EARTH OBSERVATION FOR FLOOD APPLICATIONS

PROGRESS AND PERSPECTIVES

EDITED BY

GUY J-P. SCHUMANN

ELSEVIER

Earth Observation Series

Earth Observation for Flood Applications

Page left intentionally blank

Earth Observation for Flood Applications

Progress and Perspectives

Edited by

Guy J-P. Schumann
Research and Education Department, RSS-Hydro, Dudelange, Luxembourg; School of Geographical Sciences, University of Bristol, Bristol, United Kingdom; INSTAAR, University of Colorado, Boulder, CO, United States

ELSEVIER

Elsevier
Radarweg 29, PO Box 211, 1000 AE Amsterdam, Netherlands
The Boulevard, Langford Lane, Kidlington, Oxford OX5 1GB, United Kingdom
50 Hampshire Street, 5th Floor, Cambridge, MA 02139, United States

Notices
Knowledge and best practice in this field are constantly changing. As new research and experience broaden our understanding, changes in research methods, professional practices, or medical treatment may become necessary.

Practitioners and researchers must always rely on their own experience and knowledge in evaluating and using any information, methods, compounds, or experiments described herein. In using such information or methods they should be mindful of their own safety and the safety of others, including parties for whom they have a professional responsibility.

To the fullest extent of the law, neither the Publisher nor the authors, contributors, or editors, assume any liability for any injury and/or damage to persons or property as a matter of products liability, negligence or otherwise, or from any use or operation of any methods, products, instructions, or ideas contained in the material herein.

Library of Congress Cataloging-in-Publication Data
A catalog record for this book is available from the Library of Congress

British Library Cataloguing-in-Publication Data
A catalogue record for this book is available from the British Library

ISBN: 978-0-12-819412-6

Publisher: Candice Janco
Acquisitions Editor: Louisa Munro
Editorial Project Manager: Emerald Li
Production Project Manager: Kumar Anbazhagan
Designer: Mathew Limbert

Typeset by Thomson Digital

Contents

Section 2
Estimating Flood Exposure, Damage and Risk

Section 3
Emerging Applications and Challenges

15. Emerging Techniques in Machine Learning for Processing Satellite Images of Floods

Mohammad Zare and Guy J-P. Schumann

16. Merged AMSR-E/AMSR-2 and GPM Passive Microwave Radiometry for Measuring River Floods, Runoff, and Ice Cover

G. Robert Brakenridge, Son. V. Nghiem and Zsofia Kugler

Page left intentionally blank

Contributors

Hani Ali, Willis Towers Watson, London, United Kingdom

Tyler Anderson, Cloud to Street, New York, NY, United States

Jean-Martin Bauer, World Food Programme, Congo-Brazzaville, Brazzaville, Republic of Congo

Juan Bazo, Red Cross Red Crescent Climate Centre, The Hague, The Netherlands; Universidad Tecnológica del Perú, Lima, Perú

Veronica Bell, Australian Red Cross, North Melbourne, VIC, Australia

G. Robert Brakenridge, CSDMS, INSTAAR, University of Colorado, Boulder, CO, United States

Mónica Rivas Casado, School of Water, Energy and Environment, Cranfield University, Bedfordshire, United Kingdom

Serena Ceola, Department of Civil, Chemical, Environmental and Materials Engineering (DICAM), Alma Mater Studiorum - Università di Bologna, Bologna, Italy

Marco Chini, Department of Environmental Research and Innovation, Luxembourg Institute of Science and Technology, Belvaux, Esch-sur-Alzette, Luxembourg

Walter Collischonn, Federal University of Rio Grande do Sul, Institute of Hydraulic Research (IPH), Porto Alegre, Rio Grande do Sul, Brazil

Antara Dasgupta, IITB-Monash Research Academy, Mumbai, Maharashtra, India; Department of Civil Engineering, Indian Institute of Technology Bombay, Mumbai, Maharashtra, India; Department of Civil Engineering, Monash University, Clayton, VIC, Australia

Matthias Demuzere, B-Kode VOF, Ghent, Belgium; Department of Geography, Ruhr-University Bochum, Bochum, Germany

Renato Prata de Moraes Frasson, Byrd Polar and Climate Research Center, The Ohio State University, Columbus, OH, United States

Rodrigo Cauduro Dias de Paiva, Federal University of Rio Grande do Sul, Institute of Hydraulic Research (IPH), Porto Alegre, Rio Grande do Sul, Brazil

Jéan Bienvenu Dinga, Ministère de la recherche scientifique et de l'innovation technologique (MRSIT/IRSEN), Brazzaville, Republic of Congo

Alessio Domeneghetti, Department of Civil, Chemical, Environmental and Materials Engineering (DICAM), Alma Mater Studiorum Università di Bologna, Bologna, Italy

Colin Doyle, Cloud to Street, New York, NY, United States; University of Texas, Austin, TX, United States

João Paulo Fialho Brêda, Federal University of Rio Grande do Sul, Institute of Hydraulic Research (IPH), Porto Alegre, Rio Grande do Sul, Brazil

Ayan Santos Fleischmann, Federal University of Rio Grande do Sul, Institute of Hydraulic Research (IPH), Porto Alegre, Rio Grande do Sul, Brazil

John F. Galantowicz, Atmospheric and Environmental Research, Inc., Lexington, MA, United States

Jonathon Gascoigne, Centre for Disaster Protection, London, United Kingdom

Emmalina Glinskis, Cloud to Street, New York, NY, United States

Stefania Grimaldi, Department of Civil Engineering, Monash University, Clayton, VIC, Australia

Jeff C. Ho, Cloud to Street, New York, NY, United States

Natalia Horna, Instituto Nacional de Meteorología e Hidrología Dirección de Estudios, Investigación y Desarrollo Hidrometeorológico, Quito, Ecuador

Renaud Hostache, Department of Environmental Research and Innovation, Luxembourg Institute of Science and Technology, Belvaux, Esch-sur-Alzette, Luxembourg

A.J. Kettner, CSDMS, INSTAAR, University of Colorado, Boulder, CO, United States

Abdou Khouakhi, School of Water, Energy and Environment, Cranfield University, Bedfordshire, United Kingdom

Andrew Kruczkiewicz, International Research Institute for Climate and Society, Earth Institute, Columbia University, Palisades, NY, United States; Red Cross Red Crescent Climate Centre, The Hague, The Netherlands

Zsofia Kugler, Budapest University of Technology and Economics, Budapest, Hungary

Paul Leinster, School of Water, Energy and Environment, Cranfield University, Bedfordshire, United Kingdom

Sandro Martinis, German Aerospace Center (DLR), German Remote Sensing Data Center (DFD), Weßling, Bavaria, Germany

Jesse Mason, World Food Programme, Rome, Italy

Patrick Matgen, Department of Environmental Research and Innovation, Luxembourg Institute of Science and Technology, Belvaux, Esch-sur-Alzette, Luxembourg

Paola Mazzoglio, Department of Environment, Land and Infrastructure Engineering (DIATI), Politecnico di Torino, Torino, Italy

Shanna McClain, National Aeronautics and Space Administration, Washington, DC, United States

Manoranjan Muthusamy, School of Water, Energy and Environment, Cranfield University, Bedfordshire; School of Geosciences, College of Science and Engineering, The University of Edinburgh, Edinburgh, United Kingdom

Patrick Impeti N'diaye, Agence Nationale de l'Aviation Civile (ANAC), Brazzaville, Republic of Congo

Son. V. Nghiem, Jet Propulsion Laboratory, California Institute of Technology, Pasadena, CA, United States

Fabrice Papa, University of Brasília (UnB), IRD, Institute of Geoscience, Brasília, Federal District, Brazil; University of Toulouse, *LEGOS (IRD, CNRS, CNES, UPS)*, Toulouse, France

Valentijn R.N. Pauwels, Department of Civil Engineering, Monash University, Clayton, VIC, Australia

Jeff Picton, Atmospheric and Environmental Research, Inc., Lexington, MA, United States

Michaela Rättich, German Aerospace Center (DLR), German Remote Sensing Data Center (DFD), Weßling, Bavaria, Germany

RAAJ Ramsankaran, Department of Civil Engineering, Indian Institute of Technology Bombay, Mumbai, Maharashtra, India

Mariane Moreira Ravanello, Agência Nacional de Águas e Saneamento Básico, Brasília, Brazil

Conrado Rudorff, National Center for Monitoring and Early Warning of Natural Disasters (Cemaden), São José dos Campos, São Paulo, Brazil

Guy J-P. Schumann, Research and Education Department, RSS-Hydro, Dudelange, Luxembourg; School of Geographical Sciences, University of Bristol, Bristol, United Kingdom; INSTAAR, University of Colorado, Boulder, CO, United States

Bessie Schwarz, Cloud to Street, New York, NY, United States

Nalan Senol Cabi, Willis Towers Watson, London, United Kingdom

X. Shen, Civil and Environmental Engineering, University of Connecticut, Storrs, CT; Eversource Energy Center, University of Connecticut, Storrs, CT, United States

Beth Tellman, Cloud to Street; Columbia University, New York, NY, United States

Tina Thomson, Willis Towers Watson, London, United Kingdom

Humberto Vergara, NOAA/OAR/National Severe Storms Laboratory, Norman, OK; Cooperative Institute for Mesoscale Meteorological Studies, University of Oklahoma, Norman, OK, United States

William Vu, World Food Programme, Johannesburg, South Africa

Jeffrey P. Walker, Department of Civil Engineering, Monash University, Clayton, VIC, Australia

Ruo-Qian Wang, Department of Civil and Environmental Engineering, Rutgers University, New Brunswick, NJ, United States

Olivia Warrick, Red Cross Red Crescent Climate Centre, The Hague, The Netherlands

Sam Weber, Cloud to Street, New York, NY, United States; University of California, Irvine, CA, United States

Marc Wieland, German Aerospace Center (DLR), German Remote Sensing Data Center (DFD), Weßling, Bavaria, Germany

Mohammad Zare, Research and Education Department, RSS-Hydro, Dudelange, Luxembourg; University of Luxembourg, Faculty of Science, Technology and Communication (FSTC), Institute of Civil and Environmental Engineering (INCEEN), Luxembourg, Luxembourg

Section 1

Monitoring and Modeling Flood Processes and Hazards

Page left intentionally blank

Chapter 1

Earth Observation for Flood Applications: *Progress and Perspectives*

Guy J-P. Schumann

Research and Education Department, RSS-Hydro, Dudelange, Luxembourg; Remote Sensing Solutions, Barnstable, MA, United States; School of Geographical Sciences, University of Bristol, Bristol, United Kingdom; INSTAAR, University of Colorado, Boulder, CO, United States

1 Motivation of this book

This edited book volume is a collection of chapters describing the latest progress and perspectives on the use of Earth Observation for flood applications.

It is well known that there is now a proliferation of remote sensing data, especially in the form of free imagery from Earth-observing satellites. This enables many applications in research and industry, which opens up new opportunities for science and businesses alike. With recent floods around the world becoming ever more devastating and public awareness increasing, there is a need for better science, enabling more effective solutions at a fast pace. Yet, most flood-related applications using Earth Observation still only focus on flood mapping and oftentimes with relatively little attention to scientific rigor.

The proposed book will guide the reader through the latest scientific advances in Earth Observation for a variety of flood applications and provides in-depth perspectives. It also describes new approaches to flood risk estimation and damage assessment using Earth Observation data. The book includes three parts, each containing a separate but complementary topic area under floods, which will be described by separate chapters. Each chapter will be supported by case studies and illustrative graphics.

The general topic areas dealt with in this book include flood hydrology, remote sensing of floods, and flood risk management and planning as well as flood disaster response.

The target readership for this compiled book volume includes university lecturers and teachers, and shall serve as learning and teaching material. For practitioners, the book should inspire city planning officers, flood risk management officers, and flood response officers as well as, more generally, water resource

Earth Observation for Flood Applications. http://dx.doi.org/10.1016/B978-0-12-819412-6.00001-8

managers. They can use the book as general guidance on the latest methods in Earth Observation for various flood applications.

More generally, in each chapter, readers will benefit from a clear, specific account on advances and perspective on Earth Observation for floods and will get an appreciation of the latest progress in methods and applications as well as expert perspectives as well as from illustrations of real-life application examples where methods described are demonstrated in practice.

2 Summary of content

Further sections will summarize the main messages of the chapters in this book.

2.1 Section 1: Monitoring and modeling flood processes and hazards

Monitoring and modeling flood processes and hazards using remote sensing methods and physically-based process models have been studied for almost half a century now, and, over the last 2 decades, advances have been considerable.

In terms of mapping and monitoring floods using Earth Observation (EO) data, Chapter 2 discusses progress in operational, near-real time mapping of flood duration and extent using multi-sensor satellite data, and illustrates dissemination of actionable crisis information via web-services, using Cyclone Idai in 2019 as a real-time case study. Chapter 3 highlights the value of passive microwave remote sensing (radiometry) to map flooding, and explains how competing factors reduce sensitivity to flooding or trigger false positives, and how current retrieval methods approach these challenges. The chapter also outlines recent algorithm development efforts and also discusses current downscaling capabilities as well as new approaches to improve flood mapping accuracy and usability in a variety of applications.

With regard to modeling flood processes, Chapter 4 showcases and reviews the use of remote sensing and river flood modeling in Brazil to foster our understanding of flooding regimes in large natural wetlands. The chapter shows examples suggesting the role of remote sensing in improving flood models across scales, using innovative methods, such as data assimilation and genetic algorithms. It also discusses perspectives on how current and future satellite missions, in combination with models, could help mitigate flood disasters.

In view of the upcoming Surface Water and Ocean Topography (SWOT) satellite mission, Chapter 5 outlines how satellite observations of floods have fundamentally changed the way we assess damage and coordinate first response, especially in data poor regions. In this context, the chapter gives an overview of the SWOT mission characteristics and measurement principle, describes its data products, and highlights advances in scientific methods developed to deal with this new source of data.

2.2 Section 2: Estimating flood exposure, damage, and risk

Apart from mapping and monitoring floods or improving flood modeling, satellite data are also used to estimate flood exposure, damage, and risk.

Using the 2017 floods in the Congo River basin as an example, Chapter 6 demonstrates the potential of building satellite-based flood monitoring systems to estimate flood damage and alert stakeholders. Despite non-trivial limitations of EO data, such as frequent cloud cover, inaccurate rainfall estimates, and low-resolution population data, EO-based alerting and monitoring systems could ultimately better inform local decision making, particularly in data poor regions.

Using the DFO—Flood Observatory at the University of Colorado Boulder, Chapter 7 provides an overview of satellite-based water products, developed in collaboration with various agencies and initiatives. The DFO provides EO products and services semi-operationally for assisting humanitarian aid, and, more generally, to support and encourage operational uses of remote sensing-based surface water hazard and risk information, with a vision to engage the larger hydrological community in an effort to reduce the impact of water-related natural disasters.

Taking a look at the re/insurance industry and the lack of necessary tools available with global coverage to quantify flood risk, Chapter 8 outlines how EO provides invaluable input for a number of applications, from validating and benchmarking flood solutions to estimating the exposed risks in vulnerable regions, responding to catastrophe events in real time, and increasing resilience. The chapter also discusses the ongoing challenges related to the ever-growing proliferation of EO data, products, and services, the re/insurance industry are faced with, and how relevant partnerships and community activities may present a way forward.

Further discussing the many challenges still to be solved, Chapter 9 reviews some of the most relevant EO-based open-access methods, products, and services that many research and academic institutions currently provide for detecting and near real-time monitoring of extreme hydro-meteorological events.

2.3 Section 3: Emerging applications and challenges

The third and final section of this book discusses emerging methods and technologies in the field of EO for flood applications.

Chapter 10 reviews how recent technological advances have provided an opportunity to explore the use of remote sensing within the context of flood risk management. The chapter first discusses the application of remote sensing in flood modeling, flood damage assessment, and vulnerability. It then reviews how the development of remote sensing technologies have extended the range of their application in flood management, and concludes by outlining key considerations for the use of standardized remote sensing data collection approaches to inform flood risk management activities.

Using four case studies, Chapter 11 discusses advances in the application of EO data for anticipatory action across a variety of hydro-meteorological hazards, identifying both challenges and opportunities to support anticipatory actions at scale. The chapter also provides a set of recommendations and priorities, for ensuring future growth in EO applications, is coupled with improved anticipatory humanitarian action.

With a view of providing better flood forecasting to eventually minimize damage to life and property, Chapter 12 presents a review of the current capabilities of EO data to improve flood predictions through data assimilation techniques. The challenges and opportunities of using EO data for operational flood inundation forecasting are also discussed.

In recent years, artificial intelligence (AI) has started to fundamentally change our lives, benefiting from the Big Data revolution and the Internet of Things (IoT). Flood research and applications will progress with this emerging technology, as AI is creating new flood data sources, enhancing our capability to analyze the data, even improving our accuracy of flood predictions. In this context, Chapter 13 introduces the basic concepts of AI and summarizes emerging AI applications in the field of flood hazards in terms of a number of data sources. The use of the AI-enabled Big Data is also discussed as well as opportunities and barriers of this new technology.

In a similar context, Chapter 14 discusses the many non-trivial challenges and pitfalls that new, innovative technologies, such as IoT, Big Data, cloud computing, and advanced interoperability standards in the field of EO for flood applications, bring. However, the chapter also highlights opportunities, and discusses the need for scientists, product developers, and end-users alike to manage expectations and form partnerships in order to unlock the full potential of EO for flood applications.

It is clear that decision making and planning for better management of floods requires the use of adequate models and methods. Chapter 15 reviews how, in recent years, appropriate models and algorithms, such as machine learning and deep learning have been developed and used in a number of novel research studies dealing with flood mapping. It outlines the basic concepts of machine learning methods but also discusses important challenges that remain and need to be solved if machine learning methods are to be valuable for decision-making processes related to flood management.

Chapter 16, the final chapter of this book, describes how new scientific methods in satellite microwave radiometry are used to monitor river flow changes with considerable accuracy at an appropriate temporal sampling interval for characterizing floods daily, regardless of cloud cover, over multiple decades and continuing into the future. Of course, such considerable progress demonstrates that EO has a very promising future in helping to address important flood risk issues.

Chapter 2

An Automatic System for Near-Real Time Flood Extent and Duration Mapping Based on Multi-Sensor Satellite Data

Sandro Martinis, Marc Wieland and Michaela Rättich
German Aerospace Center (DLR), German Remote Sensing Data Center (DFD), Weßling, Bavaria, Germany

1 Introduction

Floods are the most frequent and costliest natural disasters worldwide. According to figures from the United Nations Office for Disaster Risk Reduction (UNISDR), floods accounted for 43% of all 7255 disaster events recorded globally between 1998 and 2017 (CRED and UNISDR, 2018).

Numerous scientific studies as well as the work of various value adders in the frame of international emergency response mechanisms such as the Copernicus Emergency Management Service of the European Commission (Copernicus Emergency Management Service, 2019), the International Charter "Space and Major Disaster" (International Charter, 2019), or Sentinel Asia (Sentinel Asia, 2019) demonstrated the benefit of satellite-based remote sensing during rapid mapping activities in flood disaster situations. Earth Observation (EO) data have proven to provide essential large scale and detailed information on disaster situations to support adequate relief activities in near real-time (NRT).

However, single satellite missions are in general not suitable to fulfill the requirements of end users in the frame of emergency response with an eye on revisit time and coverage. The combination and the coordinated tasking of data of different satellite missions are necessary to receive a timely and complete overview about a disaster situation and to be able to monitor the evolution of inundations over time. For example, the International Charter "Space and Major Disaster," which is an association of space agencies and satellite operators, provides a unified system of currently 17 members for the coordinated rapid acquisition and delivery of satellite data in case of a disaster or crisis situation based on more than 50 operational satellite missions (Martinis et al., 2017).

Earth Observation for Flood Applications. http://dx.doi.org/10.1016/B978-0-12-819412-6.00002-X

In addition, as response time is a key element, disaster management especially benefits from the automation of algorithms to reduce time-consuming manual interactions of imaging experts in extracting crisis information from EO data. This is particularly important for global applications that use systematically acquiring satellite missions, which generate a massive daily flow of data, such as Sentinel-1 and Sentinel-2, operated by the European Space Agency (ESA) in the frame of the European Union's Copernicus Programme.

Synthetic aperture radar (SAR) sensors provide a global, continuous supply of all-weather, day-and-night image data of the Earth's surface and are therefore well suited for flood mapping and monitoring applications. Several scientific studies presented automatic approaches for SAR-based flood detection (Li et al., 2018, 2019); Amitrano et al., 2018; Tsyganskaya et al., 2018; Giustarini et al., 2017; Schlaffer et al., 2015; Pulvirenti et al., 2011; Schumann et al., 2010; Martinis et al., 2009) as well as fully automatic flood processing chains (Martinis et al., 2013, 2015b, 2018; Twele et al., 2016; Westerhoff et al., 2013). As their names imply, optical sensors make use of radiation from the optical part (i.e., visible and infrared) of the electromagnetic spectrum. As these sensors rely on solar reflectance from the Earth's surface, they are only useful for cloud-free conditions, which is a disadvantage in the context of mapping and monitoring flood events. However, during clear-sky conditions, these data are very helpful to increase the effective revisit period for flood monitoring.

Within this study, an automatic multi-sensor satellite system for NRT time flood extent and duration mapping based on multi-sensor satellite data is presented, developed by the German Aerospace Center (DLR). The system is based on four automatic processing chains for the derivation of the flood extent from Sentinel-1 and TerraSAR-X radar as well as from optical Sentinel-2 and Landsat satellite data. Due to the consistency in systematic data acquisition of Sentinel-1, the Sentinel-1 Flood Service (Twele et al., 2016; Martinis et al., 2018) has the key role in systematic flood monitoring. The two processing chains based on Landsat-8 and Sentinel-2 (Wieland and Martinis, 2019) complete the systematic monitoring capability of the system. In the frame of flood situations, a TerraSAR-X Flood Service (Martinis et al., 2013, 2015b) can be triggered on demand over a disaster affected area to increase the effective revisit period of the system or to extract the flood extent in higher detail than using the systematically acquiring sensors of up to a spatial resolution of 1 m.

Further, different flood duration layers, that is, a backward flood duration (BFD) and total flood duration (TFD) mask, are generated by using the crisis information derived from the multi-sensor system to indicate the temporal stability of an inundation over time.

The multi-sensor flood monitoring system is demonstrated based on a severe flood situation in Mozambique caused by the landfall of cyclone Idai in March 2019.

2 Satellite-based multi-sensor flood mapping system

The multi-sensor flood mapping system consists of four fully-automatic processing chains which derive the flood extent from Sentinel-1 and TerraSAR-X radar as well as from optical Landsat and Sentinel-2 satellite data in NRT. Data from other satellite missions could be integrated into the system. An overview of the system's workflow is visualized in Fig. 2.1; general characteristics of the processing chains are listed in Table 2.1. All processing chains contain the following generic steps: automatic data ingestion, preprocessing of the EO data, computation and adaption of global auxiliary data (digital elevation models, topographic slope information, and topographic indices, as well as reference water masks), classification of the flood extent, and dissemination of the crisis information, for example, via a web-client.

Further, additional flood duration layers, that is, the BFD and TFD, which show the stability of an inundation for each image element in days, is generated in NRT together with a flood duration quality (FDQ) layer by combining the flood extent products derived from the different satellite sources.

As the methodologies of the respective thematic processors need to be globally applicable to account for flood situations all over the world, delivering reliable flood extent products independent of prevailing environmental conditions and system parameters of the used satellite system (e.g., beam mode, incident angle, and spectral channels), a major focus during the implementation of the algorithms was set on reaching a high level of robustness and transferability.

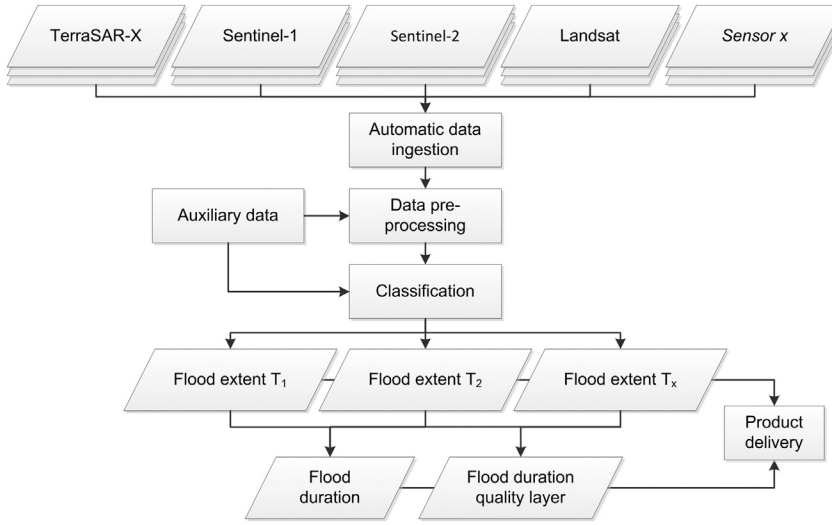

FIGURE 2.1 General workflow of DLR's satellite-based system for flood extent and duration mapping.

TABLE 2.1 General characteristics of the flood processing chains.

Processing chain	Satellite	Revisit time [d]	Resolution of products [m]	Data acquisition	Data source
TerraSAR-X Flood Service (TFS)	TerraSAR-X, TanDEM-X	11	0.24–40	On-demand	TerraSAR-X delivery server
Sentinel-1 Flood Service (S-1FS)	Sentinel-1A, Sentinel-1B	6	20	Systematic	Copernicus Open Access Hub, Direct Downlink @ DLR Neustrelitz (Europe)
Sentinel-2 Flood Service (S-2FS)	Sentinel-2A, Sentinel-2B	5	10	Systematic	Copernicus Open Access Hub
Landsat Flood Service (LFS)	Landsat-8	16	30	Systematic	USGS

The respective NRT flood processing chains are explained in detail in Section 2.1, the derivation of the combined flood duration products in Section 2.2.

2.1 NRT Flood extent mapping

2.1.1 Auxiliary datasets

Several ancillary datasets are used within the four automatic SAR- and optical data-based flood processing chains in different steps. Digital Elevation Models (DEMs) are required for terrain-correction of SAR-data, for the radiometric calibration of SAR data to sigma naught (dB), and for the calculation of terrain characteristics for post-classification improvement of the flood extent products (e.g., layover areas, slope, height above nearest drainage).

A global reference water mask is required for separating the detected open surface water extent into areas of reference water (i.e., normal water levels) and inundation areas. In order to achieve global coverage, the reference water mask is a combination of different data sources:

- Shuttle Radar Topography Mission (SRTM) Water Body Data (SWBD), which covers the Earth's surface between 56 degrees southern latitude and 60 degrees northern latitude at a spatial resolution of approximately 30 m at the equator.
- The MODIS 250 m land-water mask (MOD44W), which is used for all northern and southern latitudes and not covered by SWBD data (Carroll et al., 2009).

- For some countries, seasonal reference water masks based on Sentinel-2 and Landsat-8 time-series data have been computed offline based on DLR's Sentinel-2 and Landsat-8 Flood Services. If available, these masks are used instead of the SWBD and MODIS reference water masks as these are more up-to-date and consider effects related to seasonality of water occurrence.

All water masks are combined to a consistent global dataset, which is available as one by one degree lat/lon (WGS84) projected GeoTIFF-tiles.

The ASTER Global Digital Elevation Model Version 3 (GDEM V3) with a pixel size of 1 arc second (METI and NASA, 2019) is used for a refinement of the TerraSAR-X-based flood masks. The same terrain information is used for the optional computation of a Geocoded Incidence Angle Mask (GIM) in the preprocessing step of the TerraSAR-X Flood Service, while the SRTM 3 arc second data is used for the range Doppler terrain correction of Sentinel-1 data and the radiometric calibration to sigma naught (dB). Further, the height above nearest drainage (HAND) terrain descriptor (Rennó et al., 2008), which expresses the height difference between a DEM cell and the closest cell of the drainage network along the actual flow path, is used. As such, the index can be very well used to define flood-prone regions and consequently areas with a low probability of flood occurrence. Based on this index, areas above an empirically-derived threshold are excluded from classification of the flood extent, thereby reducing potential misclassifications in non-flood-prone regions. This helps to reduce water-lookalike areas in dependence of the hydrologic–topographic setting. The HAND index has been calculated near-globally (Twele et al., 2016) based on elevation and drainage direction information provided by the Hydrosheds mapping product (Lehner et al., 2008). Based on this index, a binary exclusion mask (termed "HAND-EM" in the following) has been calculated by Twele et al. (2016) to differentiate between flood- and non-flood-prone areas. Both binary classes are determined using an appropriate threshold value. Choosing the threshold value too high may lead to misclassifications (i.e., the inclusion of flood-lookalikes in areas much higher than the actual flood surface and drainage network) while a threshold value set too low would eliminate parts of the real flood surface. The choice of an appropriate threshold is thus critical, but could be derived through a series of empirical tests with more than 400 Sentinel-1 and TerraSAR-X scenes of different hydrological and topographical settings (Chow et al., 2016). Due to the global application scope of the flood processing chains, a rather conservative threshold of ≥ 15 m was selected to derive non-flood-prone areas.

2.1.2 TerraSAR-X Flood Service

The TerraSAR-X Flood Service (Martinis et al., 2013, 2015b) is based on data of the TerraSAR-X mission, which consist of the two satellites TerraSAR-X and TanDEM-X, operated since 2007 and 2010, respectively, in the frame of a public-private partnership (PPP) between DLR and Airbus Defense and Space.

The primary payload of TerraSAR-X and TanDEM-X is an X-band SAR sensor with a range of different acquisition modes of operation, allowing to acquire data with different swath widths, resolutions, and polarizations.

As both satellites are on-demand satellite systems, which do not follow a systematic predefined observation plan, each acquisition has to be tasked by programming the sensor over an area affected by inundations. This allows to be very flexible in adapting the acquisition parameters to the type and extent of the disaster and, therefore, to reach the highest value to support crisis management activities. In most flood situations, data are acquired in HH polarization which usually leads to the best contrast between water bodies and non-water surfaces (Martinis et al., 2015a). As also the highest contrast ratio between water and non-water surfaces appears at higher system frequencies, TerraSAR-X offers the best preconditions for a successful derivation of the flood extent.

The TerraSAR-X Flood Service (see workflow in Fig. 2.2) has been designed to process enhanced ellipsoid corrected (EEC) and ground ellipsoid corrected (GEC) TerraSAR-X amplitude imagery of all acquisition modes (Starring Spotlight, High Resolution SpotLight, SpotLight, Stripmap, ScanSAR, Wide ScanSAR), which are commonly delivered via ftp server.

In order to ensure immediate processing, the data download is triggered automatically through a Python script once the satellite scenes are available. When the download to the local file system has been completed, the data are extracted and the corresponding file structure is browsed for all relevant files, that is, the SAR data, the metadata.xml file, and the GIM. The GIM can be ordered as an optional auxiliary layer together with the EEC product and provides information on the local incidence angle for each pixel of the geocoded SAR scene and on the presence of layover and shadow regions (Infoterra, 2008). In case no GIM has been ordered jointly with the TerraSAR-X data, this layer is computed automatically during the subsequent preprocessing steps based on the ASTER GDEM. The downloaded TerraSAR-X data are reprojected to geographical coordinates (lat/lon, WGS84). This target system is also used for all global auxiliary data layer which are used in this processing chain: DEM, reference water masks, and HAND-EM.

The preprocessing of the TerraSAR-X amplitude data includes a radiometric calibration of the data to normalized radar cross-section (NRCS) σ_0 [dB] in order to take account of incidence angle-related variations of the backscatter in satellite range direction and to reduce topographic effects. The radiometrically calibrated data is rescaled to an integer value range of [0,400] in order to derive positive values during all subsequent processing steps. In order to reduce the typical speckle effect of SAR imagery, a median filter of kernel size 3×3 is finally applied on the rescaled pixels.

For the unsupervised initialization of the flood classification, a parametric tile-based thresholding procedure is applied (Martinis et al., 2009, 2015b) by labeling all pixels with a backscatter value lower than a threshold to the class "water." Thresholding algorithms only extract adequate threshold values if the scene

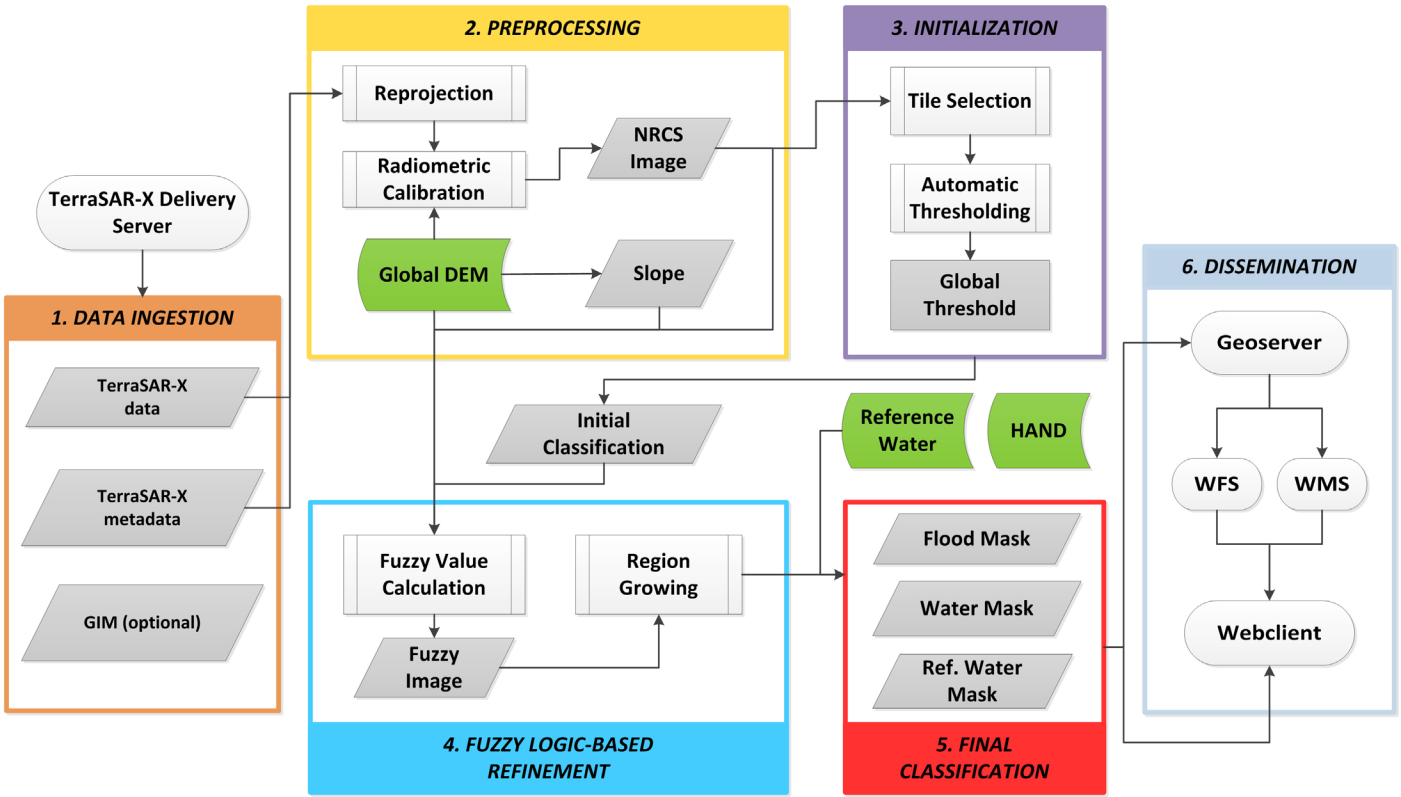

FIGURE 2.2 Workflow of the TerraSAR-X flood processing chain.

histogram is not uni-modal. Therefore, the capability of approaches to detect an adequate threshold in the histogram of the data depends on the a priori probability of the classes. If, for example, the spatial extent of water bodies in large SAR scenes is low, the class-distributions cannot be modeled reliably. Within this approach, the threshold value is automatically computed using a hierarchical tile-based thresholding procedure proposed by Martinis et al. (2009, 2015b), which solves the flood detection problem in even large-size radar data with small a priori class probabilities. The thresholding approach consists of the following processing steps: image tiling, tile selection, and sub-histogram based thresholding of a small number of tiles of the entire SAR image.

In the first step, a bi-level quadtree structure is generated based on the SAR imagery. The data are divided into N quadratic non-overlapping sub-scenes of defined size c^2 on level S^+. Each parent tile is represented by four quadratic child objects of size $(c/2)^2$ on level S^-. Variable c is empirically defined to 400 pixels. A limited number of tiles are selected out of N according to the probability of the tiles to contain a bi-modal mixture distribution of the classes "water" and "non-water." This selection step is based on statistical hierarchical relations between parent and child objects in a bi-level quadtree representation of the data. Local threshold values are computed based on the Kittler and Illingworth minimum error thresholding approach (Kittler and Illingworth, 1986) using a cost function, which is based on statistical parameterization of the sub-histograms of all selected subsets as bi-modal Gaussian mixture distributions. Finally, one global threshold τ_g is derived by computing the arithmetic mean of the individual local thresholds. This is used to initially distinct open water surfaces and non-water areas in the SAR data. The standard deviation σ_τ of the local thresholds can be used as an indicator for a successful thresholding. If σ_τ exceeds an empirically derived critical threshold τ_σ (e.g., 5.0 dB) a (sub-) histogram merging strategy is applied. In this case, τ_g is directly computed from a merged histogram which is a combination of the distributions of the selected tiles.

The initial classification result is optimized using a fuzzy logic-based post-classification approach by combining different information sources (Martinis et al., 2015b). For this purpose, a fuzzy set of four elements is built consisting of the backscatter (σ_0), digital elevation (h) and slope (s) information as well as the extent (a) of the initially extracted water objects. The elements of the fuzzy set are defined by standard S and Z membership functions (Pal and Rosenfeld, 1988), which express the degree of an element's membership m_f to the class water within the interval [0, 1], where 0 denotes minimum and 1 indicates maximum class membership. The membership degree is defined by the fuzzy thresholds x_1 and x_2 and the position of the crossover point x_c (i.e., the half width of the fuzzy curve).

The fuzzy threshold values for each element are either determined based on statistical computations or are set empirically. False positives are commonly caused by objects with a low surface roughness and therefore low backscatter similar to calm water surfaces, such as streets and bare ground or radar shadow

behind vertical objects. Elevation information is integrated into the fuzzy-logic based post-classification step to improve the classification accuracy through simple hydrological assumptions, that is, by reducing the membership degree of an image element in dependence of the height above the main water area of the initially derived water areas by applying the standard *Z* membership function.

The fuzzy thresholds of the elevation information are defined as:

$$x_{1[h]} = \mu_{h(water)} \tag{2.1}$$

and

$$x_{2[h]} = \mu_{h(water)} + f_\sigma * \sigma_{h(water)}, \tag{2.2}$$

where $\mu_{h(water)}$ and $\sigma_{h(water)}$ are the mean and standard deviation of the elevation of all initially derived water pixels. Using this fuzzy set, the number of water look-alikes in areas significantly higher in elevation than the mean elevation of the initially derived water objects is reduced. The factor f_σ is defined as:

$$f_\sigma = \sigma_{h(water)} + 3.5. \tag{2.3}$$

This function was integrated to reduce the influence of the elevation in areas of low topography. The minimum value of f_σ is defined by 0.5.

The standard *Z* function is used for describing the membership degree to open water areas according to the SAR backscatter. Full membership is assigned to image elements with a backscatter lower than the fuzzy threshold

$$x_{1[\sigma_0]} = \mu_{\sigma_0(\tau_g)}, \tag{2.4}$$

where $\mu_{\sigma_0(\tau_g)}$ is the mean backscatter of the initial flood classification result by applying τ_g to *Y*. No membership degree [0] is assigned to pixels greater than

$$x_{2[\sigma_0]} = \tau_g. \tag{2.5}$$

Slope information derived from the ASTER GDEM is integrated as a third element in the fuzzy system by applying the *Z* membership function with parameters $x_{1[sl]} = 0$ degrees, $x_{2[sl]} = 15$ degrees to reduce water look alikes in steep terrain.

The *S* membership function is applied on the extent α of the water bodies to reduce the number of dispersed small areas of low backscatter. No membership degree is further assigned to regions with a size lower than $x_{1[a]} = 250\ \text{m}^2$, maximum degree to areas with an extent greater than $x_{2[a]} = 1{,}000\ \text{m}^2$.

The average of the membership degrees is computed for each pixel in order to combine all fuzzy elements into one composite fuzzy set. Subsequently, the flood layer is calculated based on a threshold defuzzification step, which transforms each image element with a membership degree > 0.6 into a crisp value, that is, a discrete semantic class.

Region growing is performed in order to integrate pixel at the boundary of flood surfaces and non-flooded regions as well as to increase the spatial homogeneity of the detected flood plain. The initially detected water objects of the defuzzified classification result are used as seeds for dilating the water surface. The water regions are iteratively enlarged until a tolerance criterion is reached. Only image elements located in the neighborhood of the flooding are scanned to avoid the detection of water look-alikes distant from initially labeled water areas. The region growing tolerance criterion is defined by a relaxed fuzzy threshold of >0.45. Therefore, the region growing step is controlled by both the SAR backscatter and auxiliary data (slope, elevation, and extent of water bodies).

The GIM is integrated into the processing chain to eliminate open water look-alikes in areas affected by radar shadow and layover. Further, HAND-EM is applied to mask out potential misclassifications in regions with a HAND-index of ≥ 15 m above the drainage network. Finally, in order to filter out isolated flood objects, a minimum mapping unit (MMU) of 30 pixels is applied. Small land objects which are fully enclosed by water are reclassified to water based on the same MMU value. The classification result is subsequently matched with the reference water mask described in Section 2.1.1 to separate normal water bodies and flooded areas.

For dissemination of the results, the flood mask, the water mask and the reference water mask, and satellite footprints are stored in a database and published via a web-based user interface. The process chain is based on a framework of Web Processing Services standard-compliant to the Open Geospatial Consortium (OGC).

2.1.3 Sentinel-1 Flood Service

The Sentinel-1 Flood Service (Twele et al., 2016; Martinis et al., 2018) is based on Ground Range Detected (GRD) data of the Sentinel-1 mission, operated by ESA in the frame of the European Union's Copernicus Programme. It consists of two systematically acquiring satellite sensors (Sentinel-1A and Sentinel-1B) with a repeat cycle of 6 days for the constellation. The satellites are equipped with a C-Band SAR payload (5.405 GHz). Over land masses, the Interferometric Wide Swath (IW) mode is used by default, acquiring dual-polarized radar data with VV or VV/VH polarization. In contrast to the on-demand satellite mission TerraSAR-X, the Sentinel-1 mission is based on a predefined conflict-free observation scenario making optimum use of the SAR duty cycle with respect to the technical constraints of the system (Torres et al., 2012). This is a major advantage for the implementation of fully automated processing chains as the time consuming step of tasking EO data can be omitted, which increases the possibility that the peak of the flood is captured. This enhances the value of the derived crisis information for flood emergency management activities. However, in comparison to X-band SAR data like TerraSAR-X, the system parameters of Sentinel-1 are more challenging for extracting water surfaces: As the contrast between non-water and water areas decreases with increasing wavelength of the

SAR system (Drake and Shuchman, 1974), lower classification accuracies are usually achieved for C-band Sentinel-1 data. While the on-demand programming capability of TerraSAR-X permits the acquisition of HH-polarized data, which are generally considered as superior to other polarizations in the context of flood mapping (Martinis et al., 2015a), the Sentinel-1 processing chain is dependent on systematically acquired VV/VH-polarized IW-mode data. Further, most acquisition modes of X-band sensors have a higher spatial resolution than the Sentinel-1 IW mode (resolution ~20 m). This enables to extract the crisis information on the flood extent with greater detail.

The automatic Sentinel-1 processing chain is triggered through a Python-script, which routinely polls the Copernicus Open Access Hub for new acquisitions matching user-defined criteria. Using these criteria, for example, the time frame, geographical location, or orbit of suitable Sentinel-1 acquisitions can be specified. Once corresponding data are found, they are downloaded to the local file system and the thematic processor is executed. From experience, data are usually available on the Open Access Hub ~3–4 hours after data downlink. Shorter data latencies (time delays) can be achieved by receiving and preprocessing Sentinel-1 data at local ground stations. To increase the delivery times of the flood extent products using the S-1FS, this processing chain has been also implemented at the satellite ground station at DLR Neustrelitz, which allows the automatic generation of flood maps within ~1 hour after data acquisition based on directly downlinked Sentinel-1 data over an acquisition cone covering most parts of Europe. This allows reducing the time delay between sensing and product delivery significantly.

After unzipping the downloaded data, the folder structure is searched for files relevant for the further processing, namely Sentinel-1 data in GeoTIFF-format and Extensible Markup Language (XML) metadata used for radiometric calibration.

During the preprocessing step, a Range-Doppler terrain correction of Sentinel-1 data and radiometric calibration to sigma naught (dB) are performed using the Graph Processing Tool (GPT) of ESA's Sentinel Application Platform (SNAP). The GPT allows a consecutive execution of all individual preprocessing modules within a fully automated processing chain. Geometric distortions due to terrain effects are not considered in GRD imagery provided by ESA. Therefore, the GRD data have to be terrain corrected to improve the geolocation accuracy of the data. SRTM DEM tiles corresponding to a given Sentinel-1 scene are automatically downloaded by SNAP. Based on the SRTM DEM, the Sentinel-1 GRD imagery is terrain corrected and transformed to geographical coordinates (lat/lon, WGS84). After data preprocessing using SNAP, the calibrated data are filtered to reduce SAR inherent speckle noise and clipped in range and azimuth in order to remove image border noise. The result of the preprocessing is a reprojected, radiometrically calibrated, and rescaled NRCS image.

The extraction of the flood extent in Sentinel-1 data is based on the same automatic hierarchical tile-based thresholding and fuzzy-logic based

post-classification approach as applied for flood mapping in TerraSAR-X imagery described in Section 2.1.2. In addition, Sentinel-1 preevent time series data are used to compute a Sand Exclusion Layer (SEL), which is used to reduce overestimations of the flood extent related to permanent sand surfaces with a similar low backscatter as water bodies (Martinis et al., 2018). The SEL is subtracted from an automatically computed flood mask to eliminate areas that frequently have a low backscatter over time. This mainly improves the reliability of flood classification in arid regions. Due to computational reasons, the SEL is processed offline in order to be prepared in case of flood occurrence and, therefore, to be able to improve the NRT applicability of the Sentinel-1 flood service during flood rapid mapping activities.

The whole processing chain from the ingestion of Sentinel-1 data to the final classification result is implemented with an OGC compliant WPS framework (PyWPS). The processing results are stored as GeoTIFF raster files and are registered within a PostgreSQL/PostGIS database. Every output layer ("Water," "Flood," and "Reference Water") is deployed via a Geoserver as a single web mapping service (WMS) layer set and visualized within a dedicated web client (Fig. 2.3).

2.1.4 Sentinel-2/Landsat-8 Flood Service

The Sentinel-2/Landsat-8 Flood Service (Wieland and Martinis, 2019; Wieland et al., 2019) is based on multi-spectral data of the Sentinel-2 and Landsat-8 satellites. The Sentinel-2 mission is operated by ESA in the frame of the European Union's Copernicus Programme and consists of two systematically acquiring satellites (Sentinel-2A and Sentinel-2B) with a repeat cycle of 5 days for the constellation. The Landsat-8 mission is operated by NASA and USGS and consists of a single satellite with a repeat cycle of 16 days. Both satellite missions share a subset of spectral bands that are comparable in terms of their spectral bandwidth and spatial resolution. These are the Blue, Green, Red, Near Infrared (NIR), and Shortwave Infrared 1 and 2 (SWIR1 and SWIR2) bands. Therefore, these bands are used to create a generic flood service that handles both satellite sensors at once.

Fig. 2.4 shows an overview of the Sentinel-2/Landsat-8 flood service and its processing modules. Metadata and images are automatically harvested from the ESA Copernicus Open Access Hub and the USGS Earth Explorer and ingested into the flood service for preparation and analysis. The raw image bands are stacked and converted from Digital Numbers (DN) to Top of Atmosphere (TOA) reflectance. Further preparation steps, such as resampling, subsetting, pan-sharpening, or co-registration, are added depending on the particular task and study area at hand. The preprocessed image is fed into a convolutional neural network (CNN) for water segmentation that has been trained, tested, and validated on a global reference dataset of Landsat and Sentinel-2 data with six spectral bands. Clouds and cloud shadows are specifically handled by the network to remove potential biases from downstream analysis.

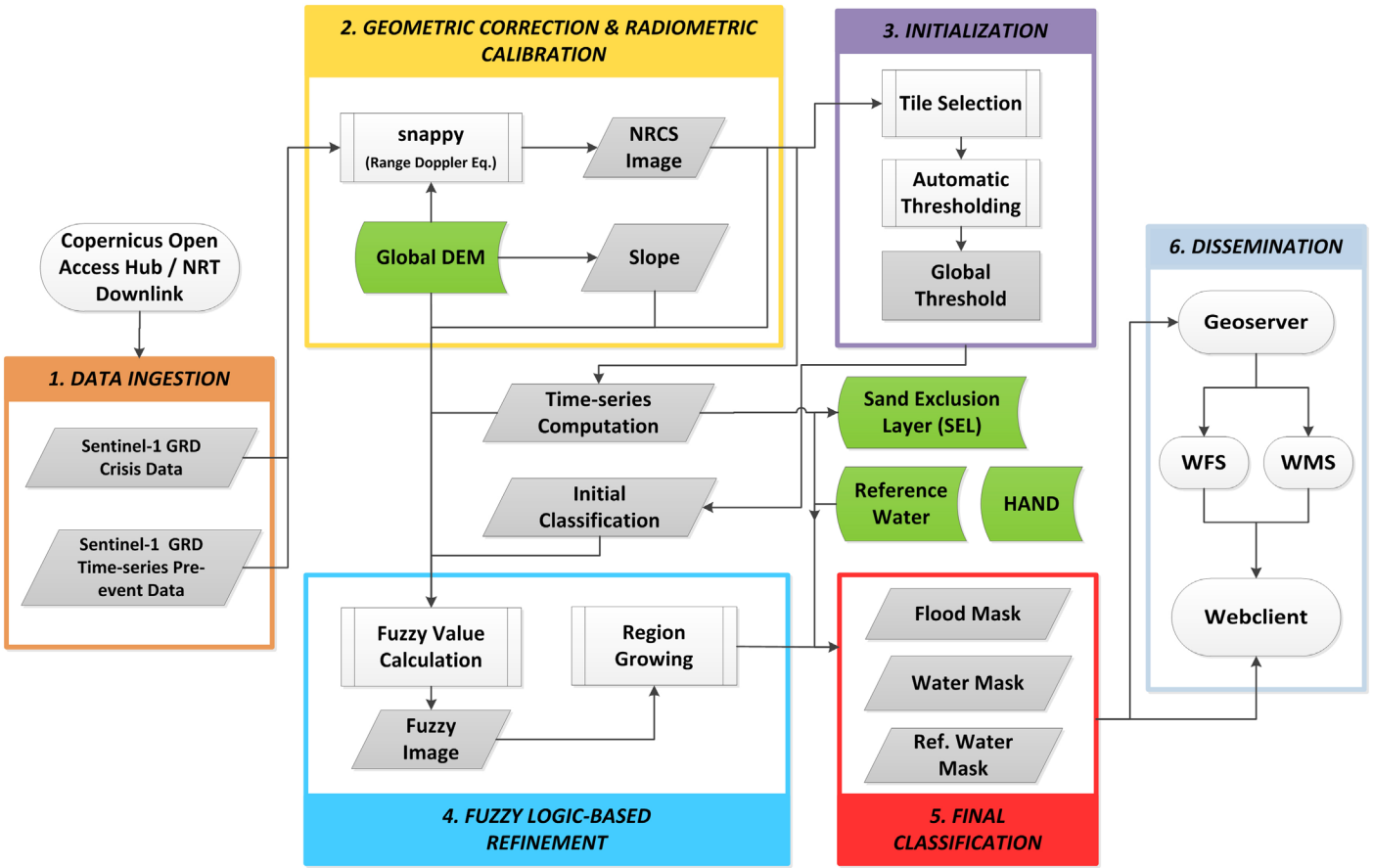

FIGURE 2.3 **Workflow of the Sentinel-1 flood processing chain.** *(Modified from Martinis et al., 2018)*

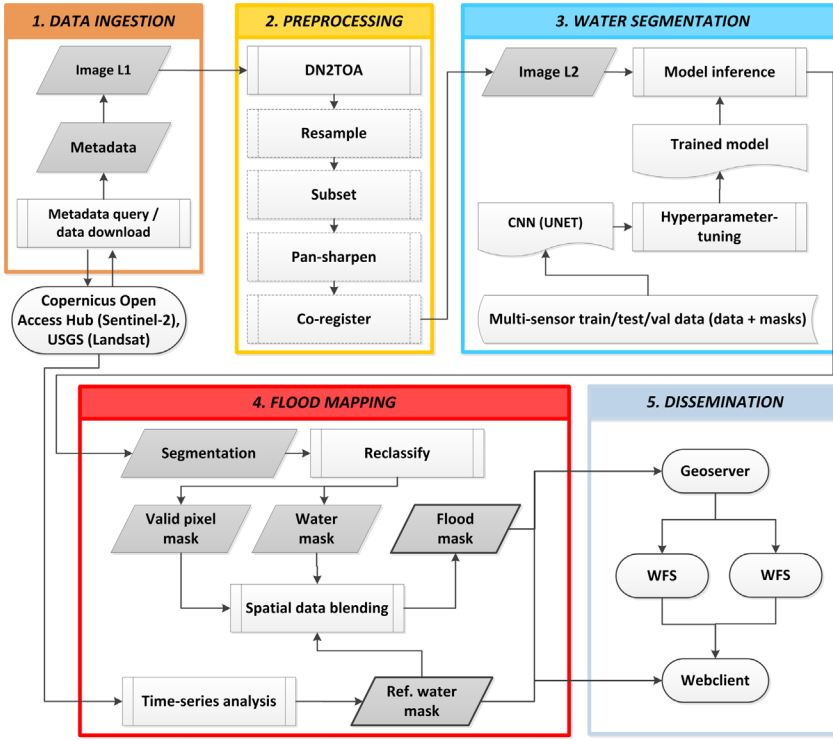

FIGURE 2.4 Workflow of the Sentinel-2/Landsat flood processing chain.

The reference dataset is globally sampled to be representative for a variety of climatic, atmospheric, and land-cover conditions (Fig. 2.5). For each sample location, Landsat and Sentinel-2 images are acquired and manually delineated to create corresponding thematic masks. Masks cover classes "Water," "Land," "Snow/Ice," "Cloud," and "Cloud shadow". Images are preprocessed and together with the corresponding thematic masks are split into non-overlapping tiles with 256 × 256 pixels size, shuffled and distributed into training (60%), validation (20%), and testing (20%) parts. The training dataset is augmented with random contrast, brightness, and rotation. The final dataset covers 94 locations, 136 images from Landsat and Sentinel-2 satellites, and is split into 1075 tiles for training (5375 tiles with augmentation) and 358 tiles for validation and testing, respectively.

The CNN is based on the U-Net architecture, which consists of encoder and decoder parts for semantic segmentation (Ronneberger et al., 2015). The encoder takes input as a multi-band image of size 256 × 256 pixels and feeds it through five convolutional blocks. The basic convolutional block consists of two 3 × 3 convolutions with Rectified Linear Unit (ReLU) activation function, batch normalization, and 2 × 2 max pooling. In the decoder part, the feature

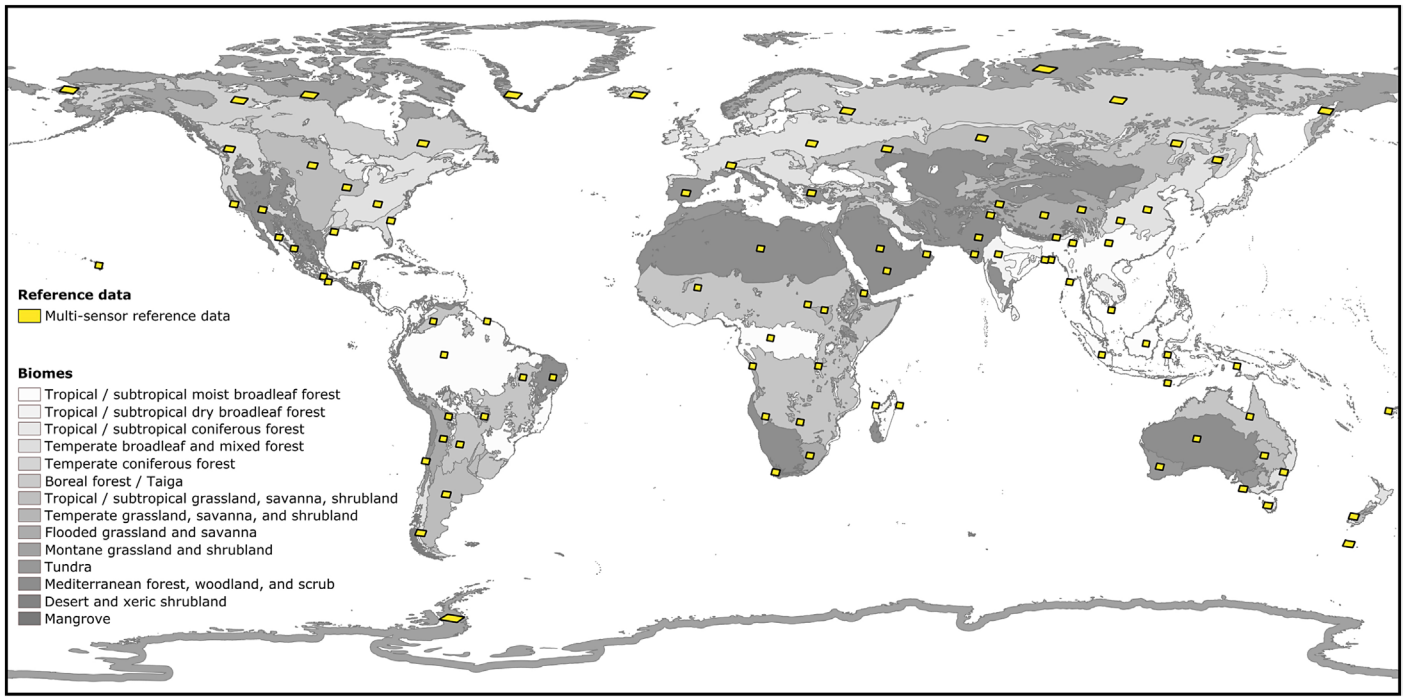

FIGURE 2.5 Sample locations of the reference dataset used for training, testing, and validation of the water segmentation method, superimposed on a global biome map that has been used as strata for sampling.

map is up-sampled by a 2×2 transpose convolution followed by a concatenation with the correspondingly cropped feature map from the decoder and two 3×3 convolutions with ReLU activation and batch normalization. At the final layer, a 1×1 convolution with softmax activation function is used to map each feature vector to the number of classes. The categorical output is computed by maximizing the predicted probability vector. We use weighted categorical cross-entropy loss and optimize the weights during training using the adaptive moment estimation algorithm (Kingma and Ba, 2015).

By reclassification of the segmentation result, we derive binary masks for water and valid pixels. A binary reference water mask is derived from time-series analysis of archive imagery and used to further distinguish permanent water bodies from temporarily flooded water. Hence, the final outputs of the flood mapping module are binary flood, valid pixel, and reference water masks.

Similar to the other flood services, the results are stored as GeoTIFF raster files and are registered within a PostgreSQL/PostGIS database. Outputs are deployed via a Geoserver as WMS and visualized within a dedicated web client.

2.2 Flood duration mapping

In order to assess the damage related to flood events, the estimation of the flood duration is a very crucial parameter as it can influence crop yield, loss of income, buildings, and infrastructure. Furthermore, it gives an indication about the temporal stability and the evolution of an inundation event and can be used to support disaster management activities in addition to single-date flood extent products by focusing relief activities to the most severely affected areas.

In order to estimate the flood duration on a regular basis and in NRT in case of disaster situations, a fully automated approach is developed (Rättich et al., 2020). Fig. 2.6 shows the workflow of the methodology.

As input automatically derived binary flood masks based on multi-sensorial EO data, the area of interest and user defined processing parameter are needed. The processor allows the user to choose the desired resolution of the output products. Furthermore, the user is able to choose the time period to be analyzed.

The first step in the preprocessing procedure is to reproject all flood masks to a uniform coordinate reference system (WGS84). The masks are clipped to the area of interest and merged if there are several observations from one satellite sensor at the same day. The resampling to a common spatial resolution is done as default according to the flood mask with the highest spatial resolution or is based on an optionally user-defined parameter.

The preprocessed flood masks serve as input for the subsequent processing where a pixel-based examination of the time series is carried out in order to the detect the start and end date of all flood periods as well as all observation gaps. Based on this, the flood duration is computed using parallel processing to reduce the processing time. Two different kinds of flood duration products are generated: the Total Flood Duration (TFD) and the Backward Flood Duration

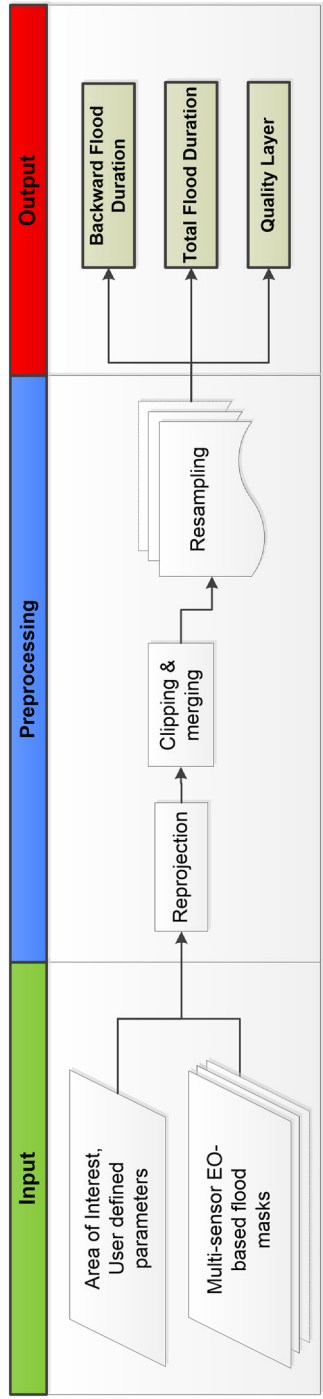

FIGURE 2.6 Workflow of flood duration estimation based on multi-sensor satellite data.

(BFD). Further a quality layer is produced in order to indicate the uncertainty related to both flood duration products. The calculation of these products is explained in more detail in the following sections.

2.2.1 Backward Flood Duration

The BFD is computed for each pixel backwards in time from the latest satellite acquisition until the beginning of the inundation event. It is an indicator for the duration of an ongoing flood event in days and should be delivered to the user in NRT in order to provide an indication of the persistency of the flooding. Fig. 2.7 shows a schematic illustration of the computation of the BFD for one single pixel i over a time period of 20 days (D_1–D_{20}). Gray pixels mark dates where no flooding is detected (DN = 0) within the EO data while blue pixel are related to dates where flooding is derived (DN = 1). White pixels are days without EO acquisitions. As soon as the latest EO acquisition is available on D_{20} the respective automatic flood processing chain is triggered in order to derive the most recent flood extent mask. The flood extent layer of D_{20} is then combined with previously derived flood extent masks in reverse order. For each pixel, the algorithm checks stepwise backwards in time if flooding is available (on D_{18}, D_{17}, D_{14}, and D_{12}) and stops when it is not covered by flooding any more on D_{11}. Finally, the duration for each pixel is computed by subtracting the latest acquisition date (D_x) from the acquisition date that indicates the beginning of the flooding:

$$BFD_i = D_{x,\ i} - D_{y,\ i}. \tag{2.6}$$

This layer is updated as soon as more up-to-date EO data are available in the time after D_{20}.

2.2.2 Total Flood Duration

TFD is computed for each pixel for a defined time period and might in contrast to the BDF cover more than one flood event. The duration of n ($n \geq 1$) flood events f is summed in order to calculate the duration of flood coverage over time in days:

$$TFD_i = \sum_{f=1}^{n} D_{d,\ i} - D_{c,\ i}, \tag{2.7}$$

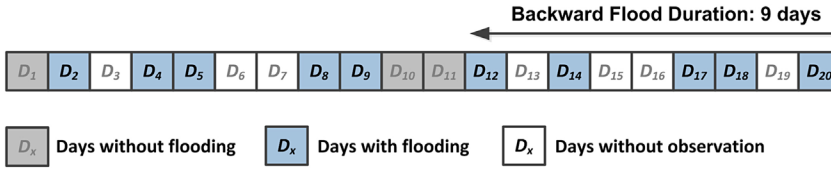

FIGURE 2.7 Schematic illustration for computing the backward flood duration of an ongoing flood situation.

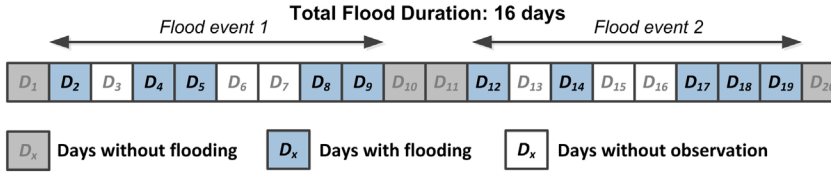

FIGURE 2.8 Schematic illustration for computing the total flood duration.

where $D_{c,i}$ is the first day with flooding (D_2 in flood event 1 and D_{12} in flood event 2 in Fig. 2.8) and $D_{d,i}$ is the last day with flooding (D_{12} in flood event 2 and D_{19} in flood event 2 in Fig. 2.8) within each single flood event.

2.2.3 Flood duration quality layer

The quality of the flood duration layers indirectly depends on the one hand on the quality of the single flood masks. The quality of the resulting open flood mask automatically derived by the respective flood processing chains has been validated within previous studies of the authors: flood masks derived by the TFS have been validated, for example, by Martinis et al. (2015b) and gained producer accuracies (PA) between 83.1% and 98.6% and user accuracies (UA) between 95.3% and 98.5%; flood masks derived by the S-1FS have been validated, for example, by Twele et al. (2016) and gained PAs between 98.2% and 99.4% and UAs between 90.0% and 92.4%; flood masks derived by the S-2FS and LFS have been validated by Wieland and Martinis (2019) and gained values of Precision between 0.79 and 0.87 and values of Recall between 0.93 and 0.99.

Furthermore the observation frequency and temporal coverage is also influencing the quality of the flood duration. In the following, the calculation of the FDQ is described which indicates the uncertainty of each pixel i of the product by taking into account the acquisition frequency and distribution of acquisitions in the frame of a flood event. By computing the BFD, the uncertainty is expressed by the sum of a pre-event uncertainty ($PreU$) and co-event uncertainty (CoU). A third term, the post-event uncertainty ($PostU$), might be added by calculating the TFD:

$$FDQ_i = \sum_{f=1}^{n} \left(PreU + CoU + PostU \right). \tag{2.8}$$

A number of flood n events f might be occurred within the defined period for calculating the FDQ. Therefore, the sum of $PreU$, CoU, and $PostU$ hast to be summarized for each flood event.

The CoU is calculated by:

$$PreU_i = D_{b,\,i} - D_{a,\,i}\,, \tag{2.9}$$

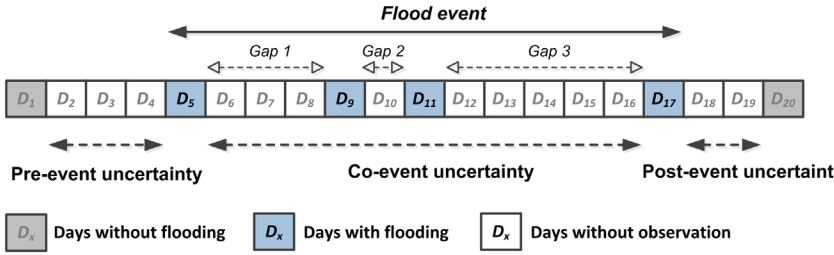

FIGURE 2.9 Schematic illustration for computing the flood duration quality layer.

where $D_{a,i}$ is the first day without information (D_2 in Fig. 2.9) after the first day where no flood is detected in the respective time period and $D_{b,i}$ is the last day without information (D_4 in Fig. 2.9) before the first day where flood is detected.

CoU is computed based on the number m of gaps g resulting from days without observation between 2 days with flooding within a single inundation event:

$$CoU_i = \sum_{g=1}^{m} \left(\left(D_{d,\,i} - D_{c,\,i} \right)^2 + \left(D_{d,\,i} - D_{c,\,i} \right) \right) * 0.5 / m, \tag{2.10}$$

where $D_{c,i}$ is the first day without information (D_6 in gap 1, D_{10} in gap 2, and D_{12} in gap 3 in Fig. 2.9) after a day with flooding in gap g and $D_{d,i}$ is the first day with flooding after this gap (D_9, D_{11}, and D_{17} in Fig. 2.9). The influence of each gap on the uncertainty is weighted according to the temporal duration of the gap. Shorter gaps with low number of days without acquisition are related to a higher quality than longer gaps with more days without acquisition.

PoU is computed by:

$$PostU_i = D_{f,\,i} - D_{e,\,i}, \tag{2.11}$$

where $D_{e,i}$ is the first day without information (D_{18} in Fig. 2.9) after the last day with flood in the defined time period and $D_{f,i}$ is the last day without information (D_{19} in Fig. 2.9) before the first day without flooding.

3 Results

3.1 Study area and dataset

In this section, the results of the automatic system for flood extent and duration mapping based on multi-sensor satellite data are presented for the torrential inundation event related to tropical cyclone Idai, which hit the east coast of Africa in March 2019.

Cyclone Idai, which formed over the Northern Mozambique Channel on March 9, made landfall near Beira City (Sofala Province, Central Mozambique) on the night of March 14–15 and caused catastrophic damage in Mozambique, Zimbabwe, and Malawi. Idai brought very strong winds and caused severe flooding due to heavy rainfall. The Tropical Cyclone Idai is regarded as one of the worst tropical cyclones on record to affect Africa and the Southern Hemisphere as a whole.

This study focuses on an area of interest (AOI) covering mainly the province of Sofala and minor parts of Manhica in Mozambique (Fig. 2.10). The AOI has a North to South expansion of ~139 km and an East to West expansion of ~ 108 km (Fig. 2.10).

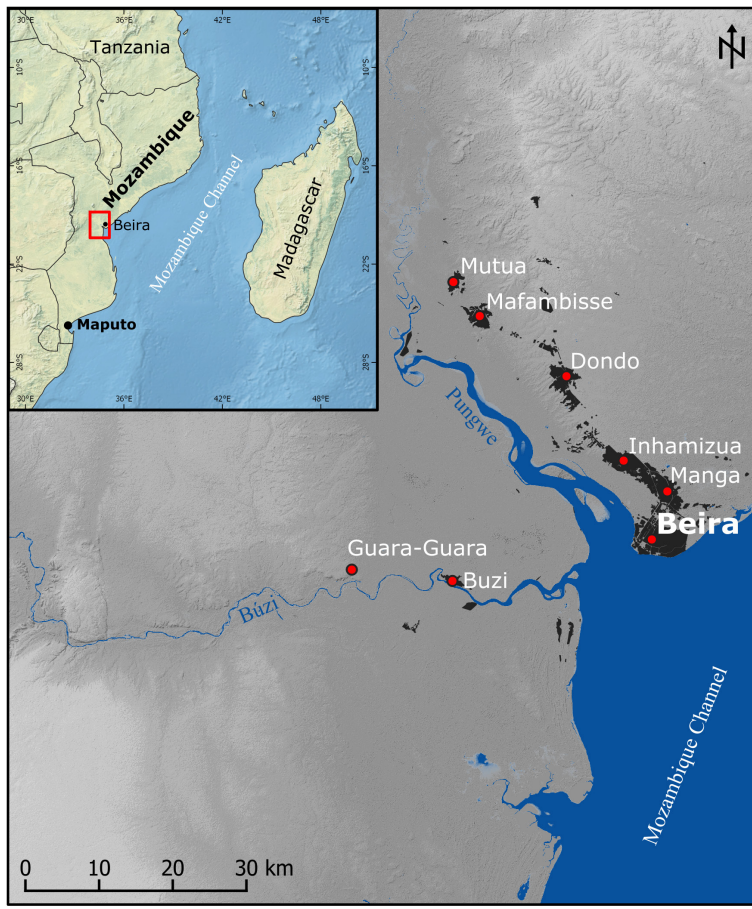

FIGURE 2.10 Study area in Mozambique. A hillshade computed based on SRTM-C band data serves as background. Map data from OpenStreetMap contributors. *(Modified from Rättich et al. (2020).)*

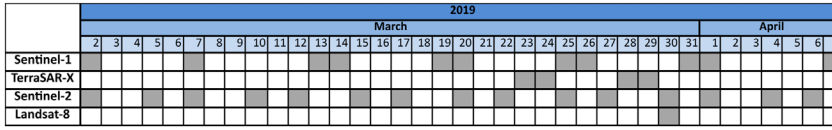

FIGURE 2.11 Temporal coverage of Sentinel-1, Sentinel-2, TerraSAR-X, and Landsat-8 data.

For this study, in total 75 satellite datasets have been used which cover the AOI within the time frame 02/03/-07/04/2019 (Fig. 2.11):

- Sentinel-1: 33 Sentinel-1 GRD IW data acquired on 11 days with a spatial resolution of ~20 m
- TerraSAR-X: 4 data ScanSAR datasets with a spatial resolution of 18.5 m
- Sentinel-2: 12 L1C scenes of the Multi-Spectral Instrument (MSI) onboard Sentinel-2 with a spatial resolution of 10 m acquired on 12 days (36 tiles à 100×100 km)
- Landsat-8: 2 scenes of the Operational Land Imager (OLI) onboard the Landsat-8 satellite with a spatial resolution of 30 m acquired on 1 day

3.2 Flood extent masks

Due to the predicted landfall of cyclone Idai, the International Charter "Space and Major Disasters" had been activated (Activation ID: 598) on March 14, 2019, by the Brazilian Disaster and Risk Management National Centre (CENAD) on behalf of Mozambique's National Institute for Disaster Management (INGC) as well as by UNITAR/UNOSAT on behalf of the International Federation of Red Cross and Red Crescent Societies (IFRC) to support disaster management activities with satellite-based crisis information. In the frame of this activity, DLR applied its automatic flood processing chains to perform a monitoring of the extent and dynamic of the flood situation over time.

Flood extent products have been automatically derived from Sentinel-1, TerraSAR-X, Sentinel-2, and Landsat-8 datasets. In Fig. 2.12 examples of flood extent products are visualized for each of these satellites. Fig. 2.12A shows a Sentinel-1 scene (HH polarization) of 19/03/2019, Fig. 2.12B shows a TerraSAR-X ScanSAR scene (HH polarization) of 23/03/2019, Fig. 2.12C shows a Sentinel-2 MSI scene of 25/03/2019, and Fig. 2.12D shows a Landsat-8 OLI scene of 30/03/2019. Fig. 2.12E–H show the derived flood extent separated from the reference water extent based on SWBD and on data of the Humanitarian OpenStreetMap Team (HOT).

Fig. 2.12 shows the temporal coverage of the used satellite data. The 37-day period between 02/03/2019 and 07/04/2019 is covered in total on 25 days by the satellite missions Sentinel-1/-2, TerraSAR-X, and Landsat-8. Due to the day- and night-imaging capability, the radar missions Sentinel-1 and TerraSAR-X

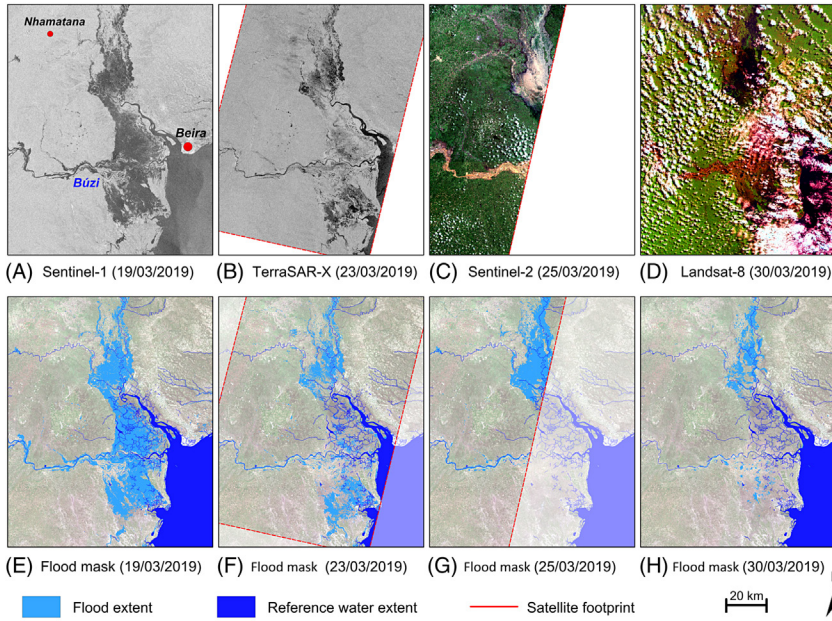

FIGURE 2.12 Exemplary results of the automatic multi-sensor flood mapping system over the study area in Mozambique. (A) Sentinel-1 of 19/03/2019 (© ESA); (B) TerraSAR-X of 23/03/2019 (© DLR); (C) Sentinel-2 (RGB: Red, Green, Blue) of 25/03/2019 (© ESA); (D) Landsat-8 (RBG: SWIR-2, NIR, Blue) of 25/03/2019 (© USGS) and (E–H) derived single-temporal flood masks and reference water masks from SWBD and data of HOT. A mosaic of four Sentinel-2 tiles (RGB: Red, Green, Blue) acquired on 02/12/2012 serves as background in E–H.

allow to derive systematically the flood extent and therefore the dynamic of the inundation event for the selected AOI.

Sentinel-2 data are highly cloud covered in the days during/after the landfall of the cyclone. However these Sentinel-2 data, together with Landsat-8, provide an added value to monitor the recession of the flooding over time after the movement of the cyclone from 17/03/2019 onwards.

Ten SAR satellite acquisitions (9 Sentinel-1 and 1 TerraSAR-X data) cover the whole AOI and are therefore used to compute the dynamic of the flood extent for the 37-days period for the study area (see Fig. 2.13). As no completely cloud-free optical dataset covering the whole AOI is available, no optical data was used for computing the dynamic of the flooded area. The classification results derived from Sentinel-1 data on 14/03/2019 (03:09 UTC) show that also before the landfall of the cyclone on the night of the 14th–15th, a significant part of the AOI is flooded (~682 km^2). The flood peak is on 19/03/2019 where more than 1,800 km^2 are flood-covered. These flooding occurred mainly in the catchment area of River Búzi in the west of the study area where a lake of ~100 km length and ~25 km width was formed.

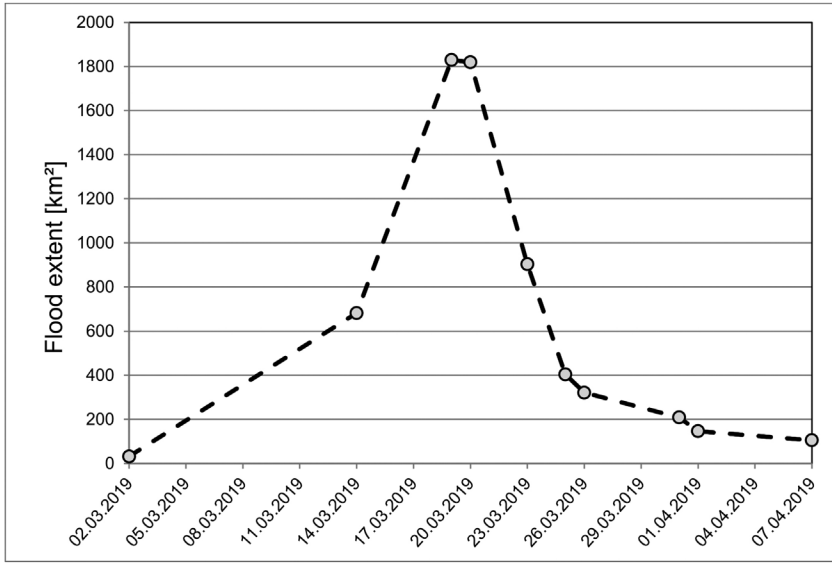

FIGURE 2.13 Evolution of the flood extent for the AOI in Mozambique derived from Sentinel-1 and TerraSAR-X data between 02/03/2019 and 07/04/2019.

Within a 5-day period between 20/03/2019 and 25/03/2019, the flood extent drastically reduced by more than 1,400 km^2 to 400 km^2. The reduction of the water extent occurred mainly in the central and southern parts of the AOI, whereas floods persisted in the northern part. In the subsequent time period until the 07/04/2019, the inundation reduced slowly by 300 km^2 to an extent of ~105 km^2.

3.3 Flood duration products

Fig. 2.14 shows the BFD at the peak of the flood event on 19/03/2019. At this stage, especially the central and southern part of the study area is already flooded since 7 days—regions which have been already flooded some days before the landfall of Idai on the night between the March 14th and 15th, 2019.

TFD in the study area in Mozambique for the observation period 02/03/2019–07/04/2019 is depicted in Fig. 2.15. As it considers all flooded pixels during this time period, it shows a larger flood extent than the BFD in Fig. 2.14. The product shows extensive inundations of 14–20 days in the southern and northern part (along Pungwe river) of the study area. The area along Búzi river was also flooded for 1–10 days. An area of more than 2,500 km^2 was flooded during the observation period. More than 1,000 km^2 was flooded for a short duration (1–2 days) and more than 1,700 km^2 area less than 1 week (1–7 days). Other regions were also inundated for longer time: in total more than 600 km^2 for 1–2 weeks and ~130 km^2 for 2–3 weeks.

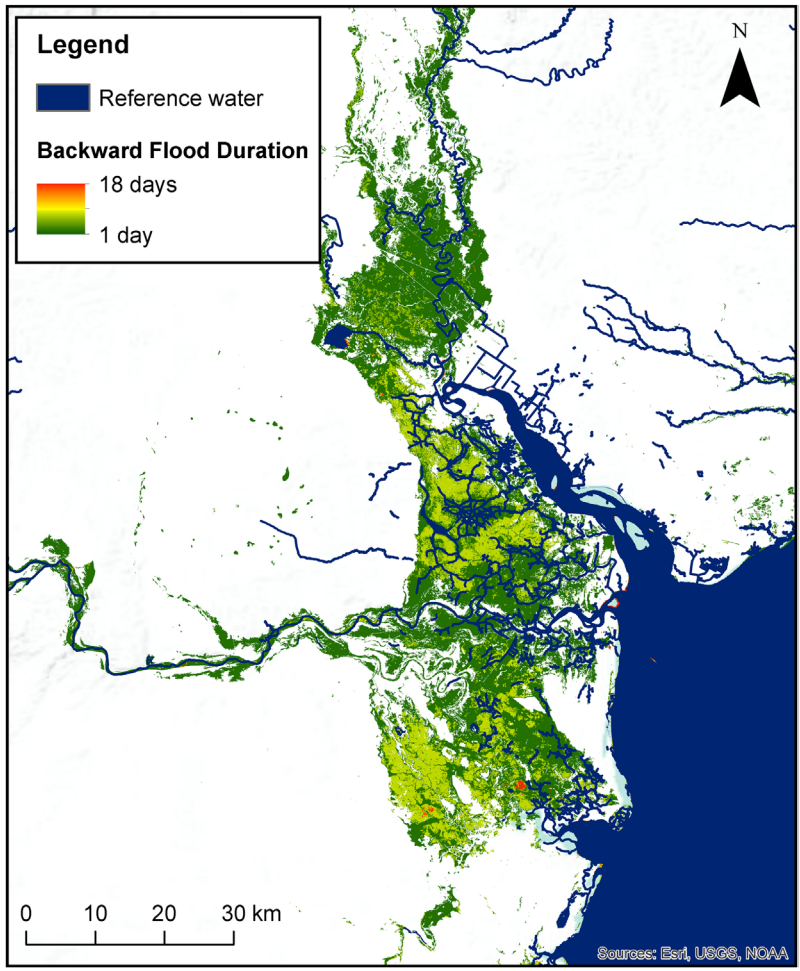

FIGURE 2.14 Backward Flood Duration over the AOI in Mozambique derived from Sentinel-1, TerraSAR-X, and Sentinel-2 data in the period 02/03/2019–19/03/2019. The reference water extent is based on SWBD and data of HOT. *(Modified from Rättich et al. (2020).)*

The quality layer for the TFD product is visualized in Fig. 2.16. It shows relative uncertainties reflecting the observation frequency and the distribution of acquisitions. Due to the high temporal coverage of satellite acquisitions for this flood event relative high certainty values between 1 and 19 are achieved for most regions. Higher uncertainties are mainly related to partial cloud coverage on one or more acquisition dates of Sentinel-2 and Landsat-8, which cause a lower availability of valid observations and the prolongation of acquisition gaps.

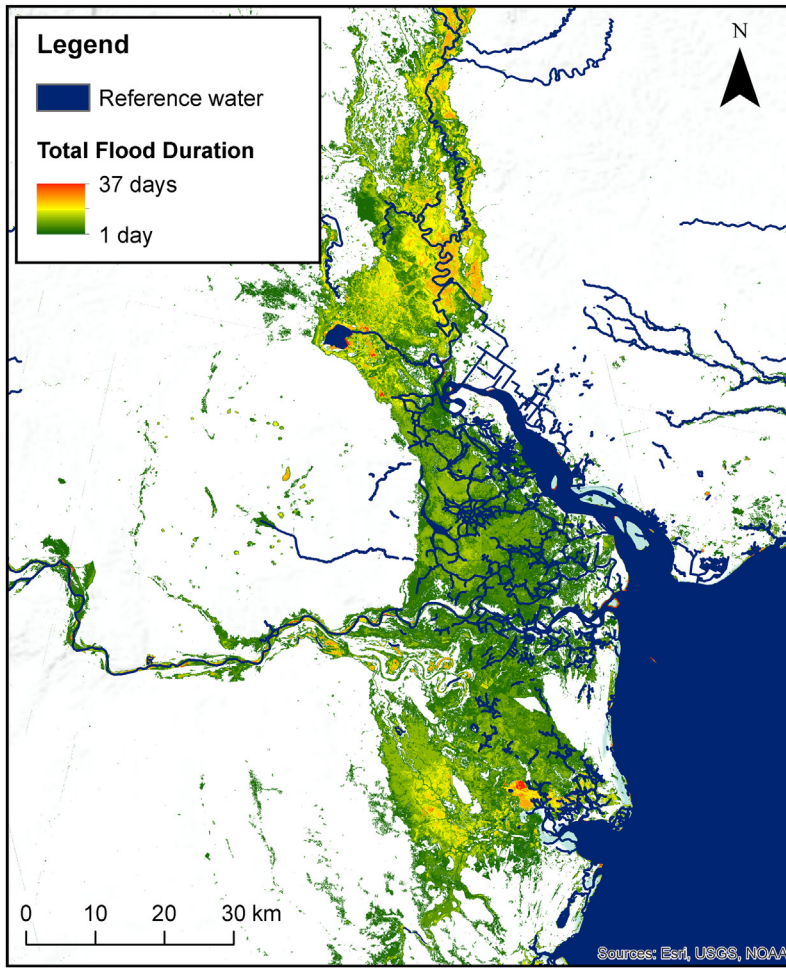

FIGURE 2.15 Total Flood Duration over the AOI in Mozambique derived from Sentinel-1, TerraSAR-X, Sentinel-2, and Landsat-8 data in the period 02/03/2019–07/04/2019. The reference water extent is based on SWBD and data of HOT. *(Modified from Rättich et al. (2020).)*

The results illustrate the usefulness of the flood duration products for a comprehensive flood monitoring at specific locations over time. The proposed approach is able to automatically generate the TFD and BFD product as well as a corresponding Flood Quality in NRT based on flood masks derived from the flood services described in Section 2. The BFD can be used as an indicator for the duration of an ongoing flood event in days and should be assessable to users involved in disaster management activities in NRT in order to provide information about the persistency of a current flood event. The TFD can be useful for scientific questions, for example, a long-term comparison of annually recurring

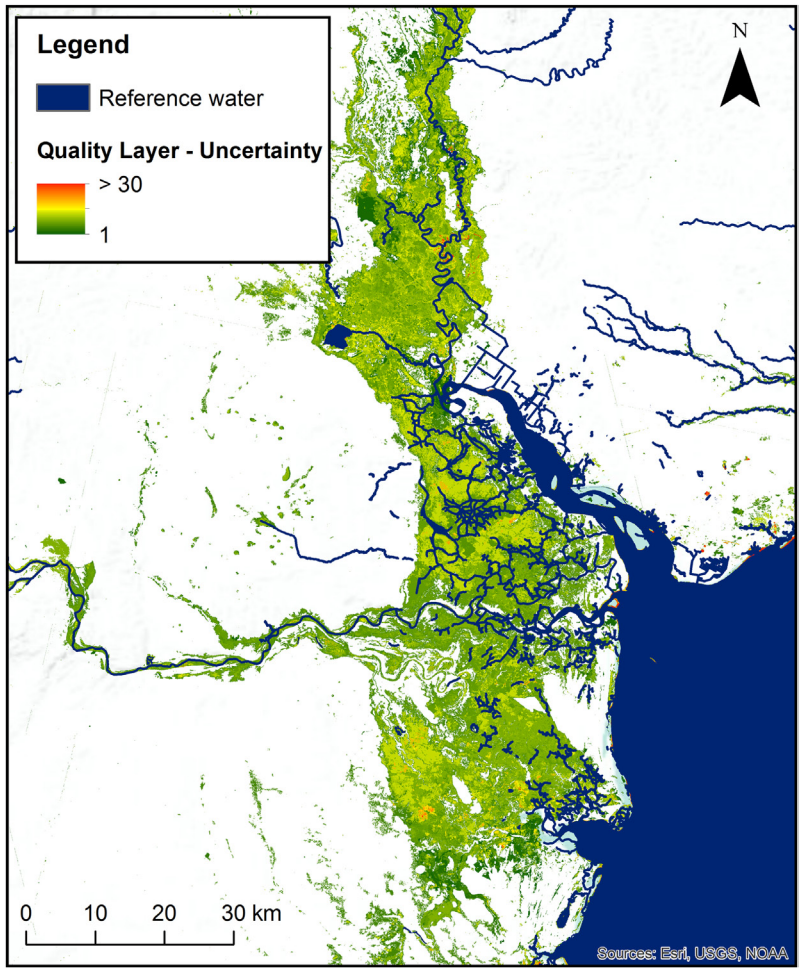

FIGURE 2.16 Quality layer for the TFD based on Sentinel-1, TerraSAR-X, Sentinel-2, and Landsat-8 data. The reference water extent is based on SWBD and data of HOT. A mosaic of four Sentinel-2 tiles (RGB: Red, Green, Blue) acquired on 02/12/2018 and 02/12/2018 is used as background. *(Modified from Rättich et al. (2020).)*

hydrological phenomena or can be used damage indicator for insurance companies providing climate risk insurance products.

4 Conclusion

Flood extent maps derived from EO data are an important information source for effective flood disaster management. Due to the fact that flood masks based on only one satellite mission are in general not sufficient to monitor the evolution of large-scale inundation event over time due to revisit time and coverage

of polar orbiting EO missions. This study presents an automatic system for NRT flood extent and duration mapping based on multi-sensor satellite data. Flood masks are automatically derived using the four satellite missions Sentinel-1, Sentinel-2, TerraSAR-X, and Landsat-8. Two different kinds of flood duration layers are computed in order to provide on the one hand NRT information about the duration of an ongoing flood for each image element within a BFD layer and on the other hand, the total duration of flood coverage for each individual pixel for a predefined time period, which could potentially cover several flood events. A quality layer is computed in addition, which gives information about the reliability of the flood duration products by taking into account pre-event, co-event and, in computing the total flood duration, also post-event uncertainties. In general, the quality of the flood duration products increases with increasing temporal resolution of the used virtual satellite constellation by combining flood masks of different sensors.

In this study, the proposed multi-sensor flood monitoring system was demonstrated over an AOI of ~15,000 km^2 in Mozambique affected by severe flood event caused by cyclone Idai in March 2019. For this purpose, 75 satellite images have been automatically analyzed within the time frame 02/03/–07/04/2019. The analysis shows the evolution of the flooding over time, with a maximum observed flood extent of more than 1,800 km^2 on 19/03/2019, at about 4 days after the landfall of the cyclone, and a fast recession of the inundation extent within the time period 20/03/–25/03/2019 by ~1,000 km^2, followed by a much slower recession to nearly pre-event conditions until 07/03/2019.

Two flood duration products, the BFD and TFD, automatically derived from preprocessed multi-sensor flood masks are useful for different applications, for example, to support disaster management or relief activities of humanitarian aid organizations. The information about regional differences in flood duration over time helps to estimate the damage from flood events more precisely enabling a more efficient response to flood situations.

Future work will focus on the integration of further satellite mission within the proposed automatic multi-sensor flood monitoring system in order to increase the temporal acquisition frequency and the quality of flood duration products. Due to the advantages of SAR in systematic flood monitoring applications, the integration of additional current (e.g., RADARSAT Constellation Mission, RCM) or future radar missions such as TanDEM-L or the High Resolution Wide Swath (HRWS) mission is of major relevance.

List of acronyms

AOI Area of Interest
BFD Backward Flood Duration
CMES Copernicus Emergency Management Service
CNN Convolutional Neural Network
CoU Co-event Uncertainty
DEM Digital Elevation Model

DLR German Aerospace Center
DN Digital Numbers
EEC Enhanced Ellipsoid Corrected
EO Earth Observation
ESA European Space Agency
FDQ Flood Duration Quality
GEC Ground Ellipsoid Corrected
GIM Geocoded Incidence Angle Mask
GPT Graph Processing Tool
GRD Ground Range Detected
HAND Height Above Nearest Drainage
HAND-EM Height Above Nearest Drainage Exclusion Mask
HOT Humanitarian Open Streetmap Team
HRWS High Resolution Wide Swath
IW Interferometric Wide Swath
LFS Landsat Flood Service
NRCS Normalized Radar Cross Section
NRT Near real-time
OGC Open Geospatial Consortium
PostU Post-event Uncertainty
PPP Public–private partnership
PreU Pre-event Uncertainty
RCM RADARSAT Constellation Mission
ReLU Rectified Linear Unit
S-1FS Sentinel-1 Flood Service
S-2FS Sentinel-2 Flood Service
SAR Synthetic Aperture Radar
SEL Sand Exclusion Layer
SNAP Sentinel Application Platform
SRTM Shuttle Radar Topgraphy Mission
SWBD SRTM Water Body Data
TOA Top of Atmosphere
TFD Total Flood Duration
TFS TerraSAR-X Flood Service
WPS Web Mapping Service
WPS Web Processing Service
XML Extensible Markup Language

References

Amitrano, D., Di Martino, G., Iodice, A., Riccio, D., Ruello, G., 2018. Unsupervised rapid flood mapping using Sentinel-1 GRD SAR images. IEEE Trans. Geosci. Remote Sens. 56 (6), 3290–3299.

Carroll, M., Townshend, J., DiMiceli, C., Noojipady, P., Sohlberg, R., 2009. A new global raster water mask at 250 meter resolution. Int. J. Digit. Earth 2 (4), 291–308.

Chow, C., Twele, A., Martinis, S., 2016. An assessment of the 'Height Above Nearest Drainage' terrain descriptor for the thematic enhancement of automatic SAR-based flood monitoring services. In: Proceedings of SPIE, SPIE Remote Sensing 2016. Edinburgh, United Kingdom.

Copernicus Emergency Management Service, 2019. https://emergency.copernicus.eu/ (accessed 10.12.2019).

CRED and UNISDR, 2018. Economic losses, poverty and disasters 1998-2017. www.preventionweb.net/knowledgebase/disaster-statistics/ (accessed 31.12.2019).

Drake, B., Shuchman, R.A., 1974. Feasibility of using multiplexed SLAR imagery for water resources management and mapping vegetation communities. Proceedings of the Ninth International Symposium on Remote Sensing of Environment. Environmental Research Institute of Michigan, April 15-19, Ann Arbor, MI, pp. 219–249.

Giustarini, L., Hostache, R., Kavetski, D., Chini, M., Corato, G., Schlaffer, S., Matgen, P., 2017. Probabilistic flood mapping using synthetic aperture radar data. Trans. Geosci. Remote Sens. 54 (12), 6958–6969.

Infoterra, 2008. Radiometric calibration of TerraSAR-X data. https://www.intelligence-airbusds.com/files/pmedia/public/r465_9_tsxx-airbusds-tn-0049-radiometric_calculations_d1.pdf (accessed 26.09.2019).

International Charter Space and Major Disaster, 2019. http://www.disasterscharter.org (accessed 10.12.2019).

Kingma, D.P., Ba, J.L., 2015. Adam: A method for stochastic optimization. In: Proceedings of the Third International Conference for Learning Representations, San Diego. arXiv:1412.6980v9.

Kittler, J., Illingworth, J., 1986: Minimum error thresholding, Pattern Recog. 19, 41–47.

Lehner, B., Verdin, K., Jarvis, A., 2008. New global hydrography derived from spaceborne elevation data. Eos Trans. AGU 89, 93–94.

Li, Y., Martinis, S., Plank, S., Ludwig, R., 2018. An automatic change detection approach for rapid flood mapping in Sentinel-1 SAR data. Int. J. Appl. Earth Obs. Geoinform. 73, 123–135.

Li, Y., Martinis, S., Wieland, M., Schlaffer, S., Natsuaki, R., 2019. Urban flood mapping using SAR intensity and interferometric coherence via Bayesian Network Fusion. Remote Sensing 11 (19), 2231.

Martinis, S., Twele, A., Voigt, S., 2009. Towards operational near real-time flood detection using a split-based automatic thresholding procedure on high resolution TerraSAR-X data. Nat. Hazards Earth Syst. Sci. 9, 303–314.

Martinis, S., Twele, A., Strobl, C., Kersten, J., Stein, E., 2013. A multi-scale flood monitoring system based on fully automatic MODIS and TerraSAR-X processing chains. Remote Sens. 5, 5598–5619.

Martinis, S., Künzer, C., Twele, A., 2015a. Flood studies using Synthetic Aperture Radar data. In: Thenkabail, P. (Ed.), Remote Sensing Handbook, vol. III–Remote Sensing of Water Resources, Disasters and Urban Studies. Taylor & Francis, London, UK, pp. 145–173.

Martinis, S., Twele, A., Kersten, J., 2015b. A fully automated TerraSAR-X based flood service. ISPRS J. Photogramm. Remote Sens. 104, 203–212.

Martinis, S., Twele, A., Plank, S., Zwenzner, H., Danzeglocke, J., Strunz, G., Lüttenberg, H., Dech, S., 2017. The International 'Charter Space and Major Disasters': DLR's contributions to emergency response world-wide. J. Photogramm. Remote Sens. Geoinform. Sci. 85, 317–325.

Martinis, S., Plank, S., Cwik, K., 2018. The use of Sentinel-1 time-series data to improve flood monitoring in arid areas. Remote Sens. 10, 583.

METI and NASA, 2019. Aster GDEM V3. https://lpdaac.usgs.gov/news/nasa-and-meti-release-aster-global-dem-version-3/a (accessed 24.09.2019).

Pal, S.K., Rosenfeld, A., 1988. Image enhancement and thresholding by optimization of fuzzy compactness. Pattern Recog. Lett. 7, 77–86.

Pulvirenti, L., Pierdicca, N., Chini, M., Guerriero, L., 2011. An algorithm for operational flood mapping from synthetic aperture radar (SAR) data using fuzzy logic. Nat. Hazards Earth Syst. Sci. 11 (2), 529–540.

Rättich, M., Martinis, S., Wieland, M., 2020. Automatic flood duration estimation based on multi-sensor satellite data. Remote Sens. 12 (4), 643.

Rennó, C.D., Nobre, A.D., Cuartas, L.A., Soares, J.V., Hodnett, M.G., Tomasella, J., Waterloo, M.J., 2008. HAND, a new terrain descriptor using SRTM-DEM: Mapping terrafirme rainforest environments in Amazonia. Remote Sens. Environ. 112, 3469–3481.

Ronneberger, O., Fischer, P., Brox, T., 2015. U-Net: Convolutional networks for biomedical image segmentation. In: Hornegger, N., Frangi, W. (Eds.), Medical Image Computing, Computer-Assisted Intervention–MICCAI 2015. In: Lecture Notes in Computer Science, vol. 9351. Springer International Publishing, Cham, Switzerland, pp. 234–241.

Sentinel Asia, 2019. Available from: https://sentinel-asia.org/ (accessed 12.10.2019).

Schlaffer, S., Matgen, P., Hollaus, M., Wagner, M., 2015. Flood detection from multitemporal SAR data using harmonic analysis and change detection. Int. J. Appl. Earth Obs. Geoinform. 38, 15–24.

Schumann, G., Di Baldassarre, G., Alsdorf, D., Bates, P.D., 2010. Near real-time flood wave approximation on large rivers from space: application to the River Po, Italy. Water Resour. Res. 46 (5), 1–8.

Torres, R., Snoeij, P., Geudtner, D., Bibby, D., Davidson, M., Attema, E., Potin, P., et al., 2012. GMES Sentinel-1 Mission. Remote Sens. Environ. 120, 9–24.

Tsyganskaya, V., Martinis, S., Marzahn, P., Ludwig, R., 2018. Detection of temporary flooded vegetation using Sentinel-1 time series data. Remote Sens. 10, 1286.

Twele, A., Cao, W., Plank, S., Martinis, S., 2016. Sentinel-1 based flood mapping: a fully automated processing chain. Int. J. Remote Sens. 37 (13), 2990–3004.

Westerhoff, R.S., Kleuskens, M.P.H., Winsemius, H.C., Huizinga, H.J., Brakenridge, G.R., Bishop, C., 2013. Automated global water mapping based on wide-swath orbital synthetic aperture radar. Hydrol. Earth Syst. Sci. 17 (2), 651–663.

Wieland, M., Li, Y., Martinis, S., 2019. Multi-sensor cloud and cloud shadow segmentation with a convolutional neural network. Remote Sens. Environ. 230, 1–12.

Wieland, M., Martinis, S., 2019. A modular processing chain for automated flood monitoring from multi-spectral satellite data. Remote Sens. 11, 2330.

Page left intentionally blank

Chapter 3

Flood Mapping with Passive Microwave Remote Sensing: Current Capabilities and Directions for Future Development

John F. Galantowicz and Jeff Picton
Atmospheric and Environmental Research, Inc., Lexington, MA, United States

1 Introduction

Passive microwave remote sensing—also known as microwave radiometry—is an unexpectedly effective way to map floods from space. Unlike other remote sensing technologies, microwave sensor data are course-resolution, producing unfocused imagery that must be heavily processed to make flood maps. Few flood mapping systems use microwave data and relatively few researchers are familiar with methods for analyzing it. Yet microwave remote sensing has unique features that make it a valuable tool for detecting floods across the globe, monitoring floods in near real–time (NRT), and analyzing historical floods to assess flood risk and prepare for future events. For example, microwave radiation penetrates clouds, which means that microwave sensors are often the first to observe a flood after rains have ceased; microwave sensors make observations day or night, which makes them more likely to observe peak flood extents; and a series of spaceborne microwave sensors have left a consistent data record extending back to 1998, allowing for historical flood reconstruction and creation of baseline flood frequency statistics against which future flood severities can be evaluated.

In this chapter, we describe the theoretical underpinnings for flood mapping from microwave radiometry and their practical application in the FloodScan flood mapping system (Galantowicz et al., 2018a,b). FloodScan is a mature, well-tested system that maps flooding in NRT. The system was originally designed for use in parametric insurance applications that prioritize automated data processing with consistency, objectivity, and reliability at continental

Earth Observation for Flood Applications. http://dx.doi.org/10.1016/B978-0-12-819412-6.00003-1

scales. FloodScan achieves these goals with its *standard flood extent depiction* (SFED) algorithm product. SFED processing relies entirely on coarse resolution passive microwave data because of its frequent coverage over more than 20 years and its ongoing availability. FloodScan's *downscaling* algorithm overcomes microwave resolution limitations to make flood maps at scales around 90 m, which is sufficiently high-resolution to assess the flood impacts on human welfare and across economic sectors on national scales.

1.1 Microwave flood mapping for sovereign risk transfer

FloodScan's SFED algorithm was originally developed for the African Risk Capacity's (ARC) sovereign-level natural disaster-risk transfer program. ARC's use case for SFED provides a case study in flood mapping system design for an end-user's application. ARC is a specialized agency of the African Union (AU) established to help African governments improve their capacities to better plan, prepare, and respond to extreme weather events and natural disasters. ARC's innovation in this regard is to structure insurance-like sovereign risk transfer programs with funds to be automatically paid out to participating states based on an algorithmic trigger. ARC has coordinated disaster insurance policies for African governments since 2014 based on this *parametric index* approach underpinned by remote sensing data. ARC's drought index incorporates satellite-based rainfall data and SFED was designed to support a flood index. ARC ties these indices to disaster response costs through vulnerability factors like household resilience and exposure to losses, working with member states to calibrate the indices to in-country records where possible. Once calibrated, ARC's program is designed to automatically trigger insurance payouts when an index crosses thresholds agreed upon in advance with the countries involved.

ARC's concept for a flood index put requirements on the SFED product that shaped how it would be derived and delivered. First, there had to be at least 20 years of historical data for index calibration against past disaster response costs. Second, historical SFED had to be produced using the same algorithm as the NRT processing system to guarantee consistency with payout triggering levels calibrated with historical data. Third, the algorithm had to be consistent across AU countries, transparently produced, and algorithmically objective to build trust with participating states and investors. And lastly, SFED production had to be reliable in NRT with a daily cadence and less than 24-hour latency to support rapid payouts while a disaster takes shape. A key SFED design trade-off was to emphasize false positive reduction at the expense of small flood detection. This approach was viewed as acceptable because the disasters of interest were expected to be large-scale events with national impacts. Nevertheless, SFED's low sensitivity to urban flooding and high noise levels near coasts (discussed later) leave a gap in flood disaster coverage that may need to be addressed by other means.

1.2 Managing flood map ambiguities in applications

Interest in rapid flood mapping for disaster response has motivated the development of additional FloodScan algorithm modes to complement the conservatively designed SFED product. These modes do away with FloodScan steps designed to filter out false positives and smooth over noise, providing timelier updates with a better chance of depicting maximum flood extents. At the same time, they expose more of the algorithm trade space between flood map performance consistency—embodied in SFED—and increased false positive risk. Users of rapidly generated flood mapping products must be aware of these trades-offs so they can make appropriate use of the data in their applications. To this end, we demonstrate three additional algorithm products designed to facilitate end-user flood map interpretation: a dual flood classification that includes flooding mapped from marginal signals; a flood occurrence probability that quantifies flood occurrence likelihood everywhere; and a flood depth estimate that shows where flood impacts may be highest. A secondary objective of these demonstration products is to encourage other flood map producers to consider the uncertainties in their products and develop similar ways to present uncertain data to end-users.

2 Methods for passive microwave remote sensing for flood mapping

Passive microwave remote sensing involves the measurement of earth-emitted thermal radiation at frequencies from 1 to 100 GHz. Microwave signals across this spectrum have varying sensitivities to a number of geophysical parameters important for environmental monitoring including land surface temperature, soil moisture, and snow cover; sea ice, temperature, and winds; and atmospheric temperature, water vapor, and clouds. Although microwave sensitivity to flooding is a natural complement to these other sensitivities, their presence requires that flood mapping methods account for them explicitly to minimize errors.

Land surface passive microwave remote sensing techniques are rooted in experimental and theoretical research that accelerated with the launch of the first satellites dedicated to environmental remote sensing in the early 1970s (Ulaby et al., 1981). By the mid 1980s much of the foundational science of microwave radiometry had been established from field and laboratory studies and the limited amount of overhead sensor data available to that point from satellites or aircrafts. More routine satellite operations began with the Scanning Multichannel Microwave Radiometer (SMMR) in 1978 followed by the Special Sensor Microwave Imager (SSM/I) series in 1987. SSM/I was the first sensor with measurement characteristics suitable for frequent flood mapping, although its resolution meant that it was only sensitive to the largest floods. Microwave sensing at resolutions more practical for flood mapping started in 1998 with TMI, which only covered the tropics, followed in 2002 by AMSR-E, which provided global coverage (Table 3.1). By leveraging passive microwave satellite data

TABLE 3.1 Microwave sensors and satellite platforms carrying them.

Sensor	Platform	Operational period	Footprint resolution		Notes
			19 GHz	37 GHz	
SSM/I[b]	DMSP F11	12/1991–5/2000	69 × 43 km	37 × 28 km	Coarsest resolution; useful for largest floods
	DMSP F13	5/1995–11/2009			
	DMSP F14	5/1997–8/2008			
	DMSP F15	12/1999–present			
TMI[c]	TRMM	12/1997–9/2014	30 × 18 km/35 × 21 km[a]	16 × 9 km/18 × 10 km[a]	Tropical orbit covers 38° S–38° N latitude
AMSR-E[d]	NASA Aqua	6/2002–10/2011	27 × 17 km	14 × 10 km	Key mission for global flood mapping algorithm development
AMSR2[e]	JAXA GCOM-W1	7/2012–present	22 × 14 km	12 × 7 km	AMSR-E successor
GMI[f]	GPM	3/2014–present	18 × 11 km	16 × 9 km	Non-Sun-synchronous orbit covers 65° S–65° N latitude
Planned future missions					
AMSR3	JAXA GOSAT-3	Launch ≥2023	—	—	AMSR2 successor
MWI[g]	DoD WSF-M	Launch ≥2022	—	—	

[a] *TMI resolution increased in August 2001 when the TRMM satellite orbital altitude was boosted from 350 to 400 km.*
[b] *Defense Meteorological Satellite Program (DMSP) Special Sensor Microwave/Imager (http://www.ncdc.noaa.gov/oa/rsad/ssmi/swath/index.html).*
[c] *Tropical Rainfall Measuring Mission (TRMM) Microwave Imager (http://trmm.gsfc.nasa.gov/).*
[d] *National Aeronautics and Space Administration (NASA) Advanced Microwave Scanning Radiometer-EOS (http://nsidc.org/data/amsre).*
[e] *Japan Aerospace Exploration Agency (JAXA) Advanced Microwave Scanning Radiometer 2, Global Change Observation Mission 1st-Water (http://www.jaxa.jp/projects/sat/gcom_w/index_e.html).*
[f] *NASA Global Precipitation Measurement (GPM) Microwave Imager (http://pmm.nasa.gov/).*
[g] *US Department of Defense (DoD) Weather Satellite Follow-on – Microwave (WSF-M) Microwave Imager.*

extending back to 1998, modern algorithms can perform retrospective processing to build a uniquely consistent historical record of flooding.

Although microwave sensors like those in Table 3.1 were originally designed for other purposes, they share a number of features that make them suitable for flood mapping. First, they use a conical scanning geometry that results in an observation beam that intersects the earth's surface at a near-constant incidence angle. From this geometry, they can separately measure changes in vertically and horizontally polarized radiation related to flooding. They also carry channels in the 19- and 37-GHz microwave bands where flooding has a large signal relative to other land surface processes and atmospheric effects are largely correctable. With the exception of SSM/I, they all make 37-GHz band measurements at better than 22-km resolution, which is a key metric for sensitivity to flood extent. And with the exception of TMI, whose tropical orbit limits its ability to reach higher latitudes, all are in orbits that provide global coverage more than once per day on average. Finally, they all measure radiation in channels useful for detecting rain, which interferes with earth-leaving signals, and snow and frozen ground, which make dry land emission hard to predict; flood mapping algorithms are unlikely to produce consistent results under these conditions.

The long passive microwave data record means that there are ample data for calibrating and training flood detection and mapping algorithms and using them to reconstruct historical flooding. For example, the Global Inundation Extent from Multi-Satellites (GIEMS), which provides monthly mean surface water extent globally, 1993–2007, on a $0.25° \times 0.25°$ grid, calibrates passive microwave remote sensing with scatterometer and visible/near-infrared data (Prigent et al., 2007). The River Watch algorithm correlates passive microwave data and river stage to estimate daily river discharge at a limited set of satellite gauging stations (Brakenridge et al., 2016). The Global Flood Detection System (GFDS) expands upon the River Watch approach to make a true global product by forgoing calibration to a runoff model and instead chooses neighboring pixels as dry land calibration points in real time (Kugler and De Groeve, 2007; De Groeve, 2010). GFDS continues to use long time series to set flood detection thresholds. The remainder of this section uses the FloodScan algorithm to illustrate passive microwave retrieval techniques. Although the methods described are specific to FloodScan, the physical principles behind the methods and many of the processing steps are shared with these other algorithms.

2.1 Estimating flooded fraction

The starting point for microwave flood detection and mapping is the contrasting ways that microwave radiation interacts with the surface-atmosphere boundary in flooded versus unflooded (*dry land*) areas. This surface interaction is quantified as the *emissivity*, the ratio between the emitted brightness temperature, T_B, and physical surface temperature, T_s (Table 3.2). Because conical-scanning

TABLE 3.2 Definition of microwave remote sensing terminology used in this chapter.

Term	Definition
Brightness temperature (herein T_B or TB)	A passive microwave sensor measurement of radiation intensity calibrated to temperature units in kelvin, K.
Polarization	The orientation of the measured microwave radiation wave relative to the Earth's surface at the point of incidence. Microwave sensors use filters to make radiation measurements representing specific polarizations.
• TB with vertical polarization (V-pol.)	A TB measurement representing radiation intensity isolated to wave oscillations in a plane perpendicular to the Earth surface at the point of incidence.
• TB with horizontal polarization (H-pol.)	A TB measurement representing radiation intensity isolated to wave oscillations tangent (horizontal) to the Earth surface at the point of incidence.
Emissivity, e_v or e_h	The ratio of V-pol. or H-pol. TB to surface temperature. Varies from 0 to 1.
Point of incidence	The central geographic location at which the sensor points during a measurement.
Earth incidence angle	The angle at which a sensor's line of sight intersects with the Earth surface.
Footprint	The relative weighting pattern in which geographic areas contribute to a microwave measurement; the peak contribution weight is typically at or near the point of incidence.
Field of view (FOV)	The pattern on the Earth surface at which the footprint contribution pattern is equal to 1/2 the peak contribution at the point of incidence. Sensor footprint FOVs are approximately elliptical. FloodScan's footprint matching process creates approximately circular composite footprint FOVs.
Footprint size or FOV size	The geographic size of the FOV, expressed either as the average FOV diameter or as the distances across the FOV major and minor axes.
Resolution	A relative term referring to the size of the geographic area represented by a sensor measurement or other quantity; FOV size is one measure of resolution and is used as such here.
Frequency or band	Central microwave frequency at which a sensor channel operates, for example, 19 GHz, 37 GHz, etc.
Channel	The combined frequency and polarization at which a sensor operates and defining a brightness temperature measurement, for example, 19 GHz vertical polarization abbreviated as 19 GHz V-pol. or 19 V.
Flooded fraction	The flooded area of a footprint as a footprint-weighed fraction of the total footprint area.
Downscaling	The conversion of lower resolution flooded fraction estimates to a flood extent depiction at a finer resolution.

sensors view the earth at near-constant oblique incidence angles, we expect some earth surface emissivity behaviors to be consistent: V-pol. emissivities are greater than H-pol.; water emissivities are less than dry land; and water lowers H-pol. emissivity more than V-pol. The goal of a microwave flood mapping algorithm is to apply these general rules to infer flooding effect's on T_B measurements at a specific place and time.

A *mixing model* approximates the way that flooded area fraction within a microwave footprint proportionately affects a T_B measurement. With the assumption that flooded and unflooded land and persistent open water areas are otherwise homogeneous, a simple mixing model can be written as:

$$T_B = f_f T_{B,f} + f_{pow} T_{B,w} + \left(1 - f_{pow} - f_f\right) T_{B,dry} \tag{3.1}$$

where f_f is *flooded fraction*, f_{pow} is *persistent open water fraction*, and dry land is the remaining fraction, $\left(1 - f_{pow} - f_f\right)$. (We use the term *persistent* instead of *permanent* to characterize the open water amount judged to be just below that of flooding.) The mixing model associates each surface type with a brightness temperature, $T_{B,x}$, emissivity, e_x, and surface temperature, T_x, which are related by:

$$T_{B,x} = \tau_{atm} e_x T_x + \tau_{atm} \left(1 - e_x\right) T_{dn} + T_{up}, \tag{3.2}$$

where τ_{atm}, T_{dn}, and T_{up} are atmospheric transmittance and downwelling and upwelling brightness temperature contributions, respectively. An algorithm could easily invert these equations for f_f if all the other terms were known. In fact, the f_{pow} and atmospheric terms can be well estimated from global static databases and numerical weather models, respectively, leaving emissivities and surface temperatures as the most significant unknowns.

A convenient way to minimize surface temperature effects is to use a polarization ratio index, PRI:

$$PRI = \frac{\left(T_{Bv} - T_{Bh}\right)}{\left(T_{Bv} + T_{Bh}\right)}, \tag{3.3}$$

where T_{Bv} and T_{Bh} are V-pol. and H-pol. data at the same microwave frequency with estimates of τ_{atm} and T_{up} effects removed. PRI carries the flooded fraction signal with a slight nonlinearity that the FloodScan algorithm adjusts for with a simple transform

$$Q = sqrt(PRI + a) + bPRI, \tag{3.4}$$

where a and b are empirical constants. When computed from microwave sensor data, Q varies linearly with water fraction from about 0.34 for dry land to 0.46 for 100% open water (Fig. 3.1).

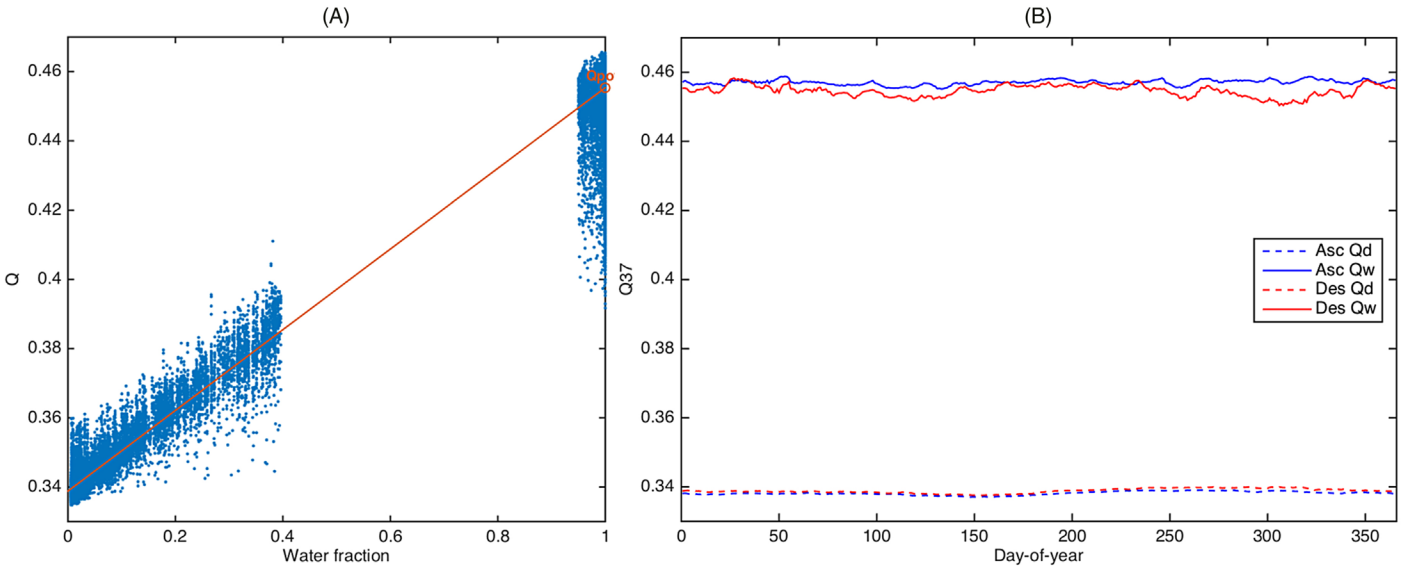

FIGURE 3.1 Empirical estimation of Q_w. (A) 37 GHz Q measured around Lake Victoria on January 1, 2003–10 with best fit line and Q_w estimate where water fraction is 1; (B) 37 GHz Q_w and Q_{dry} derived for each day of year showing Q_w seasonal variation and relative Q_{dry} stability. Note that Q_w is systematically different between ascending (daytime) and descending passes of sun-synchronous satellites. *(Credit: Original)*

If we assume that Q linearity with persistent water fraction also applies to flooded fraction, we can reformulate the mixing model Eq. (3.1) as

$$Q_{obs} = f_f Q_f + f_{pow} Q_w + \left(1 - f_{pow} - f_f\right) Q_{dry} \tag{3.5}$$

where Q_{obs} is computed from observations. Solving for flooded fraction yields

$$f_f = \frac{Q_{obs} - f_{pow} Q_w - \left(1 - f_{pow}\right) Q_{dry}}{Q_f - Q_{dry}}. \tag{3.6}$$

Of the terms in Eq. (3.6), Q_{dry} is the most difficult to estimate in real-time. We can define f_{pow} from a high-resolution reference static open water database (e.g., Hansen et al., 2013; Pekel et al., 2016); we can empirically derive Q_w (Fig. 3.1); and we can assume Q_f is equal to Q_w. This last assumption is not strictly valid because some flooding will be partially obscured by vegetation. However, given vegetation height heterogeneity and flood water depth uncertainty, an alternative model for Q_f is unlikely to be more accurate.

FloodScan's Q_{dry} model is designed to provide a conservative Q_{dry} value (i.e., leading to lower flooded fraction estimates) where conditions are most uncertain and a more liberal value where conditions are stable. The largest Q_{dry} uncertainty drivers include vegetation, soil moisture, and residual surface temperature effects. (Snow and frozen ground are detected and avoided for flood mapping.) All three are in part predictable at a place and time from their historical averages, year-to-year variability, recent history, and nearby conditions. FloodScan predicts Q_{dry} using metrics computed from historical Q time series with 31- and 61-day median filters applied to weed out most transient flooding. For each grid point and day of year, year-over-year average Q and variance statistics indicate typical Q_{dry} seasonality, rate of change, and predictability. Where Q is most predictable (e.g., evergreen forests), Q_{dry} tends to the historical average Q. Where Q_{dry} is less predictable (e.g., arid region rainy seasons), Q_{dry} tends to recent conditions propagated to the current day using historical average seasonality. Where flooding may have contaminated recent Q values, Q_{dry} tends toward a prediction based on neighboring, unflooded grid points. And finally, where regular flooding contaminates historical Q (e.g., seasonal wetlands), Q_{dry} falls back to a separate predictor based on satellite vegetation cover indices.

With Q_{dry} estimated and Eq. (3.6) executed for each Q observation, the FloodScan algorithm checks for false positives, filters noise, and produces a final daily flooded fraction estimate (Fig. 3.2). False positive flagging detects and eliminates large jumps in single observation flooded fraction (*flashes*) that are too fast and occur over scales too large to be flooding (e.g., affecting flooded fraction over more than 10,000 km^2). Flashes are likely the effects of soil moisture immediately following large scale rainstorms. After eliminating flashes, rain, and frozen conditions, the algorithm filters noise by computing a 2–3-day weighted average over all available flooded fraction values, with averaging

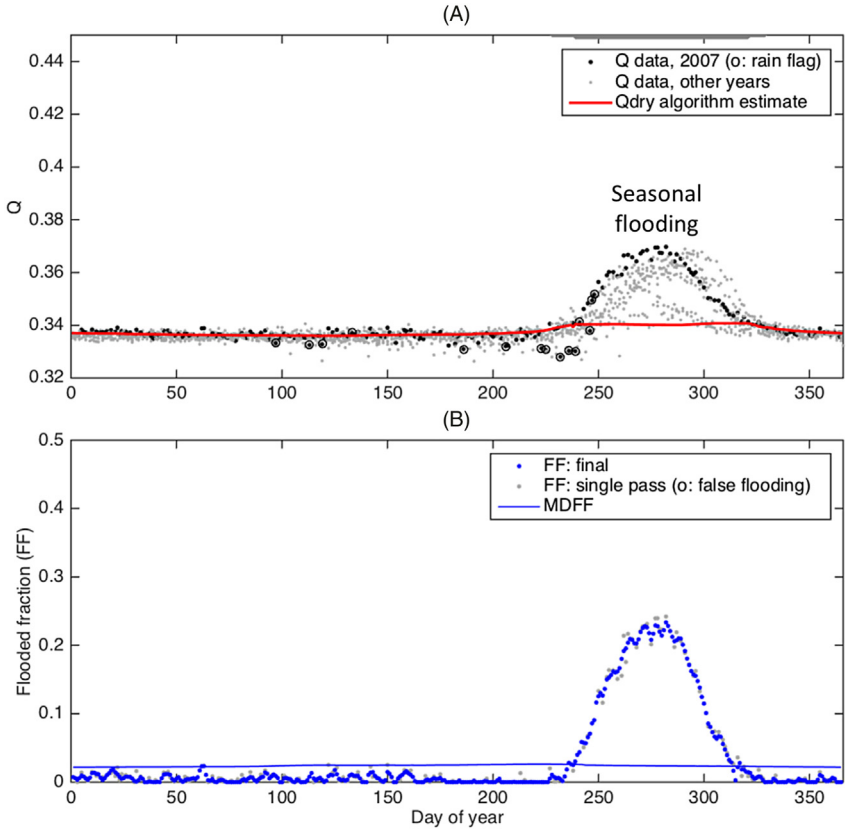

FIGURE 3.2 Time series of Q, Q_{dry}, and FloodScan flooded fraction on the Niger River, Onitsha, Nigeria, 2007. (A) Relationship between observed Q data and algorithm Q_{dry} for 2007, with Q data from other years showing year to year variance. There is minimal Q variance in the dry season (prior to day 200) relative to the wet season, whose start is marked by more frequent rain-flagged data. Rain decreases Q, causing flood false negatives if undetected. (B) Flooded fraction single pass data retrieval (Eq. (3.6)) and final algorithm estimate. Flooded fraction dry land noise falls below MDFF except at one point around day 60, which is likely to be a flood false positive. *(Credit: Original)*

period length dependent on historical noisiness. Finally, to filter out residual noise, the algorithm applies a minimum detectable flooded fraction (MDFF) threshold. MDFF varies globally and by day of year with a typical value of about 5%, meaning that about 5% flooding over a 22-km microwave footprint is typically required to confidently detect and map flooding. Although filtering by MDFF is necessary to weed out false positives in automated processing (Fig. 3.3A), it can be seen as too strict during extreme weather events when there is less uncertainty about whether or not flooding is occurring.

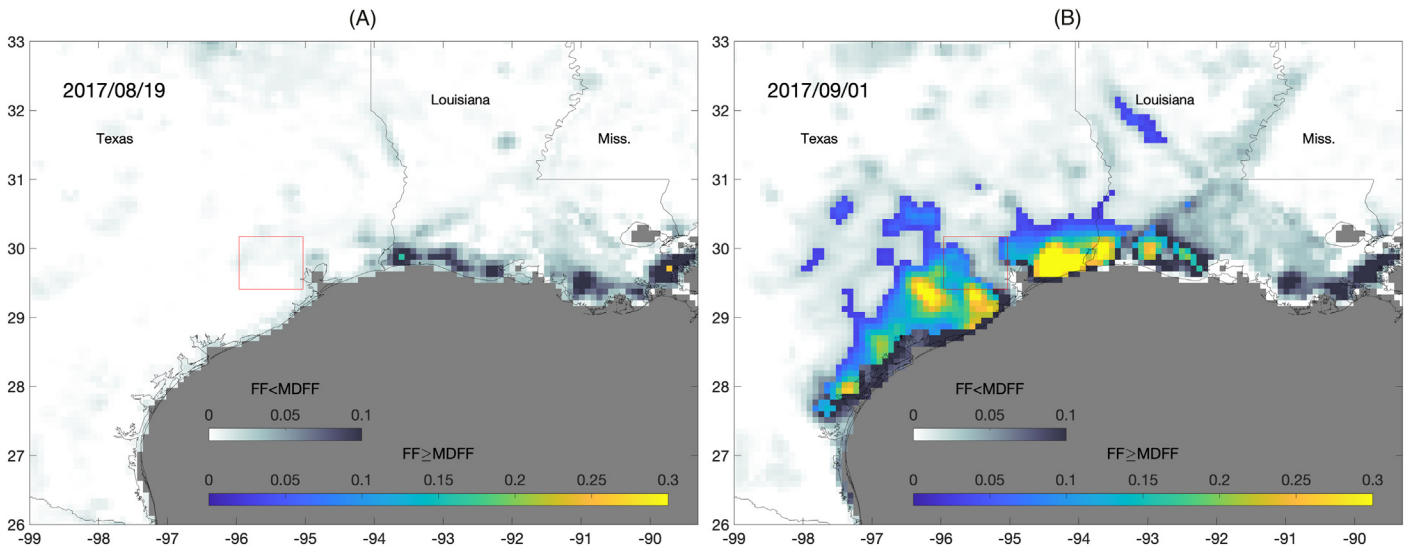

FIGURE 3.3 FloodScan flooded fraction before and after Hurricane Harvey landfall on August 25, 2017 showing the effects of MDFF. (A) August 19, 2017, when areas with flooded fraction below MDFF would likely be flood false positives if not suppressed; (B) September 1, 2017, when many areas with flooded fraction below MDFF are likely to be flooded given the amount of rainfall caused by Hurricane Harvey, notably in the Houston metro area *(red box)*. Note that MDFF is larger at the coastline by design. *(Credit: Original)*

2.2 Downscaling flooded fraction to map flooding

The idea behind downscaling is that of relative floodability: that there are inherent characteristics that make some areas more likely to be flooded than others. Relative floodability in the FloodScan context is somewhat different than that of, say, flood risk zone mapping. Whereas flood risk zones take into account the climatological probability of flooding, relative floodability is concerned specifically with the likely flood water distribution given FloodScan's flooded fraction estimates. The downscaling process effectively maps flooding pixel-by-pixel from high to low relative floodability areas until the total flood extent matches the retrieved flooded fraction.

Inputs to FloodScan's relative floodability (RF) database include a hydrologically corrected Digital Elevation Model (DEM) and historical water occurrence data. The map scale is typically 90-m for continent-wide flood mapping but can be tailored to finer scales. RF begins as the height of each point relative to a downslope streamline or other sink, an index similar to height above nearest drainage, or HAND (Nobre et al., 2011). Weighting and spatial smoothing is applied to increase RF for points nearest larger streams and to minimize discontinuities at drainage basin boundaries. Finally, RF is overridden where the annual water recurrence rate (Pekel et al., 2016) is non-zero or there is persistent open water.

FloodScan simplifies flooded fraction downscaling by first converting relative floodability to a flooded fraction threshold, f_{f0}. The flooded fraction threshold database relates each flood map point (e.g., 90-m scale) to flooded fraction (e.g., 22-km scale). With this transform, FloodScan interpolates flooded fraction to the flood map scale and evaluates $f_f > f_{f0}$ to indicate flooding. The algorithm then iteratively upscales the flood map back to flooded fractions at the microwave data scale, checks how closely the two flooded fractions match, and repeats the downscaling with adjustments until the two converge.

3 Current capabilities

The current FloodScan system includes historical datasets and an NRT processing system designed to generate SFED products that are statistically consistent with prior data. The NRT system processes incoming satellite data continuously for daily flood product updates covering North and South America and Africa. Daily historical records extend back to 1998 in most of the Americas and Africa. As currently configured, the system produces the conservative SFED product with less than 24-hours delay from the end of the nominal product day. Additional algorithm products discussed later are produced simultaneously or on demand from the same software suite.

The best way to evaluate SFED performance is through comparisons to flood maps derived from other remote sensing technologies. Direct comparisons to 20 flood maps made from 250-m resolution visible/infrared sensor

data in Africa resulted in a mean mapping accuracy of 82% (i.e., percentage of pixels in agreement; Galantowicz et al., 2018b). Additional case studies show that performance is situationally dependent. For example, coastal areas are more susceptible to false positives and false negatives, and semi-arid areas like the Sahel are likely to have false positives during the rainy season. The remainder of this section provides two SFED performance verification examples and breaks down the different sources of uncertainty in the algorithm.

3.1 Microwave flood mapping verification examples

One of FloodScan's strengths is its ability to map large scale river flooding. This capability is demonstrated by comparing the automatically generated SFED product to a Landsat false color image captured on a clear day during major river flooding in the Central United States in Spring 2018 (Fig. 3.4). The main river floodplains appear to be full, which means that FloodScan's relative floodability is a good indicator of flood likelihood. SFED misses apparent flooding in some relatively narrow floodplain sections but picks it up in others—a good demonstration of the how flood map accuracy is not strictly predicable based on flood extent alone. SFED also appears to be accurate in many areas where flood water pools while slowly draining through choke points in the hydrological system (e.g., the southeast corner of Fig. 3.4). Nevertheless, a pixel by pixel comparison is likely to show that SFED accuracy is about 80%–90% over this scene. Although an excellent score by algorithm verification standards, for end users with interests in an inaccurately mapped area the ambiguities can have serious consequences for decision making if they are not clearly presented as a part of flood map product dissemination.

The ability to update flood maps daily from microwave remote sensing make it ideal for capturing the extent of extreme floods quickly and for monitoring their evolution over time. These features are demonstrated using a *days flooded* metric computed from a series of daily SFED maps made in the aftermath of Cyclone Idai (Fig. 3.5). Idai was a massive slow-moving rainstorm that hit southeastern Africa in March 2019. After causing flooding in Malawi and moving back out to sea, Idai made landfall at Beira, Mozambique on March 14 and 15, and moved inland leaving disastrous inland flooding. By March 18, the SFED algorithm had mapped the "inland ocean" forming northwest of Beira. The SFED days flooded metric shows that flooding stayed in some areas for weeks. A flood map derived from Sentinel-1 synthetic aperture radar (SAR) data collected on March 19 and 20 shows that SFED captured most flood features. In some areas SFED flooding extends beyond the SAR-derived flood extent, which may indicate additional flooding present only during early microwave satellite passes.

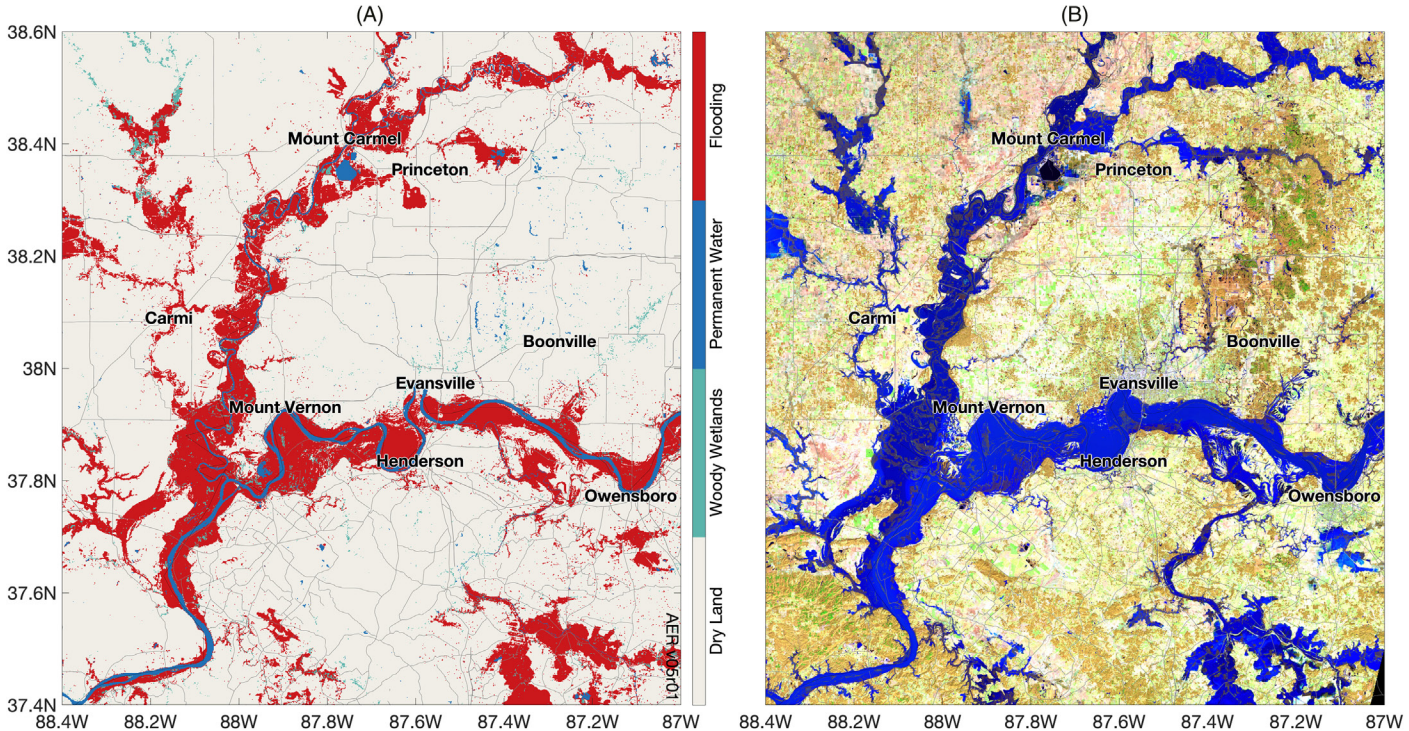

FIGURE 3.4 FloodScan-Landsat comparison, March 3, 2018, Wabash and Ohio Rivers, Indiana, Illinois, and Kentucky. (A) 90-m SFED algorithm product; (B) 30-m Landsat false color image. *(Credit: Original)*

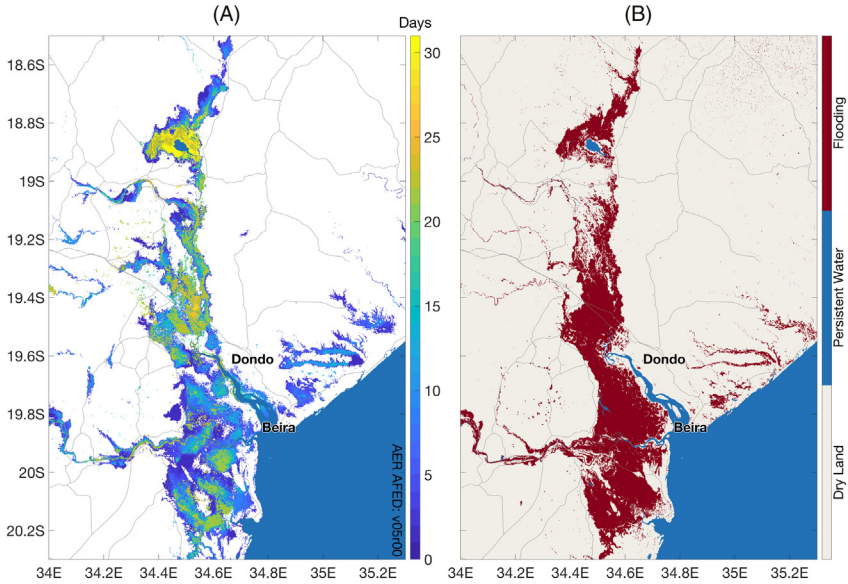

FIGURE 3.5 FloodScan-Sentinel-1 comparison, Cyclone Idai, Mozambique, March 2019. (A) SFED days flooded, March 6–April 8, 2019. (B) Flood map derived from Sentinel-1 SAR data, March 19–20, 2019. *(Credit: Original)*

3.2 Microwave flood mapping uncertainties and limitations

Understanding the uncertainties and limitations of any flood depiction method is the first step toward making practical use of the data. In many cases, flood mapping method limitations may be complemented by its strengths. For example, optical/infrared remote sensing methods make high-resolution, photo-realistic imagery whose interpretation for flood mapping is complicated by a variety of phenomenon—land cover, clouds, shadows, etc.—many of which might otherwise be measurement subjects. Similarly, hydrological models can provide near ubiquitous coverage and forecasting capabilities but are limited by the accuracy of rainfall amount, location, and timing, among other things. Selecting a flood data source for a particular application requires a user to weigh the strengths and weaknesses of each source relative to the application's needs for timeliness, accuracy, consistency, coverage, and temporal/spatial resolution.

The FloodScan method includes steps to mitigate known sources of uncertainty in its passive microwave and downscaling processing steps. As a result, the uncertainties that propagate through to FloodScan's products can be counterintuitive given what we know about microwave emission and sensing processes. Here, we list some of the major underlying uncertainty types in passive remote sensing of floods, explain how they may be expected to affect flood detection accuracy in practice, and describe alternative algorithm modes available to users to prioritize rapid updates or more sensitive flood detection over automated

processing accuracy. Although this list is drawn from FloodScan processing system features, it provides examples of the general types of algorithm and flood map product design trade-offs that would generally apply across many flood remote sensing and modeling methods.

3.2.1 Flooded fraction noise and minimum detectability threshold

Any flooded fraction algorithm component (Eq. (3.6)) can contribute noise to the flooded fraction estimate. In a well calibrated algorithm, noise is just as likely to increase or decrease flooded fraction estimates relative to the true values (e.g., Fig. 3.2). As a result, the impact of noise on flood map usage depends to a large degree on whether flooding is occurring or not: when flooding is not present, flooded fraction noise can cause false positives; when flooding is present, noise mostly affects the uncertainties on the flood map's flooded/unflooded margins.

Because flooding is rare, it is important that flooded fraction algorithms suppress false positives due to noise in flood-free, or dry land, situations to avoid false alarm fatigue. FloodScan does this by applying the MDFF threshold to flooded fraction. While this conservative approach to dry land noise is most appropriate for automatic extreme flood detection and impact assessment, it is often too conservative for emergency managers, aid providers, and others who need NRT data when a recognized flood event is already developing. To address this use case, FloodScan includes a *dual flood classification* mode that ignores the MDFF threshold to map flooding based on unfiltered flooded fraction data. If used with caution, the unfiltered mode flood products can provide guidance regarding more isolated areas with potential flooding.

3.2.2 Urban areas

Urban areas present a challenging environment for flood remote sensing. Buildings and artificial surfaces create a naturally high baseline Q_{dry}, reducing the contrast between flooded and unflooded areas. Buildings also limit the total flooded area and obscure some flooding when it occurs, further reducing the flood signal. Furthermore, rapid runoff and drainage may reduce flood duration in urban areas and therefore the chance that satellite sensors will make observations while flooding is underway. Since little can be done to correct for these limitations, it is important that flood map users be aware that flooding will generally be underestimated in urban areas and take steps to infer the true extent of at-risk areas from whatever flood extent data is available.

3.2.3 Flash false positives

By removing flooded fraction flashes, the FloodScan algorithm reduces flood false positive rates at the cost of missing or delaying some true flood detections. For example, while Hurricane Harvey dropped more than 1000 mm of rain over

southeastern Texas in August 2017, microwave sensors were unable to view the surface for several days. When microwave sensors made their first rain-free observations, the flooding was so extensive that it triggered FloodScan's flash detection. As a result, the FloodScan algorithm now includes a mode that ignores flash detections. This mode is ideal for gaining situational awareness as quickly as possible as large-scale flood events unfold. However, the mode will do poorly in automated or historical analyses where independent contextual information that confirms the likelihood of major flooding may be lacking.

3.2.4 Flood duration

Remote sensing method accuracy depends on whether satellite sensors observe a flood at its peak and this in turn depends on flood duration and satellite overpass timing. The types of satellites used for microwave remote sensing (Table 3.1) have irregular overpass intervals. For example, with combined AMSR2 and GMI sensor data, an area in the mid-latitudes is observed about 3-times per day on average, with 5% of days having just one observation and about 1% of days have no observations. Furthermore, observations cannot be made through rain and ideally multi-observation averaging is needed for good noise mitigation. As a result, at least 2-day flood duration is desirable for reliable flood detection with current satellites. Clearly, the launch of more sensors suitable for flood mapping would help fill data gaps, but this seems unlikely for the foreseeable future without radical advances in microwave remote sensing technology that reduce sensor size without compromising capabilities. An alternative FloodScan processing approach handles each satellite pass separately and skips averaging. This approach produces more rapid flood maps with more frequent updating. However, as with flash false positive detection suppression, flood maps made in this mode should be treated as more preliminary until confirmed independently or by subsequent observations.

3.2.5 Microwave footprint and persistent water uncertainty

Several factors affect a passive microwave flood mapping algorithm's ability to know the exact area represented by each observation footprint: sensor pointing, footprint matching, and interpolation to an Earth grid, to name a few. Uncertainty in footprint location mainly leads to errors in footprint-average persistent open water fraction knowledge (Eq. (3.6)) and, if flooding is present, flood location. Persistent water fraction errors are largest within 5–10 km of coastlines because this is where even small footprint location errors can make large differences in flooded fraction retrievals. Multi-day flooded fraction averaging helps reduce footprint uncertainty noise to a degree but MDFF thresholds near coastlines must be larger than in inland areas to avoid frequent false positives (Fig. 3.3). As a result, even relatively large coastal floods may go undetected and unmapped. When coastal areas are a high priority for emergency management, users have the option to use the FloodScan processing mode that skips

multiday averaging and handles each satellite pass separately. However, this mode's products are useful near coastlines only in context with inland flooding or when flooding can be confirmed by other sources.

3.2.6 Downscaling: Topography and control structure uncertainty

Flooded fraction downscaling methods have inherent ambiguities arising from their underlying assumptions about the processes that control relative floodability and drive flooding over large areas. However, uncertainties in two factors—topography and control structures—affect flood map confidence in marginal areas. DEM vertical accuracies range from less than a meter for some national models to 6–9 m for global models (e.g., Yamazaki et al., 2017). Downscaling depends on relative elevation accuracy so DEM errors can affect flood maps on a point-by-point basis or over aggregate areas with hydrological connectivity. Control structures present two problems for downscaling: they may not be represented in elevation models at all and their integrity during flooding may be unknown. Approaches for managing these uncertainties include using flood depth in flooded areas and proximity to flooding in unflooded areas as confidence indices.

3.2.7 Downscaling: Pluvial versus fluvial flooding

FloodScan's downscaling method implicitly assumes that fluvial (river) flooding conditions prevail—that water flowing down topographic gradients generally has time to reach equilibrium relative to streamlines. This means that large river flooding is better depicted than small stream and pluvial flooding. The exception is when pluvial flooding occurs far from major rivers. In this case, subtle variations in topography dictate how downscaling determines the likely location of flood water instead of the larger contrasts between floodplains and uplands. The greatest uncertainties arise when pluvial flooding occurs near fluvial flooding or in flat areas where terrain features too small to be represented in DEMs control the distribution of surface water. For these cases, a probabilistic approach to flood mapping is needed to indicate that flooding is present in the area but cannot be definitively located.

4 Directions for future development

The uncertainties and limitations of the standard FloodScan product have led to new algorithmic approaches for exposing more of the underlying data's information content. Most of these approaches are geared toward times when flood events are known to be underway and therefore conservative false positive filters are largely unnecessary. For example, the flash detection and time-averaging aspects of the algorithm may be disabled to provide daily or more frequent estimates of the latest observed flood extent. Other approaches are intended to quantify in real-time how much confidence should be placed in each flooded/unflooded indication. The products demonstrated here complement

SFED, whose role would remain for automated, low noise flood detection and depiction.

4.1 Dual flood classification

A dual flood map classification (Fig. 3.6A) allows possible but less likely flooded areas to be mapped in addition to those represented in the more conservative SFED product. In this example, the *marginal* flooding class is based on downscaling of flooded fraction even where it is below MDFF. In comparison to the Landsat false color image, the marginal flood areas are a mix of (1) areas within floodplains where the flooding is apparent in the Landsat image and (2) areas that may have saturated soils but that do not appear flooded in the Landsat image. The dual flood method is most valuable when large scale flooding has already been identified (as in this case) and there is interest in identifying marginal areas that may have been temporarily or partial affected. The method may be effective in urban areas where flood signals are generally weaker (e.g., Houston in Fig. 3.3B).

4.2 Flood occurrence probability

FloodScan's flooded fraction and downscaling steps are formulated in a way that facilitates probabilistic flood mapping (e.g., Fig. 3.6B). Remember that the Boolean SFED downscaling step maps flooding everywhere $f_f > f_{f0}$ (or $f_f - f_{f0} > 0$). Assuming f_f and f_{f0} are independent normally distributed random variables with variances σ_{FF}^2 and σ_{FF0}^2, respectively, then the variance of $\Delta f_f = f_f - f_{f0}$ is given by:

$$\sigma_{\Delta FF}^2 = \sigma_{FF0}^2 + \sigma_{FF}^2 \tag{3.7}$$

With σ_{FF} and σ_{FF0} estimates on the map grid (x,y), error function evaluations provide a model for flood probability, $\Pr[\Delta f_f(x,y) \geq 0]$. In practice, flooded fraction variance may be estimated from dry land statistics and flood map validation testing; f_{f0} variance may be computed by simulating the effective DEM uncertainty on relative floodability. With this formulation, many of the flood map uncertainties discussed earlier can be quantified in one number. For example, areas where pluvial flooding is less likely but still possible may be identified in situations where the standard product would otherwise depict flooding mainly in the floodplains.

4.3 Flood depth

Flood depth (Fig. 3.6C) is a natural extension of FloodScan's downscaling process, which already incorporates topographic information. Although the depth derivation method is generalizable to any flood extent map, it works best where flooding is not inconsistent with DEM contours (Cohen et al., 2019). In brief,

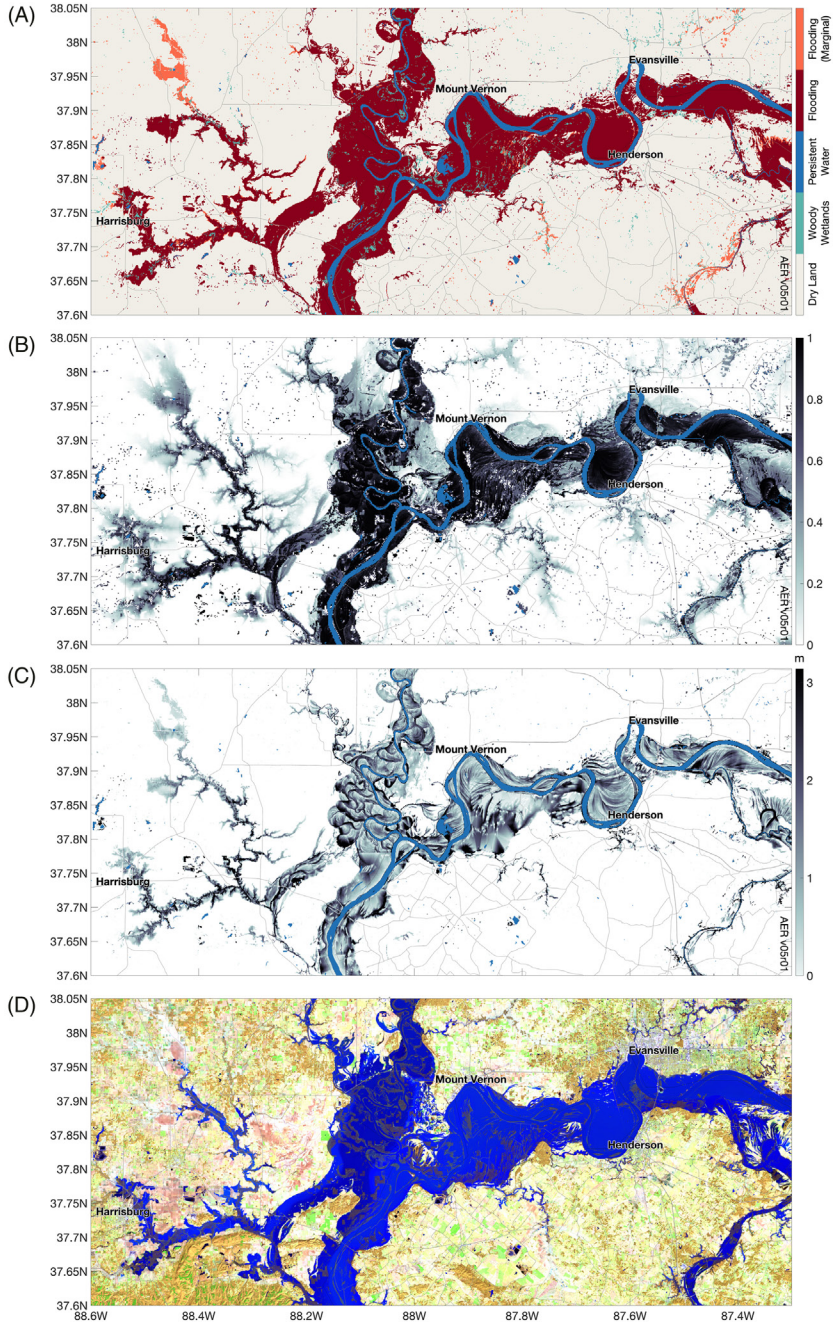

FIGURE 3.6 Advanced microwave flood mapping product examples for the same scene in Fig. 3.4. (A) Dual flood classification with the addition of a *marginal* flood category based on downscaling flooded fraction values less than MDFF; (B) flood occurrence probability; (C) flood depth derived for a flood map based on daily maximum flooded fraction; (D) Landsat false color image for comparison. *(Credit: Original)*

the method estimates flood depth by first deriving flood water height where flood edges intersect the topography and then interpolating that height over the flooded area. In this implementation, woody wetlands—which are otherwise excluded from FloodScan's downscaling process—are included in the depth interpolation step, providing a more complete flood map than SFED. Flood depth is an important index for property damage and can also serve as an index for flood likelihood—that is, the greater the flood depth the more likely that flooding in fact occurred. Flood water height itself is also valuable in its own right; it can be used at the property scale to infer the likelihood of flood impacts at various elevations.

4.4 Multi-source flood data integration

Probabilistic flood maps are the most flexible way to build up a best estimate of flooding over time from multiple data sources. A Bayesian framework, for example, allows new information like that from microwave remote sensing to update prior information like that from hydrological model forecasts. Similarly, composite flood maps can be formed from asynchronously collected remote sensing data from a variety of technologies with differing strengths and weaknesses. To build an optimal flood estimator from disparate sources, all the input data products would need to have probabilistic attributes. If feasible, the advantages for the user would be clear: a one-stop flood mapping source providing the timeliest flood maps incorporating the best available information.

5 Conclusions

Microwave remote sensing offers an alternative flood mapping perspective from other Earth observation or hydrological modeling approaches. The method's uniqueness stems from its ability to penetrate cloud cover and map flooding at night and the regularity with which microwave satellites have operated over the last two decades. Recently developed flooded fraction and downscaling algorithms have addressed many of the challenges for reliably and consistently producing accurate high-resolution flood maps from coarse resolution microwave data. A key remaining challenge is that of flood map ambiguity—how it may be reduced and represented but also how it can be communicated to end users for optimal benefit to their applications.

The set of four microwave flood mapping products described in this chapter demonstrate how a diversity of metrics can be created from a single observation type to provide users with a more complete picture of flood conditions than a Boolean flood map alone can do. Starting from a baseline high-confidence flood map (SFED), the *marginal* flood indicator provides flood maps useful in areas where, for example, there may also be insurance claims that independently confirm flood occurrence; flood depth provides a key index for damage assessment; and flood occurrence probability provides a mechanism by which users can

select their own tolerances for false negatives and false positives. The association of these or similar metrics with other flood mapping products would promote a more nuanced view of flood depiction for applications and may facilitate flood data integration across technologies.

Acknowledgments

This work was supported by the African Risk Capacity/World Food Programme (contracts QRSA-I01B-13 and QRSA-040-16) and the NASA Terrestrial Ecology Program (NNH10CC61C) and Terrestrial Hydrology Program (NNH13CH27C).

References

Brakenridge, G.R., Kettner, A., Syvitski, J., Overeem, I., De Groeve, T., Cohen, S., Nghiem, S.V., 2016. River and reservoir watch version 3.5, Experimental Satellite-Based River Discharge and Reservoir Area Measurements: Technical Summary. Available from: http://floodobservatory.colorado.edu/technical.html.

Cohen, S., Raney, A., Munasinghe, D., Loftis, J.D., Molthan, A., Bell, J., Rogers, L., Galantowicz, J., Brakenridge, G.R., Kettner, A.J., Huang, Y.-F., Tsang, Y.-P., 2019. The Floodwater Depth Estimation Tool (FwDET v2.0) for improved remote sensing analysis of coastal flooding. Nat. Hazards Earth Syst. Sci. 19, 2053–2065, https://doi.org/10.5194/nhess-19-2053-2019.

De Groeve, T., 2010. Flood monitoring and mapping using passive microwave remote sensing in Namibia. Geomatics Nat. Hazards Risk 1, 19–35, https://doi.org/10.1080/19475701003648085.

Galantowicz, J.F., Picton, J., Root, B., 2018a. ARC Flood Extent Depiction Algorithm Description Document: AFED Version V05R00, AER document P2181-AFM-ADD-V05R00-R00, AER. Lexington, MA, USA.

Galantowicz, J.F., Picton, J., Root, B., 2018b. ARC Flood Extent Depiction Algorithm Performance Document: AFED Version V05R00, AER document P1908-AFM-APD-V05R00-R00. AER, Lexington, MA, USA.

Hansen, M.C., Potapov, P.V., Moore, R., Hancher, M., Turubanova, S.A., Tyukavina, A., Thau, D., Stehman, S.V., Goetz, S.J., Loveland, T.R., Kommareddy, A., Egorov, A., Chini, L., Justice, C.O., Townshend, J.R.G., 2013. High-resolution global maps of 21st-century forest cover change. Science 342, 850–853, https://doi.org/10.1126/science.1244693.

Kugler, Z., and De Groeve, T., 2007. The Global Flood Detection System. Office of Official Publications of the European Communities, Luxembourg.

Nobre, A.D., Cuartas, L.A., Hodnett, M., Rennó, C.D., Rodrigues, G., Silveira, A., Waterloo, M., Saleska, S., 2011. Height above the nearest drainage—a hydrologically relevant new terrain model. J. Hydrol. 404, 13–29. https://doi.org/10.1016/j.jhydrol.2011.03.051.

Pekel, J.-F., Cottam, A., Gorelick, N., Belward, A.S., 2016. High-resolution mapping of global surface water and its long-term changes. Nature 540, 418–422, https://doi.org/10.1038/nature20584.

Prigent, C., Papa, F., Aires, F., Rossow, W.B., Matthews, E., 2007. Global inundation dynamics inferred from multiple satellite observations, 1993-2000. J. Geophys. Res. 112, D12107, https://doi.org/10.1029/2006JD007847.

Ulaby, F.T., Moore, R.K., Fung, A.K., Ulaby, F.T., 1981. Microwave Remote Sensing Fundamentals and Radiometry, vol. 1. In: Microwave Remote Sensing. Addison-Wesley [u.a.], Reading, Mass.

Yamazaki, D., Ikeshima, D., Tawatari, R., Yamaguchi, T., O'Loughlin, F., Neal, J.C., Sampson, C.C., Kanae, S., Bates, P.D., 2017. A high-accuracy map of global terrain elevations: Accurate Global Terrain Elevation map. Geophys. Res. Lett. 44, 5844–5853, https://doi.org/10.1002/2017GL072874.

Chapter 4

River Flood Modeling and Remote Sensing Across Scales: Lessons from Brazil

Ayan Santos Fleischmann[a], João Paulo Fialho Brêda[a], Conrado Rudorff[b], Rodrigo Cauduro Dias de Paiva[a], Walter Collischonn[a], Fabrice Papa[c,d] and Mariane Moreira Ravanello[e]

[a]Federal University of Rio Grande do Sul, Institute of Hydraulic Research (IPH), Porto Alegre, Rio Grande do Sul, Brazil; [b]National Center for Monitoring and Early Warning of Natural Disasters (Cemaden), São José dos Campos, São Paulo, Brazil; [c]University of Toulouse, LEGOS (IRD, CNRS, CNES, UPS), Toulouse, France; [d]University of Brasília (UnB), IRD, Institute of Geoscience, Brasília, Federal District, Brazil; [e]Agência Nacional de Águas e Saneamento Básico, Brasília, Brazil

Highlights

- A systematic literature review of river flood model applications in Brazil in the context of remote sensing is performed;
- Recent advances on validation and adjustment of models using remote sensing data are presented;
- Perspectives on the use of flood models and remote sensing data for flood risk management in Brazil are discussed.

1 Introduction

River overbank inundation is a key phenomenon of the terrestrial water cycle that regulates important biogeochemical processes and provides crucial ecosystem services in natural wetlands. In South America, major wetlands as the Pantanal and those in the Amazon Basin (Fig. 4.1) have drawn research attention of the scientific community for decades. Due to its large river systems, it has been called the "fluvial continent" (Kandus et al., 2018; Neiff et al., 1994), and many of the associated natural wetlands have been inventoried (Junk et al., 2015; Kandus et al., 2017; Ricaurte et al., 2019). Riverine flooding is also often related to major natural hazards due to human settlements on floodplains (Bates et al., 2014). Around 11 million people were affected by floods between 1970 and 2019 in Brazil (CRED, 2019) and, in general, flood risk has been increasing over the continent (Vörösmarty et al., 2013) besides other growing

Earth Observation for Flood Applications. http://dx.doi.org/10.1016/B978-0-12-819412-6.00004-3

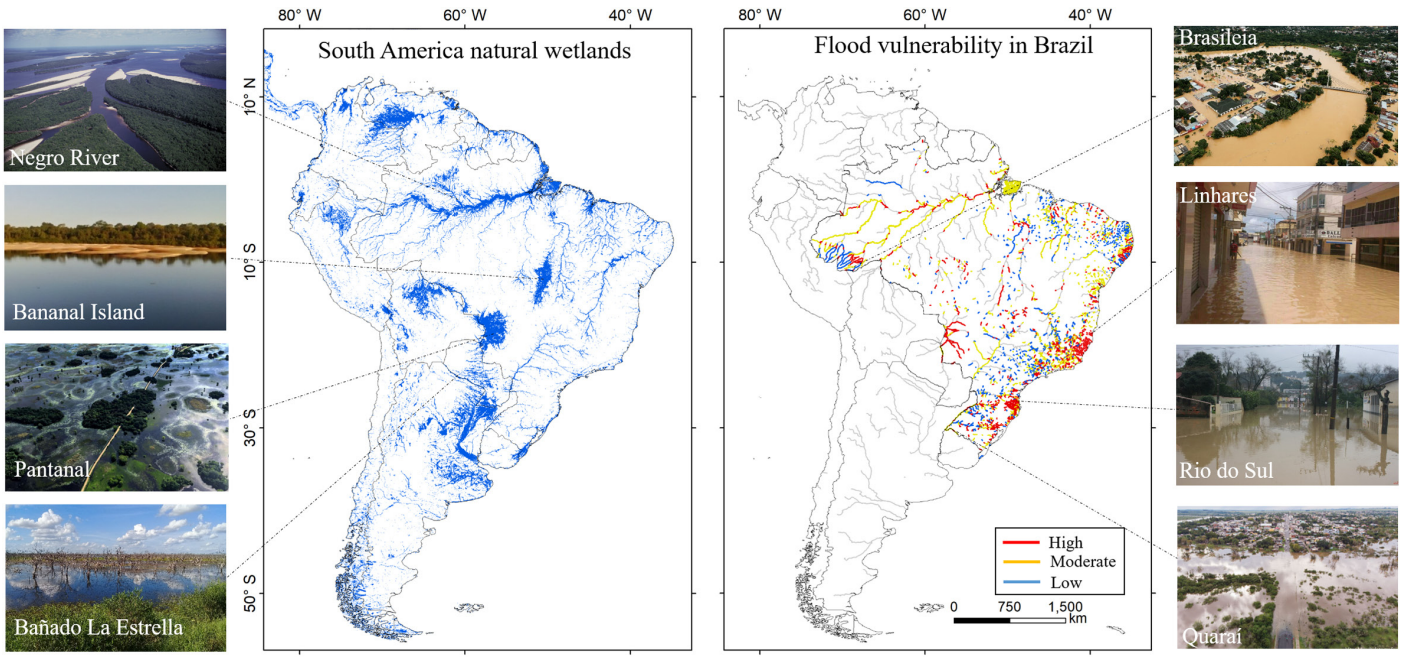

FIGURE 4.1 (A) Floodable areas in South America according to GIEMS-D15 database (Fluet-Chouinard et al., 2015), and the location of some large natural wetland systems. (B) Qualitative flood vulnerability in Brazilian rivers according to ANA (2014), and the location of some vulnerable cities: Brasiléia (Acre River), Linhares (Doce river), Rio do Sul (Itajaí-Açu river), and Quaraí (Quaraí river). *(All figures created by the authors except for those related to: Negro River (Montero and Latrubesse, 2013), Pantanal (Bergier et al., 2019), Brasileia (Sérgio Vale/Secom; available at <https://fotospublicas.com/enchente-historica-atinge-mais-de-800-familias-na-regiao-de-fronteira-com-bolivia//>; License CC BY-NC 2.0), Linhares (Corpo de Bombeiros/ES; available at <https://fotospublicas.com/corpo-de-bombeiros-espirito-santo-realiza-resgates-e-transporte-de-alimentos-para-desabrigados-das-enchentes/>; License CC BY-NC 2.0), Rio do Sul (Homero Buzzi/SDR Rio do Sul; available at <https://fotospublicas.com/chuvas-castigam-cidades-de-santa-catarina/>; License CC BY-NC 2.0) and Quaraí (courtesy by Vitor Mirailh Pereira).)*

water management issues. South America also has highly managed river systems with many large dams, such as the Magdalena and the La Plata basins—in the latter, most of the Brazilian population lives and the largest world reservoir in terms of energy production, the Itaipu Dam, is located (Angarita et al., 2017; Tucci and Clarke, 1998). In the coming decades, many new dams are planned to be built in the continent, as is the case of the Amazon River Basin (Anderson et al., 2018; Latrubesse et al., 2017).

River flood models have become fundamental tools for the management and comprehension of floods in complex river-wetland-reservoir systems. Recent developments have led to hydraulic simulation methods that are able to accurately represent the hydrodynamics of the river-floodplain-reservoir continuum that exists in many large basins (Fleischmann et al., 2019a; Shin et al., 2019), at both 1D and 2D dimensions (Mateo et al., 2014; Sampson et al., 2015; Schumann et al., 2016). Flood risk information at different scales may have distinct requirements of output variables, accuracy, and spatial and temporal resolutions, and discharge estimates are often not enough to describe flood dynamics and mitigate floods impacts. Variables other than discharge can be necessary, as water level (at-a-station or longitudinal profiles), flood extent and storage, and river velocities, or measures that translate discharges into impact estimates (e.g., expected damage associated to a given flood frequency). Understanding the uncertainty of information produced by flood models before usage is important (Hoch and Trigg, 2018; Trigg et al., 2016). Flood hazard mapping with high accuracy and resolution is required for flood mitigation projects at local scales, however, it is generally sparsely available over the globe. Regional to global scale flood models are not intended to replace more detailed local mapping, but to provide quick information on whether a location is in or out of a potential flood zone, and may be particularly helpful in areas of the world where other flood maps or resources are not readily available. The continuous spatial coverage offered by large scale models is useful for other purposes, such as flood mitigation planning by national governments, world agencies, and NGO's; integrated assessment of the effects of reservoir on downstream floodplains; and assessments of climate change impact on regional flood risk.

Flood models require hydrometric, land cover, and topographical data, which are obtained through different techniques, from ground measurements to remote sensing and hydraulic model calibration. Topographical data define the geometry of rivers and floodplains, and hydrometric observations are used as model inputs (boundary conditions) and for calibration/validation (e.g., with observations of water surface elevation, high flood marks, or flood extent maps). Remote sensing is playing an important role in improving databases for regions such as Brazil, characterized by the low density of suitable data for inundation modeling. Over the past 2 decades, the Brazilian National Hydro-meteorological Network (http://www.snirh.gov.br/) operated by agencies as ANA (National Water and Sanitation Agency) and CPRM (Brazilian Geological Survey) has expanded in climatological and real-time monitoring of river stage and discharge, river cross-section profiles, and altimetry referencing of stream gauges.

This was an important milestone that fostered positive feedbacks of improvements in both remote sensing and hydrological modeling products. Indeed, Brazilian river systems (and Amazon in special) were the focus of many developments in the field of remote sensing of wetlands (Uereyen and Kuenzer, 2019), mainly due to the size of some rivers and their particular environments (Kandus et al., 2018), leading to new methods for the estimation of flood extent based on active and passive microwave and radar data (Aires et al., 2013; Arnesen et al., 2013; Hamilton et al., 2002; Hess et al., 2003, 2015; Sippel et al., 1994), water levels from radar altimeters (Calmant et al., 2008; Paris et al., 2016; Santos da Silva et al., 2010), and water storage variation from GRACE (Gravity Recovery And Climate Experiment), InSAR (interferometric synthetic aperture radar), and other techniques (Alsdorf et al., 2000, 2007, 2010; Cao et al., 2018; Frappart et al., 2008; Lee et al., 2020; Papa et al., 2013).

Recently, the increase in production of high resolution and accurate DEM's from stereophotogrammetry, SAR interferometry, or LiDAR (light detection and ranging) has been the main driver of progress for inundation modeling at the local scale, while global bare earth DEM's with processing for vegetation removal set up new opportunities for flood modeling at larger scales (O'Loughlin et al., 2016; Yamazaki et al., 2017). Estimation of river geometry is also improving considerably (Allen and Pavelsky, 2018; Frasson et al., 2019). For large scales, machine learning and cloud processing enabled the creation of global width databases from remote sensing data (Allen and Pavelsky, 2018; Yamazaki et al., 2019).

Capabilities for water level monitoring of rivers and wetlands are also increasing (Calmant et al., 2008). For instance, while current radar altimetry missions as Sentinel-3 and Jason-3 are mainly used on large water bodies and have temporal resolution of 30 and 10 days, respectively, ICESat-2 (LiDAR altimeter technology) has a lower intertrack distance and smaller footprints which permits accurate observation over narrower rivers (Fig. 4.2B). However, ICESat-2 repeats its orbit every 91 days and LiDAR data are susceptible to weather conditions (i.e., clouds). The future Surface Water and Ocean Topography (SWOT) satellite mission will be different from these nadir altimetry sensors due to its swath mapping radar interferometer, and will provide not only surface water level but also surface water extent measurements. It is expected to observe most river reaches over 100 m width and 10 km long with a level precision of 10 cm, at least once every 21 days (Biancamaria et al., 2016; Prigent et al., 2016), providing time and spatial continuous observations of rivers and their respective floodplains across scales (Fig. 4.2C).

Finally, the number of high-resolution flood extent products is also increasing. Dynamic databases at regional to global scales are now available, based on downscaling of original coarse resolution products from multisatellite missions (Aires et al., 2017) or passive microwave data (Parrens et al., 2019), or classification of optical imagery as Landsat (Pekel et al., 2016). Although high-resolution flood extent extraction from SAR data requires adjustment for each application, it has been improved considerably through missions as

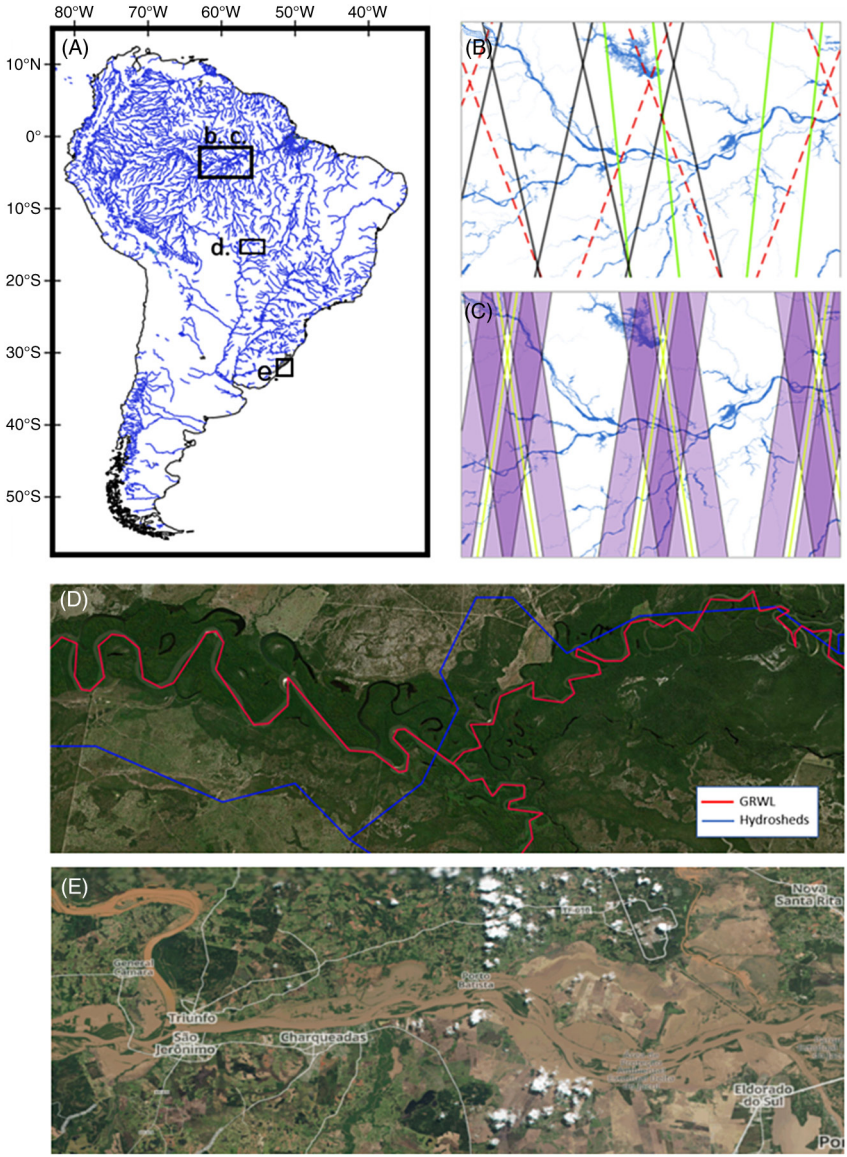

FIGURE 4.2 Examples of available remote sensing products for flood monitoring and modeling. (A) River network in South America from the GRWL database *(blue lines)*; (B) a sample of 10-days interval groundtracks of the nadir altimetry missions ICESat-2 *(green)*, Sentinel-3 *(black)*, and Jason-3 *(red)*; (C) a sample of 10-days interval swath *(purple)* and nadir *(light green)* groundtracks of SWOT mission. (D) Comparison between the GRWL *(red)* and the 500 m resolution based HydroSheds *(blue)* drainage networks. (E) RapidEye (6.5 m spatial resolution) image of the 2015 flood in the Jacuí River, Southern Brazil (available at <https://www.planet.com/explorer/>; license CC BY-SA 4.0). Location of figures B, C, D and E are presented in Figure A.

JERS-1 and its successor ALOS-PALSAR (Arnesen et al., 2013; Ferreira-Ferreira et al., 2015; Hess et al., 2015). New optical data as those from RapidEye and CubeSat also promise a revolution in terms of spatial and temporal resolution for monitoring floods extent dynamics (Santilli et al., 2018) (Fig. 4.2E).

In this chapter, we address the complementarity between flood models and remote sensing at different scales in the Brazilian context, considering some recent scientific developments carried out in Brazilian rivers. The chapter is structured as follows. First, a systematic literature review of flood model applications in Brazil in the context of remote sensing is presented (Section 2). Some recent experiences on the use of remote sensing for flood modeling in Brazil are then presented (Section 3). Finally, a discussion is provided on the current status of flood hazard mapping and real-time monitoring and forecasting in Brazil at different scales, followed by some perspectives on the use of remote sensing to improve it (Section 4).

2 Literature review on river flood modeling in Brazil

In order to understand how river flood models have been applied to Brazilian river systems in terms of model type, study area, and use of remote sensing data, a systematic literature review was performed with a Scopus search (Elsevier, 2019) for articles published since 2000. Considering that the definition of a river flood model is not straightforward, only those studies involving an explicit analysis of flood extent simulated by process-based hydrological or river hydraulic models were considered. This means that articles addressing only variables as water level or discharge were not included. In the context of this chapter, we define by river flood model: (1) a process-based hydrological model that has any kind of flood routing able to represent inundation processes (i.e., from a simple kinematic wave model coupled to an inundation method to more complex flow routing methods); or (2) a hydraulic model that considers the shallow water equations (or its simplifications) at any dimension (1D, 2D, or 3D). Some studies with lake (both natural and manmade systems) and estuary hydrodynamic simulation that did not focus on flood dynamics were not considered here, since they did not analyze flood extent estimation, and the modeled flooded area domain was usually predefined.

The non-exhaustive search was performed by looking for research articles containing words in their abstract/title/keywords related to: (1) flood modeling (hydrodynamic model, hydrodynamic simulation, hydraulic model, hydraulic simulation, inundation, flow routing, flood, wetland, and their variants); and (2) Brazilian regions (Brazil, South America, main hydrological regions according to Brazil's National Water and Sanitation Agency—ANA, the Amazon major basins, and their variants). Articles from subject areas with small relevance for floods in the context of this chapter were not considered (e.g., medicine), and a few articles of notable relevance that were not obtained with the proposed search framework were manually included. Besides, all articles in the Brazilian Journal of Water Resources (RBRH; "*Revista Brasileira de Recursos Hídricos*") archive, that involved flood models, were assessed.

Initially, around 2700 research articles were obtained, which were then manually filtered to consider only those with flood extent analysis, yielding 55 studies (the complete list is provided as Supplementary Material S1). This analysis does not include consultancy reports and other non-research articles and activities, which may alter to some extent the conclusions on how river flood models have been applied in Brazil. To address it, in Section 4 we describe some current operational and practical engineering uses of flood models and remote sensing in Brazil.

There has been a clear temporal increase in publications related to flood model applications in Brazil (Fig. 4.3A), with 40% of the studies being published since 2016. Only 33% of the papers focused at local scales (i.e., city or reach scale), while global and regional applications were more common. This figure may be biased since global models papers that do not explicitly mention a

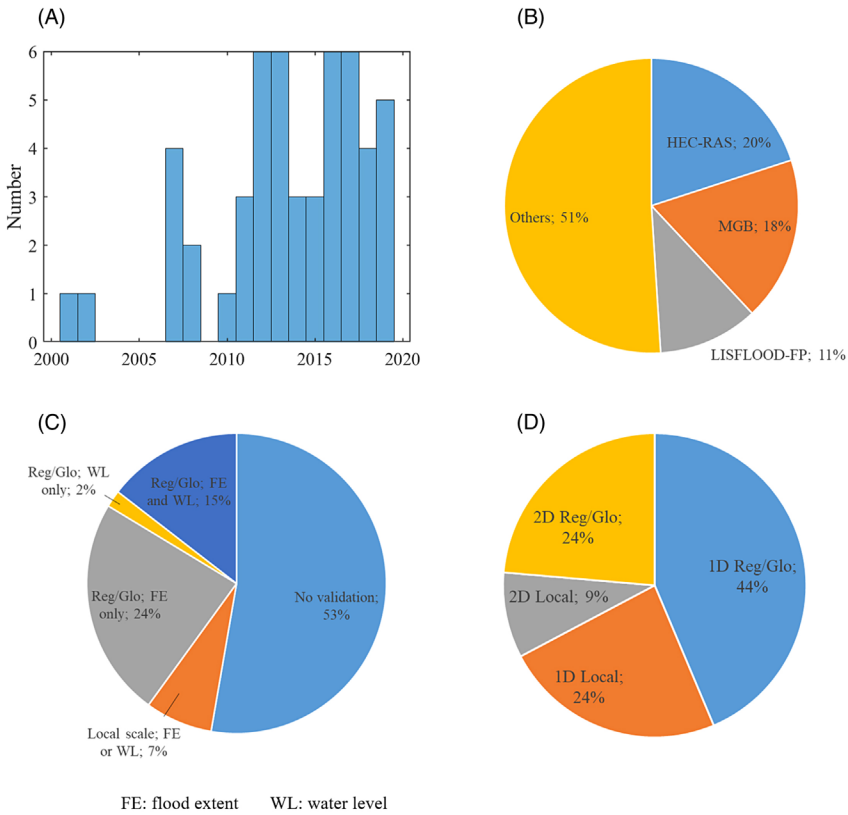

FIGURE 4.3 Summary of publications since 2000 that analyzed flood extent estimated by river flood models in Brazil. (A) Number of articles published per year. (B) Main models used. (C) Validation with remote sensing datasets (water level or flood extent) for applications at different scales (local; regional; and global (Reg/Glob)). (D) Dimensionality (1D or 2D) of applications at different scales (local; regional; and global (Reg/Glo)).

Brazilian region was not considered in the analysis. In the same way, there may have been international research articles with case studies in Brazil that did not mention it in the abstract/title/keywords.

The most commonly used models in Brazil are HEC-RAS (20%), MGB (18%), and LISFLOOD-FP (11%) (Fig. 4.3B). HEC-RAS has been the main model for applications at local scale (56% of the local applications). Regarding model dimensionality, most of the papers (68%) involved 1D modeling, and only 24% of the local scale applications used 2D modeling (Fig. 4.3C). This is interesting since many recent models have been developed worldwide to allow a relatively easy setup of 2D models, especially for urban areas (e.g., LISFLOOD-FP and HEC-RAS 2D) (Brunner et al., 2015; Sosa et al., 2020).

By far, the Amazon region is the most studied area in Brazil (40%), and many of these articles focused on understanding flooding processes in very large wetlands and their impacts on biogeochemical cycles (53% of all articles used this justification). Some of these studies have considered the Amazon as a proof-of-concept test case for large scale hydraulic modeling and remote sensing data assimilation (Brêda et al., 2019; Wilson et al., 2007), especially because of the overall pristine regions that are still existent, the global relevance of the Amazon system, and the large dimensions of its rivers that allow a good satellite data use. For instance, Wilson et al. (2007) were the first to set up a hydraulic model to a very large domain, and applied it to a 240 × 125 km area of the Central Amazon. On the other hand, there are many other large wetlands in Brazil (Fig. 4.1) that still require a better comprehension of their flood dynamics and provide equally challenging modeling difficulties, for example, the huge Pantanal wetlands, which have been addressed by a few flood models only (e.g., Bravo et al., 2012; Paz et al., 2010).

Remote sensing has been widely used in flood models, especially for estimation of floodplain topography with DEM's. Regarding validation of simulated flood extent with remote sensing, it depends on the scale. Within the analyzed articles, only three did it at local scale (Alcoforado and Cirilo, 2001; Pinel et al., 2019; Rudorff et al., 2014a). More must be done in this sense for tackling flood hazard at the scale of cities. On the other hand, regional scale validation has been intensively carried out (Luo et al., 2017; Paiva et al., 2013a; da Paz et al., 2011; Wilson et al., 2007; Yamazaki et al., 2011), especially for the Amazon region and with the products by Prigent et al., 2007 (GIEMS) and Hess et al. (2003). It was found that 35% of all studies involved quantitative model assessment with metrics as the Critical Success Index (CSI, also called Fit metric; Bates and De Roo, 2000), while 9% adopted a qualitative assessment (e.g., visual comparison without quantitative comparison between observed and simulated estimates). Other remote sensing data have also been used, as water levels derived from satellite altimetry. Fig. 4.3C shows that 47% of the studies involved validation of either flood extent or water level. It was also shown that 41% of the studies used one of the two types of observations for validation of regional/global scale models. Interestingly, only a few combined both

information (17% of the papers), and this sets the necessity of better validating flood models with multiple variables. The main data source of altimetry used is Hidroweb-Theia (available at http://hydroweb.theia-land.fr/?lang=en&), which contains hundreds of water level time series obtained at virtual stations worldwide. Looking for other studies applying satellite altimetry to flood models in Brazil that do not analyze simulated flood extent maps (which were not included in this review), there are just a few additional cases, with applications on the Amazon Basin (Garambois et al., 2017) and the whole South American continent (Emery et al., 2018; Siqueira et al., 2018).

A large part of the studies (47%) justified their research for better understanding flood hazard, especially in the case of local scale studies. However, more must be done in this context, and the country needs its own studies regarding flood risk at different scales, given its particularities related to being located in a tropical region with complex river systems, the remoteness of some urban centers, and the ungauged character of many rivers. Flood risk studies that are locally relevant for the Brazilian context are missing, especially considering the great opportunities with remote sensing data. Consultancy projects on flood hazard usually does not use remote sensing data except for DEM's, possibly given the difficulties of obtaining it at very detailed, reach scales: many images are not free, or are not available for quick floods that recede within a few days. Furthermore, many water resources engineers are still not trained for the use of advanced remote sensing observations.

In the past, hydrological models (i.e., simple rainfall-runoff models) were mainly used to predict river discharges, but now their current capabilities allow users to assess other variables as water levels, flood extent, and water velocity at the basin or larger scales (Fleischmann et al., 2019b; Schumann et al., 2013, 2016; Yamazaki et al., 2012). However, our analysis suggested that a few studies addressed flood extent, and to a much lesser extent variables as flood storage and water velocity (few exceptions do exist, as Dias et al. (2011) and Pinel et al. (2019)), and we should move forward to better estimate them (Chávarri et al., 2013; Schumann et al., 2016). Finally, we highlight that here we only considered flood models in the sense of process-based hydrological/hydraulic models, but there are many alternative flood mapping methods being applied and developed in Brazil (Nobre et al., 2016; Speckhann et al., 2018). Regional to national scale assessment on floods have also been developed, for example, related to flood trends and non-stationarity, and regionalization techniques (Bartiko et al., 2019; Cassalho et al., 2019; Lima et al., 2015, 2017; Steffen and Gomes, 2018).

3 Improving river flood models with remote sensing data across scales: some lessons from Brazil

The following sections summarize some recent studies on the application of river flood models in Brazil in the context of the satellite era, from model validation (Section 3.1) to parameter estimation (Section 3.2), and data assimilation

and model calibration (Section 3.3). Section 3.4 then provides cross-scale comparison studies between flood models, which provide valuable information on the needs of improvements for large scale models.

3.1 Model validation

Most efforts of river flood model validation with remote sensing have been performed with water levels (especially nadir satellite altimetry) and flood extent data (usually based on optical, passive microwave, and SAR sensors), and some experiences in Brazil are presented here. Most studies using satellite altimetry were performed at regional scale for natural wetlands in the Amazon Basin. These wetlands can be classified as river floodplains and interfluvial wetlands (less connected to rivers and associated to local runoff). Each wetland type requires different processing techniques (Seyler et al., 2009), and although most studies focused on main river floodplains (Paiva et al., 2013a; Siqueira et al., 2018; Trigg et al., 2009; Yamazaki et al., 2012), recent cases have performed the validation of interfluvial wetlands dynamics (Fleischmann et al., 2020a) (left panel in Fig. 4.4A). The latter study compared 1D and 2D versions of the MGB hydrological-hydrodynamic model (Collischonn et al., 2007) to simulate complex wetland systems, and showed the overall satisfactory capacity of 1D models to represent river floodplains as the Branco (validation with altimetry from Envisat), and their difficulties in simulating interfluvial wetlands that are more dependent on local runoff and have a lower level amplitude (validation with Sentinel3-A SRAL mission). On the other hand, at the continental scale, a total of 880 virtual stations along rivers from THEIA/Hydroweb website was used for validation of the 1D MGB model application in South America, showing the potentiality of these data, in addition to in situ gauges, for the Amazon, Orinoco, and La Plata basins (Fig. 4.4A) (Siqueira et al., 2018). These results confirm what was shown from the review in Section 2, in the sense that just a few local scale models used satellite altimetry data for model validation. Many river reaches under flood risk are associated to fast hydrographs, with rising limbs occurring within a few hours, which hampers the use of many altimetry data because of the too long repeat cycle. Small rivers are also difficult to be monitored, and new products as ICESat (Ice, Cloud and land Elevation Satellite) may be interesting given their higher accuracy (in detriment of low temporal resolution), for example, for estimating water surface slope. ICESat was used for validating the simulated river-floodplain-reservoir continuum along Itaipu Dam in Paraná River (Fleischmann et al., 2021), what is very promising given recent developments in large scale hydrodynamic modeling of reservoirs (Fleischmann et al., 2019a).

Remotely sensed flood extent data have also been used mainly for regional to continental scale applications. One exception is the case study by Rudorff et al. (2014a), who validated the local inundation extent predictions using remotely sensed flood maps produced by Arnesen et al. (2013) for the Curuai

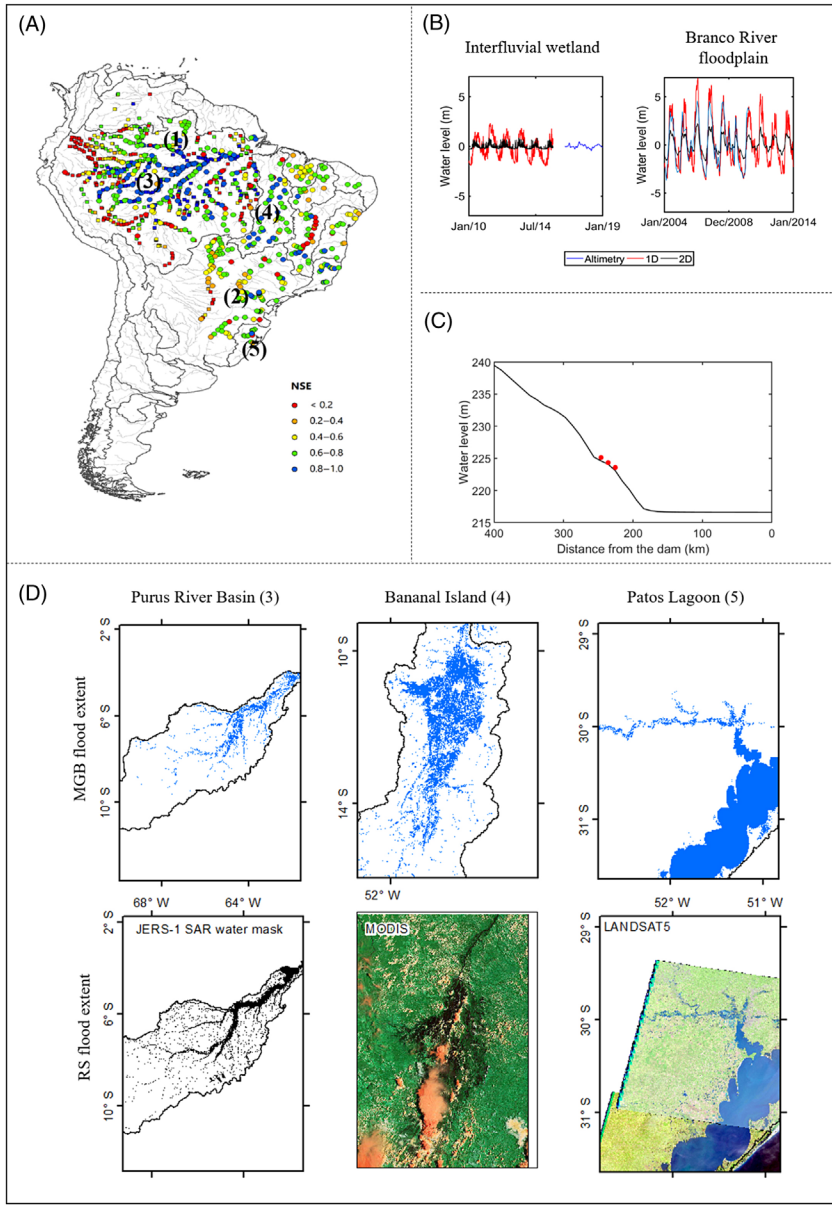

FIGURE 4.4 Validation of MGB model water levels for (A) South America (Siqueira et al., 2018), where *squares* refer to satellite altimetry and *circles* to in situ data, and (B) Negro River Basin (Amazon), where two locations are presented (interfluvial wetland and Branco river floodplain) (Fleischmann et al., 2020a). (C) Longitudinal water level profile simulated with the MGB model along Itaipu dam with validation from ICESat data (Fleischmann et al., 2021). (D) Simulated flood extent with MGB model in the Bananal Island, Purus River Basin, and Patos Lagoon regions. The regions are located in Figure A. *(Figures created by the authors.)*

floodplain in Central Amazon. More attempts should be done by the Brazilian community to validate flood hazard models with remote sensing data (e.g., Sentinel-1 SAR data). At the regional scale, examples include validation of flood extent in the natural wetlands of Pantanal (da Paz et al., 2011), Bananal Island (Pontes et al., 2017), Patos Lagoon (Lopes et al., 2018), and Amazon (Paiva et al., 2013a), with estimates from different satellites (Fig. 4.4B). These validation experiments showed the complementarity of both remote sensing and modeling approaches in estimating flood extents—even if there are still high uncertainties related to both approaches.

3.2 Direct parameter estimation

Remote sensing is capable to provide direct estimation of parameters as river length, river width, and floodplain topography. For large rivers, water masks based on optical imagery (e.g., 30 m Landsat images) have been developed (e.g., Global Surface Water/GSWE database; Pekel et al., 2016) and used to infer river widths (e.g., GRWL database; Allen and Pavelsky, 2018). For small rivers, however (e.g., < 30 m), other methods are required, and hydraulic geometry theory (i.e., geomorphic relationships) has been used to fulfill it (Beighley et al., 2009; Neal et al., 2012; Paiva et al., 2013a; Yamazaki et al., 2012). Fig. 4.5 presents an example of geomorphic relations derived for different sub-basins of the Upper Paraná River Basin in Brazil, based on the relationship between drainage area and width, which in turn was computed by dividing, for each unit-catchment that comprises the basin, its surface water (GWSE, Fig. 4.5B) by its river length. For large rivers, GRWL widths are available and an example is provided in Fig. 4.5C.

In current hydrodynamic models, channel length is usually directly estimated through the river network formed by a flow direction map. In some cases, upscaling (Yamazaki et al., 2009) and meandering factors (Oki and Sud, 1998) were used to adjust these estimates. However, accurate estimation of river length is important to better predict water surface slopes and other fluvial parameters (Frasson et al., 2019), and the inclusion of better estimates as those provided by GRWL and MERIT-Hydro has the potential to improve flood models. Fig. 4.2D shows a comparison for an area in the complex Pantanal wetlands in Central Brazil between the recent GRWL drainage in comparison to a version of Hydrosheds (Lehner et al., 2013) based on a 500 m flow direction map, highlighting the capabilities of the new high-resolution databases.

Floodplain topography can also be directly estimated with DEM's. Rudorff et al. (2014a) studied a 120×60 km section of the lower Amazon River with a thorough application of ground-survey and remote sensing data to run hydraulic simulations and assess uncertainties in predictions of water level, inundation extent, and river-floodplain exchanges. They identified that a bias in SRTM (-4.4 m for the lower Amazon floodplain near Óbidos) due to the residual motion error of the interferometric baseline was an important source of error in

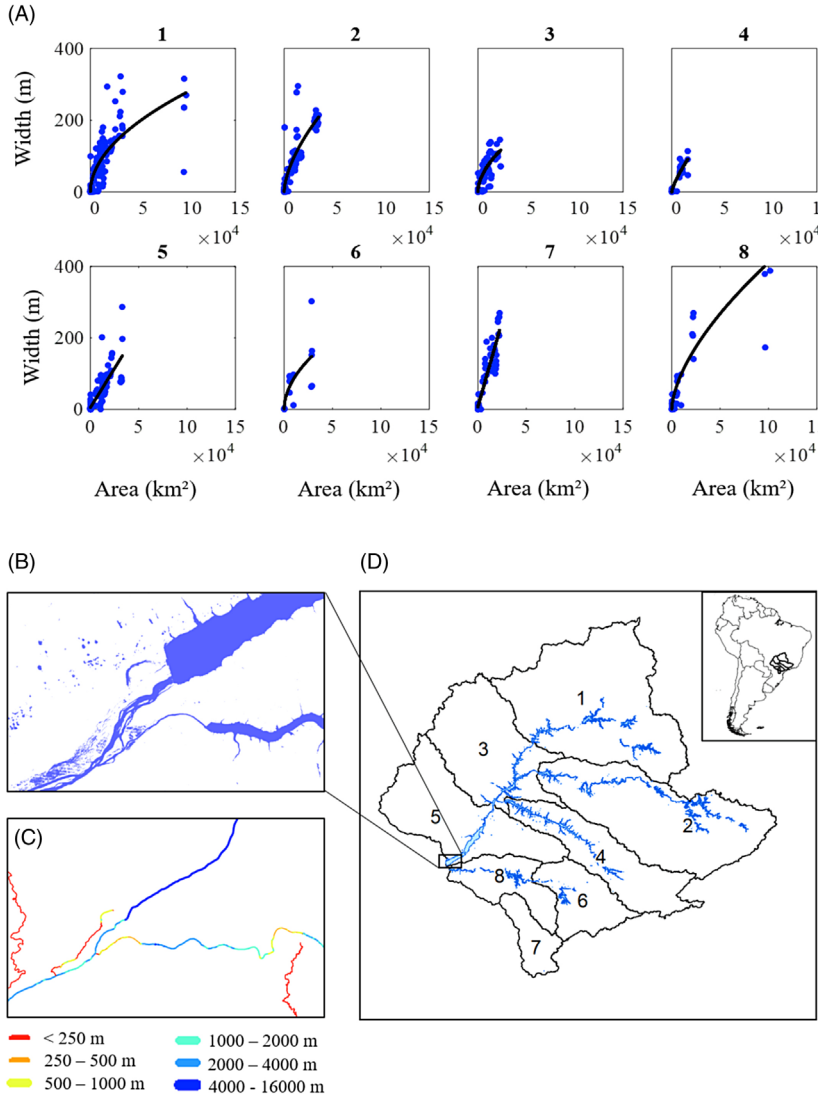

FIGURE 4.5 (A) Geomorphic relationships between river width and drainage area for different sub-basins of the Upper Paraná River Basin based on the GSWE (Global Surface Water Extent) water mask. (B) Detail of the GSWE mask and (C) the GRWL width database for the region of the confluence between Paranapanema and Paraná mainstem rivers. (D) Location of the study areas in the Upper Paraná River Basin. *(Figures created by the authors.)*

hydraulic simulations. They used satellite altimetry data (ICESat GLA14 land product) as an independent ground elevation reference for SRTM error assessment over the floodplain. These findings became important motivations for efforts of further corrections in SRTM at a global scale (Yamazaki et al., 2017).

In turn, floodplain roughness coefficients were spatially assigned through a land cover map produced based on time series of Radarsat-1 S2 and complementary Landsat TM data (Silva et al., 2010). After careful corrections to SRTM and merge with data from an extensive bathymetry survey, Rudorff et al. (2014b) achieved accurate representation of the inundation dynamics in terms of inundation extent, water surface elevation, overbank, and channelized river-floodplain exchange flows. The simulations were then applied in studies of floodplain hydrology (Rudorff et al., 2014b), sediment fluxes (Rudorff et al., 2018), and lake hydrodynamics (Augusto-Silva et al., 2019).

Another study (Fassoni-Andrade et al., 2020) proposed a new methodology to estimate floodplain topography from a combination of flood extent frequency and water level duration curves, assuming that a given pixel will have a bottom height equal to the water level whose probability of exceedance (from the duration curve) is equivalent to the flood frequency of that pixel. The authors tested it by using the GSWE and water level data (in situ and satellite altimetry) for two natural lakes and 12 hydropower reservoirs in Brazil. On the natural lakes, the root mean squared deviation (RMSD) of bed elevation was 0.18 m in lake Poopó (Bolivia) and 1.4 m in lake Curuai (Amazon basin), while for reservoirs, the relative RMSD was about 6%. The floodplain topography obtained with this new methodology is now being applied to improve river flood modeling.

3.3 Data assimilation and model calibration

Depth and roughness parameters are not directly observed through remote sensing. Thus, methods have been developed to indirectly estimate channel effective depth using satellite altimetry, by, for example, inverting hydraulic equations (Garambois and Monnier, 2015; Tourian et al., 2017) and assimilating altimetry data into hydrodynamic models using ensemble approaches (Yoon et al., 2012). Brêda et al. (2019) recently showed how altimetry data can be assimilated to adjust parameters as bed elevation and roughness, in a large scale hydraulic model of a 1100 km flat reach of the Madeira River in the Amazon (slope ~3 cm/km; Fig. 4.6A). The authors proposed a method to explicitly estimate errors covariance (thus avoiding an ensemble approach) for the Kalman Filter step, using hydraulic traditional concepts as backwater effects and the Manning's equation. The Kalman Filter with explicit covariance performed similarly to a global optimization algorithm used for model calibration, which is more computationally expensive. The method was able to reduce water surface elevation errors from 5 to 1.5 m, which is crucial for regional/global flooding simulations. The authors tested different satellite altimetry missions (Envisat, ICESat-1, and Jason-2) and inter-track distances proved relevant to the assimilation performance. Jason-2 maximum inter-track distance is about 315 km and its performance was far worse than for Envisat and ICESat (80 and 30 km, respectively). Thus, current satellite altimetry missions demonstrated potential to be a valuable resource to be explored in regional flood modeling, especially to reduce errors of water

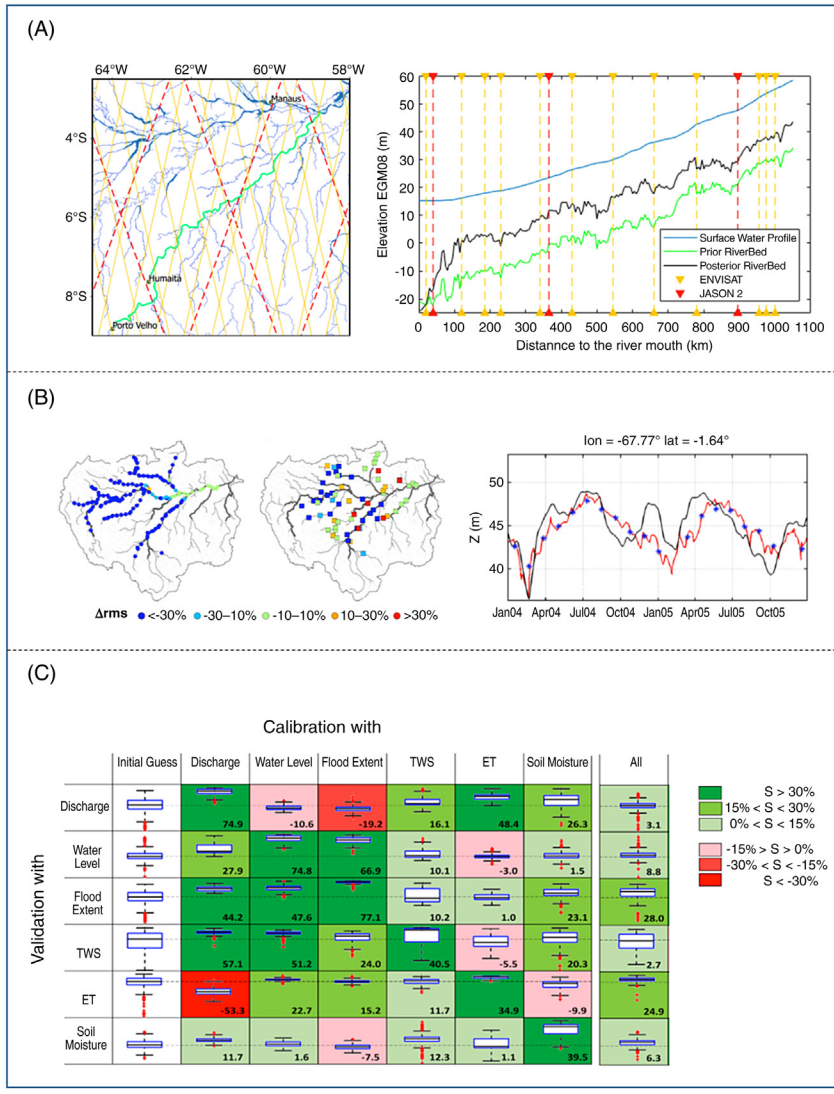

FIGURE 4.6 (A) Correction of channel bathymetry with satellite altimetry data assimilation (DA), with the display (left column) of the studied reach *(green)*, GRWL water mask *(blue)*, Jason-2 *(red)*, and Envisat groundtracks *(yellow)*. The longitudinal profile adopted on the hydrodynamic model of the Madeira River from Porto Velho to the river mouth is presented on the right panel, showing prior *(green)* and posterior *(black)* adjusted riverbeds, and satellite virtual stations (Brêda et al., 2019). (B) DA in the Amazon Basin (Paiva et al., 2013b), displaying in the left panel the altimetry (*circle*—assimilation) and in situ (*square*—validation) water level stations with performance of simulated water level (variation of RMSE). In the right panel, a water level time series is presented for the Japurá River with Envisat observations *(blue)*, and simulation with *(red)* and without DA *(black)*. (C) Multi-variable calibration of the MGB model in the Purus River Basin with five remotely sensed variables, summarized as boxplots of KGE metrics for all optimal solutions, which are compared to the first generation (initial guess); colors and performance metric values refer to a skill score index (Oliveira et al., 2020).

surface elevation. Synthetic data of other planned/recent missions (ICESat-2 and SWOT) were also tested and showed equivalent results.

Remote sensing data assimilation can also be performed to correct model state variables as water levels, discharge, and soil/vegetation variables as soil water storage. Paiva et al. (2013b) used the Ensemble Kalman Filter on the MGB for the whole Amazon Basin for improving streamflow forecast (Fig. 4.6B) through assimilation of Envisat altimetry and in situ discharge data. Altimetry assimilation led to 44% (15%) reduction in water levels (discharge) errors, presenting better results closer to assimilation sites. This model version with data assimilation was then used by Paris et al. (2016) to estimate rating curves by linking modeled discharges to satellite altimetry virtual stations, allowing a near real-time monitoring of more than 100 tributaries on the Amazon River Basin, given the latency of newly available altimetry data. This methodology is now being applied to the Congo and Niger river basins (Paris et al., 2018). On streams that were not observed through satellite altimetry, results by Paiva et al. (2013b) showed that water levels barely improved or even deteriorated in some cases. This suggests that a denser network of satellite altimetry data could produce even more accurate outputs, which could be achieved with the combination of several altimetry missions or probably the SWOT mission alone. Wongchuig et al. (2020) assimilated SWOT-like data, that is, surface water level and extent and discharge, on an MGB model application in the Purus River Basin (Amazon). The authors corrupted the model parameters with typical uncertainties of global models and used the Ensemble Kalman Filter to retrieve outputs from the "original model." Results indicate that assimilating SWOT observations will significantly reduce global/continental hydrological model errors, and that SWOT observations have potential to support flood studies across different scales.

Other remote sensing observations than satellite altimetry can be also used to improve hydrological-hydrodynamic models. In special, there is a need to develop models that are "right for the right answers" (Kirchner, 2006), in the sense that many variables should be simultaneously evaluated to assess the model capability to representing different processes. Oliveira et al., 2020 tested the impact of different types of remote sensing observations on the calibration and validation of the MGB hydrological-hydrodynamic model in the Purus River Basin (Amazon). The authors applied the MOCOM-UA automatic calibration scheme to adjust river hydraulic, soil, and vegetation parameters with observations of terrestrial water storage (TWS; GRACE), soil moisture (SMOS), evapotranspiration (ET; MOD16), water level (Jason-2), and inundated area extent (ALOS-PALSAR). One-at-a-time calibration runs were performed considering each of these observations in order to understand the capacity of the calibration with individual observations to improve the performance of other variables. Results indicated that, by calibrating the model with in situ discharges, it was possible to improve the performance for river-floodplain (water levels and flood extent) and TWS variables, but it was less effective for soil moisture and even degraded

ET estimates (Fig. 4.6C; second column). In turn, by calibrating the model with water levels or flood extent (Fig. 4.6C; third and fourth columns), which are highly correlated variables, the model was able to satisfactorily represent these two variables and TWS and ET, but degraded discharge. This may have occurred because discharge is an integrating variable, while water level and flood extent are more related to local (at-a-station) measurements. Studies like this highlight the necessity of understanding deficiencies in model structure, for example, a poor soil-vegetation dynamics representation leading to difficulties in representing ET when calibrating with discharge, as well as uncertainties in observations. Additional tests investigated the benefits of calibrating the model with all variables together (right column in Fig. 4.6C), and showed that it was able to improve most of the water cycle variables (although to a lesser extent than when calibrating with individual variables). However, the range of the obtained calibrated parameters (e.g., river width and depth and vegetation surface resistance) was large, and highlighted the issue of parameter equifinality on model predictions.

3.4 Cross-scale comparisons between flood models

Flood models are required at different scales, and this sets up the necessity of cross-scale comparisons to understand the capability of different model configurations to predict variables of interest (Fleischmann et al., 2019b; Hoch and Trigg, 2018; Trigg et al., 2016). For example, what is the accuracy requirement for each scale? Fleischmann et al. (2019b) proposed three criteria to define whether a hydraulic model is locally relevant. A large scale model should have errors close or smaller than (1) the accuracy requirement for a particular application, (2) typical errors obtained from reach scale models (i.e., large scale models will seldom have higher accuracy than these models), and (3) observations uncertainties.

Recent studies have performed cross-scale comparisons for Brazilian rivers. Siqueira et al., (2018) presented a comparison between global models and a more regionally based, continental hydrological-hydrodynamic model for South America (MGB-SA model). Results indicated substantial biases in streamflow predictions from current global hydrological models. The capability of MGB-SA to simulate extreme flood discharges was further assessed by (Fleischmann et al., 2020b) for the great 1983 floods that occurred in the continent. The model was able to adequately represent peak discharges (mean absolute percentage error for hundreds of analyzed gauges yielded 34%). While discharge is an aggregating variable from the whole upstream basin, accurate representation of water levels is more local-dependent and more challenging.

To further understand the accuracy of current regional to global models, Fleischmann et al., (2019b) compared three different versions (continental, regional, and local approaches) of the 1D MGB model at the Itajaí-Açu River Basin (see Rio do Sul city in Fig. 4.1) using different information of floodplain

topography (from global to locally derived DEM), cross-section (from global to locally surveyed data), and reach length (from 15 to 1 km). Model predictions were compared to a benchmark, detailed HEC-RAS model (Fig. 4.7). The study showed that current regional to global models are capable of estimating locally relevant discharges if forced with runoff from a calibrated rainfall-runoff model. In turn, they have difficulties to estimate water levels and flood extents with high accuracies. The use of a locally derived DEM at 30 m did not lead to major impacts on the 1D model simulations in comparison to SRTM. On the other hand, the factor that improved the large scale models the most was the adoption of more detailed and distributed cross section information (i.e., not using simple geomorphic relationships for the whole basin), what highlights the relevance of new methods of incorporating distributed remote sensing data

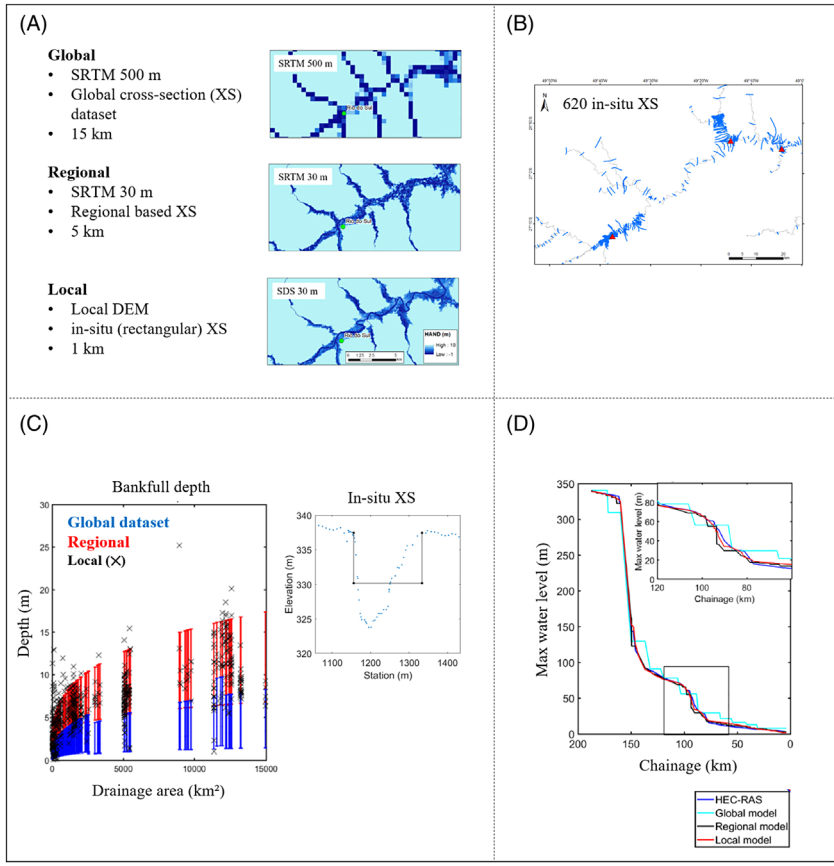

FIGURE 4.7 (A) Cross-scale comparison between hydraulic models at global, regional and local scales. (B) A detailed hydraulic model was set up as a benchmark. (C) Cross-section bankfull depth parameter as estimated for different scales based on rectangular cross sections. (D) Model predictions of maximum water levels for different scales. *(Adapted from Fleischmann et al. (2019b).)*

into flood models. Satellite data are even more important given constraints in using cross-section estimates from in situ gauge stations, since the best location for placing monitoring gauges is not necessarily representative of the reach hydraulics. This was shown by Meyer et al. (2018) for different Brazilian rivers by comparing celerity-discharge curves at reach scales with those obtained from in situ cross-sections located in the gauge stations.

4 Hydrological monitoring and modeling tools for flood risk management in Brazil

Many Brazilian riverside cities are under high flood risk (Fig. 4.1) and in need of information to improve management practices. Deriving adequate flood risk information requires accurate hazard mapping for the impact analysis. A flood early warning system is one possible strategy of risk mitigation, as communicating forecasts enables actions to prevent the loss of life and property. Another important benefit of an early warning system is that its development fosters production of risk maps and forecasting tools. In Brazil, the National Water and Sanitation Agency (ANA) has launched the National Water Security Plan (PNSH—http://pnsh.ana.gov.br) that focuses on flood control with a national view but linked to a basin level. The PNSH presented two main initiatives regarding flood management: the diagnosis of the problem, based on the Flood Vulnerability Atlas, and a broad inventory of infrastructure interventions as well as analyses of required strategic interventions. The inventory reveals an indirect measure of flood impacted basins, since some solutions have already been designed for some regions. Within PNSH, the country-wide vulnerability map (Fig. 4.1; ANA, 2014) was created at the state level and involved a qualitative analysis (with interviews with local water authorities, civil defense, and other stakeholders) of reaches with frequent flood problems associated to high damages and losses, yielding three categories of vulnerability (high, moderate, and low). However, the methodology is rather simplistic in comparison to the engineering methods for regional flood risk assessment that employs river flood models and remote sensing data. The focus of this final section is to summarize the currently available systems for flood hazard mapping (Section 4.1) and real-time monitoring and forecasting (Section 4.2) across scales for the Brazilian context (Table 4.1), and to provide some perspectives on the use of remote sensing and hydrological modeling tools for flood risk management.

4.1 Flood hazard mapping

Recent advances in global flood frequency analysis and inundation modeling paved the way for flood hazard mapping at large scales (Alfieri et al., 2014, 2015; Dottori et al., 2016; Sampson et al., 2015). A few global flood hazard maps were completed and made available online (Table 4.1). A Global Flood Partnership (GFP) study compared global flood models in Africa (Trigg et al., 2016), and

TABLE 4.1 Examples of available flood hazard maps and flood monitoring (M) and forecasting systems (F) for Brazil at different scales. M/F types are presented in parentheses to describe the systems.

Scale	Flood hazard assessment		Real-time flood monitoring (M) and forecasting systems (F)	
	Availability	Applicability	Availability	Applicability
Global	JRC (10–500 year floods)[a] Fathom (5–1000 year floods)[b] FL-GLOBAL-GLOFRIS (5–1000 year floods)[c] FM Global (100 and 500 year)[x]	Low accuracy and resolution	Copernicus Emergency Management Service (includes services of: Mapping[f] and Global Flood Awareness System/GloFAS[g]) **(M/F)** GLOFFIS[h] **(M/F)** Global Flood Monitoring System[i] **(M/F)** Disasters Charter[j] **(M)** Global Flood Partnership[k] **(M)** Global Flood Observatory[l] **(M)** Global Flood Detection System [w] **(M)** Global Flood Monitor[m] **(M)** FloodScan[n] **(M)** FloodList (Reports on major floods around the world)[o] **(M)**	Country-wide flood mitigation and planning Global to continental flood strategies by world agencies, NGO's Forecasting lead time: short to medium to long term ranges Low accuracy and resolution
Regional	Santa Catarina State Paraíba do Sul River Basin[d] Doce River Basin	Moderate to high accuracy and resolution	National Center for Monitoring and Early Warning of Natural Disasters (Cemaden) **(M/F)**[p] SACE (CPRM) for 16 basins in Brazil[e] **(M/F)** ANA Situation rooms (*"Sala de Situação"*)[q] **(M/F)** Santa Catarina State System[r] **(M/F)** Rio Grande do Sul State System[s] **(M/F)** Amazon State System[t] **(M/F)**	State- and country-based flood mitigation and planning Forecasting lead time: short to medium to long term ranges Moderate accuracy and resolution

Local	Specific sites where river engineering projects have required field surveys (e.g., lower Madeira River); SACE (CPRM) for seven flood vulnerable Brazilian cities[e]	High accuracy and resolution	Real-time monitoring in the Itajaí River basin[u] **(M/F)** Flood forecasting at Paraíba do Sul River Basin[d] **(M/F)** Real-time monitoring and forecasting in the Iguaçu River Basin and União da Vitória city[v] **(M/F)**	Flood mitigation at city/reach/basin level Forecasting lead time: very short to medium ranges High accuracy and resolution

[a] *(Dottori et al., 2016); available at <https://data.jrc.ec.europa.eu/collection/id-0054>)*
[b] *(Sampson et al., 2015); available at <https://www.fathom.global/fathom-global>*
[c] *(Ward et al., 2013; Winsemius et al., 2013); Available at <https://www.geonode-gfdrrlab.org/people/profile/GLOFRIS/?limit=20&offset=0>*
[d] *Available at <http://gripbsul.ana.gov.br/SisprecR05.html>*
[e] *Available at <https://www.cprm.gov.br/sace/index_bacias_monitoradas.php>*
[f] *Available at <https://emergency.copernicus.eu/mapping/ems/emergency-management-service-mapping>*
[g] *Available at <https://www.globalfloods.eu/>*
[h] *Available at <http://globalfloodforecast.com/glossis/index.htm>*
[i] *(Wu et al., 2014); Available at <http://flood.umd.edu/>*
[j] *Available at <https://disasterscharter.org/>*
[k] *(De Groeve et al., 2015); Available at <https://gfp.jrc.ec.europa.eu/support-service>.*
[l] *(Brakenridge et al., 2005; Brakenridge, 2020); Available at <https://floodobservatory.colorado.edu>*
[m] *(de Bruijn et al., 2019); Available at <https://www.globalfloodmonitor.org/about>*
[n] *Available at <http://product.aer.com/index.php/floodscan/>*
[o] *Available at <http://floodlist.com/>*
[p] *Available at <https://www.cemaden.gov.br/>*
[q] *Available at <https://www.ana.gov.br/sala-de-situacao>*
[r] *Forecasting system for most vulnerable sites, available at <http://ciram.epagri.sc.gov.br/index.php?option=com_content&view=article&id=2224&Itemid=250>)*
[s] *(Fan et al., 2019; Nectoux et al., 2019); Available at <http://www.saladesituacao.rs.gov.br/>*
[t] *Available at <http://hidro.sipam.gov.br/>*
[u] *Available at <https://defesacivil.itajai.sc.gov.br/telemetria>*
[v] *Available at <https://www.copel.com/mhbweb/paginas/bacia-iguacu.jsf>*
[w] *(Brakenridge et al., 2005); Available at <https://www.gdacs.org/flooddetection/>*
[x] *Available at <https://www.fmglobal.com/research-and-resources/nathaz-toolkit/flood-map>*

showed that there are still many disagreements among them, and that improvements in resolution and accuracy are needed for predictions of extreme streamflow, and the respective flood extent and water elevation. We exemplify here a case study in the Porto Velho city in the Madeira River (Amazon) where four floods have occurred over the last six years (2014–2019) (Fig. 4.8). In 2014, when two run-of-the-river mega dams (Jirau and Santo Antônio) were in the final phase of construction, Porto Velho was hit with the largest flood on record of the Madeira River (Germano et al., 2014; Santos et al., 2017). The river discharge peaked at 58,560 m^3s^{-1} with a return period of about 300 years (average annual peak discharge at Porto Velho is 17,980 $m^3\ s^{-1}$). The water level

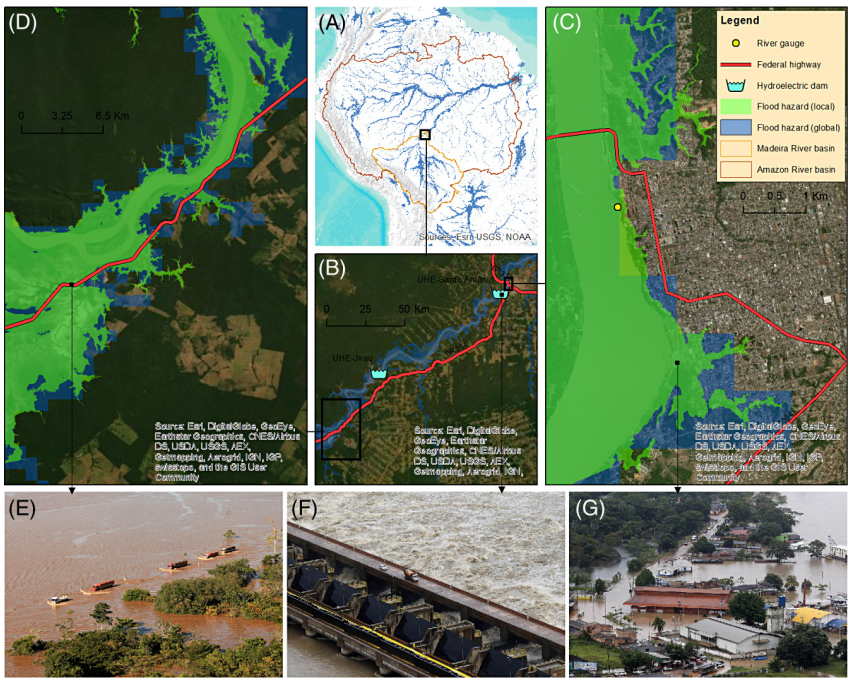

FIGURE 4.8 (A) Global flood hazard map (Dottori et al., 2016) for the return period of 50 year *(light blue)* over the Amazon Basin. The region of the Madeira River watershed upstream from Porto Velho is highlighted. (B) Overview of the Lower Madeira River encompassing the city of Porto Velho, two run-of-the-river dams and the BR-364 highway. Comparisons between global (Dottori et al., 2016) and local (HEC-RAS model based on high precision DEM) inundation models at streamflow conditions of about 60,000 $m^3\ s^{-1}$ for river reaches in (C) the urban area of Porto Velho and (D) the section of the highway with the highest exposure to flooding. Photographs of the 2014 historical flooding: (E) the federal highway submerged; (F) the Santo Antônio Dam; and (G) flooding around the municipal marketplace. *(Photo in panel E is from Secom/Acre; available at <https://fotospublicas.com/cheia-rio-madeira-bloqueia-br-364-e-isola-acre/>; License CC BY-NC 2.0. Photos in panels F and G from Adalberto Marques / Integração Nacional; available at <https://fotospublicas.com/rio-madeira-causa-enchente-em-porto-velho-devido-chuvas/>; License CC BY-NC 2.0.)*

remained above flood stage for about three months displacing 2230 people, closing a main federal highway (BR-364), and causing over R$ 455 million in damage. Dottori et al. (2016) produced global flood hazard maps based on the flood frequency analysis of GloFAS streamflow climatology. The differences in flood extent among the results for different streamflow return periods from GloFAS and a local scale HEC-RAS model are within expected ranges for Porto Velho. However, higher resolution and accuracy in water level and flood extent predictions are needed for decision making at the local scale.

At local scales, the Brazilian Geological Survey (CPRM) has carried out flood hazard mapping (2–100 year) (http://www.cprm.gov.br/sace/index_manchas_inundacao.php) for seven flood vulnerable cities in Brazil: Ponte Nova, Governador Valadares and Colatina (Doce River), Porto Velho (Madeira River), São Sebastião do Caí and Montenegro (Caí River), and Teresina (Parnaíba River). The methodology ranged from simplified projections of in situ water levels for different return periods into locally derived DEM's (Caí river) to HEC-RAS model applications (calibrated with locally estimated extreme flood extents) with a locally derived DEM and in situ surveyed cross-sections (Doce and Parnaíba rivers). Locally derived DEM's involved multiple sources, as aerophotogrammetry and local topographical surveys. Another regional scale example is the flood hazard mapping of Paraíba do Sul River Basin. In this case, the HEC-HMS hydrological model was coupled to HEC-RAS to generate hazard maps, and a flood forecasting system was also developed (http://gripbsul.ana.gov.br/Sisprec.html).

Regarding improved datasets in Brazil for flood hazard modeling, some states have invested in the acquisition of high resolution DEM's (1–5 m), such as Santa Catarina (1 m resolution based on aerophotogrammetry; available in (http://sigsc.sds.sc.gov.br/); see studies by Fleischmann et al. (2019b) and Speckhann et al. (2018)) and Pernambuco states (ongoing World Bank funded 1 m LiDAR survey; data for around one fourth of the state are already available; http://www.pe3d.pe.gov.br/). This latter survey was prompted to assist flood mitigation efforts after major floods occurred in the Una River in 2010–11.

Flood hazard information is currently underused in Brazil for local and regional planning, even where accurate local scale studies are available. There are great opportunities for improving and applying regional models, and there are just a few cases of flood hazard assessment that use remote sensing in the country. Furthermore, flood hazard mapping requires hydrological and hydraulic modeling of floodplains and the consideration of a cascade of uncertainties through several components of the model, and systematic uncertainty assessments are needed along with new approaches to constrain uncertainty and communicate it to the broader community.

4.2 Real-time flood monitoring and forecasting systems

Regarding current real-time flood monitoring and forecasting systems in Brazil, ANA has created in 2009 a situation room (*Sala de situação*) to monitor

major hydrological related disasters in Brazil (floods and droughts). ANA is also assisting Brazilian states to develop their own situation rooms through capacity building and financial support. There are currently 20 states (out of 27 federative units) with their own systems, at different levels of development. One case of success has been developed since November 2018 in the Rio Grande do Sul state (available at <http://www.saladesituacao.rs.gov.br/>; Fan et al., 2019; Nectoux et al., 2019), with operational forecasts for 25 large basins in the state. The MGB hydrological model runs with hourly observed precipitation (forcing) and discharges (for data assimilation) up to the forecast initial time, and is then fed with numerical rainfall prediction from WRF (5 km), Eta (40 km), and GEFS (100 km) models. Daily reports are sent to the State Civil Defense. Fig. 4.9A presents an example of the system application for the 2019 January floods, which displaced thousands of people in the state. The system has been very helpful for local and regional Civil Defense operations.

To date, most forecasting (or early-warning) systems in Brazil were developed for predicting reservoir inflows and enhancing dam operation (Araujo et al., 2014; Fan et al., 2016; Schwanenberg et al., 2015), but recent efforts have improved systems for flood forecasts at flood vulnerable reaches (Casagrande et al., 2017; Fan et al., 2016). In the Upper Iguaçu River, where Foz do Areia dam backwater effects may increase floods in the upstream União da Vitória city, an operational system led by COPEL company provides forecasts for the city location with a 5-days lead time (Araujo et al., 2014; available at <https://www.copel.com/mhbweb/paginas/bacia-iguacu.jsf>).

The Alert System for Critical Events by CPRM ("*Sistema de Alerta de Eventos Críticos*" (SACE); available at <https://www.cprm.gov.br/sace/index_bacias_monitoradas.php>) currently monitors 16 basins (Amazonas, Paraguay, Doce, Caí, Muriaé, Acre, Madeira, Parnaíba, Taquari, Branco, Xingu, Mundaú, Uruguai, Velhas, Itapecuru, and Pomba) with automatic collection of sub-hourly precipitation and discharge data (most gauges in Brazil monitoring network are still non-automatic with local observers performing observations twice a day), and provides forecasts for most of them, mainly with empirical (data-driven) models and lead times varying with basin size (e.g., 3 months for the Amazon river at Manaus and 5 h for the Mundaú river at União dos Palmares). Fig. 4.9B shows an example of the Madeira River Basin SACE system.

Another important advance for real-time flood monitoring in Brazil relates to the establishment of the National Center for Monitoring and Early Warning of Natural Disasters (Cemaden) in 2011 with the mission of fostering scientific, technological, and innovative capacity to improve early warning systems of natural disasters. In addition to ANA, CPRM, and other agencies, Cemaden continuously monitors hydrometeorological conditions across the nation with assessment of risk of natural disasters and issuance of early warnings to the

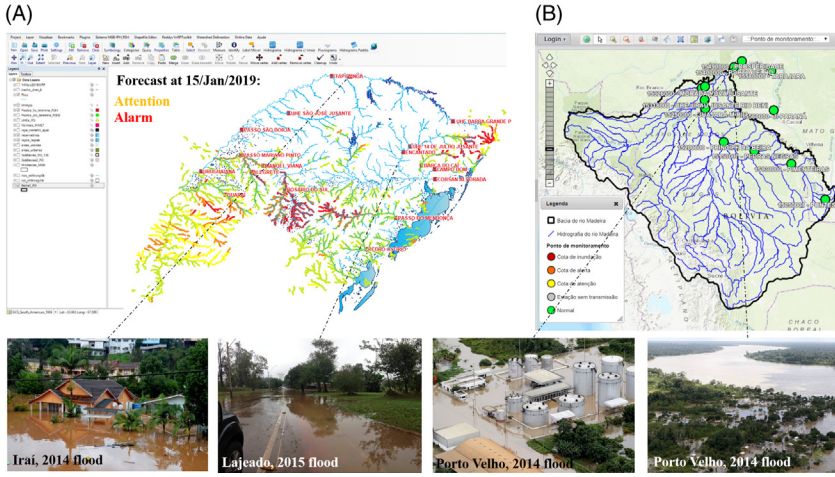

FIGURE 4.9 Real-time flood monitoring and forecasting systems for (A) the Rio Grande do Sul state and (B) the Madeira River Basin, which is 1 of the 16 currently available systems from the Geological Survey of Brazil (SACE/CPRM). *(Photos in Figure A from Iraí city from Fernando Sucolotti/ AI/ Prefeitura Iraí; available at <https://fotospublicas.com/retrospectiva-2014-cotidiano//>; License CC BY-NC 2.0; and from Lajeado city (courtesy by Amanda Wajnberg Fadel). Photos in Figure B from Adalberto Marques/Integração Nacional; available at <https://fotospublicas.com/rio-madeira-causa-enchente-em-porto-velho-devido-chuvas/>; License CC BY-NC 2.0.)*

Disaster and Risk Management National Center (Cenad). Cemaden expanded Brazil's hydrometeorological monitoring network with additional 9 weather radars, over 4750 rain gauges, and 300 river gauges.

At the global scale, the Copernicus Emergency Management Service (EMS), which has been in operation since April 1st 2012, includes multiple platforms and uses satellite imagery and other geospatial data to provide mapping service in cases of natural disasters, human-made emergency situations, and humanitarian crises throughout the world. The Global Flood Awareness System (GloFAS) provides information for alert and preparedness, while the Mapping Services provide post-event assessments for emergency response and recovery phases of a disaster upon request from authorized users. In the latter case, data processing of SAR imagery, digital elevation models, and other available datasets are used. Operationally, Cemaden uses GloFAS for streamflow forecasts, while higher resolution hydrological forecasting systems remain under development. The EMS Mapping service has not been activated for any past flood in Brazil, and in the case of a large flood disaster an activation as "associated user" would be beneficial, since currently the nation lacks an operational flood mapping service.

Another relevant global initiative is the International Charter "Space and Major Disasters" through which satellite data are made available for the benefit

of disaster management. By combining Earth Observation assets from different space agencies, the Charter allows resources and expertise to be coordinated for rapid response to major disaster situations; thereby helping civil protection authorities and the international humanitarian community. In Brazil, it was activated 9 times for flood disasters in the period of January 2000 to January 2020. The first activation was in November 2008 when heavy rainfall caused severe flooding and landslides in the Southern Brazilian state of Santa Catarina, leaving more than 20,000 people homeless. Flood mapping for emergency response was produced with ENVISAT1-ASAR radar data at spatial resolution of 14.8 m.

The GFP is another initiative that aims to gather worldwide stakeholders (scientists, users, private, and public organizations) to deal with operational flood risk management (Alfieri et al., 2018; De Groeve et al., 2015). Some cases of success activation of the network were reported by Alfieri et al. (2018), including the 2017 South Asia and the 2017 Hurricane Harvey (USA) floods. In addition to these tools, other real-time flood monitoring at global scales include the Global Flood Detection System, first based on AMSR-E microwave radiometer data (https://www.gdacs.org/flooddetection/), the Global Flood Monitor, based on social media (de Bruijn et al., 2019) (https://www.globalfloodmonitor.org/about), and the Global Flood Monitoring System, based on hydrological modeling (http://flood.umd.edu/) (Table 4.1).

The use of remote sensing based monitoring can largely improve flood management in Brazil, especially if used in combination with river flood models. This includes the provision of water surface extent climatology (Aires et al., 2017; Pekel et al., 2016) and operational mapping products for emergency response. For instance, satellite altimetry water levels have been used in Brazil for operational gap filling and series updating, as well as monitoring of ungauged reaches in transboundary basins (Da Silva et al., 2014). One example is the Madeira River in the Amazon (Fig. 4.9B) (Seyler et al., 2009), which receives water from Bolivia and Peru, so that the current alert system misses important data monitoring. Near real-time discharge monitoring using altimetry-modeled discharge rating curves as proposed by Paris et al. (2016) is very promising in such cases (Section 3.3). Furthermore, satellite based real-time monitoring of meteorological conditions is already performed by some flood monitoring systems in Brazil, as GOES16 in the Amazon State system (available at <http://hidro.sipam.gov.br/>), and other products as those from GPM and MERGE are operationally used.

5 Conclusion

Brazil presents large natural wetlands which provide important ecosystem services, but its territory is also associated to major riverine flood risk along many cities. Remote sensing data are very promising to be used in combination with

river flood models in order to improve our understanding and predictability of floods. This topic is addressed in this chapter by discussing the current Brazilian context on flood monitoring and forecasting, as well as hazard estimation, and considering the country's particularities due to its location in a tropical region with complex river systems, the remoteness of many urban centers, and the ungauged character of many of its rivers.

A systematic literature review was performed, and provided some interesting views on the need for future research in Brazil regarding river flood model applications, and especially on the use of satellite based flood extent and water level data. For instance, more efforts are required to foster model calibration and validation with remote sensing on Brazilian urban areas under flood risk, in special when dealing with 2D hydraulic models—to date, most studies in this sense were performed for regional scales and in the Amazon Basin. On the other hand, there has been an increase in the use of remote sensing data in recent years.

Recent experiences in Brazilian rivers on the integration of river flood models and remote sensing were presented, and highlighted the different opportunities now available. These include the estimation of river cross-section depth and roughness parameters with data assimilation and genetic calibration algorithms, and floodplain topography direct estimation from detailed in situ survey as well as from a new method that combines water mask and surface water level time series. Cross-scale model comparisons (from global to local scales) are also very important to better understand the capabilities of large scale models. Comparison exercises in Brazil (Itajaí-Açu and Madeira river basins as well as a South America scale study) provided valuable insights on the capabilities of current models, showing that although current global models are capable of simulating river discharges (given a prior rainfall-runoff parameter calibration), there is still a need to use more distributed information of cross-sections (bankfull width and depth, roughness) to achieve better predictions of water levels and flood extent.

Finally, we discussed some of the current efforts by national and international organizations to monitor and forecast floods in real-time and to estimate flood hazard in Brazil, and provided perspectives on how current and future satellite missions, in combination with hydrological models, could help to mitigate flood related disasters. We conclude by calling Brazilian agencies and organizations to work closer to international initiatives on disaster management (e.g., GFP, Disasters Charter), and that more efforts be invested on training operational users on the use of newly available datasets and modeling techniques.

Supplementary material S1

Table 4.2 lists the 55 studies identified with Scopus search that were published since 2000 and included analysis of flood extent simulated by flood models in Brazil.

TABLE 4.2 List of the 55 studies identified with Scopus search that were published since 2000 and included analysis of flood extent simulated by flood models in Brazil.

1	Alcoforado, R., Cirilo J.A	Sistema de Suporte à Decisão para Análise, Previsão e Controle de Inundações	2001	10.21168/rbrh.v6n4.p133-153
2	Mascarenhas, F.C.B., Miguez, M.G.	Urban flood control through a mathematical cell model	2002	10.1080/02508060208686994
3	Mascarenhas, F.C.B., Miguez, M.G., Magalhes, L.P.C.	MODCEL: An integrated cell model for river basin simulation	2007	10.2495/RM070081
4	Meller, A., Paiva, E.	Simulação Hidrodinâmica 1D de Inundações em Sistema de Drenagem Urbana	2007	10.21168/rbrh.v12n2.p81-92
5	Miguez, M.G., Mascarenhas, F.C.B., Prodanoff, J.H.A., Magalhes, L.P.C.	Simulating floods in urban watersheds: Hydrodynamic modeling of macro, micro-drainage and flows over streets	2007	10.2495/WRM070601
6	Wilson, M.D., Bates, P., Alsdorf, D., Forsberg, B., Horritt, M., Melack, J., Frappart, F., Famiglietti, J.	Modeling large-scale inundation of Amazonian seasonally flooded wetlands	2007	10.1029/2007GL030156
7	Bonnet, M.P., Barroux, G., Martinez, J.M., Seyler, F., Moreira-Turcq, P., Cochonneau, G., Melack, J.M., Boaventura, G., Maurice-Bourgoin, L., León, J.G., Roux, E., Calmant, S., Kosuth, P., Guyot, J.L., Seyler, P.	Floodplain hydrology in an Amazon floodplain lake (Lago Grande de Curuaí)	2008	10.1016/j.jhydrol.2007.10.055
8	Coe, M.T., Costa, M.H., Howard, E.A.	Simulating the surface waters of the Amazon River basin: Impacts of new river geomorphic and flow parameterizations	2008	10.1002/hyp.6850

9	Decharme B., Douville H., Prigent C., Papa F., Aires F.	A new river flooding scheme for global climate applications : Off-line evaluation over South America	2008	10.1029/2007JD009376
10	Paz, A., Collischonn, W., Tucci, C	Simulação Hidrológica de Rios com Grandes Planícies de Inundação	2010	10.21168/rbrh.v15n4.p31-43
11	Paiva, R.C.D., Collischonn, W., Tucci, C.E.M.	Large scale hydrologic and hydrodynamic modeling using limited data and a GIS based approach	2011	10.1016/j.jhydrol.2011.06.007
12	Paz, A.R.D., Collischonn, W., Tucci, C.E.M., Padovani, C.R.	Large-scale modeling of channel flow and floodplain inundation dynamics and its application to the Pantanal (Brazil)	2011	10.1002/hyp.7926
13	Yamazaki, D., Kanae, S., Kim, H., Oki, T.	A physically based description of floodplain inundation dynamics in a global river routing model	2011	10.1029/2010WR009726
14	Getirana, A.C.V., Boone, A., Yamazaki, D., Decharme, B., Papa, F., Mognard, N.	The hydrological modeling and analysis platform (HyMAP): Evaluation in the Amazon basin	2012	10.1175/JHM-D-12-021.1
15	Miguez-Macho, G., Fan, Y.	The role of groundwater in the Amazon water cycle: 1. Influence on seasonal streamflow, flooding and wetlands	2012	10.1029/2012JD017539
16	Paiva, R.C.D., Collischonn, W., Bonnet, M.P., De Gonçalves, L.G.G.	On the sources of hydrological prediction uncertainty in the Amazon	2012	10.5194/hess-16-3127-2012
17	Stacke, T., Hagemann, S.	Development and evaluation of a global dynamical wetlands extent scheme	2012	10.5194/hess-16-2915-2012
18	Yamazaki, D., Baugh, C.A., Bates, P.D., Kanae, S., Alsdorf, D.E., Oki, T.	Adjustment of a spaceborne DEM for use in floodplain hydrodynamic modeling	2012	10.1016/j.jhydrol.2012.02.045

(*Continued*)

TABLE 4.2 List of the 55 studies identified with Scopus search that were published since 2000 and included analysis of flood extent simulated by flood models in Brazil. (*Cont.*)

19	Yamazaki, D., Lee, H., Alsdorf, D.E., Dutra, E., Kim, H., Kanae, S., Oki, T.	Analysis of the water level dynamics simulated by a global river model: A case study in the Amazon River	2012	10.1029/2012WR011869
20	Ringeval B., Decharme B., Piao S.L., Ciais P., Papa F., De Noblet-Ducoudré N., Prigent C., Friedlingstein P., Gouttevin I., Koven C., Ducharne A.	Modeling sub-grid wetland in the ORCHIDEE global land surface model: Evaluation against river discharges and remotely sensed data	2012	10.5194/gmd-5-941-2012
21	Baugh, C.A., Bates, P.D., Schumann, G., Trigg, M.A.	SRTM vegetation removal and hydrodynamic modeling accuracy	2013	10.1002/wrcr.20412
22	Beck, V., Gerbig, C., Koch, T., Bela, M.M., Longo, K.M., Freitas, S.R., Kaplan, J.O., Prigent, C., Bergamaschi, P., Heimann, M.	WRF-Chem simulations in the Amazon region during wet and dry season transitions: Evaluation of methane models and wetland inundation maps	2013	10.5194/acp-13-7961-2013
23	De Paiva, R.C.D., Buarque, D.C., Collischonn, W., Bonnet, M.-P., Frappart, F., Calmant, S., Bulhões Mendes, C.A.	Large-scale hydrologic and hydrodynamic modeling of the Amazon River basin	2013	10.1002/wrcr.20067
24	Langerwisch, F., Rost, S., Gerten, D., Poulter, B., Rammig, A., Cramer, W.	Potential effects of climate change on inundation patterns in the Amazon Basin	2013	10.5194/hess-17-2247-2013
25	Paiva, R.C.D., Collischonn, W., Buarque, D.C.	Validation of a full hydrodynamic model for large-scale hydrologic modeling in the Amazon	2013	10.1002/hyp.8425
26	Veról, A., Miguez, M., Mascarenhas, F	Propagação da Onda de Ruptura de Barragem Através de um Modelo Quasi-2D	2013	10.21168/rbrh.v18n1.p165-176

27	Da Paz, A.R., Collischonn, W., Bravo, J.M., Bates, P.D., Baugh, C.	The influence of vertical water balance on modelling Pantanal (Brazil) spatio-temporal inundation dynamics	2014	10.1002/hyp.9897
28	Rudorff, C.M., Melack, J.M., Bates, P.D.	Flooding dynamics on the lower Amazon floodplain: 2. Seasonal and interannual hydrological variability	2014	10.1002/2013WR014714
29	Rudorff, C.M., Melack, J.M., Bates, P.D.	Flooding dynamics on the lower Amazon floodplain: 1. Hydraulic controls on water elevation, inundation extent, and river-floodplain discharge	2014	10.1002/2013WR014091
30	Ringeval B., Houweling S., Van Bodegom P.M., Spahni R., Van Beek R., Joos F., Röckmann T	Methane emissions from floodplains in the Amazon Basin: challenges in developing a process-based model for global applications	2014	10.5194/bg-11-1519-2014
31	Cestari Jr, E., Sobrinho, M., Oliveira, J	Study of wave propagation to assist in the preparation of the external emergency action plan-PAE	2015	10.21168/rbrh.v20n3.p689-697
32	Neto, A., Cirilo, J., Dantas, C., Silva, E.	Caracterização da formação de cheias na bacia do rio Una em Pernambuco: simulação hidrológica-hidrodinâmica	2015	10.21168/rbrh.v20n2.p394-403
33	Pontes, Collischonn, Fan, Paiva, Buarque	Hydrologic and hydraulic large-scale modeling with inertial flow routing	2015	10.21168/rbrh.v20n4.p888-904
34	Cabral, S.L., Campos, J.N.B., Silveira, C.S., Teixeira, F.A.A.	Integration of GIS, HEC/HMS and HEC/RAS in mapping urban flood area: Application to the Granjeiro River basin in Ceará State | Integração do sig, HEC/HMS e HEC/RAS no mapeamento de área de inundação urbana: Aplicação à bacia do rio granjeiro-ce	2016	NA

(*Continued*)

TABLE 4.2 List of the 55 studies identified with Scopus search that were published since 2000 and included analysis of flood extent simulated by flood models in Brazil. (*Cont.*)

35	Monte B.E.O., Costa D.D., Chaves M.B., de Oliveira Magalhães L., Uvo C.B.	Hydrological and hydraulic modelling applied to the mapping of flood-prone areas [Modelagem hidrológica e hidráulica aplicada ao mapeamento de áreas inundáveis]	2016	10.21168/rbrh.v21n1.p152-167
36	Neto, A., Batista, L., Coutinho, R.	Methodologies for generation of hazard indicator maps and flood prone areas: municipality of Ipojuca/PE	2016	10.21168/rbrh.v21n2.p377-390
37	Paz, A.R., Serra, L.S., Silva, M.R.F., Meller, A.	Reducing computational runtime of two-dimensional urban inundation model by dynamic domain reshaping	2016	10.1061/(ASCE)HE.1943-5584.0001375
38	Revilla-Romero, B., Wanders, N., Burek, P., Salamon, P., de Roo, A.	Integrating remotely sensed surface water extent into continental scale hydrology	2016	10.1016/j.jhydrol.2016.10.041
39	Sorribas, M.V., Paiva, R.C.D., Melack, J.M., Bravo, J.M., Jones, C., Carvalho, L., Beighley, E., Forsberg, B., Costa, M.H.	Projections of climate change effects on discharge and inundation in the Amazon basin	2016	10.1007/s10584-016-1640-2
40	Getirana, A., Kumar, S., Girotto, M., Rodell, M.	Rivers and Floodplains as Key Components of Global Terrestrial Water Storage Variability	2017	10.1002/2017GL074684
41	Hoch, J.M., Haag, A.V., Van Dam, A., Winsemius, H.C., Van Beek, L.P.H., Bierkens, M.F.P.	Assessing the impact of hydrodynamics on large-scale flood wave propagation – A case study for the Amazon Basin	2017	10.5194/hess-21-117-2017
42	Hoch, J.M., Neal, J.C., Baart, F., Van Beek, R., Winsemius, H.C., Bates, P.D., Bierkens, M.F.P.	GLOFRIM v1.0-A globally applicable computational framework for integrated hydrological-hydrodynamic modelling	2017	10.5194/gmd-10-3913-2017

43	Lauerwald, R., Regnier, P., Camino-Serrano, M., Guenet, B., Guimberteau, M., Ducharne, A., Polcher, J., Ciais, P.	ORCHILEAK (revision 3875): A new model branch to simulate carbon transfers along the terrestrial-aquatic continuum of the Amazon basin	2017	10.5194/gmd-10-3821-2017
44	Luo, X., Li, H.-Y., Ruby Leung, L., Tesfa, T.K., Getirana, A., Papa, F., Hess, L.L.	Modeling surface water dynamics in the Amazon Basin using MOSART-Inundation v1.0: Impacts of geomorphological parameters and river flow representation	2017	10.5194/gmd-10-1233-2017
45	Pontes, P.R.M., Fan, F.M., Fleischmann, A.S., de Paiva, R.C.D., Buarque, D.C., Siqueira, V.A., Jardim, P.F., Sorribas, M.V., Collischonn, W.	MGB-IPH model for hydrological and hydraulic simulation of large floodplain river systems coupled with open source GIS	2017	10.1016/j.envsoft.2017.03.029
46	de OLIVEIRA, G.G., Flores, T., Bresolin Junior, N.A., Haetinger, C., Eckhardt, R.R., Quevedo, R.P.	Analysis of the susceptibility to flooding in the Forqueta river basin, RS, Brazil | Análise da suscetibilidade a inundações e enxurradas na bacia hidrográfica do Rio Forqueta, RS, Brasil	2018	NA
47	Fadel, A.W., Marques, G.F., Goldenfum, J.A.	Damage risk mapping as a flood management and adaptation measure | Mapeamento do risco de prejuízo como medida de gestão e adaptação às inundações	2018	NA
48	Fadel, A.W., Marques, G.F., Goldenfum, J.A., Medellín-Azuara, J., Tilmant, A.	Full Flood Cost: Insights from a Risk Analysis Perspective	2018	10.1061/(ASCE)EE.1943-7870.0001414
49	Lopes, V.A.R., Fan, F.M., Pontes, P.R.M., Siqueira, V.A., Collischonn, W., Motta Marques, D.D.	A first integrated modeling of a river-lagoon large-scale hydrological system for forecasting purposes	2018	10.1016/j.jhydrol.2018.08.011

(*Continued*)

TABLE 4.2 List of the 55 studies identified with Scopus search that were published since 2000 and included analysis of flood extent simulated by flood models in Brazil. (*Cont.*)

50	Fleischmann, A., Collischonn, W., Paiva, R., Tucci, C.E.	Modeling the role of reservoirs versus floodplains on large-scale river hydrodynamics	2019	10.1007/s11069-019-03797-9
51	Fleischmann, A., Paiva, R., Collischonn, W.	Can regional to continental river hydrodynamic models be locally relevant? A cross-scale comparison	2019	10.1016/j.hydroa.2019.100027
52	Hoch, J.M., Eilander, D., Ikeuchi, H., Baart, F., Winsemius, H.C.	Evaluating the impact of model complexity on flood wave propagation and inundation extent with a hydrologic-hydrodynamic model coupling framework	2019	10.5194/nhess-19-1723-2019
53	Pinheiro V.B., Naghettini M., Palmier L.R.	Uncertainty estimation in hydrodynamic modeling using Bayesian techniques [Estimação de incertezas na modelagem hidrodinâmica por meio de técnicas Bayesianas]	2019	10.1590/2318-0331.241920180110
54	Vieira L.M.D.S., Fontes A.S., Simões A.L.A.	Analysis of physical mechanisms of human body instability for the definition of hazard zones present in emergency action plans of dams. Case study: Santa helena dam, bahia [Análise de mecanismos físicos de instabilidade do corpo humano para a definição de zonas de risco presentes em planos de ação emergencial de barragens. Estudo de caso: barragem de santa helena, bahia]	2019	10.1590/2318-0331.241920180185
55	Pinel, S., Bonnet, M., Silva, J., Sampaio, T., Garnier, J., Catry, T., Calmant, S., Freagoso, C., Moreira, D., Marques, D., Seyler, F	Flooding dynamics within an Amazonian floodplain: water circulation patterns and inundation duration	2019	10.1029/2019WR026081

References

Aires, F., Papa, F., Prigent, C., 2013. A long-term, high-resolution wetland dataset over the Amazon Basin, downscaled from a multiwavelength retrieval using SAR data. J. Hydrometeorol. 14, 594–607, https://doi.org/10.1175/JHM-D-12-093.1.

Aires, F., Miolane, L., Prigent, C., Pham, B., Fluet-Chouinard, E., Lehner, B., Papa, F., 2017. A global dynamic long-term inundation extent dataset at high spatial resolution derived through downscaling of satellite observations. J. Hydrometeorol. 18, 1305–1325, https://doi.org/10.1175/JHM-D-16-0155.1.

Alcoforado, R., Cirilo, J., 2001. Sistema de Suporte à Decisão para Análise, Previsão e Controle de Inundações. Rev. Bras. Recur. Hídricos. 6 (4), 133–153, https://doi.org/10.21168/rbrh.v6n4.p133-153.

Alfieri, L., Salamon, P., Bianchi, A., Neal, J., Bates, P., Feyen, L., 2014. Advances in pan-European flood hazard mapping. Hydrol. Process. 28, 4067–4077, https://doi.org/10.1002/hyp.9947.

Alfieri, L., Feyen, L., Dottori, F., Bianchi, A., 2015. Ensemble flood risk assessment in Europe under high end climate scenarios. Glob. Environ. Chang. 35, 199–212, https://doi.org/10.1016/j.gloenvcha.2015.09.004.

Alfieri, L., Cohen, S., Galantowicz, J., Schumann, G.J.P., Trigg, M.A., Zsoter, E., Prudhomme, C., Kruczkiewicz, A., Coughlan de Perez, E., Flamig, Z., Rudari, R., Wu, H., Adler, R.F., Brakenridge, R.G., Kettner, A., Weerts, A., Matgen, P., Islam, S.A.K.M., de Groeve, T., Salamon, P., 2018. A global network for operational flood risk reduction. Environ. Sci. Policy 84, 149–158, https://doi.org/10.1016/j.envsci.2018.03.014.

Allen, G.H., Pavelsky, T.M., 2018. Global extent of rivers and streams. Science 361, 585–588, https://doi.org/10.1126/science.aat0636.

Alsdorf, D.E., Melack, J.M., Dunne, T., Mertes, L.A.K., Hess, L.L., Smith, L.C., 2000. Interferometric radar measurements of water level changes on the Amazon flood plain. Nature 404, 174–177, https://doi.org/10.1038/35004560.

Alsdorf, D., Bates, P., Melack, J., Wilson, M., Dunne, T., 2007. Spatial and temporal complexity of the Amazon flood measured from space. Geophys. Res. Lett. 34, 1–5, https://doi.org/10.1029/2007GL029447.

Alsdorf, D., Han, S.C., Bates, P., Melack, J., 2010. Seasonal water storage on the Amazon floodplain measured from satellites. Remote Sens. Environ. 114, 2448–2456, https://doi.org/10.1016/j.rse.2010.05.020.

ANA, 2014. VULNERABILIDADE A INUNDAÇÕES DO BRASIL [WWW Document]. Available from: https://metadados.ana.gov.br/geonetwork/srv/pt/metadata.show?uuid=2cfa808b-b370-43ef-8107-5c3bfd7acf9c (accessed 1.9.20.).

Anderson, E.P., Jenkins, C.N., Heilpern, S., Maldonado-Ocampo, J.A., Carvajal-Vallejos, F.M., Encalada, A.C., Rivadeneira, J.F., Hidalgo, M., Cañas, C.M., Ortega, H., Salcedo, N., Maldonado, M., Tedesco, P.A., 2018. Fragmentation of Andes-to-Amazon connectivity by hydropower dams. Sci. Adv. 4, eaao1642, https://doi.org/10.1126/sciadv.aao1642.

Araujo, A., Breda, A., Freitas, C., Gonçalves, J.E., Calveti, L., Almeida, M.I., Silveira, R.B., 2014. Hydrological and meteorological forecast combined systems for flood alerts and reservoir management: the Iguaçu river basin case. In: Sixth International Conference on Flood Management, São Paulo. 1–10.

Angarita, H., Wickel, A.J., Sieber, J., Chavarro, J., Maldonado-Ocampo, J.A., Herrera-R, G.A., Delgado, J., Purkey, D., 2017. Large-scale impacts of hydropower development on the Mompós Depression wetlands, Colombia. Hydrol. Earth Syst. Sci. Discuss. 22 (5), 1–39, https://doi.org/10.5194/hess-2017-544.

Arnesen, A.S., Silva, T.S.F., Hess, L.L., Novo, E.M.L.M., Rudorff, C.M., Chapman, B.D., McDonald, K.C., 2013. Monitoring flood extent in the lower Amazon River floodplain using ALOS/PALSAR ScanSAR images. Remote Sens. Environ. 130, 51–61, https://doi.org/10.1016/j.rse.2012.10.035.

Augusto-Silva, P.B., MacIntyre, S., de Moraes Rudorff, C., Cortés, A., Melack, J.M., 2019. Stratification and mixing in large floodplain lakes along the lower Amazon River. J. Great Lakes Res. 45, 61–72, https://doi.org/10.1016/j.jglr.2018.11.001.

Bartiko, D., Oliveira, D.Y., Bonumá, N.B., Chaffe, P.L.B., 2019. Spatial and seasonal patterns of flood change across Brazil. Hydrol. Sci. J. 64, 1071–1079, https://doi.org/10.1080/02626667.2019.1619081.

Bates, P.D., De Roo, A.P.J., 2000. A simple raster-based model for flood inundation simulation. J. Hydrol. 236 (1–2), 54–77, https://doi.org/10.1016/S0022-1694(00)00278-X.

Bates, P.D., Neal, J.C., Alsdorf, D., Schumann, G.J.P., 2014. Observing global surface water flood dynamics. Surv. Geophys. 35, 839–852, https://doi.org/10.1007/s10712-013-9269-4.

Beighley, R.E., Eggert, K.G., Dunne, T., He, Y., Gummadi, V., Verdin, K.L., 2009. Simulating hydrologic and hydraulic processes throughout the Amazon River Basin. Hydrol. Process. 23, 1221–1235, https://doi.org/10.1002/hyp.7252.

Bergier, I., Silva, A.P.S., Abreu, U.G.P., de Oliveira, L.O.F., de Tomazi, M., Dias, F.R.T., Urbanetz, C., Nogueira, É., Borges-Silva, J.C., 2019. Could bovine livestock intensification in Pantanal be neutral regarding enteric methane emissions? Sci. Total Environ. 655, 463–472, https://doi.org/10.1016/j.scitotenv.2018.11.178.

Biancamaria, S., Lettenmaier, D.P., Pavelsky, T.M., 2016. The SWOT mission and its capabilities for land hydrology. Surv. Geophys. 37, 307–337, https://doi.org/10.1007/s10712-015-9346-y.

Brakenridge, R.G., 2020. Global Active Archive of Large Flood Events [WWW Document]. Available from: https://floodobservatory.colorado.edu/Archives/index.html.

Brakenridge, G.R., Nghiem, S.V., Anderson, E., Chien, S., 2005. Space-based measurement of river runoff. EOS 86 (19), 185–188, https://doi.org/10.1029/2005EO190001.

Bravo, J.M., Allasia, D., Paz, A.R., Collischonn, W., Tucci, C.E.M., 2012. Coupled hydrologic-hydraulic modeling of the Upper Paraguay River Basin. J. Hydrol. Eng. 17, 635–646, https://doi.org/10.1061/(ASCE)HE.1943-5584.0000494.

Brêda, J.P.L.F., Paiva, R.C.D., Bravo, J.M., Passaia, O.A., Moreira, D.M., 2019. Assimilation of satellite altimetry data for effective river bathymetry. Water Resour. Res. 55 (9), 7441–7463, https://doi.org/10.1029/2018wr024010.

Brunner, G.W., Piper, S.S., Jensen, M.R., Chacon, B., 2015. Combined 1D and 2D hydraulic modeling within HEC-RAS. In: World Environmental and Water Resources Congress 2015: Floods, Droughts, and Ecosystems—Proceedings of the 2015 World Environmental and Water Resources Congress. https://doi.org/10.1061/9780784479162.141.

Calmant, S., Seyler, F., Cretaux, J.F., 2008. Monitoring continental surface waters by satellite altimetry. Surv. Geophys. 29, 247–269, https://doi.org/10.1007/s10712-008-9051-1.

Cao, N., Lee, H., Jung, H.C., Yu, H., 2018. Estimation of water level changes of large-scale Amazon wetlands using ALOS2 ScanSAR differential interferometry. Remote Sens. 10 (6), 966, https://doi.org/10.3390/rs10060966.

Casagrande, L., Tomasella, J., dos Santos Alvalá, R.C., Bottino, M.J., de Oliveira Caram, R., 2017. Early flood warning in the Itajaí-Açu River basin using numerical weather forecasting and hydrological modeling. Nat. Hazards 88, 741–757, https://doi.org/10.1007/s11069-017-2889-0.

Cassalho, F., Beskow, S., de Mello, C.R., de Moura, M.M., 2019. Regional flood frequency analysis using L-moments for geographically defined regions: An assessment in Brazil. J. Flood Risk Manag. 12 (2), e12453, https://doi.org/10.1111/jfr3.12453.

Chávarri, E., Crave, A., Bonnet, M.P., Mejía, A., Santos Da Silva, J., Guyot, J.L., 2013. Hydrodynamic modelling of the Amazon River: Factors of uncertainty. J. South Am. Earth Sci. 44, 94–103, https://doi.org/10.1016/j.jsames.2012.10.010.

Collischonn, W., Allasia, D., da Silva, B.C., Tucci, C.E.M., 2007. The MGB-IPH model for large-scale rainfall-runoff modelling. Hydrol. Sci. J. 52 (5), 878–895, https://doi.org/10.1623/hysj.52.5.878.

CRED, 2019. EM-DAT website [WWW Document]. Available from: https://www.emdat.be/.

da Paz, A.R., Collischonn, W., Tucci, C.E.M., Padovani, C.R., 2011. Large-scale modelling of channel flow and floodplain inundation dynamics and its application to the Pantanal (Brazil). Hydrol. Process. 25, 1498–1516, https://doi.org/10.1002/hyp.7926.

Da Silva, J.S., Calmant, S., Seyler, F., Moreira, D.M., Oliveira, D., Monteiro, A., 2014. Radar altimetry aids managing gauge networks. Water Resour. Manag. 28, 587–603, https://doi.org/10.1007/s11269-013-0484-z.

de Bruijn, J.A., de Moel, H., Jongman, B., de Ruiter, M.C., Wagemaker, J., Aerts, J.C.J.H., 2019. A global database of historic and real-time flood events based on social media. Sci. Data 6, 311, https://doi.org/10.1038/s41597-019-0326-9.

De Groeve, T., Thielen-del Pozo, J., Brakenridge, R., Adler, R., Alfieri, L., Kull, D., Lindsay, F., Imperiali, O., Pappenberger, F., Rudari, R., Salamon, P., Villars, N., Wyjad, K., 2015. Joining forces in a global flood partnership. Bull. Am. Meteorol. Soc. 96, ES97–ES100, https://doi.org/10.1175/BAMS-D-14-00147.1.

Dias, C.M., Pastore, D.H., Borma, L.S., Bevilacqua, L., 2011. Modelling and numerical simulation of the velocity field in the Parque Estadual do Cantão (TO), Brazil. Math. Comput. Model. 53, 1575–1581, https://doi.org/10.1016/j.mcm.2010.06.021.

Dottori, F., Salamon, P., Bianchi, A., Alfieri, L., Hirpa, F.A., Feyen, L., 2016. Development and evaluation of a framework for global flood hazard mapping. Adv. Water Resour. 94, 87–102, https://doi.org/10.1016/j.advwatres.2016.05.002.

Elsevier, 2019. Scopus [WWW Document]. Available from: https://www.scopus.com/ (accessed 1.6.20.).

Emery, C.M., Paris, A., Biancamaria, S., Boone, A., Calmant, S., Garambois, P.A., Da Silva, J.S., 2018. Large-scale hydrological model river storage and discharge correction using a satellite altimetry-based discharge product. Hydrol. Earth Syst. Sci. 22, 2135–2162, https://doi.org/10.5194/hess-22-2135-2018.

Fan, F.M., Paiva, R.C.D., Collischonn, W., 2016. Hydrological forecasting practices in Brazil. In: Flood Forecasting. Elsevier, pp. 41–66. https://doi.org/10.1016/B978-0-12-801884-2.00002-5.

Fan, F.M., Fleischmann, A.S., Siqueira, V., Nectoux, M., Giacomelli, L., 2019. Flood forecasting system for the State of Rio Grande do Sul, Brazil. In: European Geosciences Union General Assembly. EGU, Vienna, Austria.

Fassoni-Andrade, A., Paiva, R., Fleischmann, A., 2020. Lake bathymetry and active storage from satellite observations of flood frequency. Water Resour. Res. 56 (7), 1–18.

Ferreira-Ferreira, J., Silva, T.S.F., Streher, A.S., Affonso, A.G., de Almeida Furtado, L.F., Forsberg, B.R., Valsecchi, J., Queiroz, H.L., de Moraes Novo, E.M.L., 2015. Combining ALOS/PALSAR derived vegetation structure and inundation patterns to characterize major vegetation types in the Mamirauá Sustainable Development Reserve, Central Amazon floodplain. Brazil. Wetl. Ecol. Manag. 23, 41–59, https://doi.org/10.1007/s11273-014-9359-1.

Fleischmann, A., Brêda, J., Passaia, O., Correa, S., Fan, F., Paiva, R., Marques, G., Collischonn, W., 2021. Regional scale hydrodynamic modeling of the river-floodplain-reservoir continuum https://doi.org/10.1002/essoar.10506204.1.

Fleischmann, A., Collischonn, W., Paiva, R., Tucci, C.E., 2019a. Modeling the role of reservoirs versus floodplains on large-scale river hydrodynamics. Nat. Hazards 99, 1075–1104, https://doi.org/10.1007/s11069-019-03797-9.

Fleischmann, A., Paiva, R., Collischonn, W., 2019b. Can regional to continental river hydrodynamic models be locally relevant? A cross-scale comparison. J. Hydrol. X 3, 100027, https://doi.org/10.1016/j.hydroa.2019.100027.

Fleischmann, A., Paiva, R., Collischonn, W., Siqueira, V., Paris, A., Moreira, D., Papa, F., Al Bitar, A., Parrens, M., Aires, F., Garambois, P-A., 2020a. Trade-offs between 1D and 2D regional river hydrodynamic models. Water Resour. Res. 56 (8), e2019WR026812.

Fleischmann, A.S., Siqueira, V.A., Wongchuig, S.C., Collischonn, W., de Paivade, R.C.D., 2020b. The great 1983 floods in South American large rivers: a continental hydrological modeling approach. Hydrol. Sci. J. 65 (8), 1358–1373.

Fluet-Chouinard, E., Lehner, B., Rebelo, L.M., Papa, F., Hamilton, S.K., 2015. Development of a global inundation map at high spatial resolution from topographic downscaling of coarse-scale remote sensing data. Remote Sens. Environ. 158, 348–361, https://doi.org/10.1016/j.rse.2014.10.015.

Frappart, F., Papa, F., Famiglietti, J.S., Prigent, C., Rossow, W.B., Seyler, F., 2008. Interannual variations of river water storage from a multiple satellite approach: A case study for the Rio Negro River basin. J. Geophys. Res. 113, D21104, https://doi.org/10.1029/2007JD009438.

Frasson, R.P., de, M., Pavelsky, T.M., Fonstad, M.A., Durand, M.T., Allen, G.H., Schumann, G., Lion, C., Beighley, R.E., Yang, X., 2019. Global relationships between river width, slope, catchment area, Meander wavelength, sinuosity, and discharge. Geophys. Res. Lett. 46, 3252–3262, https://doi.org/10.1029/2019GL082027.

Garambois, P., Monnier, J., 2015. Inference of effective river properties from remotely sensed observations of water surface. Adv. Water Resour. 79, 103–120, https://doi.org/10.1016/j.advwatres.2015.02.007.

Garambois, P.A., Calmant, S., Roux, H., Paris, A., Monnier, J., Finaud-Guyot, P., Samine Montazem, A., Santos da Silva, J., 2017. Hydraulic visibility: Using satellite altimetry to parameterize a hydraulic model of an ungauged reach of a braided river. Hydrol. Process. 31, 756–767, https://doi.org/10.1002/hyp.11033.

Germano, A.D.O., Castilho, A., Candido, M., Reis, F., 2014. Flood of 2014 in Madeira River. In: XXI Simpósio Brasileiro de Recursos Hídricos. ABRHidro, Brasília, pp. 1–8.

Hamilton, S.K., Sippel, S.J., Melack, J.M., 2002. Comparison of inundation patterns among major South American floodplains 107, 1–14.

Hess, L.L., Melack, J.M., Novo, E.M.L.M., Barbosa, C.C.F., Gastil, M., 2003. Dual-season mapping of wetland inundation and vegetation for the central Amazon basin. Remote Sens. Environ. 87, 404–428, https://doi.org/10.1016/j.rse.2003.04.001.

Hess, L.L., Melack, J.M., Affonso, A.G., Barbosa, C., Gastil-buhl, M., Novo, E.M.L.M., 2015. Wetlands of the lowland Amazon Basin: Extent, vegetative cover, and dual-season inundated area as mapped with JERS-1 synthetic aperture radar. Wetlands. 35, 745–756. https://doi.org/10.1007/s13157-015-0666-y.

Hoch, J., Trigg, M.A., 2018. Advancing global flood hazard simulations by improving comparability, benchmarking, and integration of global flood models. Environ. Res. Lett. 14 (3), 034001, https://doi.org/10.1088/1748-9326/aaf3d3.

Junk, W.J., Wittmann, F., Schöngart, J., Piedade, M.T.F., 2015. A classification of the major habitats of Amazonian black-water river floodplains and a comparison with their white-water counterparts. Wetl. Ecol. Manag. 23, 677–693, https://doi.org/10.1007/s11273-015-9412-8.

Kandus, P., Minotti, P.G., Fabricante, I., Ramonell, C., 2017. Identificación y Delimitación de Regiones de Humedales de Argentina, in: Regiones de Humedales de Argentina. Ministerio de Ambiente y Desarrollo Sustentable, Fundación Humedales/Wetlands International, Universidad Nacional de San Martín y Universidad de Buenos Aires, Buenos Aires, pp. 31–48.

Kandus, P., Minotti, P.G., Morandeira, N.S., Trilla, G.G., González, E.B., Martín, L.S., Gayol, M.P., Kandus, P., Minotti, P.G., Morandeira, N.S., 2018. Remote sensing of wetlands in South America: status and challenges. Int. J. Remote Sens. 39, 993–1016, https://doi.org/10.1080/01431161.2017.1395971.

Kirchner, J.W., 2006. Getting the right answers for the right reasons: Linking measurements, analyses, and models to advance the science of hydrology. Water Resour. Res. 42 (3), W03S04, https://doi.org/10.1029/2005WR004362.

Latrubesse, E.M., Arima, E.Y., Dunne, T., Park, E., Baker, V.R., D'Horta, F.M., Wight, C., Wittmann, F., Zuanon, J., Baker, P.A., Ribas, C.C., Norgaard, R.B., Filizola, N., Ansar, A., Flyvbjerg, B., Stevaux, J.C., 2017. Damming the rivers of the Amazon basin. Nature 546, 363–369, https://doi.org/10.1038/nature22333.

Lee, H., Yuan, T., Yu, H., Jung, H.C., 2020. Interferometric SAR for Wetland Hydrology: An overview of methods, challenges, and trends. IEEE Geosci. Remote Sens. Mag. 8 (1), 120–135, https://doi.org/10.1109/MGRS.2019.2958653.

Lehner, B., Verdin, K., Jarvis, A., 2013. HydroSHEDS Technical Documentation Version 1.2. EOS Trans. https://doi.org/World Wildlife Fund US, Washington, DC. Available from: <http://hydrosheds.cr.usgs.gov>.

Lima, C.H.R., Lall, U., Troy, T.J., Devineni, N., 2015. A climate informed model for nonstationary flood risk prediction: Application to Negro River at Manaus, Amazonia. J. Hydrol. 522, 594–602, https://doi.org/10.1016/j.jhydrol.2015.01.009.

Lima, C.H.R., Aghakouchak, A., Lall, U., 2017. Classification of mechanisms, climatic context, areal scaling, and synchronization of floods: The hydroclimatology of floods in the Upper Paraná River basin, Brazil. Earth Syst. Dyn. 8 (4), 1071–1091, https://doi.org/10.5194/esd-8-1071-2017.

Lopes, V.A.R., Fan, F.M., Pontes, P.R.M., Siqueira, V.A., Collischonn, W., da Motta Marques, D., 2018. A first integrated modelling of a river-lagoon large-scale hydrological system for forecasting purposes. J. Hydrol. 565, 177–196, https://doi.org/10.1016/j.jhydrol.2018.08.011.

Luo, X., Li, H.-Y., Leung, L.R., Tesfa, T.K., Getirana, A., Papa, F., Hess, L.L., 2017. Modeling surface water dynamics in the Amazon Basin using MOSART-Inundation v1.0: impacts of geomorphological parameters and river flow representation. Geosci. Model Dev. 10, 1233–1259, https://doi.org/10.5194/gmd-10-1233-2017.

Mateo, C.M., Hanasaki, N., Komori, D., Tanaka, K., Kiguchi, M., Champathong, A., Sukhapunnaphan, T., Yamazaki, D., Oki, T., 2014. Assessing the impacts of reservoir operation to floodplain inundation by combining hydrological, reservoir management, and hydrodynamic models. Water Resour. Res. 50, 7245–7266, https://doi.org/10.1002/2013WR014845.

Meyer, A., Fleischmann, A., Collischonn, W., de Paiva, R.C.D., Jardim, P., 2018. Empirical assessment of flood wave celerity-discharge relationships at local and reach scales. Hydrol. Sci. J. 63 (15–16), 2035–2047.

Montero, J.C., Latrubesse, E.M., 2013. The igapó of the Negro River in central Amazonia: Linking late-successional inundation forest with fluvial geomorphology. J. South Am. Earth Sci. 46, 137–149, https://doi.org/10.1016/j.jsames.2013.05.009.

Neal, J., Schumann, G., Bates, P., 2012. A subgrid channel model for simulating river hydraulics and floodplain inundation over large and data sparse areas. Water Resour. Res. 48, 1–16, https://doi.org/10.1029/2012WR012514.

Nectoux, M., Giacomelli, L., Fan, F.M., Fleischmann, A.S., Siqueira, V., Custodio, M., Collischonn, W., 2019. PREVISÃO DE CHEIAS E PRODUÇÃO DE AVISOS NO ESTADO DO RIO GRANDE DO SUL ATRAVÉS DA SALA DE SITUAÇÃO SEMA/RS E MODELO MGB. In: Anais Do XXIII SBR.H. ABRHidro, Foz do, Iguaçu.

Neiff, J.J., Iriondo, M.H., Carignan, R., 1994. Large tropical South American wetlands: An overview, in: Link, G.L., Naiman, R.J. (Eds.), The Ecology & Management of Aquatic-Terrestrial Ecotones. University of Washington, pp. 155–165.

Nobre, A.D., Cuartas, L.A., Momo, M.R., Severo, D.L., Pinheiro, A., Nobre, C.A., 2016. HAND contour: A new proxy predictor of inundation extent. Hydrol. Process. 30 (2), 320–333, https://doi.org/10.1002/hyp.10581.

Oliveira, A.M., Fleischmann, A.S., de Paiva, R.C.D., 2020. On the contribution of remote sensing-based calibration to model multiple hydrological variables. Earth Sp. Sci. Open Arch., 1–31. doi: 10.1002/essoar.10502160.1.

O'Loughlin, F.E., Paiva, R.C.D., Durand, M., Alsdorf, D.E., Bates, P.D., 2016. A multi-sensor approach towards a global vegetation corrected SRTM DEM product. Remote Sens. Environ. 182, 49–59, https://doi.org/10.1016/j.rse.2016.04.018.

Oki, T., Sud, Y.C., 1998. Design of Total Runoff Integrating Pathways (TRIP)—A Global River Channel Network. Earth Interact. 2 (1), 1–37. https://doi.org/10.1175/1087-3562(1998)002<0001:dotrip>2.3.co;2.

Paiva, R., Buarque, D.C., Collischonn, W., Bonnet, M.P., Frappart, F., Calmant, S., Bulhões Mendes, C.A., 2013a. Large-scale hydrologic and hydrodynamic modeling of the Amazon River basin. Water Resour. Res. 49, 1226–1243, https://doi.org/10.1002/wrcr.20067.

Paiva, R., Collischonn, W., Bonnet, M.P., De Gonçalves, L.G.G., Calmant, S., Getirana, A., Santos Da Silva, J., 2013b. Assimilating in situ and radar altimetry data into a large-scale hydrologic-hydrodynamic model for streamflow forecast in the Amazon. Hydrol. Earth Syst. Sci. 17, 2929–2946, https://doi.org/10.5194/hess-17-2929-2013.

Papa, F., Frappart, F., Güntner, A., Prigent, C., Aires, F., Getirana, A.C.V., Maurer, R., 2013. Surface freshwater storage and variability in the Amazon basin from multi-satellite observations, 1993-2007. J. Geophys. Res. Atmos. 118 (21), 11951–11965, https://doi.org/10.1002/2013JD020500.

Paris, A., Dias de Paiva, R., Santos da Silva, J., Medeiros Moreira, D., Calmant, S., Garambois, P.A., Collischonn, W., Bonnet, M.P., Seyler, F., 2016. Stage-discharge rating curves based on satellite altimetry and modeled discharge in the Amazon basin. Water Resour. Res. 52 (5), 3787–3814, https://doi.org/10.1002/2014WR016618.

Paris, A., Calmant, S., Gossett, M., Fleischmann, A.S., Garambois, P., Andriambelosom, J., Siqueira, V.A., Silva, J.S. da, Conchy, T., de Paiva, R.C.D., Collischonn, W., 2018. Long term chronicles and near real time discharges estimates derived from satellite altimetry, hydrological modelling and remote sensing observations in ungauged basins. In: Remote Sensing and Hydrology Symposium, ICRS-IAHS, Córdoba, Spain.

Parrens, M., Bitar, A., Al, Frappart, F., Paiva, R., Wongchuig, S., Papa, F., Yamasaki, D., Kerr, Y., 2019. High resolution mapping of inundation area in the Amazon basin from a combination of L-band passive microwave, optical and radar datasets. Int. J. Appl. Earth Obs. Geoinf. 81, 58–71, https://doi.org/10.1016/j.jag.2019.04.011.

Paz, A.R., Bravo, J.M., Allasia, D., Collischonn, W., Tucci, C.E.M., 2010. Large-scale hydrodynamic modeling of a complex river network and floodplains. J. Hydrol. Eng. 15, 152–165, https://doi.org/10.1061/(ASCE)HE.1943-5584.0000162.

Pekel, J., Cottam, A., Gorelick, N., Belward, A.S., 2016. High-resolution mapping of global surface water and its long-term changes. Nature 540, 418–422, https://doi.org/10.1038/nature20584.

Pinel, S., Bonnet, M., S. Da Silva, J., Sampaio, T.C., Garnier, J., Catry, T., Calmant, S., Fragoso, C.R., Moreira, D., Motta Marques, D., Seyler, F., 2019. Flooding dynamics within an Amazonian floodplain: water circulation patterns and inundation duration. Water Resour. Res. 56 (1), e2019WR026081 https://doi.org/10.1029/2019WR026081.

Pontes, P.R.M., Fan, F.M., Fleischmann, A.S., de Paiva, R.C.D., Buarque, D.C., Siqueira, V.A., Jardim, P.F., Sorribas, M.V., Collischonn, W., 2017. MGB-IPH model for hydrological and hydraulic simulation of large floodplain river systems coupled with open source GIS. Environ. Model. Softw. 94, 1–20, https://doi.org/10.1016/j.envsoft.2017.03.029.

Prigent, C., Lettenmaier, D.P., Aires, F., Papa, F., 2016. Toward a high-resolution monitoring of continental surface water extent and dynamics, at Global Scale: from GIEMS (Global Inundation Extent from Multi-Satellites) to SWOT (Surface Water Ocean Topography). Surv. Geophys. 37, 339–355, https://doi.org/10.1007/s10712-015-9339-x.

Prigent, C., Papa, F., Aires, F., Rossow, W.B., Matthews, E., 2007. Global inundation dynamics inferred from multiple satellite observations, 1993-2000. J. Geophys. Res. Atmos. 112 (D12), 1–13, https://doi.org/10.1029/2006JD007847.

Ricaurte, L.F., Patiño, J.E., Zambrano, D.F.R., Arias-G, J.C., Acevedo, O., Aponte, C., Medina, R., González, M., Rojas, S., Flórez, C., Estupinan-Suarez, L.M., Jaramillo, Ú., Santos, A.C., Lasso, C.A., Nivia, A.A.D., Calle, S.R., Vélez, J.I., Acosta, J.H.C., Duque, S.R., Núñez-Avellaneda, M., Correa, I.D., Rodríguez-Rodríguez, J.A., Vilardy Q, S.P., Prieto-C, A, Rudas-Ll, A., Cleef, A.M., Finlayson, C.M., Junk, W.J., 2019. A classification system for Colombian Wetlands: an essential step forward in open environmental policy-making. Wetlands 39, 971–990, https://doi.org/10.1007/s13157-019-01149-8.

Rudorff, C.M., Melack, J.M., Bates, P.D., 2014a. Flooding dynamics on the lower Amazon floodplain: 1. Hydraulic controls on water elevation, inundation extent, and river-floodplain discharge. Water Resour. Res. 50, 619–634, https://doi.org/10.1002/2013WR014091.

Rudorff, C.M., Melack, J.M., Bates, P.D., 2014b. Flooding dynamics on the lower Amazon floodplain: 2. Seasonal and interannual hydrological variability. Water Resour. Res. 50, 635–649, https://doi.org/10.1002/2013WR014714.

Rudorff, C.M., Dunne, T., Melack, J.M., 2018. Recent increase of river-floodplain suspended sediment exchange in a reach of the lower Amazon River. Earth Surf. Process. Landforms 43, 322–332, https://doi.org/10.1002/esp.4247.

Sampson, C.C., Smith, A.M., Bates, P.D., Neal, J.C., Alfieri, L., Freer, J.E., 2015. A high-resolution global flood hazard model. Water Resour. Res. 51, 7358–7381, https://doi.org/10.1002/2015WR016954.

Santilli, G., Vendittozzi, C., Cappelletti, C., Battistini, S., Gessini, P., 2018. CubeSat constellations for disaster management in remote areas. Acta Astronaut. 145, 11–17, https://doi.org/10.1016/j.actaastro.2017.12.050.

Santos da Silva, J., Calmant, S., Seyler, F., Rotunno Filho, O.C., Cochonneau, G., Mansur, W.J., 2010. Water levels in the Amazon basin derived from the ERS 2 and ENVISAT radar altimetry missions. Remote Sens. Environ. 114, 2160–2181, https://doi.org/10.1016/j.rse.2010.04.020.

Santos, L.B.L., Carvalho, T., Anderson, L.O., Rudorff, C.M., Marchezini, V., Londe, L.R., Saito, S.M., 2017. An RS-GIS-based comprehensive impact assessment of floods—A case study in Madeira River, Western Brazilian Amazon. IEEE Geosci. Remote Sens. Lett. 14, 1614–1617, https://doi.org/10.1109/LGRS.2017.2726524.

Schumann, J.-P., Neal, J.C., Voisin, N., Andreadis, K.M., Pappenberger, F., Phanthuwongpakdee, N., Hall, A.C., Bates, P.D., Schumann, C., 2013. A first large scale flood inundation forecasting model. Water Resour. Res. 49, 6248–6257, https://doi.org/10.1002/wrcr.20521.

Schumann, G.J.P., Stampoulis, D., Smith, A.M., Sampson, C.C., Andreadis, K.M., Neal, J.C., Bates, P.D., 2016. Rethinking flood hazard at the global scale. Geophys. Res. Lett. 43, 10249–10256, https://doi.org/10.1002/2016GL070260.

Schwanenberg, D., Fan, F.M., Naumann, S., Kuwajima, J.I., Montero, R.A., Assis dos Reis, A., 2015. Short-term reservoir optimization for flood mitigation under meteorological and hydrological forecast uncertainty: Application to the Três Marias Reservoir in Brazil. Water Resour. Manag. 29, 1635–1651, https://doi.org/10.1007/s11269-014-0899-1.

Seyler, F., Calmant, S., da Silva, J., Filizola, N., Cochonneau, G., Bonnet, M.P., Costi, A.C.Z., 2009. Inundation risk in large tropical basins and potential survey from radar altimetry: Example in the Amazon Basin. Mar. Geod. 32 (3), 303–319, https://doi.org/10.1080/01490410903094809.

Shin, S., Pokhrel, Y., Miguez-Macho, G., 2019. High-resolution modeling of reservoir release and storage dynamics at the continental scale. Water Resour. Res. 55, 787–810, https://doi.org/10.1029/2018WR023025.

Silva, T.S.F., Costa, M.P.F., Melack, J.M., 2010. Spatial and temporal variability of macrophyte cover and productivity in the eastern Amazon floodplain: A remote sensing approach. Remote Sens. Environ. 114, 1998–2010, https://doi.org/10.1016/j.rse.2010.04.007.

Sippel, S.J., Hamilton, S.K., Melack, J.M., Choudhury, B.J., 1994. Determination of inundation area in the Amazon River floodplain using the SMMR 37 GHz polarization difference. Remote Sens. Environ. 48, 70–76, https://doi.org/10.1016/0034-4257(94)90115-5.

Siqueira, V.A., Paiva, R.C.D., Fleischmann, A.S., Fan, F.M., Ruhoff, A.L., Pontes, P.R.M., Paris, A., Calmant, S., Collischonn, W., 2018. Toward continental hydrologic–hydrodynamic modeling in South America. Hydrol. Earth Syst. Sci. 22, 4815–4842, https://doi.org/10.5194/hess-22-4815-2018.

Sosa, J., Sampson, C., Smith, A., Neal, J., Bates, P., 2020. A toolbox to quickly prepare flood inundation models for LISFLOOD-FP simulations. Environ. Model. Softw. 123, 104561, https://doi.org/10.1016/j.envsoft.2019.104561..

Speckhann, G.A., Borges Chaffe, P.L., Fabris Goerl, R., Abreu, J.J., de Altamirano Flores, J.A., 2018. Flood hazard mapping in Southern Brazil: a combination of flow frequency analysis and the HAND model. Hydrol. Sci. J. 63, 87–100, https://doi.org/10.1080/02626667.2017.1409896.

Steffen, P.C., Gomes, J., 2018. Clustering of historical floods observed on Iguaçu River. In: União da Vitória, Paraná. RBRH 23. https://doi.org/10.1590/2318-0331.231820170107.

Tourian, M.J., Elmi, O., Mohammadnejad, A., Sneeuw, N., 2017. Estimating river depth from SWOT-type observables obtained by satellite altimetry and imagery. Water (Switzerland) 9 (10), 753, https://doi.org/10.3390/w9100753.

Trigg, M.A., Wilson, M.D., Bates, P.D., Horritt, M.S., Alsdorf, D.E., Forsberg, B.R., Vega, M.C., 2009. Amazon flood wave hydraulics. J. Hydrol. 374, 92–105, https://doi.org/10.1016/j.jhydrol.2009.06.004.

Trigg, M.A., Birch, C.E., Neal, J.C., Bates, P.D., Smith, A., Sampson, C.C., Yamazaki, D., Hirabayashi, Y., Pappenberger, F., Dutra, E., Ward, P.J., Winsemius, H.C., Salamon, P., Dottori, F., Rudari, R., Kappes, M.S., Simpson, A.L., Hadzilacos, G., Fewtrell, T.J., 2016. The credibility challenge for global fluvial flood risk analysis. Environ. Res. Lett. 11, 094014, https://doi.org/10.1088/1748-9326/11/9/094014.

Tucci, C.E.M., Clarke, R.T., 1998. Environmental issues in the la Plata Basin. Int. J. Water Resour. Dev. 14 (2), 157–173, https://doi.org/10.1080/07900629849376.

Uereyen, S., Kuenzer, C., 2019. A review of Earth Observation-based analyses for major river basins. Remote Sens. 11, 2951, https://doi.org/10.3390/rs11242951.

Vörösmarty, C.J., Bravo de Guenni, L., Wollheim, W.M., Pellerin, B., Bjerklie, D., Cardoso, M., D'Almeida, C., Green, P., Colon, L., 2013. Extreme rainfall, vulnerability and risk: a continental-scale assessment for South America. Philos. Trans. R. Soc. A Math. Phys. Eng. Sci. 371 (2002), 20120408, https://doi.org/10.1098/rsta.2012.0408.

Ward, P.J., Jongman, B., Weiland, F.S., Bouwman, A., Van Beek, R., Bierkens, M.F.P., Ligtvoet, W., Winsemius, H.C., 2013. Assessing flood risk at the global scale: Model setup, results, and sensitivity. Environ. Res. Lett. 8, 044019, https://doi.org/10.1088/1748-9326/8/4/044019.

Wilson, M.D., Bates, P., Alsdorf, D., Forsberg, B., Horritt, M., Melack, J., Frappart, F., Famiglietti, J., 2007. Modeling large-scale inundation of Amazonian seasonally flooded wetlands. Geophys. Res. Lett. 34, 4–9, https://doi.org/10.1029/2007GL030156.

Winsemius, H.C., Van Beek, L.P.H., Jongman, B., Ward, P.J., Bouwman, A., 2013. A framework for global river flood risk assessments. Hydrol. Earth Syst. Sci. 17, 1871–1892, https://doi.org/10.5194/hess-17-1871-2013.

Wongchuig, S., Paiva, R., Biancamaria, S., Collischonn, W., 2020. Assimilation of future SWOT-based river elevations, surface extent observations and discharge estimations into uncertain global hydrological models. Journal of Hydrology 590, 125473.

Wu, H., Adler, R.F., Tian, Y., Huffman, G.J., Li, H., Wang, J., 2014. Real-time global flood estimation using satellite-based precipitation and a coupled land surface and routing model. Water Resour. Res. 50 (3), 2693–2717, https://doi.org/10.1002/2013WR014710.

Yamazaki, D., Oki, T., Kanae, S., 2009. Deriving a global river network map and its sub-grid topographic characteristics from a fine-resolution flow direction map. Hydrol. Earth Syst. Sci. 13, 2241–2251, https://doi.org/10.5194/hess-13-2241-2009.

Yamazaki, D., Kanae, S., Kim, H., Oki, T., 2011. A physically based description of floodplain inundation dynamics in a global river routing model. Water Resour. Res. 47, 1–21, https://doi.org/10.1029/2010WR009726.

Yamazaki, D., Lee, H., Alsdorf, D.E., Dutra, E., Kim, H., Kanae, S., Oki, T., 2012. Analysis of the water level dynamics simulated by a global river model: A case study in the Amazon River. Water Resour. Res. 48, 1–15, https://doi.org/10.1029/2012WR011869.

Yamazaki, D., Ikeshima, D., Tawatari, R., Yamaguchi, T., O'Loughlin, F., Neal, J.C., Sampson, C.C., Kanae, S., Bates, P.D., 2017. A high-accuracy map of global terrain elevations. Geophys. Res. Lett. 44 (11), 5844–5853, https://doi.org/10.1002/2017GL072874.

Yamazaki, D., Ikeshima, D., Sosa, J., Bates, P.D., Allen, G., Pavelsky, T., 2019. MERIT Hydro: A high-resolution global hydrography map based on latest topography datasets. Water Resour. Res. 55 (6), 5053–5073, https://doi.org/10.1029/2019WR024873.

Yoon, Y., Durand, M., Merry, C.J., Clark, E.A., Andreadis, K.M., Alsdorf, D.E., 2012. Estimating river bathymetry from data assimilation of synthetic SWOT measurements. J. Hydrol. 464–465, 363–375, https://doi.org/10.1016/j.jhydrol.2012.07.028.

Page left intentionally blank

Chapter 5

Using the Surface Water and Ocean Topography Mission Data to Estimate River Bathymetry and Channel Roughness

Renato Prata de Moraes Frasson[#]
Byrd Polar and Climate Research Center, The Ohio State University, Columbus, OH, United States

1 Introduction

Quantifying water fluxes is the key to understand the global hydrological cycle and to perform accurate assessments of water availability (Oki and Kanae, 2006). Nevertheless, the uncertainty associated with estimation of key fluxes, such as the river discharge toward the oceans is high, as one can infer from the divergence in estimates found in the literature, for example, 37103 km^3/year (Dai et al., 2009) or 45103 km^3/year (Oki and Kanae, 2006). Despite the importance of the characterization of hydrological regimes and hydraulic properties of rivers, the global network of stream gages is in decline (Pavelsky et al., 2014). In addition to their thinning numbers, reluctance in sharing information across borders (Gleason and Hamdan, 2015; Hossain et al., 2014; Sneddon and Fox, 2006; Sneddon and Fox, 2012; Wolf et al., 1999) combined with the highly heterogeneous stream gage density among countries (Alsdorf et al., 2007) prevents us from resolving the propagation of hydrological events through channels, floodplains, and lakes in global scale (Alsdorf and Lettenmaier, 2003).

Alsdorf and Lettenmaier (2003) recognized the need to accurately measure world-wide discharge and highlighted the measurement accuracy needed by a satellite mission to fulfill such objective. Alsdorf et al. (2007) proposed an early design of a satellite carrying a Ka-band Radar Interferometer (KaRIn) that could address the needs of hydrologic community as well as allow the tracking of mesoscale ocean currents in line with the requirements presented by

#. Now at the Jet Propulsion Laboratory, California Institute of Technology, Pasadena, CA, United States

Earth Observation for Flood Applications. http://dx.doi.org/10.1016/B978-0-12-819412-6.00005-5

Fu and Rodriguez (2004), which led to the development of the Surface Water and Ocean Topography mission (SWOT).

The SWOT mission is scheduled to launch in 2022 and has an anticipated duration of 36 months. The first 3 months are dedicated to launch and payload check, followed by 3 months of calibration during which SWOT will fly on a fast-sampling-limited spatial-coverage orbit, before transitioning to the final orbit, where it will remain for at least 30 months as described in the SWOT science requirements document (Desai, 2018). During its operation, the satellite will measure water surface elevation, slope, and inundation area of rivers wider than 100 m and possibly as narrow as 50 m as well as measure inundation area and water surface elevation of lakes with area larger than or equal to 62,500 m^2, often reported as $(250\ m)^2$, as shape can play a role on measurement accuracy and detectability of lakes and reservoirs (Solander et al., 2016).

This chapter introduces the measurement principles of the SWOT satellite and its anticipated sources of uncertainty in Section 2 and provides a concise description of the SWOT data products for rivers in Section 3. Section 4 demonstrates how the observed changes in water surface elevation and river width can be used to estimate cross-sectional area changes and anomalies. Section 5 describes methods that can estimate unobservable hydraulic properties of rivers and allow the calculation of river discharge. We end the chapter in Section 6, which provides insights on active areas of research and development pertaining the estimation of hydraulic properties of river reaches and discharge.

2 Surface water and ocean topography mission characteristics and measurement principle

The main instrument onboard the SWOT satellite is the Ka-band Radar Interferometer (KaRIn), which operates at a frequency of 35.75 GHz, with an associated wavelength of 8.6 mm (Biancamaria et al., 2016; Fjørtoft et al., 2014). KaRIn will illuminate the surface of the earth at near nadir angles extending from 0.6 to 3.9 degrees on both right and left sides of the spacecraft as illustrated by Fig. 5.1. Given SWOT's altitude of 890.5 km and assuming flat terrain below the satellite, the swath would be 50 km wide, with a swath gap of 20 km centered immediately below the flight path.

SWOT's temporal sampling will depend on the latitude of interest. During a 20.86-day cycle, a location can be observed by more than 1 pass, which is defined as the path the satellite takes as it travels from its most southern position to its most northern position (ascending pass) and from its most northern position toward its most southern position (descending pass). At lower latitudes, that is, between 20 degrees South and 20 degrees North, locations will be typically observed by 1 or 2 passes, with the number of passes increasing as latitude increases (Biancamaria et al., 2016). Areas sampled by more than 1 pass will experience uneven time sampling, an issue discussed by Frasson et al. (2019d) and exemplified in Fig. 5.2.

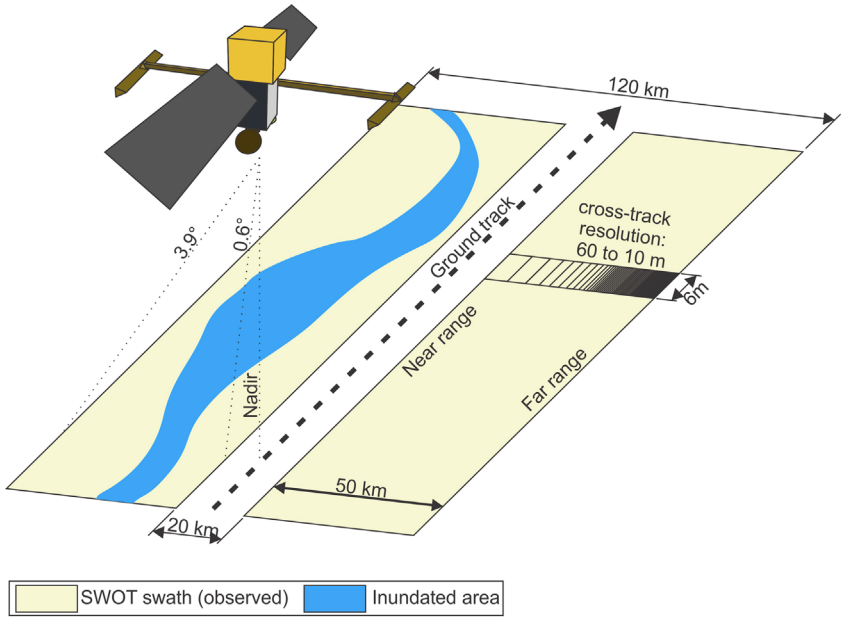

FIGURE 5.1 SWOT's viewing geometry showing the right and left swaths, the inner swath gap, and illustrating the sensor resolution, shown as *black rectangles* in the right swath that become progressively narrower toward the far range. *(Modified from Frasson et al. (2019d).)*

Land, water, buildings, or other surfaces within SWOT's swaths will reflect a fraction of the incident beam toward SWOT's two antennas. Because the antennas are separated by 10 m, the echo from a target on the surface will travel slightly different distances to each antenna, giving rise to a difference in phase between the signals received by the left and the right antennas. Provided that the targets are bright enough, the phase difference (ϕ) can be estimated.

Considering a total phase difference of $\phi + n\,2\pi$, where n is an integer value and $|\phi| < 2\pi$, SWOT will only be able to retrieve ϕ. Therefore, ϕ combined with the position of the spacecraft during image acquisition, and the range to the target does not contain sufficient information to determine a unique solution for the latitude, longitude, and elevation of a target as illustrated in Fig. 5.3. Using a reference Digital Elevation Model (DEM) allows the identification of the correct value of n (phase unwrapping) and the geolocation of targets, that is, the identification of latitude, longitude, and elevation, provided that the elevation difference between two neighboring targets is less than half of an ambiguity height, which varies from 8 m at the near range to 52 m at the far range according to equation 5 in Fjørtoft et al. (2014). Steeper scenes require more complex phase unwrapping algorithms such as Statistical-cost, Network-flow PHase-Unwrapping algorithm (SNAPHU) by Chen and Zebker (2001).

Incorrect phase unwrapping will lead to both vertical and horizontal shifts as one can see in Fig. 5.3. The presence of the horizontal shift may allow for

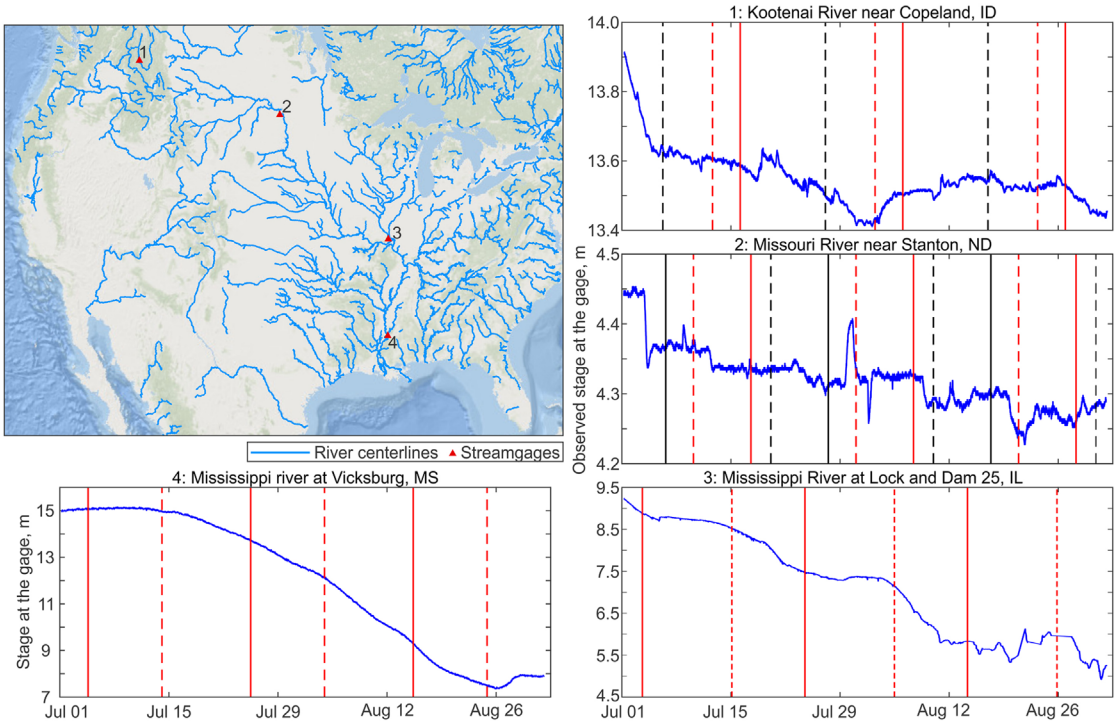

FIGURE 5.2 Examples of how SWOT will sample four different locations over the United States. The map on the upper left corner shows the locations of the four gages, marked by the *red triangles* numbered from 1 to 4. Panels 1–4 show how the stage at each gage varies over 2 months *(blue line)*, with the *vertical lines* showing the time of passes assuming a mission start day of January 1, 2019. Each *vertical line* color and pattern represent a different pass overlooking the location. *Vertical lines* with the same color and pattern are separated by 20.86 days.

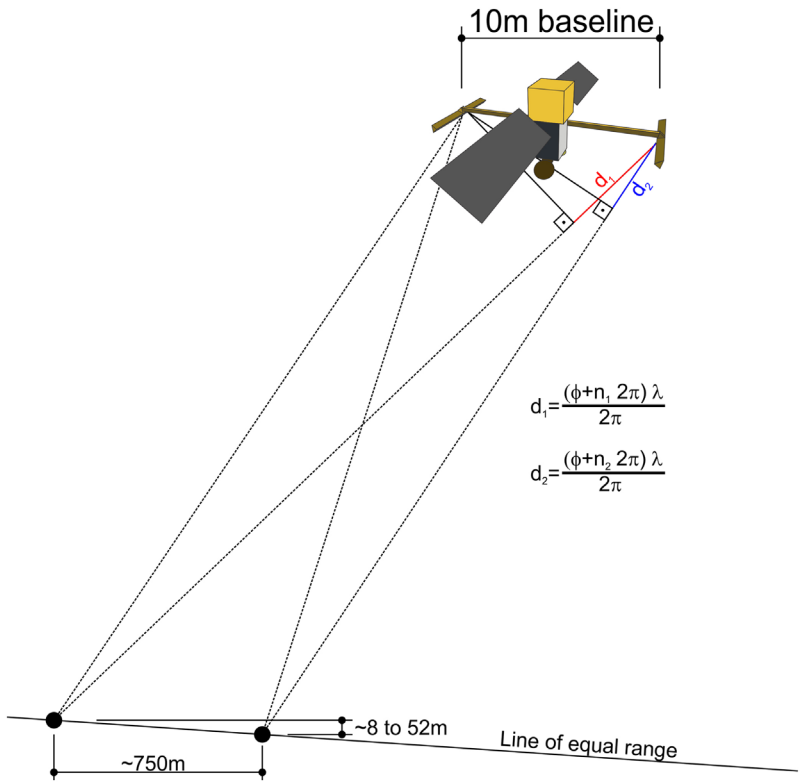

FIGURE 5.3 Illustration of two possible solutions for target position due to phase ambiguity. Both locations are possible solutions to the position of the target, the identification of the correct location is done with the help of a reference DEM. The selection of the wrong solution leads to vertical errors of a multiple of the ambiguity height as well as a horizontal shift.

correction of the phase unwrapping error if the correct waterbody can still be identified. More information on the formation of interferograms, phase unwrapping, and geolocation can be found in chapter 15 of Ulaby et al. (2014) as well as Fjørtoft et al. (2014).

The intensity of the signal reflected by different surfaces toward the satellite depends on the incidence angle, surface type, and roughness. Using an airplane-mounted Ka-Band interferometer, Fjørtoft et al. (2014) demonstrated that at a frequency similar to SWOT (35 GHz as opposed to 35.75 GHz) and at SWOT-like incidence angles, water will appear much brighter than land in the radar images. The expected difference in backscattering coefficient will allow the distinction between water and land targets.

In a perfect world, in the absence of measurement noise and signal attenuation, it would be possible to geolocate any target, regardless of the strength of the echo returning from a surface target. In reality, returns from land will generally lack the power to allow accurate determination of the phase difference perceived

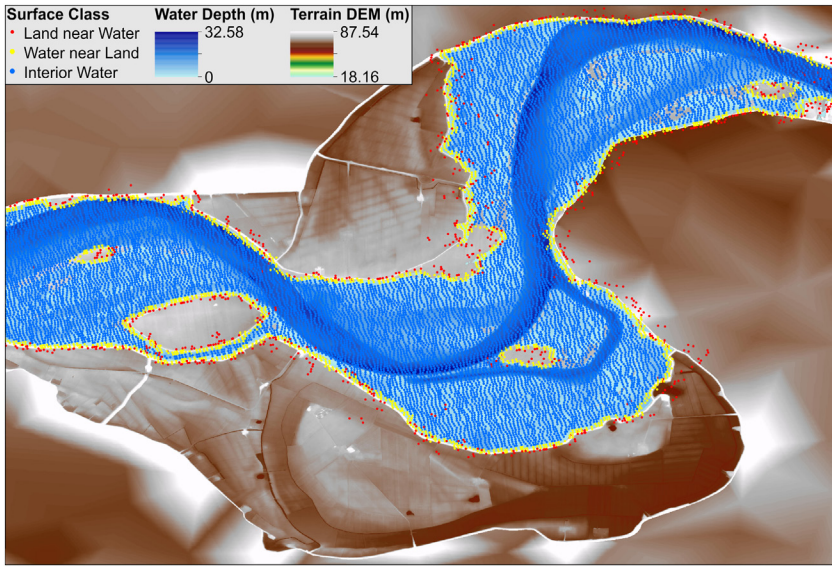

FIGURE 5.4 Example of a simulated SWOT pixel cloud showing a scene over the Po River in Italy. The *green* to *brown* color ramp represents the terrain DEM, whereas the light *blue* to *dark blue* color represent the water depth. *Blue* and *yellow circles* represent simulated SWOT returns from water and *red circles* show simulated returns from land in the vicinity of the river. Land returns display much larger latitude, longitude, and elevation uncertainty, evident here by the spread of the points, at times far from the river banks. *(Courtesy of Rui Wei.)*

by the two antennas, which will make land targets exceedingly noisy. Fig. 5.4 shows an example of geolocated returns colored by surface type. Land targets appear scattered around the river banks as opposed to more regularly located water targets, which include two classes: water near land and interior water.

On occasion, water may appear dark, a situation that the SWOT community calls dark water, which could lead to two issues: the target may be incorrectly classified as land, which can cause underestimation of river width and inundation area; or, if the target is classified as water despite appearing dark, its latitude, longitude, and height will have unusually high errors. Dark water occurs due to specular reflection over the water surface preventing the signal to be reflected to the satellite, which can happen if the water surface is smooth in comparison to the signal wavelength. Under usual circumstances, wind and turbulence will provide the surface roughness needed to prevent specular reflection over water features. However, dark water is possible during days with particularly calm winds and low flow velocities.

SWOT illuminates surfaces at the right and left sides of its groundtrack using different polarizations, allowing the satellite to identify if echoes are coming from the right or left swaths. However, if two or more targets located in the same swath have the same range to the satellite, they will be undistinguishable. Fig. 5.5 shows an example where one of the river banks is at the same range as a water target, in which case, returns from terrain will contami-

nate returns from water, a situation called terrain layover. The end result is generally a positive bias in water surface heights, with magnitude that depends on the ratio between the land and water brightness, the orientation of the river with respect to the swath, the position on the swath, and the complexity of the terrain. Using simulated SWOT data, Frasson et al. (2017) shows layover induced biases could amount to as much as 14 cm in the Sacramento River in sections with widths varying between 80 and 150 m, with levees running parallel to the SWOT groundtrack, a narrow river for SWOT, running in the worst direction with respect to the groundtrack when it comes to layover. Fjørtoft et al. (2014) describes the conditions that lead to terrain layover and suggests ways to remove biased pixels, however exclusion of biased pixels may lead to increased random errors due to the reduction of the number of retained pixels and may ultimately be detrimental to the measurement of narrow rivers.

Additionally, changes in media quality, that is, atmospheric properties, such as moisture content, refractive index, and others, can add propagation delays to the radar signal, leading to increased geolocation errors. Lastly, errors in the orientation of the spacecraft affect the precision the SWOT measurements. A comprehensive breakout of the height and slope errors for hydrologic applications can be found in Esteban-Fernandez (2013). Fig. 5.6 shows the overall

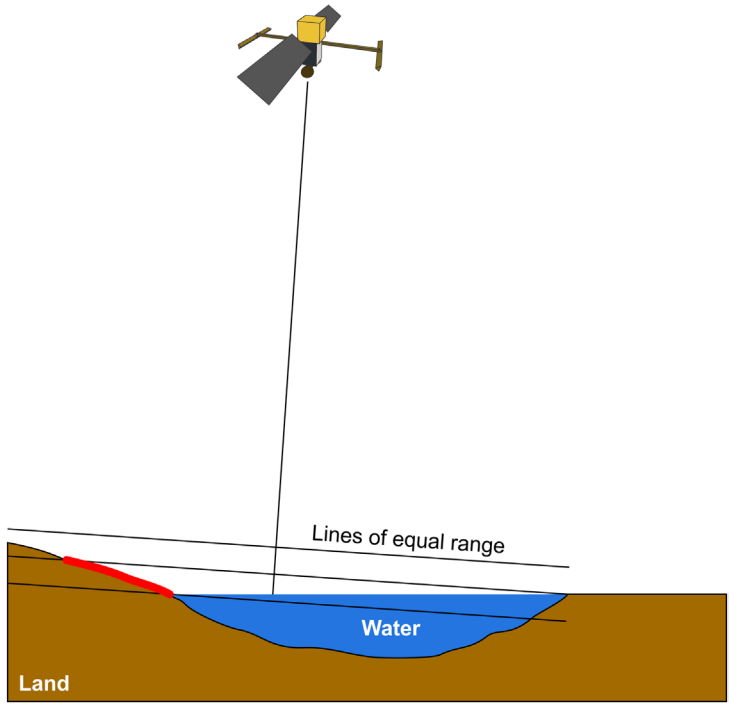

FIGURE 5.5 Illustration of a waterbody prone to layover errors. Distinct targets located at the same range to the radar cannot be distinguished by SWOT. When water and land targets (section highlighted in *red*) have the same range, the resulting estimated elevation will be biased.

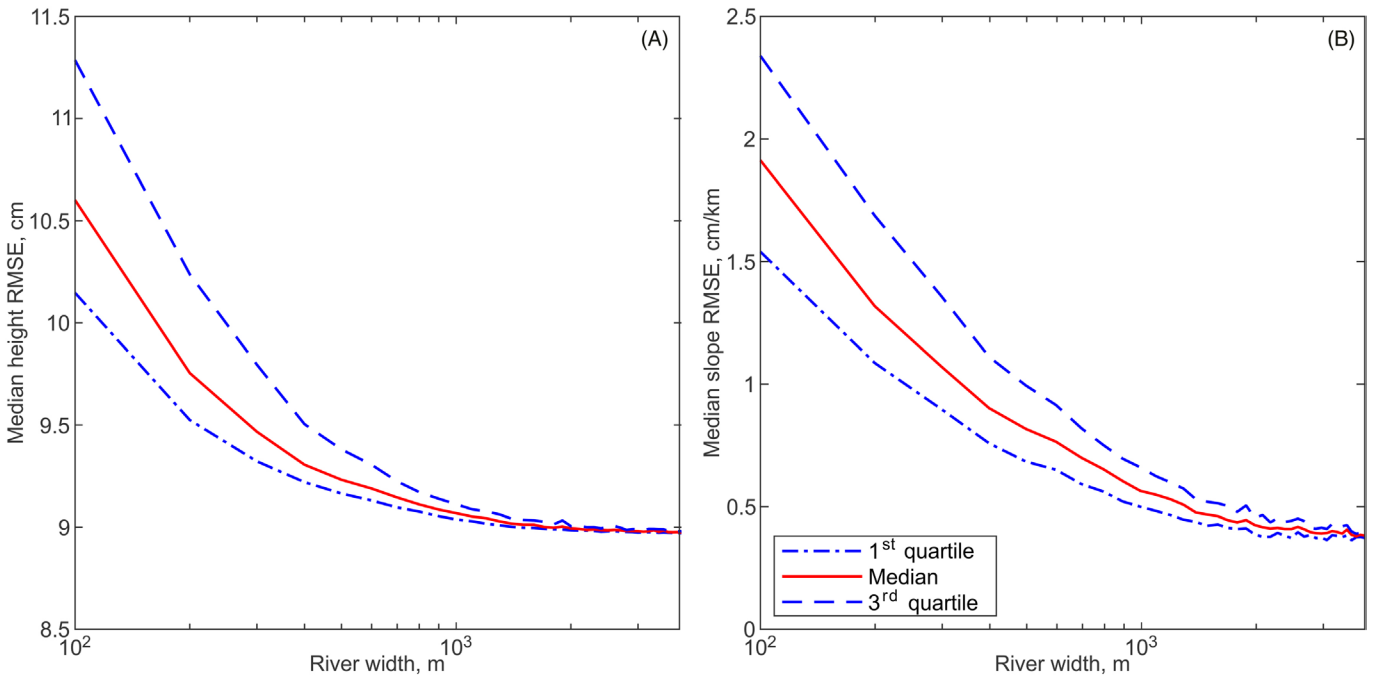

FIGURE 5.6 (A) Expected median height root mean square error versus river width, (B) Expected median slope root mean square error versus river width. Values computed over 10 km reaches assuming errors caused by thermal noise, terrain layover, media delays, and spacecraft attitude.

estimated height and slope errors at the 10 km reach scale as a function of river width, which includes thermal noise, estimated layover errors, and accounting for the budgeted amount for media and attitude errors.

3 SWOT data products

SWOT main river data products will be the pixel cloud, river nodes, reaches, and the raster product. The products vary in resolution, level of uncertainty, and in content. Fig. 5.7 illustrates the interplay between spatial resolution and measurement uncertainty. This section provides more details on the products that are relevant for discharge estimation, that is, the pixel cloud, nodes, and reaches.

The pixel cloud is the highest resolution product. It is the closest product to the raw SWOT measurements, with each pixel containing information on the latitude and longitude, surface type, fraction of the pixel covered by water, elevation above the geoid and ellipsoid, geophysical corrections, and quality flags. Due to uncertainties in the process of geolocation, the pixels no longer lay on a regular grid, but instead resemble a cloud of points, giving rise to the name of the product.

Surface types are classified as interior water, water near land, land near water, land, and potentially dark water. Interior water pixels are surrounded by other water pixels; therefore, they are more likely to cover an area that contains only water. Water near land are water pixels that contain at least one neighboring pixel classified as land. Such pixels can be mixed pixels, with a water fraction less than 100%. Land near water cover predominantly land, but have at least one neighbor classified as water, they are likely to have a water fraction greater than 0. Land pixels have all neighboring pixels classified as land or land near water, they are unlikely to contain a water fraction greater than 0 and tend to have high geolocation errors (Fig. 5.4). Finally, dark water pixels are pixels believed to be water, but appeared dark.

Most current estimates of the water surface elevation uncertainties conducted with synthetic data over the Po River (in Italy) generated by the SWOT hydrology simulator indicate that pixel height errors expressed in terms of mean absolute errors could vary from 1.5 to 1.6 m for interior water pixels and 2.26 to 2.42 m for water near land (Domeneghetti et al., 2018). Although the Po River runs predominantly from west to east, an orientation that is largely perpendicular to the SWOT ground track, minimizing the potential for layover, Domeneghetti et al. (2018) show that layover biases are still present in river bends. Moreover, layover biases can potentially be higher for narrower rivers and for rivers running in parallel to the ground track.

The next step in terms of resolution is the node product. Nodes are points located every 200 m along river centerlines and because they represent an aggregation of pixels, they are expected to show smaller levels of height uncertainty (Frasson et al., 2017). The pixel to node assignment is executed by searching for the nearest node to each pixel, accounting for continuity of water bodies.

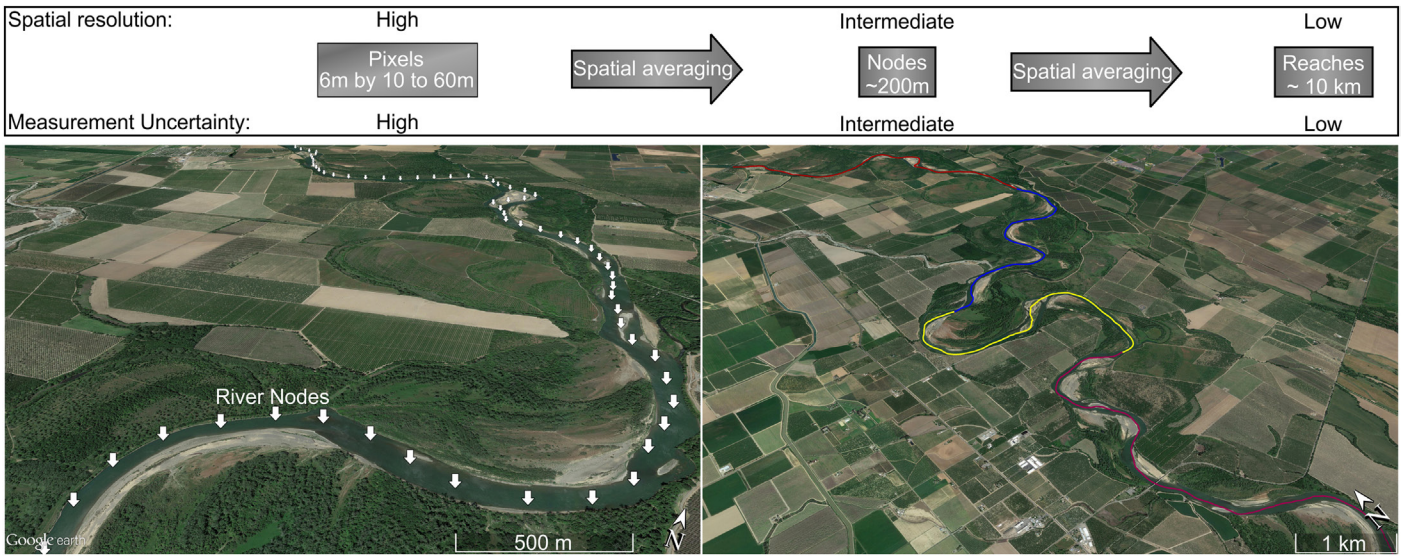

FIGURE 5.7 **Schematic tradeoff between resolution and measurement uncertainty followed by illustrations of river reaches and nodes over the Sacramento River, in California.**

Node heights are computed as the median elevation computed over all water pixels associated to a node while node widths are computed as the sum of the water surface area from all pixels associated to the node, divided by the distance between nodes.

Height uncertainty in nodes still prevents the accurate calculation of node to node water surface slope in most rivers. In order to further reduce height uncertainty, nodes are grouped into reaches that are approximately 10 km long. Reach slopes are computed with linear regression applied to nodes located within a reach and the reach averaged elevation is computed by evaluating the fitted line at the center of the reach. Similarly to the computation of node widths, reach averaged widths are computed by adding the inundated area that belongs to a reach, divided by the reach length.

4 Measuring channel cross-sectional geometry

The estimation of discharge requires knowledge of reach cross-sectional area, which is not directly measured by SWOT. Durand et al. (2014) proposed the decomposition of the reach cross-sectional area (A_t) into the cross-sectional area at the lowest stage (A_0) and the cross-sectional area change from time 0 to time t (δA_t):

$$A_t = A_0 + \delta A_t \tag{5.1}$$

where A_0 is not directly observed by SWOT and δA_t calculated by, for example, using trapezoidal integrals over a time series of observed heights and widths. The unobservable area would then be estimated using a Mass-Conserved Flow Law Inversion (MCFLI) method described by Gleason et al. (2017) and here, in Section 5.1. Alternatively, it could be estimated by fitting theoretical profiles to height and width measurements, for example, Mersel et al. (2013) and Schaperow et al. (2019).

In the interest of allowing better prior estimates of the reference cross-sectional area, Hagemann et al. (2017) proposed a similar decomposition to Eq. (5.1), however, instead of using the lowest flow as the reference cross-sectional area, Hagemann, Gleason, and Durand proposed the use of the cross-sectional area at median flow instead ($\bar{A}$) so that the cross-sectional area would be estimated as:

$$A_t = \bar{A} + \Delta A_t \tag{5.2}$$

where ΔA_t represents the cross-sectional area change between $\bar{A}$ and the time t, referred to as cross-sectional area anomaly at time t.

Both δA_t and ΔA_t can be estimated by accruing the changes in top width and water surface elevation using the trapezoidal area calculation scheme as suggested by Durand et al. (2014), or be estimated by fitting relationships between observed reach averaged stage and width. Since height and width errors are not

expected to be highly correlated, cross-sectional area changes calculated from height-width relationships are likely to carry smaller uncertainties, provided that the fitting method is appropriate for a situation when both variables carry uncertainties. An example of such method is the error in variables approach (Fuller, 1987), which was implemented to SWOT data by Durand et al. (2018).

Fig. 5.8A shows an example of a continuous piecewise linear function fitted to width height pairs generated with 10 cycles of simulated SWOT data assuming 2 passes per cycle over a reach of the Ohio River in the United States. The points were divided into three subdomains intended to represent changes in the channel geometry as illustrated in Fig. 5.8B, that is, subdomain 1 representing flow in the main channel, and subdomains 2 and 3 representing inundation of the flood plain. The three fitted lines are constrained to meet at subdomain boundaries, thus allowing the identification of a slope and intercept for subdomain 2, despite the lack of points.

Due to the reduced number of points in subdomains 2 and 3, the width-height relationships at these domains are less reliable and more prone to change

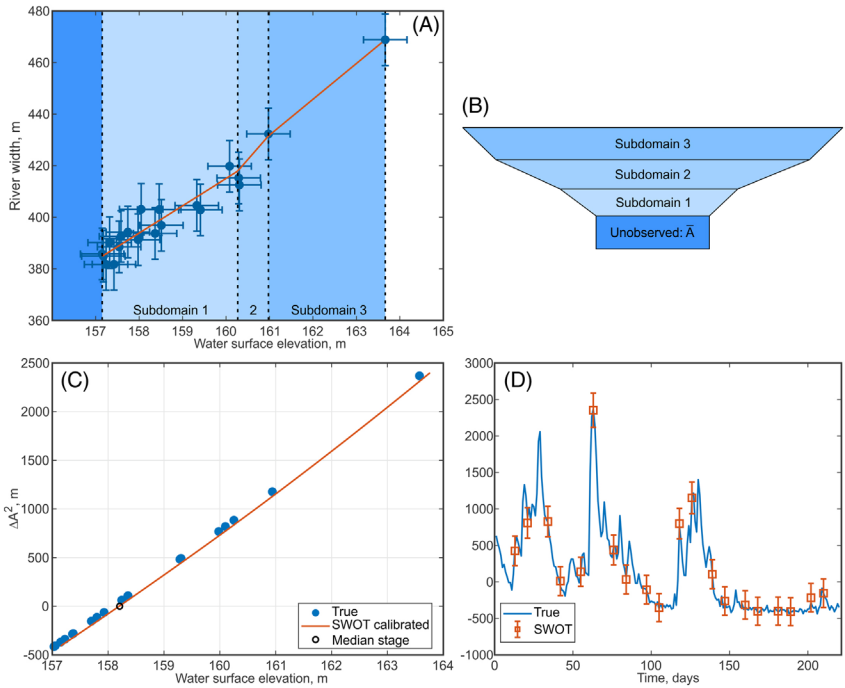

FIGURE 5.8 (A) Piecewise linear curves constrained to meet at subdomain boundaries fitted to 20 pairs of height-width measurements, (B) example of a theoretical cross-section that would yield H-W curves similar to those in (A), (C) resulting cross-sectional area as a function of height, (D) time series of ΔA for an example reach over the Ohio River compared to cross-sectional areas derived from a hydraulic model with no synthetic SWOT data added to it.

when new data is acquired, especially if high flow events are sampled. Considering three domains with boundaries transitioning from subdomain 1 to 2 and 2 to 3 at H_1 and H_2, respectively, and a linear fit between width and height described by:

$$\begin{aligned} W(H) &= p_{1,1} \cdot H + p_{2,1} && \text{for } H \le H_1 \\ W(H) &= p_{1,2} \cdot H + p_{2,2} && \text{for } H_1 < H \le H_2 \\ W(H) &= p_{1,3} \cdot H + p_{2,3} && \text{for } H > H_2 \end{aligned} \tag{5.3}$$

where $p_{1,i}$ is a fit parameter that describes the change in width with respect to the change in height for subdomain i = 1 to 3, and $p_{2,i}$ is the fitted intercept for subdomains i = 1 to 3; the curve relating the cross-sectional area anomaly at time t (ΔA_t) and stage can be derived by:

$$\Delta A_t = \int_{\overline{H}}^{H_t} W(H)\, dH \tag{5.4}$$

which, given Eq. (5.3) and assuming that $\overline{H} \le H_1$, yields:

$$\begin{aligned} \Delta A_t &= \frac{p_{1,1} \cdot \left(H_t^2 - \overline{H}^2\right)}{2} + p_{2,1} \cdot \left(H_t - \overline{H}\right) \text{ for } H_t \le H_1 \\ \Delta A_t &= \frac{p_{1,1} \cdot \left(H_1^2 - \overline{H}^2\right)}{2} + p_{2,1} \cdot \left(H_1 - \overline{H}\right) + \frac{p_{1,2} \cdot \left(H_t^2 - H_1^2\right)}{2} + p_{2,2} \cdot \left(H_t - H_1\right) \text{ for } H_1 < H_t \le H_2 \\ \Delta A_t &= \frac{p_{1,1} \cdot \left(H_1^2 - \overline{H}^2\right)}{2} + p_{2,1} \cdot \left(H_1 - \overline{H}\right) + \frac{p_{1,2} \cdot \left(H_2^2 - H_1^2\right)}{2} + p_{2,2} \cdot \left(H_2 - H_1\right) + \\ &\quad + \frac{p_{1,3} \cdot \left(H_t^2 - H_2^2\right)}{2} + p_{2,3} \cdot \left(H_t - H_2\right) + \text{for } H_t > H_2 \end{aligned} \tag{5.5}$$

The resulting curve is shown in Fig. 5.8C, which yields the time series cross-sectional area change as shown in Fig. 5.8D. The estimated ΔA_t are compared to cross-sectional area anomalies computed by hydraulic model of the Ohio River (Adams et al., 2010) used to generate the simulated noisy SWOT data, and therefore are assumed as the truth.

5 Estimating cross-sectional area, roughness, and discharge

5.1 Mass-Conserved Flow Law Inversion methods

Discharge algorithms created to support the SWOT mission employ simple hydraulic laws to estimate discharge. For example, the Metropolis Manning (MetroMan), developed by Durand et al. (2014), Garambois-Monnier (GaMo) discharge algorithm developed by Garambois and Monnier (2015), and the Bayesian At-many-stations-hydraulic geometry-Manning (BAM) method developed by Hagemann et al. (2017) use modified forms of Manning's equation

for discharge estimation. Common among MetroMan, GaMo, and BAM are the assumption that the river reaches are wide, that is, width >> depth, therefore the wetted perimeter is essentially equal to the river width. Giving this assumption, the Manning-Strickler equation can be written as:

$$Q = \frac{1}{n} \cdot A^{5/3} \cdot W^{-2/3} \cdot \sqrt{S_f} \tag{5.6}$$

where n stands for the friction coefficient, A represents the wetted cross-sectional area, W stands for the top width, and S_f for the friction slope.

The second assumption is that the friction slope is equal to the water surface slope. Although this simplification is only true for uniform flow, it can be assumed for reaches with low Froude numbers, typically less than 0.3 as shown by Garambois and Monnier (2015). Under such assumptions, the Manning-Strickler equation reduces to:

$$Q = \frac{1}{n} \cdot A^{5/3} \cdot W^{-2/3} \cdot \sqrt{S} \tag{5.7}$$

where S represents the water surface slope.

The cross-sectional area can be rewritten with Eq. (5.2), which gives us the form:

$$Q = \frac{1}{n} \cdot \left(\overline{A} + \Delta A\right)^{5/3} \cdot W^{-2/3} \cdot \sqrt{S} \tag{5.8}$$

used by the early versions of MetroMan and BAM. The initial iteration of discharge algorithms was benchmarked by Durand et al. (2016), who found that at least one of the five tested algorithms could retrieve discharge with relative root mean square errors of 35% or better for 14 out of the 16 test cases containing non-braided rivers. Additionally, Durand et al. (2016) suggested that allowing the friction coefficient to vary as a function of flow conditions, such as discharge or depth, can lead to improvements in discharge retrieval, particularly at low flows.

The initial findings of Durand et al. (2016) were based on river models and synthetic data. Later, Tuozzolo et al. (2019a) demonstrated with field observations that the Manning-Strickler equation can better describe the discharge in river reaches when the roughness coefficient is allowed to vary with either stage or discharge. As a response to those findings, new SWOT discharge algorithms that use the Manning Strickler equation adopted a roughness parameterization such as:

$$n = n_0 \left(\frac{\overline{A} + \Delta A_t}{W_t} \right)^b \tag{5.9}$$

where n is essentially a time-varying effective roughness that depends on three static parameters: n_0, b, and $\overline{A}$ and two time-varying quantities that can be

directly observed by SWOT: the cross-sectional area anomaly at time t (ΔA_t) and top width at time t (W_t).

Combining Eqs. (5.8) and (5.9) applied to a river reach r at a point in time t, gives:

$$Q_{r,t} = \frac{1}{n_{0,r}\left(\frac{\overline{A}_r + \Delta A_{r,t}}{W_{r,t}}\right)^{b_r}} \cdot \left(\overline{A}_r + \Delta A_{r,t}\right)^{5/3} \cdot W_{r,t}^{-2/3} \cdot \sqrt{S_{r,t}} \tag{5.10}$$

where the subscript r identifies the reach and t the point in time. Variables with only one subscript, that is $n_{0,r}$, b_r, and $\overline{A}_r$ are constant in time, but variable in space, those with two subscripts vary in both time and space. Discharge estimation with Eq. (5.10) requires knowledge of $\Delta A_{r,t}$, $W_{r,t}$, and $S_{r,t}$, which are observable by SWOT, and parameters $n_{0,r}$, b_r, and $\overline{A}_r$, which need to be estimated. Discharge algorithms based on the MCFLI approach estimate the non-observable parameters by applying the continuity equation between a set of contiguous reaches, typically 4–6 reaches, and across time, with a minimum of 6 observations in time.

MCFLI algorithms differ in how they simplify and discretize the continuity equation. Starting from the one-dimensional continuity equation:

$$\frac{\partial Q_{r,t}}{\partial x} + \frac{\partial A_{r,t}}{\partial t} = q_{r,t} \tag{5.11}$$

where x represents the flow distance and $q_{r,t}$ represents contributions from lateral flows, the first approximation is to assume the contribution of lateral flows to be negligible, that is, $q_{r,t} = 0$. This approximation is justified by applying the MCFLI method on sets of reaches that do not contain tributaries. In practice, overland flow, groundwater gains and losses, evaporation, and the presence of unavoidable tributaries joining the set of reaches can degrade the quality of the estimated parameters. Methods to address mass imbalance are discussed in Section 6.

Additionally, the algorithms make one of the following assumptions before discretizing Eq. (5.11): either they neglect the rate of change of the cross-sectional area with respect to time, or they attempt to resolve the cross-sectional area. The first approach yields the simplest discretization scheme, that is, in a point in time, the set of connected reaches have equal values of discharge. This approach is used by BAM, which makes the algorithm more applicable to locations with sparser time sampling.

The second approach retains the time derivative of the cross-sectional area, in which case the discretized version of Eq. (5.11) for an internal reach using the finite differences approach becomes:

$$\frac{Q_{dn} - Q_{up}}{\Delta x} + \frac{A_{r,t+1} - A_{r,t}}{\Delta t} = 0 \tag{5.12}$$

where Q_{dn} represents the downstream discharge interpolated to the boundary between reaches r − 1 and r, averaged between time steps t and t + 1, Q_{up} represents the upstream discharge interpolated to the boundary between reaches r + 1 and r, averaged between time steps t and t + 1, Δx represents the reach length, $A_{r,t+1}$ and $A_{r,t}$ stand for the cross-sectional area for reach r at time steps t + 1 and t, respectively, and Δt represents the time interval between time steps t + 1 and t. This approach is currently adopted by MetroMan. Given the need to average discharges between time steps and the consideration of cross-sectional area change between time steps, this form requires reaches to be simultaneously observed and may experience performance degradation at exceedingly sparse time sampling.

The optimum selection of sets of reaches used for the application of MCFLI methods requires a balance of four needs. First, the set must avoid the inclusion of tributaries; second, the set must contain at least 2 reaches and preferably 4–6 for the application of the method, third, the uncertainty in the observations must be low enough to allow the observation of flow dynamics, which is achieved by increasing reach length until uncertainties are acceptable; the fourth need is for reaches in a set to be simultaneously observed, or for at least subsets of 2 or more reaches to be simultaneously observed, which when combined include all reaches in a set.

The avoidance of tributaries is illustrated in Fig. 5.9. The figure shows the confluence between the Cedar and the Iowa rivers, which later join the upper Mississippi River with the alternating colors identifying river reaches. Panel A shows an example of mass-conserved set of reaches located between the confluences of the Cedar and Iowa rivers and Iowa and Mississippi rivers, which were picked to avoid tributaries joining within the set. Similarly, panel B shows a set on the upper Mississippi river, which does not include visible tributaries. The centerlines shown in Fig. 5.9 represent a new iteration of the Global River Width from Landsat (GRWL) database (Allen and Pavelsky, 2018), including manual processing and corrections to improve river topology executed by Altenau et al. (2018).

The last piece of information needed before the MCFLI methods can be applied is an initial estimate of discharge for the set of reaches. Since the initial MCFLI methods were based on Bayesian methods, this initial estimate is often called prior information. For MetroMan and BAM, this prior estimate of discharge is used to define prior distributions for the $\overline{A}$ and roughness parameters. Although the algorithms are designed to produce improved estimates of discharge as well as to produce flow law parameters that allow the reproduction of discharge dynamics, a fraction of the initial discharge biases may remain unmitigated, especially if the inversion window does not contain enough variation in flow conditions. This is well demonstrated by Tuozzolo et al. (2019b) who ran three different discharge algorithms using AirSWOT observations of stage, width, and slope over four reaches in the Willamette River in Oregon, United States. Despite successfully retrieving discharge in the study area, Tuozzolo

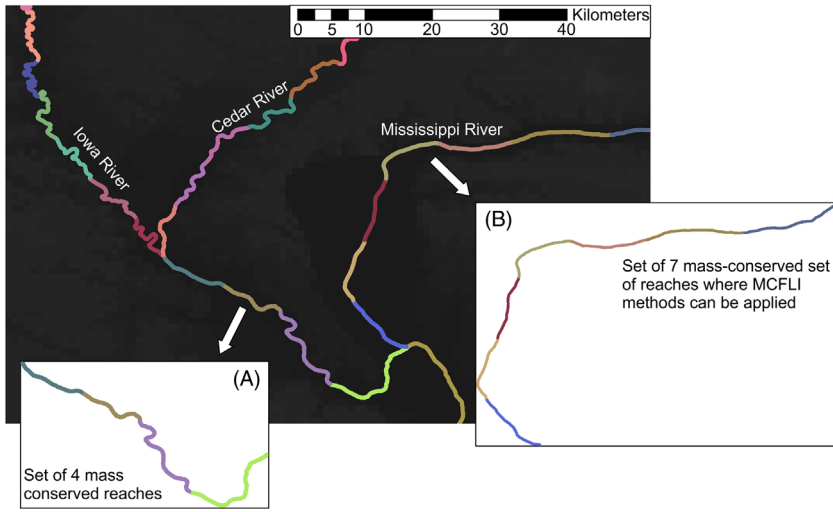

FIGURE 5.9 ***Solid lines*** **representing the centerlines of the upper Mississippi River and tributaries near the border of Iowa and Illinois in the United States showing two confluences:** Iowa and Cedar rivers and Iowa and Mississippi rivers. Background shows the Global 30 Arc-second elevation model. The *solid lines* are drawn in alternating colors, representing how the rivers are segmented into reaches. Panel A shows a set of mass conserved reaches in the Iowa River, which begins at the Cedar-Iowa River confluence and ends where the Iowa River joins the upper Mississippi. Panel B shows a similar set of mass conserved reaches that begins at the confluence between the Mississippi and the Rock rivers and ends at the confluence between the Mississippi and the Iowa rivers.

and collaborators identified a dependence of biases in the final estimates of discharge on biases in the prior estimate of discharge.

As SWOT is intended to produce global estimates of river discharge, prior discharge estimates are needed globally. Two sources are currently available for running world-wide MCFLI inversions: the first is mean annual flow based on 50 years of discharge estimates made by the model WBMSed (Cohen et al., 2014) mapped on river centerlines by Frasson et al. (2019c), which were organized into a publicly available dataset that can be obtained from Frasson et al. (2019b). A second possible source is the database compiled by Lin et al. (2019), which extends beyond the areas observed by the Shuttle Radar Topography mission, which is described in detail by Farr, 2007. The next section describes an application of MetroMan to two sets of reaches in the Seine River using SWOT-like data produced with a hydraulic model.

5.2 Illustration of the application of MetroMan for discharge estimation in the Seine River

We demonstrate the implementation of MetroMan using the Seine River in France as an example. We constructed two synthetic mass conserved cases shown in Fig. 5.10 based on a 1-year long hydrodynamic simulation of the Seine

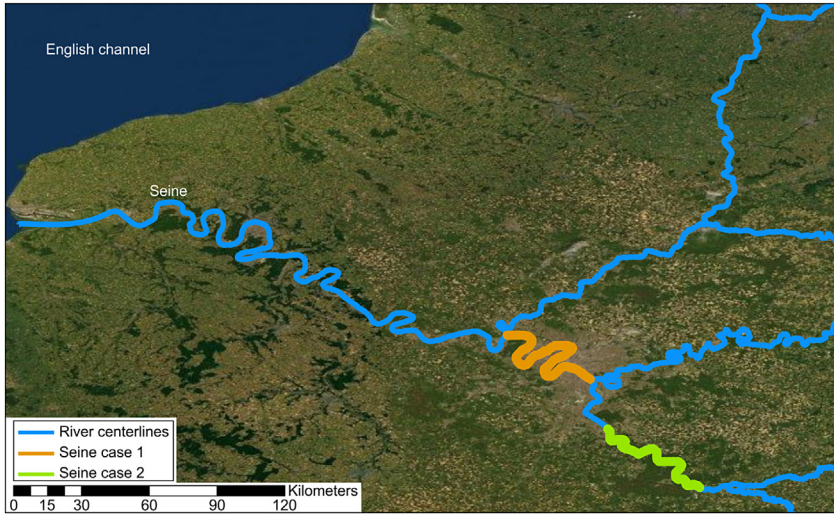

FIGURE 5.10 Location of two sets of mass conserved reaches on the Seine River (France) where the MCFLI method can be applied.

built by Even et al. (1998). We extracted cross-sectional top widths and water surface elevations from the hydrodynamic model output and used these cross-sectional values as proxies for node widths and elevations. By aggregating the synthetic nodes, we built reaches, over which we computed time series of reach averaged water surface elevation, slope, river width, and cross-sectional area anomaly. Additionally, we extracted the discharge from the hydraulic model, which we treated as the true discharge used in the evaluation of our estimations. This synthetic dataset as well as others are available from Frasson et al. (2019a).

An important step in the estimation of flow law parameters by MetroMan is the definition of the inversion window. Measurements inside the inversion window are used for the estimation of $n_{0,r}$, b_r, and $\overline{A}_r$ shown in Eqs. (5.9) and (5.10), which are later used to estimate discharge for all times when measurements of height, width, and slope are available. When selecting the inversion window, the user should attempt to maximize the observed flow conditions as that allows for better constraining the flow parameters b_r and $\overline{A}_r$, while avoiding out-of-bank flow, where atypical values of the effective roughness coefficient caused by, for example, vegetation and debris as well as important deviations from one dimensional flow can affect the inversion process.

MetroMan and other algorithms have been successfully deployed with as little as 6 days of measurements obtained with an airplane mounted Ka-band Radar interferometer called AirSWOT (Tuozzolo et al., 2019b). However, a larger number of measurements is desirable, with 20–30 days of measurements being commonly used in previous trial runs (Durand et al., 2016). Given inversion windows including 20–30 measurements over 4–5 reaches, run times are on the

order of minutes. Increasing the number of measurements inside the inversion window above 50 can lead to inversion times on the order tens of minutes, while inclusion of 150 and more measurements can lead to run times in excess of 6 h using a typical desktop machine.

We initialized MetroMan using an estimate of the mean annual flow equal to 205 m^3/s based on 50 years of discharge estimates made by the model WBMSed (Cohen et al., 2014) and no ancillary information, in a situation that aimed to reproduce an ungaged basin scenario. The algorithm was set to run a Markov chain of 10,000 iterations with the first 2,000 iterations being discarded as burn-in. We used the inversion windows shown in Fig. 5.11, from day 195 to 335, assuming one synthetic SWOT pass every 7 days, leading to 20 days of measurements inside the inversion window. Both upstream and downstream models were segmented into 4 reaches defined based on inspection of the water surface profiles, with the intent of having homogeneous water surface slopes within each reach.

Using the resulting estimates of $n_{0,r}$, b_r, and $\overline{A}_r$, we calculated discharge for all days for which we had synthetic measurements of water surface height, width, and slope. The resulting hydrograph showing the average discharge

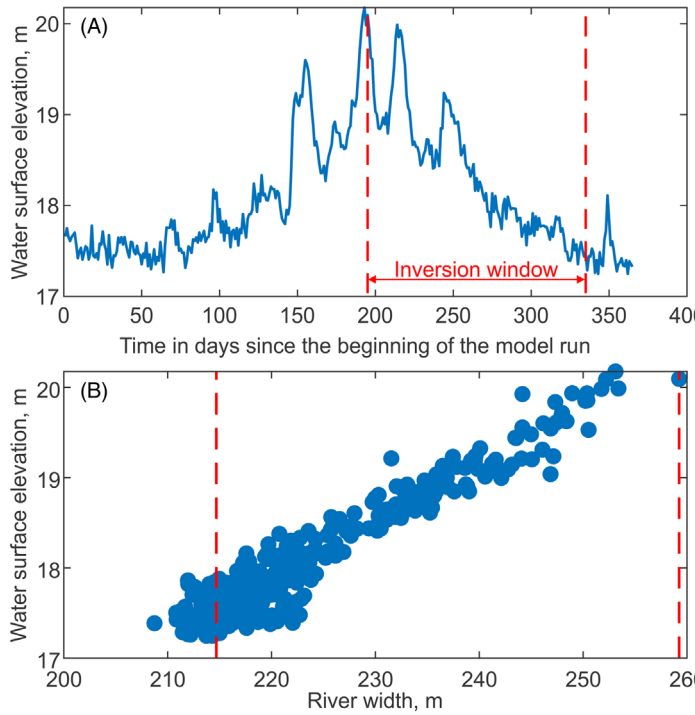

FIGURE 5.11 Selection of the days used for estimation of flow law parameters. Time series of water surface elevation and river width generated from a hydraulic model of the river Seine.

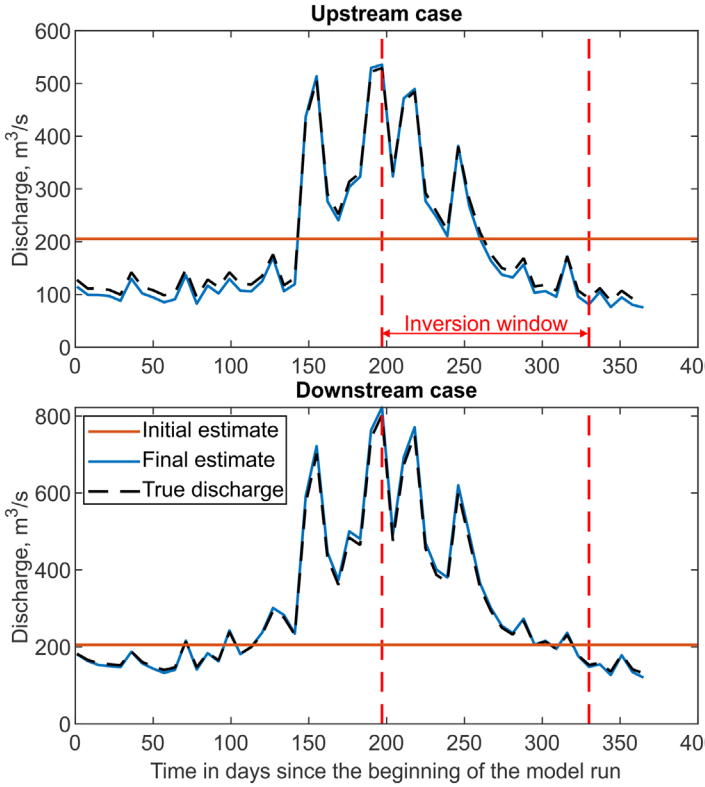

FIGURE 5.12 Hydrograph of spatially averaged discharge for the two synthetic cases constructed over the river Seine. The horizontal *solid line* shows the initial estimate of discharge generated by a hydrologic model used to initialize MetroMan. The *blue solid line* represents the average discharge for each case calculated with the flow law parameters estimated by MetroMan, the *dashed black line* represents the true discharge used to force the hydrodynamic model from where we created the synthetic SWOT observations. The inversion window highlights the days used for the estimation of the flow law parameters.

among the 4 reaches for each time step is in Fig. 5.12. The blue solid line represents the discharge calculated with the flow parameters estimated by MetroMan, the dashed black line shows the modeled discharge, which we treat as true discharge in the domain, the horizontal solid line shows the estimate of mean annual flow used to initialize MetroMan.

The quality of the inversions shown in Fig. 5.12 can be assessed with several metrics. Here we present estimates of the root mean square error normalized by the true mean annual flow (NRMSE), the Nash-Sutcliffe Efficiency (NSE), the remaining bias normalized by the true mean annual flow (nbias), the normalized residual standard deviation ($n\sigma_e$), and the coefficient of determination (r^2). Each metric shows a different angle of the error characteristics, while NRMSE tends to give an overall sense of the errors with respect to usual flow conditions,

TABLE 5.1 Error metrics for discharge inversions executed with MetroMan over two cases shown in Figs. 5.11 and 5.12. NRMSE stands for the normalized root mean square error, NSE for the Nash-Sutcliffe Efficiency, nbias for the normalized bias, and r^2 for the coefficient of determination.

Case	NRMSE	NSE	nbias	$n\sigma_e$	r^2
Upstream	5.6%	0.993	−4.6%	3.2%	0.999
Down-stream	3.4%	0.997	1.6%	3.1%	0.999

it bundles biases and random fluctuations, which are better captured by nbias and $n\sigma_e$, respectively. The error metrics for the two cases is shown in Table 5.1. It is worth noticing that this example contains no complications such as violations of mass conservation, complex planforms such as anastomosing or braided reaches, and no observation uncertainty.

6 Perspectives and future directions

Realistically, it is not always possible to define sets of mass conserved reaches, either because tributaries could be too narrow to be seen by SWOT or because consecutive confluences prevent the construction of sets of reaches. Additionally, if storm events happen to be present inside the inversion window, overland flow could be non-negligible and ground water fluxes, either adding to the river discharge or leading to losses are of difficult observation and estimation. In such cases, lateral flows need to be accounted for, so that mass conservation is not violated. Nickles et al., 2020 present a study case that uses globally available estimates of runoff to calculate lateral inflows. The study demonstrates that even if poor estimates of the lateral inflows are accounted for, MetroMan can successfully estimate discharge in reaches in the Muskingum River.

Other promising methods for the estimation of discharge using SWOT observations include variational data assimilation (Brisset et al., 2018; Oubanas et al., 2018a,b). Such methods have the potential to produce more accurate discharge measurements as well as depth and cross-sectional area estimates than MCFLI methods, however, they have considerably higher computational costs, which prevents them from delivering global near real-time estimates of discharge. Although considerable effort is being spent in operationalizing such methods, their application remains restricted to basin level estimates of discharge, where the computational domain is limited and the need for accuracy is greater. Hybrid methods that perform one-time parameter estimation via data assimilation into more complex flow laws and estimate discharge operationally using simpler flow laws with static parameters offer a compromise between the

high computational costs of performing assimilation at each time step and the simplicity of the MCFLI methods. One example of such methods is the Hierarchical Variational Discharge Inversion (HiVDI) method proposed by Larnier et al., 2020 and Garambois et al. (2020).

Considerable efforts to generate better initial estimates of discharge are underway. Two avenues are being explored: decreasing the biases in mean annual flow estimates as well as producing estimates of different flow quantiles. Lin et al. (2019) built a dataset of world rivers containing such estimates of discharge. The dataset was built using machine learning leveraging tens of thousands of stream gages distributed over the world. Meanwhile, the MCFLI methods are being adapted to make use of multiple flow quantiles for better estimation of prior distributions for flow law parameters. Furthermore, while estimates of flow quantiles with as little biases as possible are needed, the dataset produced by Lin and others also contains robust estimates of uncertainty, which is of utmost importance when using Bayesian methods such as BAM and MetroMan.

References

Adams, T., Chen, S., David, R., Shade, T., Lee, D., 2010. The Ohio River Community HEC-RAS Model (Techinical Report). American Society of Civil Engineering, Reston, Virginia.

Allen, G.H., Pavelsky, T.M., 2018. Global extent of rivers and streams. Science 361 (6402), 585–588. doi: 10.1126/science.aat0636.

Alsdorf, D.E., Lettenmaier, D.P., 2003. Tracking fresh water from space. Science 301 (5639), 1491–1494. doi: 10.1126/science.1089802.

Alsdorf, D.E., Rodríguez, E., Lettenmaier, D.P., 2007. Measuring surface water from space. Rev. Geophys. 45 (2), 1–24. doi: 10.1029/2006rg000197.

Altenau, E.H., et al., 2018. Enhancing the SWOT A Priori Global River Database. A.G.U. Fall Meeting, Washington D.C.

Biancamaria, S., Lettenmaier, D.P., Pavelsky, T.M., 2016. The SWOT mission and its capabilities for land hydrology. Surv. Geophys. 37 (2), 307–337. doi: 10.1007/s10712-015-9346-y.

Brisset, P., Monnier, J., Garambois, P.-A., Roux, H., 2018. On the assimilation of altimetric data in 1D Saint–Venant river flow models. Adv. Water Resour. 119, 41–59, https://doi.org/10.1016/j.advwatres.2018.06.004.

Chen, C.W., Zebker, H.A., 2001. Two-dimensional phase unwrapping with use of statistical models for cost functions in nonlinear optimization. J. Opt. Soc. Am. A 18 (2), 338–351. doi: 10.1364/JOSAA.18.000338.

Cohen, S., Kettner, A.J., Syvitski, J.P.M., 2014. Global suspended sediment and water discharge dynamics between 1960 and 2010: Continental trends and intra-basin sensitivity. Glob. Planet. Change 115, 44–58, https://doi.org/10.1016/j.gloplacha.2014.01.011.

Dai, A., Qian, T., Trenberth, K.E., Milliman, J.D., 2009. Changes in continental freshwater discharge from 1948 to 2004. J. Climate 22 (10), 2773–2792. doi: 10.1175/2008jcli2592.1.

Desai, S., 2018. Surface Water and Ocean Topography mission (SWOT), Science Requirements Document JPL document D-61923 Revision B, Jet Propulsion Laboratory. https://swot.jpl.nasa.gov/docs/D-61923_SRD_Rev_B_20181113.pdf (accessed on 03.03.2019.).

Domeneghetti, A., et al., 2018. Characterizing water surface elevation under different flow conditions for the upcoming SWOT mission. J. Hydrol. 561, 848–861, https://doi.org/10.1016/j.jhydrol.2018.04.046.

Durand, M., et al., 2016. An intercomparison of remote sensing river discharge estimation algorithms from measurements of river height, width, and slope. Water Resour. Res. 52, 4527–4549. doi: 10.1002/2015wr018434.

Durand, M., et al., 2014. Estimating reach-averaged discharge for the River Severn from measurements of river water surface elevation and slope. J. Hydrol. 511, 92–104. doi: 10.1016/j.jhydrol.2013.12.050.

Durand, M., Pavelsky, T., Hagemann, M., 2018. Enhanced width: can we use river height measurements to improve river width?, SWOT Science Team Meeting, Montreal, Canada.

Esteban-Fernandez, D., 2013. SWOT mission performance and error budget JPL D-79084 Revision A, Jet Propulsion Laboratory. http://swot.jpl.nasa.gov/files/SWOT_D-79084_v5h6_SDT.pdf.

Even, S., et al., 1998. River ecosystem modelling: application of the PROSE model to the Seine river (France). Hydrobiologia 373 (0), 27–45. doi: 10.1023/A:1017045522336.

Farr, T.G., et al., 2007. The Shuttle Radar Topography mission. Rev. Geophys. 45 (2), RG2004. doi: 10.1029/2005rg000183.

Fjørtoft, R., et al., 2014. KaRIn on SWOT: Characteristics of near-nadir Ka-band interferometric SAR imagery. IEEE Trans. Geosci. Remote Sens. 52 (4), 2172–2185. doi: 10.1109/tgrs.2013.2258402.

Frasson, R.P.d.M., Durand, M., Rodriguez, E., 2019a. Compilation of hydraulic models for the study of the spatial averaging on ow laws, Zenodo. doi:10.5281/zenodo.3463541

Frasson, R.P.d.M., et al., 2019b. Global database of river width, slope, catchment area, meander wavelength, sinuosity, and discharge, Zenodo. doi:https://doi.org/10.5281/zenodo.2579160

Frasson, R.P.d.M., et al., 2019c. Global relationships between river width, slope, catchment area, meander wavelength, sinuosity, and discharge. Geophys. Res. Lett. 46 (6), 3252–3262. doi: 10.1029/2019GL082027.

Frasson, R.P.d.M., Schumann, G.J.-P., Kettner, A.J., Brakenridge, G.R., Krajewski, W.F., 2019d. Will the Surface Water and Ocean Topography (SWOT) satellite mission observe floods? Geophys. Res. Lett. 46 (17–18), 10435–10445. doi: 10.1029/2019gl084686.

Frasson, R.P.d.M., et al., 2017. Automated river reach definition strategies: Applications for the Surface Water and Ocean Topography mission. Water Resour. Res. 53 (10), 8164–8186. doi: 10.1002/2017wr020887.

Fu, L.L., Rodriguez, E., 2004. High-resolution measurement of ocean surface topography by radar interferometry for oceanographic and geophysical applications. In: Sparks, R., Hawkesworth, C., (Eds.), The State of the Planet: Frontiers and Challenges in Geophysics. American Geophysical Union, Washington D.C., pp. 209–224. DOI:10.1029/150GM17.

Fuller, W.A., 1987. Measurement Error Models. John Wiley & Sons, New York, 432 pp.

Garambois, P.A., et al., 2020. Variational estimation of effective channel and ungauged anabranching river discharge from multi-satellite water heights of different spatial sparsity. J. Hydrol. 581, 124409, https://doi.org/10.1016/j.jhydrol.2019.124409.

Garambois, P.A., Monnier, J., 2015. Inference of effective river properties from remotely sensed observations of water surface. Adv. Water Resour. 79, 103–120. doi: 10.1016/j.advwatres.2015.02.007.

Gleason, C., Garambois, P.A., Durand, M.T., 2017. Tracking river flows from space. EOS, 98. doi: 10.1029/2017EO078085.

Gleason, C.J., Hamdan, A.N., 2015. Crossing the (watershed) divide: Satellite data and the changing politics of international river basins. Geogr. J. 183 (1), 2–15. doi: 10.1111/geoj.12155.

Hagemann, M.W., Gleason, C.J., Durand, M.T., 2017. BAM: Bayesian AMHG-Manning inference of discharge using remotely sensed stream width, slope, and height. Water Resour. Res. 53 (11), 9692–9707. doi: 10.1002/2017WR021626.

Hossain, F., et al., 2014. Proof of concept of an altimeter-based river forecasting system for transboundary flow inside Bangladesh. IEEE J. Selected Topics Appl. Earth Obs. Remote Sens. 7 (2), 587–601. doi: 10.1109/jstars.2013.2283402.

Larnier, K., Monnier, J., Garambois, P.A., Verley, J., 2020. River discharge and bathymetry estimation from SWOT altimetry measurements. Inverse Prob. Sci. Eng. 1−31. doi: 10.1080/17415977.2020.1803858.

Lin, P., et al., 2019. Global reconstruction of naturalized river flows at 2.94 million reaches. Water Resour. Res. 55 (8), 6499–6516. doi: 10.1029/2019WR025287.

Mersel, M.K., Smith, L.C., Andreadis, K.M., Durand, M.T., 2013. Estimation of river depth from remotely sensed hydraulic relationships. Water Resour. Res. 49 (6), 3165–3179. doi: 10.1002/wrcr.20176.

Nickles, C., Beighley, E., Durand, M., Prata de Moraes Frasson, R., 2020. Integrating Lateral Inflows Into a SWOT Mission River Discharge Algorithm. Water Resources Research 56 (10). doi: 10.1029/2019WR026589, e2019WR026589.

Oki, T., Kanae, S., 2006. Global hydrological cycles and world water resources. Science 313 (5790), 1068–1072. doi: 10.1126/science.1128845.

Oubanas, H., et al., 2018a. Discharge estimation in ungauged basins through variational data assimilation: The potential of the SWOT mission. Water Resour. Res. 54 (3), 2405–2423, https://doi.org/10.1002/2017WR021735.

Oubanas, H., Gejadze, I., Malaterre, P.-O., Mercier, F., 2018b. River discharge estimation from synthetic SWOT-type observations using variational data assimilation and the full Saint-Venant hydraulic model. J. Hydrol. 559, 638–647. doi: 10.1016/j.jhydrol.2018.02.004.

Pavelsky, T.M., et al., 2014. Assessing the potential global extent of SWOT river discharge observations. J. Hydrol. 519, 1516–1525. doi: 10.1016/j.jhydrol.2014.08.044.

Schaperow, J.R., Li, D., Margulis, S.A., Lettenmaier, D.P., 2019. A curve-fitting method for estimating bathymetry from water surface height and width. Water Resour. Res. 55 (5), 4288–4303. doi: 10.1029/2019WR024938.

Sneddon, C., Fox, C., 2006. Rethinking transboundary waters: A critical hydropolitics of the Mekong basin. Political Geogr. 25 (2), 181–202, http://dx.doi.org/10.1016/j.polgeo.2005.11.002.

Sneddon, C., Fox, C., 2012. Water, geopolitics, and economic development in the conceptualization of a region. Eurasian Geogr. Econom. 53 (1), 143–160. doi: 10.2747/1539-7216.53.1.143.

Solander, K.C., Reager, J.T., Famiglietti, J.S., 2016. How well will the Surface Water and Ocean Topography (SWOT) mission observe global reservoirs? Water Resour. Res. 52 (3), 2123–2140. doi: 10.1002/2015wr017952.

Tuozzolo, S., et al., 2019a. The impact of reach averaging Manning's equation for an in-situ dataset of water surface elevation, width, and slope. J. Hydrol. 578, 123866, https://doi.org/10.1016/j.jhydrol.2019.06.038.

Tuozzolo, S., et al., 2019b. Estimating river discharge with swath altimetry: A proof of concept using AirSWOT observations. Geophys. Res. Lett. 46 (3), 1459–1466, https://doi.org/10.1029/2018GL080771.

Ulaby, F.T., Long, D.G., Blackwell, W.J., Elachi, C., Sarabandi, K., 2014. Microwave Radar and Radiometric Remote Sensing. University of Michigan Press.

Wolf, A.T., Natharius, J.A., Danielson, J.J., Ward, B.S., Pender, J.K., 1999. International river basins of the world. Int. J. Water Resour. Dev. 15 (4), 387–427. doi: 10.1080/07900629948682.

Section 2

Estimating Flood Exposure, Damage and Risk

Page left intentionally blank

Chapter 6

From Cloud to Refugee Camp: A Satellite-Based Flood Analytics Case-Study in Congo-Brazzaville

Jeff C. Ho[a], William Vu[b], Beth Tellman[a,c], Jean Bienvenu Dinga[d], Patrick Impeti N'diaye[e], Sam Weber[a,f], Jean-Martin Bauer[g], Bessie Schwarz[a], Colin Doyle[a,h], Matthias Demuzere[i,j], Tyler Anderson[a] and Emmalina Glinskis[a]

[a]Cloud to Street, New York, NY, United States; [b]World Food Programme, Johannesburg, South Africa; [c]Columbia University, New York, NY, United States; [d]Ministère de la recherche scientifique et de l'innovation technologique (MRSIT/IRSEN), Brazzaville, Republic of Congo; [e]Agence Nationale de l'Aviation Civile (ANAC), Brazzaville, Republic of Congo; [f]University of California, Irvine, CA, United States; [g]World Food Programme, Congo-Brazzaville, Brazzaville, Republic of Congo; [h]University of Texas, Austin, TX, United States; [i]B-Kode VOF, Ghent, Belgium; [j]Department of Geography, Ruhr-University Bochum, Bochum, Germany

1 Introduction

A community's ability to absorb a shock and prevent a flood from becoming a disaster is a key to its long-term resilience. However, governments, communities, and other government actors can only reliably reduce the number of deaths and protect their economies if they know where vulnerable people and assets are at key moments to make risk mitigation decisions. For flood preparedness, the identification of people and assets most exposed to flooding would enable the government and World Food Program (WFP) to prepare aid and plan response, as well as rezone assets and design protective infrastructure. For emergency response, reliable flood information would enable the government to better locate people for immediate rescue and aid and would enable WFP to provide faster food relief. This would reduce the number of deaths, injuries, illnesses associated with the flood, and more precisely allocate scarce resources. Such a solution would have several co-benefits, which include increased transparency and

Earth Observation for Flood Applications. http://dx.doi.org/10.1016/B978-0-12-819412-6.00006-7

accountability of aid, and improved communication between decision-makers and the public.

Much of the loss of life and suffering from catastrophic flooding comes in the days and weeks following an initial event. During this time, communities are stranded, receiving little to no aid, and lack access to the capital needed to recover. In November of 2017, the city of Impfondo in the Republic of the Congo (a.k.a. the Congo) experienced a serious flood event, leaving 5000 people in need of food assistance (Bauer, 2018). However, the WFP did not learn of the flood for an entire month after it occurred, and once they did receive some information of it, there continued to be unclear information about the size of the flood and the need for food which delayed the response. Alerts about the flood initially came from word of mouth, and later from field staff deployed from the capital.

WFP in collaboration with Cloud to Street developed a pilot for the 2018/2019 rainy season to assess if a flood information service based on satellite imagery could provide valuable information for monitoring floods. Cloud to Street sought to assess whether satellite imagery could deliver useable and impactful data on flooding to UN, WFP, and to the Congolese government ministries. For WFP, this would mean reducing response times by rapidly assessing if, where, and how much food relief was required. For the Congolese government, this would mean providing information on flooding located in remote parts of the country where there is little regular contact. The goal of both stakeholders was to improve on the benchmark set by the November 2017 Impfondo flood event of detecting a flood in several days instead of several weeks (Fig. 6.1).

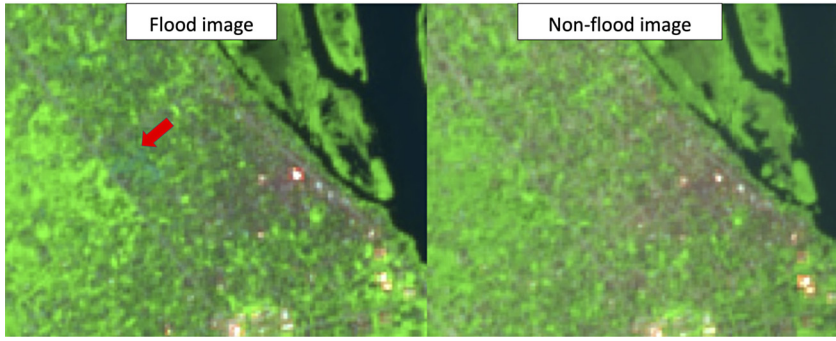

FIGURE 6.1 Sentinel-2 images showing visual differences during a flood event in Impfondo (left) and also when no flood is occurring (right). Sentinel-2 images are visualized using Shortwave-Infrared, Near-Infrared, and Red bands instead of true color Red, Green, and Blue bands to highlight that flooding is discernible in such imagery. *Red arrow* in flood image points to blue corresponding to areas confirmed as flooding, leading to the pilot to test an operationalized satellite-based flood monitoring system. Flood image captured on November 14, 2017 and processed in Google Earth Engine.

2 Congo-Brazzaville local decision-making context

2.1 User design exercise for local stakeholders

Through this pilot, Cloud to Street implemented user design methods for assessing the true needs and capacities of its users. Starting this pilot (and all of Cloud to Street's other projects thereafter) with these "user design" methods—not prescribed technological solutions—helped ensure that we built products based on the end users' needs and that they could unlock the value of what they received, leading to solutions inspiring long term use of the tool.

The exercises included:

1. Stakeholder mapping
   a. Participants were asked to identify all groups and individuals involved when a serious flood event occurs.
   b. By placing Post-it notes on a large piece of paper, users then mapped the lines of communication between the stakeholders and the order of information and actions flows in this system by asking: Who first reports the flood? Who declares officially whether a flood occurs?
   c. This is done in small groups—in most cases participants are divided by agency or department—and afterward the groups come back together as a larger group to compare their maps.
   d. The differences in the maps created revealed some inadeqaute coordination and accountability in emergency response.
2. Timeline analysis
   a. Participants were asked to describe a specific flood event and the steps taken, by first drawing a line in the wall with a tick mark in the middle. This line represents the timeline of the flood and the tick mark is the first day of the event.
   b. The users then walked through the major events in the timeline, recording who performed what action at what time.
   c. The 2017 Impfondo flood was used as the example here.
3. Counterfactual example and scenario discussion
   a. Next, we showed the prototype of the Cloud to Street flood information tool monitoring the country, as well as the flood maps created for the last major disaster (sometimes these maps must be made on the fly). We asked what they would have done had they seen these maps and the analytics right after the flood started.
   b. Then we drew a second timeline on the wall under the first and discussed hypothetical steps that could be taken with the information currently in the prototype, including what information users would have wanted that they did not see in the prototype at present.

The user design exercise conducted in this pilot was unknown to WFP previously, and was suggested as a standard checklist WFP officers could use by WFP staff. Overall the process proved essential for identifying key local stakeholder

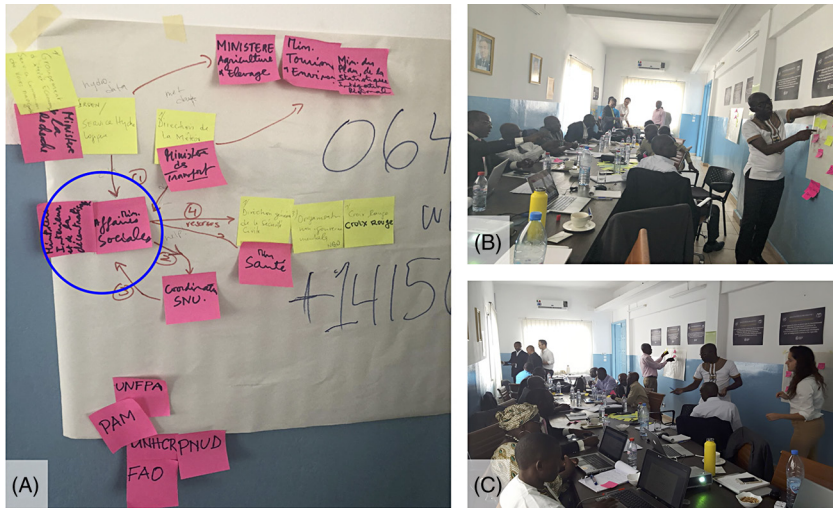

FIGURE 6.2 Communication capacity for flood emergencies in Republic of the Congo. (A) A prototypical stakeholder map drawn by a government ministry user communicating the chain of command for responding to floods. *Blue circle* shows the Ministry of Social Affairs at the center of other actors, something disputed by that particular ministry. These maps were the result of a Cloud to Street exercise with the local government (B,C). *(Sam Weber)*

groups, clarifying the chain of command, identifying where information could improve the flood response process, and profiling the flood capacity in general. See Fig. 6.2 for outputs of the exercises.

2.2 Local stakeholders

Within the Congolese government, three main stakeholder groups were involved. These were the Ministry of Social Affairs, the Meteorology Office, and the HydroMet Office. Users from up to 12 or more government agencies were additionally involved, including the Ministry of the Interior, the police, and the weather service.

Lack of clear coordination between various stakeholder groups made it difficult to clearly assign responsibility to specific ministries during a serious flood event. During a fact-finding session initiated by Cloud to Street prior to service implementation (see Section 2.1), this was confirmed when each group drew a stakeholder map to communicate their understanding of which ministry was responsible during a flood emergency: there was no consensus on chain of command or process. For example, multiple ministries pointed to the Ministry of Social Affairs as ultimately responsible, but representatives from Social Affairs were not aware of that understanding (Fig. 6.2A).

Communication between field agents in more remote areas of the Congo and the country government staff located in Brazzaville was also limited. Most

communication must happen via radio and cannot happen via phone due to lack of a reliable cellular network. Updates from field agents in different parts of the country did not appear to come at regular intervals, as indicated by the 2017 Impfondo event. Moreover, each agency had a different network of field agents, and some ministries do not have personnel on the ground in certain areas that who would be able to respond during an emergency.

2.3 Limited existing data availability

Compounding the coordination problems among users were the limited tools which could be brought to bear on flood issues (Fig. 6.3). As the Republic of the Congo is a country which has experienced conflict over the past several decades, only approximately 13 out of the more than 80 historical hydrological gauges are currently operational (Fig. 6.3B). Rainfall data is also limited, with information recorded manually and reported once a month via phone to Brazzaville from over 15 points around the country (Fig. 6.3C).

2.4 Technical capacity for using satellite-derived information

Beyond the limited tools available, there was also limited capacity for understanding and using publicly available tools, which could improve existing processes. Few government ministry officers have staff with appropriate science and engineering training to understand how to use data from satellites. Only the HydroMet office has the technical capacity to process or use satellite informa-

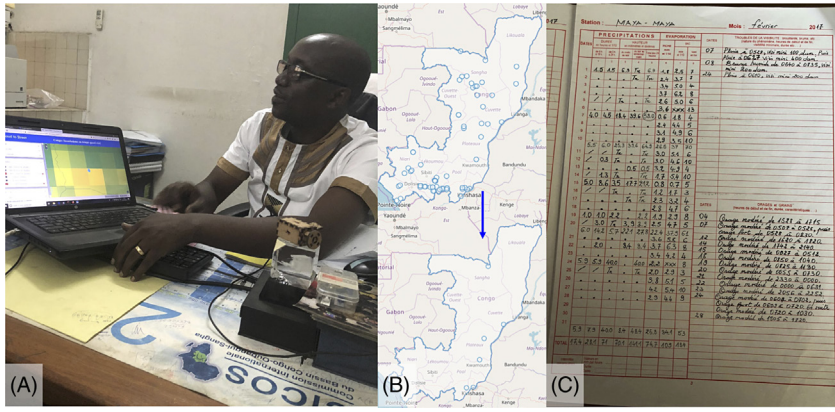

FIGURE 6.3 Existing flood information limitations for Republic of the Congo. (A) Government official from the HydroMet office comparing the rainfall gauge data used locally to satellite derived gridded rainfall data. (B,C) Current tools for flood monitoring in Congo showing (B) the reduced number of gauges due to past conflict (top, historical gauge locations; bottom current gauge locations) and (C) the manual data collection process for collecting rainfall data. *(Photo A by Sam Weber, map by Jeff. C. Ho, and photo C by Bessie Schwarz.)*

tion, and only two employees in this office had this capacity. Moreover, slow internet speeds and low bandwidth further limit the ability to ingest and process such data.

3 Methodology of Cloud to Street's flood monitoring system

Cloud to Street designed and implemented an automated, online flood and rainfall monitoring tool for local stakeholders, provided as a service within an interactive dashboard for government and WFP users (Fig. 6.4). The system locally optimizes global flood detection algorithms and satellite rainfall data to generate flood analysis and reports (Fig. 6.5) that can be verified from the ground and shared through WhatsApp alerts daily.

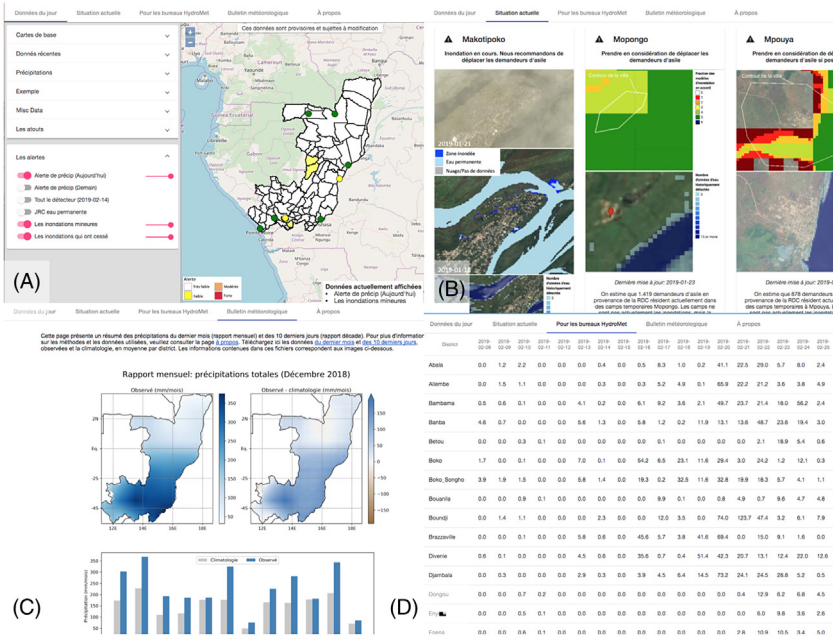

FIGURE 6.4 The main pages of Cloud to Street's Near Real-Time flood monitoring dashboard. (A) "Recent data" page showing map of precipitation alerts by district, with locations of observed flooding situations throughout the country. Collapsible groups of layers on left allow for displaying of different precipitation, flood, and contextual information. "Report a flood" button in blue allows users to manually report a flood to Cloud to Street. (B) "Current situation" page summarizing the latest information on each flooding situation using satellite imagery, flood model results, and rainfall levels. (C) "Meteorological bulletin" page providing monthly and 10-day summaries of rainfall throughout the country compared to historical averages. (D) "Daily rainfall for the HydroMet office" page providing automatic daily precipitation data for two weeks before and after the current date, allowing power users to download tabular data for use in their own reports and analyses. *(Photos by Sam Weber.)*

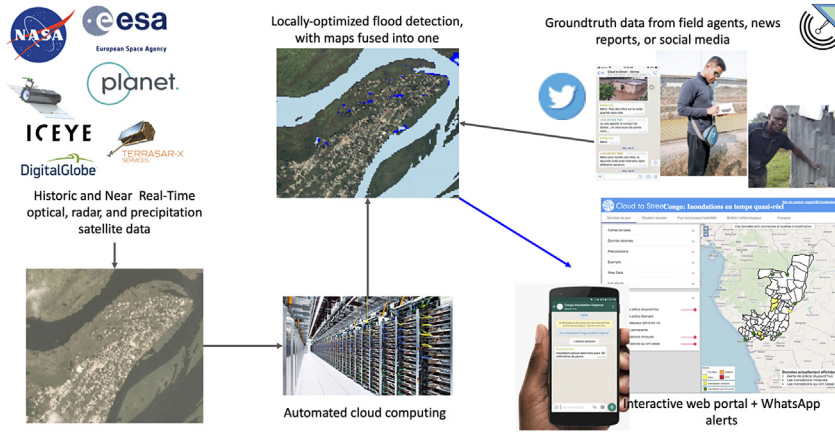

FIGURE 6.5 Cloud to Street's approach. Starting with optical, radar, and precipitation satellite data, and leveraging automated cloud computing and groundtruth data from field agents, news reports, or social media, we perform locally-optimized flood detection. The results are then presented in an interactive dashboard combining flood analysis and reports (Fig. 6.4). *(Bessie Schwarz.)*

This service had three main features:

1. A user-centered dashboard and offline tools customized for the most important local flood needs based on the required information to reduce flood vulnerability.
2. Flood information leveraging the best available science, satellites, and community intelligence.
3. Day-to-day support and local capacity building to make sure users understand the data and can use the information to make decisions.

The flood maps in the system were derived from NASA's MODIS (Aqua and Terra), Landsat 7 and 8, and ESA's Sentinel 1 and Sentinel 2. MODIS maps use 2 images daily at 250-m resolution while the Landsat maps use at least 1 image about every 2 weeks at 30-m resolution. Sentinel 1 and 2 maps use at least 1 image at 10-m resolution every 3 days. For specific flood events, commercial satellite imagery from Planet (PlanetScope, 3-m resolution; RapidEye, 5-m resolution; SkySat, 0.72-m resolution) and DigitalGlobe (WorldView-3, 1.24-m resolution; WorldView-4, 1.24-m resolution; Ikonos, 3.2-m resolution; GeoEye, 1.65-m resolution; QuickBird, 2.16-m resolution) were used when available. Algorithms used are described in greater detail in Tellman et al. (in press).

Past precipitation rates (millimeter/day—mm/day) were retrieved from GSMaP (JAXA Earth Observation Research Center) and provided as maps for the past 12, 24, 48, 72, and 96 h on GSMaP's native 0.1 degree (~10 km) resolution.

4 Results of the pilot

4.1 Overall system performance

During the pilot, Cloud to Street reported on eight flood events and assessed the flood risk of four additional desired sites with asylum seekers. Five of the eight events were identified using public satellite tools and three were reported by local stakeholders in urban areas. Cloud to Street identified that flooding impacted 33 homes in Makotipoko, 26 homes in Mossaka (Fig. 6.6), at least 11 homes in Nkayi, and also identified flooded roads and the risk of larger potential flooding in Ouesso and Sembe.

4.2 Flood risk for asylum seeker sites: a rapid response success

On December 28, 2018, Cloud to Street was made aware of a situation where around 16,000 asylum seekers from the neighboring countries of Democratic Republic of Congo crossed the border and sought refuge in several sites along the Congo River on the Republic of the Congo side (Fig. 6.7). The UN Refugee agency (UNHCR) was concerned about the flood risk of these sites, and sought information from external sources. Cloud to Street mobilized quickly, providing an initial briefing on the flood risk based on historical flood patterns by December 29. By January 3, we added additional information from six flood models (Trigg et al., 2016) to provide a more comprehensive assessment of flood

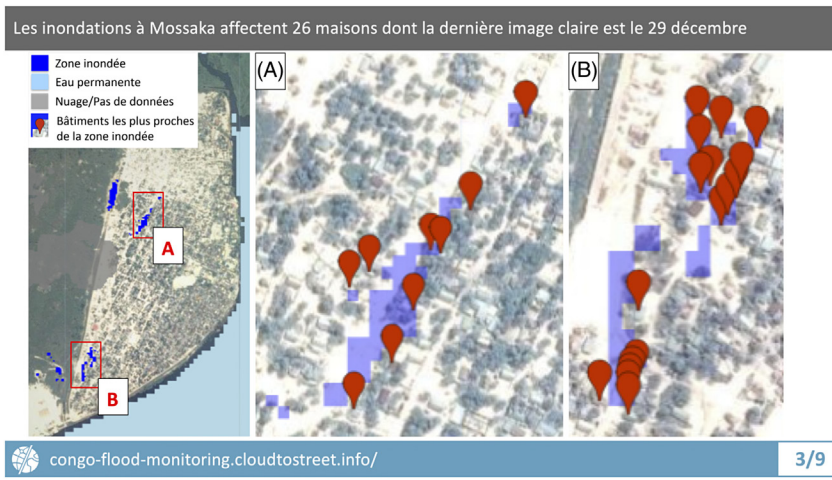

FIGURE 6.6 Satellite-based flood analytics report in French presented to local stakeholders showing 26 homes impacted by flooding in Mossaka, Republic of the Congo. This is one example of a flood detected by Cloud to Street's flood monitoring system and provided to government stakeholders in the local language. The title of the report can be translated in English to "Floods in Mossaka affected 26 homes in last clear image on December 29" and the caption items, in order, as "Flooded area," "Permanent water," "Clouds/No data," and "Buildings closest to the flooded area."

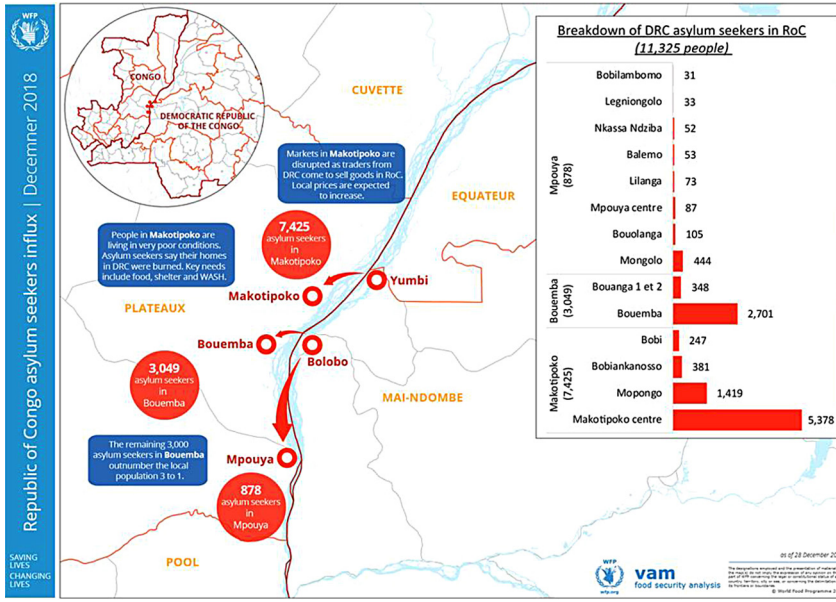

FIGURE 6.7 Asylum seekers situation report, 28 December 2018, showing the location and population of 4 settlements and an estimated over 11,000 people. *(World Food Programme.)*

risk, and emailed recommendations to UNHCR (Fig. 6.8). At that point, daily checks of the four main asylum seeker sites were added to the Cloud to Street monitoring system in case flooding occurred, which also included providing daily information on our "Current Situation" cards for local decision makers.

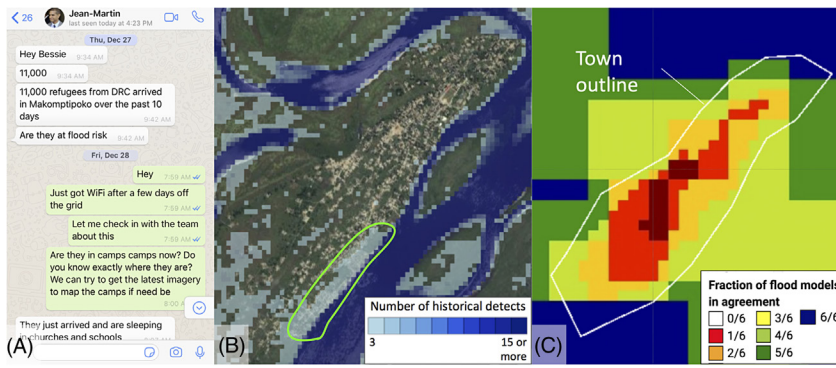

FIGURE 6.8 (A) Cloud to Street's received news of asylum seeker sites that were potentially at risk of flooding. WFP was dispatching food aid to these sites and needed to know whether some sites should be relocated. (B) Historical flood frequency map for one site (Makotipoko) showing number of years with flooding detected historically (1984–2018) in areas where buildings exist (green outline). (C) Location of the 25 year flood plain based on six flood models from Trigg et al. (2016) showing high model agreement in some areas of Makotipoko. The data in (B) and (C) were used to make recommendations to relocate refugees from Makotipoko. *(Analysis and maps by Jeff C. Ho, Sam Weber, and Beth Tellman.)*

On January 16, formal recommendations were presented to UNHCR and then the information was conveyed to local government actors on the ground.

On February 8, UNHCR reported that the government agreed to provide a recommendation for refugees to move from the highest risk site (Makotipoko) to one of the sites with lower risk (Bouemba). Makotipoko was the site with the largest number of refugees, with 5,378 in Makotipoko center alone, and 2,000 more in the surrounding areas. While exact numbers of refugees moved is unavailable, the estimated flood risk of over 7,000 refugees was reduced based on the provided information. This therefore represented an important success for the usefulness of satellite information on flood risk in decision making.

In November 2019, during the following rainy season, the Republic of the Congo experienced severe flooding due to overflowing dams upstream in the Central African Republic. As a follow-up to the original pilot, Cloud to Street detected flooding in Makotipoko using PlanetScope imagery (Fig. 6.9), validating the decision to reccomend moving refugees from the high-risk site.

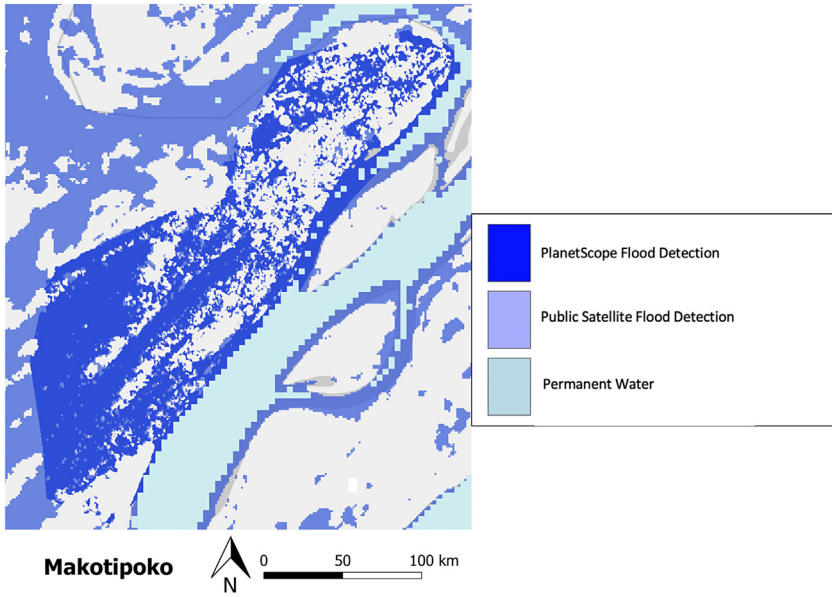

FIGURE 6.9 Flooding detected in Makotipoko combining flood maps from commercial PlanetScope imagery captured on November 23, 2019 and from all public satellite imagery (Landsat-8, Sentinel-2, Sentinel-1) captured between October 24 and December 10, 2019. This flood event occurred after the decision to recommend moving at-risk refugee camps. This information thus reduced the impact of that flooding on the refugees who ultimately decided to move. *(Map and analysis by Tyler Anderson.)*

4.3 Communication and technical capacity building

The system was designed to provide useable flood information for government users to incorporate into their decision-making process. The initial assumption had been that government users would check the pages of the dashboard regularly or would check the dashboard when alerted. However, as the pilot proceeded, it was found that more direct communication through WhatsApp allowed for greater uptake of flood alert information based on monitoring web visits to the dashboard from Congo-Brazzaville using Google Analytics. Therefore, we created a local WhatsApp group with representatives from different government ministries and other local stakeholders and subsequently sent out daily summaries of the "Current Situation" page to that group (Fig. 6.10A). This allowed for confirmation from users on the ground about situations observed with Cloud to Street's system (Fig. 6.10B).

The WhatsApp group served as a focal point of coordination among ministries who had previously lacked a common source of information around flooding. For example, on January 7, 2019, from M. Dinga from the HydroMet Office, "Je propose que nous travaillons ensemble à chaque intervention" (I propose that we work together for each intervention). In addition, a representative from the Ministry of the Interior reported in the January monthly conference call that photos shared in the group, in addition to reports from other ministries where flooding was occurring throughout the city, alerted them to flooding, they otherwise would not have identified.

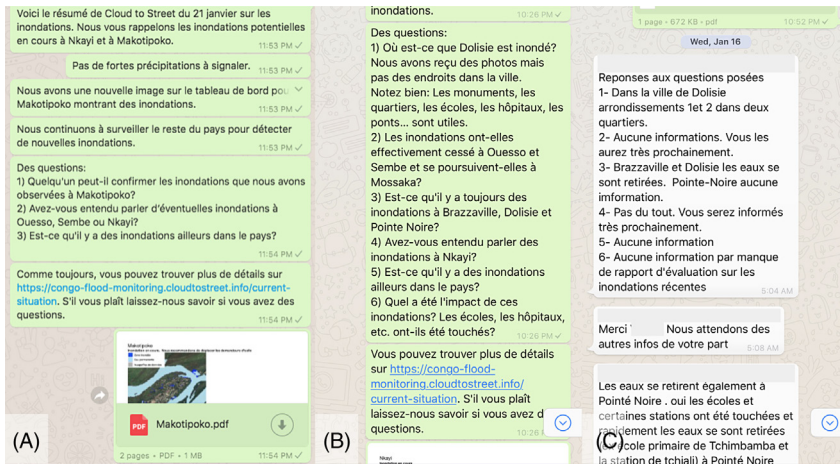

FIGURE 6.10 Screenshots from Cloud to Street's local WhatsApp group with representatives from government ministries and other local stakeholders (names and phone numbers redacted for privacy). (A) An example flood summary from January 21 sent with PDF summaries of situations on the "Current Situation" page as well as questions for local stakeholders. (B,C) A longer list of questions plus responses from multiple users from January 16. *(Jeff C. Ho)*

FIGURE 6.11 Photos of (A) initial training on Cloud to Street's system on November 2 and (B) the final monthly conference call attended by stakeholders on February 25, 2019. *(Photos by William Vu)*

Cloud to Street added to local capacity of the government ministries through training at the pilot's onset in October, monthly updates starting in December, and shared coordination around flooding through the WhatsApp group. On November 2, 2018, 18 officials from 7 government ministries attended a training session on the Cloud to Street System and each received a training certificate (Fig. 6.11). During subsequent monthly conference calls attended by stakeholders, they received new information from the system.

A final meeting was held with local stakeholders to review the service provided. Representatives from the government gave the following testimonials of the system (translated from the original French):

- "Cloud to Street's service provides the evidence and models that scientifically can help us make better decisions in our work, especially in work on refugee or asylum seeker situations. This was evident with their analysis and recommendation for the DRC asylum seekers in Makotipoko."—Chief of Staff, Ministry of Social Affairs
- "Cloud to Street would have helped us to react in a number of days to major flood situations, like the one in Impfondo in 2017, instead of a number of weeks."—Chief of Staff, Ministry of Social Affairs
- "If Cloud to Street's system existed in 2017, we would have been able to evacuate and potentially relocate those vulnerable to the major flooding in Impfondo."—Government attendee
- "The Cloud to Street dashboard and WhatsApp group provided the infrastructure to detect and respond more quickly to floods that previously did not exist." Victor Batekouaou—Director of Prevention and Risk Reduction to Catastrophe, Ministry of Social Affairs

4.4 Technical challenges

Flash flooding also occurred in three urban areas in the Southern part of the country (Brazzaville, Pointe Noire, and Dolisie), but the system was not designed for detecting flooding in such areas. Cloud to Street obtained commercial imagery from optical (DigitalGlobe) and experimental radar (ICEYE) sensors for these situations, but these images either did not provide useful information (ICEYE) or did not provide information in a timely manner (DigitalGlobe). Cloud to Street provided support for these situations through the WhatsApp group coordinating local efforts from different ministries, and also by providing rainfall information. Although such floods are arguably the most dangerous and costly for the country, unfortunately the feasibility of near real-time urban flood detection from satellites remains an ongoing scientific challenge: thus far, urban flood mapping has only been demonstrated on large scale flooding in isolated cases (e.g., Chini et al., 2019), and not been demonstrated operationally in flood monitoring services.

Cloud to Street also discovered that precipitation and flood detection algorithms were relatively noisy, and even when hindcasted historically for the Impfondo 2017 event would not be able to provide a dispositive alert. Therefore, early on in the pilot, Cloud to Street explored proxies and other contextual information that would aid in triangulating the detection of flood events for Republic of the Congo. For example, river levels were a useful proxy for the risk of flooding in Impfondo—that is, Impfondo occurred when normally-seasonal rivers became full of water. However, there were few documented historical events which were used to locally calibrate the satellite detection algorithms (primarily just Impfondo in 2017), and the global satellite algorithms that have been successfully implemented elsewhere were particularly noisy in Congo due to the high proportion of forested land cover in the country. Floods cannot be detected under regions under dense canopy cover using optical or radar sensors, save for L-band SAR sensors, but the moderate resolution existing sensors (e.g. ALOS-2) has a revisit time of 14 days. Coarse resolution (25 km) daily inundation fraction can be obtained through fusion of passive/microwave sensors through SWAMPS (Jensen & Mcdonald, 2019).

Using commercial imagery was also slower and more limited than initially expected. We engaged three commercial imagery providers for this pilot: DigitalGlobe (~1 m optical), Planet (3 m optical), and ICEYE (1 m radar), and each had distinct issues that prevented their use in providing high quality flood maps for decision making. Cloud to Street tasked DigitalGlobe satellites to collect imagery over Brazzaville during urban flooding there; however, cloud-free imagery was not able to be collected until 1 month later, after flooding had already ended. Planet Imagery was available daily or every few days over many sites in Congo; however, imagery could only be visualized with the visible light spectrum (i.e., red, green, blue) in their proprietary viewer, so that other visualizations required to detect flooding (i.e., using the near-infrared signal)

were not accessible for daily flood monitoring. Cloud to Street further engaged ICEYE to collect two very high-resolution radar images over Pointe Noire during urban flooding there; however, the images were still experimental and the images were not well-calibrated, leading to vastly different signals and limited use for flood detection. Later experiments as of November 2019 revealed that ICEYE data had improved in calibration. Of the three commercial providers explored, Planet provided the most value as their imagery could be purchased and downloaded once floods had been detected via the public satellite sensors and used for confirmation.

5 Conclusions and recommendations

Given the scientific and technical limitations of the system as implemented, this case study reveals three clear directions for future research and flood services.

1. More work is necessary for urban flood detection from satellite remote sensing. Advances need to be made both on the algorithm-development side with publicly available satellite sensors (e.g., Sentinel-1) and also on the operationalizing side, evaluating how algorithms perform "in the field" on real events that may be typical for a tropical country like the Republic of the Congo. Due to dense canopy cover, active sensors, especially L-band SAR that can detect water through canopies available at coarse resolution (25 km, via SWAMPS, see Jensen and McDonald 2019) or moderate resolution (100 m, currently revisits every 14 days with ALOS-2 but soon every 8 days with the 2020 SAOCOM mission), are important to capture the full extent of floods in many areas.
2. The development of a globally consistent library of events for local calibration of satellite flood-detection algorithms and other flood alert triggers is necessary to operationalize satellite-based flood monitoring systems in countries like the Republic of the Congo. Although some databases currently exist (e.g., the Dartmouth Flood Observatory (http://floodobservatory.colorado.edu/), or from Tellman et al., inpress), these typically contain only the largest events. For smaller events such as Impfondo 2017, such a library of flood events will be critical for developing an operational flood monitoring system.
3. The importance of fusion of flood information from multiple sensors is clear from this case study. No one sensor performed best for operational flood monitoring. The combination of public and commercial satellites, with precipitation information and information from flood models, was necessary for providing actionable recommendations to decision makers.

The primary lessons from this case study are not scientific. This case study has demonstrated that operationalizing scientific algorithms for flood monitoring is extremely difficult, and at least part of the difficulty owes to the challenging decision-making context in under-resourced countries. The example of

the flood risk analysis of the asylum seeker sites provides evidence to suggest that existing information from satellite-based flood analytics can indeed inform local decision making and provides optimism for operationalizing flood monitoring from satellites in the future.

Acknowledgments

Thanks to Planet for providing Skysat and Planetscope imagery for Makotipoko. Thanks to the Ministry of Social Affairs for the Republic of Congo for their coordination. Thanks to the WFP Innovation Accelerator for funding this project.

References

Bauer, J.M., 2018. Cloud on the horizon: Rebooting flood mapping in Congo. World Food Programme Insight. Available from: https://insight.wfp.org/cloud-on-the-horizon-rebooting-flood-mapping-in-congo-c8c4fdae66ef.

Chini et al., 2019. Sentinel-1 InSAR coherence to detect floodwater in urban areas: Houston and Hurricane Harvey as a test case. Remote Sens. 11 (2), 107. doi.org/10.3390/rs11020107.

Jensen, K., Mcdonald, K., 2019. Surface water microwave product series version 3: a near-real time and 25-year historical global inundated area fraction time series from active and passive microwave remote sensing. IEEE Geosci. Remote Sens. Lett. 16 (9), 1402–1406. https://doi.org/10.1109/LGRS.2019.2898779.

Tellman, B., Sullivan, J., Doyle, C., in press. Global flood observation with multiple satellites: Applications in Rio Salado, Argentina, and the Eastern Nile Basin. In: Wu, H., (Ed.) Global Drought and Flood Prediction. American Geophysical Union Books.

Trigg, M.A., Birch, C.E., Neal, J.C., Bates, et al., 2016. The credibility challenge for global fluvial flood risk analysis. Environ. Res. Lett. 11 (9), 094014. doi: 10.1088/1748-9326/11/9/094014.

Further reading

Brakenridge, R., Anderson, E., 2006. MODIS-based flood detection, mapping and measurement: The potential for operational hydrological applications. In: Transboundary Floods: Reducing Risks through Flood Management. Springer, Netherlands, pp. 1–12.

Du, Y., Zhang, Y., Ling, F., Wang, Q., Li, W., Li, X., 2016. Water bodies' mapping from Sentinel-2 Imagery with Modified Normalized Difference Water Index at 10-m spatial resolution produced by sharpening the SWIR band. Remote Sens. 8 (4), 354. https://doi.org/10.3390/rs8040354.

FAO, ITU, 2019. Delivering remote flood analytics as a scalable service. In: E-Agriculture in Action: Big Data for Agriculture, FAO and ITU, Bangkok. http://www.fao.org/3/ca5427en/ca5427en.pdf.

Feyisa, G.L., Meilby, H., Fensholt, R., Proud, S.R., 2014. Automated Water Extraction Index: A new technique for surface water mapping using Landsat imagery. Remote Sens. Environ. 140, 23–35. https://doi.org/10.1016/j.rse.2013.08.029.

Lin, Y.N., Yun, S.H., Bhardwaj, A., Hill, E.M., 2019. Urban flood detection with Sentinel-1 multitemporal synthetic aperture radar (SAR) observations in a Bayesian Framework: a case study for Hurricane Matthew. Remote Sens. 11 (15), 1778. https://doi.org/10.3390/rs11151778.

Li, Y., Martinis, S., Wieland, M., Schlaffer, S., Natsuaki, R., 2019. Urban flood mapping using SAR intensity and interferometric coherence via Bayesian Network Fusion. Remote Sens. 11 (19), 2231. https://doi.org/10.3390/rs11192231.

Twele, A., Cao, W., Plank, S., Martinis, S., 2016. Sentinel-1-based flood mapping: a fully automated processing chain. Int. J. Remote Sens. 37 (13), 2990–3004. https://doi.org/10.1080/01431161.2016.1192304.

Tarpanelli, A., Camici, S., Nielsen, K., Brocca, L., Moramarco, T., Benveniste, J., 2019. Potentials and limitations of Sentinel-3 for river discharge assessment. Adv. Space Res. https://doi.org/10.1016/j.asr.2019.08.005.

Tellman, B., Sullivan, J., Doyle, C., Kettner, A., Brakenridge, G.R., Erickson, T., Slayback, D.A., 2017. A global geospatial database of 5000 + historic flood event extents. AGU Fall Meeting Abstracts.

Yang, X., Pavelsky, T.M., Allen, G.H., Donchyts, G., 2019. RivWidthCloud: An automated Google Earth Engine algorithm for river width extraction from remotely sensed imagery. IEEE Geosci. Remote Sens. Lett. 17 (2), 217–221. https://doi.org/10.1109/LGRS.2019.2920225.

Zajic, B., 2019. How flood mapping from space protects the vulnerable and can save lives. Planet Blog. Available from: https://www.planet.com/pulse/how-flood-mapping-from-space-protects-the-vulnerable-and-can-save-lives/.

Chapter 7

DFO—Flood Observatory

A.J. Kettner[a], G. Robert Brakenridge[a], Guy J-P. Schumann[a,b,c,d] and X. Shen[e,f]
[a]INSTAAR, University of Colorado, Boulder, CO, United States; [b]Research and Education Department, RSS-Hydro, Dudelange, Luxembourg; [c]Remote Sensing Solutions, Barnstable, MA, United States; [d]School of Geographical Sciences, University of Bristol, Bristol, United Kingdom; [e]Civil and Environmental Engineering, University of Connecticut, Storrs, CT, United States; [f]Eversource Energy Center, University of Connecticut, Storrs, CT, United States

1 Introduction

Freshwater is a vital and indispensable resource for humankind. However, the availability and spatial distribution of freshwater at any time is not even around the world. This unequal distribution leads frequently to severe drought or flood disasters, significantly impacting humanity. Over the last decade, 83% of all disasters triggered by natural hazards were caused by extreme weather- and climate-related events and this has been increasing by 35% since the 1990s (IFRC, 2020). Gauge-based hydrological monitoring systems help society to better understand freshwater availability throughout the year and monitor hydrological disasters. For rivers, they typically continuously measure stage height (water level with respect to a fixed datum) which is then converted to discharge with the use of in-situ measurements with a current meter, which provides velocity and flow width and depth. Thus, a "rating curve" is produced, and the stage information can be converted to discharge units. So far, when it comes to flooding, ground-based gauging station observations have limitations: (1) political boundaries, as rivers frequently cross borders but hydrological data is often not shared. This leaves nations downstream often unaware of, for example, the timing and or magnitude of an extreme event heading their way; or (2) the inability to capture the severity of an event due to overtopping or destruction of a gauging station while a flood disaster is unfolding (Klemas, 2015). This happens often, whereas satellite sensors are unaffected. Also, even if stage heights of such devastating events are monitored and made available, conventional streamflow monitoring systems do not capture the often-associated extensive inundation extent, in which much water is entering into temporary floodplain storage. Airborne missions and satellites have the capacity to track the extent of vast inundated areas and how they evolve over time; they can complement hydrological records obtained on the ground. Also, satellite information is not

Earth Observation for Flood Applications. http://dx.doi.org/10.1016/B978-0-12-819412-6.00007-9

restricted by political boundaries. Applying satellite data to track and map flood extents has been intermittently performed since the mid 1970s (McGinnis and Rango, 1975). However, usage of satellite data greatly advanced during the last 2 decades, during which the number of satellite missions carrying instruments that can be utilized to map flooding has increased considerably (Schumann et al., 2018). Various first-response agencies such as the UN World Food Programme now routinely incorporate satellite-based flood products into their response efforts.

The need for timely and accurate flood information is more urgent than ever as flooding remains the most common natural hazard worldwide, impacting people of all continents in both developed and less developed countries. Over the last decade of the 20th century alone, 46% of the natural hazards were floods (EM_DAT, 2020) that directly impacted 1.4 billion people, claiming 100,000 fatalities worldwide (Jonkman, 2005), causing alone more fatalities than any other natural hazard in the USA (Klemas, 2015). That more and more people are affected by flooding can partly be explained by expanding human population. Since the 1950s, population increased from 2.5 to 6.5 billion in 2005 (United Nations 1962, 1973, 2007) and is expected to be approximately 10 billion by the 2070s (Bongaarts, 2009). Additionally, Najibi and Devineni (2018) concluded from a 30-year (1985–2015) global assessment that flood frequency increased at the global scale, particularly in the tropics, southern subtropics, and mid-latitudes. This was especially the case for moderate- and long-duration floods; frequency remained unchanged for short-duration floods. However, objective data on this topic is not easily obtained: floods as a global geophysical phenomenon are, as noted, not easily measured.

By 2050, Jongmans et al. (2012) estimated a 31% increase of people exposed to the 1 in a 100-year river flood compared to current estimates. By then the total exposed assets by river flooding alone is expected to be increased to $126 trillion, up by 250% from 2010. Desai et al. (2015) indicated that all types of flooding are contributing currently to a global average annual loss of $104 billion. And the annual loss will almost certainly become worse in the coming decades given some evidence of increases in flood frequency over the last 30-years (Najibi and Devineni, 2018). The increase in exposed assets in flood-prone zones and additional changes in baseline conditions such as climate change (Kettner et al., 2018), drainage basin properties, river modifications, sea level rise, all will likely amplify this trend.

Unlike, for example, precipitation measurements organized through the World Meteorological Organization (WMO), the hydrological community has not been very successful in establishing a global hydrological network of observations through which measurements and novel measurement technologies could be exploited (Vereecken et al. 2015). Efforts that come closest have resulted in the Global Runoff Data Centre (GRDC), which is operating under the auspices of the WMO (GRDC, 2008). However, not all countries contribute their hydrological data and for those that do, often only data of a subset of

the available gauging stations is provided, sometimes with a multiyear time lag between the actual measurement and the data being publicly available. The GRDC archives relevant information of just one type of flooding, fluvial flood disasters. Outside of our work, there is no global effort to archive data of other common types of flood disasters, for example, flooding due to pluvial or storm surge events.

The DFO—Flood Observatory (DFO) is a not-for profit entity, now hosted at the Institute of Arctic and Alpine Research (INSTAAR) at the University of Colorado, Boulder, and has been operating since 1995. DFO's mission is to:

> *(1)* Acquire and preserve for public use a digital map record of the Earth's changing surface water, including but not limited to changes related to floods, droughts, wetlands, shorelines, lakes, and reservoirs; *(2)* Conduct remote sensing-based water measurement and mapping in "near real time" for humanitarian purposes; *(3)* Support and encourage operational uses of remote sensing-based surface water information; and *(4)* Conduct scientific research making use of these data products.

DFO is actively testing and further developing remote sensing and modeling capabilities, assembling a global hydrological record, and establishing online automated data services to further enable easy access to daily-updated surface water products. These records serve first responders during a natural disaster and can also improve flood risk assessments. Or they can be used in tandem with hydrological modeling to facilitate weather-based flow and inundation predictions. DFO collaborates with relief agencies and emergency managers during and after major flood events, and with operational water organizations worldwide for data sharing and further development of technical capabilities. It collaborates with NASA—Goddard Space Flight Center; with the Joint Research Centre of the European Commission, Italy; with a research group at the University of Maryland; with the Department of Civil & Environmental Engineering at the University of Connecticut; and with the Surface Dynamics Modeling Laboratory, University of Alabama. As hosted at the University of Colorado, DFO is funded over 10 years on a per-project basis by NASA, the US Geological Survey, the World Bank, the Development Bank of Latin America, the United Nations Office for Disaster Risk Reduction UNDRR (formerly known as UNISDR), and the European Commission's Global Disaster Alert and Coordination System (GDACS) at the Joint Research Centre.

Here we present an overview of what flood observatory hydrological data products and some case studies on how products can be applied and end with some future perspectives.

2 Hydrological data products

Multiple hydrological datasets have been developed by DFO. Some are automatically updated over time, others require additional manual input (e.g. per-flood event maps). Of the products described later, "flood extent maps" derived

from MODIS are automated as well as "estimated water discharge" from microwave radiometer satellite data. All other products require a certain amount of personnel labor. The most-used datasets are discussed below.

2.1 Flood extent maps

Near-real time satellite-derived flood inundation maps are valuable to agencies for disaster monitoring, relief efforts, evaluating flood control measures, and to settle damage claims (Smith, 1997; Follum et al., 2020). DFO uses ample sources of freely available optical satellite data to map flood extent: data from the Moderate Resolution Imaging Spectroradiometer MODIS sensor onboard Aqua and Terra, from LandSat missions, from Sentinel-2 imagery, and from the Visible and Infrared Imager/Radiometer Suite VIIRS onboard the NASA/NOAA satellite Suomi. These data sources have varying revisiting time and spatial resolutions (Table 7.1). Depending on the application, one or more data sources can be utilized for deriving flood extents. NASA Goddard Space Flight Center has implemented DFO-developed algorithms (Brakenridge and Anderson, 2006) to detect flooding from MODIS data. The derived flood extent maps have a global coverage and are made available on a daily basis since 2013

TABLE 7.1 Satellite data used by DFO to map flood extent at a global scale.

Sensor	Satellite	Horizontal resolution flood extent maps at nadir (m)[a]	Repeat interval
Optical:			
Multispectral Instrument	Sentinel-2	~10–20	5 days at the equator, with 2–3 days at mid-latitudes
Multispectral Scanner (MSS) & Thematic Mapper (TM) & Enhanced Thematic Mapper Plus (ETM +)	LandSat 1–8	~30	16 days
MODIS	Terra and Aqua	~250	1 day for each satellite
VIIRS	Suomi	~375	1 day
Radar:			
C-band Synthetic Aperture Radar (SAR)	Sentinel 1	~10–30	Location variable, ~2–6 days (Torres et al., 2012; Potin et al., 2018)

[a]*The horizontal resolution of the DFO end products is provided.*

within a few hours of the satellite overpass. For the other optical data sources (Table 7.1), data is typically processed upon request. Flood extent can be measured from these optical products when clouds or vegetation are not in the line of sight of the water surface. Where needed, commercial optical imagery provide significantly higher spatial resolution.

The following products are developed from the global daily MODIS-based flood inundation maps: (1) Current daily water extent data: a 3-day composition of imaged surface water. The 3 days of data are included to overcome missing values due to clouds and at the same time give an almost near-real time representation of the surface water extent; (2) The 2-week flooded area: a 14-day composition of surface water to provide even greater spatial coverage despite changing cloud cover, and thus image the severity of major flooding; (3) January till current flood area: water extent of the current year from January onward, which is updated monthly. This product highlights the extent of flood events, which happened earlier during a calendar year; (4) Annual flood inundation area: showing from 2013 onward annual flood extents. When processing the entire MODIS data archive, this may eventually be extended to 2000; (5) Flood hazard maps (or occurrence maps): a multiyear water extent which indicates how often an area was flooded in the time series of years. (6) Persistent water layer: this shows where water is detected most of the time: lakes and reservoirs, shorelines, and the larger rivers.

Radar products such as synthetic aperture radar (SAR) data can also be used to map flood extents and have the advantage of not being hindered by clouds or nightly overpasses. SAR data availability and temporal and spatial resolutions improved in recent years with the launch of the non-commercial satellites Sentinel-1(a & b) and the commercial satellites TerraSAR-X, Radarsat-2, and COSMO-SkyMed (Wagner et al., 2009; Schumann et al., 2018). The volume of high-resolution data challenge processing times (Shen et al., 2019) and data storage requirements are very large if global mapping of surface water change is the goal. DFO presently produces flood extent maps from SAR on an event base, only, for locations where flooding is occurring. Initiatives such as the "RAPID," Radar-Produced Inundation Diary, led by Shen et al. (2019) or future initiatives by other organizations may overcome these challenges (Fig. 7.1).

2.2 Water discharge

Historical and current information regarding river discharge is essential, not only from a water management, energy, or global change perspective but also to better control and forecast flooding (Van Dijk et al., 2016). However, the number of ground-based gauging stations is declining (Shiklomanov et al., 2002; Alsdorf et al., 2003), and data that are measured by gauging stations is often not shared. Although freshwater is considered an indispensable resource for humankind, there is still no adequate ground-based global network of river discharge stations. Efforts from the 1990s onward have shown that this gap can be

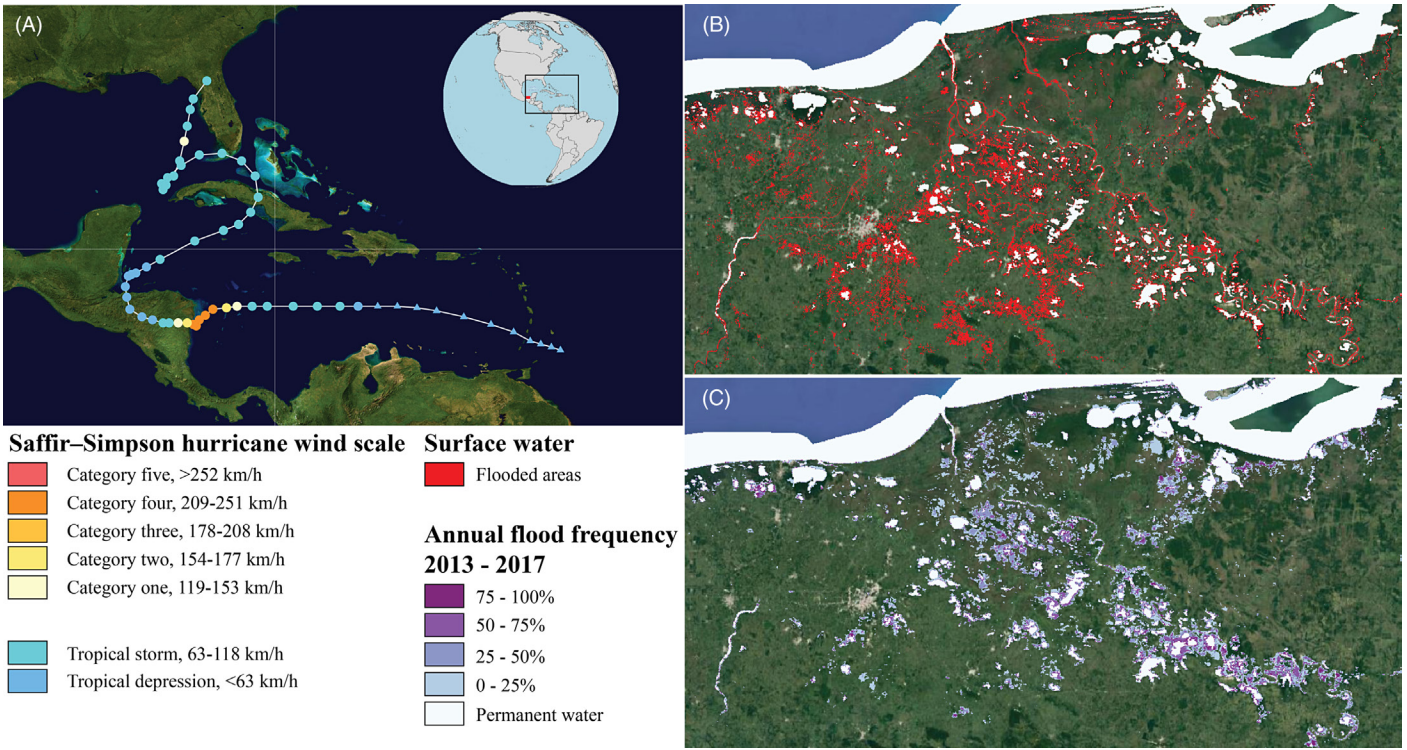

FIGURE 7.1 (A) Track of Hurricane Eta that made landfall as a category 4 hurricane south of Puerto Cabezas, Nicaragua, on November 4, 2020. As a result, eight countries of Central America (Nicaragua, Honduras, Guatemala, El Salvador, Costa Rica, Panama, Belize, and Mexico) were impacted by severe flooding due to heavy rainfall and or storm surge, resulting in at least 160 fatalities. (B) Severe flooding of parts of southern Mexico as observed by Sentinel 1 SAR data (processed at the University of Connecticut; X. Shen). (C) Flood frequency for the same area of southern Mexico for the period 2013–17 as observed by MODIS data from satellites Terra and Aqua, showing how frequently in the five years times series the area was flooded.

overcome by utilizing various satellite sensors (Smith, 1997; Smith et al., 1995, 1996; Van Dijk et al., 2016).

To capture flooding and peak discharge, satellite sensors with a relatively high temporal resolution are needed. With a near-daily repeat intervals, the microwave band at 36.5 GHz (e.g., TRMM, AMSR-E, AMSR2, GMP) has been successfully applied to measure water discharge at a global scale (Brakenridge et al., 2007, 2012). This band is responsive to physical temperature and emissivity and is very sensitive to water/land proportion within an image pixel. By applying a ratio between a river pixel and a nearby dry cell, the physical temperature-driven changes can be cancelled out, resulting in a ratio that indicates changes in within-river-pixel water area. And surface water area changes reflect changes in water discharge. As at a ground-based gauging station of a given river cross profile where discharge can be referred by measured stage height (depth) or flow velocity, a regression can be applied to estimation the relationship between intermittent observed (or modeled) water discharges and the satellite-observed ratio (water discharge signal). Where no observed discharge is available, DFO uses the Water Balance Model, WBM (Wisser et al., 2008) to develop independent discharge estimates at a discharge measurement site, and for comparison to the coeval and co-located satellite-observed water area estaimate. The microwave ratio signal used by the DFO is first processed (daily) by the Global Flood Detection System at the Joint Research Centre, JRC, of the European Commission (De Groeve, 2010), and this signal is averaged using a 4-day running mean to overcome intermittent missing days and to reduce signal noise. Water discharges are estimated from January 1998 onward by applying the regression equation to the microwave signal ratio.

DFO is providing discharge data on a daily basis of several hundred satellite-based gauging stations, using the earlier-described method. For each station, using the complete discharge record from January 1998 onward, a low flow threshold, flood frequency analysis, monthly runoff, and the regression analysis are provided together with an uncertainty analysis, using the Nash–Sutcliffe statistical method (Nash and Sutcliffe, 1970). Displayed on a world map, the current discharge status of each station is provided as either: low flow, normal flow, moderate flooding, or major flooding (Fig. 7.2). DFO also applies the earlier-described method, to reservoirs to proxy water storage from extent status. DFO intends to expand the array of rivers and reservoirs being monitored.

2.3 Active archive of large flood events

Since 1985, collected information on large flood events that occurred around the world has been recorded in a database. Both news reports and orbital remote sensing to detect floods are used and have been used in the past. Each flood event is assigned a unique DFO ID and a natural hazard Glide-Number when available (Guha-Sapir et al., 2011). These IDs are coupled with information on flood duration, cause, location, start and end dates, and socioeconomic impacts

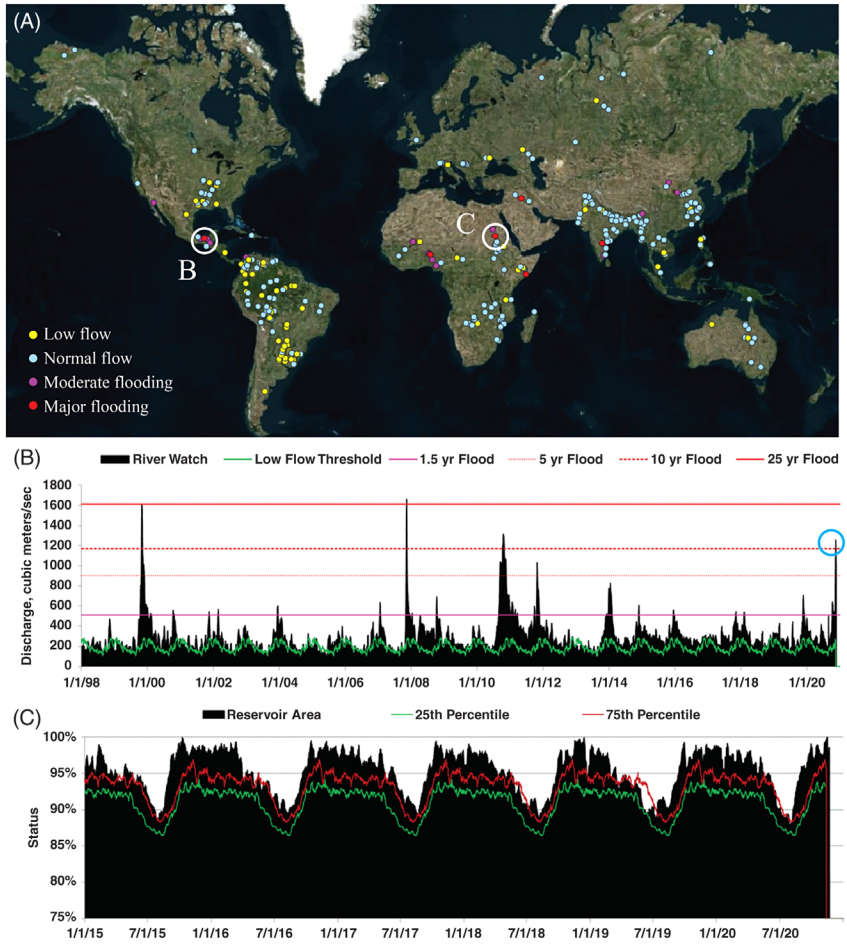

FIGURE 7.2 (A) Satellite-based river discharge and reservoir area measurements for several hundred sites and their status indicated by color for November 15, 2020. These measurements are updated daily. (B) Example of satellite-based daily water discharges for a period of ~22 years for the Grijalva River, Mexico (DFO site ID: 1052; http://floodobservatory.colorado.edu/SiteDisplays/1052.htm). Notice that Hurricane Eta caused severe flooding in Mexico (blue circle figure 2B), resulting in a 10-year flood event for the Grijalva River (mean discharge ~285 m^3/s; peak discharge as of November 9, 2020: 1,270 m^3/s). As of November 15, 2020, Hurricane Eta resulted in at least 160 fatalities across Central America of which 27 in Mexico. (C) Example of reservoir area measurements of the Merowe Reservoir, Sudan (DFO site ID: 11808; http://floodobservatory.colorado.edu/SiteDisplays/11808.htm).

(number of fatalities and people displaced), together with the news source and an index to characterize a flood event—based on flood severity (Kundzewicz et al., 2013). Flood severity is divided into three classes. Class 1: large flood events: significant damage to structures or agriculture; fatalities; and/or 1–2 decades-long reported interval since the last similar event. Class 1.5: very large

events: with a greater than 2 decades but less than 100 year estimated recurrence interval, and/or a local recurrence interval of at 1–2 decades and affecting a large geographic region (> 5000 km^2). Class 2: Extreme events: with an estimated recurrence interval greater than 100 years. With over 4900 entries, this is the only flood event archive that holds over 35 years of such unique data on large floods (Fig. 7.3).

Data of the archive has been supporting science studies to, for example, estimate the percentage of floods that the upcoming Surface Water and Ocean

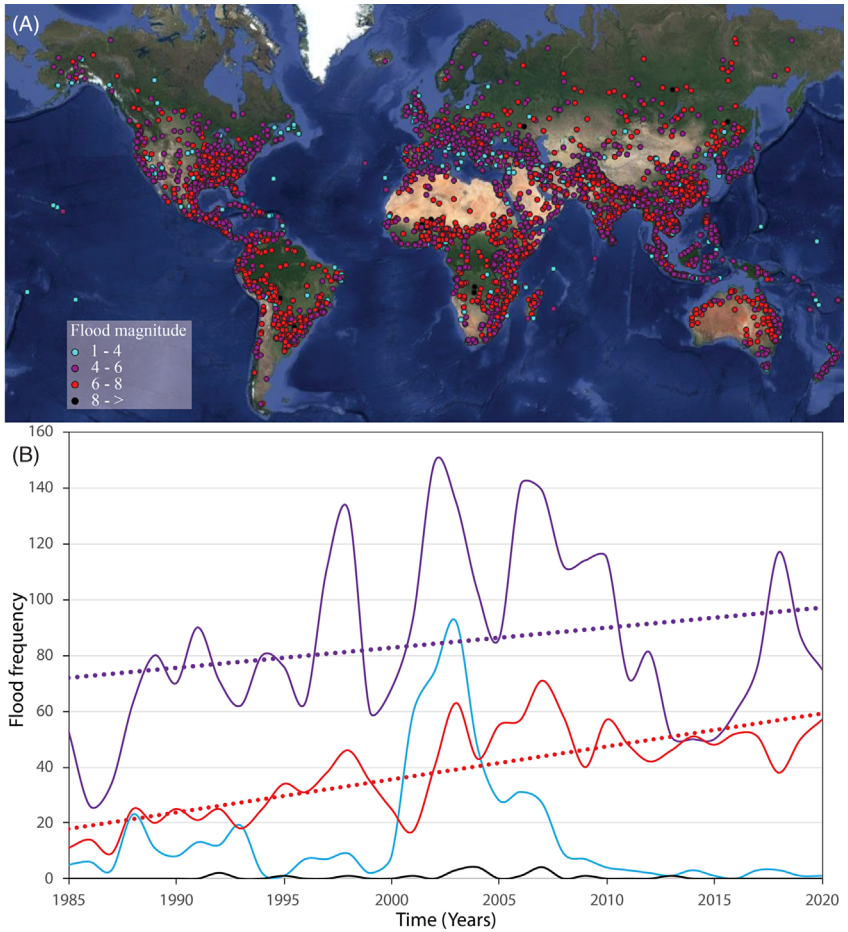

FIGURE 7.3 (A) Flood centroids of 4982 large flood events recorded since 1985 from news, governmental, instrumental, and remote sensing sources. Colors indicate the flood magnitude on a logarithmic scale as defined as the flood duration times the inundated area times the flood severity. (B) Flood frequency per year for the 4 magnitude classes, colored following the legend of Fig. 7.3A. Notice that large flood events (magnitude 4–6) and extreme flood events (magnitude 6–8) have increasing trends.

Topography (SWOT) satellite mission would have captured if it were launched and actively obtaining data from 1985 onward (Frasson et al., 2019). Other studies have used this active data archive to describe the spatial-temporal variability of large floods in Europe (Kundzewicz et al., 2013), or the global spatial distribution of flooding events (Adhikari et al., 2010).

2.4 Flood hazard maps

Risk defines the impact of a hazard to humans and resources. So, for flooding, where there are no people or human assets that can be affected by a flood hazard, there is no risk (Kron, 2005). To determine flood risk, the probability of occurrence of flooding is required (Spachinger et al., 2008). Flood hazard maps spatially display flood events of different probability, identifying flood-prone areas that may threaten life and property. Such maps are essential for building awareness, informing local government on hazard situations, for insurance purposes, and for authorities to establish areal zoning that indicate levels of restrictions (e.g., building restrictions in flood prone areas) (Hagemeier-Klose and Wagner, 2009). Many of the developed countries have established a standardized method to produce hazard maps. These often involve long time series of observed discharge records in conjunction with hydrodynamic model simulations to establish spatial flood extent for a given peak discharge with a certain return period. These methods are computationally expensive and therefore costly as model accuracy depends on high resolution digital elevation models (DEMs) and also the knowledge of channel bathymetry; both of which have commonly obtained through field-ground or airborne campaigns.

For most less-developed nations, there is limited availability of long-term time series of discharge records, and if available, these are only for a very few gauging stations. So, it is impossible to establish return periods of peak discharges with acceptable certainty. Additionally, less developed countries often do not have sufficient resources to develop the high resolution DEMs that are required for hydrodynamic modeling. Consequently, for regions with no hazard maps, planning cannot limit exposure and mitigate flood risk in a consistent and replicable manner. This is often true for the rapidly developing nations that are most in need of these hazard products (Brakenridge et al., 2017; Johnson et al., 2020).

Brakenridge (2018) describes an alternative, more practical approach to map flood hazards, where either ground or satellite-obtained discharges (discussed in Section 2.2) are used in conjunction with satellite-derived flood extent maps for actual floods. For the satellite-based obtained discharges, daily discharges can be back-processed till 1998 for any new location of interest, providing a more than 20-year discharge record to establish a Log Pearson III (for example) probability analysis of discharge return periods. Given the time length of this discharge record, frequency analysis can then provide a reasonable estimate of the 50-year recurrence interval flood. The dates associated with a particular flood frequency at a particular location can then be used to retrieve the associated

flood extent maps, for example, from the automated daily flood product of MODIS. But other archived satellite data could be processed as well (for example, if higher spatial resolution is needed). Accomplishing this for different discharge recurrence intervals for a specific location provides floodplain managers and planners valuable information of the inundation extent for a given discharge and recurrence interval (Fig. 7.4).

2.5 Flood data dissemination

Communicating risk is an important element in making people aware of the potential of flooding and provide better protection against harm (Hagemeier-Klose and Wagner, 2009). Access to long-term records of historical hydrological data is crucial to determine the scale and severity of potential risk. During or after a flood, when preparation is no longer a viable option, near-real time flood information can support relief and recovery efforts. As a result, different hydrological data needs exist depending on when information is required, before, during, or after a flood. Additionally, stakeholders can have varying hydrological information needs, and often their work method or operational framework requires data to be of a certain type, format, and/or scale.

DFO holds a variety of unique global hydrological datasets and strives to have all datasets online, freely available under the Creative Commons CC-BY-NC-SA 4.0 License (https://creativecommons.org/licenses/by-nc-sa/4.0). The DFO flood portal (https://floodobservatory.colorado.edu/) provides access to the aforementioned datasets. Flood information of currently unfolding or recent events that were impactful or for which DFO received a data request, are prominently displayed on the front page. Depending on availability, these DFO datasets are often associated with data derived from other initiatives, including flood forecast data from the Global Flood Monitoring System (GFMS), University of Maryland (Wu et al., 2012). In general, most water extent displays are made available as downloadable shapefiles and or georeferenced tiff (GEOTIFFs) composites, holding multiple layers (e.g., historical flood extent, current day flooding, and last 2-weeks flooding). Many of these individual flood layers are also provided as Web Map Service (WMS), a standard protocol developed by the Open Geospatial Consortium (OGC) for serving images of georeferenced maps over the internet. As such, each WMS layer can be included as a layer in, for example, the user's GIS system, such that the user has instant access to the latest flood information when the server site data gets updates. Daily and historical discharge observations of satellite-based gauging stations, together with its metadata that includes a quality assessment, and derived hydrological information can be obtained directly through the portal or as WMS. Additionally, the flood portal includes an interactive page where people can zoom in/out to the area of interest and display the various hydrological layers of interest.

A freely-downloadable phone app available through the Android and Apple app stores has been developed in close collaboration with Remote Sensing

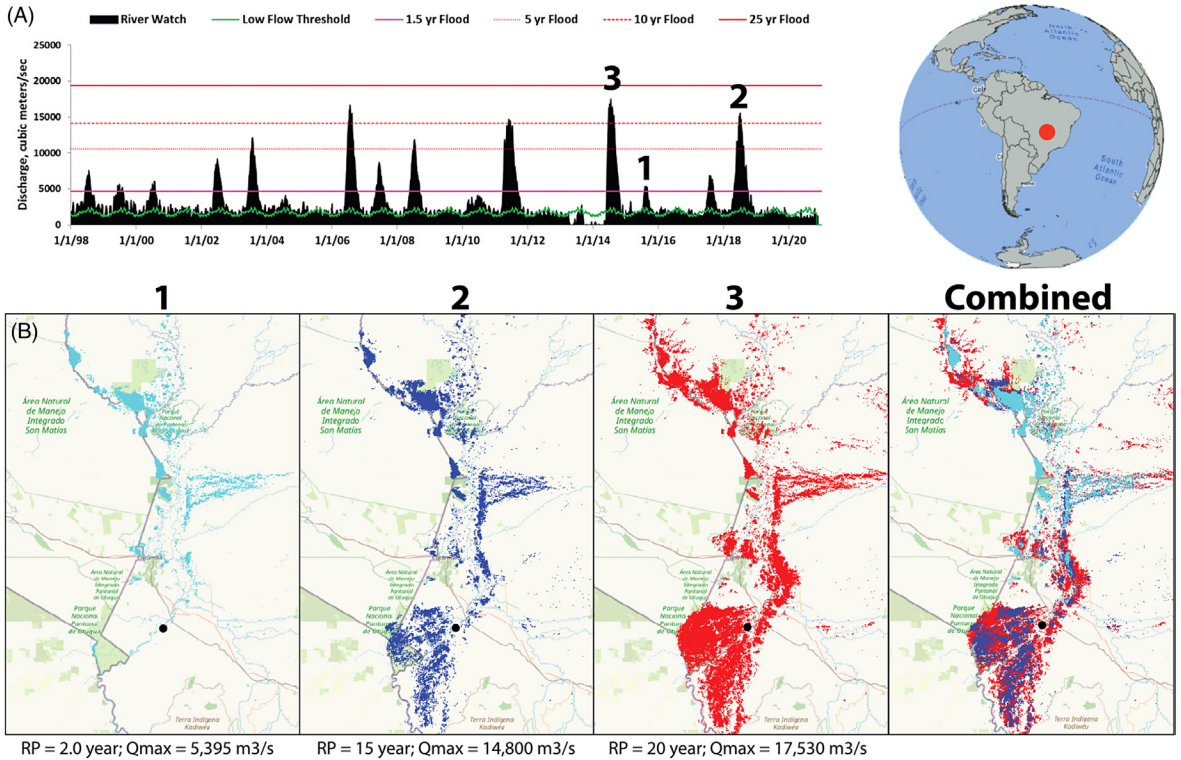

FIGURE 7.4 (A) Satellite-based daily water discharges for a period of ~22 years for the Rio Paraguay, Brazil (DFO site ID: 861; http://floodobservatory.colorado.edu/SiteDisplays/861.htm). (B) The flood extent based on three events were analyzed using MODIS imagery. Combining the flood extent with discharge peak events makes it possible to investigating the flood extent for a given discharge return period. During the month of August 2015 (event 1), discharges were just exceeding bank full (discharge = 5,395 m^3/s and has a return period of ~1 year) and the inundated area is illustrated in *light blue*. The June–July 2018 event had a return period of 10 years (4A; discharge = 14,800 m^3/s) and Fig. 7.2B shows the associated flood extent in *dark blue*. The 20-year flood (event nr. 3; 2A; discharge = 17,530 m^3/s) had a significant larger flood extent (2B, area in *red*).

Solutions, Inc. (RSS). Mobile apps increase data accessibility, especially when the users' need is outdoor, on location. First-response relief agencies such as the World Food Programme (WFP) or the Red Cross are often dispatched in the field during or immediately after a flood disaster. Having accurate, up to date flood information is essential during the decision-making process: which areas need to be evacuated first, deploy what level of resources, how to get these resources to the people in need, and where best to establish one or more emergency shelters? Where there is cell phone coverage, the DFO Floods mobile app lets a responder view current flood conditions and provides access to historical flood data. Additionally, the app has a "save layers" mode where current information can be stored on the phone such that it can be viewed in areas without Internet or cell coverage.

The DFO is developing hydrological related flood data either due to project support from external funding agencies or in response to a request that is directly received or is forwarded through the Global Flood Partnership (GFP; https://gfp.jrc.ec.europa.eu) Support Service. The GFP is an international group of volunteers of academics, research institutes, practitioners, public, and private organizations active in the field of flood risk and emergency management (Alfieri et al., 2018). The aim of GFP is to help reduce the impacts of flood disasters by fostering a community between scientists, who develop and operate flood management tools and data, and practitioners. As co-founder of GFP, DFO is actively responding to these data requests, and, to maximize access, hosts data from other providers on the DFO flood event web pages.

3 Future perspectives

The DFO—Flood Observatory is a research-driven entity, almost solely funded through a variety of grants and contracts. As part of a research institute at the University of Colorado, its goal is to continue to develop innovative methods to better understand flooding as a part of the terrestrial hydrological cycle and to make these insights available to the general public through research publications, even while gathering each day new information. Most of the work of DFO builds upon Earth Observation (EO) remote sensing data. Satellites have a limited life span and new satellites replace old ones with a possibly different set of sensors, which require the development of new algorithms to detect, measure, and map surface water. It is thus difficult to predict when and what new challenges will be investigated and made available in the future. However, some general perspectives are provided further.

Hazard products. In an ideal world, flooding (which does have many beneficial aspects for floodplain ecosystems and wetlands) would occur without significant damage to human societies and economies. In reality, increasing flood-induced fatalities and financial losses are occurring over time. To slow or even reverse these trends strategies are being developed for natural disaster prevention, preparedness, and mitigation. Over the last few decades, several have

been suggested and implemented with varying success: the Yokohama Strategy and Plan of Action for a Safer World (United Nations, 1994), the Hyogo Framework for Action (HFA) 2005–15 (United Nations, 2005), and more recently, the Sendai Framework for Disaster Risk Reduction (SFDRR) 2015–30 (United Nations, 2015). The SFDRR was adopted at the Third United Nations World Conference on Disaster Risk Reduction and built upon previous strategies. The aim of SFDRR is to "*substantially reduce disaster risk and losses in lives, livelihoods and health and in the economic, physical, social, cultural and environmental assets of persons, businesses, communities and countries*" (United Nations, 2015). It is composed of four priorities for action, one of which is directly related to the efforts of DFO: understanding disaster risk. With better knowledge of risk for a potential disaster in a certain area, a more appropriate level of preparedness or effective response can be performed. In relation to flooding, in order to better understand disaster risk, both local and global knowledge is needed on where and how frequently floods of a certain magnitude are likely to occur. Numerical model simulations have attempted to address this. However, there is skepticism about the accuracy of global flood models, partly fed by the discrepency of different models in the same events (Hoch and Trigg, 2019). A different approach would be to use long-time series of flood extents, for example, derived from satellite imagery, to identify previous flood areas. Although this does not provide information regarding the extent of flooding of a certain magnitude of a flood event, it would provide an indication of where it has been flooded in the past, and how frequently. Satellite data, although with different resolutions and revisit frequencies, is available from as early as the 1980s, and can be used to determine areas that are flooded often, versus only once in several decades. An even more useful, informative approach is described earlier, where gauging station data, either from ground-based stations or from satellite-based stations, are used in conjunction with flood extent maps to develop flood hazard maps. Currently, DFO has produced these flood hazard maps for certain regions of interest, but much further work by various organizations could very usefully address this Sendai objective.

Flood data warehouse. Whether it comes to first responders, flood risk assessments, planners or scientists, the availability of accurate, reliable flood data is of crucial importance. The DFO—Flood Observatory produces, like many other entities, hydrological data (see Section 2) that is freely available for noncommercial users. Over the last decade, more entities have started to produce similar geospatical flood data products, to the extent that there is now an increasing abundance of such from different sources. As such, end-users are now challenged by which data source to use. In the case of flood monitoring and response, this "firehose" of information can make it especially difficult for first responders within limited time: to investigate what data are available and determine which source(s) to use. This is a challenge during a single flood event, and it increaes as multiple simultaneous events or successive large events are responded to. Although each of those datasets offers unique capability, there

is to date no global decision support system for flood disasters that ingests all available data from existing systems and provides real-time critical information that can guide operational reactions on the ground. Gomes et al. (2015), Schumann and Domeneghetti (2016), and Schumann et al. (2018) argue that a step in the right direction would be to build a "one-stop-shop" (i.e., data portal), either primarily dedicated to remote sensing products of flood events or, more general to all flood related products (so from precipitation forecasts and inundation simulations to historical flood information). This one-stop-shop would not only organize and structure data availability better, thereby clarifying existing confusion over data and products; it would also add further value to the various products and services. At the same time, the end-user community would have the opportunity to provide feedback on data and products, which should be used to improve the different types of information disseminated. This one-stop-shop might be developed in collaboration with, for example, the Global Flood Partnership (GFP): where already flood-related data is loosely shared through group email. In any case, the new technologies do offer global society the opportunity to address in creative, effective, and useful ways its increasing vulnerability to this natural hazard.

References

Adhikari, P., Hong, Y., Douglas, K.R., Kirschbaum, D.B., Gourley, J., Adler, R., Brakenridge, G.R., 2010. A digitized global flood inventory (1998-2008): compilation and preliminary results. Nat. Hazards 55, 405. doi: 10.1007/s11069-010-9537-2.

Alfieri, L., Cohen, S., Galantowicz, J., Schuman, G.J-P., Trigg, M.A., Zsoter, E., Prudhomme, C., Kruczkiewicz, A., Coughlan de Perez, E., Flaming, Z., Rudari, R., Wu, H., Adler, R.F., Brakenridge, R.G., Kettner, A.J., Weerts, A., Matgen, P., Salamon, P., 2018. A global network for operational flood risk reduction. Environ. Sci. Policy 84, 149–158. doi: 10.1016/j.envsci.2018.03.014.

Alsdorf, D., Lettenmaier, D., Vörösmarty, C.J., The NASA Surface Water Working Group, 2003. The need for global, satellite-based observations of terrestrial surface waters. Eos Trans. AGU 84 (29), 269–276. doi: 10.1029/2003EO290001.

Bongaarts, J., 2009. Human population growth and the demographic transition. Philos. Trans. R. Soc. B 364, 2985–2990. doi: 10.1098/rstb.2009.0137.

Brakenridge, G.R., 2018. Flood risk mapping from orbital remote sensing. In: Schumann, G.J.-P., Bates, P.D., Heiko, A., Aronica, G.T. (Eds.), Global Flood Hazard: Applications in Modeling, Mapping, and Forecasting. American Geophysical Union and John Wiley & Sons, Inc, Hoboken, NJ, pp. 43–54. doi: 10.1002/9781119217886.ch3.

Brakenridge, G.R., Anderson, E., 2006. Modis-based flood detection, mapping and measurement: the potential for operational hydrological applications. Marsalek, J., Stancalie, G., Balint, G. (Eds.), Transboundary Floods: Reducing Risks Through Flood Management. Nato Science Series: IV: Earth and Environmental Sciences, vol. 72, Springer, Dordrechtdoi: 10.1007/1-4020-4902-1_1.

Brakenridge, G.R., Cohen, S., Kettner, A.J., De Groeve, T., Nghiem, S.V., Syvitski, J.P.M., Fekete, B.M., 2012. Calibration of satellite measurements of river discharge using a global hydrology model. J. Hydrol. 475, 123–136. doi: 10.1016/j.jhydrol.2012.09.035.

Brakenridge, G.R., Nghiem, S.V., Anderson, E., Mic, R., 2007. Orbital microwave measurement of river discharge and ice status. Water Resour. Res. 43, W04405. doi: 10.1029/2006WR005238.

Brakenridge, G.R., Syvitski, J.P.M., Niebuhr, E., Overeem, I., Higgins, S.A., Kettner, A.J., Prades, L., 2017. Design with Nature: Causation and avoidance of catastrophic floods in Myanmar. Earth-Science Reviews 165, 81–109. doi: 10.1016/j.earscirev.2016.12.009.

De Groeve, T., 2010. Flood monitoring and mapping using passive microwave remote sensing in Namibia. Geomat. Nat. Hazard Risk 1, 19–35. doi: 10.1080/19475701003648085.

Desai, B., Maskrey, A., Peduzzi, P., De Bono, A., Christian, H., United Nations Office for Disaster Risk Reduction (UNISDR), 2015. Making Development Sustainable: The Future of Disaster Risk Management, Global Assessment Report on Disaster Risk Reduction. United Nations Office for Disaster Risk Reduction (UNISDR), Genève, Suisse.

EM-DAT (Emergency Events Database), 2020. Université catholique de Louvain (UCL)—Centre for Research on the Epidemiology of Disasters (CRED). Available from: https://www.emdat.be/, (accessed 17.11. 2020.).

Follum, M.L., Vera, R., Tavakoly, A.A., Gutenson, J.L., 2020. Improved accuracy and efficiency of flood inundation mapping of low-, medium-, and high-flow events using the AutoRoute model. Nat. Hazards Earth Syst. Sci. 20 (2), 625–641.

Frasson, R.P. de M., Schumann, G.J.-R., Kettner, A.J., Brakenridge, G.R., Krajewski, W.F., 2019. Will the Surface Water and Ocean Topography (SWOT) mission observe floods? Geophys. Res. Lett. 46, 10435–10445. doi: 10.1029/2019GL084686.

Gomes, J.L., Jesus, G., Rogeiro, J., Oliveira, A., Costa, R., Fortunato, A.B., 2015. Molines—towards a responsive Web platform for flood forecasting and risk mitigation. Proc. Federated Conf. Comp. Sci. Inform. Syst. 5, 1171–1176. doi: 10.15439/2015F265.

GRDC, 2008. Report of the Eighth GRDC Steering Committee Meeting, 19 – 21 September 2007, Koblenz, Germany, https://www.bafg.de/GRDC/EN/02_srvcs/24_rprtsrs/report_10.html.

Guha-Sapir, D., Rodriguez-Llanes, J.M., Jakubicka, T., 2011. Using disaster footprints, population databases and GIS to overcome persistent problems for human impact assessment in flood events. Nat. Hazards. 58, 845. doi:10.1007/s11069-011-9775-y.

Hagemeier-Klose, M., Wagner, K., 2009. Evaluation of flood hazard maps in print and web mapping services as information tools in flood risk communication. Nat. Hazards Earth Syst. Sci. 9, 563–574. doi: 10.5194/nhess-9-563-2009.

Hoch, J.M., Trigg, M.A., 2019. Advancing global flood hazard simulations by improving comparability, benchmarking, and integration of global flood models. Environ. Res. Lett. 14, 034001. doi: 10.1088/1748-9326/aaf3d3.

International Federation of Red Cross and Red Crescent Societies (IFRC), 2020. World Disasters Report 2020 — Come heat or high water, Tackling the humanitarian impacts of the climate crisis together. ISBN 978-2-9701289-5-3.

Johnson, K.A., Wing, O.E.J., Bates, P.D., Fargione, J., Kroeger, T., Larson, W.D., Sampson, C.C., Smith, A.M., 2020. A benefit–cost analysis of floodplain land acquisition for US flood damage reduction. Nat. Sustain. 3, 56–62. doi: 10.1038/s41893-019-0437-5.

Jonkman, S.N., 2005. Global perspectives on loss of human life caused by floods. Nat. Hazards 34, 151–175. doi: 10.1007/s11069-004-8891-3.

Jongman, B., Ward, P., Aerts, J., 2012. Global exposure to river and coastal flooding: Long term trends and changes. Glob. Environ. Change 22, 823–835. doi: 10.1016/j.gloenvcha.2012.07.004.

Kettner, A.J., Cohen, S., Overeem, I., Fekete, B.M., Brakenridge, G.R., Syvitski, J.P.M., 2018. Estimating change in flooding for the 21st century under a conservative RCP forcing. In: Schumann, G.J.-P., Bates, P.D., Apel, H., Aronica, G.T. (Eds.), Global Flood Hazard: Applications in

Modeling, Mapping, and Forecasting. In: Geophysical Monograph Series, Chapter 9, Wiley. doi:10.1002/9781119217886.ch9.

Klemas, V., 2015. Remote sensing of floods and flood-prone areas: An overview. J. Coast. Res. 31 (4), 1005–1013. doi: 10.2112/JCOASTRES-D-14-00160.1.

Kron, W., 2005. Flood Risk = Hazard • Values • Vulnerability. Water Int. 30 (1), 58–68. doi: 10.1080/02508060508691837.

Kundzewicz, Z.W., Pinskwar, I., Brakenridge, G.R., 2013. Large floods in Europe, 1985-2009. Hydrol. Sci. J. 58 (1), 1–7. doi: 10.1080/02626667.2012.745082.

McGinnis, D.F., Rango, A., 1975. Earth resources satellite systems for flood monitoring. Geophys. Res. Lett. 2, 132–135. doi: 10.1029/GL002i004p00132.

Najibi, N., Devineni, N., 2018. Recent trends in the frequency and duration of global floods. Earth Syst. Dynam. 9, 757–783. doi: 10.5194/esd-9-757-2018.

Nash, J.E., Sutcliffe, J.V., 1970. River flow forecasting through conceptual models part I—A discussion of principles. J. Hydrol. 10, 282–290. doi: 10.1016/0022-1694(70)90255-6.

Potin, P., Rosich, B., Miranda, N., and Grimont, P., 2018. Sentinel-1A/-1B Mission Status. In: Proceedings of the EUSAR 2018: Twelfth European Conference on Synthetic Aperture Radar, Aachen, Germany, pp. 1–5.

Schumann, G.J.-P., Domeneghetti, A., 2016. Exploiting the proliferation of current and future satellite observations of rivers. Hydrol. Process. 30 (16), 2891–2896. doi: 10.1002/hyp.10825.

Schumann, G.J.-P., Brakenridge, G.R., Kettner, A.J., Kashif, R., Niebuhr, E., 2018. Assisting flood disaster response with Earth Observation data and products: A critical assessment. Remote Sens. 10, 1230. doi: 10.3390/rs10081230.

Shen, X., Anagnostou, E.N., Allen, G.H., Brakenridge, G.R., Kettner, A.J., 2019. Near-real-time non-obstructed flood inundation mapping using synthetic aperture radar. Remote Sens. Environ. 221, 302–315. doi: 10.1016/j.rse.2018.11.008.

Shiklomanov, A., Lammers, R., Vörösmarty, C.J., 2002. Widespread decline in hydrological monitoring threatens pan-Arctic research. Eos Trans. AGU 83 (2), 13–17. doi: 10.1029/2002EO000007.

Smith, L., 1997. Satellite remote sensing of river inundation area, stage, and discharge: a review. Hydrol. Process. 11, 1427–1439, doi:10.1002/(SICI)1099-1085(199708)11:10 < 1427::AID-HYP473 > 3.0.CO;2-S.

Smith, L.C., Isacks, B.L., Bloom, A.L., Murray, A.B., 1996. Estimation of discharge from three braided rivers using synthetic aperture radar satellite imagery. Water Resour. Res. 32, 2021–2034. doi: 10.1029/96WR00752.

Smith, L.C., Isacks, B.L., Forster, R.R., Bloom, A.L., Preuss, I., 1995. Estimation of discharge from braided glacial rivers using ERS 1 synthetic aperture radar: First results. Water Resour. Res. 31, 1325–1329. doi: 10.1029/95WR00145.

Spachinger, K., Dorner, W., Metzka, R., Serrhini, K., Fuchs, S., 2008. Flood Risk and Flood hazard maps—Visualisation of hydrological risks. IOP Conf. Ser. Earth Environ. Sci. 4, 012043. doi: 10.1088/1755-1307/4/1/012043.

Torres, R., Snoeij, P., Geudtner, D., Bibby, D., Davidson, M., Attema, E., Potin, P., Rommen, B., Floury, N., Brown, M., Navas Travera, I., Deghaye, P., Duesmann, B., Rosich, B., Miranda, N., Bruno, C., L'Abbate, M., Croci, R., Pietropaolo, A., Huchlerc, M., Rostan, F., 2012. GMES Sentinel-1 mission. Remote Sens. Environ. 120, 9–24. doi: 10.1016/j.rse.2011.05.028.

United Nations, 1962. Demographic Yearbook. United Nations, New York, NY.

United Nations, 1973. The Determinants and Consequences of Population Trends. Department of Economic and Social Affairs, Population Studies 50, United Nations, New York, NY.

United Nations, 2007. World Population Prospects: The 2006 Revision. United Nations Population Division, New York, NY.

United Nations, 2015. Sendai Framework for Disaster Risk Reduction 2015-2030, United Nations Office for Disaster Risk Reduction.

United Nations—ISDR, 1994. Yokohama Strategy and Plan of Action for a Safer World: Guidelines for Natural Disaster Prevention, Preparedness and Mitigation. UN/ISDR, Geneva.

United Nations—ISDR, 2005. Hyogo Framework for Action 2005-2015: Building the Resilience of Nations and Communities to Disasters. UN/ISDR, Geneva.

Van Dijk, A.I.J.M., Brakenridge, G.R., Kettner, A.J., Beck, H.E., De Groeve, T., Schellekens, J., 2016. River gauging at global scale using optical and passive microwave remote sensing. Water Res. Res. 52 (8), 6404–6418. doi: 10.1002/2015WR018545.

Vereecken, H., Huisman, J.A., Hendricks Franssen, H.J., Brüggemann, N., Bogena, H.R., Kollet, S., Javaux, M., van der Kruk, J., Vanderborght, J., 2015. Soil hydrology: Recent methodological advances, challenges, and perspectives. Water Res. Res. 51 (4), 2616–2633. doi: 10.1002/2014WR016852.

Wagner, W., Sabel, D., Doubkova, M., Bartsch, A., Pathe, C., 2009. The potential of Sentinel-1 for monitoring soil moisture with a high spatial resolution at global scale. In: Proceedings on Earth Observation and Water Cycle Science, Frascati, Italy. ESA Special Publications SP-674.

Wisser, D., Frolking, S., Douglas, E.M., Fekete, B.M., Vörösmarty, C.J., Schumann, A.H., 2008. Global irrigation water demand: variability and uncertainties arising from agricultural and climate data sets. Geophys. Res. Lett. 35 (24), L24408. doi: 10.1029/2008GL035296.

Wu, H., Kimball, J.S., Li, H., Huang, M., Leung, L.R., Adler, R.F., 2012. A new global river network database for macroscale hydrologic modeling. Water Resour. Res. 48, W09701. doi: 10.1029/2012WR012313.

Chapter 8

How Earth Observation Informs the Activities of the Re/Insurance Industry on Managing Flood Risk

Nalan Senol Cabi[a], Tina Thomson[a], Jonathon Gascoigne[b] and Hani Ali[a]
[a]Willis Towers Watson, London, United Kingdom; [b]Centre for Disaster Protection, London, United Kingdom

1 Introduction

Approximately 500 million people are affected by flood events worldwide annually, far more than any other category of natural catastrophe (Jha et al., 2012).

Floods are an expensive natural hazard yet, inevitably, limited historical experience alone is not enough to help quantify the risk from such catastrophes. Over the course of the last 38 years, almost 6000 events were recorded by Munich Re's NatCatService catastrophic flood/flash flood events database (Figs. 8.1 and 8.2).

It is clear from the figures that floods impact the majority of the world's population. Yet, within the re/insurance industry, flood has largely been regarded as a "secondary peril," partly due to the more visually striking spatial and temporal concentrations of damage from earthquakes and windstorms, and partly from difficulties involved in detailed flood risk modeling. Recent catastrophic events such as hurricanes Harvey, Irma, and Maria (2017), together with Super Typhoon Hagibis (2019), are forcing the industry to adjust its view, as it is also on wildfire.

Quantification of flood risk is still challenging. There are a limited number of probabilistic flood catastrophe models available; one of the widely used conventional tools to quantify flood risk in the re/insurance industry. To overcome this challenge, Earth Observation (EO) or remotely sensed data has become an essential part of tackling risk from flood, including facilitating the development of models to quantify the risk for re/insurance purposes, to enhance the exposure information available in an insurance portfolio of underwritten flood risks, and to respond to catastrophe flood events from forecasting to providing assessment during and in the immediate aftermath of an event.

Earth Observation for Flood Applications. http://dx.doi.org/10.1016/B978-0-12-819412-6.00008-0

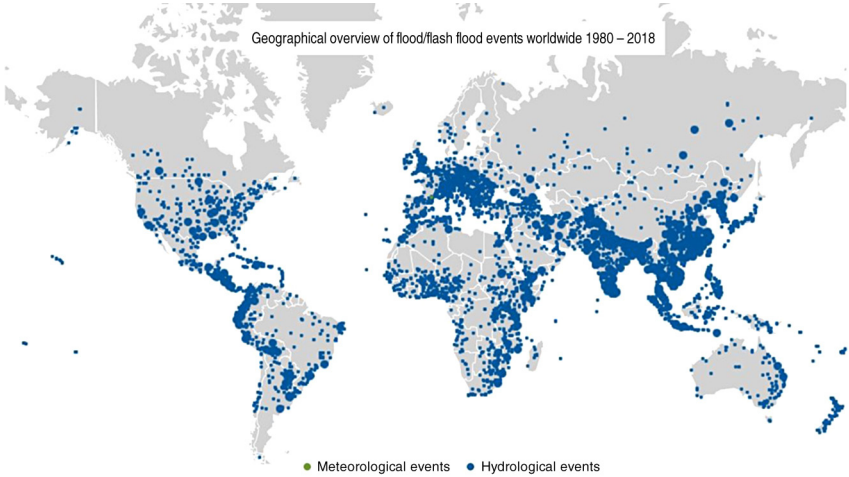

FIGURE 8.1 Geographical overview of worldwide flood/flash flood events between 1980–2018. *(Munich Re, NatCatSERVICE (2020))*

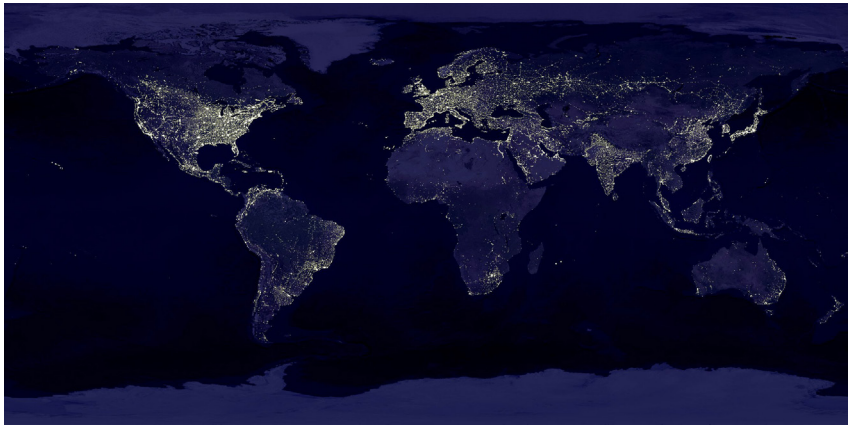

FIGURE 8.2 Earth night lights. *(Pixabay)*

Whilst satellites are becoming increasingly smaller, cheaper to build and easier to deploy, with better resolution and revisit times, the accessibility and adoption of the latest satellite technology in the re/insurance market has been slow, due to lack of expertise, and inhibiting costs and license terms. However, long records since the 1970s, albeit at varying levels of resolution, have proven useful in the integration of modeling flood risk with the likes of Landsat and MODIS. These aspects are illustrated, as the chapter discusses how catastrophe modeling has evolved, for flood specifically, in the re/insurance sector, and how EO combined with technological advancements has enabled the sophisticated modeling solutions we see today.

The model development process is explained in more detail, with examples of how particular EO datasets and derivative products are essential in the production of hazard maps and stochastic catalogs of simulated extreme events, as well as for model validation. Realistic disaster scenarios (RDS), which can either be based on an extreme historical event or plausible catastrophic flood events that could occur in the area of interest, are discussed together with their application in disaster risk management, such as event response.

The chapter looks at how the industry has evolved around technical modeling advances, in the context of insurance sector issues such as adverse selection and ensuring insurance affordability in the public eye. As such, risk management schemes and availability of open data, including EO, and associated limitations are discussed. Finally, the chapter moves onto the protection gap, highlighting the benefits EO can bring in developing regions, combined with alternative risk transfer mechanisms that complement standard reinsurance placement.

2 History of catastrophe modeling

Catastrophe modeling has played a significant role in the re/insurance market over the last 30 years, when insurance companies faced the unquantified threat of insolvency from the impact of property losses from natural catastrophic events in the late 1980s and early 1990s, notably including Hurricane Andrew in 1992. It was clear that the infrequent nature of these types of perils, which are challenging to capture through actuarial techniques alone, due to lack of sufficient historical claims data, meant that insurers tended to underestimate the cost of losses. Andrew caused record losses, costing the industry $15.5 billion at that time (O'Conner, 2017) and sending eight insurers out of business (McChristian, 2012).

Subject matter experts from disciplines such as hydrology, atmospheric physics, seismology, geographical information science (GIS), and engineering entered the industry to develop numerical estimates of frequency and severity of loss from natural hazards. Earthquake and windstorm models dominated early methodological developments, with flood models following later for a variety of reasons. Because of the challenging nature of flood risk assessment, requirements for modeling include:

- high level of geographical resolution related to underlying digital elevation model (DEM);
- sophisticated hydro-dynamic and hydraulic modeling of inundation extents (moving away from a simplistic bath-tub approach);
- computational capabilities to cope with nationwide exposures;
- capturing varying sources of flood risk from fluvial, pluvial, ground water, dam break, and storm surge; and finally
- allowing the incorporation of flood mitigation measures, notably flood defenses.

EO has been playing an important role in improving these elements, which include better DEM resolution, more detailed built environment representations, and greater clarity on flood defense locations and height.

Natural catastrophe (nat cat) models became the tool of choice of the industry in the early 1990s, since they provided the means to analyze and measure risk more accurately (ABI, 2011; LMA, 2013). Emerging spatial data handling technologies of the time based upon GIS, remote sensing, and photogrammetry allowed the fundamental aspect of diversification in insurance to be incorporated in the analyses of different perils. For example, accumulations of insured exposure at risk could be rapidly identified and proximally related to potential sources of natural hazard, be it a flood plain or fault line. Diversification means that an insurance portfolio will consist of different risk exposed elements, geographically at international scale, by line of business (such as residential, commercial, industrial property, or life), and peril, which ensures that losses balance out over time and space. The likelihood of a simultaneous California earthquake and Tokyo earthquake, or European flood, is highly unlikely, and therefore all insured "eggs are not in one basket."

Over time natural catastrophe models have become ever more sophisticated, by incorporating sets of artificial events simulated over tens of thousands of years to represent the full spectrum of possible events beyond those observed in history. Aided by increased computational power and highly detailed DEMs derived from EO data, it is now possible to model flood at national or even international scale, so capturing correlations across catchments (Dodov and Weiner, 2013).

Whilst stochastic flood model development methodologies can range from precipitation-based run-off models to extrapolating the hydrology of gauge station data, the interplay of geographical information with DEMs is fundamental in this process and drives the accuracy of hazard assessment.

Combined with the simulated event set and an intensity-damage ratio relationship, which defines the susceptibility of different property types to the inundation depth or any hazard intensity, a nat cat model outputs portfolio to location-level losses in the form of key metrics that express the probability of a loss exceeding a given return period. For example, a 1-in-100-year event loss is equal to the loss exceeding with a 1% chance in any given year. These metrics are used in understanding and quantifying the risk in terms of losses and the amount of premiums required to statistically break even on an average year, that is, the average annual loss.

As model vendors focus on developing better and high-resolution models, accompanied by higher resolution data and improved computational power, the current advancements reflect ever more sophisticated and accurate location-level flood loss estimates. They also incorporate the interplay of correlated perils such as tropical cyclone induced rainfall and flooding, the impact of changing climate signals, the cyclicity of the weather systems and, with that, the potential impact of climate change.

Nat cat models aid integration with existing underwriting and pricing workflows, hence the "technical price" view, which these models provide, has become an important metric in the annual insurance cycle and decision-making process. The accurate interpretation of such results therefore relies on understanding how these models operate, their methodologies and assumptions, and strengths and weaknesses. Guided by an increasing desire to develop a view of risk that reflects an insurance carrier's book of business, initiatives like the Oasis Loss Modelling Framework (Geneva Association, 2018b), which promote open-source platforms and plug-and-play models, are gaining momentum.

The intermediary and advisory role of reinsurance brokers has further promoted the transparency, insight and own view of risk in the vendor-re/insurance relationship. The ability to evaluate and adjust models using the latest scientific research, as facilitated through networks that are extensions of re/insurance markets, such as the Willis Research Network (WRN) or Lighthill Research Network (LRN), continues to push the boundaries of catastrophe modeling and the required EO data.

3 Methodological development of catastrophic flood risk assessment

Catastrophe models quantify risk by combining hazard information and vulnerability functions, which describe the relationship between hazard intensity and damageability of different property types. This is captured by exposures that define the risk locations and insured conditions of policies, for which a financial module then calculates the associated losses from the simulated events and hazard intensities (Fig. 8.3). Such probabilistic models allow the estimation of the distribution of the flood cost. The result can be used by the (re)insurance sector for underwriting and pricing, and also for capital reserving based on the estimation of the 200-year cost of flood as regulated by the European Solvency II directive (Dreksler et al., 2013). Due to such regulatory requirements, development of stochastic flood models becomes a priority in some European countries. Vendor companies started to develop models in data-rich territories such as Western Europe. EO data plays a significant role in overcoming limitations

FIGURE 8.3 Catastrophe model components. *(Willis Re)*

in the development of catastrophe models, especially in the hazard and the exposure components (Fig. 8.3), but also in validating the results.

Fundamentally, the hazard component includes event generation and intensity calculation, elements which try to simulate the physical characteristics of the water (hydrological) cycle (Fig. 8.4). There are different ways to simulate each stage of a water cycle. The most common starting point is simulating the precipitation field over the area of interest and identifying independent, flood-causing storms, in other words "events." After many simulations, an "event set" is built. Typically, 10,000 years or 50,000 years of simulations are needed to build a stochastic catalog to produce realistic numbers of events per year. Using a rainfall-runoff model, these simulated events are routed through the terrain and the river network. Hydraulic modeling takes the calculated remaining surface runoff and river flows (accounting for infiltration and evapotranspiration) and determines the flood depths and inundation extent. This completes the hazard component.

Instead of simulating the complexities of the precipitation field, another starting point can be using ground measurements of rainfall directly or river flow from gauges. Whilst using gauge data reduce the model development efforts, it is limited by the availability and the quality of the station data.

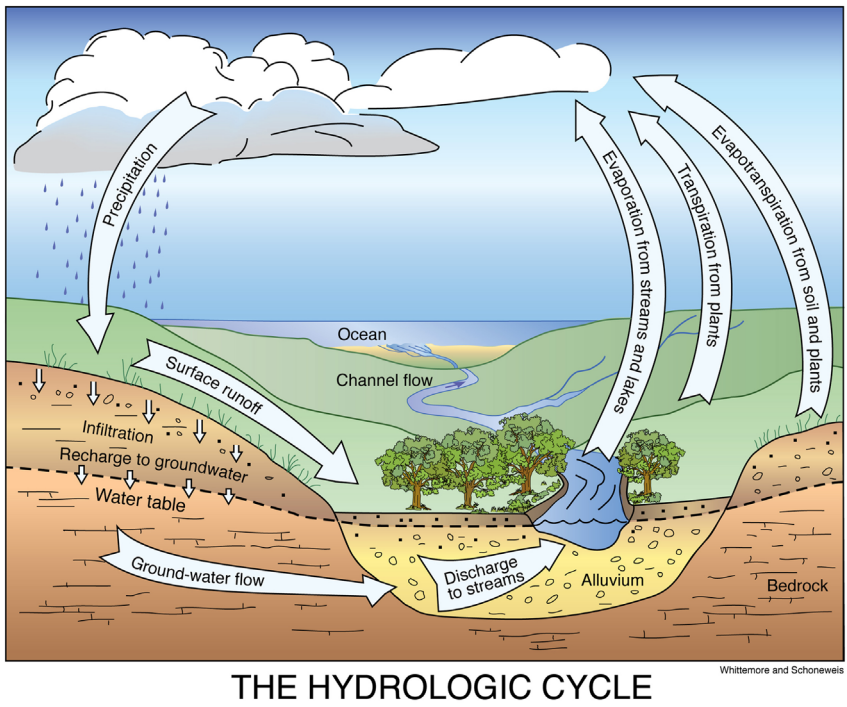

FIGURE 8.4 Water (hydrological) cycle. *(Kansas Geological Survey)*

Examples of EO data that play a crucial part in the model development process include:

- for precipitation modeling, EO data such as Realtime TRMM (Tropical Rainfall Measuring Mission) Multi-satellite Precipitation Analysis dataset;
- for rainfall-runoff modeling, soil data such as MODIS (Moderate Resolution Imaging Spectroradiometer); and
- for hydraulic modeling, terrain data such as SRTM (Shuttle Radar Topography Mission).

The exposure component provides characteristics of properties such as location, occupancy type, and total insured value. One of the key challenges here is the requirement of location level information. Most of the time, exposure data is provided in aggregate terms, that is, total value is assigned to an administrative boundary such as postcode rather than distributed to each property location. Hence, the users of these models rely on exposure disaggregation methods, for which EO data (e.g., CORINE land use land cover data, population density, nightlight imagery, etc.) can be used as a proxy (Smith et al., 2019).

In addition, EO data also play a significant role in the evaluation process of catastrophe flood models, to ensure models generate realistic loss estimates. Model performance might be evaluated by comparing simulated losses with experienced losses for a client portfolio using historical events as benchmark. Given the limited data points of experienced losses, one can only judge the performance of a model for frequent return periods.

Alternatively, one can evaluate each model component independently to ensure that the model captures the physical characteristics well. One must identify strengths and weaknesses of each component. This requires a good understanding of model methodology and input data limitations in each component. Most of the time, users do not have full access to hazard, vulnerability, and financial modules, hence model evaluation/sensitivity tests need to be created.

There are several tests one can do to evaluate the hazard component of flood models. One of the tests is the comparison of modeled event frequency distribution with observed events distribution in the area of interest.

Due to the lack of long historical time series for flood events, most of the probabilistic flood models rely heavily on the physically based model approach to capture the fundamental characteristics of the peril. For instance, the occurrence date of simulated events is expected to follow observed seasonality of the modeled region. Getting the seasonality right will create realistic antecedent soil conditions for flood events, such as ground saturation and infiltration characteristics; hence a realistic flood extent is simulated.

Both spatial and temporal distribution of stochastic events is expected to match with observations. For example, a good model is expected to capture the spatial and temporal distribution of the monsoon seasons in India (Fig. 8.5). One can expect to see more events in the catalog from June to September time frame, and/or more events impacting the south-east coast of the country during the winter monsoon months.

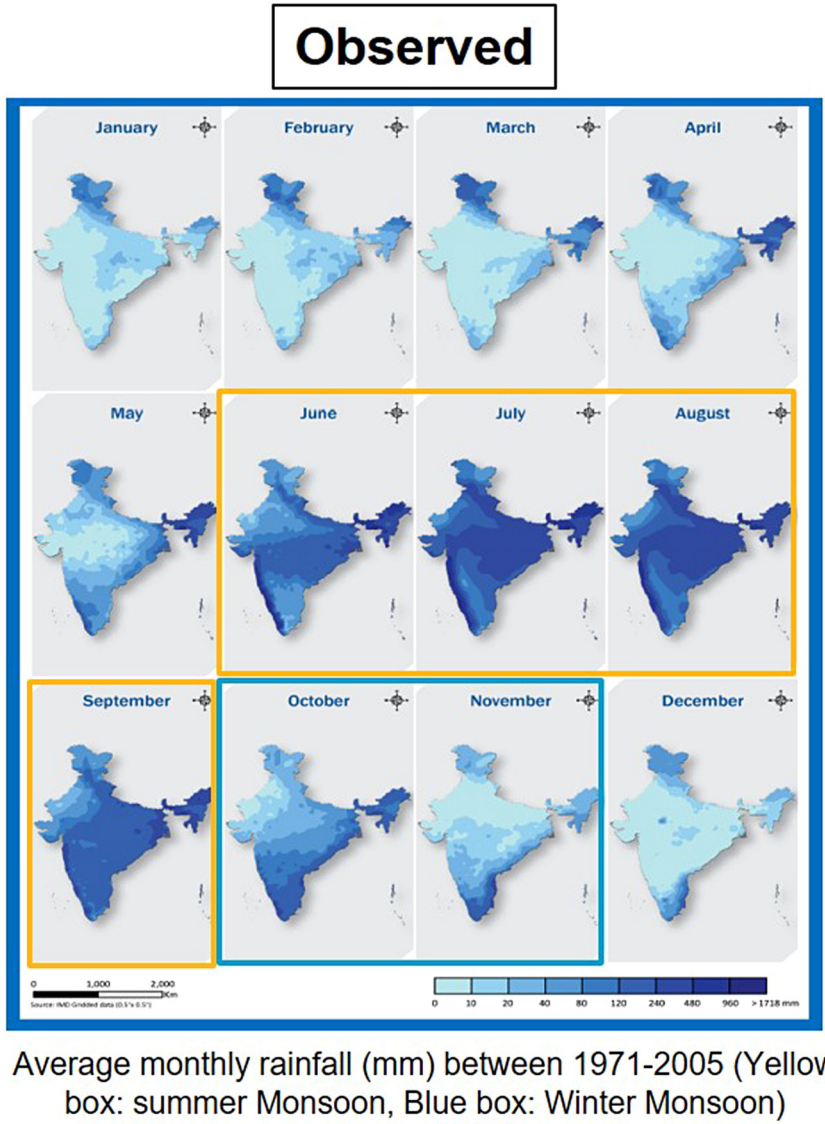

FIGURE 8.5 The image shows both spatial and temporal distributions of average monthly rainfall data. *(Central Water Commission of India)*

Historical event analysis can be a good way to justify the selection of probabilistic vendor models to quantify flood risk for a specific insurance company portfolio. If modeled losses mirror the losses experienced by the insurance company for the same historical event, then the flood model can be used to identify capital requirements.

Some vendor models have historical catalogs, that is, compilations of significant events simulated using the model's framework. The historical catalog can be used to run the simulation of an event and compare it with the experienced loss to evaluate the performance of the model. However, it is not common to have a historical catalog in flood models. Alternatively, a "similar stochastic event" can be selected as a proxy to a historical event to achieve this type of comparison. Event similarities can be defined based on simulated event return period, area impacted, etc. One can compare the similar stochastic catalog event loss as a proxy to the simulated historical event loss and compare it with the experienced loss to evaluate the performance of the model.

If there is no historical catalog and if a similar stochastic event cannot be selected then EO data can be used. For example, inundation extent from satellite imagery and event flow and depth information from river gauge records can be compared with the model's hazard outputs. This approach does not have any loss estimation and it is not for the entire event footprint, but it still provides a validation to the model's hazard component.

For example, Central Europe experienced major flooding in May and June 2010 affecting Poland, Germany, Hungary, Austria, Czech Republic, Ukraine, Slovakia, and Serbia. In Poland, on the Vistula River, levee failures caused significant flooding (Fig. 8.6). Several cities, such as Sandomierz, were inundated for couple of weeks. The observed flood extent from satellite imagery shows a relatively good agreement with the modeled hazard footprint. Overall insurance market losses for Poland due to this event were more than $3 billion (Source: MunichRe).

In addition to the use cases in model development/evaluation processes discussed earlier, EO data provide valuable insight for designing realistic disaster scenarios (RDSs). The majority of probabilistic flood models are only available for data-rich territories, such as Europe, United States, and Japan. If one needs to build a view of risk on flood, RDSs can be used to stress test client portfolios.

A recent example was the extensive flooding caused by several days of heavy rain in France in late May and early June 2016. The Loing River burst its banks causing very significant damage in numerous towns such as Nemours, Longjumeau, and Montargis. Some areas reported the worst flooding seen since 1910. The flood resulted in 4 deaths, 24 people injured, and €1.3 billion worth of damage, and is considered the worst nat cat event since 1982.

While the event was unfolding, the Copernicus Emergency Service published impacted area maps using satellite data. This is a typical product Copernicus produces during significant flood events that require emergency response. In September 2016, the Copernicus Emergency Management Service Risk and Recovery produced a detailed study of the same event using imagery from the AIRBUS SPOT6 and SPOT7 satellites. This study contained maximum flood delineation, flood water depth estimation, and flood damage assessments along the Seine River located upstream to Paris and its tributary of the Loing river, from Fontainebleau to Montargis.

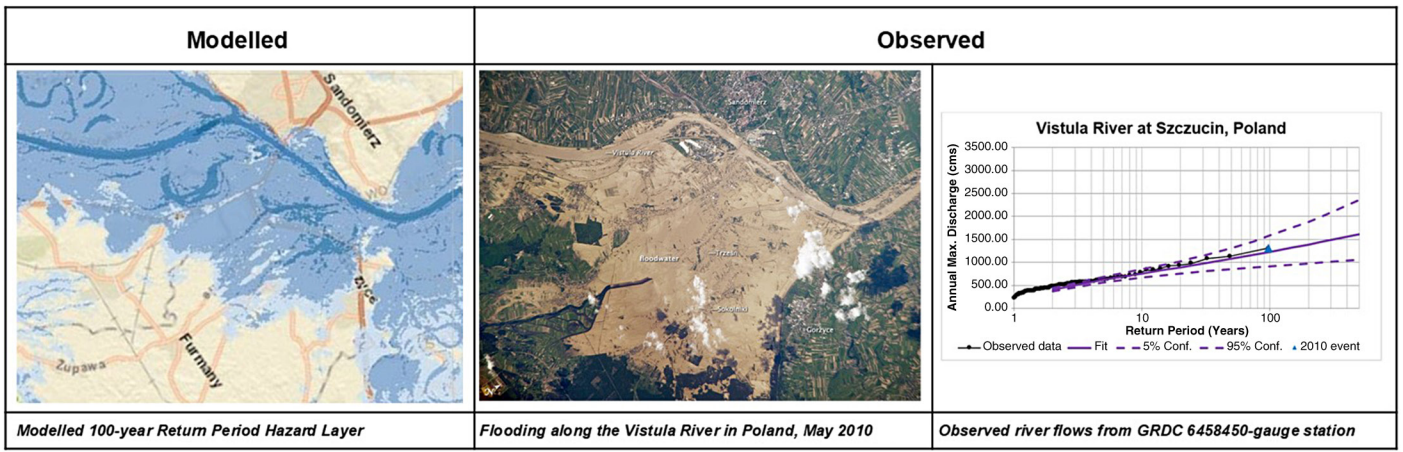

FIGURE 8.6 Observed vs, modeled flood extents from the Central Europe floods in May and June 2010, which affected the Vistula River in Poland. *(Willis Re, NASA, The Global Runoff Database (GRDC) (Source: Poland - Institute of Meteorology and Water Management - National Research Institute (IMGW-PIB) Provided by: Global Runoff Data Centre, GRDC, Koblenz, Germany: Federal Institute of Hydrology (BfG)))*

Maximum flood extent is a key input to calculate probable maximum loss (PML) due to an event. Since the intensity metric for flood is the floodwater depth, calculating accurate depths within the inundation extent will dictate the accuracy of the PML. There are different ways to estimate flood water depths from satellite imagery by combining the flood extents with DEMs. Cohen et al., 2017 developed a Floodwater Depth Estimation Tool (FwDET). As illustrated in Fig. 8.7, water depths can be estimated in the flooded area from Copernicus flood extent combined with the European Digital Elevation Model (EU-DEM 25 m).

The FwDET method allows for an automated spatially continuous floodwater depth estimation. It is based on identifying the flooded domain boundary cells on a DEM. The elevation values of the boundary cells are then assigned to cells within the flooded domain. Water depth is calculated by assigning a cell within the flooded domain to the elevation of its nearest boundary cell, which is then used to calculate the local water depth by subtracting this value from a cell's surface elevation (derived from a DEM).

The water depths calculated using the FwDET algorithm are compared to depths published by Copernicus. The results from the two methods are close despite the use of a relatively coarse resolution (30 m) DEM (Table 8.1).

When flood extent and depth information of a historical event is available, they can be used as an RDS to stress test an insurer's portfolio. Calculated hazard information of a historical event, together with observed claims information

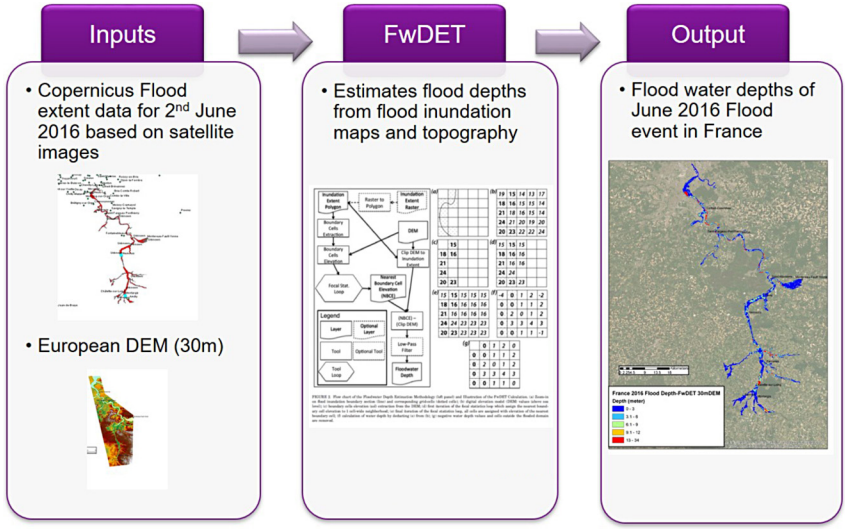

FIGURE 8.7 Methodology for generating riverine flood event hazard file using satellite images. *(Willis Re, Copernicus (with funding by the European Union), EUDEM/HYDRO -MEDDE / DE, Cohen et al., 2017)*

TABLE 8.1 The flood hazard raster generated using the 30 m DEM and FwDET tool closely matches the observations provided by the French hydrological service (http://www.hydro.eaufrance.fr) for 8 out of the 11 stations.

Station Number	Station Name	Observed Water Depth (m)	Estimated Water Depth (m) using EUDEM 30m data	Estimated Water Depth (m) by Copernicus
1	Saint-Mammes	6.8	3.44	6.68
2	Saint-Fargeau-Ponthierry	4	7.83	6.12
3	Melun	5.4	3.33	3.3
4	Corbeil-Essonnes	4.8	12.05	4.533
5	Chalette-sur-Loing	3.4	15.87	5.13
6	Montargis	3.4	0.43	1.403
7	Nemours	4.6	4.08	9.1
8	Episy	1.48	2.55	0.853
9	Episy	4.9	0.258	4.13
10	Ferrieres	1.9	2.75	3.94
11	Pannes	1.2	1.09	2.29

Willis Re, Copernicus (with funding by the European Union), EUDEM/HYDRO -MEDDE / DE, Cohen et al., 2017.

as a proxy for event loss, plays a significant role in catastrophe flood model calibration.

4 Event response

Another application of satellite images, and more generally EO technology, is to improve and update event response tools with recent data on the most impacted areas. For example, Willis Re uses satellite imagery to assess the most exposed policies after a big flood event and identify the riskiest areas with a high damage concentration. The Willis Re Event response module (eVENT Response) allows insurers to monitor claims development in near real-time during an event and to operate as quickly as possible. Re/insurers use EO data-based tools, such as Willis Re's eVENT Response, to monitor critical events and to rapidly estimate losses related to these events.

There are a variety of applications for event response, which include:

- Claims/adjusters to improve allocation of reserves, triage loss adjustment, and accelerate and validate claims payments;
- Exposure reporting to improve and coordinate business management information with more localized information, pro-active event monitoring, and more efficient allocation of resources and internal processing of data;
- Policy-holder support and preparedness to improve client experience through tailored support prior and during an event; and
- Mitigation by linking with risk engineering tools to educate clients and support them with pre-emptive plans and procedures, potentially mitigating the risk and claims costs.

For example, during hurricane Harvey affecting Texas in 2017, very high resolution (~ 0.5 m) satellite imagery was used by McKenzie Intelligent Services (MIS) to delineate the flooded area in Houston. This imagery highlighted limitations of the US nationwide Federal Emergency Management Agency's (FEMA) hazard maps, which didn't capture the flood extents associated from hurricane-induced rainfall and consequent flooding. Harvey highlighted significant modeling limitations, which did not account for a stalling hurricane over the low-lying Texan coastline and the warm waters of the Gulf of Mexico for 6 days, which intensified the hurricane and thus resulted in significant flash flooding within the major conurbation of Houston. Purportedly, the volume and weight of the flood waters permanently "sank" the city area by 0.05 m.

Event response typically evolves in accuracy over time, and in the example of MIS, a variety of methods were used to provide updates at:

- Landfall 0–24 hours: due to lack of coherent information, geospatial analysis and contextual reporting was provided;
- 6–48 hours: the Houston flood profiled at zip code level using social media and press video imagery feeds;
- 24–72 hours: National Oceanic and Atmospheric Administration (NOAA) and National Weather Service (NWS) river flow data from high water gauges were used for near real-time ground truthing, which enables the plotting and correlation of river flow data combined with the social media information streams;
- 72+ hours: low resolution (20 m) synthetic aperture radar (SAR) was used to map large scale areas of standing flood water, contrasted with pre-event SAR data to separate flooded areas into a single vector layer; and finally
- 7–10 days: very high resolution (less than 0.5 m) imagery swathes were imaged from low altitude to provide a complete view from all-source and non-traditional imagery information.

MIS was a success story and the first of its kind to operate collectively, on a shared access basis across multiple insurance syndicates of Lloyds of London. This is an essential step to enable improved access to real-time event information due to the expense otherwise being a limiting factor in the uptake of such

approaches by individual insurers. It's not only the cost and potential license issues in accessing high resolution and real-time satellite data, but also the expertise in processing the data into usable and value-add derivatives that can be readily consumed by the insurance industry. In addition, MIS has in part overcome limitations of individual sensors, such as coverage and repeat times, by combining multiple sources of information, including crowd sourcing and volunteered geographic information. On their own, these sources can be difficult to implement due to reliability of data, barriers in public perceptions, data availability, and homogeneity, which can vary greatly by country even across Europe. Nonetheless, the challenges in forecasting, irrespective of responding to flood events, are significant due to the granularity and temporal nature of this peril.

Whilst alternative for-profit solutions exist, like JBA's Flood Foresight or Weathernet, the aforementioned challenges remain an issue in the uptake of these solutions. Other open, public solutions are designed for governments and emergency responders, and can be limited in their commercial application, such as the European and Global Flood Awareness Systems (EFAS/GLOFAS). There is always an opportunity for better collaboration among public services and the insurance industry considering the greater public good and social responsibility in providing immediate aid and restoration after events, as well as promoting building resilience and other preventive measures to reduce the risk. Combined with improved access to open data, with initiatives such as open data cubes and CommonSensing, these challenges may diminish over time.

5 Relationship between private and public sector for flood risk

As exemplified in the role of event response, insurance as an institution and a product has a significant role to play in society, providing peace of mind and reducing the financial risks that individuals and businesses face. Economic growth is promoted by supporting investment decisions with the confidence of a safety net for potentially overwhelming losses as well as from the funds generated by premium collection that are invested in government securities and stock. Typically, the state becomes a default "insurer of last resort" when the limits of insurability are reached (Hoppe, 2012; Swiss Re, 2012).

A side effect of increasingly sophisticated flood model development has been an increasing opportunity for adverse risk selection in the insurance industry. This describes where insurers can potentially "cherry pick" or "red line" coverage and charge significantly higher premiums on high risk flood properties and/or provide coverage only for low flood risks, so undercutting notions of social solidarity.

Several government initiatives exist to support the public and insurance companies by further mitigating the risk from flood and other perils through government-linked compensation schemes. A survey of the approaches taken by

countries with various levels of flood risk and economic development to manage the financial impacts of floods is provided by the Organization for Economic Co-operation and Development (OECD, 2016). UK, US, and French public-private schemes for flood insurance are briefly described here, as they differ in both risk profile and cultural context.

In the United Kingdom, Flood Re is a government initiative established to overcome issues of adverse selection and unaffordable premiums by providing standardized fees for homeowners based on council tax bands (www.floodre.co.uk). This affordability is achieved by introducing a levy, charged according to insurance companies' gross written premium, which in turn allows these insurance companies to write high risk properties and cede them to the Flood Re reinsurance pool, which compensates insurers for any claims.

In the United States, the FEMA, established in 1978 to coordinate the national response to disasters when a state of emergency is declared, provides public protection against flood risk with the National Flood Insurance Program (NFIP) and governmental flood hazard maps (https://msc.fema.gov/portal/home). The US market is now moving to privatize flood insurance to overcome the current debts and financial constraints of the government. Such privatization can only be facilitated by the introduction of nationwide, sophisticated catastrophe flood models. This has been a challenge for many years considering the geographical scope and computational requirements to run such high-resolution models but several competing models are now available. This challenge is exacerbated by the increasing resolution of DEMs.

In France, a natural catastrophe compensation scheme covers losses against natural perils from windstorm and flood (https://www.ccr-re.com/en/home). The scheme has also adopted a private-public solution between government and insurers, covered by the state-backed reinsurer CCR. The scheme relies on local governments declaring a state of natural disaster, and subject to the scope, type of peril, and intensity of the disaster, any properties covered by an insurance policy will be entitled to full compensation.

Having a view of the high-risk properties is thus essential for these types of natural catastrophe schemes and requires accompanying high-resolution geographical information. This has led to more openness and availability of data, especially as a public good. Initiatives such as the Oasis open-source loss modeling framework and the Oasis hub (https://oasishub.co/) provide not just an open-source platform for plug-and-play vendor models but also provide a marketplace for relevant datasets, both free and licensed.

EO data have a role to play but is still limited by prohibitive costs, data processing capabilities, and ultimately, accessibility. There are some initiatives starting to promote the availability of DEMs, such as SRTM, with a general call for improving data resolution to support the public good. Other examples include the Dartmouth Flood Observatory (DFO), which provides an open-source, global historical event footprint data base (https://www.dartmouth.edu/~floods/), using space-based measurement, mapping, and modeling of

surface water. It mostly relies on the 250 m spatial resolution MODIS as well as high resolution imagery where available. Such data sources are vital not just for the development and benchmarking of models, but provide the input data to recreate events, stress and sensitivity test models, and verify loss outputs.

Consequently, the progression of flood models, aided by the ever-increasing resolution of remotely sensed terrain data, has led not just to changes in the insurance market in terms of how flood risk is treated, but also to new ways of mitigating against this peril.

6 Role of regulation

As part of the financial service industry, insurance is governed by stringent regulatory and risk management frameworks. Over time, this has led to the wider incorporation of catastrophe analytics into the regulatory structures known today, such as Solvency II in Europe (EIOPA, 2014). The requirements designed to ensure sufficient capital is assigned to pay for any potential claims demand a process, which is well understood, auditable, consistent, and standardized across geographies and perils.

From a governance perspective, the role of financial regulation in focusing senior management on risk has sometimes been viewed somewhat enviously by other corporate sectors (such as retail and manufacturing), where enterprise risk management can garner less attention and resources. Many advocates of tackling climate change risk, within as well as outside of business, thus welcome emerging regulation as a driver for societal engagement.

Regulatory impacts on technological and methodological advances in risk assessment can however have a stifling effect on innovation, as the requirement for standardized process-driven procedures inhibits evolution of new thinking and techniques. For example, while advancements in catastrophe models have addressed regulatory needs, challenges have arisen around model changes impacting the requirements for capital reserves over time, as well as disrupting financial instruments optimized around specific model results. For example, in 2011, vendor catastrophe modeling company RMS released a version 11 update (RMS 2012) to its US Hurricane software, taking into account the lessons learned from several recent major loss-making wind events, such as Hurricane Ike. Insured loss results from significant model changes increased from 20% to 100% (Marsh and Mclennan 2012), notably in inland areas. The Florida Commission on Hurricane Loss Projection Methodology, a unique state-based technical regulator, approved the version update but controversy ensued. Many insurance companies were hesitant to adopt the new model version impacts, undertaking individual evaluation as a form of "own view of risk." The impact on less technical audiences was more profound: rating agencies such as Standard & Poor's placed 17 catastrophe bonds, where expected loss and pricing are established by catastrophe models, on negative watch (Insurance Journal, 2011). Subsequently, third-party modeling agents AIR Worldwide came to dominance

in catastrophe bond deal issuance (Artemis, 2019), although RMS will remodel bonds as a service to their clients so that differing risk views are available to influence pricing.

It is clear from the above example that there are far-reaching consequences for many stakeholders on how natural hazard risk assessment is regulated, particularly for flood risk, which is so geographically widespread and proximate to populations. Technological developments have had and will continue to exert an impact on the relationship between private and public sector in this regard, as influenced by regulatory regime.

7 Protection gap

In insurance terms, the increasingly used phrase "protection gap" simply denotes the difference between what is paid out by insurance as financial compensation after a disaster and the total cost to an economy and its people of a catastrophic event. It's also known as underinsurance (Swiss Re, 2018).

Such a protection gap can exist in both high and low income economies for differing reasons. For example, in California, a high-risk seismic region, earthquake insurance is available, yet only around 10% of homeowners purchase such cover. For US flood coverage, the protection gap is significantly lower than for California earthquake, mainly due to activities of the government's heavily indebted National Flood Insurance Program (NFIP). For flooding damage from Hurricane Harvey in 2017, insurance compensated around 30% of residential losses.

Low income economies face differing challenges for underinsurance. On the demand-side, affordability is a significant obstacle, as is policy-holder trust in financial institutions and governments in countries characterized by weak legal and regulatory systems for enforcing payment of valid claims. Cultural and social factors around risk aversion can also play a role. In relation to Gross Domestic Product, the protection gap for property coverage in mature markets is around 59%, whereas in emerging markets it is as high as 94% (Holzheu and Turner, 2018). Fig. 8.8 illustrates this protection gap by hazard group, where hydrological events worldwide between 1980 and 2018 have the smallest proportion of economic loss that was insured.

The challenge remains to cover such global economic flood losses by insurance. This is particularly evident in less developed regions. The protection gap between economic and insured losses can be tackled through disaster risk financing (DRF) initiatives supported by national government, development banks, humanitarian agencies, non-governmental organizations (NGOs), and the private sector. DRF covers the system of budgetary and financial mechanisms to credibly pay for a specific risk, arranged before a potential shock. This can include paying to prevent and reduce disaster risk, as well as preparing for and responding to disasters.

While catastrophe models form an important part of the solution to quantify risks (they are necessary but by no means sufficient), there is limited model

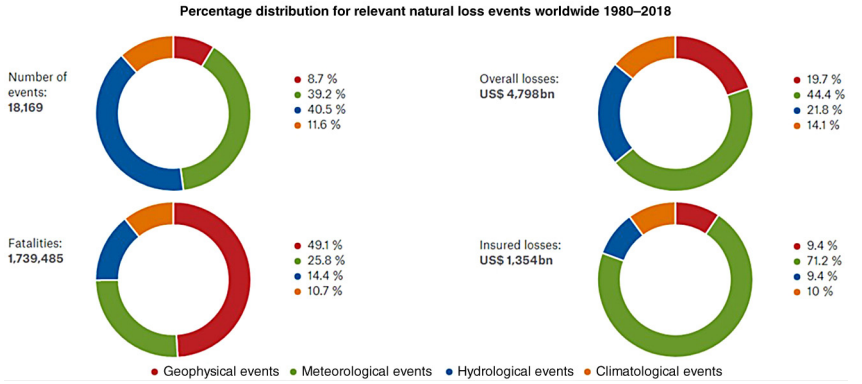

FIGURE 8.8 The protection gap. *(From 2020 Münchener Rückversicherungs-Gesellschaft, NatCatSERVICE.)*

coverage in the developing regions where data is often lacking or of low quality. Crucially, a broader range of issues must be considered if DRF approaches are to prove beneficial for development outcomes and become scalable (Clarke and Dercon, 2016). Such issues include ensuring participation and empowerment of potentially affected communities (thereby conferring legitimacy), adequate monitoring and evaluation of schemes, and taking a holistic risk perspective across disaster risk management strategies, contingency plans, climate change adaptation plans, and governmental sectoral plans. All too often, DRF instruments can be seen as supply led, supported by technologies from distant countries that are making poorly informed assumptions and are not led by development needs.

EO is nevertheless an extremely useful resource to develop models in data-scarce regions, in particular to identify river networks and to derive DEM for hydraulic modeling. EO can support the estimation of exposure information where detailed information of the built environment is not readily available.

Exposure requirements, such as location information, structural type, occupancy, era of construction, building height, and size and cost to replace a building are required to adequately estimate losses after a damaging event. There are initiatives to build such comprehensive exposure databases using remote sensing data. This is an important process to establish a credible statistical breakdown of structural and occupancy types for a given region so that consistent disaggregation of insurance portfolios can also be achieved.

The Global Earthquake Model (GEM) initiative, for example, has been working toward the development of a first comprehensive, publicly available Global Exposure Database (GED) through a consortium of leading institutions that are engaging with domain-experts from multiple countries. The aim is to better evaluate global earthquake risk and loss estimation through GEM's OpenQuake platform. While the focus is on earthquake risks, the GED4GEM project is a good example of employing multiple scales, sources, inferences

schemes, and flexibility to create taxonomy that adequately describes the build environment across the globe. Datasets include country level statistical information, urban extent grids (GRUMP), population data, and satellite land use classifications. These are combined with higher level housing inventory datasets and actual building stock accounts up to building-by-building vector databases. Satellite data includes Global Land Cover 2000 based on daily data from SPOT4, which is processed using supervised classification methods, as well as GlobCover from Envisat derived from MERIS. These datasets are vital to disaggregate and link the coarser statistical data on building counts into finer resolutions for modeling purposes.

8 Index-based parametric insurance

Index-based insurance, increasingly known as parametric insurance, has been in existence for many years originating with Chakravati, 1920, who envisaged a rainfall insurance product in India where payment would be triggered if total rainfall during a season was less than a given threshold. The limitations of data availability in this example are now obvious because short dry spells at a particular moment of crop growth can trigger large crop losses, even if a season has average aggregate rainfall—thus demonstrating a form of "basis risk". Basis risk refers to the potential for mismatch between the measures and models that determine payouts, and the losses experienced on the ground. A risk holder may receive a payout that is greater or less than expected. Agricultural insurance has seen much index insurance application due to the high cost of assessing losses with traditional indemnity losses; this is especially the case for subsistence farmers and smallholders in developing countries. Drought examples include the Weather Based Crop Insurance Scheme (WBCIS) in India, where rainfall amount is measured by weather stations, and Index-Based Livestock Insurance (IBLI) in Ethiopia, where rangeland conditions as identified by satellite (normalized difference vegetation index, NDVI).

The two fundamental components of parametric insurance are:

1. the pay-out trigger, which is typically based on observable physical characteristics (reported by an independent "calculation agent") directly related to the risk that the protection buyer seeks to cover, such as hurricane wind speed or minimum central pressure, temperature, rainfall total, etc. Such parametric triggers can also be used for catastrophe bond pay-out, such as New York Metropolitan Transit Authority's 2013 (post-hurricane Sandy) bond with a trigger based on storm surge height for a named storm; and
2. the pre-agreed pay-out amount, which should be policy-triggered.

The key advantages of parametric insurance are speed of payout, predictability of pay-out, clear claims processes to buyer and seller, the absence of loss adjuster fees, lower chance of disputes as parameters are predefined, and also reduced data requirements for modeling risk frequency and severity.

Parametric insurance is increasingly attracting attention for applications beyond weather-related disasters and also as a complement to traditional insurance because of its potential to speed up initial recovery time and to cover both specific catastrophic losses and frequency attritional losses. For example, gauges of water levels of the River Rhine have been used to trigger pay-outs not only for physical damage from flood but for business interruption losses to marine transportation due to heatwave-induced low levels in 2018. Historical data from the river gauges allowed pricing of the product and assessment of the payout amount. EO could clearly broaden the range of applications by line of business and geography thanks to the increasing density of micro-satellite constellations, for example.

Like flood risk assessment in catastrophe modeling, however, significant challenges persist for development of saleable parametric flood insurance. As stated in a 2016 OECD report: "From the perspective of the issuer, the complexity in understanding flood risk means that simple parametric triggers are unlikely to correlate well with actual losses, creating 'basis risk' for the issuer." For example, an individual weather station rainfall measurement might not capture the magnitude of inundation further away from the same event. Such a measurement might also not capture the network-aggregating nature of riverine flood.

While basis risk is the biggest challenge for parametric products, several mechanisms exist to mitigate such basis risk. Also, it should not be forgotten that basis risk exists in indemnity contracts in terms of "the small print" of policy conditions and wording leading to uncertainty in the mind of the policy-holder about what exactly they are covered for. Multiple parametric triggers can be applied to a single product, or hybrid products designed, mixing both a predefined event parameter and indemnity proof of loss. Structures may also be staggered, as with forms of forecast-based finance (Coughlan de Perez et al., 2015), allowing for progressively higher payouts for stronger storms, for example. Such features do detract though from the most appealing features of parametric products regarding speed and transparency.

For flood-specific products, basis risk is a particular problem as measures such as rainfall or river flow are more remote to likelihood and magnitude of loss than ground shaking or gust speed. Such risk can be reduced by establishing flood footprints which delineate specific areas that are affected. EO could greatly assist in near-real-time flood footprint collation. Such work has additional benefits for other audiences, such as applications in risk model validation and scenario analysis as mentioned earlier. One problem with visible spectrum sensing is the difficulty of discerning flooding in urban areas, which include concentrations of people and property risk, during stormy conditions. Successful deployment of parametric flood insurance would assist in allowing sovereign regional pools such as CCRIF (formerly Caribbean Catastrophe Risk Insurance Facility, where excess rainfall cover is available), ARC (Africa Risk Capacity), and PCRIC (Pacific Catastrophe Risk Insurance Company) to further diversify less correlated risks from differing perils. Environment-monitoring satellite services are an obvious choice for regional or global third-party reporting agencies.

9 Climate change and the finance sector beyond insurance

The insurance sector has been actively involved in considering climate change impacts for many years (Swiss Re, 1994; Dlugolecki, 2000; Geneva Association, 2018a), but this has increasingly become of more comprehensive concern for the finance sector. Regarding extreme events, which are the most familiar component of physical climate risk for the industry, even the impacts of an apparently increasingly optimistic future climate scenario, where COP21 2015 Paris Agreement carbon emissions targets lead to a temperature increase of less than 2°C by 2100, are alarming.

The Intergovernmental Panel on Climate Change SR15 report (IPCC, 2018) noted that extreme rainfall and fluvial flooding may increase in many areas, with significant increase in precipitation extremes already observed in mid-latitudes of the northern hemisphere. Heavy rainfall associated with tropical cyclones is expected to increase by 10%–15% (as seen with Hurricane Harvey in 2017, flooding Houston). Coastal flooding is likely to cost between 0.3% and 5.0% of global GDP annually by 2100 with today's level of coastal protection. More severe climate scenarios dramatically exacerbate these patterns of impact. It should be noted however that there is much more uncertainty in assessing changes in frequency and severity of extreme events, such as storm and flood, due to climate change than chronic events such as temperature change and sea level rise.

Insurance companies have to respond to a range of push and pull factors across both asset and liability sides of the balance sheet (CRO, 2019), which include severe event loss estimation, underwriting activities and reputational risk (as seen with the Unfriend Coal campaign which targeted specific insurers; ClientEarth, 2018), investor sentiment (including consideration of environmental, social, and governance (ESG) factors), and also potential emerging business opportunities.

Many stakeholders look to the insurance sector as a repository of knowledge on physical climate risk, both in terms of long datasets of hydrometeorological claims and risk quantification from 30 years of natural hazard modeling. A limitation of existing approaches is that the focus is on the likelihood of losses occurring over the next 12 months of the usual insurance policy period.

However, many modeling practices adapt relatively easily to the consideration of differing (business-relevant) time horizons and also differing future emissions pathways (Climatewise, 2019; Geneva Association, 2018b).

Several proto-regulatory initiatives are worthy to mention here in light of their needs, to lesser and greater extent, for some form of risk metric implementation around physical climate impacts.

1. The Task-force for Climate-related Financial Disclosures (TCFD), led by former Bank of England governor Mark Carney and chaired by Michael Bloomberg, came into being in December 2015 after a G20 request to provide voluntary recommendations. These recommendations are aimed at helping

companies disclose decision-useful information to enable financial markets to better understand climate-related financial risks and opportunities. TCFD focuses on the key areas of governance, strategy, risk management, and targets and metrics (TCFD, 2017). Published response to TCFD can already be seen by early mover reporting, such as by Aviva's Climate Value at Risk (Aviva, 2019). New Zealand recently announced that listed companies could soon be required by law to make any climate change-related risks to their businesses known to their shareholders (New Zealand, 2019).

2. National financial regulators are starting to define and impose climate change-related stress test scenarios to drive the insurance industry to start thinking about climate change impact on solvency requirements, capital management, and internal risk appetite setting. The UK's Prudential Regulator Authority (PRA), via Supplementary Statement 3/19 (PRA, 2019), was the first to set precedence in asking UK insurers to assess their solvency impacts against varying severities of climate change scenarios, based on UK climate change projections. Other countries will inevitably follow The Bank of England's lead in climate risk, leading candidates being other European countries, Australia, and Japan. The Network for Greening the Financial System (NGFS), formed in 2017 and now with 42 members, will also drive the TCFD agenda, with its mandate to support the goals of the Paris agreement by enhancing the role of the financial system to manage risks and mobilize capital for low-carbon investments.

Jarzabkowski et al. (2019) have reported on the role of insurance for climate adaptation and some conclusions provide potential opportunities for EO products and services:

- Recommendation 1: Invest in open-source models that provide a long-term view of climate risk and link to insurance solutions.
- Recommendation 2: Joined-up policy-making to put climate risk models at the heart of national adaptation strategies.
- Recommendation 6: Converge insurance, humanitarian, and development agendas.

Uncertainty around estimating low frequency, high severity "tail risk" combined with uncertainty around future emissions pathways, and the potential impact of increased greenhouse gas concentrations on extreme events (Weitzman, 2011) promote the use of scenario analyses for simplicity of calculation and clarity of communication. Ideally, all underlying hazard data will reside in the public domain to support transparency of analysis and corroboration of robustness, as well as to allow challenges around expert judgment and necessary assumptions. In extending the risk assessment methodologies to developing economies and the humanitarian agenda, inevitably less ground surveyed data will be available, and solutions will rely more heavily upon remotely sensed data.

For example, to estimate the impact of increased flood risk under the UK climate projections, as outlined in the PRA climate change stress test, hydrological data are used from gauge station data and increased by the scenario's percentage change to reflect the increase in surface run-off resulting from increased precipitation (e.g., 5%, 10%, and 40%, respectively). This is done to estimate a new frequency-severity relationship from a hazard point of view, such that a 1-in-100-year event may become a 1-in-70-year event under the increased precipitation run-off generated flow, which is then assumed to reflect the loss change on an exceedance probability curve to estimate the financial impact. These simplistic techniques could be elaborated by using full inundation models to estimate the changes in flood extents, to then estimate impacts on a portfolio bottom up by overlaying the extents with risk locations and associated vulnerability curves.

Risk modeling for national adaptation strategies effectively requires "industry exposure databases" (IEDs, see AIR, 2016)—inventories of built environment at risk. An IED represents 100% (insurable) market share rather than the partial coverage of insured datasets. A good example is the UK Environment Agency's "National Receptor Database" (NRD), used as part of its NaFRA (National Flood Risk Assessment) to estimate weighted annual average damages (WAAD), equivalent to average annual loss (AAL) in insurance terminology. In the short to medium term, changes in exposure have a much greater impact on losses than changes in hazard, induced by climate change (Woetzel et al., 2020).

The requirement for "asset level data" as input to risk models are also being sought beyond the insurance industry. As part of activities by the UK's Green Finance Institute, inaugurated in 2018 with joint funding from government and the City of London, a Spatial Finance Initiative (2018) has been established, involving the Alan Turing Institute, University of Oxford, and Satellite Applications Catapult. Mainstreaming geospatial capabilities enabled by space technology and data science into financial decision making globally is a key aim. Whereas insurance companies have access to policy level information on location and type of property or commercial enterprise that is covered, which can be collated in "exposure databases" that are input data to catastrophe models, other financial institutions such as asset managers or banks have much more limited data availability. Crucially, such exposure data needs to be tied to company ownership information. To this end, the "Climate risk analysis from space" report (Spatial Finance Initiative, 2018) boldly states:

- We expect that the development of a global catalog of every physical asset in the world to be already within the reach of technical feasibility.
- It is possible to train learning algorithms to recognize an asset and its features in remote imagery and then scan global imagery corpuses to identify all assets of that type.
- The launch of the CarbonSat satellite in 2020, as well as some already scheduled sun-synchronous sensors, offer the potential for more precise observation of GHG concentrations and emissions at the asset level.

- Through future research projects undertaken over multiple phases, we plan to make asset-level data and GHG emissions monitoring for each asset available for every physical asset in every sector globally, beginning with the most GHG intensive assets.

Such innovative goals clearly sit squarely with the EO community, but as much connected with climate risk analytics, a mature market to pay for such products does not yet exist. To what extent could a finance sector precompetitive space be created to assist in defraying development (and maintenance and support) costs for such asset level datasets? How could industry initiatives such as Oasis or IceBreaker One (2019) (bridging the data gaps between finance, assets, policy, and science to deliver a zero-carbon future) support such approaches with standards and frameworks? Is there a role for government-funded research councils (Hillier et al., 2019), such as UKRI (2019) (Pre-Announcement—Climate and Environmental Risk Analytics for Resilient Finance)? Or perhaps as with GoogleMaps, or even the Human Genome Project and the Celera Corporation, could a private company with large enough resources complete such an ambitious task as a global asset level database, at fractional cost and enviable speed? The field is very much open for such competition. Keenan (2019) describes the climate intelligence arms race in financial markets well, noting that, similar to catastrophe model development: "lack of transparent scientific validation and public oversight over rapidly advancing, and often proprietary, 'black box' technologies are causes of concern, both for the integrity of science and for the potential impacts on consumer behavior and public policy."

Finally, regarding the sibling catastrophe of climate change, biodiversity loss, efforts have been made to explore how financial mechanisms might support conservation of natural capital and ecosystem services. A fledgling example is The Nature Conservancy (2019) "world's first insurance policy on a coral reef" for parts of the Mesoamerican Reef in Mexico. A parametric policy has a trigger of 100 knot wind speed which, if exceeded in a predefined area, leads to a rapid insurance payout to a trust fund, allowing swift damage assessments, debris removal, and initial repairs to be carried out. Earth Observation data may not be required for parametric trigger design but information on location (and ideally type and quality) of reefs, as well as onshore exposure, or DEMs for storm surge risk may be useful in contextual event modeling, perhaps by historical scenario, that provides evidence for product pricing.

The Global Environment Facility (GEF) Trust Fund was established at the 1992 Rio Earth Summit to help tackle the world's most pressing environmental problems. In December 2019 GEF (GEF, 2019) announced 9 winners from 400 applicants for its Challenge Program for Adaptation Innovation. As much of the funding is directed at developing countries, opportunities exist here for EO support in project monitoring for blue as well as green economies.

10 Conclusions

This chapter outlines the roles of EO data in re/insurance sector applications and highlights market trends and specific use cases across that support risk assessment in both established and emerging markets, model development, and event response. Flood risk may have been seen as a "secondary" peril to windstorm and earthquake; however, it has attracted greater attention due to ever-increasing losses in terms of both frequency and severity, as well as how it may change under the influence of climate change and exposure/vulnerability change, such as increasing urbanization. We have learned how catastrophe modeling has evolved, for flood specifically, in the re/insurance sector, and how EO combined with technological advancements has enabled components of sophisticated modeling solutions we see today to estimate financial losses and societal impacts.

While existing solutions have been aided by increased computational power and higher resolution and better quality DEMs derived from EO data, making it possible to model flood hazard at national and global scale, it is clear that more needs to be done to translate research advances, data, and technology into applications that can be more easily accessed by viable business models.

We have seen successes in multi-source approaches of combining satellite, UAV video, social media, and post-event ground survey in the case of event response; hydrodynamic modeling solutions supported by increased computer processing technology; and integrating, organizing, and better understanding data through geographic information systems. Yet, more needs to be done to better harness new solutions aided by investments in training, systems, and data, as well as further fostering the private public relationship to drive the openness and transparency agenda around data. This chapter, therefore, concludes with the following recommendations:

1. The provision of higher quality, global datasets and input files, as provided by EO for model development, such as a better quality DTM and global detailed exposure data set, working in collaboration with governments, NGOs, and industry to make the data available publicly to increase the base level of flood risk understanding globally.
2. To broadly serve commercial and societal needs in risk and resilience, the ideal partnership will incorporate EO into public-private-academic collaborations that support reliable information, strong communication, joint planning, and clear ideas on roles and limitations.
3. Regulators must strive to send market signals that encourage both a level playing field and risk management discipline for market participants yet also provides space for iteration of innovative technological solutions without being overly proscriptive on methodologies.
4. The global coverage of EO technologies must be fully exploited by creative design of accompanying business models and intellectual property application to enable risk assessment tools to be developed for low income countries.

5. "Technologies of humility" should be considered to control the impulse toward creating products with even more modeled complexity, where simpler products with more transparent assumptions and documented limitations may provide a better service, by allowing risk holders to calibrate their experience against fewer variables. Additionally, simplified algorithms are required for flood simulation to enable real-time hydrodynamic modeling solutions.
6. EO providers must be prepared to listen closely and respond to a variety of user needs from an increasing range of often non-technical stakeholders, thereby avoiding being supply-led.

Whilst many positive efforts are underway from creating better quality SRTM data for public consumption, improved disaggregation methods, and industry collaborations to tackle the protection gap—for all of which EO plays a central role—challenges remain. A changing climate adds urgency to answering how the latest science can be incorporated into modeling, combined with technological and data advancements, their maintenance (often a crucially underestimated aspect), and how this can be adapted within the re/insurance industry and more broadly across finance.

From an EO perspective, machine learning, on-the-cloud imagery and parallel processing, and better awareness through digitalization, means we are certainly in an age of space technology (as well as political) disruption. Sensors ranging across the entire electromagnetic spectrum, both passive and active, geostationary ("fixed" position), sun-synchronous and polar orbiting satellite are offering new capabilities and insights that can help further advance the modeling capabilities with different views of risk reflecting potential future scenarios. However, productive assimilation of this disruption by re/insurance industry proceeds at a much slower pace. This is due in part to longstanding inertial relationships between commercial risk modeling suppliers and their clients, as well as potentially legacy methodological approaches, supported by regulatory environments that have the potential to inhibit the flexibility, efficiency, and fitness-for-purpose of the financial system.

References

ABI, 2011. Industry Good Practice for Catastrophe Modeling. A Guide to Managing Catastrophe Models as part of an Internal Model Under Solvency II, Association of British Insurers. https://www.abi.org.uk/globalassets/sitecore/files/documents/publications/public/migrated/solvency-ii/industry-good-practice-for-catastrophe-modelling.pdf.

AIR Worldwide, 2016. Modeling fundamentals: AIR industry exposure databases. Available from: https://www.air-worldwide.com/Publications/AIR-Currents/2016/Modeling-Fundamentals--AIR-Industry-Exposure-Databases/.

Artemis, 2019. Catastrophe bond and ILS risk modelling firm leaderboard. Available from: https://www.artemis.bm/dashboard/cat-bond-ils-risk-modellers/.

Aviva, 2019. Climate-related financial disclosure 2018 report.

Chakravati, J., 1920. Agricultural Insurance: A Practical Scheme Suited to Indian Conditions. Government Press, Bangalore.

Clarke, D., Dercon, S., 2016. Dull Disasters? How Planning Ahead will Make a Difference (English). World Bank Group, Washington, D.C..

ClientEarth, 2018. Insuring coal no more: An insurance scorecard on coal and climate change. Available from: https://unfriendcoal.com/clientearth-reports-uk-insurers-to-fca/.

ClimateWise, 2019. Physical risk framework: understanding the impact of climate change on real estate lending and investment portfolios. Available from: https://www.cisl.cam.ac.uk/resources/sustainable-finance-publications/physical-risk-framework-understanding-the-impact-of-climate-change-on-real-estate-lending-and-investment-portfolios.

Cohen, S., Brakenridge, G.R., Kettner, A., Bates, B., Nelson, J., McDonald, R., Huang, Y-F, Munasinghe, D., Zhang, J., 2017. Estimating floodwater depths from flood inundation maps and topography. J. Am. Water Resour. Assoc. 54 (4), 847–858.

Coughlan de Perez, E., van den Hurk, B., van Aalst, M., Jongman, B., Klose, T., Suarez, P., 2015. Forecast-based financing: an approach for catalyzing humanitarian action based on extreme weather and climate forecast. Nat. Hazards Earth Syst. Sci. 15, 895–904.

CRO Forum, 2019. The heat is on: Insurability and resilience in a Changing Climate. Available from: https://www.thecroforum.org/2019/01/24/crof-eri-2019-the-heat-is-on-insurability-and-resilience-in-a-changing-climate/.

Dlugolecki, A.F., 2000. Climate change and the insurance industry. Geneva Pap. Risk Insur. Issues Pract. 25, 582–601.

Dodov, B., Weiner, A., 2013. Introducing the AIR Inland Flood Model for the United States. AIR Currents. https://www.air-worldwide.com/publications/air-currents/2013/Introducing-the-AIR-Inland-Flood-Model-for-the-United-States/.

Dreksler, S., Allen, C., Akoh-Arrey, A., Courchene, J., Junaid, B., Kirk, J., Lowe, W., O'Dea, S., Piper, J., Shah, M., Shaw, G., Storman, D., Thaper, S., Thomas, L., Wheatley, M., Wilson, M., 2013. Solvency II Technical Provisions for General Insurers. Institute and Faculty of Actuaries. Available from: https://www.actuaries.org.uk/system/files/documents/pdf/sii-tp-wp-paper-giro40.pdf.

EIOPA, 2014. The underlying assumptions in the standard formula for the Solvency Capital Requirement calculation. Available from: https://eiopa.europa.eu/Publications/Standards/EIOPA-14-322_Underlying_Assumptions.pdf.

GEF, 2019. https://www.thegef.org/news/winners-gef-challenge-program-adaptation-innovation-announcedhallenge. Program for Adaptation Innovation announced.

Geneva Association, 2018a. Climate change and the insurance industry: taking action as risk managers and investors. https://www.genevaassociation.org/sites/default/files/research-topics-document-type/pdf_public/climate_change_and_the_insurance_industry_-_taking_action_as_risk_managers_and_investors.pdf.

Geneva Association, 2018b. Managing physical climate risk: leveraging innovations in catastrophe risk modelling. https://www.genevaassociation.org/sites/default/files/research-topics-document-type/pdf_public/ga_risk_modelling_18112018.pdf.

Hillier, J., et al., 2019. Investing in Science for Natural Hazards Insurance. Loughborough University. 10.17028/rd.lboro.c.4322666.v2.

Holzheu, T., Turner, G., 2018. The natural catastrophe protection gap: measurement, root causes and ways of addressing underinsurance for extreme events. Geneva Pap. Risk Insur. Issues Pract. 43, 37–71.

Hoppe, K., 2012. The Value of Insurance to Society. Geneva Association, Risk Management Newsletter No. 51.

Insurance Journal, 2011. S&P puts 17 cat bonds on CreditWatch/negative due to RMS model change. https://www.insurancejournal.com/news/national/2011/04/18/194986.htm.

IceBreaker One, 2019. Developing standards-based marketplaces for environmental and financial data. https://icebreakerone.org/start-here/.

Intergovernmental Panel on Climate Change (IPCC), 2018. SR15 global warming of 1.5°C. https://www.ipcc.ch/sr15/.

Jarzabkowski, P., Chalkias, K., Clarke, D., Iyahen, E., Stadtmueller, D., Zwick, A., 2019. Insurance for climate adaptation: Opportunities and limitations. Rotterdam and Washington, DC. Available from: www.gca.org.

Jha, A., Bloch, R., Lamond, J., 2012. Cities and Flooding: A Guide to Integrated Urban Flood Risk Management for the 21st Century. World Bank.

Keenan, J., 2019. A climate intelligence arms race in financial markets. Science 365 (6459), 1240–1243.

LMA, 2013. Catastrophe Modelling Guidance for Non-Catastrophe Modelers. Lloyd's Market Association. https://www.lmalloyds.com/lma/finance/Cat_Modelling_Guidance.aspx.

McChristian, L., 2012. Hurricane Andrew and Insurance: The Enduring Impact of an Historic Storm. Insurance Information Institute.

Marsh and Mclennan, 2012. Catastrophe modeling: Why all the fuss? https://www.marsh.com/us/insights/research/catastrophe-modeling.html.

New Zealand Ministry for the Environment, 2019. Climate-related financial disclosures: understanding your business risks and opportunities related to climate change. https://www.mfe.govt.nz/sites/default/files/media/Climate%20Change/Climate-related-financial-disclosures-discussion-document.pdf.

OECD, 2016. Financial Management of Flood Risk. OECD Publishing, Paris. https://doi.org/10.1787/9789264257689-en.

O'Conner, A., 2017. 25 years later: How Florida's insurance industry has changed since hurricane Andrew. Insurance Journal.

Prudential Regulation Authority, 2019. Supervisory Statement SS3/19: Enhancing banks' and insurers' approaches to managing the financial risks from climate change. https://www.bankofengland.co.uk/prudential-regulation/publication/2019/enhancing-banks-and-insurers-approaches-to-managing-the-financial-risks-from-climate-change-ss.

RMS, 2012. Principles of model validation: United States hurricane model. https://forms2.rms.com/rs/729-DJX-565/images/tc_2012_principles_model_validation_us.pdf.

Spatial Finance Initiative, 2018. Climate risk analysis from space: remote sensing, machine learning, and the future of measuring climate-related risk. https://www.spatialfinanceinitiative.com/wp-content/uploads/2019/04/Remote-sensing-data-and-machine-learning-in-climate-risk-analysis.pdf.

Swiss Re, 1994. Global Warming: Element of Risk. Swiss Reinsurance Company, Zurich.

Swiss Re, 2012. Flood—An Underestimated Risk: Inspect, Inform, Insure. Swiss Reinsurance Company. https://media.swissre.com/documents/Flood.pdf.

Swiss Re, 2018. Closing the Protection Gap—Disaster Risk Financing: Smart Solutions for the Public Sector. Swiss Reinsurance Company.

Smith, A., Bates, P., Wing, O., Sampson, C., Quinn, N., Neal, J., 2019. New estimates of flood exposure in developing countries using high-resolution population data. Nat. Commun. 10, 1814. doi: 10.1038/s41467-019-09282-y.

Task Force on Climate-related Financial Disclosures, 2017. Recommendations of the task force on climate-related financial disclosures: Final report. https://www.fsb-tcfd.org/wp-content/uploads/2017/06/FINAL-TCFD-Report-062817.pdf.

The Nature Conservancy, 2019. Insuring nature to ensure a resilient future. https://www.nature.org/en-us/what-we-do/our-insights/perspectives/insuring-nature-to-ensure-a-resilient-future/.

UKRI, 2019. Pre-announcement—Climate and environmental risk analytics for resilient finance. https://nerc.ukri.org/funding/application/currentopportunities/pre-announcement-climate-and-environmental-risk-analytics-for-resilient-finance/.

Weitzman, M., 2011. Fat-tailed uncertainty in the economics of catastrophic climate change. Rev. Environ. Econom. Policy 5 (2), 275–292.

Woetzel, J., et al., 2020. Climate Risk and Response: Physical Hazards and Socioeconomic Impacts. McKinsey Global Institute.

Page left intentionally blank

Chapter 9

Flood Detection and Monitoring with EO Data Tools and Systems

Paola Mazzoglio[a], **Alessio Domeneghetti**[b] **and Serena Ceola**[b]
[a]*Department of Environment, Land and Infrastructure Engineering (DIATI), Politecnico di Torino, Torino, Italy;* [b]*Department of Civil, Chemical, Environmental and Materials Engineering (DICAM), Alma Mater Studiorum - Università di Bologna, Bologna, Italy*

1 Introduction

According to several disaster databases like the Emergency Events Database (EM-DAT; www.emdat.be) and Munich Re's NatCatSERVICE, an increasing trend in terms of frequency and severity of flood events emerges by analyzing the data related to the most recent years. Now more than ever, precise near real-time information on ongoing flood events can reduce the socioeconomic impact of flooding. In this context, remote sensing represents a highly valuable source of observational data that could provide valuable information, which alleviate the decline of in-field surveys and gauging stations at the global level (Domeneghetti et al., 2019), especially in remote areas and developing countries (Collischonn et al., 2008; Xue et al., 2013). The wide spatial extent of these products has provided benefits to regions that might not have otherwise been able to set up local models and observation programs (Alfieri et al., 2018).

Global (or quasi-global) early warning systems are key instruments for both early forecasting (for better preparedness) and early detection, as well as for an effective response and crisis management (Revilla-Romero et al., 2014) of hydrological extreme events. A correct estimation of both flooded and potentially flooded areas has a direct impact on the reliability of flood risk assessment, especially considering that for large parts of the Earth's surface, the time series of annual maxima are short and fragmented. This becomes even more relevant in densely inhabited areas where growing capital density and population growth contribute to increase flood risk.

During last decades, considerable effort has been spent toward increasing the precision and the timeliness of remote sensing data and Earth Observation (EO)-derived maps (Schumann and Domeneghetti, 2016). The launch of new satellite missions has further improved EO-based flood mapping.

Earth Observation for Flood Applications. http://dx.doi.org/10.1016/B978-0-12-819412-6.00009-2

Moreover, an increasing number of organizations and researchers have committed their efforts to the exploitation of satellite observations for flood identification and monitoring. Among all, the Global Flood Partnership (GFP), a global network of scientists, users, private and public organizations active in flood-risk management and reduction, shares its experimental products when flooding is taking place (Alfieri et al., 2018). The success of the GFP comes from being part of a global forum built with the aim of testing and improving, in a collaborative manner, research tools in real emergency management situations, further increasing the ability to provide complete near real-time information by merging different sources. The whole framework was tested in South Asia (Alfieri et al., 2018) and in the United States (Cohen et al., 2017).

Operational and research challenges regarding satellite-based quantitative precipitation measurements are instead studied by the International Precipitation Working Group (IPWG; www.isac.cnr.it/~ipwg/index.html), cosponsored by the permanent Working Group of the Coordination Group for Meteorological Satellites (CGMS) and the World Meteorological Organization (WMO).

With the aim to provide a concise but complete overview of flood monitoring performed with EO data, this chapter starts with a description of currently available satellite data (Section 2). Then, in Section 3, services developed for an EO-based monitoring of precipitation events are reviewed. Section 4 focuses on systems and hydrological models for flood monitoring based on satellite data. Finally, Section 5 summarizes previous sections, highlighting the pros and cons of current approaches.

2 EO data for flood detection, monitoring, and assessment

2.1 Rainfall datasets

High-resolution satellite-derived precipitation products can provide valuable information when it is necessary to know in near real-time the spatial distribution of precipitation and its temporal evolution (Michaelides et al., 2009).

Near real-time rainfall estimations are performed using infrared (IR), visible (VIS), and microwave (MW) wavelengths. Relevant examples are Precipitation Estimation from Remotely Sensed Information using Artificial Neural Networks (PERSIANN; Hsu et al., 1997), the Climate Prediction Center (CPC) Morphing technique (CMORPH; Joyce et al., 2004), the Tropical Rainfall Measuring Mission (TRMM) Multi-satellite Precipitation Analysis (TMPA; Huffman et al., 2007), the Global Satellite Map Product (GSMaP; Ushio et al., 2009), and the Integrated Multi-satellitE Retrievals for Global Precipitation Measurement (IMERG; Huffman et al., 2019). IMERG data represent an important step forward in satellite precipitation estimation thanks to the high spatial/temporal resolution and the global spatial coverage. Detailed information on the 3D structure of precipitation events are currently available thanks to advanced

spaceborne radar instruments like GPM's Dual-frequency Precipitation Radar (DPR).

The original PERSIANN dataset (Hsu et al., 1997) was improved by the Center for Hydrometeorology and Remote Sensing (CHRS) at the University of California, Irvine, releasing PERSIANN-CCS, a quasi-global (60°N–60°S) high-resolution (≈ 4 km) real-time precipitation product based on IR data acquired by geostationary satellites as the sole input (Hong et al., 2004). This algorithm separates cloud images into distinctive cloud patches, extracts cloud features (like coldness, geometry, and texture), clusters cloud patches into subgroups, and calibrates cloud-top temperature and rainfall relationship using gauge-corrected radar hourly rainfall data (Hong et al., 2004). A further step forward was possible thanks to PERSIANN Dynamic Infrared-Rain rate model (PDIR), which improved PERSIANN-CSS algorithm by using climatological data to construct a dynamic brightness temperature—rain rate relationship, increasing the capture of warm precipitation and cloud patches (Nguyen et al., 2019b). PDIR's improvement is also linked to an expansion of the cloud classification system that now includes monthly sets of cloud types.

These global rainfall datasets are characterized by geographically-dependent accuracy. More specifically, higher accuracy is reached in tropics and subtropic latitudes, while the quality of IR images acquired by geostationary satellites tends to suffer at high latitude due to steep view angles (Wright, 2018). An orographic correction proved to be necessary to reduce the processes leading to an orographic enhancement of precipitation (Vicente et al., 2002). Furthermore, passive MW estimation performs better over the oceans than over heterogeneous land surfaces and complex terrains, where the highly variable emissivity of soils and vegetation is much higher than the one of the water (Michaelides et al., 2009).

It is important to note that every rainfall measurement represents a spatial and temporal average over its grid cell, not allowing a finer-scale variability analysis and making flood modeling in fast-responding areas a difficult task. Moreover, biases and random errors that characterize this type of rainfall estimation are propagated during hydrologic modeling, posing limitations on the use of these products in flood forecasting (Nikolopoulos et al., 2013).

The possibility of retrieving rainfall estimations from soil moisture measurements performed by satellite, through a kind of a "bottom-up" approach (SM2RAIN; Brocca et al., 2014), is showing promising results. However, the potential of such indirect estimation of rainfall pattern for flood monitoring on near real-time application is still under investigation.

Table 9.1 summarizes key aspects of previously mentioned datasets. More detailed overviews of currently adopted techniques for satellite-based rainfall measurements are available in Levizzani and Cattani (2019), Sun et al. (2018), and Michaelides et al. (2009).

TABLE 9.1 Spatio-temporal characteristics of the main satellite-based rainfall datasets.

Dataset name	Spatial resolution	Temporal resolution	References
Precipitation Estimation from Remotely Sensed Information using Artificial Neural Networks (PERSIANN)	0.25° × 0.25°	60°N–60° S	Hsu et al. (1997)
Precipitation Estimation from Remotely Sensed Information using Artificial Neural Networks - Cloud Classification System (PERSIANN-CSS)	0.04° × 0.04°	60° N–60° S	Hong et al. (2004)
Precipitation Estimation from Remotely Sensed Information using Artificial Neural Networks - Dynamic Infrared-Rain rate model (PDIR)	0.04° × 0.04°	60° N–60° S	Nguyen et al. (2019b)
Climate Prediction Center (CPC) Morphing technique (CMORPH)	0.25° × 0.25°	60° N–60° S	Joyce et al. (2004)
Tropical Rainfall Measuring Mission (TRMM) Multi-satellite Precipitation Analysis (TMPA)	0.25° × 0.25°	50° N–50° S	Huffman et al. (2007)
Global Satellite Map Product (GSMaP)	0.1° × 0.1°	60° N–60° S	Ushio et al. (2009)
Integrated Multi-satellitE Retrievals for Global Precipitation Measurement (IMERG)	0.1° × 0.1°	90° N–90° S	Huffman et al. (2019)

2.2 Satellite optical and radar imagery

Optical images, in particular very high-resolution ones, are currently adopted to evaluate the ground situation (e.g., flood extent and dynamic, as well as damages induced by the inundations) (Voigt et al., 2007). Their use, however, provides useful information only in absence of clouds over the area of interest. Considering that flood events are often linked to adverse weather conditions, these data are limited to some cases (Matgen et al., 2011; Schumann and Moller, 2015).

Synthetic Aperture Radar (SAR), instead, measures the strength and the round-trip time of a microwave signal emitted by a radar antenna that can penetrate clouds. These instruments illuminate the Earth's surface (being independent from solar illumination) and build an image from the energy reflected back to the antenna (i.e., the backscatter). The brightness value of each image pixel is directly linked to the strength of the backscatter, which in turn depends on several factors that characterize surfaces, like soil composition and related dielectric

constant, roughness, and inclination. Generally, rough surfaces appear bright, while flat surfaces result dark; drier objects appear dark, while wetter objects become light. A flat water body, however, represents an exception: it acts as a flat surface and reflects the signal off from the radar. This important aspect allows extracting the flood extent, even if, in some cases, the accuracy of this delineation is deeply affected by particular ground conditions, like vegetation partially covered by water, buildings surrounded by water, shadows, etc. Although using a single image could provide reliable information, it is widely recognized that considering at least a pair of SAR images acquired during the flood event allows estimating the flood extent with greater accuracy (Matgen et al., 2011).

Valuable information for a near real-time mapping is currently provided by high-resolution SAR missions, like COSMOSky-Med, RADARSAT, Sentinel-1, TanDEM-X, TerraSAR-X, and the most recent Iceye.

2.3 Digital Elevation Models (DEMs): a glance to global, open-access spaceborne products

Precise representation of global terrain is essential to support any hydrological and hydraulic modeling and many studies have investigated the topographic role on hydraulic investigations (e.g., Hawker et al., 2018 and reference therein). High-resolution sensing techniques (e.g., GPS, LiDAR, etc.) are known to provide the best accuracy surveys; however, they require costs that are not compatible with resources of many communities. Thus, spaceborne DEMs represent the primary alternative in many parts of the globe.

Among mostly used DEMs, there is the Shuttle Radar Topography Mission (SRTM; obtained during an 11-day mission in February 2000), which provides land elevation retrieved with radar interferometry technique at near-global scale (80%) at 30 and 90 m resolution (Farr et al., 2007). Lately, higher spatial resolution global DEMs, such as Advanced Spaceborne Thermal Emission and Reflection Radiometer-Global DEM (ASTER GDEM; Tachikawa et al., 2011a) and Advanced Land Observing Satellite (ALOS; Tadono et al., 2014) have been developed using stereo viewing of optical satellite images, with the latter providing more accurate elevation data than previous missions (Courty et al., 2019). However, all satellite-derived DEMs are affected by several errors, such as system noise (i.e., speckle and stripe noise; Rodriguez et al., 2006), as well as beam reflection of water bodies, tree canopies, or building that contribute to DEM bias and elevation overestimation (Yamazaki et al., 2017; Ekeu-wei and Blackburn, 2018).

In the last decade, many attempts have been made to curb such errors and treat the spaceborne products to identify globally available off-the-shelf modified DEMs that can be readily applied in hydrological applications. O'Loughlin et al. (2016) reduced average SRTM's vertical bias using data from ICESat GLAS (Zwally et al., 2002) and information on vegetation height (Simard et al., 2011), forest canopy density, and climate regionalization maps (Broxton et al., 2014). Another example is represented by the global EarthEnv-DEM90

TABLE 9.2 Characteristics of most used open-source globally available spaceborne DEMs.

DEM	Spatial resolution [m]	Vertical error [m]	References
SRTM	30–90	± 16	Rodriguez et al. (2006); Farr et al. (2007)
ASTER GDEM	30	± 25	Tachikawa et al. (2011a,b)
ACE 2 GDEM	1000	> 10	Varga and Bašić (2015)
GTOP30	1000	9–30	Varga and Bašić (2015)
ALOS	30	± 5	Tadono et al. (2014); Jilani et al. (2017)
GMTED2010	250	26–30	Danielson and Gesch (2011); Pakoksung and Takagi (2016)
[a]Bare-Earth SRTM	90	4.85–12.64	Sampson et al. (2015); O'Loughlin et al. (2016)
[a]EarthEnv-DEM90	90	4.13–10.55	Robinson et al. (2014); Tan et al. (2015)
[a]MERIT DEM	90	± 2	Yamazaki et al. (2017)

[a]*indicates DEMs obtained after error removing or data combination.*
Modified from Ekeu-wei and Blackburn (2018).

(Robinson et al., 2014; Tan et al., 2015), which has been obtained integrating several products (ASTER GDEM2, CGIAR-CSI SRTM V4.1, and Global Land Survey Digital Elevation Model) by means of delta surface filling and adaptive DEM noise smoothing methodology, improving the overall DEM accuracy.

Recently, Yamazaki et al. (2017) developed the Multi-Error-Removed Improved-Terrain DEM (MERIT DEM) obtained after removing several error sources, such as absolute bias, stripe noise, speckle noise, and tree height bias. Demanding to Ekeu-wei and Blackburn, 2018, (and reference therein) for a larger review and additional details, Table 9.2 summarizes the peculiarities of most common global satellite DEMs.

3 EO-based monitoring of precipitation events

3.1 Center for Hydrometeorology and Remote Sensing Data Portal

The Center for Hydrometeorology and Remote Sensing (CHRS) at the University of California, Irvine (UCI), recently developed a Data Portal (https://chrsdata.eng.uci.edu) for quick access to their products (Fig. 9.1). PERSIANN, PERSIAN—Cloud Classification System (PERSIANN-CCS), PERSIANN—Climate Data Record (PERSIANN-CDR), and PERSIANN Dynamic Infrared-Rain

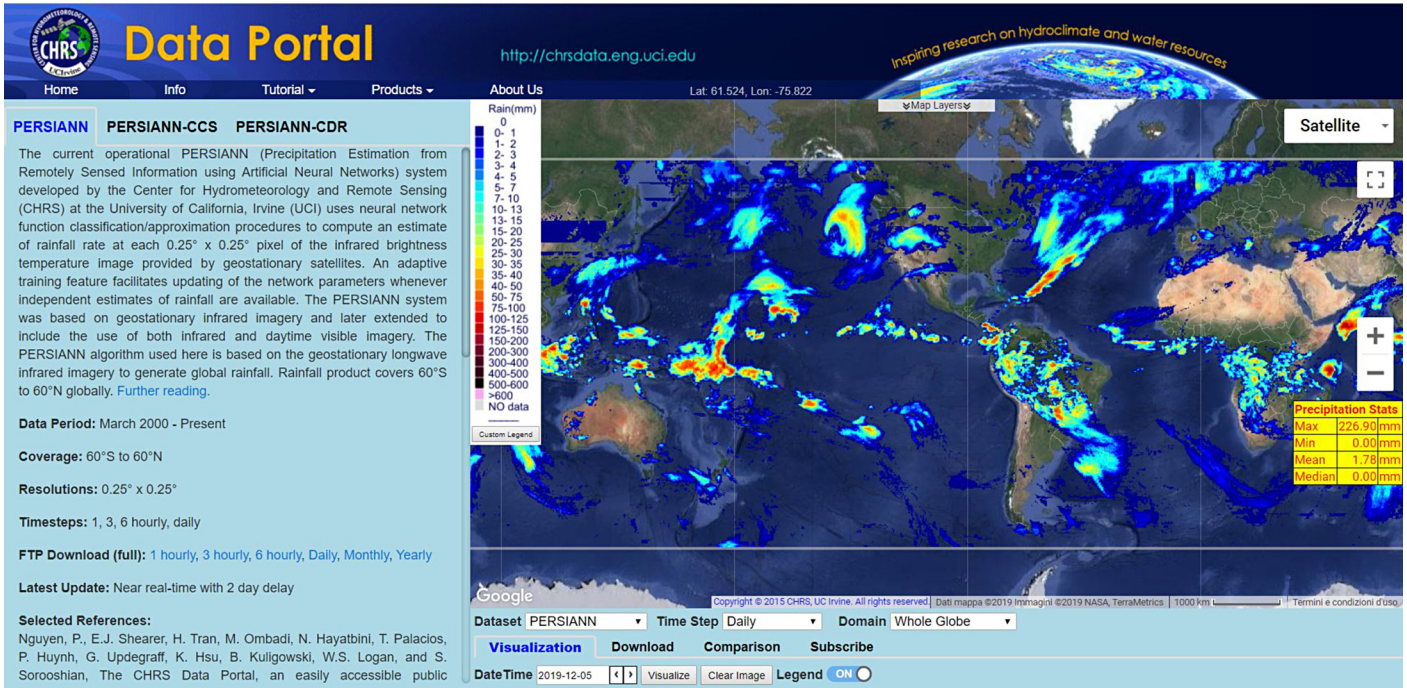

FIGURE 9.1 **Data Portal developed by The Center for Hydrometeorology and Remote Sensing (CHRS).**

rate model (PDIR) are customizable in their spatiotemporal extent and are available for visualization, download, comparison, and subscription (Nguyen et al., 2019a).

The Comparison tool implemented in the Data Portal compares PERSIANN datasets with other external datasets directly available on the data repository, generates a downloadable report of the characteristics of each dataset and establishes direct numerical and graphic comparisons between them (Nguyen et al., 2019a).

The Portal gives access also to other services, like iRain (https://irain.eng.uci.edu), a data visualization platform. iRain was originally developed to provide information based on PERSIANN-CCS. The new update is instead based on PDIR. Rain totals are available for different time intervals: 3, 6, 12, 24, 48, and 72 hours. A 3-hour rain animation over the past 72 hours is also accessible. A spatial query allows to access additional statistics over specific areas selected by the user. Moreover, iRain identifies and tracks extreme precipitation events globally (Fig. 9.2). Every extreme event is characterized by a short report containing storm statistics like maximum rainfall intensity (mm/3 h), average rainfall intensity (mm/3 h), maximum accumulated rainfall, storm coverage area, total rain volume, storm duration, and storm status. By clicking on identified events, the user is able to visualize a 3-hour animation of every single event over the past 72 hours (both in terms of spatial evolution and accumulated rainfall). End-users can subscribe, using their email, and setup rainfall alerts after having chosen a rainfall intensity over a specific time period (i.e., a rainfall threshold) and a location.

Additional information (like radar or rain gauge measurements) is accessible where available (additional layers have partial coverage and are concentrated mainly in the United States of America).

A mobile app named "iRain UCI" is available for iOS and Android as a complement to the iRain website. Users can report local rainfall information as a supplement of CHRS data by means of a crowdsourcing functionality. Crowdsourced information is visible on iRain portal.

3.2 ITHACA Extreme Rainfall Detection System

The Extreme Rainfall Detection System (ERDS; http://erds.ithacaweb.org), developed and implemented by ITHACA, is a service for the monitoring and forecasting of rainfall events characterized by a global spatial coverage. ERDS is also an early-warning system (EWS) designed for the identification of extreme rainfall events, convective storms, tropical storms, and heavy rainfall induced by cyclones and hurricanes.

The system is currently performing two different analyses. The first one is a near real-time rainfall monitoring based on NASA GPM IMERG Early run half-hourly data, a near real-time product characterized by a $0.1° \times 0.1°$ spatial resolution, a quasi-global spatial coverage and a 4-hour latency (Huffman

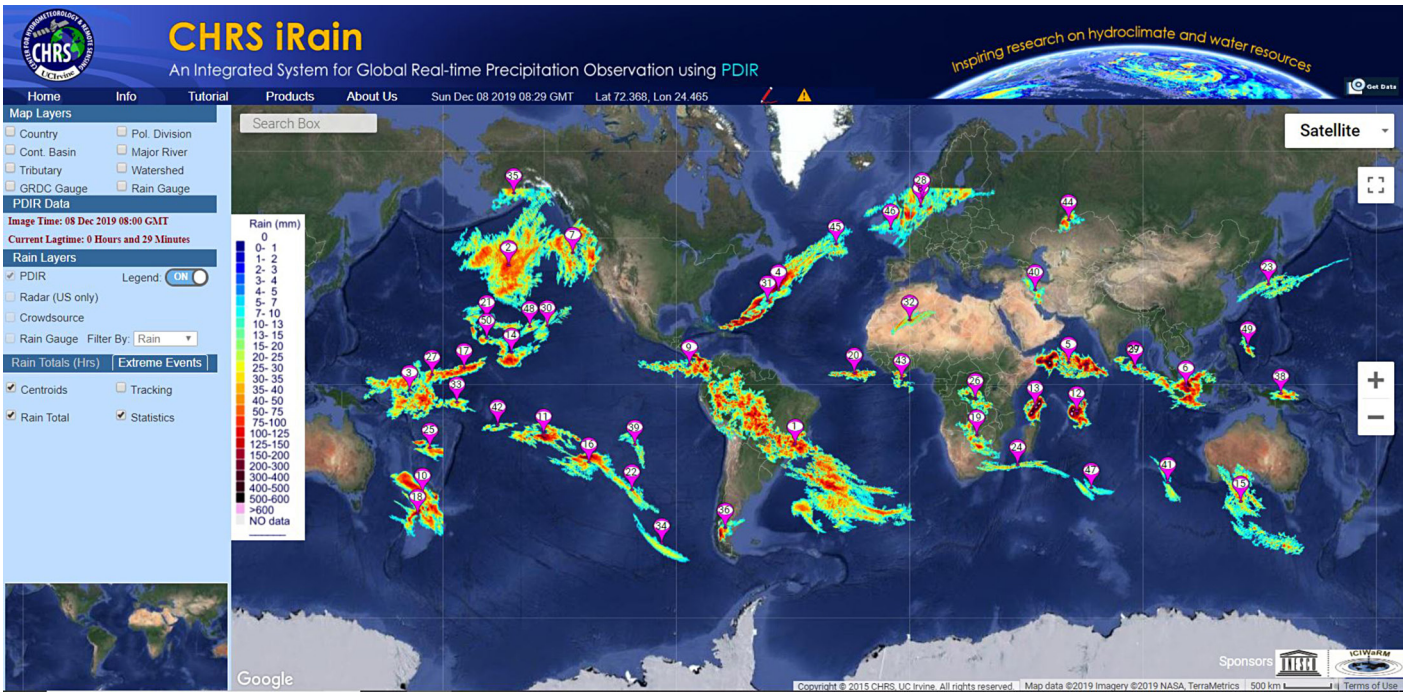

FIGURE 9.2 Example of extreme precipitation events identified by the iRain Data Portal, developed by The Center for Hydrometeorology and Remote Sensing (CHRS).

et al., 2019). Near real-time accumulated rainfall maps based on GPM are updated on an hourly basis. The second one, instead, takes advantages of the output of the Global Forecast System (GFS) deterministic weather prediction model, characterized by a 0.25° × 0.25° spatial resolution and a global spatial coverage (NCEP, 2015). GFS data are used to provide accumulated rainfall forecasts with a 12-hour update.

The extreme rainfall identification, performed at the same resolution of the input data, is based on the concept of activation threshold: an exceptional rainfall event is identified when the rainfall amount exceeds a specific threshold value (Mazzoglio et al., 2019a). Threshold values are data-dependent (values based on GPM data are different from the ones retrieved from GFS data), site-specific, and time-dependent (threshold values increase as the aggregation interval increases). The system is working using five different aggregation intervals (12, 24, 48, 72, and 96 hours). Shorter aggregation intervals would be characterized by a significant number of false alarms in the heavy rainfall identification, especially when GPM data are used (Mazzoglio et al., 2019a).

The outputs produced by ERDS are made available in two different formats through a WebGIS application (erds.ithacaweb.org). Specifically, the data can be downloaded in GeoTiff format, thus guaranteeing users to be able to view it in a geographic information system (GIS) environment and to use it for further analysis. The same data are also available through a Web Map Service (WMS), making them accessible even by non-expert users.

The system proved to provide reliable information based on GPM data (using the before mentioned aggregation intervals) for the near-real identification of heavy rainfall events characterized by duration greater than GPM latency (Mazzoglio et al., 2019a,b). It is important to highlight that the system may fail in the timely identification of intense rainfall events affecting small basins due to the combination of the coarse spatial resolution of satellite measurements and the latency in the availability of the data. The extreme rainfall detection performed using GPM data is in fact characterized by a 4-hour delay (due to GPM data latency plus the time required for data download and processing). Further studies aimed at developing a temporal and spatial downscaling of satellite precipitation measurements could contribute to offer a more accurate output, especially for localized heavy rainfall events.

The global accuracy evaluation of this EWS is currently undergoing. Fig. 9.3 shows the most affected areas, according to ERDS, during the heavy rainfall event that affected the South of Spain between September 11 and 14, 2019. The figure shows the number of alerts provided by ERDS, using GPM data as input and a 24-hour aggregation interval, compared to the Areas of Interest mapped by Copernicus Emergency Management Service (CEMS) in Rapid Mapping mode during the activation EMSR388—Flood in the Southeast of Spain. CEMS was triggered on September 12, 2019 at 13:37 UTC. Table 9.3, instead, shows the time of the first alert issued by ERDS. As reported in this table, the system was able to provide timely alerts over the most affected areas, especially when GFS data are used as input.

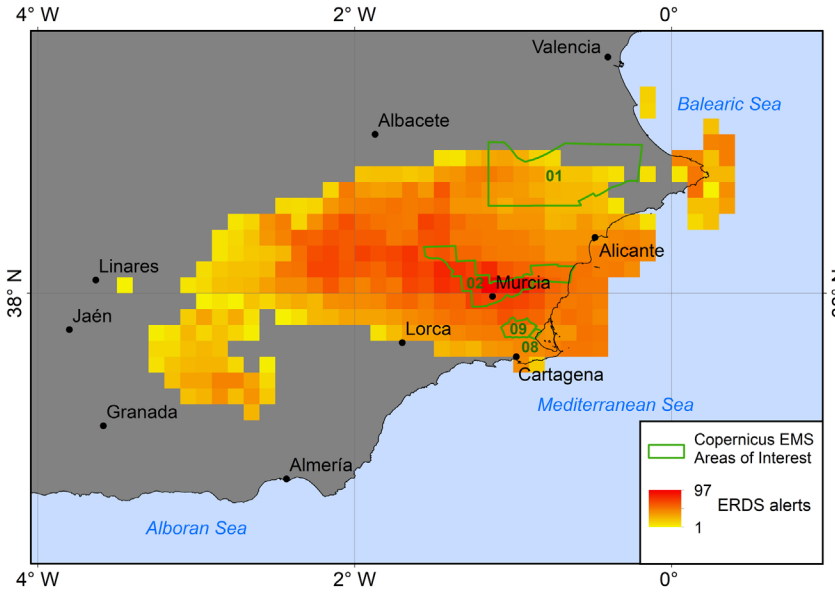

FIGURE 9.3 Numbers of alerts provided by ERDS from 11/09/2019 00:00 UTC until 16/09/2019 23:59 UTC using GPM data as input over a 24-hour aggregation interval, compared to the Areas of Interest mapped by Copernicus Emergency Management Service (2019 European Union), EMSR388.

TABLE 9.3 Date and time of the first alert provided by ERDS, using both GPM and GFS data as input.

Aggregation interval	First alert based on GPM data		First alert based on GFS data	
	Date	Time	Date	Time
12-hour	12/09/2019	08:00 UTC	12/09/2019	00:00 UTC
24-hour	12/09/2019	09:00 UTC	12/09/2019	00:00 UTC
48-hour	11/09/2019	23:00 UTC	11/09/2019	00:00 UTC
72-hour	12/09/2019	06:00 UTC	10/09/2019	00:00 UTC
96-hour	12/09/2019	07:00 UTC	no alerts	no alerts

4 Systems and hydrological models for flood monitoring

4.1 Dartmouth Flood Observatory—River and Reservoir Watch project

The Dartmouth Flood Observatory (DFO) monitors surface water across the globe for research, humanitarian, and water management applications. Among its several tools and projects, the River and Reservoir Watch (Version 3.7) allows to routinely survey surface water via satellite passive microwave sensors

(e.g., AMSR-E, AMSR-2, TRMM, and GPM) and measure river discharge changes on a daily basis across the entire globe at a 10 km grid resolution (Brakenridge et al., 2007; Van Dijk et al., 2016). The River and Reservoir Watch is a cooperative project between the University of Colorado, the GDACS-GFDS (Global Disaster Alert Coordination System-Global Flood Detection System; see Section 4.3 of this Chapter for more details) of the European Commission Joint Research Centre, the University of Alabama, and NASA's Jet Propulsion Laboratory (JPL).

Microwave sensors detect water and land areas at low and high emission, respectively. Thus, lower signals indicate increased water coverage. This satellite-observed signal is easily translated into discharge data (m^3/s) and surface runoff (mm/day) using site-specific rating equations. Similarly to stage-discharge rating curves applied at in-situ gauging stations, a rating equation, based either on a linear regression or a second-order polynomial, is applied to derive discharge from microwave emission. The microwave satellite-observed signal is provided by the Global Flood Detection System (GFDS). Overall, there are nearly 10,000 measurement sites across the globe, although only 334 sites are used and continuously monitored for the River and Reservoir Watch tool (i.e., the majority of them is poorly located or not even located on rivers). Discharge values are obtained from WBM global runoff models (Cohen et al., 2011), using a 5-year comparison (2003–2007) window for model calibration (i.e., WBM modeled monthly mean daily, maximum daily, and minimum daily discharges are compared against observed microwave emission; see also Brakenridge et al., 2012). A calibration by using in-situ gauging stations is also performed, where data are available (i.e., particularly across the United States). Each monitored site is provided with discharge and runoff data (available by clicking on each site display on the map at http://floodobservatory.colorado.edu/DischargeAccess.html) updated twice a day at 2:30 a.m. and 2:30 p.m. Local Denver Time. The River and Reservoir Watch tool allows monitoring river discharge values in near-real time, by detecting low-flow, normal-flow, moderate-flooding, and major-flooding conditions. Among many operational uses of these data, flood warnings and flood risk evaluation are the most relevant ones. The River and Reservoir Watch tool provides annual and monthly runoff values, and an evaluation of any trend in the 10-year recurrence interval flood over the period of record, thus easily allowing a clear detection in flood risk. In particular, extreme events, such as major floods, are identified as anomalies in a time series of discharge values at a given site by measuring the size of a flood event, namely by evaluating the number of standard deviations from the mean. For example, a flood magnitude equal to 2 identifies small and regular floods, whereas a magnitude of 4 represents large and unusual floods.

4.2 NASA's near real-time Global Flood Mapping product

Near real-time (NRT) Global Flood Mapping is a global-scale product developed at NASA Goddard's Hydrology Laboratory to timely and effectively

detect floods using available satellite data resources (https://floodmap.modaps.eosdis.nasa.gov/index.php).

This product uses Moderate Resolution Imaging Spectroradiometer (MODIS) instrument, onboard NASA's Terra and Aqua satellites, to provide twice a day (i.e., Terra and Aqua overpass the equator at 10:30 a.m. and 1:30 p.m. local solar time) high-resolution data at 250 m on surface water and flood water extent. LANCE (Land Atmosphere Near real-time Capability for EOS; https://lance-modis.eosdis.nasa.gov) system at NASA processes MODIS images and combines data from all orbits falling within a $10° \times 10°$ tile for each satellite, each day. Water is detected through an algorithm developed by the Dartmouth Flood Observatory, using a ratio of MODIS optical Band 1 and 2, and a threshold on Band 7, over a multi-day product window (i.e., 2-day, 3-day, and 14-day). A pixel is classified as MODIS Surface Water (MSW) if it is identified as water over at least 2 out of 4 (or 3 out of 6) observations, for the 2-day (or 3-day) composite. This multi-day water detection is needed to overcome issues with incomplete coverage (i.e., cloudiness) and cloud and terrain shadows, whose spectra incorrectly appear like water. A terrain shadow masking is now routinely applied to all products, thus eliminating this issue. A cloud shadow masking is applied, but only to single-day products. Detected surface water (MSW) is then compared against a reference layer showing permanent water (i.e., rivers, lakes, and oceans) to identify and isolate flood water surface. Namely, MSW pixels located outside the reference surface water layer are classified as MODIS Flood Water (MFW). The reference surface water layer (from NASA MODIS MOD44W) shows a few weaknesses (i.e., it is seasonally static and out of date in a few places), but it is the best available product at this stage. MSW and MFW do not present any indication of insufficient clear data to detect water extent, that is, less than 2 (or 3) clear observations in the 2-day (or 3-day) composite product. To overcome this deficiency, the MODIS Water Product (MWP) provides detailed information (Table 9.4). Despite some limitations (i.e., cloud and terrain shadows, dense vegetation, and limited detection of small floods) NASA NRT Global Flood Mapping is a powerful product comparable to the Dartmouth Flood Observatory River and Reservoir Watch project.

TABLE 9.4 NASA MODIS NRT Global Flood Mapping: MODIS Water Product description.

MODIS Water Product (MWP)	0	Insufficient data to make water determination (cloudy, missing images, swath gaps, or bad data values).
	1	No water detected.
	2	Water detected, coinciding with reference water, classified as "not flood".
	3	Water detected, beyond reference water, classified as flood.

While the River and Reservoir Watch project may have more accurate products as experts have been involved in building the flood extent maps, NRT Global Flood Mapping provides more timely products, generated automatically within several hours of satellite overpass, although not checked for errors.

4.3 Global Disaster Alert Coordination System

The Global Disaster Alert Coordination System (GDACS; www.gdacs.org) is a cooperation framework between the United Nations and the European Commission developed in order to provide timely alerts and facilitate information exchange in the first phase after major disasters. The system collects near real-time information to provide multi-hazards disaster alerting for earthquakes, tsunamis, tropical cyclones, floods, and volcanoes. Moreover, GDACS provides access to coordination tools and operational services, like the Global Flood Detection System (GFDS; www.gdacs.org/floodmerge).

GFDS is an experimental system that provides daily detection of major riverine floods at a spatial resolution of $0.09° \times 0.09°$ using passive microwave satellite observations (Revilla-Romero et al., 2015). The technique was originally developed at the Dartmouth Flood Observatory and then it was modified at the Joint Research Centre (JRC) of the European Commission. The aim of GFDS is to provide high-frequency satellite-based flow information substituting the missing on-site gauging in many parts of the world (Kugler et al., 2007).

GFDS has used a different combination of passive microwave sensor since 1998 (Revilla-Romero et al., 2015). JAXA Advanced Microwave Scanning Radiometer 2 (AMSR2) and GPM passive microwave sensors are currently used to monitor surface water extent. In order to minimize the influence of clouds and local ground factors, brightness temperature (at a frequency of 36.5 GHz) measured by these sensors is normalized into a water signal that represents the amount of surface water in each pixel (Brakenridge et al., 2007). When a significant increase of the surface water is detected (compared to the reference value), the system flags it as flood and the flood magnitude is defined as the number of standard deviations above the long-term mean. This anomaly ranges from high positive values (as in the case of large flood events) to negative values (dry conditions). Because it adapts automatically to different land surface characteristics, this methodology has the capability to be applied systematically over the entire globe (Kugler et al., 2007).

4.4 University of Maryland's Global Flood Monitoring System

The Global Flood Monitoring System (GFMS; http://flood.umd.edu/; Wu et al., 2014) is an experimental scheme funded by NASA and developed at the University of Maryland. GFMS uses real-time TRMM Multi-satellite Precipitation Analysis (TMPA) and Global Precipitation Measurement (GPM) Integrated MultisatellitE Retrievals for GPM (IMERG) precipitation maps

as input to a hydrological model settled to provide a nearly global coverage (3-hour frequency within the range 50°N–50°S). The hydrological and flow-routing processes are modeled coupling the Variable Infiltration Capacity land surface model (VIC; Liang et al., 1994) with the recently developed physically based Dominant River Tracing Routing model (DRTR; Wu et al., 2012). VIC solves the full water and energy balances considering the subgrid heterogeneity of infiltration capacity for different land cover types and elevation bands, thus enabling a proper balance in terms of appropriate performance in runoff calculation and computational load at nearly-global scale (Wu et al., 2014). Hydrographic parameters for the runoff-routing scheme (e.g., drainage area, flow direction, channel width, and slope) are obtained at 1 km grid-cell resolution (Wu et al., 2012).

In addition to several hydrological variables (e.g., soil moisture, evapotranspiration, etc.), the GFMS provides an estimate of the expected discharge (m^3/s) and the surface water storage (routed runoff), namely the water depth (mm) above dry ground of each computational cell, which is used for defining whether a cell is flooded or not, based on statistical thresholds. Global maps available online show the spatial distribution of the natural surface water constrained in the river channels and overflowing in flood-prone areas. In particular, the inundation map at a given time (updated every 3 hours) is defined as the amount of the routed runoff at the net of the referential water coverage (i.e., the 95th percentile value map of the surface storage estimate retrieved by means of an extended model retrospective simulation; see Wu et al., 2012 for additional details). A cell is considered flooded once the water depth is larger than 10 mm. The current version of GFMS does not consider man-made constructions interfering with the natural river systems (such as dams, embankments, retentions areas). Finally, in addition to real-time flood estimation and monitoring, the system can provide short-term (4–5 days) flood forecasting at 1/8th degrees spatial resolution by referring to numerically predicted precipitations (e.g., GEOS-5; (Molod et al., 2012)). Maps of the cumulated rainfall observed from satellite during last 1–3 and 7 days are also provided.

The GFMS has been evaluated by means of a retrospective simulation carried out over a 15-year period (1998–2012) for which a large dataset of gauge streamflow observations (more than 1000; from Global Runoff Data Centre—GRDC) and reported flood events across the globe (more than 2000; from Dartmouth Flood Observatory—DFO) were available. Using real-time precipitation dataset (i.e., TRMM TMPA), the system detected about 87% of flood events greater than 1-day duration across the globe. In general, better performances are obtained concerning longer duration events (3-day instead of 1-day events). In the light of the topographic limit (anthropic elements are not considered), the system works better in case of fewer dams: for 3-day events over basins with limited number of dams, the detection probability is nearly 0.9, while the false alarm ratio is 0.6. Validation performed with real-time precipitation across the tropics (30°S–30°N) shows a mean Nash-Sutcliffe Coefficient of 0.19 for 28%

of the gauging stations, while the performance rises up to 0.33 over 51% of the same gauges considering a monthly scale (Wu et al., 2014).

Concluding, the GFMS represents a suitable tool for many international relief and water management agencies (such as, UN World Food Program, national and regional security agencies in developing countries) since it is capable of providing real-time (as well as short-term forecasts) publicly available flood estimate for a large part of the globe.

5 Conclusions

Publicly-available EO datasets, tools for direct monitoring of extreme hydrometeorological events and hydrological models for flood monitoring based on satellite measurements were briefly reviewed in this chapter.

An overview of the characteristics of currently available EO datasets is reported in Section 2. Concerning the rainfall measurement from satellite, significant progress has been made in the last few years thanks to NASA/JAXA GPM mission. Nevertheless, an accurate high-resolution rainfall measurement from space is still a challenging problem. Efforts are required for increasing both the temporal/spatial resolution and the accuracy of global datasets. Perhaps, a higher spatiotemporal coverage is hindered by the continual loss of satellites due to ageing (Levizzani and Cattani, 2019). Good spatial and temporal resolutions of rainfall intensity are obtained using VIS/IR satellite observations. However, due to the intrinsic limits of the relationship between cloud brightness temperature and rainfall, it would be advisable to invest in increasing the number of passive microwave instruments. Smallsats (i.e., satellite of small size and mass, typically lower than 500 kg) are among the alternatives being explored (Levizzani and Cattani, 2019). These considerations are also valid for SAR missions: a greater number of SAR instruments could provide a shorter revisit time.

Concerning applied hydrology, the growing fidelity and resolution of remotely sensed datasets have fostered the development of techniques and modeling chains that attempt to forecast floods and droughts globally, which would not have been possible in the absence of remotely sensed precipitation data. Thanks to recent advances in numerical codes, processor speed and computing architecture, substantial progresses in the field of flood monitoring have been achieved.

Tools for the monitoring of extreme rainfall events by means of precipitation measurement performed by satellites were summarized in Section 3. Services like ITHACA Extreme Rainfall Detection System and CHRS iRain are able to identify extreme events with a global spatial coverage in near real-time. As additional not-EO-based features, a tracking analysis is performed by iRain, while ERDS integrates a near real-time monitoring with the output of a weather prediction model (i.e., GFS).

Systems and hydrological models for flood monitoring were finally reviewed in Section 4. As highlighted in Section 4.4, major limitation concerns man-made constructions not currently taken into account by global-scale flood mod-

els. When optical data are used as input, a multi-day water detection is needed to overcome incomplete coverage due to cloudiness and shadows, whose spectra incorrectly appears like water. However, several flood event types put a strain on available tools (many rivers should be monitored at a much smaller scale than the one that typically characterizes freely-available EO images with daily revisit time).

From an end-user perspective, some of these operational services might result not intuitive. Minimum technical prerequisites are often necessary for a conscious understanding of the outputs provided by the available systems. Moreover, the full potential of these tools could be explored only when their complete integration will be possible. In the wake of these considerations, to unlock the full potential for EO data in flood disaster response, Schumann et al. (2016) suggested a stronger collaboration between agencies, product developers, and decision-makers.

References

Alfieri, L., Cohen, S., Galantowicz, J., Schumann, G.J.P., Trigg, M.A., Zsoter, E., Prudhomme, C., Kruczkiewicz, A., Coughlan de Perez, E., Flamig, Z., Rudari, R., Wu, H., Adler, R.F., Brakenridge, R.G., Kettner, A., Weerts, A., Matgen, P., Islam, S.A.K.M., de Groeve, T., Salamon, P., 2018. A global network for operational flood risk reduction. Environ. Sci. Policy 84, 149–158. doi: 10.1016/j.envsci.2018.03.014.

Brakenridge, R.G., Cohen, S., Kettner, A.J., De Groeve, T., Nghiem, S.V., Syvitski, J.P.M., Fekete, B.M., 2012. Calibration of satellite measurements of river discharge using a global hydrology model. J. Hydrol. 475, 123–136. doi: 10.1016/j.jhydrol.2012.09.035.

Brakenridge, G.R., Nghiem, S.V., Anderson, E., Mic, R., 2007. Orbital microwave measurement of river discharge and ice status. Water Res. Res. 43, 1–16. doi: 10.1029/2006WR005238.

Brocca, L., Ciabatta, L., Massari, C., Moramarco, T., Hahn, S., Hasenauer, S., Kidd, R., Dorigo, W., Wagner, W., Levizzani, V., 2014. Soil as a natural rain gauge: Estimating global rainfall from satellite soil moisture data. J. Geophys. Res. Atmos. 119, 5128–5141. doi: 10.1002/2014JD021489.

Broxton, P.D., Zeng, X., Sulla-Menashe, D., Troch, P.A., 2014. A global land cover climatology using MODIS data. J. Appl. Meteorol. Climatol. 53, 1593–1605. doi: 10.1175/JAMC-D-13-0270.1.

Cohen, S., Alfieri, L., Brakenridge, G.R., Coughlan, E. Galantowicz, J.F., Hong, Y., Kettner, A.; Nghiem, S.V., Prados, A.I., Rudari, R., Salamon, P., Trigg, M., Weerts, A., 2017. Rapid-response flood mapping during Hurricanes Harvey, Irma and Maria by the Global Flood Partnership (GFP). AGU Fall Meeting Abstracts. adsabs.harvard.edu/abs/2017AGUFMNH23E2822C.

Cohen, S., Ketter, A.J., Syvitski, J.P.M., Fekete, B.M., 2011. WBMsed, a distributed global-scale riverine sediment flux model: Model description and validation. Comp. Geosci. 53, 80–93. doi: 10.1016/j.cageo.2011.08.011.

Collischonn, B., Collischonn, W., Tucci, C.E.M., 2008. Daily hydrological modeling in the Amazon basin using TRMM rainfall estimates. J. Hydrol. 360, 207–216. doi: 10.1016/j.jhydrol.2008.07.032.

Courty, L.G., Soriano-Monzalvo, J.C., Pedrozo-Acuña, A., 2019. Evaluation of open-access global digital elevation models (AW3D30, SRTM, and ASTER) for flood modelling purposes. J. Flood Risk Manag. 12, 1–14. doi: 10.1111/jfr3.12550.

Danielson, J.J., Gesch, D.B., 2011. Global multi-resolution terrain elevation data 2010 (GMTED2010). United States Geological Survey Open-File Report. doi.org/10.3133/ofr20111073.

Domeneghetti, A., Schumann, G.J.P., Tarpanelli, A., 2019. Preface: Remote sensing for flood mapping and monitoring of flood dynamics. Remote Sens. 11, 943. doi: 10.3390/rs11080943.

Ekeu-wei, I.T., Blackburn, G.A., 2018. Applications of open-access remotely sensed data for flood modelling and mapping in developing regions. Hydrology 5, 39. doi: 10.3390/hydrology5030039.

Farr, T.G., Rosen, P.A., Caro, E., Crippen, R., Duren, R., Hensley, S., Kobrick, M., Paller, M., Rodriguez, E., Roth, L., Seal, D., Shaffer, S., Shimada, J., Umland, J., Werner, M., Oskin, M., Burbank, D., Alsdorf, D., 2007. The Shuttle Radar Topography Mission. Rev. Geophys. 45, RG2004. doi: 10.1029/2005RG000183.

Hawker, L.P., Rougier, J., Neal, J.C., Bates, P.D., Archer, L., Yamazaki, D., 2018. Implications of simulating global digital elevation models for flood inundation studies. Water Resour. Res. 54, 7910–7928. doi: 10.1029/2018WR023279.

Hong, Y., Hsu, K.L., Sorooshian, S., Gao, X., 2004. Precipitation estimation from remotely sensed imagery using an artificial neural network cloud classification system. J. Appl. Meteorol. 43 (12), 1834–1852. doi: 10.1175/jam2173.1.

Hsu, K.L., Gao, X., Sorooshian, S., Gupta, H.V., 1997. Precipitation estimation from remotely sensed information using artificial neural networks. J. Appl. Meteorol. 36, 1176–1190, doi.org/10.1175/1520-0450(1997)036 < 1176:PEFRSI > 2.0.CO;2.

Huffman, G.J., Adler, R.F., Bolvin, D.T., Gu, G., Nelkin, E.J., Bowman, K.P., Hong, Y., Stocker, E.F., Wolff, D.B., 2007. The TRMM Multisatellite Precipitation Analysis (TMPA): Quasi-global, multiyear, combined-sensor precipitation estimates at fine scales. J. Hydrometeorol. 8, 38–55. doi: 10.1175/JHM560.1.

Huffman, G.J., Bolvin, D.T., Nelkin, E.J., Tan, J., 2019. Integrated Multi-satellitE Retrievals for GPM (IMERG) Technical Documentation. Available from: https://pmm.nasa.gov/sites/default/files/document_files/IMERG_doc_190909.pdf (accessed 27.02.2020.).

Jilani, R., Munir, S., Siddiqui, P., 2017. Application of ALOS data in flood monitoring in Pakistan. In: Proceedings of the First PI Symposium of ALOS Data Nodes, Kyoto, Japan, 10 July 2017.

Joyce, R.J., Janowiak, J.E., Arkin, P.A., Xie, P., 2004. CMORPH: A method that produces global precipitation estimates from passive microwave and infrared data at high spatial and temporal resolution. J. Hydrometeorol. 5, 487–503, doi.org/10.1175/1525-7541(2004)005 < 0487:CAMTPG > 2.0.CO;2.

Kugler, Z., De Groeve, T., Brakenridge, G.R., Anderson, E., 2007. Towards a Near-Real Time Global Flood Detection System (GFDS). Proceedings of the Tenth International Symposium on "Psysical Measurements and Signatures in Remote Sensing" ISPMSRS07. Available from: https://www.isprs.org/proceedings/xxxvi/7-C50/papers/P37.pdf (accessed 27.02.2020.).

Levizzani, V., Cattani, E., 2019. Satellite remote sensing of precipitation and the terrestrial water cycle in a changing climate. Remote Sens. 11, 2301. doi: 10.3390/rs11192301.

Liang, X., Lettenmaier, D.P., Wood, E.F., Burges, S.J., 1994. A simple hydrologically based model of land surface water and energy fluxes for general circulation models. J. Geophys. Res. Atmos. 99, 14415–14428. doi: 10.1029/94JD00483.

Matgen, P., Hostache, R., Schumann, G., Pfister, L., Hoffmann, L., Savenije, H.H.G., 2011. Towards an automated SAR-based flood monitoring system: Lessons learned from two case studies. Phys. Chem. Earth 36 (7–8), 241–252. doi: 10.1016/j.pce.2010.12.009.

Mazzoglio, P., Laio, F., Balbo, S., Boccardo, P., Disabato, F., 2019a. Improving an extreme rainfall detection system with GPM IMERG data. Remote Sens. 11, 677. doi: 10.3390/rs11060677.

Mazzoglio, P., Laio, F., Sandu, C., Boccardo, P., 2019b. Assessment of an extreme rainfall detection system for flood prediction over Queensland (Australia). Proceedings 18, 1. doi: 10.3390/ECRS-3-06187.

Michaelides, S., Levizzani, V., Anagnostou, E., Bauer, P., Kasparis, T., Lane, J.E., 2009. Precipitation: Measurement, remote sensing, climatology and modeling. Atmos. Res. 94, 512–533. doi: 10.1016/j.atmosres.2009.08.017.

Molod, A., Takacs, L., Suarez, M., Bacmeister, J., Song, I.S., Eichmann, A., 2012. The GEOS-5 Atmospheric General Circulation Model: Mean Climate and Development from MERRA to Fortuna. In: Suarez, M.J. (Ed.), Technical Report Series on Global Modeling and Data Assimilation, vol. 28.

National Centers for Environmental Prediction/National Weather Service/NOAA/U.S. Department of Commerce, 2015. NCEP GFS 0.25 Degree Global Forecast Grids Historical Archive. Research Data Archive at the National Center for Atmospheric Research, Computational and Information Systems Laboratory, Boulder, CO. doi.org/10.5065/D65D8PWK (27.02.2020.).

Nguyen, P., Shearer, E.J., Tran, H., Ombadi, M., Hayatbini, N., Palacios, T., Huynh, P., Braithwaite, D., Updegraff, G., Hsu, K., Kuligowsli, B., Logan, W.S., Sorooshian, S., 2019a. The CHRS data portal, an easily accessible public repository for PERSIANN global satellite precipitation data. Sci. Data 6, 1–10. doi: 10.1038/sdata.2018.296.

Nguyen, P., Shearer, E.J., Ombadi, M., Gorooh, V.A., Hsu, K., Sorooshian, S., Logan, W.S., Ralph, M., 2019b. PERSIANN Dynamic Infrared-Rain rate model (PDIR) for high-resolution, real-time satellite precipitation estimation. Bull. Am. Meteorol. Soc. 101 (3), E286–E302. doi.org/10.1175/BAMS-D-19-0118.1.

Nikolopoulos, E.I., Anagnostou, E.N., Borga, M., 2013. Using high-resolution satellite rainfall products to simulate a major flash flood event in northern Italy. J. Hydrometeorol. 14, 171–185. doi: 10.1175/JHM-D-12-09.1.

O'Loughlin, F.E., Paiva, R.C.D., Durand, M., Alsdorf, D.E., Bates, P.D., 2016. A multi-sensor approach towards a global vegetation corrected SRTM DEM product. Remote Sens. Environ. 182, 49–59. doi: 10.1016/j.rse.2016.04.018.

Pakoksung, K., Takagi, M., 2016. Digital elevation models on accuracy validation and bias correction in vertical. Modeling Earth Syst. Environ. 2, 11. doi: 10.1007/s40808-015-0069-3.

Revilla-Romero, B., Thielen, J., Salamon, P., De Groeve, T., Brakenridge, G.R., 2014. Evaluation of the satellite-based Global Flood Detection System for measuring river discharge: influence of local factors. Hydrol. Earth Syst. Sci. 18, 4467–4484. doi: 10.5194/hess-18-4467-2014.

Revilla-Romero, B., Hirpa, F.A., Pozo, J.T.-D., Salamon, P., Brakenridge, R., Pappenberger, F., De Groeve, T., 2015. On the use of global flood forecasts and satellite-derived inundation maps for flood monitoring in data-sparse regions. Remote Sens. 7, 15702–15728. doi: 10.3390/rs71115702.

Robinson, N., Regetz, J., Guralnick, R.P., 2014. EarthEnv-DEM90: A nearly-global, void-free, multi-scale smoothed, 90 m digital elevation model from fused ASTER and SRTM data. ISPRS J. Photogramm. Remote Sens. 87, 57–67. doi: 10.1016/j.isprsjprs.2013.11.002.

Rodriguez, E., Morris, C.S., Belz, J.E., 2006. A global assessment of the SRTM performance. Photogramm. Eng. Remote Sens. 72, 249–260. doi: 10.14358/PERS.72.3.249.

Sampson, C.C., Smith, A.M., Bates, P.D., Neal, J.C., Alfieri, L., Freer, J.E., 2015. A high- resolution global flood hazard model. Water Resour. Res. 51, 7358–7381. doi: 10.1002/2015WR016954.

Schumann, G.J.P., Moller, D.K., 2015. Microwave remote sensing of flood inundation. Phys. Chem. Earth 83-84, 84–95. doi: 10.1016/j.pce.2015.05.002.

Schumann, G.J.P., Domeneghetti, A., 2016. Exploiting the proliferation of current and future satellite observations of rivers. Hydrol. Process. 30, 2891–2896. doi: 10.1002/hyp.10825.

Schumann, G.J.P., Frye, S., Wells, G., Adler, R., Brakenridge, R., Bolten, J., Murray, J., Slayback, D., Policelli, F., Kirschbaum, D., Wu, H., Cappelaere, P., Howard, T., Flamig, Z., Clark, R., Stough, T., Chini, M., Matgen, P., Green, D., Jones, B., 2016. Unlocking the full potential of Earth Observation during the 2015 Texas flood disaster. Water Resour. Res. 52, 3288–3293. doi: 10.1002/2015WR018428.

Simard, M., Pinto, N., Fisher, J.B., Baccini, A., 2011. Mapping forest canopy height globally with spaceborne Lidar. J. Geophys. Res. Biogeosci. 116, G04021. doi: 10.1029/2011JG001708.

Sun, Q., Miao, C., Duan, Q., Ashouri, H., Sorooshian, S., Hsu, K.L., 2018. A review of global precipitation data sets: data sources, estimation, and intercomparisons. Rev. Geophys. 56, 79–107. doi: 10.1002/2017RG000574.

Tachikawa, T., Hato, M., Kaku, M., Iwasaki, A., 2011a. Characteristics of ASTER GDEM version 2. Proceeding of 2011 IEEE International Geoscience and Remote Sensing Symposium (IGARSS), Vancouver, British Coumbia, pp. 3657–3660. doi:10.1109/IGARSS. 2011.6050017.

Tachikawa, T., Kaku, M., Iwasaki, A., Gesch, D.B., Oimoen, M.J., Zhang, Z., Danielson, J.J., Krieger, T., Curtis, B., Haase, J., Abrams, M., Carabajal, C., 2011b. ASTER Global Digital Elevation Model Version 2—Summary of validation results.

Tadono, T., Ishida, H., Oda, F., Naito, S., Minakawa, K., Iwamoto, H., 2014. Precise Global DEM Generation by ALOS PRISM. ISPRS Annals of Photogrammetry, Remote Sensing and Spatial Information Sciences. ISPRS Ann. Photogramm. Remote Sens. Spatial Inform. Sci. Volume II-4, 71–76. doi: 10.5194/isprsannals-II-4-71-2014.

Tan, M.L., Ficklin, D.L., Dixon, B., Ibrahim, A.L., Yusop, Z., Chaplot, V., 2015. Impacts of DEM resolution, source, and resampling technique on SWAT-simulated streamflow. Appl. Geogr. 63, 357–368. doi: 10.1016/j.apgeog.2015.07.014.

Ushio, T., Sasashige, K., Kubota, T., Shige, S., Okamoto, K., Aonashi, K., Inoue, T., Takahashi, N., Iguchi, T., Kachi, M., Oki, R., Morimoto, T., Kawasaki, Z.I., 2009. A kalman filter approach to the global satellite mapping of precipitation (GSMaP) from combined passive microwave and infrared radiometric data. J. Meteorol. Soc. Japan 87 A, 137–151. doi: 10.2151/jmsj.87A.137.

Van Dijk, A.I.J.M., Brakenridge, G.R., Kettner, A.J., Beck, H.E., De Groeve, T., Schellekens, J., 2016. River gauging at global scale using optical and passive microwave remote sensing. Water Resour. Res. 52, 6404–6418. doi: 10.1002/2015WR018545.

Varga, M., Bašić, T., 2015. Accuracy validation and comparison of global digital elevation models over Croatia. Int. J. Remote Sens. 36, 170–189. doi: 10.1080/01431161.2014.994720.

Vicente, G.A., Davenport, J.C., Scofield, R.A., 2002. The role of orographic and parallax corrections on real time high resolution satellite rainfall rate distribution. Int. J. Remote Sens. 23, 221–230. doi: 10.1080/01431160010006935.

Voigt, S., Kemper, T., Riedlinger, T., Kiefl, R., Scholte, K., Mehl, H., 2007. Satellite image analysis for disaster and crisis-management support. IEEE Trans. Geosci. Remote Sens. 45 (6), 1520–1528. doi: 10.1109/TGRS. 2007.895830.

Wright, D.B., 2018. Rainfall information for global flood modeling. In: Schumann, G.J-P., Bates, P.D., Apel, H., Aronica, G.T. (Eds.), Global Flood Hazard. Wiley, pp. 17–42. doi:10.1002/9781119217886.ch2.

Wu, H., Adler, R.F., Tian, Y., Huffman, G.J., Li, H., Wang, J., 2014. Real-time global flood estimation using satellite-based precipitation and a coupled land surface and routing model Huan. Water Resour. Res. 50, 2693–2717. doi: 10.1002/2013WR014710.

Wu, H., Kimball, J.S., Li, H., Huang, M., Leung, L.R., Adler, R.F., 2012. A new global river network database for macroscale hydrologic modeling. Water Resour. Res. 48, W09701. doi: 10.1029/2012WR012313.

Xue, X., Hong, Y., Limaye, A.S., Gourley, J.J., Huffman, G.J., Khan, I.K., Dorji, C., Chen, S., 2013. Statistical and hydrological evaluation of TRMM-based Multi-satellite Precipitation Analysis over the Wangchu Basin of Bhutan: Are the latest satellite precipitation products 3B42V7 ready for use in ungauged basins? J. Hydrol. 499, 91–99. doi: 10.1016/j.jhydrol.2013.06.042.

Yamazaki, D., Ikeshima, D., Tawatari, R., Yamaguchi, T., O'Loughlin, F., Neal, J.C., Sampson, C.C., Kanae, S., Bates, P.D., 2017. A high-accuracy map of global terrain elevations. Geophys. Res. Lett. 44, 5844–5853. doi: 10.1002/2017GL072874.

Zwally, H.J., Schutz, B., Abdalati, W., Abshire, J., Bentley, C., Brenner, A., Bufton, J., Dezio, J., Hancock, D., Harding, D., Herring, B., Minster, B., Quinn, K., Palm, S., Spinhirne, J., Thomas, R., 2002. ICESat's laser measurements of polar ice, atmosphere, ocean, and land. J. Geodynam. 34, 405–445. doi: 10.1016/S0264-3707(02)00042-X.

Page left intentionally blank

Section 3

Emerging Applications and Challenges

Page left intentionally blank

Chapter 10

Emerging Remote Sensing Technologies for Flood Applications

Mónica Rivas Casado[a], Manoranjan Muthusamy[a,b], Abdou Khouakhi[a] and Paul Leinster[a]

[a]*School of Water, Energy and Environment, Cranfield University, Bedfordshire, United Kingdom;*
[b]*School of Geosciences, College of Science and Engineering, The University of Edinburgh, Edinburgh, United Kingdom*

1 Introduction

Remote sensing is now used in a wide range of flood risk management applications, which include emergency response, flood extent, and damage assessment, and the development of robust flood risk management strategies. Such applications rely on the use of flood models to predict the extent of the flooding for given storm events, as well as the velocity and depth of the water affecting flooded areas. Flood models generally rely on remote sensing data from multiple sources to generate model predictions. The rapid advancement in remote sensing monitoring and data collection over the last decade has facilitated modeling activities. For example, in England, high-resolution digital terrain models (DTMs) and digital surface models (DSMs) of up to 25 cm resolution are available free of charge from the Environment Agency (EA) (Environment Agency, inpress). In addition, NASA's Shuttle Radar Topography Mission (SRTM) has been providing a global 30 m resolution Digital Elevation Model (DEM) free of charge since 2015 (NASA, inpress). This increased availability of DEM together with other remote sensing data including aerial imagery from both air and space has facilitated the use of 2D flood modeling regardless of the source of the flooding.

The application of remote sensing data in flood modeling can broadly be divided based on: (1) flood types (i.e., pluvial, fluvial, and coastal); (2) model types (i.e., 1D and 2D); and (3) modeling phases (i.e., model calibration phase and model set up phase). Although 1D models are rarely used on their own for flood modeling, they are useful when building 1D-2D coupled hydrodynamic models. In Section 1.1, we provide an overview of the application of flood

Earth Observation for Flood Applications. http://dx.doi.org/10.1016/B978-0-12-819412-6.00010-9

modelling based on the different phases of the modeling process—model set-up and calibration. Then in Section 1.2, we discuss the application of remote sensing in flood damage and vulnerability assessments.

1.1 Remote sensing for flood modeling

1.1.1 Model setup

A 2D flood model typically requires products derived from remote sensing as input data, primarily DSMs and/or DTMs. The resolution of such products can vary from scales finer than 25 cm to scales coarser than 1 km depending on the flood types and spatial scale of the model. For example, in the case of pluvial modeling where detailed urban surface dynamics needs to be captured, the required resolution can be as small as a few centimeters. This accuracy can only be obtained using remote sensing data. For pluvial or coastal modeling, DEMs can be coarser depending on the terrain dynamics. In most cases, the accuracy and detail (resolution) of flood predictions depends upon the resolution of the DEM used to obtain the flood estimates. In addition to the terrain, waterbodies (e.g., rivers, canals, drainage network) also need to be represented in flood models. Depending on the complexity of the water bodies, it can either be directly represented in a DEM or by means of a 1D-2D coupled model which has the capability of representing waterbodies and associated structures. In a typical coupled model, waterbodies and the associated structures such as canals and drainage networks are represented in 1D to consider the overtopping/overflow aspects and are then coupled with a 2D model to predict the floodwater propagation over a surface.

Remote sensing is also used to characterize waterbody channels using primarily echo-sounding based bathymetry where sound pulses are used to measure water depth (Hellequin et al. 2003). Although originally developed for marine application, echo-sounding soon became useful in inland water measurements (Dost and Mannaerts, 2008; Kasvi et al., 2019). Laser-based remote sensing techniques such as LiDAR have also become widely used to measure inland water bathymetry (Abdallah et al., 2013; Kriechbaumer et al., 2016). These techniques have their limitations due to their cost and the influence of water clarity and movement on the measurements. However, due to the spatial coverage it is possible to achieve within limited time periods and the rapid technological advancements, they are widely used for inland and coastal bathymetry measurements.

Remote sensing can also be used to measure rainfall, one of the main inputs for pluvial flood modelling, using both active and passive techniques. Examples of active remote sensing include weather radar measurements (Wilson and Brandes, 1979; Thorndahl et al., 2017). Passive approaches to measure rainfall are possible at microwave and infrared wavelengths (Leijnse et al., 2007). Although ground-based point rainfall measurements are still widely used for flood modeling due to their high accuracy, remote sensing precipitation mea-

surements are preferred in large scale flood models (>10 km) as they provide greater aerial and temporal coverage. It has also become a common practice to use a merged rainfall product in flood modeling where ground-based point measurments and remote sensing measurements are combined to produce a better rainfall estimation using advanced Kriging methods such as spatio-temporal co-kriging (Sideris et al., 2014).

1.1.2 Model calibration

A major challenge with flood modeling is its calibration, especially for pluvial flood models. Typically pluvial flood depths are estimated from watermarks on buildings and structures if available and even where they are used, they are not always reliable measures. In fluvial flooding, water levels are usually calibrated by means of gauging stations. However, these measurements also become unreliable once the river is out of bank. Remote sensing therefore has an important role to play in calibrating and ground truthing flood models. Both flood extent and flood depths can be measured, although the latter is more challenging (Schumann et al., 2009).

Images taken by unmanned aerial vehicles (UAVs), aircraft and satellites in combination with classification algorithms can be used to calibrate flood extents. Examples of these data types include aerial photographs (Néelz et al., 2006), and Landsat (Khan et al., 2011), which are produced by either optical or microwave sensors. Microwave sensors, such as synthetic aperture radar (SAR) can penetrate through objects such as clouds and vegetation and provide clear images of the inundated area even during cloudy weather conditions. However, optical sensors, especially in the near infrared, are useful as they provide a clear distinction between water and land as these spectral bands are strongly absorbed by water, yet reflected by land.

Satellite data provides large area coverage, although the level of detail is limited. When higher resolution images are required, for example, to capture the flood dynamics in an urban environment, manned and unmanned aircraft systems (UAS) are preferred. UAS are emerging as an important means of providing high resolution data under challenging environmental conditions in a cost effective way.

As floodwater is often muddy and carrying debris, it is challenging and in some cases impossible to measure floodwater depths using remote sensing methods.

1.2 Remote sensing for the assessment of flood damages and vulnerability

Regardless of flood type, remote sensing data, mostly aerial images, can be used to assess flood damage (Klemas, 2015). As discussed in Section 1.1.2, these data can be collected from space or the air. Flood damage is generally assessed by comparing aerial images of the flooded area before and after an event. This

FIGURE 10.1 Land use flood depth map obtained by overlaying predicted 2D flood inundation map and land use map—Storm Desmond floods (5–6/12/2015), Cockermouth, Cumbria, United Kingdom. Attribution statement: Contains OS data © Crown Copyright and database.

information can be used in combination with other data such as predicted flood maps or ground-based damage surveys (e.g., door-to-door surveys) to provide a better estimation of the damage. Further, by overlaying predicted 2D flood maps onto land use maps, damage for each land use type can be estimated. The map in Fig. 10.1 indicates the flood depth estimations for different land use types for the market town of Cockermouth (England). Flood vulnerability can be assessed in a similar way using a flood map together with population data and other vulnerability measures. The vulnerability of other land use types such as roads and farmland can also be assessed using a flood map and corrosponding vulnerability measures.

Loss adjusters within the insurance sector typically use flood risk models to estimate the damage caused by a flood event to individual properties. Financial algorithms were used by Rivas et al. (2018) to calculate the direct tangible losses to residential properties based on data collected using UAS. The high resolution imagery enabled the identification of damaged goods that were deposited outside households as a consequence of a flood event. Visual inspection of the imagery enabled an assessment to be made of the locations within the town where properties had been affected by the flooding and the relative impact on each household. The financial algorithms were based on multiple variables, including: house type (e.g., terraced, bungalow), house age (i.e., historic period), and flood depth. The derived losses for the market town of Cockermout were estimated to be £10 million within the surveyed area. The information obtained from the combined use of remote sensing and flood modeling could be used to

further inform flood risk management measures such as the best locations for property level flood resilience and resistance approaches.

2 Extending the use of emerging remote sensing technologies

This section provides examples from the literature and ongoing work on the novel applications of remote sensing in relation to physically-based modeling and machine learning (ML). The examples for physically-based models mainly use freely available remote sensing data in the United Kingdom. The ML section provides examples from the literature of recent developments.

2.1 Remote sensing data in physically-based flood modeling

2.1.1 Remote sensing methods for flood type identification (Muthusamy et al., 2019)

Many flood events are caused by more than one type of flooding, for example, fluvial, pluvial, and coastal. It is therefore important when assessing the most appropriate mitigation measures to understand better the spatial extent, flood depth, and flood damage associated with the different sources. For example, the deployment of resources, during an event and the identification of evacuation routes, requires an understanding of the predicted spatial and temporal propagation of flooding from all sources. To capture the spatial and temporal dynamics of a flood event correctly requires the incorporation of all sources of flooding in the modeling process (Chen et al., 2010; Apel et al., 2016). Remote sensing data can be used effectively in combination with ground-based data to simulate and analyze composite flood events. In the following example, a conceptual remote sensing-based, integrated approach is used to model a composite flood event and allocate the damages to the different sources of flooding.

Cockermouth, a town located in Cumbria, United Kingdom, is historically known for fluvial flooding. The town center is located at the confluence of two rivers (Fig. 10.2). However, during recent flood events, including three in 2015, on more detailed analysis, it was evident that the town was also affected by pluvial flooding. In this study, a high-resolution DEM was produced for Cockermouth from a composite DSM and a DTM obtained from the EA (Fig. 10.2). Then, using this DEM, a 2D flood model was developed in HEC-RAS (v5) 2D. The flood event caused by storm Desmond in 2015 (5–6/12/2015) was selected for this study. Simulations were carried out with and without a contribution from pluvial flooding to compare the difference in the properties affected by the flooding in terms of both flood area and flood depth. These models were also used to compare the fluvial and combined (pluvial and fluvial) flood damage areas for different land-use types. The numbers of residential properties affected by fluvial and combined flooding were then compared using a combination of modeled results and UAS data. Fig. 10.3 shows a comparison of the properties

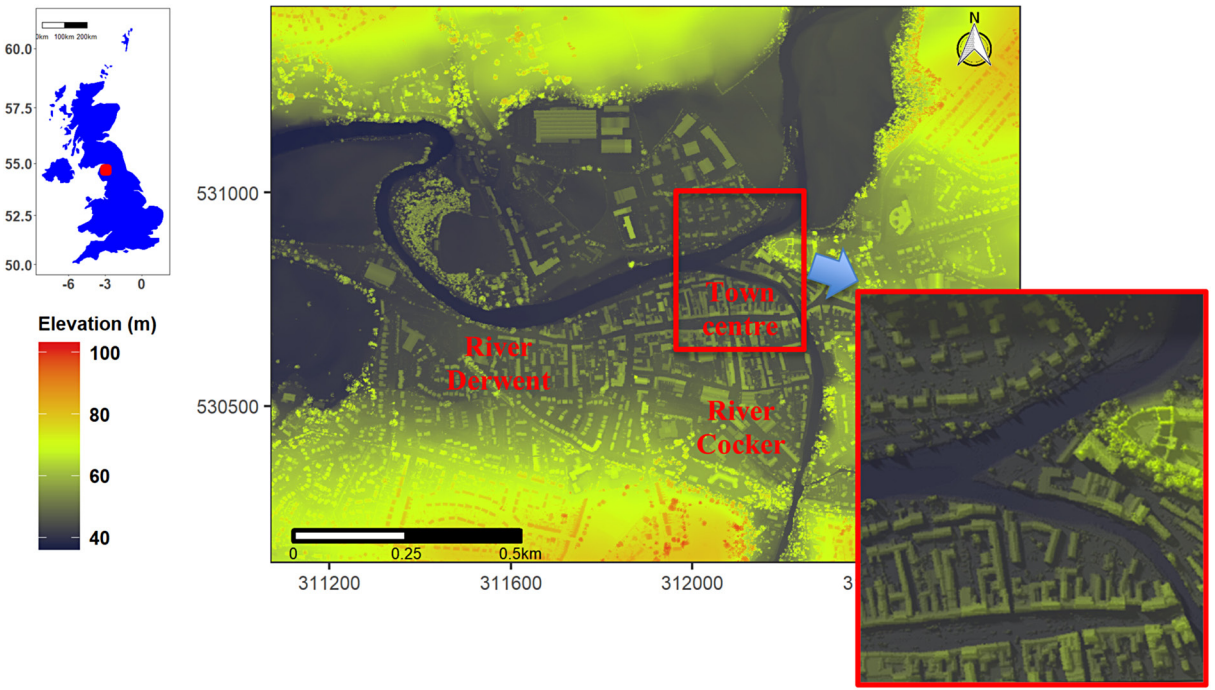

FIGURE 10.2 Digital Elevation Model (DEM) of the study site (Cockermouth, Allerdale, Cumbria, UK). Data collected by the Environment Agency (EA) in 2015; DEM derived from photogrammetry techniques applied to aerial imagery collected from aircraft. The zoomed window shows a 3D image of the river confluence and a part of the town center. *(Attribution statement: From Environment Agency copyright and/or database right 2019. All rights reserved (Environment Agency, inpress).)*

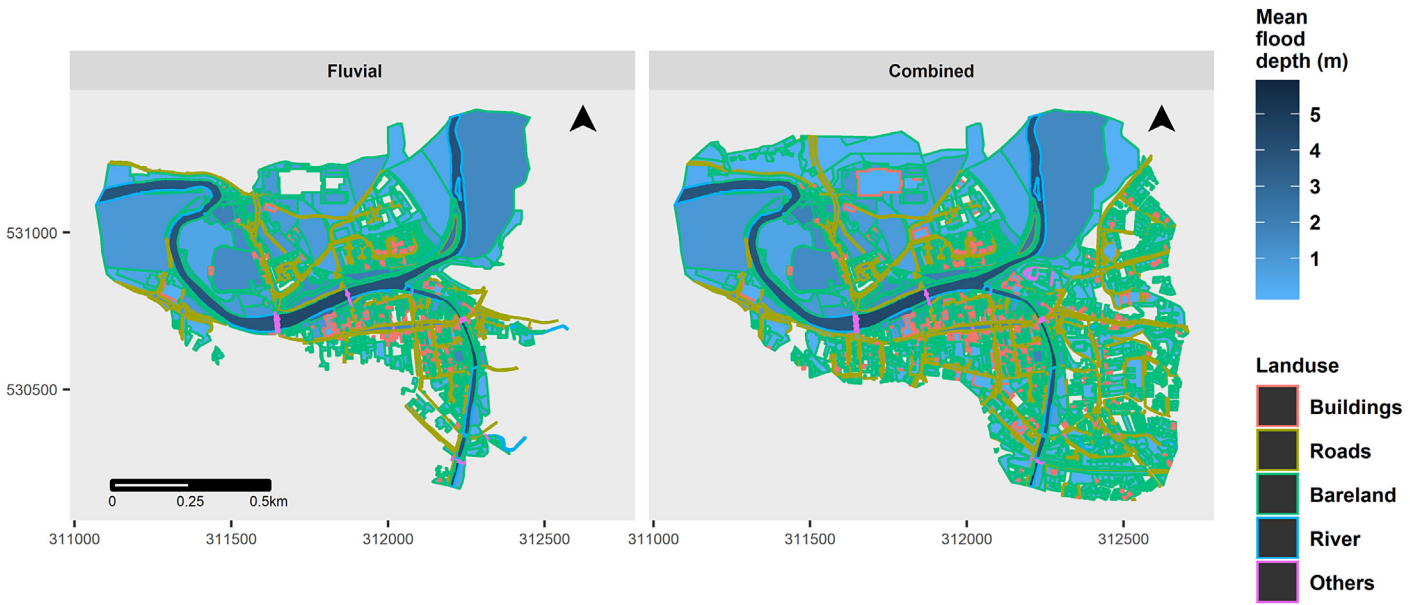

FIGURE 10.3 Flood depth (m) obtained from HEC-RAS (v5) 2D for fluvial flooding and combined (fluvial and pluvial) flooding scenarios, combined with land use map. *(Attribution statement: Contains OS data © Crown Copyright and database)*

impacted by fluvial and combined (pluvial + fluvial) flooding for different land use types.

This study demonstrates how remote sensing, hydrological modeling, and flood damage data at a property level can be used together to differentiate between the flood extents and damage caused by fluvial, pluvial, and combined fluvial and pluvial flooding in the same event. Most of the data used in this study were obtained via remote sensing methods, including aircraft, satellites, and UASs and demonstrates the benefits of developing a remote sensing-based framework to enhance the current practice in the estimation of flood extent and damage from different sources. This framework can also be extended to include real-time flood calibration/prediction by making use of remote sensing data collected as a flood propagates. However, such an extended framework needs to take into account the data and model processing times as real-time flood prediction cannot be based on time-consuming modeling processes. Section 2.2 discusses how this can be addressed using ML approaches, which have much faster processing times than physically based models such as the one used in this study.

2.1.2 Remote sensing to enhance flood modeling capabilities

DEM resolution plays a major role in the accuracy of flood modeling. The terrains in urban catchments are highly variable due to the buildings and infrastructure. The complexity of urban landscapes requires high-resolution DEMs sometimes as fine as a few centimeters. This is why most commonly used data such as the Shuttle Radar Topography Mission (SRTM) with a resolution of 30 m is not sufficient for small urban catchments. With such low resolution, drainage networks including small water courses, both natural and man-made, cannot be represented, which can result in an over-prediction of flood extent and depth (Ozdemir et al., 2013). However, with the advancement in remote sensing methods, such as Light Detection and Ranging (LIDAR) some countries provide higher resolution DEM. For example, in England, high-resolution DTM and DSM of up to 25 cm resolution are available free of charge from the EA (Environment Agency, inpress). With DEMs available at various resolutions, it is important to understand how the resolution of a DEM affects the flood modeling and the optimal resolution that is required to model a given catchment. Studies show that the effect of the DEM resolution in relation to the flood extent and depth calculated by a model depends on the flood type and the catchment characteristics (Saksena and Merwade 2015; Ozdemir et al., 2013). In the following example, the effect of DEM resolution on the pluvial flood modeling results was determined for Storm Desmond in Cockermouth using DEM resolutions of 1 and 50 m. The 1 m DSM and 1 m DTM obtained from the EA (Environment Agency, inpress) were used to generate both the 1 m and, by sub-sampling, the 50 m DEMs. These DEMs were then used to develop 2D fluvial flood models in HEC-RAS (v5) 2D for the study site. The results, as presented in Fig. 10.4, were compared to quantify the effect of different resolution DEMs. As the

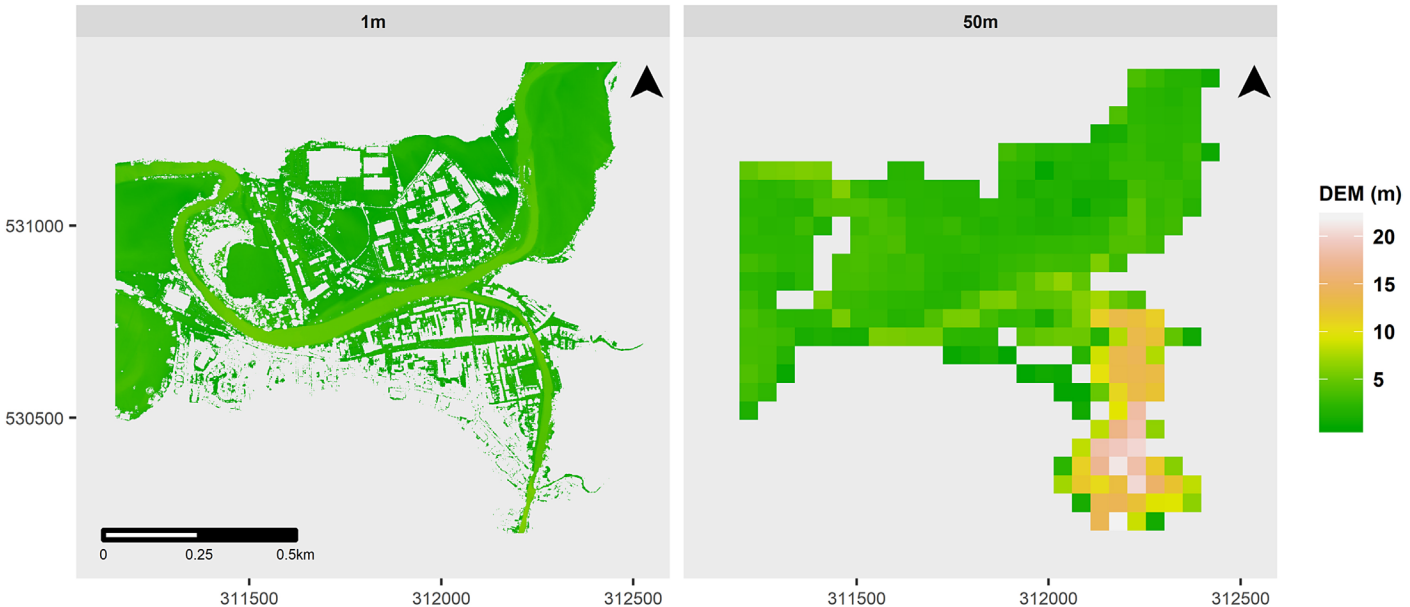

FIGURE 10.4 **Flood maps produced for different resolution DEM obtained from HEC-RAS (v5) 2D.**

resolution increases so does the majority of the flood depth estimations. The flood depths in the areas close to the River Cocker show the largest increase. The main reason for this is the increasing lack of definition of the river channel with an associated reduction in the depth of the river resulting in reduced river channel conveyance. This then leads to an increase in the flood extent and depth especially in the immediate vicinity of the river. The effect is not as marked for the River Derwent (Fig. 10.2) which is much wider than the River Cocker. Also many of the areas showing as not being flooded using the 1 m resolution DEM due to the influence of buildings are indicated as being flooded when using the 50 m resolution DEM as a result of the buildings being smoothed out

The approach outlined earlier can help decide what the optimal resolution is for a DEM in a particular type of topography and can be used in the design of data collection protocols for remote sensing. The results also demonstrate the importance of accurate representation of river channels and banks in 2D flood models. It may therefore be appropriate in some situations to use a composite DEM by merging a high resolution product for the river channel and banks with freely available lower resolution DEMs for the surrounding terrain.

2.2 Machine learning and remote sensing for flood applications

The application of ML including deep learning (DL) and remote sensing technologies in hydrology have shown remarkable potential in recent years. Remotely sensed data are increasingly being used to build ML models, for example, to predict flood risk in a specific area (e.g. Bui et al., 2019; Chapi et al., 2017) or to map flooded areas during a flood event (e.g. Feng et al., 2015; Sarker et al., 2019). The current upsurge of publicly accessible Earth Observation data (e.g., satellite imagery) and advancements in both computing technology and ML algorithms have provided powerful tools for use in flood risk management applications.

ML is a branch of artificial intelligence (AI), where processes automatically learn from past experience and act without being explicitly programmed to do so. A ML model relies on a broad range of input training data such as historical flood events and other associated data from multi-sensor satellites. The data often requires preprocessing and transformation. For example, predicting river flow would require structuring the data into input and output formats and scaling the datasets within a specific range. The data are then split into two subsets for training and testing, where the testing dataset might typically comprise about 80% of the data with the remaining 20% retained for testing. A ML model is trained and optimized using the training subset. A separate set of test data is then used to evaluate the model's performance. Following these testing steps, real-time data are fed into the model to make predictions (Fig. 10.5).

Many ML algorithms and architectures have been used in flood hydrology. Artificial neural networks (ANNs) are one of the most widely used algorithms for predicting both short- and long-term hydrological variables such as river

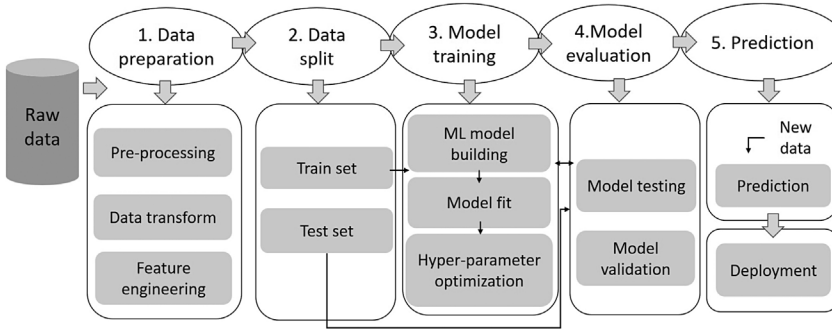

FIGURE 10.5 A simple machine learning (ML) pipeline.

flow discharge and flood levels (Maier and Dandy, 2000; Fahimi et al., 2017; Dawson and Wilby, 2001; Kim and Barros, 2001). Other commonly used algorithms include decision trees, support vector machines, and ensemble ML models such as random forest (Mosavi et al., 2018).

DL algorithms are another type of ML based on multilayer ANNs. DL has gained popularity in areas such as pattern recognition, object detection, and image classification. DL can be applied to regression problems such as predicting the value of flood discharge, or classification problems such as classifying flooded and non-flooded areas from imagery trained with predefined flood labels. For instance, Yang and Cervone (2019) used a large number of aerial photographs to train a DL model to classify rapidly flooded areas and assess flood damage. Another example involves the prediction of river discharge using deep recurrent neural networks (Le et al., 2019; Xiang et al., 2020).

ML and remote sensing data have been combined in a number of flood related applications including flood prediction (Kim and Barros, 2001; Shortridge et al., 2016; Zhou et al., 2018) flood risk assessment (Alipour et al., 2020; Bui et al., 2019; Chapi et al., 2017; Mojaddadi et al., 2017; Shahabi et al., 2020), and monitoring and mapping (Amitrano et al., 2018; Feng et al., 2015; Gebrehiwot et al., 2019; Ireland et al., 2015; Sarker et al., 2019).

ML models have been used extensively for flood prediction with varying predictive lead-times, often at the catchment scale. These models typically use multivariate datasets comprising meteorological, hydrometric, and catchment characteristics, and may include additional remotely sensed information such as soil moisture and land cover (Zhou et al., 2018; Shortridge et al., 2016; Kim and Barros, 2001). Other ML studies have used remote sensing products to extract flood conditioning factors (i.e., factors that have a relationship to flooding), such as slope, aspect, soil types, and other indices, in order to predict flood risk, damage, and flood susceptibility (Shahabi et al., 2020; Chapi et al., 2017; Alipour et al., 2020; Bui et al., 2019).

One rapidly emerging area of interest is coupling ML with physically-based (hydrologic and hydraulic) models. ML and remote sensing data can

be leveraged to increase the predictive power of such physically-based models, to correct their biases and improve model accuracy (Yang et al., 2019; Zhang et al., 2018; Ahmad et al., 2010; Puttinaovarat and Horkaew, 2020; Tian et al., 2018; Bui et al., 2019; Zhou et al., 2018).

Flood assessment and flood extent mapping is another key example where ML and DL are increasingly being used together with remotely sensed data. The growth of high-resolution satellite data and UAS imagery has generated large volumes of spatial data with high spatiotemporal resolution. Many recent studies have combined remote sensing and ML to identify flood extents, by classifying pixels into "flooded" and "not flooded" (Schnebele and Cervone, 2013; Feng et al., 2015; L. Yang and Cervone, 2019; Gebrehiwot et al., 2019; Ireland et al., 2015; Sarker et al., 2019). Remote sensing combined with ML can also be used in rapid flood damage assessments to help with disaster response (Li et al., 2018; Amitrano et al., 2018; Mojaddadi et al., 2017; Yang and Cervone, 2019).

In previous sections, we described the use of UASs in the village of Cockermouth to quantify flood damage (direct tangible losses) at residential property level and to differentiate the flood damages caused by fluvial, pluvial, and a combination of the two. This application could be further developed via the use of ML techniques by training a DL classifier to detect damage automatically within UAS images and the associated source of the flooding, fluvial or pluvial, in real time. Such an application requires the collection of UAS images that are processed and transmitted in real time. Current requirements for data collection and photogrammetric processing restrict the development of real-time applications when geomatic products (e.g., orthoimage or DEM) for the totality of the surveyed area are required. However, this limitation can be overcome by the on-board analysis of individual frames as soon as they are captured. Such applications will make a significant contribution to the rapid estimation of flood impacts. The approach could also be adapted to assist emergency responders identify flood evacuation routes.

3 Remote sensing and flood management

Effective flood risk management strategies require many organizations with different accountabilities and responsibilities to work together. In England, these are outlined in the National Flood Emergency Framework (Defra, 2014). These include the Department for Environment, Food and Rural Affairs (Defra), the EA, Lead Local Flood Authorities (LLFAs), and District Councils and Internal Drainage Boards (IDBs). Defra is responsible for Flood and Coastal Erosion Risk Management Policy. The EA, which is a Non-Departmental Publicly Funded Body, and the largest of the Defra group of organizations, is responsible for maintaining a strategic overview of all aspects of flooding. The LLFAs, which are the County and Unitary Councils, are responsible for developing and maintaining local flood risk management strategies. The EA is responsible for

addressing flood risk from main rivers, reservoirs, estuaries, and the sea, LLFAs for surface water and groundwater and District Councils and IDBs for ordinary water courses.

An effective flood risk management program has a number of components. These include: (1) the underpinning policy and governance arrangements, (2) flood risk assessments and plans that rely on intelligence from previous events, data, models, and maps, (3) a clear set of flood risk reduction measures such as property level resistance and resilience and catchment management measures and major flood risk management schemes, (4) operational and maintenance activities, (5) a reliable monitoring and forecasting program (e.g., weather), (6) spatial planning and development controls, (7) flood incident management and emergency response including rescue, and (8) recovery.

When localized flooding occurs in England, the response is lead by local emergency responders (Defra, 2010). For flood events that affect larger areas (lower level national flood events), the emergency response is coordinated and managed by Defra. Incidents which are classified as having a serious impact are coordinated by Defra through the Cabinet Office Briefing Room (A) (COBRA) whereas catastrophic events are coordinated by the Civil Contingencies Secretariat within COBRA (Defra, 2014).

Over the past 20 years, remote sensing technologies have been used increasingly in various aspects of flood risk management. These applications can be categorized in terms of their use as follows (Salmoral et al., 2020):

- before an event in developing DEMs, flood extent modeling, flood risk assessments, the design of new flood risk management schemes, identifying safe shelter points and evacuation routes, the condition of flood risk management assets and maintenance;
- in the period immediately prior to a flood event in flood forecasting and flood warning including assessing a need for the evacuation of people;
- during an event to inform responders about actual flood extents and depths, flood sources and routes, and whether these are as expected from models, whether evacuation routes remain clear, identifying blockages that need to be cleared, breaches in structures in need of repair, people in need of rescue and provision of emergency relief supplies;
- post-events as part of damage and impact assessments, the ground truthing of flood models and flood risk assessments, assessing the performance of flood risk management structures, and identifying the source of the flooding.

Remote sensing data has become a fundamental part of many flood risk management activities in the "before and post event" categories outlined earlier. The EA has established a specialist team (Geomatics) to carry out, oversee, and commission as appropriate, such work (Salmoral et al., 2020). This ensures the data is gathered and utilized in a structured way. They are also responsible for being aware of developments in remote sensing technologies that can be applied to the wider flood risk management activities in the EA.

Informed flood risk management decisions require a consistent approach, agreed methodologies and standards for geomatic products, catchment flood models, and the design of physical flood risk management schemes and structures. The use of non-standard remote sensing products and the associated derived flood extents and depths could result in sub-optimal decisions being taken with respect to the design, development, and operation of, and investment in, flood risk management measures. A central data acquisition team ensures that flood management can be carried out in an efficient and effective way. They then provide the remote sensing data, geomatic products, and underpinning data for others in the EA, partners and stakeholders to use.

Central coordination of data acquisition requires a detailed knowledge of how the information will be used before, during, and after an event and the impact of ambient conditions on the surveying process. For example, the use of remote sensing technologies during an event tends to be on a more ad-hoc basis and is affected by factors such as: deployment time, the scale, and duration of the flooding, the frequency with which repeat data can be obtained, whether there are multiple locations that need to be assessed, the resolution of the sensing system, the weather conditions, the timeliness in obtaining the outputs. Standardization of data collection under this varied range of underlying conditions is challenging and requires careful planning.

Similarly, there are challenges to the routine use of satellite and plane based remote sensing products during an event. Flooding associated with surface water and in rapid response catchments can occur and then subside in a matter of hours. This means that any technology used in support of such flood event response must be able to be deployed quickly. It is likely that they will need to be used by the emergency responders. Satellites and planes are unlikely to be able to be deployed in a timely manner to gather meaningful data to assist in the response.

In addition, satellites are not always over areas that are flooded and even when they are available, the data are only refreshed on a periodic basis. In addition, satellites and planes may not be able to provide data because of the prevailing weather conditions. It is therefore unlikely that emergency responders will want to rely on data sources that are intermittent and on occasions may not be available. For these reasons, UASs based remote sensing systems tend to be used during flood events.

UAS are readily available in the market and affordable, with a wide range of platforms suitable for different applications. They can be used by various organizations including the EA, the local council, emergency responders, and insurance companies. Often, they are used to provide images that can be streamed back to control rooms to inform and clarify situations and assist in their immediate tasks. Such images can be used in a range of ways including: strategic and tactical situation awareness; to check the extent and location of flooding; whether evacuation routes remain clear and safe shelter points available; to identify people at risk and those who are trapped, blockages in water ways, the need for maintenance activities; to assist identify and then repair breaches in

flood risk management structures; impacted buildings and infrastructure and damage assessment.

Although there are clear benefits in the collection of standardized remote sensing information, there is not an established framework in England to define how to use UASs and for what purpose before, during, and after a flood event and how best to disseminate the data and images collected. As a result, sometimes data contains underlying errors, missing information, or cannot be used for the objective for which it was gathered. Data and images that are collected during events will often be analyzed post–event, for example, to better understand flood extents and depths, property and infrastructure impacts, to ground truth flood models and flood risk assessments, to identify the sources of the flooding, and the performance of flood risk management structures. Such information is vital if the most appropriate flood risk reduction and mitigation approaches are to be implemented. Lack of consistency in UAS data potentially will result in sub-optimal management decisions. It is clear that a purpose driven and strategically coordinated approach is required to determine how best to use remote sensing approaches and technologies to inform flood risk management activities, including incident response. This will reduce duplication of effort and costs, ensure the timely capture of important data that can be used to inform current and future flood risk management activities and encourage the uptake of novel and disruptive technologies such as UAS.

References

Abdallah, H., Bailly, J., Baghdadi, N.N., Saint-Geours, N., Fabre, F., 2013. Potential of space-borne LiDAR sensors for global bathymetry in coastal and inland waters. IEEE J. Sel. Topics Appl. Earth Obs. Remote Sens. 6 (1), 202–216. doi: 10.1109/JSTARS. 2012.2209864.

Ahmad, Sajjad, Kalra, Ajay, Stephen, Haroon, 2010. Estimating soil moisture using remote sensing data: A machine learning approach. Adv. Water Resour. 33 (1)doi: 10.1016/j.advwatres.2009.10.008, Elsevier Ltd: 69–80.

Alipour, Atieh, Ahmadalipour, Ali, Abbaszadeh, Peyman, Moradkhani, Hamid, 2020. Leveraging machine learning for predicting flash flood damage in the Southeast US. Environ. Res. Lett. 15 (2) doi: 10.1088/1748-9326/ab6edd, IOP Publishing.

Apel, H., Martínez Trepat, O., Hung, N.N., Chinh, D.T., Merz, B., Dung, N.V., 2016. Combined fluvial and pluvial urban flood hazard analysis: Concept development and application to Can Tho City, Mekong Delta, Vietnam. Nat. Hazards Earth Syst. Sci. 16 (4), 941–961. doi: 10.5194/nhess-16-941-2016, Copernicus Publications.

Bui, D.T., Ngo, P.-T.T., Pham, T.D., Jaafari, A, Minh, N.Q., Hoa, P.V., Samui, P., 2019. A novel hybrid approach based on a swarm intelligence optimized extreme learning machine for flash flood susceptibility mapping. Catena 179, 184–196. doi: 10.1016/j.catena.2019.04.009.

Chapi, K., Singh, V.P., Shirzadi, A, Shahabi, H., Tien Bui, D., Pham, B.T., Khosravi, K., 2017. A novel hybrid artificial intelligePnce approach for flood susceptibility assessment. Environ. Model. Softw. 95, 229–245. doi: 10.1016/j.envsoft.2017.06.012, Elsevier Ltd.

Chen, A.S., Djordjević, S., Leandro, J., Savić, D.A., 2010. An analysis of the combined consequences of pluvial and fluvial flooding. Water Sci. Technol. 62 (7), 1491–1498. doi: 10.2166/wst.2010.486.

Dawson, C.W., Wilby, R.L., 2001. Hydrological modelling using artificial neural networks. Prog. Phys. Geogr. 25 (1), 80–108. doi: 10.1177/030913330102500104.

Defra, 2010. Flood and Water Management Act 2010. London, UK.

Defra, 2014. The National Flood Emergency Framework for England. London, UK.

Donato, A., Di Martino, G., Iodice, A., Riccio, D., Ruello, G., 2018. Unsupervised rapid flood mapping using Sentinel-1 GRD SAR images. IEEE Trans. Geosci. Remote Sens. 56 (6), 3290–3299. doi: 10.1109/TGRS. 2018.2797536.

Dost, R.J.J., Mannaerts, C.M., 2008. Generation of lake bathymetry using sonar, satellite imagery and GIS. In: Dangermond, J. (Ed.), Proceedings of the 2008 ESRI International User Conference: GIS, Geaography in Action, August 4-8, 2008, San Deigo, Florida. ESRI, Redmond, USA.

Environment Agency, inpress. "Environment Agency—Data."

Farzad, F., Yaseen, Z.M., El-shafie, A., 2017. Application of soft computing based hybrid models in hydrological variables modeling: A comprehensive review. Theor. Appl. Climatol 128 (3-4), 875–903. doi: 10.1007/s00704-016-1735-8.

Feng, Q., Liu, J., Gong, J., 2015. Urban flood mapping based on unmanned aerial vehicle remote sensing and random forest classifier-A case of Yuyao, China. Water (Switzerland) 7 (4), 1437–1455. doi: 10.3390/w7041437.

Gebrehiwot, A., Hashemi-Beni, L., Thompson, G., Kordjamshidi, P., Langan, T.E., 2019. Deep convolutional neural network for flood extent mapping using unmanned aerial vehicles data. Sensors (Switzerland) 19 (7), 1486. doi: 10.3390/s19071486.

Hellequin, L., Boucher, J., Lurton, X., 2003. Processing of high-frequency multibeam echo sounder data for seafloor characterization. IEEE J. Ocean. Eng. 28 (1), 78–89. doi: 10.1109/JOE. 2002.808205.

Ireland, G., Volpi, M., Petropoulos, G.P., 2015. Examining the capability of supervised machine learning classifiers in extracting flooded areas from Landsat TM imagery: A case study from a Mediterranean flood. Remote Sens. 7 (3), 3372–3399. doi: 10.3390/rs70303372.

Kasvi, E., Salmela, J., Lotsari, E., Kumpula, T., Lane, S.N., 2019. Comparison of remote sensing based approaches for mapping bathymetry of shallow, clear water rivers. Geomorphology 333, 180–197. doi: 10.1016/j.geomorph.2019.02.017.

Khan, S.I., Hong, Y., Wang, J., Yilmaz, K.K., Gourley, J.J., Adler, R.F., Brakenridge, G.R., Policelli, F., Habib, S., Irwin, D., 2011. Satellite remote sensing and hydrologic modeling for flood inundation mapping in lake Victoria Basin: Implications for hydrologic prediction in ungauged basins. IEEE Trans. Geosci. Remote Sens. 49 (1), 85–95. doi: 10.1109/TGRS. 2010.2057513.

Kim, G., Barros, A.P., 2001. Quantitative flood forecasting using multisensor data and neural networks. J. Hydrol. 246 (1–4), 45–62. doi: 10.1016/S0022-1694(01)00353-5.

Klemas, V., 2015. Remote sensing of floods and flood-prone areas: An overview. J. Coast. Res. 314, 1005–1013. doi: 10.2112/jcoastres-d-14-00160.1.

Kriechbaumer, T., Blackburn, K., Everard, N., Casado, M.R., 2016. Acoustic Doppler current profiler measurements near a Weir with Fish Pass: Assessing solutions to compass errors, spatial data referencing and spatial flow heterogeneity. Hydrol. Res. 47 (3)doi: 10.2166/nh.2015.095, Nordic Association for Hydrology.

Le, X.H., Ho, H.V., Lee, G., Jung, S., 2019. Application of long short-term memory (LSTM) neural network for flood forecasting. Water (Switzerland) 11 (7), 1387. doi: 10.3390/w11071387.

Leijnse, H., Uijlenhoet, R., Stricker, J.N.M., 2007. Hydrometeorological application of a microwave link: 2. Precipitation. Water Resour. Res. 43 (4) doi: 10.1029/2006WR004989, John Wiley & Sons, Ltd..

Li, Y., Martinis, S., Plank, S., Ludwig, R., 2018. An automatic change detection approach for rapid flood mapping in Sentinel-1 SAR data. Int. J. Appl. Earth Obs. Geoinf. 73, 123–135. doi: 10.1016/j.jag.2018.05.023.

Maier, H.R., Dandy, G.C., 2000. Neural networks for the prediction and forecasting of water resources variables: A review of modelling issues and applications. Environ. Model. Softw. 15 (1), 101–124. doi: 10.1016/S1364-8152(99)00007-9.

Mojaddadi, H., Pradhan, B., Nampak, H., Ahmad, N., Ghazali, A.H.B., 2017. Ensemble machine-learning-based geospatial approach for flood risk assessment using multi-sensor remote-sensing data and GIS. Geomatics Nat. Hazards Risk 8 (2), 1080–1102. doi: 10.1080/19475705.2017.1294113, Taylor & Francis.

Mosavi, A., Ozturk, P., Chau, K.-W., 2018. Flood prediction using machine learning, literature review. Water 10 (11), 1536. doi: 10.20944/preprints201810.0098.v1.

Muthusamy, M., Casado, M.R., Salmoral, G., Irvine, T., Leinster, P., 2019. A remote sensing based integrated approach to quantify the impact of fluvial and pluvial flooding in an urban catchment. Remote Sens. 11 (5), 577. doi: 10.3390/rs11050577.

NASA, inpress. "Shuttle Radar Topography Mission - Data."

Néelz, S., Pender, G., Villanueva, I., Wilson, M., Wright, N.G., Bates, P., Mason, D., Whitlow, C., 2006. Using remotely sensed data to support flood modelling. Proc. Inst. Civil Eng. Water Manag. 159 (1), 35–43. doi: 10.1680/wama.2006.159.1.35.

Ozdemir, H., Sampson, C.C., de Almeida, G.A.M., Bates, P.D., 2013. Evaluating scale and roughness effects in urban flood modelling using terrestrial LIDAR data. Hydrol. Earth Syst. Sci. 17 (10), 4015–4030. doi: 10.5194/hess-17-4015-2013, Copernicus Publications.

Puttinaovarat, S., Horkaew, P., 2020. Flood forecasting system based on integrated big and crowdsource data by using machine learning techniques. IEEE Access 8, 5885–5905. doi: 10.1109/ACCESS. 2019.2963819.

Saksena, S., Merwade, V., 2015. Incorporating the effect of DEM resolution and accuracy for improved flood inundation mapping. J. Hydrol. 530, 180–194. doi: 10.1016/j.jhydrol.2015.09.069, Elsevier B.V..

Salmoral, G., Casado, M.R., Muthusamy, M., Butler, D., Menon, P.P., Leinster, P., 2020. Guidelines for the use of unmanned aerial systems in flood emergency response. Water 12 (2), 521. doi: 10.3390/w12020521, MDPI AG.

Sarker, C., Mejias, L., Maire, F., Woodley, A., 2019. Flood mapping with convolutional neural networks using spatio-contextual pixel information. Remote Sens. 11 (19), 1–25. doi: 10.3390/rs11192331.

Schnebele, E., Cervone, G., 2013. Improving remote sensing flood assessment using volunteered geographical data. Nat. Hazards Earth Syst. Sci. 13, 669–677. doi: 10.5194/nhess-13-669-2013.

Schumann, G., Bates, P.D., Horritt, M.S., Matgen, P., Pappenberger, F., 2009. Progress in Integration of Remote Sensing–Derived Flood Extent and Stage Data and Hydraulic Models. Rev. Geophys. 47 (4) doi: 10.1029/2008RG000274, John Wiley & Sons, Ltd..

Shahabi, H., Shirzadi, A., Ghaderi, K., Omidvar, E., Al-Ansari, N., Clague, J.J., Geertsema, M., et al., 2020. Flood detection and susceptibility mapping using Sentinel-1 remote sensing data and a machine learning approach: Hybrid intelligence of bagging ensemble based on k-nearest neighbor classifier. Remote Sens. 12 (2), 266. doi: 10.3390/rs12020266.

Shortridge, J.E., Guikema, S.D., Zaitchik, B.F., 2016. Machine learning methods for empirical streamflow simulation: A comparison of model accuracy, interpretability, and uncertainty in seasonal watersheds. Hydrol. Earth Syst. Sci. 20 (7), 2611–2628. doi: 10.5194/hess-20-2611-2016.

Sideris, I.V., Gabella, M., Erdin, R., Germann, U., 2014. Real-time radar–rain-gauge merging using spatio-temporal co-kriging with external drift in the Alpine Terrain of Switzerland. Quart. J. R. Meteorol. Soc. 140 (680), 1097–1111. doi: 10.1002/qj.2188, John Wiley & Sons, Ltd.

Thorndahl, S., Einfalt, T., Willems, P., Nielsen, J.E., Veldhuis, M-.C., 2017. Weather radar rainfall data in urban hydrology. Hydrol. Earth Syst. Sci. 21 (3), 1359–1380. doi: 10.5194/hess-21-1359-2017.

Tian, Y., Xu, Y.P., Yang, Z., Wang, G., Zhu, Q., 2018. Integration of a parsimonious hydrological model with recurrent neural networks for improved streamflow forecasting. Water (Switzerland) 10 (11), 1655. doi: 10.3390/w10111655.

Wilson, J.W., Brandes, E.A., 1979. Radar measurement of rainfall—A summary. Bull. Am. Meteorol. Soc. 60 (9), 1048–1060. doi: 10.1175/1520-0477(1979)060<1048:RMORS>2.0.CO;2, American Meteorological Society.

Xiang, Z., Yan, J., Demir, I., 2020. A rainfall-runoff model with LSTM-based sequence-to-sequence learning. Water Resour. Res. 56 (1) doi: 10.1029/2019WR025326, e2019WR025326. https://doi.org/10.1029/2019WR025326.

Yang, L., Cervone, G., 2019. Analysis of remote sensing imagery for disaster assessment using deep learning: A case study of flooding event. Soft Comput. 23 (24), 13393–13408. doi: 10.1007/s00500-019-03878-8, Springer Berlin Heidelberg.

Yang, T., Sun, F., Gentine, P., Liu, W., Wang, H., Yin, J., Du, M., Liu, C., 2019. Evaluation and machine learning improvement of global hydrological model-based flood simulations. Environ. Res. Lett. 14 (11), 114027. doi: 10.1088/1748-9326/ab4d5e, IOP Publishing.

Zhang, D., Hølland, E.S., Lindholm, G., Ratnaweera, H., 2018. Hydraulic modeling and deep learning based flow forecasting for optimizing inter catchment wastewater transfer. J. Hydrol. 567, 792–802. doi: 10.1016/j.jhydrol.2017.11.029, Elsevier B.V..

Zhou, J., Peng, T., Zhang, C., Sun, N., 2018. Data pre-analysis and ensemble of various artificial neural networks for monthly streamflow forecasting. Water (Switzerland) 10 (5), 628. doi: 10.3390/w10050628.

Chapter 11

Earth Observations for Anticipatory Action: Case Studies in Hydrometeorological Hazards

Andrew Kruczkiewicz[a,b], Shanna McClain[c], Veronica Bell[d], Olivia Warrick[b], Juan Bazo[b,e], Jesse Mason[f], Humberto Vergara[g,h] and Natalia Horna[i]

[a]International Research Institute for Climate and Society, Earth Institute, Columbia University, Palisades, NY, United States; [b]Red Cross Red Crescent Climate Centre, The Hague, The Netherlands; [c]National Aeronautics and Space Administration, Washington, DC, United States; [d]Australian Red Cross, North Melbourne, VIC, Australia; [e]Universidad Tecnológica del Perú, Lima, Perú; [f]World Food Programme, Rome, Italy; [g]NOAA/OAR/National Severe Storms Laboratory, Norman, OK, United States; [h]Cooperative Institute for Mesoscale Meteorological Studies, University of Oklahoma, Norman, OK, United States; [i]Instituto Nacional de Meteorología e Hidrología Dirección de Estudios, Investigación y Desarrollo Hidrometeorológico, Quito, Ecuador

1 Introduction

As flooding and drought accounts for the majority of all global weather-related hazards, disaster risk reduction for hydrometeorological hazards receives significant attention (United Nations Office for Disaster Risk Reduction, 2018), however, impact profiles of hydrometeorological hazards vary significantly across type. For example, riverine floods occur near riverbanks and often in areas known to be at risk for flooding, while flash floods can be caused by extreme rainfall, dam or levee breaks, rapid and/or unplanned settlement, and/or mudslides and debris (Xia et al., 2011; Zaharia et al., 2017). For flash floods, rainfall intensity, location, topography, land cover, and land use (including soil type, vegetation, urban development) are each contributing factors, while presenting disparate challenges in risk model parameterization compared to riverine and coastal floods (Gallus, 1999; Zampieri et al., 2005; Georgakakos 2006). Furthermore, with increasing urbanization, flooding is leading to increased impact on lives and livelihoods, and one of the most common factors, both direct and indirect, in humanitarian emergencies that necessitate a large-scale response (Faccini et al., 2015; Cutter et al. 2018). In determining risk of impact from any

Earth Observation for Flood Applications. http://dx.doi.org/10.1016/B978-0-12-819412-6.00011-0

flood type, it is necessary to understand both the geophysical and non-geophysical factors (Wahl et al., 2015; Couasnon et al., 2020; Bevacqua et al., 2020). For example, some locations are at low risk of flooding from a geophysical perspective (e.g., spatial and temporal anomalies of inundated land), while socioeconomic factors such as the inability to evacuate due to health or low economic standing can significantly increase risk of impact when a flood occurs (Chakraborty et al., 2020).

In recent years, there has been growing momentum within the humanitarian and risk management communities to shift from disaster response to anticipatory action (or early action—in this chapter "anticipatory action" will address both terms)—the ability to provide critical support to at-risk communities prior to a disaster occurring (Stephens et al., 2015; Ruth et al., 2017). This is done through the development of predefined Standard Operating Procedures (SOPs), such as the Red Cross's Early Action Protocols (EAPs), that determine how to prioritize taking anticipatory actions to decrease the impact of disasters, such as floods, if and when a hydrometeorological forecast exceeds a given threshold of magnitude and probability (Coughlan de Perez et al., 2016). These thresholds are determined by reviewing historical disasters, including the magnitude of geophysical hazard and the associated impact on people, their assets, and/or their livelihoods. When triggered, a financial instrument is activated, automatically releasing funds for humanitarian anticipatory actions to minimize impact.

Fortunately, Earth observation (EO) data availability to support the understanding of hydrometeorological hazards and associated risk of impact is increasing, however data availability does not necessarily equate to discoverability, accessibility, and usefulness (Giuliani et al., 2017). EO can provide information on both the geophysical characteristics that drive flood and drought magnitude and impact, but increasingly they are providing the non-geophysical socioeconomic data that enables an improved understanding of vulnerability, infrastructure, and damage categorization, that in turn enhances the understanding of exposure (Muis et al., 2015). These dynamics are challenging even in the most data-rich contexts, while in data-sparse locations, including many fragile states and regions that are experiencing armed conflict, a robust understanding of them is near impossible (Mason et al., 2015). The ability to connect the humanitarian and EO communities and to convene dialog, presents opportunities for new types of sustainable partnerships and mutually beneficial engagement opportunities related to various hazards including hydrometeorological such as droughts, floods (Nauman et al., 2021) and landslides, tropical cyclones, heat waves and scenarios where multiple types of geophysical and non-geophysical hazards overlap in time and geographic areas.

2 Case study: flash flood anticipatory action in Ecuador

While operational anticipatory action systems (such as Forecast-based Financing from Red Cross and Start Network's Anticipation Window) for riverine floods exist, there has been significantly less progress in developing similar

systems for flash floods (Rohwerder, 2017; MacLeod et al., 2021). Providing accurate forecasts for the rainfall element of a flash flood forecast at sufficiently frequent temporal intervals is one of the primary challenges (Demeritt et al., 2010). Data assimilation at appropriate spatiotemporal scales also presents unique challenges specific to impact-based flash flood forecasting, in particular related to socioeconomic data elements (Hapuarachchi et al., 2011; Kruczkiewicz et al., 2018a). While these and other geophysical and socioeconomic challenges initially led to the de-prioritization of flash floods as a focus hazard, recently there has been increased interest within the humanitarian community to better understand the predictability of flash floods, the types of actions that can be taken to decrease their impact, and the appropriate lead times relative to develop an operational anticipatory action system (Nielsen et al., 2020).

Previous work on anticipatory action related to flash floods has identified various pathways forward. This includes the development of an approach inspired by riverine flood Forecast-based Financing (FbF), an anticipatory action approach initially developed by Red Cross Red Crescent Climate Centre, German Red Cross, The International Federation of Red Cross Red Crescent Societies (IFRC), and the World Food Programme (WFP). However, due to the lack of historical flash flood impact data, and availability of flash flood forecasts that are not necessarily "fit for purpose" to support anticipatory action (including FbF), the NASA GEO global flash flood risk project (Flash Flood Risk Project) has identified opportunities for flash flood FbF development at appropriate lead times which both allow for early action to take place, and account for the spatial and temporal constraints of a sufficiently skillful forecast. More specifically, a primary goal of the Flash Flood Risk Project is development of the first EAP for flash floods. Ecuador emerged as priority area to explore development of a national level EAP for flash floods for three primary reasons: (1) the strategic plan of the Ecuador Red Cross has identified flash floods as a priority hazard of interest, (2) Ecuador Red Cross and Instituto Nacional de Meteorología e Hidrología (INAMHI—The National Meteorological and Hydrological Service of Ecuador) is actively collaborating on hazards other than flash floods (Jokinen, 2019), (3) Ecuador has experienced a notable increase in flash flood risk in recent years (Morán-Tejeda et al., 2016).

The Ensemble Framework for Flash Flood Forecasting (EF5), used by the United States National Oceanic and Atmospheric Agency's National Weather Service for operational flash flood warnings, was identified as a potentially valuable process for understanding flash flood forecasting potential over Ecuador (Flamig et al., 2020). As an initial approach for describing the geophysical dynamics within the flash flood EAP development process, EF5 has been configured for Ecuador. Through a combination of Digital Elevation Model (DEM) data, HydroSHEDS data from NASA's Shuttle Radar Topography Mission (SRTM), and NASA's Integrated Multi-satellitE Retrievals for GPM (IMERG) data integrated into EF5, a range of flooding magnitudes can be understood (Lehner et al., 2008; Huffman et al., 2019). If not for EO, the project goals of both developing improved flash flood forecasts for streamflow and for impact

(and thus development of the EAP) would be at the least significantly more difficult and at most, not possible.

One of the key challenges identified from recent experiences with anticipatory action program development is that the trigger development process can differ significantly across organizations, geographic areas of interest, hazards and lead time, among other variables (Pichon, 2019). Further, the role of EO varies depending on the type of hazard, and thus also across flood types. However, bridging connections between EO and anticipatory action can offer opportunities to prioritize discussions around the ethical production of risk-informed products, their dissemination, and the accountability of the data provider in connection to decision makers in the field (Schumann, 2019). This work is ongoing as a collaborative effort between Ecuadorian Red Cross, INAMHI, Columbia University-IRI, University of Oklahoma, Red Cross Red Crescent Climate Centre, NASA, and the Group on Earth Observations.

Although regional or local geospatial datasets can be used to configure EF5, an objective of the Flash Flood Risk Project is to develop a process, which can potentially be used to extend flash flood FbF beyond Ecuador. EOs are, therefore, key in providing geospatial information readily available at the global scale. For example, DEM data and its derivatives are central to EF5's computational domain and mapping of its forecast products. HydroSHEDS (Lehner et al., 2008), which is mainly based on observations from NASA's SRTM, provides these datasets at various resolutions. Exploratory work has begun to assess the forecast value in using a higher pixel resolution than that of the 5-km global implementation of EF5 (Clark et al., 2017). Fig. 11.1 shows a comparison of flow accumulation at 1-km (Fig. 11.1A) and at 5-km (Fig. 11.1B), which depict the characterization of stream networks based on DEM at both pixel resolutions. Additionally, a-priori estimation of model parameters has been completed following the methodology described in Vergara et al. (2016) and Clark et al. (2017).

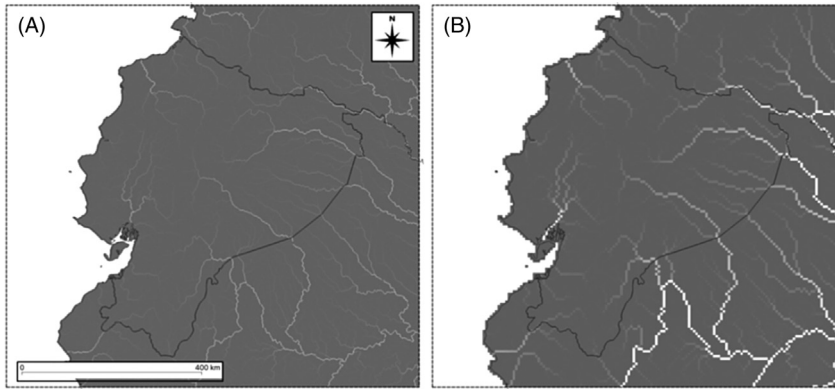

FIGURE 11.1 Flow accumulation grid used in EF5 at different pixel resolution. (A) 1-km and (B) 5-km.

A critical parameter in EF5 for describing a range of flooding magnitudes owing to different levels of human intervention to the land is the percentage of impervious surface. This parameter can be derived from the impervious surfaces dataset (Elvidge et al., 2007), based partially on NASA's MODIS land cover and SRTM (Gao et al., 2017). Last, and as the most important element in EF5, precipitation estimates are derived from NASA's Integrated Multi-satellitE Retrievals for GPM (IMERG; Huffman et al., 2019) product, which offers high spatiotemporal resolution with global coverage. The opportunity for iteration of EF5 implementation, and EAP development, beyond Ecuador elevates IMERG over other satellite-based products currently used in flash flood forecasting for potential application in both the same region (Leon et al., 2020) and in other regions (Alsumaiti et al., 2020; Ma et al., 2020; Saouabe et al., 2020).

While it is clear that EO has enabled the availability of data that could potentially be useful for anticipatory action systems (such as FbF), there are significant challenges that leave a gap between availability and use for decision making related to disaster risk reduction and resilience. The opportunity in creating EO-driven tools and derived data for integration within disaster management standard operating procedure lies in coupling novel technical approaches in EO data processing with novel partnerships. This coupling should be integrated within the roles and responsibilities of a "translator," "integrator,'" and/or "broker"—a person or people (or organization) that is tasked to understand the opportunities and constraints of each the geophysical, socioeconomic, and policy aspects of EA systems, to convene discussions, and to facilitate implementation. To that point, identifying and describing the specific roles and responsibilities for each partner has been key to the initial success of the Flash Flood Risk Project.

As the National Meteorological and Hydrological Service in Ecuador, INAMHI is responsible for issuing flash flood warnings and alerts, and in the context of the project, for sharing information on systems and processes to ensure that any project output is supporting their current policies and standard operative procedures and/or future goals. Further, they led analyses in various basins including: Francisco de Orellana (Coca), Cañar, and Zarumilla. These included a baseline study, assessment of extreme values, streamflow modeling, threshold definition, and real time analysis (Fig. 11.2) (Usamah et al., 2015; Manz et al., 2017). Conscious of the need to build-off of these previous studies, and with the possibility to broaden the study area, a group of experts from INAMHI's Hydrology, Climatology, Meteorology, and Modeling division designed the collaboration between the Ecuadorian Red Cross and the NASA GEO Global Flash Flood Risk Project. Through several meetings and a workshop, INAMHI presented a general overview of the information that is available for the model calibration and validation activities, which included an assessment of events detected by automatic hydrological stations (*http://186.42.174.236/HidroInamhiV2/Front-End/#*) in the Andes. With these ongoing efforts on policy and science related to flash flood risk, the first EAP for flash floods is progressing and is expected to be finalized in 2021.

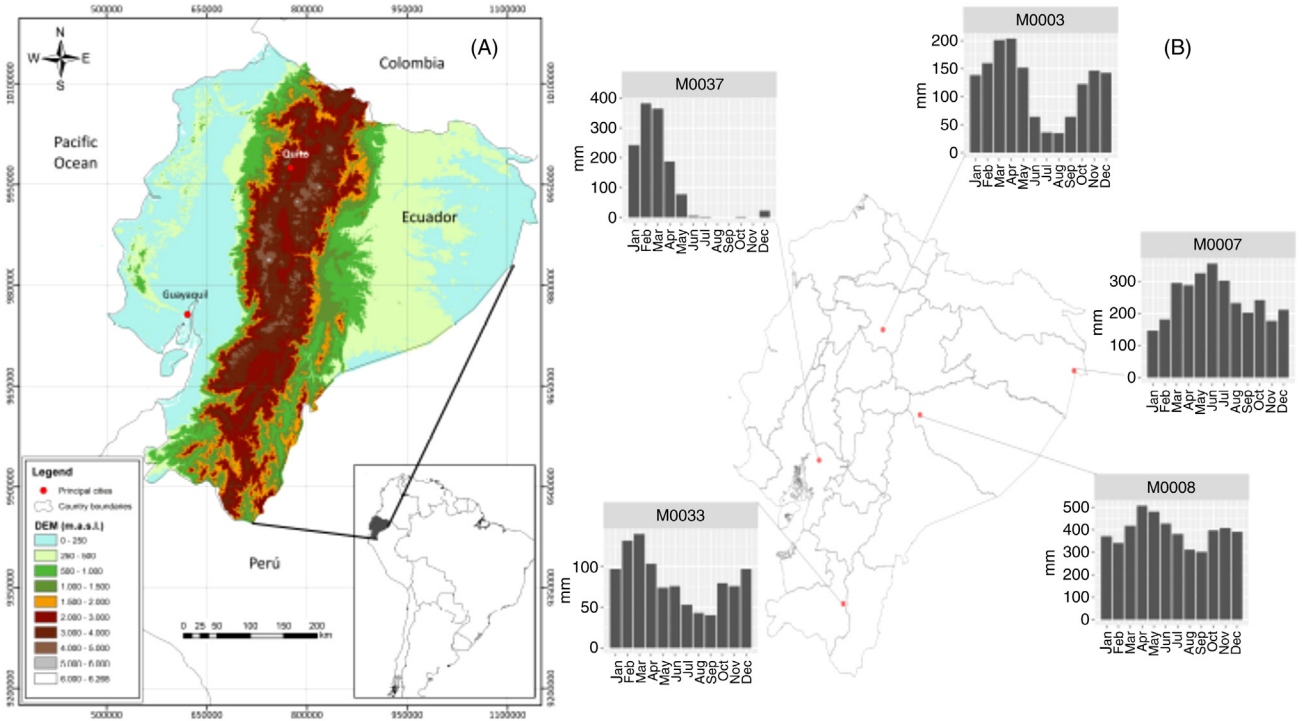

FIGURE 11.2 (A) Topographic map of Ecuador showing elevation. (B) Rainfall for five representative INAMHI meteorological stations. Rainfall is shown as a monthly average from 2000 to 2019.

3 Case study: intense rainfall anticipatory action and response in Peru

The Peruvian Red Cross National Society (PRC) has implemented an EAP for extreme rainfall. This EAP addresses flooding related to extreme rainfall during the summer months (between December and April), landslides, and riverine flooding due to overflow and failure of dikes. Anticipatory actions will be activated based on forecasts from The Multisectoral Committee for the National Study of El Niño (ENFEN) and the Peruvian National Meteorological and Hydrological Service (SENAMHI), which afford PRC a window of time to act before the extreme event begins (Aguirre et al., 2019). The EAP is developed for cross-timescale risk assessment and early action including seasonal, monthly, and weekly forecast-based triggers using the 90th and 95th percentiles as danger levels in seasonal and 5-day rainfall forecasts, respectively.

The EAP for extreme rainfall includes parameters derived from EO data, such as vegetation, historical precipitation data, and timing and spatial extent of historical flood events. These parameters informed the development of historical impact maps, which are essential for identifying which areas should be prioritized (and deprioritized) for the implementation of anticipatory actions (Ceccato et al., 2017). The main variables from EO that were used to develop the EAP are Normalized Difference Vegetation Index (NDVI) (derived from various sensors including from MODIS and the Landsat Program) and precipitation data from the Global Precipitation Measurement (GPM) V6. From 2000 to 2019, the mean annual precipitation values were calculated and historical floods were identified from Sentinel-2 through The Copernicus Emergency Management Service (Copernicus EMS). The analysis for the raw dataset was calculated in Google Earth Engine (GEE) and data processing was performed through QGIS. Fig. 11.1 shows the flood extension for the Piura River in March 2017, driven by the El Niño Costero (Coastal El Niño). All of the computational analysis was carried out by the Red Cross FbF team in Peru.

In addition to anticipatory action, EO has been useful in humanitarian response, such as during the 2017 El Niño Costero event in northern Peru (Son et al., 2020; McClain et al., 2021). After El Niño Costero driven floods, various agencies such as The Copernicus Programme, NASA, and ESA were activated during January to March 2017 (Novoa and Finer, 2017). The Civil Protection Agency of Peru reported 97 fatalities and 184,112 people affected, mostly in the cities of Piura, Trujillo, and Chiclayo. The main satellites that the Peruvian government used were from the European Satellite Agency (ESA) and other agencies, supported by Copernicus. A variety of SAR (synthetic aperture radar) sensors were used including RADARSAT-2 and TerraSAR-X and data from Sentinel missions 1&2, COSMOS-SkyMed, GeoEye-1, WorldView1, Deimos, and Pleiades (European Commission, 2017).

The experience gained through the efforts outlined in this case study could be adopted as a set of international best practices in support the Sendai Framework to augment existing capacities in using geospatial information and

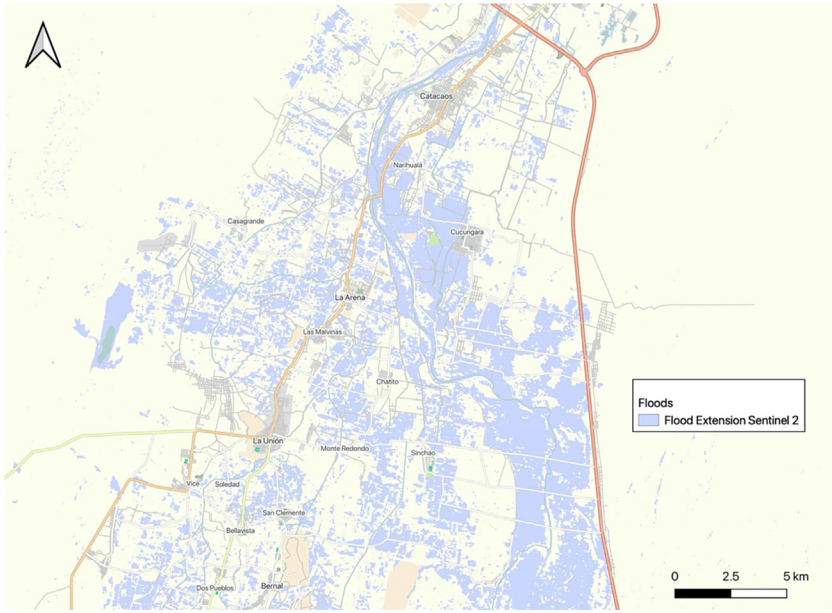

FIGURE 11.3 Flood extension map over March 2017 for flooding of the Piura River, Peru related to the El Niño Costero event. Calculated with Google Earth Engine using Sentinel 2. *(Peruvian Red Cross Forecast-based Financing team.)*

services across phases of disaster risk management related to flood risk and extreme rainfall (Whitcraft et al., 2019). The elements worth considering include the activities associated with the identification of spatial and temporal scales (including lead time) of interest from the humanitarian community, and subsequent activities around their integration within the trigger development process (Fig. 11.3).

4 Case study: the 2020 Southwest Pacific dry season and COVID-19

Many Pacific Islanders rely heavily on household and community rainwater harvesting and surface water for freshwater security (Hadwen et al., 2015). During the dry season (approximately May to October for most Pacific countries), careful water management and drinking water safety practices are essential to ensure clean water is consistently available to meet basic household needs (Elliott et al., 2017). This is particularly the case during anomalously dry periods where in some Pacific islands, as little as 10 days without rainfall can lead to failure of household rainwater harvesting systems (White, 2016). The dual risks of the water shortage and COVID-19 during the 2020 Southwest and Central Pacific dry season presented an unprecedented set of decisions around resource allocation for reducing risk.

EOs have begun to be used by Red Cross National Societies (NS) in the Pacific islands region to improve understanding of meteorological drought risk (Luchetti et al., 2016; Kelman, 2019). The COVID-19 global pandemic situation in 2020 increased the importance of ensuring sufficient, reliable, and safe household and community water supply in Pacific Islands. In early- and mid-2020, as the pandemic spread across the world, most Pacific Island countries remained free of COVID-19. From March 2020, Pacific NS began conducting hygiene campaigns and distribution of hand sanitizer, antibacterial soap, and disinfectant to limit risk of virus transmission.

COVID-19 risk reduction behavioral measures being promoted required reliable and safe water supply for hand-washing, general increased personal hygiene practices, and frequent disinfection of household surfaces. These behavior measures increased household water demand at a time when the threat of locations going into "lockdown" increased and travel was restricted between main and outer islands, rural areas, and urban centers. In a region where regular movement of family between communities and islands is common, these measures increased pressure on local water supply. As this period coincided with the South West Pacific dry season, IFRC Pacific Country Cluster Support Team (CCST) utilized EO derived seasonal rainfall forecasts to identify NSs in need of prioritized distribution of hand sanitizer, and funding for safe and secure drinking water programs and water hardware.

The Australian Community Climate Earth-System Simulator—Seasonal (ACCESS–S) is a dynamical forecast modeling system produced over a global domain, including the Pacific Islands region (Hudson et al., 2017). ACCESS-S uses ocean, atmosphere, ice, and land observations to initiate outlooks for the season ahead based on a 99-member ensemble, allowing for improved forecasts at various timescales including subseasonal (Gregory et al., 2020). The default ACCESS-S land and atmosphere model components operate at an approximate resolution of 60 km in the atmosphere and 25 km over the ocean, a significant improvement and opportunity to increase understanding of climate and climate impacts in the Pacific island region (Marshall and Hendon 2019). Outlooks derived from ACCESS-S are available at a subseasonal (weekly and fortnightly) and seasonal (1 month and 3 months) scale at multiple lead times (weeks/months before the forecast period).

To increase the value of these outlooks, IFRC worked with the Australian Bureau of Meteorology to develop a simple alert system, "Early Action Rainfall Watch" (EAR Watch), for anomalously dry and wet conditions early warning across Pacific island countries and divisions. Graduated alerts represent a combination of (1) the probability of drier, near normal or wetter than normal conditions (tercile probability method) in the upcoming 3-month period and (2) skill using the Linear Error in Probability Space (LEPS) method, alert 3 being high likelihood (Fig. 11.4).

The ACCESS-S-derived EAR Watch provides greater coverage than previous methods which used a statistical model providing outlooks for specific in-situ

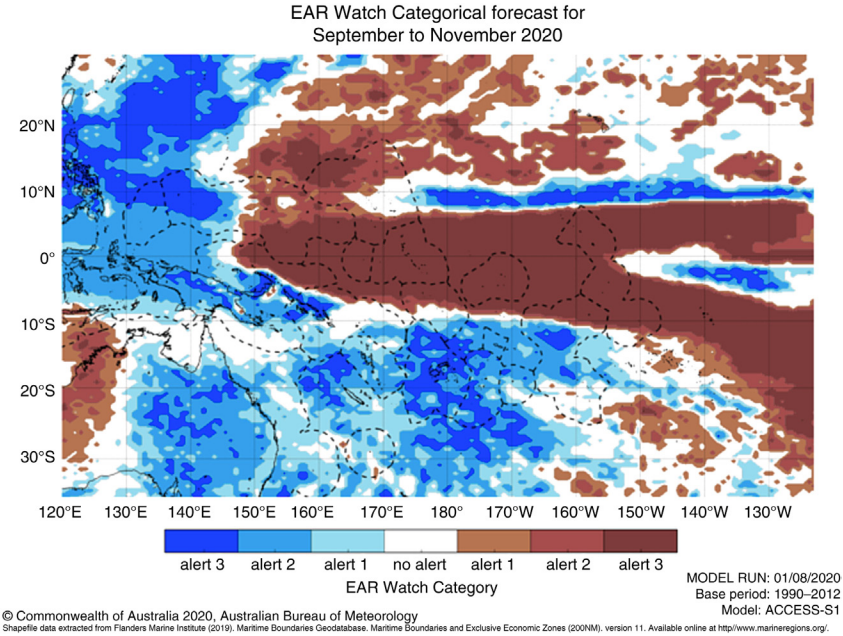

FIGURE 11.4 Early Action Rainfall Watch produced 1 August 2020 for the target period September to November, 2020. The *darker browns* indicate higher likelihood of drier than normal conditions (such as in the central equatorial Pacific), with *blues* indicating higher likelihood of wetter than normal conditions.

station points only, thus limiting locations at which outlooks could be integrated into disaster risk reduction decision making. The EAR Watch alert system was used in combination with location-specific meteorological drought status derived from station data, and consideration of water supply vulnerability. This enabled early identification of locations most at risk of water insecurity in the months ahead.

While the use of EO for anticipatory action is in its infancy in the Pacific, nonetheless, basic applications to prevent compound disasters during the South West Pacific dry season have identified a number of gaps and lessons that will be useful going forward. In particular, standardized, systematic, and regularly updated data on water system vulnerability at as fine a scale as possible would greatly assist regional humanitarian organizations to accurately assess drought risk and enable more accurate targeting and prioritization of anticipatory action support.

5 Case study: the use of Earth Observations for climate and disaster risk reduction within The World Food Programme

WFP uses EO data in numerous ways, from facilitating an understanding of baseline risk to supporting the development of emergency response protocols to address the impacts of hydrometeorological shocks. The use, generation,

management, and presentation of EO data at WFP cross-cuts numerous divisions that together form an integrated disaster risk management (DRM) approach to a changing climate and evolving needs. Anticipatory actions are one component of WFP's DRM strategy, utilizing EO data to define how to visualize and respond to a climate shock, often in near-real time, through to mitigating the impacts before they affect lives and livelihoods.

As conflicts and climate change affect an increasing number of people, and increase the number of people coping with reduced food security, WFP is innovating approaches to aid affected populations. One such innovation is the use of FbF, which aims to connect early warning systems (EWS) to anticipatory actions and pre-positioned financing, to implement them. The challenges lie in needing high resolution, high-quality, long-term EO data in some of the most remote and data sparse locations globally to support the development and implementation of these emergency programs.

To support the delivery of humanitarian aid in the most vulnerable communities, there is a need to prioritize on a sub-national level based on both historical weather-data and the livelihood types within the focus areas. Having increased confidence that a flood or other climate hazard is imminent or will likely occur at some point in the future only addresses some of the challenges faced by humanitarian organizations in prioritizing disaster risk reduction activities. Humanitarian organizations also need to identify which communities will be most impacted, when, for what duration, and how to support the households most at-risk in mitigating potential impacts. This requires extensive data sets on past floods, rainfall, temperatures, dry spells, and a deep understanding of how communities have adapted and are willing to adapt to changing seasons and severe weather (World Food Programme, 2014). In Mozambique, WFP is supporting partners in developing an integrated risk management approach to drought using a combination of EO data from the national meteorological service (INAM), the Climate Hazards Group InfraRed Precipitation with Station data (CHIRPS), and satellite imagery from MODIS to support analysis of vegetation cover and land temperature (Nnachi, 2019). The assimilation of these data represents a new approach for WFP for mitigating the impacts of drought by offering both a historical analysis of past impacts to support program prioritization and the ability to predict future impacts within the occurrence of drier than average conditions, and subsequent drought.

Unlike floods, droughts are slow-onset in nature, and offer opportunities to mitigate impacts on households across various timescales. These phased activities can be characterized in three broad categories: (1) actions that are implemented before the season begins to address risk and build resilience; (2) actions implemented midseason, with support from EO data, to identify and contain worsening conditions; and (3) late-season activities that support an early response to likely increasing food needs.

For example, in Mozambique seasonal forecasts are being downscaled using information from EO analysis and subsequently operationalized to provide

skillful forecasts months before the rainfall season begins. During the cropping season, MODIS and Sentinel-2 data provides early indications of vegetation health and extent, while seasonal forecasts can provide information for the remaining rainfall season and consequent harvests. This type of early warning offers humanitarian organizations and relevant stakeholders the information needed to implement time-sensitive anticipatory activities that can prevent or mitigate the impacts from drought, such as ensuring sustainable access to safe water, providing drought resistant and short-cycle crop seeds, and empowering communities to make risk-informed choices. Moreover, the mid-season activities are developed to protect vulnerable people and contain worsening conditions considering the window to prevent impacts has passed. In some scenarios, fully protecting vulnerable people from a drought shock may not be possible and therefore the early warnings from both forecast and observed information is also being used to ensure a timely and effective humanitarian response, through pre-positioned food, aid, and funding offering robust drought risk-management in Mozambique.

WFP has been supporting partner governments' investment in EO data to help develop an understanding of baseline risk, develop climate-informed anticipatory action plans, and support improved weather-forecasting skill. However, delivering aid, such as cash transfers, for use prior to a disaster is of little benefit if the necessary time needed to purchase items and/or services in anticipation of the disaster is not possible. WFP benefits from the extensive network of EOs which improves initial geophysical conditions, mid-season assessments, and validation of forecasts, the latter being extremely important if donors and governments are to offer funds before a natural hazard has become a humanitarian disaster. Encouraging the UN and its partners to better integrate information from EO data and forecasts to increase reliable warning of impending crises and to act earlier to mitigate impact from disasters is increasingly a priority.

Looking toward the future and recognizing the importance of addressing the interface between conflict, food security, and climate change, WFP is supporting governments in building a comprehensive climate-risk financing strategy through inclusive-insurance programs. These climate finance programs, such as FbF, are enabled by high-quality, high-resolution EO data to develop parametric indices that support accurate trigger points to efficiently address climate shocks of different frequency, severity, and geographical impact (Makaudze and Miranda, 2010; Black et al., 2016; Jensen et al., 2019). As part of an effort to strengthen this integrated programming approach, WFP is currently assessing the feasibility and potential costs and benefits of integrated climate risk financing in Malawi, Bangladesh, and Zimbabwe.

6 Looking ahead—the future of EO and anticipatory humanitarian action

As demonstrated through these case studies, EOs have significant potential to increase the scale and precision of humanitarian action by enhancing understanding of where and when to carry out anticipatory actions, identifying

where investment in the development of anticipatory action systems should be prioritized, and affording new opportunities in monitoring and evaluation (Gros et al., 2020). However, data alone is insufficient for bridging the gaps between data and decisions and in acknowledgement of the constraints identified throughout this chapter, we highlight options to pair EO and anticipatory humanitarian action.

First, improved partnerships between the EO and anticipatory action communities are necessary. Earth observing communities include a variety of organizations such as space agencies, commercial data companies, and academic research entities—groups that do not traditionally have significant knowledge of humanitarian systems and programming. Similarly, the humanitarian sector engages subject matter experts and policy specialists capable of developing programming to manage fragile and crisis-affected systems, with greater focus on qualitative data than geophysical. Incentivizing engagement among these entities should include a structured process of learning in order to adapt programming to include considerations of each other's approaches (Nauman et al., 2021).

Additionally, the sharing of interdisciplinary approaches and providing opportunities to facilitate data application from national to community level for improved humanitarian outcomes (i.e., "last mile" approaches) is crucial if a mutually beneficially, and sustainable, partnership is desired (Shrestha et al., 2021, Wilkinson et al., 2021). Effective collaboration between scientists, government and non-government actors, private sector, civil society organizations, and local communities has the potential to result in tailored, contextually appropriate user-centered products and services that benefit those most vulnerable to identified risks, however this goal must be articulated at the onset of the partnership development process and decisions (such as those related to resource allocations) should be made to ensure that this remains a focus (Kruczkiewicz et al., 2018b; Hewitt et al., 2020). Further, through partnerships such as these, trust and respect can be built between otherwise diverse communities in a way that enables sustained collaboration and success, with additional opportunities for systematic reflection and evaluation of approaches (Bischiniotis et al., 2020; Wagner and Jaime, 2020). Before establishing best practices around the roles and responsibilities of such partnerships, a prerequisite step could be to review existing partnerships present in applied EO programming to better understand to what extent they involve mutually benefit collaboration.

Finally, EO data derived products should require the communication of uncertainty along with their suggested use, and/or require validation with local data and indigenous knowledge, in order to increase levels of trust and greater confidence in their relevance to decision making (Kettle and Dow, 2016; Vincent et al., 2018). A translator acting between the EO and humanitarian community can promote the identification of the types of decisions that can or cannot be made with particular forecasts and early warning models, with the goal of shifting the mindset of the EO community to reward and incentivize the development of tools and products that are tailored to inform action.

References

Aguirre, J., Ugarte, D.D.L.T., Bazo, J., Quequezana, P., Collado, M., 2019. Evaluation of early action mechanisms in Peru regarding preparedness for El Niño. Int. J. Disaster Risk Sci. 10 (4), 493–510.

Alsumaiti, T.S., Hussein, K., Ghebreyesus, D.T., Sharif, H.O., 2020. Performance of the CMORPH and GPM IMERG products over the United Arab Emirates. Remote Sens. 12 (9), 1426.

Bevacqua, E., Vousdoukas, M., Zappa, G., Hodges, K., Shepherd, T., Maraun, D., Mentaschi, L., Feyen, L., 2020. Global projections of compound coastal meteorological extremes.

Bischiniotis, K., de Moel, H., van den Homberg, M., Couasnon, A., Aerts, J., Nobre, G.G., Zsoter, E., van den Hurk, B., 2020. A framework for comparing permanent and forecast-based flood risk-reduction strategies. Sci. Total Environ. 720, 137572.

Black, E., Greatrex, H., Young, M., Maidment, R., 2016. Incorporating satellite data into weather index insurance. Bull. Am. Meteorol. Soc. 97 (10), ES203–ES206.

Ceccato, P., Connor, S., Dinku, T., Kruczkiewicz, A., Lessel, J., Sweeney, A., Thomson, M.C., 2017. Integrating remotely sensed climate and environmental information into public health. Integrating Scale in Remote Sensing and GIS. CRC Press, pp. 304–335.

Chakraborty, L., Rus, H., Henstra, D., Thistlethwaite, J., Scott, D., 2020. A place-based socioeconomic status index: Measuring social vulnerability to flood hazards in the context of environmental justice. Int. J. Disaster Risk Reduct. 43, 101394.

Clark, R.A., et al., 2017. Hydrological modeling and capacity building in the Republic of Namibia. Bull. Amer. Meteor. Soc. 98, 1697–1715, https://doi.org/10.1175/BAMS-D-15-00130.1.

Couasnon, A., Eilander, D., Muis, S., Veldkamp, T.I., Haigh, I.D., Wahl, T., Winsemius, H.C., Ward, P.J., 2020. Measuring compound flood potential from river discharge and storm surge extremes at the global scale. Nat. Hazards Earth Syst. Sci. 20 (2), 489–504.

Coughlan de Perez, E.R., Van den Hurk, B., Van Aalst, M.K., Amuron, I., Bamanya, D., Hauser, T., Jongma, B., Lopez, A., Mason, S.J., Mendler de Suarez, J. and Pappenberger, F., 2016. Action-based flood forecasting for triggering humanitarian action. Hydrol. Earth Syst. Sci. 20, 3549–3560.

Cutter, S.L., Emrich, C.T., Gall, M., Reeves, R., 2018. Flash flood risk and the paradox of urban development. Nat. Hazards Rev. 19 (1), 05017005.

Demeritt, D., Nobert, S., Cloke, H., Pappenberger, F., 2010. Challenges in communicating and using ensembles in operational flood forecasting. Meteorol. Appl. 17 (2), 209–222.

Elliott, M., MacDonald, M.C., Chan, T., Kearton, A., Shields, K.F., Bartram, J.K., Hadwen, W.L., 2017. Multiple household water sources and their use in remote communities with evidence from Pacific Island countries. Water Resour. Res. 53 (11), 9106–9117.

Elvidge, C., Tuttle, B., Sutton, P., Baugh, K., Howard, A., Milesi, C., Bhaduri, B., Nemani, R., 2007. Global distribution and density of constructed impervious surfaces. Sensors 7, 1962–1979, https://doi.org/10.3390/s7091962.

European Commission, 2017. Emergency Management Service—Mapping. Available from: https://emergency.copernicus.eu/mapping/list-of-components/EMSR199.

Faccini, F., Luino, F., Sacchini, A., Turconi, L., 2015. Flash flood events and urban development in Genoa (Italy): lost in translation. Engineering Geology for Society and Territory, 5, Springer, Cham, pp. 797–801.

Flamig, Z.L., Vergara, H., Gourley, J.J., 2020. The ensemble framework for flash flood forecasting (EF5) v1.2: Description and case study. Geosci. Model Dev. Discuss. 13 (10), 4943–4958, https://doi.org/10.5194/gmd-2020-46, in review.

Gallus, Jr., W.A., 1999. Eta simulations of three extreme precipitation events: Sensitivity to resolution and convective parameterization. Weather Forecasting 14 (3), 405–426.

Gao, Z., Long, D., Tang, G., Zeng, C., Huang, J., Hong, Y., 2017. Assessing the potential of satellite-based precipitation estimates for flood frequency analysis in ungauged or poorly gauged tributaries of China's Yangtze River basin. J. Hydrol. 550, 478–496.

Georgakakos, K.P., 2006. Analytical results for operational flash flood guidance. J. Hydrol. 317 (1–2), 81–103.

Giuliani, G., Nativi, S., Obregon, A., Beniston, M., Lehmann, A., 2017. Spatially enabling the Global Framework for Climate Services: Reviewing geospatial solutions to efficiently share and integrate climate data & information. Clim. Services 8, 44–58.

Gregory, P., Vitart, F., Rivett, R., Brown, A., Kuleshov, Y., 2020. Subseasonal forecasts of tropical cyclones in the Southern Hemisphere using a dynamical multimodel ensemble. Weather Forecasting 35 (5), 1817–1829.

Gros, C., Easton-Calabria, E., Bailey, M., Dagys, K., de Perez, E.C., Sharavnyambuu, M., Kruczkiewicz, A., 2020. The effectiveness of forecast-based humanitarian assistance in anticipation of extreme winters: Evidence from an intervention for vulnerable herders in Mongolia. Disasters. https://doi.org/10.1111/disa.12467

Hadwen, W.L., Powell, B., MacDonald, M.C., Elliott, M., Chan, T., Gernjak, W., Aalbersberg, W.G., 2015. Putting WASH in the water cycle: Climate change, water resources and the future of water, sanitation and hygiene challenges in Pacific Island Countries. J. Water Sanit. Hyg. Dev. 5 (2), 183–191.

Hapuarachchi, H.A.P., Wang, Q.J., Pagano, T.C., 2011. A review of advances in flash flood forecasting. Hydrol. Process. 25 (18), 2771–2784.

Hewitt, C.D., Allis, E., Mason, S.J., Muth, M., Pulwarty, R., Shumake-Guillemot, J., Bucher, A., Brunet, M., Fischer, A.M., Hama, A.M., Kolli, R.K., 2020. Making society climate resilient: International progress under the Global Framework for Climate Services. Bull. Am. Meteorol. Soc. 101 (2), E237–E252.

Hudson, D., Alves, O., Hendon, H.H., Lim, E.P., Liu, G., Luo, J.J., MacLachlan, C., Marshall, A.G., Shi, L., Wang, G., Wedd, R., 2017. ACCESS-S1: the new Bureau of Meteorology multi-week to seasonal prediction system. J. South. Hemisphere Earth Syst. Sci. 67 (3), 132–159.

Huffman, G.J., Stocker, E.F., Bolvin, D.T., Nelkin, E.J., Jackson Tan, 2019. GPM IMERG Final Precipitation L3 Half Hourly 0.1 degree x 0.1 degree V06. Greenbelt, MD.

Jensen, N., Stoeffler, Q., Fava, F., Vrieling, A., Atzberger, C., Meroni, M., Mude, A., Carter, M., 2019. Does the design matter? Comparing satellite-based indices for insuring pastoralists against drought. Ecol. Econom. 162, 59–73.

Jokinen, T., 2019. Forecast-based Financing: Transformation or a faster way to transfer funds? University of Helsinki.

Kelman, I., 2019. Pacific island regional preparedness for El Niño. Environ. Dev. Sustain. 21 (1), 405–428.

Kettle, N.P., Dow, K., 2016. The role of perceived risk, uncertainty, and trust on coastal climate change adaptation planning. Environ. Behav. 48 (4), 579–606.

Kruczkiewicz, A., Greatrex, H., Braun, M., Flamig, Z., Nielsen, M., Llamanzares, B., Caniglia, D., Ahmadul, H., Baugh, C., Coughlan, E., 2018a. Forecast-based Financing for Flash Floods: Challenges and Opportunities. AGUFM, 2018, pp. PA22A-17.

Kruczkiewicz, A., Sayeed, S., Hansen, J., Furlow, J., Rose, A., Dinh, D., 2018b. Review of Climate Services Governance Structures: Case Studies from Mali, Jamaica, and India. CCAFS Working Paper no. 236, Wageningen, Netherlands.

Lehner, B., Verdin, K., Jarvis, A., 2008. New global hydrography derived from spaceborne elevation data. EOS Trans. AGU 89 (10), 93–94.

Leon, K., Acuña, J., Llauca, H., Lavado, W., Suarez, W., Ordoñez, J., Felipe, O., 2020. Implementation of a flood forecasting system in a transboundary river basin, Peru-Ecuador. In: EGU General Assembly Conference Abstracts, p. 12927. European Geophysical Union.

Luchetti, N.T., Sutton, J.R., Wright, E.E., Kruk, M.C., Marra, J.J., 2016. When El Niño rages: How satellite data can help water-stressed islands. Bull. Am. Meteorol. Soc. 97 (12), 2249–2255.

Ma, M., Wang, H., Jia, P., Tang, G., Wang, D., Ma, Z., Yan, H., 2020. Application of the GPM-IMERG products in flash flood warning: a case study in Yunnan, China. Remote Sens. 12 (12), 1954.

MacLeod, D., Kilavi, M., Mwangi, E., Ambani, M., Osunga, M., Robbins, J., Graham, R., Rowhani, P., Todd, M.C., 2021. Are Kenya Meteorological Department heavy rainfall advisories useful for forecast-based early action and early preparedness for flooding? Nat. Hazards Earth Syst. Sci. 21 (1), 261–277.

Makaudze, E.M., Miranda, M.J., 2010. Catastrophic drought insurance based on the remotely sensed normalised difference vegetation index for smallholder farmers in Zimbabwe. Agrekon 49 (4), 418–432.

Manz, B., Páez-Bimos, S., Horna, N., Buytaert, W., Ochoa-Tocachi, B., Lavado-Casimiro, W., Willems, B., 2017. Comparative ground validation of IMERG and TMPA at variable spatiotemporal scales in the tropical Andes. J. Hydrometeorol. 18 (9), 2469–2489.

Mason, S.J., Kruckiewicz, A., Ceccato, P., Crawford, A., 2015. Accessing and using climate data and information in fragile, data-poor states. International Institute for Sustainable Development.

Marshall, A.G., Hendon, H.H., 2019. Multi-week prediction of the Madden–Julian oscillation with ACCESS-S1. Clim. Dynam. 52 (5–6), 2513–2528.

McClain, S.N., Kruczkiewicz, A., Owens, M., Ndugwa, R., Bader, D., Braneon, C., 2021. Building risk-informed communities: applications of Earth Observation data. In: Kavvada, A., Cripe, D., Friedl, L. (Eds.), Earth Observation Applications and Global Policy Frameworks. AGU and John Wiley & Sons, Inc, Washington DC.

Morán-Tejeda, E., Bazo, J., López-Moreno, J.I., Aguilar, E., Azorín-Molina, C., Sanchez-Lorenzo, A., Vicente-Serrano, S.M., 2016. Climate trends and variability in Ecuador (1966-2011). Int. J. Climatol. 36 (11), 3839–3855.

Muis, S., Güneralp, B., Jongman, B., Aerts, J.C., Ward, P.J., 2015. Flood risk and adaptation strategies under climate change and urban expansion: A probabilistic analysis using global data. Sci. Total Environ. 538, 445–457.

Nauman, C., Anderson, E., de Perez, E.C., Kruczkiewicz, A., McClain, S., Markert, A., Griffin, R., Suarez, P., 2021. Perspectives on flood forecast-based early action and opportunities for Earth observations. J. Appl. Remote Sens. 15 (3), 032002.

Nielsen, M., Greatrex, H. and Kruczkiewicz, A., 2020, January. A systematic review of flash flood risk, vulnerability and impact. In: 100th American Meteorological Society Annual Meeting. AMS.

Nnachi, U., 2019. Linking Humanitarian and Development Interventions into A Joint Resilience Continuum: World Food Programme (WFP) and International Fund for Agricultural Development (IFAD) Collaboration on Building Climate Resilience in Nepal, El Salvador and Ethiopia, Doctoral dissertation, NUI Galway.

Novoa, S., Finer, M, 2017. High Resolution Images of the Flooding in Peru, 57, MAAP.

Pichon, F., 2019. Anticipatory humanitarian action: what role for the CERF? Moving from rapid response to early action. Overseas Development Institute.

Rohwerder, B., 2017. Flexibility in funding mechanisms to respond to shocks. Institute of Development Studies, Governance, Social Development, Humanitarian, Conflict.

Ruth, A., Fontaine, L., Coughlan, E.R., Kampfer, K., Wyjad, K., Destrooper, M., Amuron, I., Choularton, R., Burer, M., Miller, R., 2017. Forecast-based financing, early warning and early action: a cutting-edge strategy for the International Humanitarian Community. The Routledge Companion To Media and Humanitarian Action. Routledge, pp. 31–46.

Saouabe, T., El Khalki, E.M., Saidi, M.E.M., Najmi, A., Hadri, A., Rachidi, S., Jadoud, M., Tramblay, Y., 2020. Evaluation of the GPM-IMERG precipitation product for flood modeling in a semi-arid mountainous basin in Morocco. Water 12 (9), 2516.

Schumann, G.J.P., 2019. The need for scientific rigour and accountability in flood mapping to better support disaster response. Hydrol. Process. 33 (24), 3138–3142.

Shrestha, M.S., Gurung, M.B., Khadgi, V.R., Wagle, N., Banarjee, S., Sherchan, U., Parajuli, B., Mishra, A., 2021. The last mile: Flood RISK communication for better preparedness in Nepal. Int. J. Disaster Risk Reduct., 102118.

Son, R., Wang, S.S., Tseng, W., et al., 2020. Climate diagnostics of the extreme floods in Peru during early 2017. Clim. Dyn. 54, 935–945, https://doi.org/10.1007/s00382-019-05038-y.

Stephens, E., Coughlan de Perez, E., Kruczkiewicz, A., Boyd, E., Suarez, P., 2015. Forecast based Action. Red Cross/Red Crescent Climate Centre, The Netherlands.

United Nations Office for Disaster Risk Reduction (UNDRR), 2018. The Human Cost of Weather-related Disasters. Available from: https://www.unisdr.org/files/46796_cop21weatherdisastersreport2015.pdf.

Usamah, M., Páez, S., Rebotier, J., Roberts, J., Martínez, I., 2015. Serie reflexiones académicas: la vulnerabilidad y los riesgos estudios de caso en el Ecuador. Universidad de Cuenca, PYDLOS, Available from: http://dspace.ucuenca.edu.ec/handle/123456789/21729.

Vergara, H., Kirstetter, P.E., Gourley, J.J., Flamig, Z.L., Hong, Y., Arthur, A., Kolar, R., 2016. Estimating a-priori kinematic wave model parameters based on regionalization for flash flood forecasting in the Conterminous United States. J. Hydrol. 541, 421–433.

Vincent, K., Daly, M., Scannell, C., Leathes, B., 2018. What can climate services learn from theory and practice of co-production? Clim. Services 12, 48–58.

Wagner, M., Jaime, C., 2020. An Agenda for Expanding Forecast-Based Action to Situations of Conflict. Global Public Policy Institute.

Wahl, T., Jain, S., Bender, J., Meyers, S.D., Luther, M.E., 2015. Increasing risk of compound flooding from storm surge and rainfall for major US cities. Nat. Clim. Change 5 (12), 1093–1097.

Whitcraft, A.K., Becker-Reshef, I., Justice, C.O., Gifford, L., Kavvada, A., Jarvis, I., 2019. No pixel left behind: Toward integrating Earth Observations for agriculture into the United Nations Sustainable Development Goals framework. Remote Sens. Environ. 235, 111470.

White, I., 2016. Multi Country Drought Preparedness and Response Plan Design: Summary of Hot Spot Analysis Based on Historic Rainfall Data, Solomon Islands. UNICEF Pacific.

Wilkinson, E., Arvis, B., de Suarez, J.M., Weingärtner, L., Jaime, C., Grainger, N., Simonet, C., Bazo, J., Kruczkiewicz, A., 2021. Preparing for extreme weather in the Eastern Caribbean. Overseas Development Institute. Working Paper 603.

World Food Programme, 2014. A WFP approach to operationalise resilience: Part 1: Integrated Context Analysis. Available from: https://documents.wfp.org/stellent/groups/public/documents/communications/wfp264472.pdf.

Xia, J., Falconer, R.A., Lin, B., Tan, G., 2011. Modelling flash flood risk in urban areas. Proceedings of the Institution of Civil Engineers-Water Management, vol. 164, Thomas Telford Ltd., pp. 267–282.

Zaharia, L., Costache, R., Prăvălie, R., Ioana-Toroimac, G., 2017. Mapping flood and flooding potential indices: a methodological approach to identifying areas susceptible to flood and flooding risk. Case study: the Prahova catchment (Romania). Front. Earth Sci. 11 (2), 229–247.

Zampieri, M., Malguzzi, P., Buzzi, A., 2005. Sensitivity of quantitative precipitation forecasts to boundary layer parameterization: a flash flood case study in the Western Mediterranean. Nat. Hazards Earth Syst. Sci. 5(4), 603–612.

Page left intentionally blank

Chapter 12

Earth Observation and Hydraulic Data Assimilation for Improved Flood Inundation Forecasting

Antara Dasgupta[a,b,c], Renaud Hostache[d], RAAJ Ramsankaran[b], Stefania Grimaldi[c], Patrick Matgen[d], Marco Chini[d], Valentijn R.N. Pauwels[c] and Jeffrey P. Walker[c]

[a]IITB-Monash Research Academy, Mumbai, Maharashtra, India; [b]Department of Civil Engineering, Indian Institute of Technology Bombay, Mumbai, Maharashtra, India; [c]Department of Civil Engineering, Monash University, Clayton, VIC, Australia; [d]Department of Environmental Research and Innovation, Luxembourg Institute of Science and Technology, Belvaux, Esch-sur-Alzette, Luxembourg

1 Introduction

The devastation caused by the surface water flooding is widely acknowledged in scientific literature, as now there is the need to better coordinate prediction and monitoring efforts (Schumann et al., 2016). Current global flood forecasting systems, primarily consist of a numerical weather prediction and hydrological model cascade, which provide predictions of streamflow (Emerton et al., 2016). For example, the Global Flood Awareness System (GloFAS, Alfieri et al., 2013) provides forecast probabilities of the streamflow exceeding predefined flood severity thresholds, in the global channel network with a lead time of up to a month (Hirpa et al., 2018). GloFAS is the first globally concerted effort toward operational flood forecasting, which could potentially offset the disproportionate impacts of flooding on developing nations where the necessary expertise and infrastructure might be lacking (Uhe et al., 2019). However, the lack of corresponding inundation information severely prohibits the direct translation of GloFAS forecasts into actionable insights for flood mitigation. As flood extent estimates are not provided, pre-emptively assessing risk and damage based on GloFAS predictions is nearly impossible.

Although there exists a widespread scientific consensus regarding the inclusion of hydraulic flood inundation models into global forecasting chains, there are mainly two reasons why this has not been materialized yet. The first, pertains to the availability of sufficient computational resources for operational

Earth Observation for Flood Applications. http://dx.doi.org/10.1016/B978-0-12-819412-6.00012-2

real-time ensemble forecasts of flood inundation. To put this in perspective, hydrological model calibration studies use thousands (Pappenberger et al., 2005) to a million model runs (Moradkhani et al., 2005a) within a research scenario, while GloFAS (real world scenario) can only use 51. This is primarily because a trade-off between computational time and prediction accuracy becomes absolutely critical in an operational scenario where time is of essence (Sanders and Schubert, 2019). Moreover, in an ensemble forecasting model cascade, these 51 GloFAS outputs are inputs to a hydraulic model, a task which requires even more time and even larger computational capabilities. Recent advances in scientific computing prowess suggest that integrating flood inundation models into forecasting chains might now be feasible (Bates et al., 2017; Ward et al., 2015). However, extensive investigations into the computational demand versus accuracy trade-off are essential to realize this operationally.

The second reason is related to the data required for the implementation of flood inundation models (Bates, 2012; Bates et al., 2014). Typically, this necessarily includes information on upstream (rainfall or inflow) and downstream (outflow or water levels) boundary conditions, channel geometry, and floodplain topography. Among these, the floodplain topography and channel geometry are arguably the most critical factors which determine the accuracy of the simulated flood propagation. While the channel bathymetry controls the streamflow thresholds and thereby the timing at which the river banks are overtopped or breached, the topographic representation of the floodplain connectivity and flow pathways dominates the resulting floodplain inundation patterns (Schumann et al., 2014). The uncertainty contributed by forecast inflow compounds topographic errors, often leading to highly erroneous predictions of inundation extent (Hostache et al., 2018). Current global Digital Elevation Models (DEMs), such as those from the Shuttle Radar Topography Mission (SRTM) or from the Advanced Spaceborne Thermal Emission and Reflection Radiometer (ASTER) mission exhibit large vertical errors to the order of several meters (Chen et al., 2018). These errors are exacerbated over complex topography and cannot resolve microtopographic variations in low gradient regions, limiting their utility toward generating flood predictions with high accuracy (Chu and Lindenschmidt, 2017; Grimaldi et al., 2019; Schumann and Bates, 2018).

Studies have explored a variety of bias correction (Kumar et al., 2019; Pramanik et al., 2010; Sanders, 2007), vegetation and artefact removal (Hirt, 2018; Yamazaki et al., 2017, 2012), artificial enforcement of drainage networks (Gallant et al., 2011; Yamazaki et al., 2019), and DEM merging techniques (O'Loughlin et al., 2016; Pham et al., 2018; Robinson et al., 2014; Wang et al., 2018; Yue et al., 2017) to improve the quality of global DEMs for flood modeling. For example, the global Multi Error Removed Improved Terrain (MERIT) DEM (Yamazaki et al., 2017) removed absolute bias, stripe noise, speckle noise, and tree height bias from a merged SRTM3 and AW3D elevation product. The resulting MERIT DEM showed significant improvements, especially in the representation of microtopographic variations and channel

networks in flat terrains. In spite of this, Schumann & Bates (2018) observe that these improved topographic datasets still exhibit vertical errors much larger than those acceptable for flood inundation forecasting.

Recent literature has explored the possibility of a high resolution global DEM based on TanDEM-X data, reporting sub-meter vertical accuracy in simulated water surface elevations (WSEs), indicating suitability for flood applications (Archer et al., 2018). Moreover, the TanDEM-X 90 (~1 arc second) product was also found to exhibit lower vertical errors than the MERIT DEM, for all land-use classes except tree-covered regions (Hawker et al., 2019). However, the development and provision of a global product is still a long-term goal which would need extensive testing, as even small vertical errors can strongly impact flood forecasting accuracy especially at local scales (Schumann and Bates, 2018). As Hawker et al. (2019) demonstrate, the choice of an appropriate global DEM for floodplain applications should ideally be determined through an assessment of the predominant land cover in the region. While this recommendation is feasible on a case to case basis for research purposes, it also implies that when using any one of the global DEMs for operational forecasting, large vertical errors may still exist in one or more of the underlying land cover regions. Consequently, in order to prepare for the imminent integration of flood inundation models into global forecasting systems, methods to reduce the uncertainty contributed by topography need to be developed urgently (Fleischmann et al., 2019).

Earth Observation (EO) data have the potential to provide independent observations of surface water flood dynamics (Bates et al., 2014), which can be used to improve flood inundation predictions in near real-time as shown in Fig. 12.1. The primary objective of data assimilation is to optimally combine model trajectory and observed data, improving the agreement between them (Schumann et al., 2009). Data assimilation (DA) can be interpreted as a dynamic technique in that sense, where the observations are used to update model forecasts in an online manner (Smith et al., 2011). The implementation of DA techniques also allows extending the temporal coverage of instantaneous satellite-based flood observations, through integration with a continuous dynamic process-based hydraulic flood inundation models (Lahoz et al., 2010). In fact studies like the one of Hostache et al. (2018) have shown that forecast errors can be reduced more than 50% at the assimilation time step, while improvements can persist for more than 48 hours. EO-datasets which can be assimilated into flood models to improve forecast skill include water levels (WLs) (Matgen et al. 2010), inundation volumes (Revilla-Romero et al., 2016), and inundated area (Hostache et al. 2018).

While the inundated area can be directly derived from optical and microwave images, satellite altimeters provide water level observation with typical footprint sizes in the order of kilometers (Hossain et al., 2014; Huang et al., 2018b; Paiva et al., 2013; Schneider et al., 2018; Tourian et al., 2017). However, satellite altimetry is currently unable to resolve water levels in narrow channels at local and catchment scales (Biancamaria et al., 2016; Grimaldi et al., 2016;

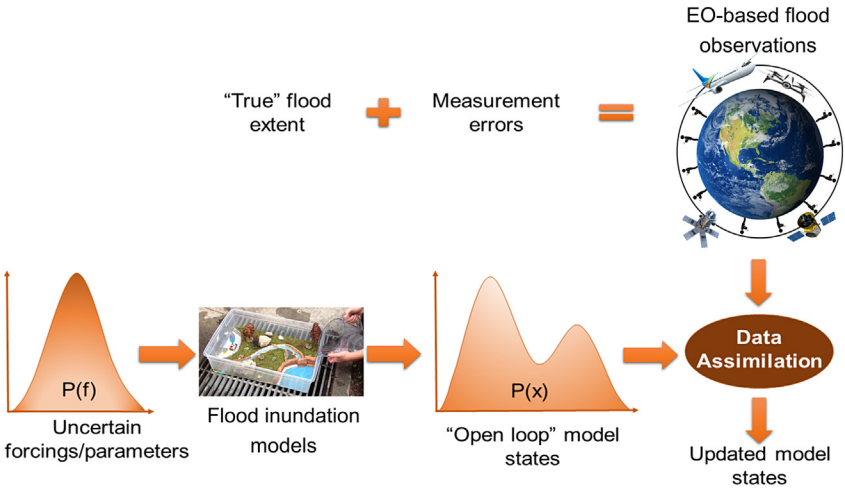

FIGURE 12.1 Schematic of the Earth Observation data assimilation problem in hydraulic modeling. Here, Earth Observations are interpreted as "truth" plus errors, as satellite-derived flood extents are expected to encompass the "true" flood extent even though a major component of measurement errors are also expected to be present in the observation. *(Adapted after Moradkhani (2008).)*

Schumann et al., 2018; Schumann et al., 2014b), which is problematic as almost 25% of global rivers have widths <120 m (Frasson et al., 2019). Indeed, for narrow channels the surrounding topography can also significantly impact the echo shape returned to radar altimeters, adding uncertainties to the corresponding WSE (Grimaldi et al., 2016). Although some innovative research is ongoing in this direction which promises future improvements (Bauer-Gottwein et al., 2015; Kim et al., 2019; Kim and Sharma, 2019; Michailovsky et al., 2012), especially with respect to the potential of swath altimetry for hydraulic flood inundation modeling applications (Alessio Domeneghetti et al., 2018b; Pitcher et al., 2018; Tuozzolo et al., 2019). The upcoming SWOT (Surface Water Ocean Topography) mission with an expected launch date of 2021, will use swath altimetry to provide observations of WSE, widths, and slopes simultaneously for rivers wider than 100 m (Baratelli et al., 2018). Inverse modeling can then be used to remotely derive discharge and bathymetry information (slope and geometry) as well as flow velocity values within a hindcasting data assimilation framework (Baratelli et al., 2018; Brisset et al., 2018; Domeneghetti et al., 2018a,b; Durand et al., 2008; Kim et al., 2019; Oubanas et al., 2018a,b; Prigent et al., 2016; Revel et al., 2019; Yoon et al., 2012). Investigative studies preparing for the SWOT mission, have successfully demonstrated the value of combining virtual swath altimetry measurements with hydrodynamic models, for improved modeled depth and discharge estimates. Therefore, the SWOT satellite is expected to revolutionize hydraulic data assimilation research, as remote sensing-based spatially distributed water levels will be available to modelers for the very first time.

While multiple studies have noted that the processing of optical satellite imagery to extract inundated areas is relatively straightforward (Lacava et al., 2019; Ogilvie et al., 2015; Oliveira et al., 2019), cloud persistence during flood events hinders their systematic use in flood monitoring (Huang et al., 2018a,b). Per contra, synthetic aperture radar (SAR) sensors which use active imaging techniques are capable of cloud penetration and capturing observations through the day and night. SAR sensors are thus uniquely suited to flood mapping applications, especially for small to medium catchments, where flood events are quick and inundation often recedes before clouds have dissipated (Schumann and Moller, 2015). Moreover, satellite-based flood extents can be overlaid on DEMs, to obtain shoreline WLs after a number of postprocessing steps (Mason et al., 2012; Matgen et al., 2007a and 2007b; Schumann et al., 2007). In fact, comparisons of WLs derived from LiDAR and topographic contours with those derived from the global SRTM DEM, demonstrated that even coarse resolution DEMs have the potential to support flood modeling (Schumann et al., 2008). Recent years have witnessed the development of a variety of data assimilation techniques, which are designed to enhance the exploitation of the available satellite-derived WL datasets for flood model improvements (Domeneghetti et al., 2019). However, research in this direction has also revealed a number of caveats in the WL derivation process that must be effectively addressed to unlock the full potential of EO-data for flood disaster management (Schumann and Domeneghetti, 2016).

This chapter provides a discussion on the issues related to the integration of EO-data with hydraulic flood forecasting models within a data assimilation framework, with an aim to harmonize and present the current progress in finding feasible solutions. Therefore, it is important to note that this chapter focuses exclusively on the use of EO-based hydraulic data assimilation to improve predictions of floodplain inundation extent, water level, and flow velocity. This implies that studies on the assimilation of satellite altimetry for improved discharge modeling, for example, are not within the scope of this chapter and accordingly have not been covered. Consequently, an overview of the state of the art of data assimilation techniques proposed for flood inundation model improvements is presented first. Next, the estimation of relevant hydraulic model states and fluxes using flood data assimilation is described. Furthermore, some selected case studies from recent literature which demonstrate the potential of EO-based data assimilation for improved flood inundation forecasting are presented. Finally, future work and open research questions in EO-based data assimilation for flood applications have been elucidated.

2 Principles of data assimilation

Mathematical models of environmental system dynamics can be used effectively to generate future predictions of the system behavior, provided that the initial states of the system are known (Lakshmivarahan and Lewis, 2010). Here,

states refer to the condition of a given dynamic physical system at a particular instant in time. For example, water depth and flow velocities are hydraulic system states. Unfortunately, observational data defining all the states of an environmental system are extremely rare. Moreover, the models as well as the initial states contain inherent inaccuracies, which can lead to significant discrepancies between the predicted and actual states of the system (Lahoz et al., 2010). Integrating observations of the system into the model can therefore improve state estimates while simultaneously providing information on the associated uncertainties.

State estimation is an inverse problem which can be solved using data assimilation based on feedback design techniques. In environmental data assimilation where the models are complex and non-linear, with large number of state variables (often in the order of ~10^8), system dynamics are often multi-scale, unstable, and chaotic (Nichols, 2010). Typically a large number of observations are also available through EO satellites, although their uneven spatiotemporal distribution makes the data assimilation problem ill-posed, and the state estimates sensitive to observation errors. DA can be used either to update model states and/or parameters in real time or to re-analyze model predictions. In the first case, model states and/or parameters are sequentially updated each time an observation is available, therefore dynamically feeding observations back into the model as they become available. In the second case, many observations over a given time window are integrated "at once" to update model state variables and/or parameters and compute an optimal state trajectory (see Fig. 12.2). When focusing on the retrieval of model parameters, DA can be applied for calibrating in an optimal way uncertain models. Among the various available DA techniques that have been recently used in hydrodynamic modeling, one can cite three main families, namely variational methods, Ensemble Kalman Filters (EnKFs), and Particle Filters (PFs). Among variational methods, the one that has recently retained most attention is the 4DVAR. Originally developed for meteorological applications, the latter is based on optimal theory control.

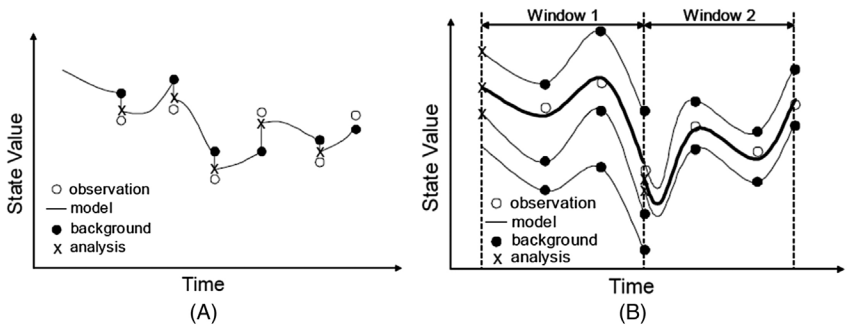

FIGURE 12.2 Schematic of the (A) sequential and (B) variational data assimilation approaches. *(Taken from Walker and Houser (2005).)*

Provided that relevant observations are used, 4DVAR is very efficient for the retrieval of initial and boundary conditions as well as optimal parameter values (Lai and Monnier, 2009). However, it involves the non-trivial development of the adjoint code (i.e., inverse model) of the considered model necessary for computing the derivatives of a predefined quadratic cost function. Ensemble-based filters require comparatively less model developments and they are more directed toward sequential DA. Filters based on the EnKF assume the uncertainty of the observation and the model to be normally distributed while PFs relax this assumption allowing to consider any kind of observation uncertainty distribution (Plaza et al., 2012; Matgen et al., 2010). EnKFs use covariance matrices to estimate model and observation uncertainties and can be resource demanding especially when a large number of observations are assimilated (Mason et al., 2012). Instead, PFs compute prior and posterior probabilities base only on a weighting procedure (De Lannoy et al., 2007). A few studies have also adapted EnKFs and PFs for taking into account all observations "at once" (Hostache et al., 2015; Yoon et al., 2012). The derived so-called smoothers are comparable to variational methods in the sense that observations within a predefined time window are used to estimate the parameters and/or state variables (Plaza et al., 2012). In general, the data assimilation problem can be formulated as the task of finding the best estimates of system states $\mathbf{x}$ from a (noisy) dynamic model of the system given a (noisy) observations $\mathbf{y}$, (Walker and Houser, 2005). In order to demystify the large amount of jargon typically associated with data assimilation, a list of terminology adapted from Walker and Houser (2005) has been provided in Table 12.1.

2.1 Sequential data assimilation

Commonly used sequential data assimilation methods include direct insertion (Mazzoleni et al., 2015), statistical/successive correction, optimal/statistical interpolation, analysis correction, nudging (Patil and Ramsankaran, 2018), 3D-variational (Smith et al., 2013), Kalman filter and variants (Evensen, 2003), particle filter and variants (Arulampalam et al., 2002; Elvira et al., 2017), and evolutionary algorithm and variants (Dumedah, 2012). While some of the approaches like direct insertion, nudging, and optimal interpolation offer ease of implementation, observational or background uncertainty is often ignored. The widely popular sequential algorithm known as the Kalman filter, allows the use of uncertainty estimates in models and observations. However, the linearization of model equations is necessarily required, which can cause instability in solutions and make the assimilation problem intractable for highly non-linear systems common to geophysics. The variants of the ensemble Kalman filter, particle filter, and evolutionary filters, while computationally more intensive, allow the full representation of model and observation uncertainties. These filters are therefore better suited for geophysical applications, as the models as well as EO satellites are known to contain a variety of inherent uncertainties which must be acknowledged.

TABLE 12.1 Commonly used data assimilation terminology, after Walker and Houser (2005).

DA term	Definition
State	Condition of a given physical system, for example, water depth and flow velocities are hydraulic system states
State error	Deviation of the estimated state from the truth
Prognostic	A model state/flux required to propagate the model forward in time
Diagnostic	A model state/flux diagnosed from the prognostic states—not explicitly required to propagate the model
Observation	Measurement of a model diagnostic or prognostic variable
Model ensemble	Set of uniquely parameterized model realizations
Open loop	Model ensemble without any data assimilation
Error covariance matrix	Description of uncertainty in terms of standard deviations and correlations
State perturbation matrix	Matrix containing values of deviations of each individual state vector from the ensemble mean vector
Prediction	Model estimates of future states of a given system
Update	Correction to a model prediction using observations
Background	Model forecast, prediction, or state estimate prior to an update
Analysis	State estimate after an update
Innovation	Observation minus prediction, a priori residual between model prediction, and observation of system state
Gain matrix	Correction factor applied to the innovation, calculated based on the level of confidence in the model, and the observation
Tangent linear model	Linearized version of a non-linear model using the Taylor's series expansion, around a chosen equilibrium point
Adjoint	Inverse operator allowing the model to be run backwards in time

In the variants of Kalman filter, the model forecast is sequentially updated using the innovation, defined as the difference between the observation and the forecast in the observation space each time a new observation becomes available at time k. The analysis (updated forecast) is computed from the background states x_k^b and the innovation as follows:

$$x_k^a = x_k^b + \mathrm{K}\left(\mathrm{y}_k - Hx_k^b\right), \tag{12.1}$$

where x_k^a is the analysis (updated model forecast), x_k^{ab} the background (prior model forecast), K the Kalman gain, and H the linearized observation operator that maps the model state space into the observation space.

The Kalman gain $\mathbf{K}$ is a function of the relative confidence on the model and the observation, and computed based on the observation and model error covariances. In simplified terms, it determines how much of the innovation has to be incorporated in the forecast to draw the analysis in an optimal way. In contrast, PFs carry out the assimilation of the observation into the model based on a weighting procedure of an ensemble of model states called particles. As a starting point of PFs, the set of particles represent the prior probability density function $p(\mathrm{x}_k)$ at time k, as follows (van Leeuwen et al., 2019):

$$p(\mathrm{x}_k) \approx \sum_{i=1}^{N} \frac{1}{N} \delta\left(\mathrm{x}_k - x_k^i\right), \tag{12.2}$$

where δ is the Dirac delta function, and x_k^i is the model state of the i^{th} particle. PFs uses the Bayes theorem to estimate the posterior probability density $p(\mathrm{x}_k \mid \mathrm{y}_k)$, given the observation as:

$$\begin{aligned} p(\mathrm{x}_k|\mathrm{y}_k) &= \frac{p(\mathrm{y}_k|\mathrm{x}_k)}{p(\mathrm{y}_k)} p(\mathrm{x}_k) \\ &\approx \sum_{i=1}^{N} w_i \delta\left(\mathrm{x}_k - x_k^i\right) \quad , \\ with\, w_i &= \frac{p\left(\mathrm{y}_k|x_k^i\right)}{\sum_{j=1}^{N} p\left(\mathrm{y}_k|x_k^j\right)} \end{aligned} \tag{12.3}$$

where $p(\mathrm{y}_k|\mathrm{x}_k)$ is the posterior probability density, $p(\mathrm{y}_k|\mathrm{x}_k)$ the probability density of the observation for each possible model state, $p\left(\mathrm{y}_k|\mathrm{x}_k^i\right)$ the weight of the i^{th} particle, and w_i is the probability the observation given the states of the i^{th} particle. The main limitation in PFs is the potentially high number of particle necessary for accurately representing the prior and posterior probability densities especially for high dimensional systems. Many further developments of PFs have been proposed to overcome this limitation, like resampling and tempering. Readers are referred to van Leeuwen et al. (2019) for an extensive review of such methods.

2.2 Variational data assimilation

Originally, variational data assimilation techniques find the initial condition of a model via minimizing a quadratic cost function J over a pre-specified time

window, computed based on model forecast and observation. Accordingly, the usual cost function takes the following form:

$$J(x) = \frac{1}{2}\left(x^b - x\right)^{\mathrm{T}} B^{-1}\left(x^b - x\right) + \frac{1}{2}\sum_{k=0}^{N}\left(y_k - H_k\left[x_k\right]\right)^{\mathrm{T}} R^{-1}\left(y_k - H_k\left[x_k\right]\right), \tag{12.4}$$

where b refers to the background, x to the model state at initial time, k to time with available observations, N is the length of the time window of the assimilation, y_k the set of observation at time k, and $H_k\left[x_k\right]$ is the counterpart of the model prediction in the observation space. To identify the minimum of the cost function, implementations of 4DVar utilize an adjoint model to evaluate the derivatives of the cost function with respect to the initial model state x (Walker and Houser, 2005). The adjoint model can be defined as a mathematical operator, which allows evaluating the cost function sensitivity to changes in initial model states, over the assimilation window.

Variational data assimilation solves therefore an optimization problem, where the initial state vector is retrieved based on uncertain observations over a given time window. Variational schemes can also be formulated using stronger (perfect model assumption) or weaker constraints (model errors as white process noise) for the retrieval of accurate parameter or boundary condition estimates.

As the backward integration of the model is essential over the entire time window at every assimilation time step, the development of robust adjoint models is essential. However, developing the adjoint model for the complex and non-linear equations of hydrological and hydraulic models, it is a scientific challenge in itself and still impede widespread applications of variational methods in flood modeling.

3 Assimilation of Earth Observations into hydraulic flood forecasting models

Disentangling and dealing with multi source uncertainty in modeling is widely accepted as a scientific challenge in hydrological and hydraulic modeling (Blöschl et al., 2019). Accordingly, most hydraulic data assimilation studies have employed EO-data assimilation with the objective of improving flood forecasting accuracy. As this requires dynamically updating the model trajectory at each assimilation time step, as and when a new observation becomes available, most of the studies have employed sequential filtering techniques (Andreadis, 2018). A few studies have also investigated the potential of variational data assimilation approaches such as 4DVAR; although the main objective of these studies was not improving forecast accuracy in real time.

3.1 Water level assimilation using 4DVAR

These studies primarily focused on the selection of effective inputs and parameters in hindcasting scenarios, which implies that operational constraints of rapid

processing times were largely ignored. For example, Lai and Monnier (2009) proposed a method for assimilating EO-derived water level into a 2D shallow water model based on the 4DVAR algorithm for input and parameter updating and tested it in a synthetic experiment; in the study by Hostache et al. (2010) adopted the same assimilation framework and show, in a real word experiment, its efficiency for the retrieval of distributed friction parameters. Within a similar 4DVAR-based assimilation framework, Lai et al. (2014) introduced the possibility of direct flood extent assimilation—eliminating the need for a water level processing step—for distributed channel roughness estimation. In Oubanas et al. (2018a,b) synthetically generated long time series of SWOT-like observations are assimilated into a 1D shallow water model using 4DVar. The proposed methods showed enabling the retrieval of an equivalent riverbed geometry and the upstream discharge time series. More general presentation of applications of variational DA can also be found in Fletcher (2018a,b) and Lahoz et al. (2010). However, the development of the adjoint code for hydraulic models is a significant scientific challenge, which has thus far impeded the widespread application of the 4DVAR to flood data assimilation problems, specifically geared toward operational forecasting applications.

3.2 Water level assimilation using the Kalman filter and variants

The earliest studies which investigated the potential of EO-based assimilation for flood variable estimation typically used the Kalman filter (KF) and its variants (Evensen, 2003). The Kalman filter family of data assimilation approaches forecast the background error covariance matrix to calculate the Kalman gain, which determines how much of the observational information is taken up at each time step. This gain matrix is determined by the relative confidence in the model and the observations. The traditional Kalman filter approach achieves this using a standard error propagation theory on the tangent linear model, while the extended Kalman filter (EKF) uses a Taylor's series expansion for linearization (Walker and Houser, 2005). EKF allows the extension of KF to non-linear modeling problems, however, the computational cost exceeds model run times by a factor of one more than the number of assimilated observations (Habert et al., 2016). Here the computational cost is measured in terms of the number of binary matrix operations required at each time step to propagate the assimilation system forward. The Ensemble Kalman filter or EnKF, computes the error covariance matrices from an ensemble of state forecasts using the Monte Carlo approach, significantly reducing computational cost and the required ensemble size (Madsen and Canizares, 1999).

Although the studies discussed in this paragraph did not directly use EO-based flood variables for assimilation, they have been included here as they paved the way for future flood data assimilation studies. The first hydraulic data assimilation studies were by Madsen and Skotner (2005) and Neal et al. (2007), who assimilated ground gauge-based river level data at different points

along river reaches. Madsen and Skotner (2005) developed a novel hybrid assimilation technique combining a simplified Kalman filter with an error forecast model, using gain functions with predefined shapes that reflect typical error correlation structures along the reach. Neal et al. (2007) used the EnKF to simultaneously update the states and inputs of a 1D-hydrodynamic model. One major structural assumption in both studies was that the boundary conditions were the sole source of uncertainty. Both studies sequentially updated an augmented state vector including discharge and stage (Madsen and Canizares, 1999), as well as future state error covariance matrices, which were also parameterized through the assimilation scheme (see Fig. 12.3).

The error forecasting procedure allowed for an update of the inflow boundary conditions, which are known to strongly influence flood flow regimes between subsequent assimilation steps. By pre-emptively estimating and accounting for inflow errors in the assimilation framework, the forecast error reduction is rendered persistent. An autoregressive error model was used to synthetically generate and subsequently predict temporally correlated inflow errors. On testing a variety of temporal sampling intervals for field hydrometric observations of

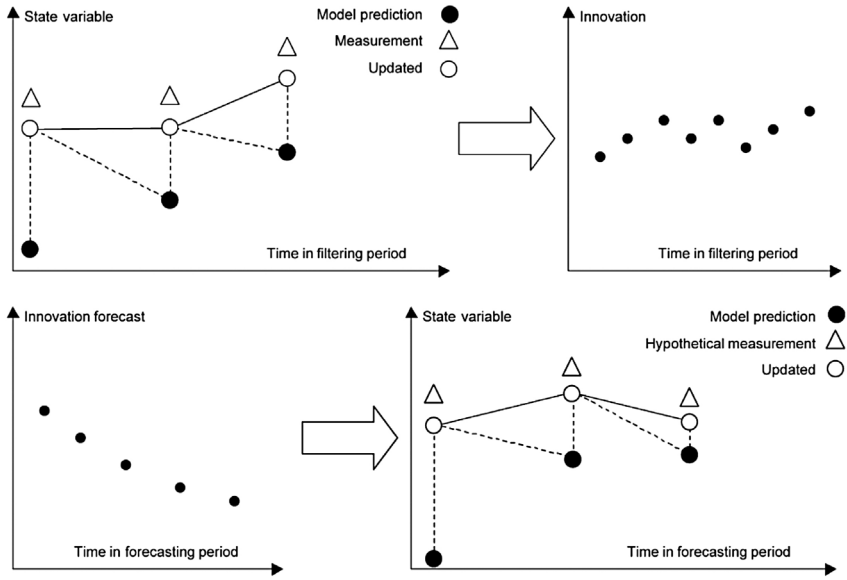

FIGURE 12.3 Illustration of the combined filtering and error forecast procedure followed by Neal et al. (2007) and Madsen & Skotner (2005). At each assimilation time step in the filtering period prior to the forecast, the innovation at all update locations is acquired, leading to a time series up to the time of the last available measurement (Row 1 plots). An error forecast model is then defined at each update location and used to propagate the innovation as per the modeled trend in the forecasting period. These future initial state error estimates are then used to update the state variables and retain the assimilation benefits for longer. *(Taken from Madsen and Skotner (2005), © Elsevier, 2005.)*

water stage, Neal et al. (2007) concluded that the state uncertainty was overestimated when the sampling rate was reduced. This indicated that the observations were assigned relatively lower weights than model predictions, when the temporal density of the measurements was low.

The following study on hydraulic data assimilation was actually geared toward the feasibility assessments of the proposed SWOT mission, then known as WatER—Water Elevation Recovery (Alsdorf et al., 2007). Through the assimilation of synthetic swath-altimetry data into the raster-based hydraulic model Lisflood-FP (Bates and De Roo, 2000) using the ensemble square root Kalman filter EnSRKF (Evensen, 2004), Andreadis et al. (2007) investigated the prospects for estimating channel flow and water depth. Errors were propagated from boundary inflows, generated by corrupting outputs obtained from the Variable Infiltration Capacity (VIC) model. Given that this was a feasibility study, synthetic spatial fields of WL were generated using the NASA JPL SWOT simulator (Fu and Rodriguez, 2004) by corrupting predictions from the "truth" model with Gaussian errors. A hydraulic data assimilation for EO-data was developed for the first time by Andreadis et al. (2007), to simultaneously update states and inputs by dynamically parameterizing the inflow error prediction model, following Madsen and Skotner (2005). The EnSRKF-based approach was successful in retrieving channel water depth and discharge from the corrupted open loop simulations. While the filter showed low sensitivity to assumed observation errors, it was highly sensitive to observation frequency; assimilation performance degraded substantially as the temporal frequency was halved.

The study by Matgen et al. (2007a,b) considered real EO-derived WL observations, as opposed to the synthetic ones used by Andreadis et al. (2007), within a sequential data assimilation framework for the very first time. As state updating is the most straightforward way to utilize EO data to correct models in real time (Grimaldi et al., 2016), this proof-of-concept study implemented a similar strategy. Water stages were derived from ERS-2 SAR and ENVISAT ASAR images, by intersecting with a LiDAR DEM using the REFIX approach of Schumann et al. (2007). Considering all the sources of uncertainty in EO-based WL estimation, an interval of values is determined from the EO-based WL estimation approach and further refined by enforcing hydraulic coherence principles (Puech et al., 2007). Subsequently, the model generated water line is updated at the time steps of the EO data acquisition, to fall within the interval of EO-derived WLs at each model cross-section (Matgen et al., 2007a,b). As the calibrated 1D HEC-RAS model already performed very well for the study reach, the reported improvements were minor and rapidly decayed within a few hours. For instance, the assimilation of ERS-2 based WLs improved forecast error by 23 cm at the assimilation time step, but this reduced to 3 cm within 3 hours of the assimilation, after which the analysis trajectory completely decayed back to the background state values within ~4.5 hours. In contrast, the assimilation of ENVISAT-derived WLs increased the deviation of the assimilated state vector from the open loop from 3 to 6 cm, which is an almost 100%

relative degradation. Although, the decay to the original model trajectory in this case was faster (~2 hours), these results can primarily be attributed to the flashy catchment characteristics, where the flood wave peaked in a few hours and receded within 3 days. This study particularly highlighted that EO-based data assimilation can even degrade model predictions when observation errors are not appropriately represented. The implication here is that some a priori quality control might be necessary to effectively filter outliers which may negatively impact forecast errors.

Extending the work of Andreadis et al. (2007), Durand et al. (2008) used data assimilation to estimate bathymetric depth and slope, through an inverse modeling approach. This study used Lisflood-FP (Bates and De Roo, 2000), errors in the upstream inflow, DEM, bathymetry, and the channel roughness parameter were considered for the first time. While there was no explicit objective toward flood forecasting, the realistic uncertainty scenario assumed in this study, made it a rather significant contribution to flood data assimilation literature. Bathymetric slope, channel roughness, and upstream inflow uncertainties were modeled as multiplicative log-normal error (MLNE) distributions, with unit mean and different coefficients of variation. Topographic uncertainty in floodplain DEM is modeled as a zero mean additive normal distribution, while bathymetric depth was estimated from the slope ensemble previously described. A novel assimilation scheme which used Monte Carlo techniques to modify a linear parameter estimator for non-linear cases was designed. Synthetic SWOT WL fields were assimilated to obtain the reach-averaged bathymetric slope and point-based bathymetric depth. Using the assimilation scheme, the reach-averaged slope was estimated within 0.30 cm/km of the truth, while an improvement of 84% was observed at the downstream point estimate of channel depth. The experiments detailed in this study corroborated the low measurement error sensitivity observed by Andreadis et al. (2007). This phenomenon was primarily attributed to the higher magnitude model errors, which likely dominate over measurement errors within the assimilation framework.

Similarly, Neal et al. (2009) built upon the earlier body of work to estimate discharge, using a combination of hydrodynamic modeling and EO-derived En-KF-based WL assimilation. This study considered the impact of incorrect bathymetry specification on the predicted flows by simulating a data limited scenario, where the channel cross-sections were simplified to a trapezoidal shape. The use of simple channel geometry led to an underestimation of hydraulic conveyance, resulting in higher predicted WLs for a given flow value. This is caused by an underrepresentation of the channel carrying capacity, resulting in an artificial increase of simulated WSEs. However, the assimilation of EO-based WLs was able to effectively improve the retrievals of observed discharge, even in the data scarce scenario where simplified channel geometries were considered. This study corroborated the findings of Matgen et al. (2007a,b), who demonstrated that SAR images may not provide useful information across the entire model domain. It was also noted that forcing the model to reproduce

observations at certain locations, may introduce measurement bias leading to model performance degradation.

The studies which exclusively used state updating or evaluated its impacts with respect to input updating, highlighted that the analysis vector rapidly decayed back to the background state trajectory immediately following the assimilation (Andreadis et al., 2007; Matgen et al., 2007a,b). Schumann et al. (2009) attributed this lack of persistence in accuracy to the dominating effect of upstream boundary conditions in hydraulic modeling. They argued that as long as errors in the initial conditions and forcing data persisted, merely reinitializing the model with an updated state vector may not serve as an adequate solution. Based on these findings, the simultaneous updating of states and inputs was recommended to obtain more persistent forecast error reductions.

Furthermore, the work of Schumann et al. (2008) showed that SAR-derived WL observations, mostly exhibit non-Gaussian probability density functions (PDF) at each cross-section. It therefore follows, that the sum of these distributions considered for the full river reach, is also strictly non-normal in form (Kitagawa, 1996). The EnKF algorithm assumes that the forecast and measurement error covariance matrices are jointly normal to make the data assimilation problem tractable; such that their respective PDFs can be sufficiently characterized using only the first and second moments of the distribution, that is, mean and covariance (Moradkhani et al., 2005b). This raised questions about the theoretical justification of employing EnKF-based assimilation schemes for EO-based hydraulic data assimilation, where states are subject to unknown disturbances (Moradkhani et al., 2005a). The conditional probabilities of strongly non-linear model trajectories can only be characterized sufficiently by tracking the higher order moments of the distribution (Moradkhani, 2008). However, the spatial coverage of EO-data implies that some observations can be discarded, for example, those that fail a normality test as suggested by Neal et al. (2009). While simple and easy to implement, this approach might reject potentially useful information. Further studies then investigated possible ways to solve the problem of obtaining persistent improvements from hydraulic data assimilation while accounting for non-Gaussian uncertainties.

3.3 Water level assimilation using the particle filter and variants

Particle filters (PF) relax the assumption of Gaussianity regarding the form of the posterior probability density functions of the models and observations, offering certain advantages over KF and variants (Moradkhani, 2008). This enables PFs to easily manage the propagation of non-Gaussian distributions through highly non-linear hydraulic models, by tracking the temporal evolution of all the moments of the full probability density function (Plaza et al., 2012). It is rendered possible to consider multiple competing distributions, by updating the probabilities of any given model being true conditioned on the observation, rather than updating the state trajectory (Arulampalam et al., 2002). Exclusively

updating the PDFs also provides the unique advantage of avoiding the hydrostatic reinitialization shock, known to cause numerical instabilities in the hydraulic model domain, as fluxes drop to zero at the assimilation time step and momentum cannot be conserved (Hostache et al., 2018).

Early implementations of the PF used the sequential importance sampling (PF-SIS) algorithm. The PF-SIS algorithm used a Sequential Monte Carlo procedure to approximate the posterior true state PDF, through a number of independent random samples called particles, sampled directly from the state-space. Subsequently, the conditional probability of a given model realization and the observation, is assigned as a weight to each particle and used to compute the expectation defined as the weighted ensemble mean. Starting with a likely proposal distribution, weights and estimates are sequentially updated at every assimilation time steps and the expectation is calculated, which is representative of the "analysis." The PF-SIS conserves mass for each particle unlike the EnKF by selecting the most likely model runs, rather than updating model states which may cause discontinuities in the hydraulic model domain (Matgen et al., 2010).

The SIS algorithm, however, suffers from several significant limitations. First, there is the problem of sample degeneracy, where most of the particles attain very low weights after assimilation steps, leading to an underrepresentation of the state-parameter space in the approximated posterior PDF. In extreme cases, only one particle will acquire the full weight of unity leading to filter collapse, implying that the model uncertainty is not accounted for anymore. The second problem pertains to the ensemble size or particles required for an effective estimation of the posterior PDF. As the true state PDF approximation is dependent on discrete random sampling, it is understandable that the estimation will improve as increase in the number of samples. In theory, this approximation process will work best as the number of particles tends to infinity; this is obvious, as discrete sampling is being used to characterize a continuous process. However, this is nearly impossible to achieve in practice, due to the huge computational demand of distributed hydraulic models.

Literature suggests several pragmatic solutions. Moradkhani et al. (2005a) suggested a variety of ensemble verification measures, to pre-emptively assess the skill and spread of the ensemble. Several resampling schemes have also been proposed, such as the Sequential Importance Resampling (SIR) algorithm. The SIR algorithm repopulates the particles by replicating the highly ranked particles, in proportion to their respective importance weights. In some cases simplistic solutions such as these may work, however, in most cases, the resampling leads to the problem of sample impoverishment. This is when only a few particles are replicated many times, the ensemble therefore containing only a few unique model realizations. In this event, the effective particle population remains spuriously high. Techniques such as inflation have also been proposed to artificially scale the error covariance matrices and compensate for the underestimation of model error covariance due to small ensemble sizes. These are used for sequential as well as variational assimilation (Browne, 2016; Evensen, 2003;

Fletcher, 2018b; Slivinski et al., 2015). Most studies use one or several of these in conjunction, to avoid filter collapse.

In this context, the study by Matgen et al. (2010) used the PF-SIR algorithm to assimilate synthetic EO-derived WLs into a coupled hydrological-hydraulic model. The PF-SIR algorithm was chosen primarily to relax the assumption of Gaussianity. Global weighting procedures such as the one used here, consider WLs simulated by a particular model realization along the entire channel reach as one particle. Weights at each cross-section were computed using a Gaussian PDF and aggregated through multiplication, by assuming (perhaps unrealistically) mutual statistical independence. The PF-based assimilation was able to retrieve the truth, even when errors of up to 5 m were introduced in the synthetic WLs. This implied that for completely ungauged catchments, WLs extracted from a combination of coarse resolution satellite data and global DEMs, could also be useful to effectively constrain flood forecast errors (Schumann et al., 2008a,b). Consistently with previous findings (Andreadis et al., 2007; Matgen et al., 2007a,b), input updating was identified as a crucial aspect in retaining improvements to the model state trajectory. Interestingly, the study also found that a higher frequency of observations is required during the rising limb than during recession, as the errors in the precipitation are unpredictably compounded through the modeling cascade, resulting in increased model forecast errors.

In order to address the gap of defining a suitable spatially and temporally variable non-Gaussian distribution of observations, Giustarini et al. (2012) suggested using the full empirical distribution of WLs. Employing the empirical distribution with no assumptions about its form, finally allowed the optimal utilization of the advantages of PF over KF variants. At each cross-section, a histogram of the EO-derived WLs is computed, which is subsequently used to define the local likelihood of each particle. The final aggregation to global weights is achieved by following the approach proposed by Matgen et al. (2010). Two different case studies were presented in Giustarini et al. (2012), using coarse and high-resolution EO datasets, respectively; temporally persistent improvements in discharge estimation were obtained for both cases. Numerical experiments performed in this study, interestingly revealed a trade-off between WL and discharge estimation accuracy, particularly in regions where channel bathymetry is poorly specified.

3.4 Filter localization and flood extent assimilation

In a pioneering study, which highlighted the possibility of degrading model forecasts through assimilation for the first time, Giustarini et al. (2011) demonstrated that the use of global weighting procedures always leads to compromise solutions. Using synthetic and real experiments, assimilating field data at the cross-sections where EO-derived WLs were available, this study argued that a single model run cannot perform equally well along the entire river reach. In

fact the study showed that defining global weights as a product of local weights as proposed by Matgen et al. (2010), could even lead to the propagation of local scale systematic model errors over the whole domain. Global weights were found to favor acceptable solutions all over the domain, rather than well performing solutions locally. To avoid this problem, Giustarini et al. (2011) proposed the use of filter localization. Using a model setup identical to Matgen et al. (2010), the assimilation was implemented by considering the model simulated WL at each cross-section as a separate particle. Local weights were calculated for each particle, by comparing with the corresponding EO-WLs, using uniform as well as normal PDFs. While this study advocated the use of filter localization techniques going forward, it also warned of potentially introducing bias into the model predictions, as a function of local inconsistencies in the calibrated model. The use of local PF for diagnosing and correcting model errors was recommended for hindcasting applications, while inflow correction was identified as a major research gap for forecasting problems.

Filter localization only updates the states close to the observation location, reducing the weight given to observations spatially disconnected from the estimated state variable (Fig. 12.4). The impact of using small ensemble sizes can then be minimized, primarily by decreasing the state-parameter subspace in which the analysis is conducted (García-Pintado et al., 2013). The study by García-Pintado et al. (2015) also investigated this issue through a series of SAR-derived WL assimilation experiments, based on the ensemble transform Kalman filter (ETKF) with and without localization. ETKF (Hunt et al., 2007) is an adaptation of the square root form of the EnKF. More specifically, the EnSRKF implementation explicitly updates both the ensemble mean and the

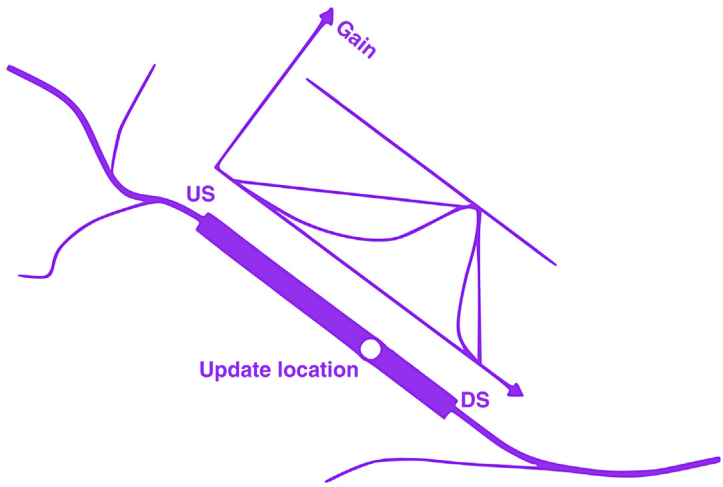

FIGURE. 12.4 Illustration of filter localization for an example observation update location in 1-D. US = upstream and DS = downstream. *(Adapted from Madsen and Skotner (2005).)*

error covariance at each assimilation time step to theoretically match the KF. The ETKF additionally introduces a transform matrix to ensure a symmetric solution (García-Pintado et al., 2013). Results obtained by García-Pintado et al. (2015), corroborated the need for filter localization to avoid the development of spurious correlations, within the forecast error covariance matrix (García-pintado et al., 2014). The use of a flow distance based spatial domain localization metric was recommended, although further testing for channel networks with varied geometries is required. Simultaneous estimation of states and inputs proved necessary for persistent reductions in forecast error as in earlier studies (Neal et al., 2009). The use of localized ETKF for simultaneous parameter estimation (lumped channel roughness and distributed bathymetry) was also investigated, although the results proved to be inconclusive in terms of forecast improvements. Possible reasons could be the localization distance or the error covariance chosen for the stochastic generation of bathymetry estimates, as the standalone experiments on channel friction demonstrated adequate convergence. The findings highlighted that further experiments might be warranted to effectively tune the localization radii and the reach correlation length used in the bathymetry error generation model for improved forecast accuracies. Experimental results were corroborated by the findings of other studies, where empirical localization was found to significantly improve state estimation (Revel et al., 2019; Yamazaki et al., 2018).

As most studies observed and Schumann et al. (2009) incisively pointed out, the problem of local uncertainties stemming from the measurement bias of EO-derived WLs, required the development of more mature retrieval methods (Andreadis and Schumann, 2014; García-Pintado et al., 2013). Moreover, the use of the same DEM both to retrieve the EO-derived WLs and for the implementation of the hydraulic model leads to adding the DEM uncertainty twice in the resulting predictions. While this might be an acceptable risk where highly accurate LiDAR-based elevation data are available, in the case of coarse resolution global topography this could severely impact the forecast error. Moreover, using the same elevation data additionally violates a basic principle of data assimilation, which mandates the use of model independent observations to improve the accuracy of subsequent predictions. Furthermore, even with the advent of sophisticated thinning algorithms for the automatic derivation and appropriate subsample of EO-WLs (Mason et al., 2012), manual intervention is often still necessary (Hostache et al., 2018).

Recent studies have, therefore, focused on the development of techniques capable of directly assimilating flood extents into flood forecasting modeling cascades, rather than water levels (Hostache et al., 2018; Lai et al., 2014; Revilla-Romero et al., 2015, 2016; Shastry and Durand, 2019). Lai et al. (2014) and Revilla-Romero et al. (2016) both interpret inundation extents as a function of the internal model states to develop the cost function for assimilation, that is, water depth and discharge, respectively. The 4D-Var filter was used in the proof of concept study by Lai et al. (2014), for the assimilation of a

MODIS-derived flood extent map (250 m) to optimize a lumped friction parameter, with no particular aim toward forecasting. In contrast, Revilla-Romero et al. (2016) use the EnKF to assimilate dimensionless surface water extent observations (0.1°× 0.1°) satellite-derived from the Global Flood Detection System (http://www.gdacs.org/flooddetection), to improve near real-time (NRT) global flood forecasts. The EO-derived flood extents were interpreted as inundation volumes; the difference between the simulated and observed (interpreted) value, was used to update the models within the EnKF framework. The study was conducted on a global scale and gauge validation demonstrated improvements for a major portion (~60%) of those evaluated. Although the use of EnKF was perhaps not theoretically justified, significant improvements were noted in practice.

Adopting a different approach, Hostache et al. (2018) directly assimilated SAR-derived flood extents using a PF-based assimilation framework. Through a comparison of modeled cell wet-dry status and satellite observed flood probabilities, improvements of up to 50% were obtained in forecast WLs at the assimilation time step. Inundation extents were retrieved from ENVISAT ASAR (resampled to 75 m) into the hydraulic model LISFLOOD-FP. As modeled flood extents are derived based on simulated water depth, the variation in the number of wet-dry cells at most time steps is limited. Consequently, the development of an extent based cost function with enough sensitivity to isolate the best performing ensemble members and drive the assimilation is a scientific challenge (Lai et al., 2014). Hostache et al. (2018) used a number of pragmatic mathematical solutions to facilitate the direct assimilation of flood extents in a real case. For example, the posterior variance was artificially inflated to avoid degeneracy. Although this technical solution enabled a more realistic representation of forecast uncertainty, some more advanced solution should be proposed. Thus, the development of novel flood extent assimilation techniques to optimally combine flood inundation models with EO-flood extents still remains an open scientific challenge (Van Wesemael et al., 2019).

4 Observation operators and characteristics

One common issue highlighted by previous studies was the possible degradation of forecast skill, caused by the introduction of measurement bias in (highly erroneous) observations. Although the issue of observation timing (Giustarini et al., 2011; Matgen et al., 2010) and frequency (Andreadis et al., 2007; Neal et al., 2009) was briefly discussed in a few studies, the first explicit discussion and assessment was provided by García-Pintado et al. (2013). Similarly, Andreadis and Schumann (2014) evaluated assimilation performance sensitivity to the observation spatial location for the very first time. Further studies in this direction, evaluated the impact of domain length (Cooper et al., 2018), observation error correlations (Waller et al., 2018), and observation operators used to calculate the innovation (Cooper et al., 2019).

In order to assess the impact of acquisition timing, García-Pintado et al., (2013) used an ETKF based assimilation strategy in conjunction with LISFLOOD-FP, with a synthetic experiment based on the July 2007 flood event in the widely researched Severn Catchment, United Kingdom (Mason et al., 2010; Neal et al., 2011; Schumann et al., 2011). An error free model was considered with no parametric uncertainty, to independently evaluate the impacts of observation timing on inflow error correction, through several satellite first visit and revisit scenarios. Results illustrated that frequent assimilation during the decreasing limb does not lead to sensible improvement in the forecast, implying that post peak overpass frequency could be reduced when considering budget limited scenarios. However, as satellite flood extents which are used to derive the WLs for assimilation can only be informative for out-of-bank flows, the first visit time should ideally closely follow channel overtopping. Corroborating the findings of Matgen et al. (2010), the results of García-Pintado et al. (2013) demonstrated that multiple observations were necessary during the rising limb of the hydrograph, as additional errors are continuously introduced at the upstream boundary.

Subsequently, Andreadis and Schumann (2014) assessed the spatial observation impact on the forecast skill of hydraulic models, through the LETKF formulation of Hunt et al. (2007) within an ensemble sensitivity (ES) framework (Liu and Kalnay, 2008). In the ES method, the LETKF cost function is modified such that each term can be calculated from the previously initialized ensemble forecasts. This eliminates the need for generating forecasts after the assimilation step. The cost function can be pre-emptively computed for each observation time and for different lead times, simply by selecting the appropriate time steps for the forecasts and observations (Andreadis and Schumann, 2014). Using a continuous annual large-scale implementation of LISFLOOD-FP for the Ohio River, this seminal study showed for the very first time, that observations acquired during low flows consistently degrade forecast error. A synthetic study was conducted where model errors stemming from inflows, parameters, topography, and channel network delineation were considered. The observations were not explicitly assimilated, rather their impact was evaluated by just replacing the state and observation variables in the cost function equation. This allowed previously unused observations, such as river channel width and inundated area, to be considered alongside WSE. On assimilating WLs, the largest improvements in forecast accuracy could be obtained during peak flows, although the error reductions decayed after 5–11 days in some locations and eventually led to forecast degradation. Interestingly, the findings indicated that the assimilation of channel top width mostly degraded forecast skill, while inundated area assimilation mostly resulted in improvements. Further examination revealed that the improvements possible from the assimilation of either observed variable, could be considered as a direct function of the variability (e.g., see Figure 10 in Andreadis and Schumann (2014)). Authors also recommended the use of these methods to plan targeted satellite acquisitions, over reaches that would either

maximize the forecast error reduction or from the locations of fastest growing errors (Langland, 2006). For example, the study was able to identify three river reaches where observations had a positive impact on the forecasts for a lead time of up to 11 days ahead. If EO data were acquired covering those areas, forecast improvements could be maximized while minimizing costs incurred.

The study by Cooper et al. (2018) showed that the hydrostatic reinitialization shock, caused by the fluxes dropping to zero just after the update step in hydraulic data assimilation, could be minimized by applying preassimilation velocities. This pragmatic solution was able to significantly reduce the root mean squared error values obtained just after the assimilation time. Using idealized synthetic domain topography, the study also demonstrated that persistence of error reductions from WL assimilation could be improved by simply considering a longer domain length. The WL observations in different parts of the domain are usually strongly correlated, thereby allowing the ETKF to effectively update downstream WLs. State augmentation was used to simultaneously update model states and parameters, resulting in clear improvements in forecast accuracy at all times. This finding also suggest an interdependence between parametric and inflow errors, due to similar forecast error characteristics obtained from both. Furthermore, the joint-state parameter estimation using EO-derived WLs is able to effectively detect and compensate for biases introduced in either or both.

In a study similar to Andreadis and Schumann (2014), the impact of observation quality on flood data assimilation was investigated by Waller et al., 2018. Through numerical experiments, the authors showed that statistical averages of observation-minus-background and observation-minus-analysis residuals can be useful for the estimation of error correlations in EO-derived WLs. Using the same flood event as García-Pintado et al. (2015), an analysis of observation error and spatiotemporal correlation was elucidated. Spatial analysis showed that the observed forecast error correlations were independent of observation errors. In terms of observation timing, the observations exhibit similar error standard deviations although the correlation length is fairly short. This is expected as this is the most dynamic part of the flood event, where ongoing precipitation is continuously adding errors to the domain while each tributary and sub-catchment respond differently. As the flood wave progresses, standard deviation decreases, while the correlation length scale increases. Given that such observation error assessments are possible at a relatively low computational cost, the authors recommend its use in the identification of data anomalies.

Sensitivity to observation operators was examined by Cooper et al. (2019) using the same idealized test domain as Cooper et al. (2018). In this study, backscatter from a SAR image was directly assimilated to improve hydraulic model forecasts for the first time. Inflow and parametric uncertainty was considered, in a synthetic experiment based on the 2012 River Severn flood event, to compare the performance of a WL-based and a backscatter based observation operator. SAR images were generated using a Gaussian mixture model, using the parameters empirically derived by Giustarini et al. (2016). These parameters

were perturbed within 1% of the values to obtain an ensemble of observed SAR images. The number of backscatter observations used was limited to match the number of satellite WL observations that can typically be expected, to facilitate an intercomparison of the observation operators independent of observation frequency. For instance, WLs indirectly retrieved using SAR-based flood maps and DEMs, are only able to provide reliable estimates at specific shoreline locations which are unobstructed by riparian vegetation. Conversely, the assimilation of backscatter observations means that an observation could be available at every pixel, and thus the number of values used would need to be limited artificially, to enable an unbiased comparison against a WL based operator.

The new backscatter operator generally performs better than the WL operator in all the test cases considered in this study. Using backscatter directly also eliminated the need for multiple image processing steps and the water level derivation, which has been identified as a major source of uncertainty (Schumann et al., 2009). The authors acknowledge that the new operator can exclusively work well in conditions where a clear separation exists between the land-water distributions of backscatter response. As this is rarely the case in reality where backscatter is affected by multiple sources of uncertainty (Schumann, 2019), the effectiveness of this operator has to be tested using a real case study. Moreover, directly using the backscatter values, removes the advantage offered by the probabilistic flood maps produced using a combination of the SAR backscatter, texture, or ancillary data (Dasgupta et al., 2018; Grimaldi et al., 2020).

5 Case studies

Almost all studies assimilating flood information into hydraulic models derive these from SAR images. This is mainly due to the capability of SAR sensors to acquire images day and night and to penetrate cloud cover. This makes SAR systems a lot more suitable for operational and near real-time applications such as sequential data assimilation as floods are due to heavy rainfall closely linked to important cloud covers. In the following section, we propose two case studies based on the paper by Giustarini et al. (2011) and Hostache et al. (2018) that assimilated SAR-derived information into flood inundation models.

5.1 Assimilation of SAR-derived water levels into a hydraulic model

The first study by Giustarini et al. (2011) sequentially assimilate WSE data derived from satellite SAR images into a 1-D hydraulic model of the Alzette River (Luxembourg). The proposed assimilation framework uses a PF with sequential importance resampling. The method employed for deriving WSE from Envisat and ERS images is based on the algorithm proposed by Hostache et al. (2009). The latter first maps flood extent from a SAR image based on a dual thresholding, therefore providing fuzzy flood extent limits. Next, the most reliable information is selected from the fuzzy flood extent limits based on land

use and topography information. This thinned information is then superimposed with a high accuracy digital elevation model in order to locally estimate fuzzy WSE data at the limit of the flood extent in the form of plausible intervals of WSEs. Eventually, based on predetermined flow paths, the intervals of WSE are constrained (i.e., their width is reduced) based on the hydraulic rule stating that WSEs decrease from upstream to downstream in a subcritical flow regime. This last step allows for substantially reducing WSE observation uncertainty.

For assimilating WSE observation derived from one ERS-2 and one ENVISAT SAR images, the study by Giustarini et al. (2011) evaluated two variants of Particle Filter with SIR: one with a global and one with a local particle weighting procedure. In both scenarios, the ensemble of model forecasts (i.e., particles) is generated using an ensemble of upstream boundary conditions of the hydraulic model (streamflow hydrographs generated using an ensemble of hydrologic model simulations with perturbed parameter sets, initial conditions and precipitation data).

This study confirms the finding of Matgen et al. (2010) in showing, as well in a real experiment, a substantial forecast improvement as a result of the assimilation of satellite SAR derived information into a hydraulic model. Moreover, Giustarini et al. (2011) highlighted the need for envisaging bias in the observation. According to the authors, the localized PF is the preferred solution when assimilating unbiased and/or very accurate observations as it helps to retrieve the true water surface line at the assimilation time. However, in poorly gauged basins where satellite image are the only available data source, the PF with a global weighting procedure is to be recommended. Moreover this study shows the complementarity between in situ measurements and satellite data in the proposed data assimilation framework as the combination of both datasets yields better forecast accuracy. Indeed, as argued by the authors, whereas in situ data are point measurement, but with high accuracy and high temporal sampling, satellite data provide instantaneous information with comparatively larger uncertainty but spatially distributed over potentially large areas.

5.2 Assimilation of SAR-derived flood extent maps into a flood forecasting model chain

The second study by Hostache et al. (2018) assimilates probabilistic flood map (PFM) derived from satellite SAR images into a flood forecasting system composed of a conceptual rainfall-runoff model and a 2-D shallow water model of the Severn and Avon Rivers (United Kingdom). The proposed assimilation framework uses a PF with sequential importance sampling, meaning that only particle weights are updated during the assimilation.

The motivation for assimilating flood extent instead of WSE information is that flood extent information can be derived from SAR data automatically and rather straightforwardly, while the assessment of WSE requires high accuracy topography (not available at a global scale) data and involves many additional

steps that cannot be easily automated. According to the authors, this hampers the assimilation of WSE information operationally and in near real-time. The automated method employed for deriving probabilistic flood maps from Envisat images is based on the algorithm proposed by Giustarini et al. (2016). This image processing approach assigns each pixel a probability of being flooded based on its backscatter values. To do so, the probability density functions of "water" and "non-water" pixels is first parameterized based on the image histogram. Next the probability of each pixel being flooded given its backscatter value is computed based on the Bayes theorem using the previously parameterized distributions and assuming a prior probability of any pixel corresponding to water equal to 0.5. The Envisat Wide Swath Mode (WSM) image archive is exploited to derive 11 probabilistic flood maps over 4 different flood events of markedly different magnitudes.

For the sequential assimilation of PFM, Hostache et al. (2018) assumed that the dominant source of uncertainty in their flood forecasting models come from the rainfall uncertainty. They consequently perturbed the rainfall predictions of the ERA-interim database in order to emulate an ensemble of rainfall forecast. This ensemble of forcings is therefore propagated though the hydrological and hydraulic models allowing for simulating an ensemble of flood extent maps.

During the analysis (i.e., assimilation) steps, authors proposed to estimate the posterior probability of each particle (probability of the particles given the observation) by first estimating the particle likelihood (probability of the observation knowing the particle state) at the pixel scale and then multiplying the local pixel likelihoods to derive a global likelihood assuming, as usual in a PF, that observation errors are spatially independent. The weights of the particle, representing the posterior particle distribution, are eventually computed by normalizing the model global likelihood. To estimate probability of the observation knowing the particle states, the following likelihood is proposed in Hostache et al. (2018):

$$p\left(y_{k,j}^{i}|x_{k,j}^{i}\right) \approx y_{k,j}^{i} \times x_{k,j}^{i} + \left(1 - y_{k,j}^{i}\right) \times \left(1 - x_{k,j}^{i}\right), \tag{12.5}$$

where i indicates the particle number, k the assimilation time step number, j the pixel number, $y_{k,j}^{i}$ the probability being water in the observed flood map, and $x_{k,j}^{i}$ the model prediction, taking values of 1 for pixels predicted as flooded and 0 otherwise.

Moreover, in the proposed assimilation framework, a power coefficient is used when computing the posterior particle weights in order to combat sample degeneracy by inflating the posterior distribution variance. As acknowledged by authors, this is only a practical solution that nevertheless efficiently helps in keeping some variance in the posterior distribution.

The experimental results of this study show that, although flood extent is not a state variable of the model, errors of forecast water levels are reduced by more than 50% at the assimilation time step. Moreover, forecast improvements persist

over subsequent time steps for 24 to a few days. However, after 1 or a few days, forecast improvements vanish as the best-performing particles at the assimilation time step do not maintain their high performance forever. The degradation of forecast improvement appears earlier when hydrological conditions change rapidly. Authors conclude that one of the main limitation of such an assimilation framework was the satellite revisit times, but this may reduce with increasing near real-time satellite images availability.

6 Opportunities and challenges

As data assimilation algorithms are extremely sensitive to observation characteristics, several innovative possibilities emerge. First, optimal acquisition strategies can be designed which allow maximum improvements in forecast skill while minimizing costs, based on the relationships between observation characteristics and assimilation performance (Andreadis, 2018). Assimilation experiments can be used to inform acquisition planning, thereby optimizing the location, timing, and frequency of satellite-based flood observations to best support hydraulic forecasting of inundation. Similarly, assimilation can help to diagnose localized discrepancies, in model implementation or even parameterization.

In certain scenarios, integrating observations acquired at specific timings or locations have no impact on the assimilation and can even lead to model degradation. This phenomenon is typically a function of localized dominating model errors, although in rare cases, observation errors or the assimilation algorithm itself could also lead to similar problems. For example, Schumann and Andreadis (2016) insightfully utilized this particular feature to objectively identify reaches which could especially benefit from high resolution topography. Using the LETKF-based ensemble sensitivity approach employed by Andreadis and Schumann (2014), optimum locations for LiDAR acquisitions along the Lower Zambezi River were identified, such that maximum improvements in accuracy could be obtained at minimum costs. The authors also demonstrate local improvements of up to 78% in risk estimates, which is substantial from an emergency management perspective.

In spite of the significant advances made toward hydraulic data assimilation of EO-data for improved operational food inundation forecasting, several areas still require extensive research. An objective estimation of the computational demand versus accuracy trade-off, considering the precision needs of the various stakeholders involved, is the first challenge which needs to be addressed. The representation of model uncertainties ideally requires a large number of simulations to effectively explore the state parameter space. However, in practice each hydraulic model run on a global or even continental-scale, may require several hours of computational time depending on the grid resolution. As Schumann et al. (2014) demonstrated, higher resolution models are required to efficiently resolve local scale flow pathways. Studies have shown that higher resolution modeling is now possible at much larger scales, as a consequence of

the giant strides in scientific computing (Dottori et al., 2016; Quinn et al., 2019; Schumann et al., 2013; Uhe et al., 2019). Additionally, nested modeling approaches could be used to maximize computational efficiency. The work of Mason et al. (2015), for instance, shows that it might be possible to pre-emptively diagnose, areas of large vertical errors in the specified DEM. Subsequently, these highly uncertain sub-domains of the hydraulic model, can serve as the focus of local scale high resolution modeling using LiDAR acquisitions, significantly improving flood forecast skill (Fleischmann et al., 2019; Schumann and Andreadis, 2016).

Another significant challenge for effectively utilizing EO-based data assimilation for improved flood forecasts is the adequate representation of anthropogenic factors like hydraulic infrastructure in models (Andreadis, 2018). Large hydroelectric or irrigation dam reservoirs, often form a substantial portion of catchment storage capacity, yet data on reservoir operations are seldom available in the public domain (Do et al., 2010). Although alternative methods to determine factors like irrigation supply and demand are currently being explored in literature (Brocca et al., 2018; Zaussinger et al., 2018), significant uncertainties are remained in the accurate estimation of flood regulation measures (Schumann et al., 2018). Moreover, the implementation of flood control structures in the DEM is absolutely vital for capturing the actual inundation patterns observed on ground. In fact, misrepresentation of structures can be especially expensive in terms of risk management, in the rare case of a breach which can suddenly inundate large regions. Attempts are underway to develop global maps of control structures using EO-data, although several difficult challenges still remain (Wood et al., 2018).

The integration of other diverse datasets, for example, point observations of water levels and velocities from crowd-sourcing or depth Doppler maps of inundation from GNSS reflectometry, is another significant challenge that faces the flood data assimilation community. Using alternative datasets requires an objective estimation of the associated uncertainty and some data sources such as crowd-sourcing are still rather young in this direction. A lot of research is ongoing, where the potential utility of crowd-sourced and citizen science observations for flood inundation modeling is being investigated (Assumpção et al., 2018; Zheng et al., 2018). Significant progress has been made in this direction, but the filtering and standardization of the available data remain challenging (Mazzoleni, 2016). Alternative observations of flow velocities are also becoming available (Assumpção et al., 2018; Fujita et al., 2007; Muste et al., 2011), which soon might be available to the flood data assimilation community. There is also a need to integrate the research progress in the assimilation of soil moisture (Patil and Ramsankaran, 2018) and evapotranspiration (Hartanto et al., 2017) in hydrological models with hydraulic data assimilation frameworks, such that the utilization of EO-data for flood inundation forecasting can be optimally harmonized.

The final challenge is the translation of flood extent and depth estimates, into hazard and risk estimates, which are more relevant to the stakeholders (Ward

et al., 2015). In fact open source models exist, which can integrate hydraulic model outputs with socioeconomic risk factors, for example, the GLOFRIS (Global Flood Risk) framework (Winsemius et al., 2013), yet the delivery of maps and inundation forecasts in often only in scientific terms. Open Street Maps (OSM) which uses local knowledge of citizen scientists, to maintain a detailed global vector database of road/rail/waterways and buildings, is yet another rich resource which could potentially revolutionize flood emergency management. Maps of inundation could be intersected with the richly detailed OSM GIS layers, with structured crowd-sourced local information about assets at risk (Ward et al., 2015). The humanitarian benefits of the progress in flood inundation modeling can only be quantified through an evaluation of the impacts of improved forecasts on corresponding risk and hazard estimates (Pappenberger et al., 2015).

Schumann and Andreadis (2016) conducted such analyses for the first time in flood inundation modeling literature; although in streamflow forecasting this is a widely recommended practice (Cloke et al., 2013; Pappenberger et al., 2015; Wetterhall et al., 2013). In this context, the High Resolution Settlement Layer (HRSL) developed by Facebook in association with the Centre for International Earth Science Information Network (CIESIN) can also prove to be a valuable resource. HRSL provides gridded population density estimates for 33 countries, at a ~30 m resolution for the year 2015, based on recent census data and high-resolution 50 cm DigitalGlobe imagery (https://www.ciesin.columbia.edu/data/hrsl/). This dataset could be readily used to quantify the change in risk estimates resulting from improved flood data assimilation techniques. Developing comprehensive forecasting frameworks which synergize the progress in EO, numerical modeling, data assimilation, and scientific computing to enhance global flood hazard estimates, could significantly increase flood resilience. In light of urbanization and climate change exacerbating the number and impacts of extreme weather events, developing effective techniques to minimize global flood hazard are urgently required.

7 Summary and perspectives

This chapter presented an overview of the challenges and opportunities associated with the online integration of EO data with hydraulic flood inundation models using data assimilation techniques. The general principles of data assimilation were first discussed, along with a mathematical discussion on the theoretical background of different types of assimilation schemes. This was followed by a critical evaluation of the progress in EO-based hydraulic data assimilation studies, where the evolution of techniques with respect to the current state-of-the-art was presented. Selected case studies which were pivotal to the advancement of hydraulic data assimilation algorithms were then discussed. Finally, the challenges in hydraulic data assimilation were systematically examined and the opportunities with respect to improved flood forecasting were

summarized. A synthesis of all the relevant literature in this direction revealed the following gaps:

1. Diagnostic assessments of localized flood flow behavior need to be undertaken to identify which portions of the model domain could benefit the most from data assimilation. In fact, the possibility of forecast degradation as a consequence of assimilating in highly erroneous model sub-domains makes answering this question quite crucial.
2. The impact of assimilating highly uncertain observations needs to be further investigated, especially with respect to completely ungauged catchments. In this regard, efficient methods for quality control of the assimilated observations while retaining the maximum amount of information possible, also need to be designed.
3. Filter localization methods, which consider hydraulic relationships to objectively identify optimal regions of observation influence, need to be developed, to support operational applications of hydraulic data assimilation. Similarly, advanced techniques to artificially inflate the error covariance need to be considered, which allow a comprehensive representation of model uncertainties even with limited ensemble members.
4. Effective spatial cost functions, which are sensitive to subtle changes in the model state variable in question, need to be designed to better quantify the innovation and optimize the possible forecast improvements through assimilation. In this context, techniques to synthetically scale the objective function values such that the sensitivity to changes in state can be enhanced also need to be explored.

Research on hydraulic data assimilation of Earth Observations of floods, is relatively new and many scientific challenges remain. The availability of different flood observations from diverse sources will only increase in future and the hydraulic data assimilation community needs to evolve rapidly to keep up with the pace of advancements in measurement techniques. Estimates of associated uncertainty will vary based on each observation technique and the measured variable in question. In order to unlock the full potential of EO data for hydraulic flood inundation forecasting, it is imperative to objectively estimate these uncertainties and remain cognizant of them during the assimilation process (Schumann et al., 2016). Harmonizing the progress in hydraulic modeling, data assimilation, and measurement techniques through the development of operational forecasting systems, is required to ensure the optimal utilization of EO-data and can finally result in tangible humanitarian benefits.

References

Alfieri, L., Burek, P., Dutra, E., Krzeminski, B., Muraro, D., Thielen, J., Pappenberger, F., 2013. GloFAS-global ensemble streamflow forecasting and flood early warning. Hydrol. Earth Syst. Sci. 17, 1161–1175, https://doi.org/10.5194/hess-17-1161-2013.

Alsdorf, D.E., Rodriguez, E., Lettenmaier, D.P., 2007. Measuring surface water from space. Rev. Geophys. 45, 1–24. doi: 10.1029/2006RG000197.1.INTRODUCTION.

Andreadis, K.M., 2018. Data assimilation and river hydrodynamic modeling over large scales. In: Global Flood Hazard, Applications in Modeling, Mapping, Forecasting, vol. 233. In: Geophysical Monograph, Series. American Geophysical Union and Wiley, pp. 229–237.

Andreadis, K.M., Clark, E.A., Lettenmaier, D.P., Alsdorf, D.E., 2007. Prospects for river discharge and depth estimation through assimilation of swath-altimetry into a raster-based hydrodynamics model. Geophys. Res. Lett. 34, 1–5. doi: 10.1029/2007GL029721.

Andreadis, K.M., Schumann, G.J.P., 2014. Estimating the impact of satellite observations on the predictability of large-scale hydraulic models. Adv. Water Resour. 73, 44–54. doi: 10.1016/j.advwatres.2014.06.006.

Archer, L., Neal, J.C., Bates, P.D., House, J.I., 2018. Comparing TanDEM-X data with frequently-used DEMs for flood inundation modelling. Water Resour. Res. 54 (12), 10,205–10,222. doi: 10.1029/2018WR023688.

Arulampalam, M.S., Maskell, S., Gordon, N., Clapp, T., 2002. A tutorial on particle filters for online nonlinear/non-GaussianBayesian tracking. IEEE Trans. Signal Process. 50, 174–188. doi: 10.1109/78.978374.

Assumpção, T.H., Popescu, I., Jonoski, A., Solomatine, D.P., 2018. Citizen observations contributing to flood modelling: opportunities and challenges. Hydrol. Earth Syst. Sci. 22, 1473–1489.

Baratelli, F., Flipo, N., Rivière, A., Biancamaria, S., 2018. Retrieving river baseflow from SWOT spaceborne mission. Remote Sens. Environ. 218, 44–54. doi: 10.1016/j.rse.2018.09.013.

Bates, P.D., 2012. Integrating remote sensing data with flood inundation models: how far have we got? Hydrol. Process. 26, 2515–2521. doi: 10.1002/hyp.9374.

Bates, P.D., De Roo S a P.J., 2000. A simple raster based model for flood inundation simulation. J. Hydrol. 236, 54–77. doi: 10.1016/S0022-1694(00)00278-X.

Bates, P.D., Neal, J., Sampson, C., Smith, A., Trigg, M., 2017. Progress toward hyperresolution models of global flood hazard. Risk Modeling for Hazards and Disasters. Elsevier Inc.doi: 10.1016/B978-0-12-804071-3.00009-4.

Bates, P.D., Neal, J.C., Alsdorf, D., Schumann, G.J.P., 2014. Observing global surface water flood dynamics. Surv. Geophys. 35, 839–852. doi: 10.1007/s10712-013-9269-4.

Bauer-Gottwein, P., Jensen, I.H., Guzinski, R., Bredtoft, G.K.T., Hansen, S., Michailovsky, C.I., 2015. Operational river discharge forecasting in poorly gauged basins: the Kavango River basin case study. Hydrol. Earth Syst. Sci. 19, 1469–1485. doi: 10.5194/hess-19-1469-2015.

Biancamaria, S., Lettenmaier, D.P., Pavelsky, T.M., 2016. The SWOT mission and its capabilities for land hydrology. Surv. Geophys. 37, 307–337. doi: 10.1007/s10712-015-9346-y.

Blöschl, G., Bierkens, M.F.P., Chambel, A., Cudennec, C., Destouni, G., Fiori, A., Kirchner, J.W., McDonnell, J.J., Savenije, H.H.G., Sivapalan, M., Stumpp, C., Toth, E., Volpi, E., Carr, G., Lupton, C., Salinas, J., Széles, B., Viglione, A., Aksoy, H., Allen, S.T., Amin, A., Andréassian, V., Arheimer, B., Aryal, S.K., Baker, V., Bardsley, E., Barendrecht, M.H., Bartosova, A., Batelaan, O., Berghuijs, W.R., Beven, K., Blume, T., Bogaard, T., Borges de Amorim, P., Böttcher, M.E., Boulet, G., Breinl, K., Brilly, M., Brocca, L., Buytaert, W., Castellarin, A., Castelletti, A., Chen, X., Chen, Y., Chen, Y., Chifflard, P., Claps, P., Clark, M.P., Collins, A.L., Croke, B., Dathe, A., David, P.C., de Barros, F.P.J., de Rooij, G., Di Baldassarre, G., Driscoll, J.M., Duethmann, D., Dwivedi, R., Eris, E., Farmer, W.H., Feiccabrino, J., Ferguson, G., Ferrari, E., Ferraris, S., Fersch, B., Finger, D., Foglia, L., Fowler, K., Gartsman, B., Gascoin, S., Gaume, E., Gelfan, A., Geris, J., Gharari, S., Gleeson, T., Glendell, M., Gonzalez Bevacqua, A., González-Dugo, M.P., Grimaldi, S., Gupta, A.B., Guse, B., Han, D., Hannah, D., Harpold, A., Haun, S., Heal, K., Helfricht, K., Herrnegger, M., Hipsey, M., Hlaváčiková, H., Hohmann,

C., Holko, L., Hopkinson, C., Hrachowitz, M., Illangasekare, T.H., Inam, A., Innocente, C., Istanbulluoglu, E., Jarihani, B., Kalantari, Z., Kalvans, A., Khanal, S., Khatami, S., Kiesel, J., Kirkby, M., Knoben, W., Kochanek, K., Kohnová, S., Kolechkina, A., Krause, S., Kreamer, D., Kreibich, H., Kunstmann, H., Lange, H., Liberato, M.L.R., Lindquist, E., Link, T., Liu, J., Loucks, D.P., Luce, C., Mahé, G., Makarieva, O., Malard, J., Mashtayeva, S., Maskey, S., Mas-Pla, J., Mavrova-Guirguinova, M., Mazzoleni, M., Mernild, S., Misstear, B.D., Montanari, A., Müller-Thomy, H., Nabizadeh, A., Nardi, F., Neale, C., Nesterova, N., Nurtaev, B., Odongo, V.O., Panda, S., Pande, S., Pang, Z., Papacharalampous, G., Perrin, C., Pfister, L., Pimentel, R., Polo, M.J., Post, D., Prieto Sierra, C., Ramos, M.-H., Renner, M., Reynolds, J.E., Ridolfi, E., Rigon, R., Riva, M., Robertson, D.E., Rosso, R., Roy, T., Sá, J.H.M., Salvadori, G., Sandells, M., Schaefli, B., Schumann, A., Scolobig, A., Seibert, J., Servat, E., Shafiei, M., Sharma, A., Sidibe, M., Sidle, R.C., Skaugen, T., Smith, H., Spiessl, S.M., Stein, L., Steinsland, I., Strasser, U., Su, B., Szolgay, J., Tarboton, D., Tauro, F., Thirel, G., Tian, F., Tong, R., Tussupova, K., Tyralis, H., Uijlenhoet, R., van Beek, R., van der Ent, R.J., van der Ploeg, M., Van Loon, A.F., van Meerveld, I., van Nooijen, R., van Oel, P.R., Vidal, J.-P., von Freyberg, J., Vorogushyn, S., Wachniew, P., Wade, A.J., Ward, P., Westerberg, I.K., White, C., Wood, E.F., Woods, R., Xu, Z., Yilmaz, K.K., Zhang, Y., 2019. Twenty-three unsolved problems in hydrology (UPH)—a community perspective. Hydrol. Sci. J. 64 (10), 1141–1158. doi: 10.1080/02626667.2019.1620507.

Brisset, P., Monnier, J., Garambois, P.A., Roux, H., 2018. On the assimilation of altimetric data in 1D Saint–Venant river flow models. Adv. Water Resour. 119, 41–59. doi: 10.1016/j.advwatres.2018.06.004.

Brocca, L., Tarpanelli, A., Filippucci, P., Dorigo, W., Zaussinger, F., Gruber, A., Fernández-Prieto, D., 2018. How much water is used for irrigation? A new approach exploiting coarse resolution satellite soil moisture products. Int. J. Appl. Earth Obs. Geoinf. 73, 752–766. doi: 10.1016/j.jag.2018.08.023.

Browne, P.A., 2016. A comparison of the equivalent weights particle filter and the local ensemble transform Kalman filter in application to the barotropic vorticity equation. Tellus A Dyn. Meteorol. Oceanogr. 68 (1), 30466. doi: 10.3402/tellusa.v68.30466.

Chen, H., Liang, Q., Liu, Y., Xie, S., 2018. Hydraulic correction method (HCM) to enhance the efficiency of SRTM DEM in flood modeling. J. Hydrol. 559, 56–70. doi: 10.1016/j.jhydrol.2018.01.056.

Chu, T., Lindenschmidt, K.E., 2017. Comparison and validation of Digital Elevation Models derived from InSAR for a Flat Inland Delta in the high latitudes of Northern Canada. Can. J. Remote Sens. 43, 109–123. doi: 10.1080/07038992.2017.1286936.

Cloke, H., Pappenberger, F., Thielen, J., Thiemig, V., 2013. Operational European flood forecasting. In: Environmental Modeling: Finding Simplicity in Complexity, second ed. John Wiley & Sons, Inc., pp. 415–434. https://doi.org/10.1002/9781118351475.ch25.

Cooper, E.S., Dance, S.L., García-Pintado, J., Nichols, N.K., Smith, P., 2019. Observation operators for assimilation of satellite observations in fluvial inundation forecasting. Hydrol. Earth Syst. Sci. 23, 2541–2559, https://doi.org/10.5194/hess-2018-589.

Cooper, E.S., Dance, S.L., Garcia-Pintado, J., Nichols, N.K., Smith, P.J., 2018. Observation impact, domain length and parameter estimation in data assimilation for flood forecasting. Environ. Model. Softw. 104, 199–214, https://doi.org/10.1016/j.envsoft.2018.03.013.

Dasgupta, A., Grimaldi, S., Ramsankaran, R.A.A.J., Pauwels, V.R.N., Walker, J.P., 2018. Towards operational SAR-based flood mapping using neuro-fuzzy texture-based approaches. Remote Sens. Environ. 215, 313–329, https://doi.org/10.1016/j.rse.2018.06.019.

Do, H.X., Westra, S., Leonard, M., Gudmundsson, L., 2010. Global-scale prediction of flood timing using atmospheric reanalysis. Water Resour. Res. 56 (1), 1–27.

De Lannoy, G.J.M., Reichle, R.H., Houser, P.R., Pauwels, V.R., Verhoest, N.E., 2007. Correcting for forecast bias in soil moisture assimilation with the ensemble Kalman filter. Water Resour. Res. 43, W09410.

Domeneghetti, A., Schumann, G.J.P., Frasson, R.P.M., Wei, R., Pavelsky, T.M., Castellarin, A., Brath, A., Durand, M.T., 2018a. Characterizing water surface elevation under different flow conditions for the upcoming SWOT mission. J. Hydrol. 561, 848–861, https://doi.org/10.1016/j.jhydrol.2018.04.046.

Domeneghetti, A., Schumann, G.J.P., Tarpanelli, A., 2019. Preface: Remote sensing for flood mapping and monitoring of flood dynamics. Remote Sens. 11 (8), 943, https://doi.org/10.3390/rs11080940.

Domeneghetti, A., Tarpanelli, A., Grimaldi, L., Brath, A., 2018b. Flow duration curve from satellite: Potential of a lifetime SWOT mission. Remote Sens. 10, 1–23, https://doi.org/10.3390/rs10071107.

Dottori, F., Salamon, P., Bianchi, A., Alfieri, L., Hirpa, F.A., Feyen, L., 2016. Development and evaluation of a framework for global flood hazard mapping. Adv. Water Resour. 94, 87–102, https://doi.org/10.1016/j.advwatres.2016.05.002.

Dumedah, G., 2012. Formulation of the evolutionary-based data assimilation, and its implementation in hydrological forecasting. Water Resour. Manag. 26, 3853–3870, https://doi.org/10.1007/s11269-012-0107-0.

Durand, M., Andreadis, K.M., Alsdorf, D.E., Lettenmaier, D.P., Moller, D., Wilson, M., 2008. Estimation of bathymetric depth and slope from data assimilation of swath altimetry into a hydrodynamic model. Geophys. Res. Lett. 35, 1–5, https://doi.org/10.1029/2008GL034150.

Elvira, V., Miguez, J., Djurie, P.M., 2017. Adapting the number of particles in sequential Monte Carlo methods through an online scheme for convergence assessment. IEEE Trans. Signal Process. 65, 1781–1794, https://doi.org/10.1109/TSP.2016.2637324.

Emerton, R.E., Stephens, E.M., Pappenberger, F., Pagano, T.C., Weerts, A.H., Wood, A.W., Salamon, P., Brown, J.D., Hjerdt, N., Donnelly, C., Baugh, C.A., Cloke, H.L., 2016. Continental and global scale flood forecasting systems. Wiley Interdiscip. Rev. Water 3, 391–418, https://doi.org/10.1002/wat2.1137.

Evensen, G., 2004. Sampling strategies and square root analysis schemes for the EnKF. Ocean Dyn. 54, 539–560, https://doi.org/10.1007/s10236-004-0099-2.

Evensen, G., 2003. The Ensemble Kalman Filter: Theoretical formulation and practical implementation. Ocean Dyn. 53, 343–367, https://doi.org/10.1007/s10236-003-0036-9.

Fleischmann, A., Paiva, R., Collischonn, W., 2019. Can regional to continental river hydrodynamic models be locally relevant? A cross-scale comparison. J. Hydrol. X 3, 100027, https://doi.org/10.1016/j.hydroa.2019.100027.

Fletcher, S.J., 2018a. Observation space variational data assimilation methods. Data Assim. Geosci. 1, 753–763. doi: 10.1016/B978-0-12-804444-5.00018-0.

Fletcher, S.J., 2018b. Variational data assimilation. In: Data Assimilation for the Geosciences, first ed. Elsevier, pp. 673–703. https://doi.org/10.1016/b978-0-12-804444-5.00016-7.

Frasson, R.P., de, M., Pavelsky, T.M., Fonstad, M.A., Durand, M.T., Allen, G.H., Schumann, G., Lion, C., Beighley, R.E., Yang, X., 2019. Global relationships between river width, slope, catchment area, Meander wavelength, sinuosity, and discharge. Geophys. Res. Lett. 46, 3252–3262, https://doi.org/10.1029/2019GL082027.

Fu, L., Rodriguez, E., 2004. High-resolution measurement of ocean surface topography by radar interferometry for oceanographic and geophysical applications. In: Sparks, R.S.J., Hawkesworth, C.J., (Eds.), The State of the Planet: Frontiers and Challenges in Geophysics, Geophysical

Monograph Series. American Geophysical Union, pp. 209–224. https://doi.org/http://dx.doi.org/10.1029/150GM17.

Fujita, I., Watanabe, H., Tsubaki, R., 2007. Development of a non-intrusive and efficient flow monitoring technique: The space-time image velocimetry (STIV). Int. J. River Basin Manag. 5, 105–114, https://doi.org/10.1080/15715124.2007.9635310.

Gallant, J.C., Dowling, T.I., Read, A.M., Wilson, N., Tickle, P., Inskeep, C., 2011. 1 second SRTM Derived Products User Guide 106. Geoscience Australia.

García-pintado, J., Mason, D.C., Dance, S.L., 2014. Moderation of ensemble covariances for data assimilation of satellite-based water level observations into flood modeling. Geophys. Res. Abs. 16, 11618.

García-Pintado, J., Mason, D.C., Dance, S.L., Cloke, H.L., Neal, J.C., Freer, J., Bates, P.D., 2015. Satellite-supported flood forecasting in river networks: A real case study. J. Hydrol. 523, 706–724, https://doi.org/10.1016/j.jhydrol.2015.01.084.

García-Pintado, J., Neal, J.C., Mason, D.C., Dance, S.L., Bates, P.D., 2013. Scheduling satellite-based SAR acquisition for sequential assimilation of water level observations into flood modelling. J. Hydrol. 495, 252–266, https://doi.org/10.1016/j.jhydrol.2013.03.050.

Giustarini, L., Hostache, R., Kavetski, D., Chini, M., Corato Giovanni, Schlaffer, S., Matgen, P., 2016. Probabilistic flood mapping using synthetic aperture radar data. IEEE Trans. Geosci. Remote Sens. 54, 6958–6969.

Giustarini, L., Matgen, P., Hostache, R., Dostert, J., 2012. From SAR-derived flood mapping to water level data assimilation into hydraulic models. In: Remote Sensing for Agriculture, Ecosystems, and Hydrology XIV. SPIE Remote Sensing, Edinburgh, United Kingdom, pp. 85310U. https://doi.org/10.1117/12.974655.

Giustarini, L., Matgen, P., Hostache, R., Montanari, M., Plaza, D., Pauwels, V.R.N., De Lannoy, G.J.M., De Keyser, R., Pfister, L., Hoffmann, L., Savenije, H.H.G., 2011. Assimilating SAR-derived water level data into a hydraulic model: a case study. Hydrol. Earth Syst. Sci. 15, 2349–2365, https://doi.org/10.5194/hess-15-2349-2011.

Grimaldi, S., Li, Y., Pauwels, V.R.N., Walker, J.P., 2016. Remote sensing-derived water extent and level to constrain hydraulic flood forecasting models: Opportunities and challenges. Surv. Geophys. 37, 977–1034, https://doi.org/10.1007/s10712-016-9378-y.

Grimaldi, S., Schumann, G.J.-P., Shokri, A., Walker, J.P., Pauwels, V.R.N., 2019. Challenges, opportunities and pitfalls for global coupled hydrologic-hydraulic modeling of floods. Water Resour. Res. 55, 1–24, https://doi.org/10.1029/2018WR024289.

Grimaldi, S., Xu, J., Li, Y., Pauwels, V.R.N., Walker, J.P., 2020. Flood mapping under vegetation using single SAR acquisitions. Remote Sens. Environ. 237, 111582, https://doi.org/10.1016/j.rse.2019.111582.

Habert, J., Ricci, S., Le Pape, E., Thual, O., Piacentini, A., Goutal, N., Jonville, G., Rochoux, M., 2016. Reduction of the uncertainties in the water level-discharge relation of a 1D hydraulic model in the context of operational flood forecasting. J. Hydrol. 532, 52–64, https://doi.org/10.1016/j.jhydrol.2015.11.023.

Hartanto, I.M., van der Kwast, J., Alexandridis, T.K., Almeida, W., Song, Y., van Andel, S.J., Solomatine, D.P., 2017. Data assimilation of satellite-based actual evapotranspiration in a distributed hydrological model of a controlled water system. Int. J. Appl. Earth Obs. Geoinf. 57, 123–135, https://doi.org/10.1016/j.jag.2016.12.015.

Hawker, L., Neal, J.C., Bates, P., 2019. Accuracy assessment of the TanDEM-X 90 Digital Elevation Model for selected floodplain sites. Remote Sens. Environ. 232, 111319, https://doi.org/10.1016/j.rse.2019.111319.

Hirpa, F.A., Salamon, P., Beck, H.E., Lorini, V., Alfieri, L., Zsoter, E., Dadson, S.J., 2018. Calibration of the Global Flood Awareness System (GloFAS) using daily streamflow data. J. Hydrol. 566, 595–606, https://doi.org/10.1016/j.jhydrol.2018.09.052.

Hirt, C., 2018. Artefact detection in global digital elevation models (DEMs): The Maximum Slope Approach and its application for complete screening of the SRTM v4.1 and MERIT DEMs. Remote Sens. Environ. 207, 27–41, https://doi.org/10.1016/j.rse.2017.12.037.

Hossain, F., Maswood, M., Siddique-E-Akbor, A.H., Yigzaw, W., Mazumdar, L.C., Ahmed, T., Hossain, M., Shah-Newaz, S.M., Limaye, A., Lee, H., Pradhan, S., Shrestha, B., Bajracahrya, B., Biancamaria, S., Shum, C.K., Turk, F.J., 2014. A promising radar altimetry satellite system for operational flood forecasting in flood-prone bangladesh. IEEE Geosci. Remote Sens. Mag. 2, 27–36, https://doi.org/10.1109/MGRS.2014.2345414.

Hostache, R., Chini, M., Giustarini, L., Neal, J., Kavetski, D., Wood, M., Corato, G., Pelich, R.M., Matgen, P., 2018. Near-real-time assimilation of SAR-derived flood maps for improving flood forecasts. Water Resour. Res. 54, 5516–5535, https://doi.org/10.1029/2017WR022205.

Hostache, R., Lai, X., Monnier, J., Puech, C., 2010. Assimilation of spatially distributed water levels into a shallow-water flood model. Part II: Use of a remote sensing image of Mosel River. J. Hydrol. 390, 257–268, https://doi.org/10.1016/j.jhydrol.2010.07.003.

Hostache, R., Matgen, P., Giustarini, L., Teferle, F.N., Tailliez, C., Iffly, J.F., Corato, G., 2015. A drifting GPS buoy for retrieving effective riverbed bathymetry. J. Hydrol. 520, 397–406, https://doi.org/10.1016/j.jhydrol.2014.11.018.

Hostache, R., Matgen, P., Schumann, G., Puech, C., Hoffmann, L., Pfister, L., 2009. Water level estimation and reduction of hydraulic model calibration uncertainties using satellite SAR images of floods. IEEE Trans. Geosci. Remote Sens. 47 (2), 1–10.

Huang, C., Chen, Y., Zhang, S., Wu, J., 2018a. Detecting, extracting, and monitoring surface water from space using optical sensors: A review. Rev. Geophys. 56, 333–360, https://doi.org/10.1029/2018RG000598.

Huang, Q., Long, D., Du, M., Zeng, C., Li, X., Hou, A., Hong, Y., 2018b. An improved approach to monitoring Brahmaputra River water levels using retracked altimetry data. Remote Sens. Environ. 211, 112–128, https://doi.org/10.1016/j.rse.2018.04.018.

Hunt, B.R., Kostelich, E.J., Szunyogh, I., 2007. Efficient data assimilation for spatiotemporal chaos: A local ensemble transform Kalman filter. Phys. D Nonlinear Phenom. 230, 112–126, https://doi.org/10.1016/j.physd.2006.11.008.

Kim, D., Yu, H., Lee, H., Beighley, E., Durand, M., Alsdorf, D.E., Hwang, E., 2019. Ensemble learning regression for estimating river discharges using satellite altimetry data: Central Congo River as a Test-bed. Remote Sens. Environ. 221, 741–755, https://doi.org/10.1016/j.rse.2018.12.010.

Kim, S., Sharma, A., 2019. The role of floodplain topography in deriving basin discharge using passive microwave remote sensing. Water Resour. Res. 55 (2), 1707–1716, https://doi.org/10.1029/2018WR023627.

Kitagawa, G., 1996. Monte Carlo filter and smoother for non-Gaussian nonlinear state space models. J. Comput. Graph. Stat. 5, 1–25, https://doi.org/https://doi.org/10.1080/10618600.1996.10474692.

Kumar, A., Dasgupta, A., Lokhande, S., Ramsankaran, R.A.A.J., 2019. Benchmarking the Indian National CartoDEM against SRTM for 1D hydraulic modelling. Int. J. River Basin Manag. 17, 1–10, https://doi.org/10.1080/15715124.2019.1606816.

Lacava, T., Ciancia, E., Faruolo, M., Pergola, N., Satriano, V., Tramutoli, V., 2019. On the potential of RST-FLOOD on visible Infrared Imaging Radiometer Suite data for flooded areas detection. Remote Sens. 11, 598, https://doi.org/10.3390/rs11050598.

Lahoz, W., Khattatov, B., Menard, R., Nichols, N.K., Talagrand, O., Kalnay, E., Buehner, M., Cohn, S.E., Huang, X.-Y., Lynch, P., Thepaut, J.-N., Anderrson, E., Charlton-Perez, A., Swinbank, R., Rood, R.B., Yudin, V., Errera, Q., Elbern, H., Strunk, A., Nieradzik, L., Haines, K., Houser, P.R., Walker, J.P., De Lannoy, G.J.M., Bosilovich, M.G., Masutani, M., Schlatter, T.W., Errico, R.M., Stoffelen, A., Woollen, J.S., Emmitt, G.D., Riishojgaard, L.-P., Lord, S.J., Lewis, S.R., 2010. Data Assimilation: Making Sense of Observations, first ed. Springer-Verlag Berlin Heidelberg, London, https://doi.org/10.1007/978-3-540-74703-1.

Lai, X., Liang, Q., Yesou, H., Daillet, S., 2014. Variational assimilation of remotely sensed flood extents using a 2-D flood model. Hydrol. Earth Syst. Sci. 18, 4325–4339, https://doi.org/10.5194/hess-18-4325-2014.

Lai, X., Monnier, J., 2009. Assimilation of spatially distributed water levels into a shallow-water flood model. Part I: Mathematical method and test case. J. Hydrol. 377, 1–11, https://doi.org/10.1016/j.jhydrol.2009.07.058.

Lakshmivarahan, S., Lewis, J.M., 2010. Forward Sensitivity Approach to dynamic data assimilation. Adv. Meteorol. 2010, 1–2.

Langland, R.H., 2006. Issues in targeted observing. Q. J. R. Meteorol. Soc. 131, 3409–3425, https://doi.org/10.1256/qj.05.130.

Liu, J., Kalnay, E., 2008. Estimating observation impact without adjoint model in an ensemble Kalman filter. Q. J. R. Meteorol. Soc. 134, 1327–1335, https://doi.org/10.1002/qj.280.

Madsen, H., Canizares, R., 1999. Comparison of extended and ensemble Kalman filters. Int. J. Numer. Methods Fluids 31, 961–981.

Madsen, H., Skotner, C., 2005. Adaptive state updating in real-time river flow forecasting—A combined filtering and error forecasting procedure. J. Hydrol. 308, 302–312, https://doi.org/10.1016/j.jhydrol.2004.10.030.

Mason, D.C., Garcia-Pintado, J., Cloke, H.L., Dance, S.L., 2015. The potential of flood forecasting using a variable-resolution global Digital Terrain Model and flood extents from synthetic aperture radar images. Front. Earth Sci. 3, 1–14, https://doi.org/10.3389/feart.2015.00043.

Mason, D.C., Schumann, G.J.-P., Neal, J.C., Garcia-Pintado, J., Bates, P.D., 2012. Automatic near real-time selection of flood water levels from high resolution Synthetic Aperture Radar images for assimilation into hydraulic models: A case study. Remote Sens. Environ. 124, 705–716, https://doi.org/10.1016/j.rse.2012.06.017.

Mason, D.C., Speck, R., Devereux, B., Schumann, G.J.P., Neal, J.C., Bates, P.D., 2010. Flood detection in urban areas using TerraSAR-X. IEEE Trans. Geosci. Remote Sens. 48, 882–894, https://doi.org/10.1109/tgrs.2009.2029236.

Matgen, P., Montanari, M., Hostache, R., Pfister, L., Hoffmann, L., Plaza, D., Pauwels, V.R.N., De Lannoy, G.J.M., De Keyser, R., Savenije, H.H.G., 2010. Towards the sequential assimilation of SAR-derived water stages into hydraulic models using the Particle Filter: proof of concept. Hydrol. Earth Syst. Sci. 14, 1773–1785, https://doi.org/10.5194/hess-14-1773-2010.

Matgen, P., Schumann, G., Henry, J.-B., Hoffmann, L., Pfister, L., 2007a. Integration of SAR-derived river inundation areas, high-precision topographic data and a river flow model toward near real-time flood management. Int. J. Appl. Earth Obs. Geoinf. 9, 247–263, https://doi.org/10.1016/j.jag.2006.03.003.

Matgen, P., Schumann, G., Pappenberger, F., Pfister, L., 2007. Sequential assimilation of remotely sensed water stages in flood inundation models. In: Proceedings of Symposium HS3007 at IUGG2007. Perugia, Italy, pp. 78–88.

Mazzoleni, M., 2016. Improving flood prediction assimilating uncertain crowdsourced data into hydrologic and hydraulic models. Delft University of Technology and UNESCO-IHE Institute for Water Education.

Mazzoleni, M., Alfonso, L., Chacon-Hurtado, J., Solomatine, D., 2015. Assimilating uncertain, dynamic and intermittent streamflow observations in hydrological models. Adv. Water Resour. 83, 323–339, https://doi.org/10.1016/j.advwatres.2015.07.004.

Michailovsky, C.I., McEnnis, S., Berry, P.A.M., Smith, R., Bauer-Gottwein, P., 2012. River monitoring from satellite radar altimetry in the Zambezi River basin. Hydrol. Earth Syst. Sci. 16, 2181–2192, https://doi.org/10.5194/hess-16-2181-2012.

Moradkhani, H., 2008. Hydrologic remote sensing and land surface data assimilation. Sensors 8, 2986–3004, https://doi.org/10.3390/s8052986.

Moradkhani, H., Hsu, K.-L., Gupta, H., Sorooshian, S., 2005a. Uncertainty assessment of hydrologic model states and parameters: Sequential data assimilation using the particle filter. Water Resour. Res. 41, 1–17, https://doi.org/10.1029/2004WR003604.

Moradkhani, H., Sorooshian, S., Gupta, H.V., Houser, P.R., 2005b. Dual state-parameter estimation of hydrological models using ensemble Kalman filter. Adv. Water Resour. 28, 135–147, https://doi.org/10.1016/j.advwatres.2004.09.002.

Muste, M., Ho, H.C., Kim, D., 2011. Considerations on direct stream flow measurements using video imagery: Outlook and research needs. J. Hydro-Environment Res. 5, 289–300, https://doi.org/10.1016/j.jher.2010.11.002.

Neal, J., Schumann, G., Bates, P., Buytaert, W., Matgen, P., Pappenberger, F., 2009. A data assimilation approach to discharge estimation from space. Hydrol. Process. 23, 3641–3649, https://doi.org/10.1002/hyp.7518.

Neal, J., Schumann, G., Fewtrell, T., Budimir, M., Bates, P., Mason, D., 2011. Evaluating a new LISFLOOD-FP formulation with data from the summer 2007 floods in Tewkesbury, UK. J. Flood Risk Manag. 4, 88–95, https://doi.org/10.1111/j.1753-318X. 2011.01093.x.

Neal, J.C., Atkinson, P.M., Hutton, C.W., 2007. Flood inundation model updating using an ensemble Kalman filter and spatially distributed measurements. J. Hydrol. 336, 401–415, https://doi.org/10.1016/j.jhydrol.2007.01.012.

Nichols, N.K., 2010. Mathematical concepts of data assimilation. In: Lahoz, W. (Ed.), Data Assimilation. Springer Berlin Heidelberg, Berlin, Heidelberg, pp. 13–39, https://doi.org/10.1007/978-3-540-74703-1_2.

O'Loughlin, F.E., Paiva, R.C.D., Durand, M., Alsdorf, D.E., Bates, P.D., 2016. A multi-sensor approach towards a global vegetation corrected SRTM DEM product. Remote Sens. Environ. 182, 49–59, https://doi.org/10.1016/j.rse.2016.04.018.

Ogilvie, A., Belaud, G., Delenne, C., Bailly, J.-S., Bader, J.-C., Oleksiak, A., Ferry, L., Martin, D., 2015. Decadal monitoring of the Niger Inner Delta flood dynamics using MODIS optical data. J. Hydrol. 523, 368–383, https://doi.org/10.1016/j.jhydrol.2015.01.036.

Oliveira, E.R., Disperati, L., Cenci, L., Pereira, L.G., Alves, F.L., 2019. Multi-Index Image Differencing Method (MINDED) for flood extent estimations. Remote Sens. 11, 1–29.

Oubanas, H., Gejadze, I., Malaterre, P.O., Durand, M., Wei, R., Frasson, R.P.M., Domeneghetti, A., 2018a. Discharge estimation in ungauged basins through variational data assimilation: The potential of the SWOT mission. Water Resour. Res. 54, 2405–2423, https://doi.org/10.1002/2017WR021735.

Oubanas, H., Gejadze, I., Malaterre, P.O., Mercier, F., 2018b. River discharge estimation from synthetic SWOT-type observations using variational data assimilation and the full Saint-Venant hydraulic model. J. Hydrol. 559, 638–647, https://doi.org/10.1016/j.jhydrol.2018.02.004.

Paiva, R.C.D., Collischonn, W., Bonnet, M.P., De Gonçalves, L.G.G., Calmant, S., Getirana, a., Santos Da Silva, J., 2013. Assimilating in situ and radar altimetry data into a large-scale hydrologic-hydrodynamic model for streamflow forecast in the Amazon. Hydrol. Earth Syst. Sci. 17, 2929–2946, https://doi.org/10.5194/hess-17-2929-2013.

Pappenberger, F., Beven, K., Horritt, M., Blazkova, S., 2005. Uncertainty in the calibration of effective roughness parameters in HEC-RAS using inundation and downstream level observations. J. Hydrol. 302, 46–69, https://doi.org/10.1016/j.jhydrol.2004.06.036.

Pappenberger, F., Ramos, M.H., Cloke, H.L., Wetterhall, F., Alfieri, L., Bogner, K., Mueller, A., Salamon, P., 2015. How do I know if my forecasts are better? Using benchmarks in hydrological ensemble prediction. J. Hydrol. 522, 697–713, https://doi.org/10.1016/j.jhydrol.2015.01.024.

Patil, A., Ramsankaran, R., 2018. Improved streamflow simulations by coupling Soil Moisture Analytical Relationship in EnKF based hydrological data assimilation framework. Adv. Water Resour. 121, 173–188, https://doi.org/10.1016/J.ADVWATRES.2018.08.010.

Pham, H.T., Marshall, L., Johnson, F., Sharma, A., 2018. A method for combining SRTM DEM and ASTER GDEM2 to improve topography estimation in regions without reference data. Remote Sens. Environ. 210, 229–241, https://doi.org/10.1016/j.rse.2018.03.026.

Pitcher, L.H., Pavelsky, T.M., Smith, L.C., Moller, D.K., Altenau, E.H., Allen, G.H., Lion, C., Butman, D., Cooley, S.W., Fayne, J., Bertram, M., 2018. AirSWOT InSAR mapping of surface water elevations and hydraulic gradients across the Yukon Flats Basin, Alaska. Water Resour. Res. 55 (2), 937–953, https://doi.org/10.1029/2018WR023274.

Plaza, D.A., De Keyser, R., De Lannoy, G.J.M., Giustarini, L., Matgen, P., Pauwels, V.R.N., 2012. The importance of parameter resampling for soil moisture data assimilation into hydrologic models using the particle filter. Hydrol. Earth Syst. Sci. 16, 375–390, https://doi.org/10.5194/hess-16-375-2012.

Pramanik, N., Panda, R.K., Sen, D., 2010. One dimensional hydrodynamic modeling of river flow using DEM extracted river cross-sections. Water Resour. Manag. 24, 835–852, https://doi.org/10.1007/s11269-009-9474-6.

Prigent, C., Lettenmaier, D.P., Aires, F., Papa, F., 2016. Toward a high-resolution monitoring of continental surface water extent and dynamics, at Global Scale: from GIEMS (Global Inundation Extent from Multi-Satellites) to SWOT (Surface Water Ocean Topography). Surv. Geophys. 37, 339–355, https://doi.org/10.1007/s10712-015-9339-x.

Puech, C., Hostache, R., Raclot, D., Matgen, P., 2007. Estimation of flood water levels by merging DEM and satellite imagery using hydraulics laws through AI to enhance the estimates. In: Proceedings of Second Space for Hydrology Workshop. ESA, Geneva, pp. 1–7.

Quinn, N., Bates, P.D., Neal, J., Smith, A., Wing, O., Sampson, C., Smith, J., Heffernan, J., 2019. The spatial dependence of flood hazard and risk in the United States. Water Resour. Res. 55, 1890–1911, https://doi.org/10.1029/2018WR024205.

Revel, M., Ikeshima, D., Yamazaki, D., Kanae, S., 2019. A physically based empirical localization method for assimilating synthetic SWOT observations of a continental-scale river: A case study in the Congo basin. Water (Switzerland) 11 (4), 829. https://doi.org/10.3390/w11040829.

Revilla-Romero, B., Hirpa, F.A., del Pozo, J.T., Salamon, P., Brakenridge, R., Pappenberger, F., de Groeve, T., Pozo, J.T. del, Salamon, P., Brakenridge, R., Pappenberger, F., de Groeve, T., 2015. On the use of global flood forecasts and satellite-derived inundation maps for flood monitoring in data-sparse regions. Remote Sens. 7, 15702–15728, https://doi.org/10.3390/rs71115702.

Revilla-Romero, B., Wanders, N., Burek, P., Salamon, P., de Roo, A., 2016. Integrating remotely sensed surface water extent into continental scale hydrology. J. Hydrol. 543, 659–670, https://doi.org/10.1016/j.jhydrol.2016.10.041.

Robinson, N., Regetz, J., Guralnick, R.P., 2014. EarthEnv-DEM90: A nearly-global, void-free, multi-scale smoothed, 90m digital elevation model from fused ASTER and SRTM data. ISPRS J. Photogramm. Remote Sens. 87, 57–67, https://doi.org/10.1016/j.isprsjprs.2013.11.002.

Sanders, B.F., 2007. Evaluation of on-line DEMs for flood inundation modeling. Adv. Water Resour. 30, 1831–1843, https://doi.org/10.1016/j.advwatres.2007.02.005.

Sanders, B.F., Schubert, J.E., 2019. PRIMo: Parallel raster inundation model. Adv. Water Resour. 126, 79–95, https://doi.org/10.1016/J.ADVWATRES.2019.02.007.

Schneider, R., Tarpanelli, A., Nielsen, K., Madsen, H., Bauer-Gottwein, P., 2018. Evaluation of multi-mode CryoSat-2 altimetry data over the Po River against in situ data and a hydrodynamic model. Adv. Water Resour. 112, 17–26, https://doi.org/10.1016/j.advwatres.2017.11.027.

Schumann, G., Bates, P.D., Horritt, M.S., Matgen, P., Pappenberger, F., 2009. Progress in integration of remote sensing-derived flood extent and stage data and hydraulic models. Rev. Geophys. 47, 1–20, https://doi.org/10.1029/2008RG000274.

Schumann, G., Brakenridge, G., Kettner, A., Kashif, R., Niebuhr, E., 2018. Assisting flood disaster response with Earth Observation data and products: A critical assessment. Remote Sens. 10, 1230, https://doi.org/10.3390/rs10081230.

Schumann, G., Cutler, M., Black, A., Matgen, P., Pfister, L., Hoffmann, L., Pappenberger, F., 2008a. Evaluating uncertain flood inundation predictions with uncertain remotely sensed water stages. Int. J. River Basin Manag. 5124, 37–41, https://doi.org/10.1080/15715124.2008.9635347.

Schumann, G., Hostache, R., Puech, C., Hoffmann, L., Matgen, P., Pappenberger, F., Pfister, L., 2007. High-resolution 3-D flood information from radar imagery for flood hazard management. IEEE Trans. Geosci. Remote Sens. 45, 1715–1725, https://doi.org/10.1109/TGRS.2006.888103.

Schumann, G., Matgen, P., Cutler, M.E.J.E.J., Black, a., Hoffmann, L., Pfister, L., 2008. Comparison of remotely sensed water stages from LiDAR, topographic contours and SRTM. ISPRS J. Photogramm. Remote Sens. 63, 283–296, https://doi.org/10.1016/j.isprsjprs.2007.09.004.

Schumann, G., Matgen, P., Pappenberger, F., 2008b. Conditioning water stages from satellite imagery on uncertain data points. IEEE Geosci. Remote Sens. Lett. 5, 810–813.

Schumann, G.J.-P., Bates, P.D., 2018. The need for a high-accuracy. Open-access global DEM. Front. Earth Sci. 6, 225, https://doi.org/10.3389/FEART.2018.00225.

Schumann, G.J.-P., Bates, P.D., Neal, J.C., Andreadis, K.M., 2014. Technology: Fight floods on a global scale. Nature 507, 169, https://doi.org/10.1038/507169e.

Schumann, G.J.-P., Frye, S., Wells, G., Adler, R.F., Brakenridge, R., Bolten, J., Murray, J., Slayback, D., Policelli, F., Kirschbaum, D., Wu, H., Cappelaere, P., Howard, T., Flamig, Z., Clark, R., Stough, T., Chini, M., Matgen, P., Green, D., Jones, B., Plicelli, F., Kirschbaum, D., Wu, H., Cappelaere, P., Howard, T., Flamig, Z., Clark, R., Stough, T., Chini, M., Matgen, P., Green, D., Jones, B., 2016. Unlocking the full potential of Earth observation during the 2015 Texas flood disaster. Water Resour. Res. 52, 3288–3293, https://doi.org/10.1002/2015WR017126.

Schumann, G.J.-P., 2019. The need for scientific rigour and accountability in flood mapping to better support disaster response. Hydrol. Process. 33 (24), 3138–3142, https://doi.org/10.1002/hyp.13547.

Schumann, G.J., Moller, D.K., 2015. Microwave remote sensing of flood inundation. Phys. Chem. Earth 83–84, 84–95, https://doi.org/10.1016/j.pce.2015.05.002.

Schumann, G.J., Neal, J.C., Voisin, N., Andreadis, K.M., Pappenberger, F., Phanthuwongpakdee, N., Hall, A.C., Bates, P.D., 2013. A first large-scale flood inundation forecasting model. Water Resour. Res. 49, 6248–6257, https://doi.org/10.1002/wrcr.20521.

Schumann, G.J.P., Andreadis, K.M., 2016. A method to assess localized impact of better floodplain topography on flood risk prediction. Adv. Meteorol. 2016, https://doi.org/10.1155/2016/6408319.

Schumann, G.J.P., Bates, P.D., Neal, J.C., Andreadis, K.M., 2014b. Measuring and mapping flood processes. Hydro-Meteorological Hazards, Risks, and Disasters. Elsevier Inc., https://doi.org/10.1016/B978-0-12-394846-5.00002-3.

Schumann, G.J.P., Domeneghetti, A., 2016. Exploiting the proliferation of current and future satellite observations of rivers. Hydrol. Process. 30, 2891–2896, https://doi.org/10.1002/hyp.10825.

Schumann, G.J.P., Neal, J.C., Mason, D.C., Bates, P.D., 2011. The accuracy of sequential aerial photography and SAR data for observing urban flood dynamics, a case study of the UK summer 2007 floods. Remote Sens. Environ. 115, 2536–2546, https://doi.org/10.1016/j.rse.2011.04.039.

Shastry, A., Durand, M., 2019. Utilizing flood inundation observations to obtain floodplain topography in data-scarce regions. Front. Earth Sci. 6, 1–10, https://doi.org/10.3389/feart.2018.00243.

Slivinski, L., Spiller, E., Apte, A., 2015. A Hybrid particle-Ensemble Kalman filter for Lagrangian data assimilation. Mon. Weather Rev. 143, 195–211, https://doi.org/http://dx.doi.org/10.1175/MWR-D-14-00051.1.

Smith, P.J., Dance, S.L., Nichols, N.K., 2011. A hybrid data assimilation scheme for model parameter estimation: Application to morphodynamic modelling. Comput. Fluids 46, 436–441, https://doi.org/10.1016/j.compfluid.2011.01.010.

Smith, P.J., Thornhill, G.D., Dance, S.L., Lawless, a.S., Mason, D.C., Nichols, N.K., 2013. Data assimilation for state and parameter estimation: Application to morphodynamic modelling. Q. J. R. Meteorol. Soc. 139, 314–327, https://doi.org/10.1002/qj.1944.

Tourian, M.J., Schwatke, C., Sneeuw, N., 2017. River discharge estimation at daily resolution from satellite altimetry over an entire river basin. J. Hydrol. 546, 230–247, https://doi.org/10.1016/j.jhydrol.2017.01.009.

Tuozzolo, S., Lind, G., Overstreet, B., Mangano, J., Fonstad, M., Hagemann, M., Frasson, R.P.M., Larnier, K., Garambois, P.-A., Monnier, J., Durand, M., 2019. Estimating river discharge with swath altimetry: A proof of concept using AirSWOT observations. Geophys. Res. Lett. 46 (3), 1459–1466, https://doi.org/10.1029/2018GL080771.

Uhe, P., Mitchell, D., Bates, P., Sampson, C., Smith, A., ISLAM, A.S., 2019. Enhanced flood risk with 1.5°C global warming in the Ganges-Brahmaputra-Meghna basin. Environ. Res. Lett. 14 (7), 074031, https://doi.org/10.1088/1748-9326/ab10ee.

van Leeuwen, P.J., Künsch, H.R., Nerger, L., Potthast, R., Reich, S., 2019. Particle filters for high-dimensional geoscience applications: A review. Q. J. R. Meteorol. Soc. 145, 2335–2365, https://doi.org/10.1002/qj.3551.

Van Wesemael, A., Landuyt, L., Lievens, H., Verhoest, N.E.C., 2019. Improving flood inundation forecasts through the assimilation of in situ floodplain water level measurements based on alternative observation network configurations. Adv. Water Resour. 130, 229–243, https://doi.org/10.1016/j.advwatres.2019.05.025.

Walker, J.P., Houser, P.R., 2005. Hydrologic data assimilation. Adv. water Sci. Methodol., 233, https://doi.org/10.5772/1112.

Waller, J.A., García-Pintado, J., Mason, D.C., Dance, S.L., Nichols, N.K., 2018. Technical note: Analysis of observation uncertainty for flood assimilation and forecasting. Hydrol. Earth Syst. Sci. Discuss. 22 (7), 3983–3992. https://doi.org/10.5194/hess-22-3983-2018.

Wang, X., Holland, D.M., Gudmundsson, G.H., 2018. Accurate coastal DEM generation by merging ASTER GDEM and ICESat/GLAS data over Mertz Glacier, Antartica. Remote Sens. Environ. 206, 218–230, https://doi.org/10.1016/j.rse.2017.12.041.

Ward, P.J., Jongman, B., Salamon, P., Simpson, A., Bates, P., De Groeve, T., Muis, S., de Perez, E.C., Rudari, R., Trigg, M.a., Winsemius, H.C., 2015. Usefulness and limitations of global flood risk models. Nat. Clim. Chang. 5, 712–715, https://doi.org/10.1038/nclimate2742.

Wetterhall, F., Pappenberger, F., Alfieri, L., Cloke, H.L., Thielen-Del Pozo, J., Balabanova, S., Danˇhelka, J., Vogelbacher, a., Salamon, P., Carrasco, I., Cabrera-Tordera, a.J., Corzo-Toscano, M., Garcia-Padilla, M., Garcia-Sanchez, R.J., Ardilouze, C., Jurela, S., Terek, B., Csik, a., Casey, J., Stankunavicˇius, G., Ceres, V., Sprokkereef, E., Stam, J., Anghel, E., Vladikovic,

D., Alionte Eklund, C., Hjerdt, N., Djerv, H., Holmberg, F., Nilsson, J., Nyström, K., Sušnik, M., Hazlinger, M., Holubecka, M., 2013. HESS Opinions "forecaster priorities for improving probabilistic flood forecasts". Hydrol. Earth Syst. Sci. 17, 4389–4399, https://doi.org/10.5194/hess-17-4389-2013.

Winsemius, H.C., Van Beek, L.P.H., Jongman, B., Ward, P.J., Bouwman, A., 2013. A framework for global river flood risk assessments. Hydrol. Earth Syst. Sci. 17, 1871–1892, https://doi.org/10.5194/hess-17-1871-2013.

Wood, M., Jong, S.M.De, Straatsma, M.W., 2018. Locating flood embankments using SAR time series: A proof of concept. Int. J. Appl. Earth Obs. Geoinf. 70, 72–83, https://doi.org/10.1016/j.jag.2018.04.003.

Yamazaki, D., Baugh, C.a., Bates, P.D., Kanae, S., Alsdorf, D.E., Oki, T., 2012. Adjustment of a spaceborne DEM for use in floodplain hydrodynamic modeling. J. Hydrol. 436-437, 81–91, https://doi.org/10.1016/j.jhydrol.2012.02.045.

Yamazaki, D., Ikeshima, D., Sosa, J., Bates, P.D., Allen, G., Pavelsky, T., 2019. MERIT Hydro: A high-resolution global hydrography map based on latest topography datasets. Water Resour. Res. 55, 5053–5073, https://doi.org/10.1029/2019WR024873.

Yamazaki, D., Ikeshima, D., Tawatari, R., Yamaguchi, T., O'Loughlin, F., Neal, J.C., Sampson, C.C., Kanae, S., Bates, P.D., 2017. A high-accuracy map of global terrain elevations. Geophys. Res. Lett. 44, 5844–5853, https://doi.org/10.1002/2017GL072874.

Yamazaki, D., Revel, M., Kanae, S., 2018. Model based observation localization weighting function for Amazon mainstream. J. Jpn. Soc. Civil Eng. 74 (5), 157–162.

Yoon, Y., Durand, M., Merry, C.J., Clark, E.a., Andreadis, K.M., Alsdorf, D.E., 2012. Estimating river bathymetry from data assimilation of synthetic SWOT measurements. J. Hydrol. 464-465, 363–375, https://doi.org/10.1016/j.jhydrol.2012.07.028.

Yue, L., Shen, H., Zhang, L., Zheng, X., Zhang, F., Yuan, Q., 2017. High-quality seamless DEM generation blending SRTM-1, ASTER GDEM v2 and ICESat/GLAS observations. ISPRS J. Photogramm. Remote Sens. 123, 20–34, https://doi.org/10.1016/j.isprsjprs.2016.11.002.

Zaussinger, F., Dorigo, W., Gruber, A., Tarpanelli, A., Filippucci, P., Brocca, L., 2018. Estimating irrigation water use over the contiguous United States by combining satellite and reanalysis soil moisture data. Hydrol. Earth Syst. Sci. 23, 897–923.

Zheng, F., Tao, R., Maier, H.R., See, L., Savic, D., Zhang, T., Chen, Q., Assumpção, T.H., Yang, P., Heidari, B., Rieckermann, J., Minsker, B., Bi, W., Cai, X., Solomatine, D., Popescu, I., 2018. Crowd sourcing methods for data collection in geophysics: State of the art, issues, and future directions. Rev. Geophys. 56, 698–740, https://doi.org/10.1029/2018RG000616.

Further Reading

Briggs, J., Dowd, M., Meyer, R., 2013. Data assimilation for large-scale spatio-temporal systems using a location particle smoother. Environmetrics 24, 81–97. doi: 10.1002/env.2184.

Schumann, G., Di Baldassarre, G., Alsdorf, D., Bates, P.D., 2010. Near real-time flood wave approximation on large rivers from space: Application to the River Po, Italy. Water Resour. Res. 46, 1–8, https://doi.org/10.1029/2008WR007672.

Schumann, G., Pappenberger, F., Matgen, P., 2008c. Estimating uncertainty associated with water stages from a single SAR image. Adv. Water Resour. 31, 1038–1047, https://doi.org/10.1016/j.advwatres.2008.04.008.

Schumann, G.J.P., Andreadis, K.M., Bates, P.D., 2014a. Downscaling coarse grid hydrodynamic model simulations over large domains. J. Hydrol. 508, 289–298, https://doi.org/10.1016/j.jhydrol.2013.08.051.

Chapter 13

Artificial Intelligence for Flood Observation

Ruo-Qian Wang
Department of Civil and Environmental Engineering, Rutgers University, New Brunswick, NJ, United States

1 Introduction

In the last few years, artificial intelligence (AI) is increasingly becoming powerful. It can diagnose diseases, write financial analytics, drive cars, trade stocks, and even compose hit music and produce trailers for horror movies. The most remarkable milestone might be the moment when the AI program, AlphaGo, demonstrated a superior art to beat Lee Sedol, an 18-time world champion at the most sophisticated game invented in human history—Go (Holcomb et al., 2018). From a science and engineering perspective, could AI be harnessed to benefit our society, for example, predict and manage natural disasters—such as floods—better than humans can?

A computer game and a flood are obviously two very different fields. But AI is being more frequently adopted in flooding related research. This chapter is targeted to demonstrate important advances in AI's applications in flood related study. Due to the limited time and the author's knowledge, this chapter cannot and will not exhaust the relevant studies—actually it's almost impossible because new flood studies using AI are being published every week and many AI-related flood papers scattered across a wide spectrum of literature and can be traced to a few decades ago. However, this chapter is planned to follow and comment on the general trend and the frontier of the field with a "review" of reviews and highlights of typical studies. This chapter provides a general road map of the field and points the topics that the readers are most interested in for further studies.

This chapter is organized in the following structure: Section 2 reviews the definition and major application of AI; Section 3 describes the AI's application in extracting flood information from crowdsourcing data (social media and mobile phone apps); Section 4 reviews the video surveillance camera data in flood monitoring; Section 5 highlight the need for more studies to use the emerging AI enabled Big Data in flood research. The chapter ends with a summary and outlook of the future research directions.

Earth Observation for Flood Applications. http://dx.doi.org/10.1016/B978-0-12-819412-6.00013-4

2 What's AI?

AI is intelligence demonstrated by machines. In contrast to the pursuit of general machine intelligence, the AI concept used in engineering and applied science is machine learning, which is the study of algorithms and statistical models that computer systems use to perform a specific task without using explicit instructions, relying on patterns and inference instead.

To explain the general idea of machine learning, let's take a look of the general function,

$$y = f(x),$$

where x and y are the input and output of the function f. Machine learning is the task to find a general function, without knowing the structure or knowledge of f itself, to replace f within a limited error. In machine learning tasks, x is usually known, and y is either completely, partially known, or unknown. Accordingly, machine learning can be classified into three categories, that is, supervised learning (y is known), semi-supervised learning (y is partially known), and unsupervised learning (y is unknown). The process to tune a machine learning model that is targeted to approximate f is called "training."

The common machine learning algorithms include Linear Regression, Logistic Regression, Decision Tree, Support Vector Machine, Naive Bayes, k-Nearest Neighbor, K-Means, Random Forest, and Dimensionality Reduction Algorithms. Recent years witnessed the rising of deep learning algorithms, which uses multiple layers to progressively extract higher level features from the raw input and were found useful in many practical applications such as Natural Language Processing and Computer Vision.

Thanks to the development of AI, the unconventional data sources, often described as "Big Data," become possible to provide useful information for engineering application such as flood monitoring. This chapter is targeted to outline the advances from this perspective.

3 Extracting flood information from crowdsourcing data using AI

Recently, pluvial flooding (flooding due to heavy precipitation) and nuisance flooding (flooding due to sea-level rise, also called "sunny day flooding") become grave concerns in the flooding research (Rosenzweig et al., 2018; Moftakhari et al., 2018). Different from the traditional fluvial flooding, it is more challenging to collect data for these chronical, spreading, and low magnitude flood events. Traditional flood monitoring means are limited, for example, the sensor network is expensive to install and maintain in the city area, insurance reports are usually inaccessible and delayed in time, and government survey is incomplete in coverage and inaccurate in the record (Wang et al., 2018a). In addition, many cities lack an early warning mechanism to prepare and

mitigate the impact. Citizen science and crowdsourcing are providing an alternative and innovative solutions to the data collection need and the hope is to use AI to automatically process the unconventional "Big Data" for contributing to early warning systems and flood forecasting model validations (See, 2019). Another hope is to expect crowdsourcing to supplement data obtained from more traditional sources through data fusion and eventually improve the data coverage and resolution in space and time taking its advantage in continuous coverage in time and high spatial resolution in space. Crowdsourcing is also expected to play a significant role in developing countries where basic flood warning and monitoring infrastructure is pooled constructed and maintained so that crowdsourcing can enable badly needed data collection to fill the gap, particularly due to its relatively low implementation cost.

Two review papers that are targeted to exhaust the development in the crowdsourcing/citizen science field worth mentioning here. Zheng et al. (2018) reviewed crowdsourcing-based data acquisition methods that have been used in a broad spectrum, covering seven domains of geophysics including weather, precipitation, air pollution, geography, ecology, surface water, and natural hazard management. They proposed a new framework to categorize the studies and highlighted the common issues in data acquisition methods. They include the management of crowdsourcing projects, data quality, data processing, and data privacy. See (2019) focused on the current activities in citizen science and crowdsourcing with respect to applications of pluvial flooding. They developed four themes to describe the flooding research: (1) applications relevant during a flood event, which includes automated street flooding detection using crowdsourced photographs and sensors, analysis of social media, and online and mobile applications for flood reporting; (2) applications related to post-flood events; (3) the use of citizen science and crowdsourcing for model development and validation; and (4) the development of integrated systems. They pointed out that advances in the use of citizen science and crowdsourcing data can benefit the other three topics.

3.1 Extracting flood information from social media data

There are majorly two data sources in crowdsourcing flood monitoring, namely social media and mobile phone app. Social media was first used in the damage assessment study after the Haiti earthquake (Muralidharan et al., 2011). It was later used in flood monitoring such as in Jongman et al. (2015) and Fohringer et al. (2015).

In the pilot studies, social media data were processed manually, which is a slow and expensive process and cannot be used in real-time monitoring. AI has shown the potential to address these problems. Wang et al. (2018a) created a new method using AI to automatize the process, in which Natural Language Processing techniques are applied to the data collected from Twitter. They could use topic modeling to filter the relevant topic and Name Entity Recognition

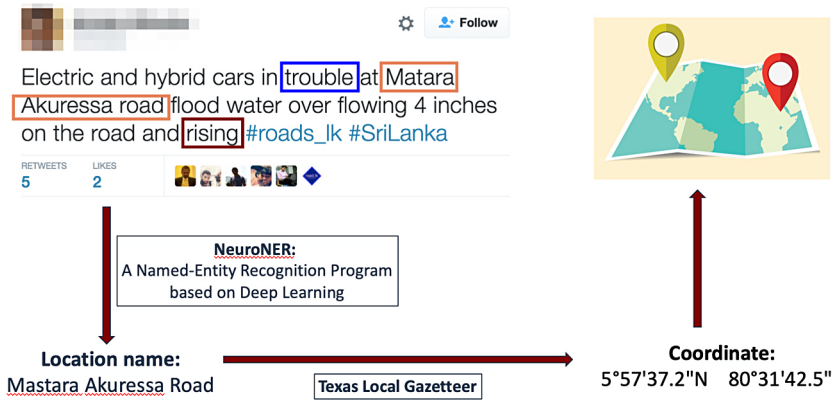

FIGURE 13.1 Process of Twitter flood monitoring (Wang, 2018).

to extract the flood location information. They found that the Big Data-based flood monitoring approaches can complement the existing means of flood data collection and the validation against precipitation data showed a good correlation. They further developed the method to use local gazetteers to achieve high location accuracy and applied the improved method to the flood of Hurricane Harvey in 2017 (Fig. 13.1) (Wang et al., 2020). They demonstrated that social media can effectively inform the diaster rescue phases and serve as a passive hotline to inform the disaster management. Asmai et al. (2019) conducted a more general study. They used the topic modeling approach of Term Frequency-Inverse Document Frequency (TF-IDF) to automatically filter the flooding topic, but the location name was not extracted. So, their flood prediction is general in geolocation.

Interested readers may consult to a more detailed review on the progress in this direction of Yu et al. (2019). They focused on the practical applications of employing social media data for a wide range of public applications, including environmental monitoring, water resource managing, disaster and emergency response. They further pointed out that the creative ideas and new values could be conveyed through a 4Ws (What, Why, When, hoW) model. They also mentioned controversial issues associated with social media data such as data collection, data quality management, fake news detection, privacy issues, etc.

Although social media is shown to potentially provide useful information in flood monitoring, the concern on the data quality is grave, which could significantly limit it in practical applications. This issue is not expected to be quickly resolved in the near future. So researchers have started to explore the "niche" application for this emerging technology, one of which is in the emergency response and rescue activities. As mentioned in Kankanamge et al. (2019), highly reliable in-situ location information is critical for rescue efforts during and after disasters, but often not easy or even possible to access. They reviewed the recent

development in this direction and found disaster reduction to be promising in assisting policymakers and disaster risk managers to make informed decisions before, during and after disasters. They also found an increasing trend of literature in focusing on volunteer crowdsourcing between 2006 and 2018.

Aware of the challenge in data quality, another recent trend of using social media flood data is to fuse the data with other data sources, for example, remote sensing. The fusion will benefit both the data types and improve the data coverage through the complementing characteristics. Qi et al. (2019) provided an overview on the integration and joint analysis of remote sensing and social media data in urban observation applications. Four opportunities were identified in exploiting the value of social media data: to investigate the relationship among humans, environment, and urban, to help urban planning, to manage urban disaster, and to monitor urban environment. The future possibilities to combine remote sensing and social media data were exciting and it was believed to profoundly change the future research and practice.

3.2 Extracting flood information from mobile device data

Smart phones have fundamentally changed the lifestyle and business in the world. As a reliable means of citizen science data collection, smart phones have also been used to enable flood monitoring. In comparison to social media data, observation from mobile phone is better in quality through the customized design of smart phone apps. Wang et al., 2018a has shown that the mobile phone app, MyCoast, can be useful in the application of observing the coastal flood (Fig. 13.2). Computer vision scheme was applied in automatic processing of the mobile phone data in recognizing the flood scenes.

The geolocation information is usually available through the volunteered mobile phone data from the GPS positioning service of smart phones. However,

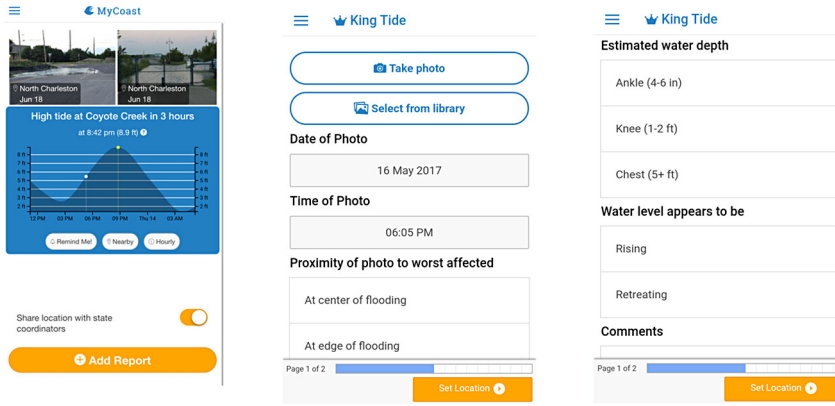

FIGURE 13.2 Graphic user interface of MyCoast (Wang et al., 2018b).

it is challenging when the collected data, for example, photos, have no geolocation information. This is often in the case that the original mobile phone app is not designed for the purpose and the study was aimed to use the existing data that were collected through the past studies with other intentions. Kim and Ham (2019) presented a novel geospatial localization method to address such problem using distant objects based participatory sensing. The proposed geospatial localization process consists of a geographic coordinate conversion, mean-shift clustering, deep learning-based object detection, magnetic declination adjustment, line of sight equation formulation, and the Moore-Penrose generalized inverse method. The experiments were conducted in Houston and College Station in Texas to evaluate the accuracy of the proposed method. The experimental results demonstrated a reasonable reliability with distance errors of 1.5–27.8 m in the cases that the distance from observers to the objects of interest were 17–296 m. AI is playing a significant role in the study that has the potential to enable rapid data collection over large urban areas, especially beneficial for disaster preparedness.

4 Extracting flood information from surveillance video cameras using AI

Another field that AI has enabled is extracting flood information from surveillance video cameras. Video surveillance equipments, which are readily available in many cities and can record urban waterlogging processes in video form, have become potential data sources that flood researchers start to tap on. Better than crowdsourcing data, video cameras can provide more reliable objective water depth information. For example, Jiang et al. (2018, 2019) invented an approach to extract urban waterlogging depths from video images based on machine learning methods and Golparvar and Wang (2020) developed a monoplotting based flood extent mapping scheme (Fig. 13.3). The latter study focusing on the high tide flood in Newport Beach, California, showed that advanced computer visioon schemes can effectively map the flood extent from images collected through social media. The method was shown effective in mining and utilizing urban waterlogging depth information from video images. The low economic cost, good accuracy, high spatiotemporal resolution, and wide coverage are some of the attractive features of the proposed method.

Similarly, Moy de Vitry et al. (2019) performed a study on estimating water depth from surveillance camera systems. A deep convolutional neural network (DCNN) was employed to detect floodwater in surveillance footage and a qualitative flood index was developed to ensure the estimation consistent. The study trained the model with 1218 flooding images collected from the Internet from six surveillance videos. They cover a range of flooding and lighting conditions. The study reported a 75% correlation to the actual water level fluctuation on average.

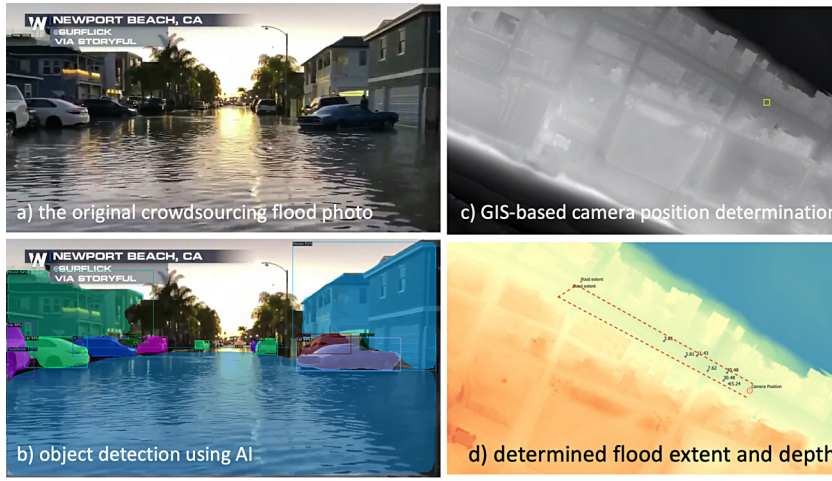

AI and GIS supported flood extent and depth mapping
(a) The original photo collected from social media
(b) Object detection using AI
(c) GIS-based camera position determination
(d) Determined camera position in Google map
(e) Determined flood extent and depth

Reference: Golparvar and Wang (2020)

FIGURE 13.3 An example of AI-supported camera monitoring of flooding extent and depth. (Jiang et al., 2019).

5 Progress in using AI extracted and processed data

The rise of the reviewed unconventional data sources enabled by AI provides a great opportunity to revolutionize the flood monitoring and prediction. However, relatively speaking, still very limited effort has been made to use the new data sources to improve our understanding and prediction of flood events (Maskey, 2019).

A recent effort in this direction by Wang et al. (2018b) is highlighted, who developed a new holistic framework for using information collected from multiple sources for setting parameters of a 2D flood model. They used a Cellular Automata based model CADDIES to simulate surface water flood inundation. Social media were used to set model parameters and investigate the infiltration and drainage system capacity in an urban flood environment. The results of processing terrain datasets indicated that the representation of urban micro-features is critical to the accuracy of modeling results and deeper study is needed to explore the best practice in using social media for flood modeling.

6 Summary and future research directions

This chapter uses the method of "review of the reviews" and highlights the typical studies to examine the frontier development of the application of "Big Data" enabled by AI. This chapter first reviews the definition of AI and then overview the rise of unconventional data sources including crowdsourcing data and surveillance camera videos. The focus is on the application of AI that was designed to enable these new data sources for flood monitoring. Here a series of observations are made through this review. First, the AI application in flood monitoring is very new: for example, the earliest paper for social media application in natural hazard is less than 10 years old; social media application in flooding is less than 5 years old; and the involvement of AI to enable automatic data mining is even younger. This emerging field still has a great potential in the future. Second, AI is the key to practical use of the Big Data. Featured as the 3 "Vs"—volume, velocity, and variety, Big Data is almost impossible to be used in flood modeling and prediction without AI. Third, data quality control is difficult in the AI-enabled big data. There is no universal or highly transferrable method in the field. This issue significantly prevents the scaling up of the method from places to places. Better AI models are still in need to improve the data quality. On the other hand, designing the protocol in data collection to address the data quality issues is still needed to improve our practice of data collection in the future.

Predicting the future is dangerous, but an outlook could at least inspire the future studies to focus on the important issues emerging from the literature (at least at the current stage). From the author's perspective, the future studies should focus on the following areas to better harness the power of AI and incubate a healthy and sustainable research field.

1. Finding the "niche" application of crowdsourcing data

   Data quality is still the major issue in AI related data processing. Using such data as the major data source to validate and understand the holistic picture of floods is still far from practical. Future researchers are encouraged to focus on particular areas that have less requirement of data quality and complete coverage to sustain the interest of AI-based flood monitoring studies. One example is the rescue and emergency response, in which field highly localized and detailed information is needed and big data could play a more important role there.
2. Fusion and assimilation of the AI-enabled big data
   Data fusion and assimilation can combine different data sources to improve flood estimate and forecasting. This field is still less explored than the data mining field and many "lower-hanging fruits" are more likely to be in this direction.
3. Innovative future AI application
   AI is a fast developing field. New methods and applications are emerging from the community every day. Chasing the pace is not easy but if a quick

application of the proved methods could be established, large improvement of the flood monitoring field can be expected.

4. Personalized data service
   Another idea that has been discussed in the field for years is to harness the power of AI to provide personalized data service for the end users. AI combining big data has the power to collect data from each user and customize the information for personal level communication. Researchers have discussed the possibilities to use this advantage to solicit better data volunteering and make better information for personal decisions (Wang et al., 2018a). Research following this direction may have a better chance to make an impact.

Acknowledgment

The lead author would like to acknowledge the support of Rutgers University Research Council Seeding Grant and EOAS seeding grant.

References

Asmai, S.A., Abidin, Z.Z., Basiron, H., Ahmad, S., 2019. An intelligent crisis-mapping framework for flood prediction. Int. J. Recent Technol. Eng. 8 (2S8), 1304–1310.

Fohringer, J., Dransch, D., Kreibich, H., Schröter, K., 2015. Social media as an information source for rapid flood inundation mapping. Nat. Hazards Earth Syst. Sci. 15 (12), 2725–2738.

Holcomb, S.D., Porter, W.K., Ault, S.V., Mao, G., Wang, J., 2018. Overview on DeepMind and its AlphaGo Zero AI. In: Proceedings of the 2018 International Conference on Big Data and Education, ACM, pp. 67–71.

Golparvar, B., Wang, R.Q., 2020. AI-supported citizen science to monitor high-tide flooding in newport beach, California. In Proceedings of the 3rd ACM SIGSPATIAL International Workshop on Advances in Resilient and Intelligent Cities, pp. 66–69.

Jiang, J., Liu, L., Cheng, C., Huang, J., Xue, A., 2019. Automatic estimation of urban waterlogging depths from video images based on ubiquitous reference objects. Remote Sens. 11 (5), 587.

Jiang, J., Liu, J., Qin, C-.Z., Wang, D., 2018. Extraction of urban waterlogging depth from video images using transfer learning. Water 10 (10), 1485.

Jongman, B., Wagemaker, J., Romero, B., de Perez, E., 2015. Early flood detection for rapid humanitarian response: harnessing near real-time satellite and Twitter signals. ISPRS Int. J. Geoinfo. 4 (4), 2246–2266.

Kankanamge, N., Yigitcanlar, T., Goonetilleke, A., Kamruzzaman, M., 2019. Can volunteer crowdsourcing reduce disaster risk? A systematic review of the literature. Int. J. Disaster Risk Reduct. 35, 101097.

Kim, H., Ham, Y., 2019. Participatory sensing-based geospatial localization of distant objects for disaster preparedness in urban built environments. Automat. Constr. 107, 102960.

Maskey, S., 2019. How can flood modelling advance in the “big data” age? J. Flood Risk Manag. 12, e12560.

Moftakhari, H.R., AghaKouchak, A., Sanders, B.F., Allaire, M., Matthew, R.A., 2018. What is nuisance flooding? Defining and monitoring an emerging challenge. Water Resour. Res. 54 (7), 4218–4227.

Moy de Vitry, M., Kramer, S., Wegner, J.D., Leitão, J.P., 2019. Scalable flood level trend monitoring with surveillance cameras using a deep convolutional neural network. Hydrol. Earth Syst. Sci. 23 (11), 4621–4634.

Muralidharan, S., Rasmussen, L., Patterson, D., Shin, J.H., 2011. Hope for Haiti: An analysis of Facebook and Twitter usage during the earthquake relief efforts. Public Relat. Rev. 37 (2), 175–177.

Qi, L., Li, J., Wang, Y., Gao, X., 2019. Urban observation: Integration of remote sensing and social media data. IEEE J. Sel. Top. Appl. Earth Obs. Remote Sens. 12 (11), 4252–4264.

Rosenzweig, B.R., McPhillips, L., Chang, H., Cheng, C., Welty, C., Matsler, M., Iwaniec, D., Davidson, C.I., 2018. Pluvial flood risk and opportunities for resilience. WIREs Water 5 (6), e1302.

See, L.M., 2019. A review of citizen science and crowdsourcing in applications of pluvial flooding. Front. Earth Sci. 7, 44.

Wang, R.Q., 2018. Big data of urban Flooding: dance with social media, citizen science, and artificial intelligence. In: Proceedings of Twentieth EGU General Assembly Conference Abstracts, vol. 20. Vienna, Austria, pp. 404.

Wang, R.Q., Hu, Y., Zhou, Z., Yang, K., 2020. Tracking flooding phase transitions and establishing a passive hotline with AI-enabled social media data. IEEE Access 8, 103395–103404.

Wang, R-.Q., Mao, H., Wang, Y., Rae, C., Shaw, W., 2018a. Hyper-resolution monitoring of urban flooding with social media and crowdsourcing data. Comput. Geosci. 111, 139–147.

Wang, Y., Chen, A.S., Fu, G., Djordjević, S., Zhang, C., Savić, D.A., 2018b. An integrated framework for high-resolution urban flood modelling considering multiple information sources and urban features. Environ. Model. Softw. 107, 85–95.

Yu, Y., Zhu, Y., Wan, D., Zhao, Q., Shu, K., Liu, H., 2019. Applications of social media in hydroinformatics: A survey. arXiv preprint arXiv:1905.03035.

Zheng, F., Tao, R., Maier, H.R., See, L., Savic, D., Zhang, T., Chen, Q., et al., 2018. Crowdsourcing methods for data collection in geophysics: state of the art, issues, and future directions. Rev. Geophys. 56 (4), 698–740.

Chapter 14

The Full Potential of EO for Flood Applications: Managing Expectations

Guy J-P. Schumann

Research and Education Department, RSS-Hydro, Dudelange, Luxembourg; Remote Sensing Solutions, Barnstable, MA, United States; School of Geographical Sciences, University of Bristol, Bristol, United Kingdom; INSTAAR, University of Colorado, Boulder, CO, United States

1 Introduction

The occurrence of flooding is a natural process and in many regions of the world regular flooding sustains biodiversity, ecosystems, and agriculture. However, when rivers burst their banks at above normal conditions, flooding can pose significant risks to people, livelihoods, exposed assets, and the environment. The level of impact depends on the magnitude of the event, the type of flood, and the degree of vulnerability of people and exposed assets. At a global level, flood frequency and impact seem to be increasing every year and certainly making the past years a flood rich period (Lane, 2009). With a possible intensification of the hydrological cycle (Hirmas et al., 2018), large and unprecedented events may become more frequent than expected One of the most notable recent disasters was without a doubt Cyclone Idai in early 2019, which caused widespread, unprecedented flooding in Mozambique and surrounding countries (Fig. 14.1). Entire nations have been devastated and complete recovery from this disaster will hardly be possible for most people in these regions (Schumann, 2019).

Recent high-magnitude floods have covered spatial scales well beyond what has been observed or measured in the past and are frequently surpassing traditional regional measurement and also disaster response coverage, thus highlighting the need for data and monitoring coverages that can only be provided by remote sensing platforms (i.e., satellite and airborne sensors). Remote sensing, in its true definition, is the acquisition of information about an object or phenomenon without making physical contact with the object, but is now more commonly referred to as the scanning of the Earth by satellite or high-flying

Earth Observation for Flood Applications. http://dx.doi.org/10.1016/B978-0-12-819412-6.00014-6

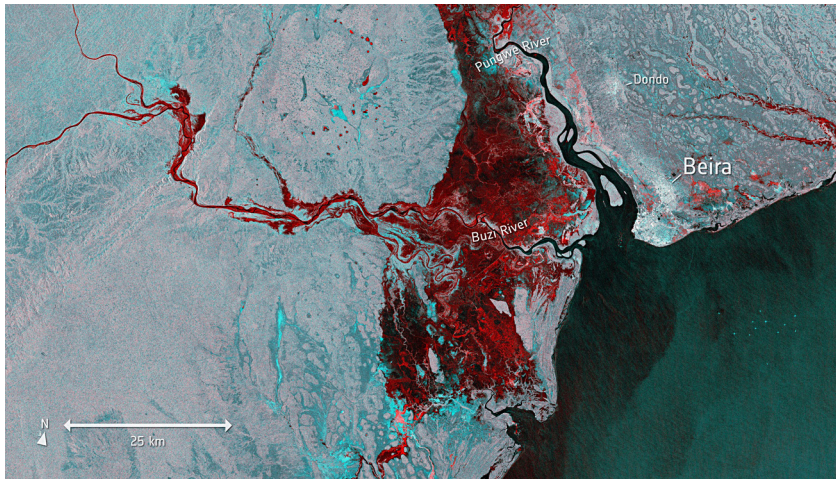

FIGURE 14.1 Millions of people in Mozambique, Malawi, and Zimbabwe have been affected by Cyclone Idai. The image shown is from the Copernicus Sentinel-1 SAR satellite and shows the extent of flooding, depicted in *red*, around the port town of Beira in Mozambique on 19 March. *(Image contains modified Copernicus Sentinel data (2019), processed by ESA, CC BY-SA 3.0 IGO.)*

aircraft and therefore slowly becoming popularly synonymous with the science of Earth Observation (EO) (Schumann, 2017).

Remote sensing of flood event processes and variables can be beneficial to many sectors and activities, including flood risk mitigation planning, disaster relief services, global (re-)insurance markets, and research of course. However, the amount and quality of information available varies greatly with location, spatial scales, and time. Remote sensing of floods can complement ground-based observations and be integrated with computer models of flooding for event re-analysis, such as demonstrated by Schumann et al. (2011) and for flood forecasting (see Hossain et al. (2014), e.g., using radar altimetry) in order to augment the amount of information available to end-users, decision-makers, and scientists.

However, before using remote sensing data or products for flood mapping, monitoring, and prediction, it is important to engage with end-users to understand their needs, requirements, and their preferred timeline as well as the appropriate spatial resolution of the delivered products. Based on a survey among hydrologists in Europe (Blyth, 1997), Fig. 14.2 shows the requirement in terms of spatial resolution and turnaround time for different flood management sectors. For instance, flood mapping for emergency response assistance could be done at any spatial resolution and accuracy may be less important but data or products should be made available within 48 hours, preferably even within the first 12–24 hours, while for the insurance industry the opposite situation would apply; spatial resolutions finer than 10 m but timeliness might actually be less important.

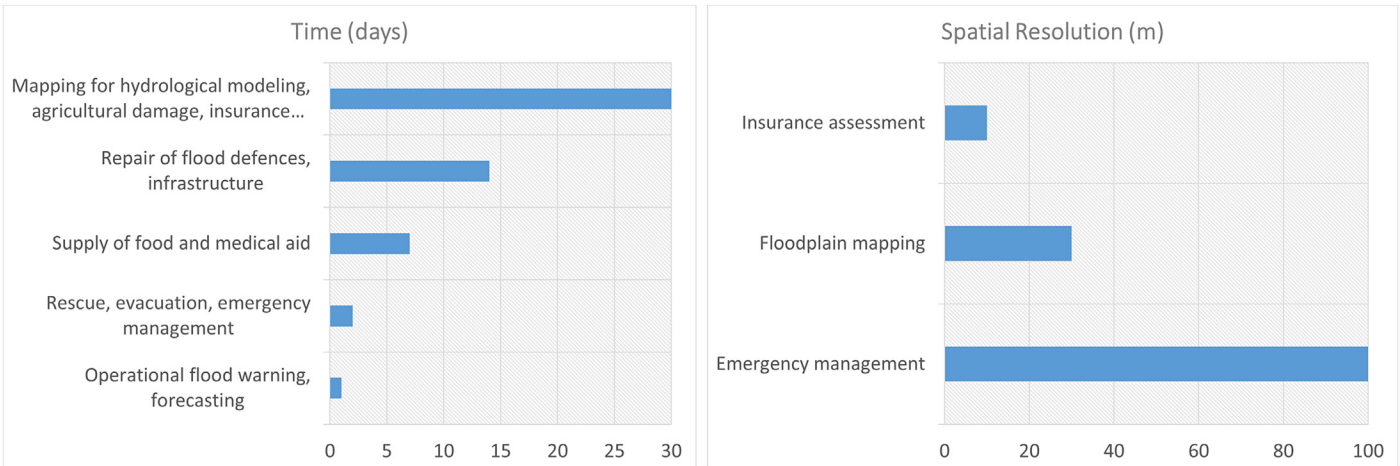

FIGURE 14.2 **End-user requirements in timeliness and spatial resolution of satellite remote sensing flood products.**

This situation seems favorable, at least at first glance, as it is in line with the fundamental physical principle that by increasing satellite swath coverage thus decreasing spatial resolution, the orbital revisit time is increased. For flood applications, however, the situation is far from ideal since in many cases, research scientists and product developers do not meet end-user needs at all and expectations are not managed adequately, leading to a lot of frustration and confusion in both camps. On the one hand, scientists most often lack understanding of end-user needs and on the other hand, decision-makers are oftentimes reluctant to use new data and methods in their operations or systems.

Nevertheless, over the past 2 decades, remote sensing has clearly been transformative in the way we now understand flood processes at different scales, model and predict floods, and also assist flood disaster response. Success stories are numerous but both the science and end-user communities need to be aware of the fundamental limitations of remote sensing of floods and manage expectations accordingly (Schumann, 2017).

The following sections in this chapter will detail this problem and highlight challenges, pitfalls, and opportunities in remote sensing applications of floods, suggesting possible ways forward.

2 How far have we got?

The potential that optical satellite images can contribute to flood science and applications has been known for over 40 years. Several studies in the early 1970s demonstrated the value of optical satellite imagery to map the evolution of flooding from space and indicated strong application potential for such maps for a number of sectors (Currey, 1977; Deutsch and Ruggles, 1978; Robinove, 1978).

The variables which both scientists and practitioners involved with flood risk management would like to measure or estimate during a flood event, and hopefully over different spatial and temporal scales, might include discharge, flow velocity and direction, water volume, depth and level, flooded area, and flood edge. Remote sensing can provide information about most of these with varying degrees of accuracy, however depth, discharge, and flow velocities can only be obtained indirectly through integration with auxiliary datasets, a hydrodynamic model, or gauging networks. Also, water volume and in some cases water level estimation requires the use of a topographic data set.

Information about floods can be obtained from a large variety of sensors. Among the most common are sensors operating in the visible to infrared (optical) range of the electromagnetic signal spectrum or in the microwave range. Radiometers that record data in the microwave range and optical sensors are passive instruments, which mean they record signals emitted by the Earth surface whereas synthetic aperture radar (SAR) or altimeters (LiDAR, radar) record the backscatter properties of the satellite-transmitted signal. The information about floods that can be retrieved from a satellite or airborne instruments operating in

the visible-to-infrared ranges depends on daylight, weather conditions (particularly clouds and rain), vegetation canopy density (especially emerging flooded vegetation or overhanging vegetation), and the chemical composition as well as the turbidity of the water (e.g., water sediment loads), all of which can vary considerably during flood events. These limitations are considerable, and the situation is oftentimes further aggravated by the fact that the satellite needs to be passing over the flood at the right time.

Despite many non-trivial issues outlined earlier and discussed in more detail in the next section, in the past 15 years, remote sensing has clearly shifted hydrological science and applications as well as model predictions from a data-poor to a data-rich environment (Bates, 2004, 2012). This is also evident in the many engineering and scientific efforts that are currently made to further augment this data-rich environment by developing satellite missions with advanced sensor technology that can be utilized for addressing research and application needs in hydrology, such as the existing European Sentinel missions, NASA's recent ICESat-2 and CYGNSS missions, the upcoming NASA/CNES SWOT mission or new commercial missions like ICEYE, and the small satellites operated by Planet Labs, Inc. Many of the existing and future satellite missions and airborne platforms provide rich datasets with great potential for enhanced monitoring, measuring, and mapping hydrological processes, including extreme events or defining climatological trends. The proliferation of free and open data from many satellites also help to improve process models and model predictions through machine learning approaches (Nevo et al., 2019), new data assimilation techniques (Andreadis and Schumann, 2014), and parameter scaling behavior (Schumann et al., 2007a), and ultimately for an exploration of the ways in which new data sources may reduce uncertainty in hydrological predictions (Schumann and Domeneghetti, 2016).

Alongside data proliferation, recent advances in distributed high-performance computing, cloud-based service infrastructure, and web application programming interfaces, allow unsupervised flood mapping algorithms to be readily and easily deployed across computing server networks and thus map floods across large areas (country-level or global level) with an unprecedented data and product latency that satisfies end-user requirements. Fig. 14.3 shows an example of such an unsupervised flood mapping algorithm developed for SAR images from ESA and other agencies missions (Hostache et al., 2012; Matgen et al., 2011).

In an editorial article of a special issue on remote sensing for flood monitoring and management, Schumann (2015) argues that with a proliferation of free EO data now and in the near future, there is an obvious need to not only understand the limitations and errors of the data and methods (Ticehurst et al., 2014) but also to develop more sophisticated data processing algorithms (Dasgupta et al., 2018) as well as robust frameworks for handling the many heterogeneous geospatial data sets (Chen et al., 2015) and for effective information management and transfer across networks.

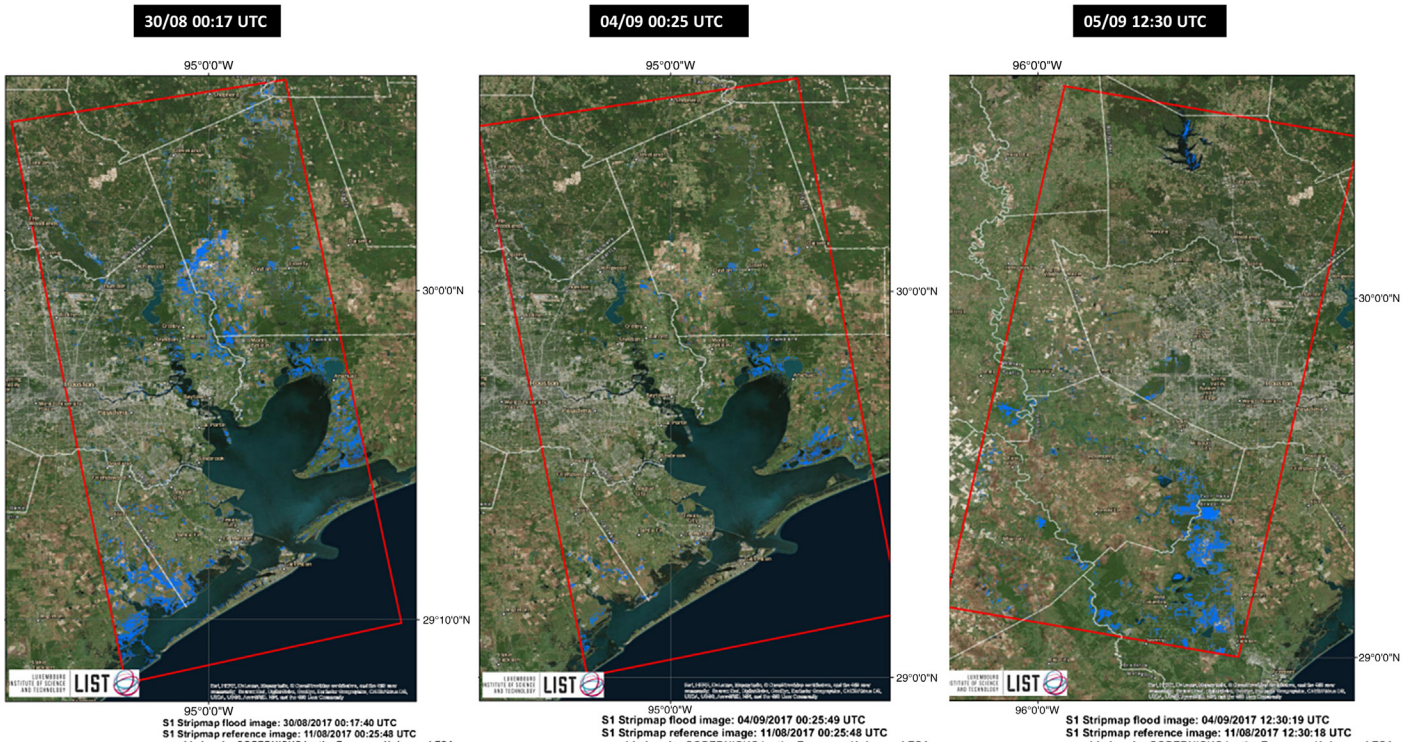

FIGURE 14.3 Example illustration of a fully automated flood mapping algorithm developed by Matgen et al. (2011) at the Luxembourg Institute of Science and Technology (LIST). Their SAR-based flood mapping software HASARD has been developed with support from ESA.

It is clear that many advances in remote sensing technologies and methods relevant to flood applications have been made in recent years but many challenges, pitfalls, and opportunities in remote sensing of floods still remain and need to be solved in order to allow unlocking the full potential of EO for flood applications.

3 Current challenges, pitfalls, and opportunities

The following sections will describe current major challenges, outline main pitfalls, and briefly discusses potential opportunities thereof.

3.1 Challenges

Clouds. Probably one of the bigger problems in optical satellite remote sensing of floods is without a doubt that of frequent, persistent and large-scale cloud cover (Fig. 14.4). This is particularly the case during short-lived but high-intensity pluvial floods (so called flash floods) and coastal floods in small- to medium-sized catchments in temperate regions where, in general, moderate-sized floods may have receded before weather conditions improve (Schumann et al., 2007a). Indeed, it seems that in many situations, microwave sensors, especially SAR, are the only realistic option to monitor and map floods reliably and routinely. Microwave sensors present an inviting alternative as the signals can penetrate clouds, work independent of daylight and during adverse weather conditions. Nonetheless, given the high orbital repeat cycle of lower resolution optical sensors, like MODIS, an automated cloud detection and masking algorithm (Foga et al., 2017; Griffin et al., 2003) can assist in generating a multi-day cloud-free composite image of a flood, such as produced by experimental NASA GSFC

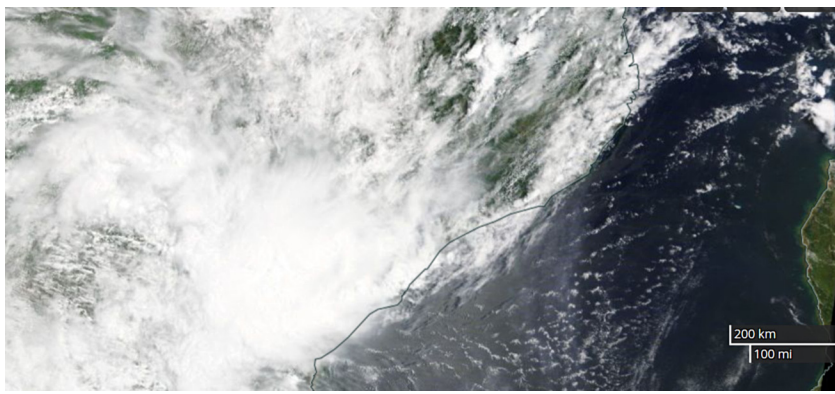

FIGURE 14.4 Typical cloudy scene from an optical satellite image during a large-scale flood event, particularly along coastal areas. Depicted here is an image of Mozambique where in mid-February 2020 hundreds were impacted by heavy rains and flooding in several central provinces (image acquisition date: February 12, 2020). *(NASA EOSDIS Worldview)*

Global Flood Mapping system (https://floodmap.modaps.eosdis.nasa.gov/). Also, merging of SAR and optical imagery could be potentially promising for surface water mapping applications (Markert et al., 2018).

Vegetation. Accurately mapping flooding beneath vegetation is for obvious reasons desirable as it allows the mapping of flooded agricultural fields, of abnormal wetland inundation, and of flooded recreational park land and forests. However, optical satellite sensors and the side-looking nature of SAR limit detection of flooding beneath vegetation. Mapping flooded vegetation or wetlands with optical satellite imagery has been achieved with only limited success (DeVries et al., 2017). In the case of SAR, vegetation typically causes diffusive and volume scattering and at short wavelengths, most signals do not penetrate dense vegetation cover (Schumann and Moller 2015). At longer radar wavelengths (e.g., L- or P-band), however, several successful approaches have been developed and been demonstrated (see e.g., Hess et al. (1990) for an extensive review), even at shorter, more commonly used wavelengths, such as C- or X-band (El Hajj et al., 2019; Grimaldi et al., 2020; Pierdicca et al., 2017; Plank et al., 2017) (Fig. 14.5). Multi-satellite data, including passive microwave, have

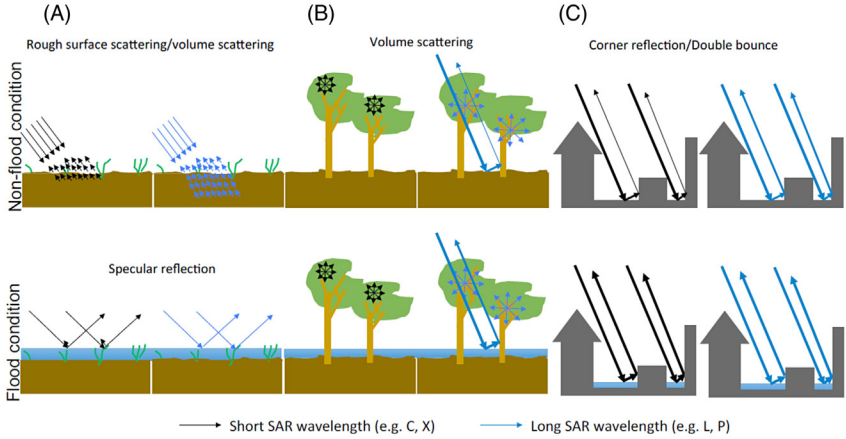

FIGURE 14.5 Schematic illustrating different backscatter mechanisms typical for short (e.g., X/C) and long (e.g., P/L) wavelength electromagnetic signals for various surface cover under non-flood and flooded conditions. Grass/soil is illustrated in (A). In this, when the cover is "dry," there is surface reflection at both short and long wavelengths due to the relative surface roughness in addition to volume backscatter from the grasses (short wavelength) and penetration into the soil itself (penetration will be greater at the long wavelengths). When flooded, the reflection becomes specular (assuming little surface roughness of the water) although emergent vegetation will create backscatter at the short wavelengths. For forest (B), short wavelength scatter will be dominated by volume scattering within the canopy and, if dense the electromagnetic energy might not penetrate to the surface. Longer wavelengths will scatter from branches and tree structure in addition to "double-bounce" surface/trunk backscatter. When inundated the "double bounce" return will be highly amplified. In urban regions (C) the "double-bounce" effect can tend to dominate at both scales, although surfaces will appear "rougher" at short wavelengths, dulling this. When flooded, the "double" and indeed multiple-bounce returns will be heightened significantly. *(Taken from Schumann and Moller (2015).)*

also been used successfully to map global wetland inundation dynamics (Prigent et al., 2012) and recent innovative approaches have looked at GNSS reflectometer technology to improve the mapping of flooded forests (Rodriguez-Alvarez et al., 2019).

Urban areas. Most people and valuable assets at risk from flooding are located in urban areas, so it is obviously desirable to map flooding in those areas. However, urban areas in flood present important challenges: inadequate spatial resolution; high building density obstructing street view; many different building types and a large variety of other man-made features, which cause a lot of signal distortion (Fig. 14.5); obstruction by cloud cover; and mixing of many different land cover types that are flooded and non-flooded. In fact due to these challenges, at present, accurate remote sensing of urban flooding seems restricted either to aerial photography (Yu and Lane, 2006), dGPS-generated wrack marks (McMillan and Brasington, 2007; Neal et al., 2009), or the use of high resolution LiDAR intensity data (Hoefle et al., 2009). Some successes have been shown using space-borne fine resolution SAR particularly sensors like TerraSAR-X or COSMO-SkyMed (Chini et al., 2012; Giustarini et al., 2013; Mason et al., 2010). However, more fundamental research is required into understanding the complex interactions between building structure and SAR signal processing as well as noise reduction and shadow/layover effects. Parts of those complex issues can be solved by employing a theoretical scattering model (Franceschetti et al., 2003) as demonstrated by Mason et al. (2014) or by making use of complementary SAR signal information contained in signal polarization modes or signal coherence (Chaabani et al., 2018; Chini et al., 2016), which has been shown recently to hold most promise for reliable operational urban flood mapping (Chini et al., 2019).

Flow depth, discharge, and velocity. As mentioned earlier, remote sensing of water depth, discharge, and flow velocities is very challenging and requires the use of cutting-edge technologies and thus, most of the time, these variables are inferred from remote sensing indirectly through integration with auxiliary datasets (Schumann et al., 2007b), a hydrodynamic model via assimilation (Andreadis et al., 2007; Andreadis and Schumann, 2014) or in-situ measurement stations (Straatsma, 2009). Measuring depth of clear river and coastal waters has been shown to be possible with green LiDAR (Kinzel et al., 2013; Zhao et al., 2017) but because of relatively high sediment content, flood waters are typically turbid and so flood depth can only really be inferred by integrating remotely sensed water level or extent with a high-accuracy digital elevation model (Cohen et al., 2019; Schumann et al., 2007b). For measuring flow velocity, image velocimetry is showing great potential, as demonstrated by Muste et al. (2014) for characterizing shallow free-surface flows. This technique quantifies the movement of small to large particles or objects moving within illuminated planes transecting the body of water—the assumption being that objects accurately follow the underlying flow. Obtaining discharge measurements for many river locations from satellites would be a game-changer. Innovative meth-

odologies have been studied using a combination of variations in river width and water level measurements from remote sensing, making some assumptions on river cross-sectional geometry (Durand et al., 2016; Tarpanelli et al., 2015). Similar methodologies are planned to be employed for retrieving instantaneous discharge of rivers wider than 50–100 m from measurements of water surface slopes, water levels, and widths by the upcoming NASA/CNES Surface Water Ocean Topography (SWOT) satellite mission, the first satellite mission dedicated to hydrology (https://swot.jpl.nasa.gov/).

Global open-access, accurate topography. It is clear that current global, open-access DEMs cannot resolve the detail of terrain features that control flooding (Schumann et al., 2014). Thus, these DEMs cannot be used to accurately simulate or predict local scale processes or impacts thereof. Even after considerable preprocessing to remove significant biases (due to vegetation and other physical structures) and to reduce inherent vertical errors, publicly available global DEMs still suffer from inaccuracies oftentimes orders of magnitude greater than length scales of the processes that are simulated (Schumann and Bates, 2018). However, as argued by Schumann et al. (2014), the technologies and funds to create a high-accuracy, open-access, global DEM are certainly available but such an undertaking would require a high-level international consortium and serious commitment of various sectors, including private industry; however, there is no doubt that the benefits of such a dataset would largely outweigh the costs (Schumann et al., 2016). Existing promising candidate technologies or datasets include of course existing and new airborne and drone LiDAR and photogrammetric DEMs, commercial high-resolution satellite DEMs, and recent developments in airborne single-pass interferometry (Faherty et al., 2020; Schumann et al., 2016).

3.2 Pitfalls

Within the major challenges described earlier, there are some pitfalls that can significantly limit the success for solutions or indeed make robust and reliable solutions difficult to develop.

For instance, the rapidly and constantly changing nature of urban landscapes and vegetation dynamics over different spatial and temporal scales poses a difficult problem for addressing the challenge of mapping inundation below vegetation canopy and in urban areas. Although characterizing and simulating or predicting the various signal interactions in these complex and dynamic environments is possible and the theoretical basis of doing so is known and robust, practical application of the mathematical models that need to be part of the solution requires expert SAR signal knowledge. Therefore, at least for the moment, promising operational solutions that have been proposed for flood mapping from SAR under different types of vegetation or urban areas are limited to only a few papers as outlined in the previous section. This is particularly true for urban flood mapping that received only recently the attention it de-

serves using complex SAR signal coherence processing (Chini et al., 2019; Li et al., 2019a,b).

Another pitfall, fairly obvious when looking at most of the published literature on remote sensing of floods, is that of relatively little scientific innovation and rigor (Schumann, 2019). Nowadays, with the popular use of web application programming interfaces or APIs for short, and the recent proliferation of online open-access satellite data and other valuable geospatial datasets, producing a more or less adequate flood map from a satellite image has become a fairly straightforward exercise and can be realized without much effort or expert knowledge. However, most of the commonly applied algorithms over large spatial coverage and across many types of imagery in a fully- or semi-automatic way are fairly dated and moreover, albeit robust and reliable, they were mostly developed for relatively "small" image data loads and often only demonstrated at case study level. Instead of faster and global processing for applications with less attention to scientific advances, there should be much more focus on scientific innovation first, especially when the goal is rapid, automated processing at global level for non-expert end-users.

3.3 Opportunities

Naturally, with challenges come many opportunities. More communities, organizations, and individual end-users want readily accessible flood maps instantly and with actual actionable information content that can be trusted (Schumann, 2018). Furthermore, many of the non-scientific or non-expert communities or end-users are becoming increasingly science-aware, and so scientific evaluation of products and services offered becomes almost a requirement in the eyes of the end-users and not only for the scientists as could be expected.

In terms of fast online data loading and processing, there is also the obvious opportunity of researching ways of how to use online analytics platforms, high-performance compute engines, and machine learning-based algorithms most efficiently.

4 Managing expectations

We have clearly entered an era of big data and the Internet of Things (IoT), in which everyone and everything is connected across networks, transmitting and receiving quasi an overload of information. In this context, Schumann et al. (2018) argued that for remote sensing of floods, the grand challenge now lies in ensuring sustainable and interoperable use as well as optimized distribution of remote sensing products and services for science and end-user applications as well as for operational flood disaster assistance. It is obvious that without a clear reality check, it is difficult to manage expectations, which is needed to match capabilities and needs.

There is no doubt that remote sensing, in particular satellite remote sensing, has seen significant progress over recent year, especially over the last 2 decades.

Alongside this, the need and desire for geospatial datasets to inform decision-making processes is also clearly increasing. However, in the context of flood disasters for instance, in recent years, response coordination between EO product developers and decision-makers during flood disasters has only slowly, albeit steadily, improved (Schumann et al., 2018), mainly because many challenges still remain and technical capabilities oftentimes are not well aligned with end-user needs. In order to address this mismatch and also the many challenges that exist in making EO data more readily usable and actionable in assisting flood management as well as flood disaster preparedness, response and resilience, the scientific community should seek closer collaboration with end-users (Hossain et al., 2016). As a result, outcomes of an effective partnership between product users and developers would be mutually beneficial and, at the same time, formal partnerships would ensure that expectations from both sides are properly managed.

5 Conclusions

The ability to observe, monitor, and measure floods and associated processes from satellites has been known since the early launch of the first Landsat satellite in the 1970s. However, until about a decade ago, satellite images, and especially those depicting a flood, have been rather difficult to obtain for free to conduct scientific analysis. Over the last decade, with the proliferation of satellite missions, largely due to the EC Copernicus Sentinel program, the increasing market potential of commercial small satellites and the IoT technologies, satellite remote sensing of floods has come a long way. Indeed, the increase in the number of peer-reviewed publications in recent years bears witness to that progress (Schumann and Moller, 2015). The main challenge now lies in turning that research progress into reliable and user-friendly applications that can be transitioned to end-user organizations.

Many of the existing and future satellite missions and airborne platforms provide rich data with great potential for enhanced monitoring, measuring, and mapping of floods, improving hydraulic models through new data assimilation techniques and parameter scaling behavior, and ultimately for an exploration of the ways in which new data sources may reduce uncertainty in flood predictions. Having said that, many challenges still lie ahead, among which the most important ones have been discussed in this chapter and are related to the development of robust, sharable, and interoperable operational mapping algorithms that are independent of satellite and image type and can be applied in a variety of environments (Schumann and Moller, 2015). Some scientific studies outlined in this chapter have introduced algorithms that are geared toward this aim but more research and applied case studies are needed to ultimately demonstrate to decision makers that EO should be an integral part of flood management and disaster relief operations.

References

Andreadis, K.M., Clark, E.A., Lettenmaier, D.P., Alsdorf, D.E., 2007. Prospects for river discharge and depth estimation through assimilation of swath-altimetry into a raster-based hydrodynamics model. Geophys. Res. Lett. 34.

Andreadis, K.M., Schumann, G.J.-P., 2014. Estimating the impact of satellite observations on the predictability of large-scale hydraulic models. Adv. Water Resour. 73, 44–54, https://doi.org/10.1016/j.advwatres.2014.06.006.

Bates, P.D., 2012. Integrating remote sensing data with flood inundation models: how far have we got? Hydrol. Process. 26 (16), 2515–2521, https://doi.org/10.1002/hyp.9374.

Bates, P.D., 2004. Invited commentary: Remote sensing and flood inundation modelling. Hydrol. Process. 18, 2593–2597.

Blyth, K., 1997. Floodnet: a telenetwork for acquisition, processing and dissemination of Earth observation data for monitoring and emergency management of floods. Hydrol. Process. 11, 1359–1375.

Chaabani, C., Chini, M., Abdelfattah, R., Hostache, R., Chokmani, K., 2018. Flood mapping in a complex environment using bistatic TanDEM-X/TerraSAR-X InSAR coherence. Remote Sens. 10, 1873, https://doi.org/10.3390/rs10121873.

Chen, N., Zhou, L., Chen, Z., 2015. A sharable and efficient metadata model for heterogeneous Earth Observation data retrieval in multi-scale flood mapping. Remote Sens. 7, 9610, https://doi.org/10.3390/rs70809610.

Chini, M., Papastergios, A., Pulvirenti, L., Pierdicca, N., Matgen, P., Parcharidis, I., 2016. SAR coherence and polarimetric information for improving flood mapping. In: 2016 IEEE International Geoscience and Remote Sensing Symposium (IGARSS), Beijing, China. https://doi.org/10.1109/IGARSS.2016.7730976.

Chini, M., Pelich, R., Pulvirenti, L., Pierdicca, N., Hostache, R., Matgen, P., 2019. Sentinel-1 InSAR coherence to detect floodwater in urban areas: Houston and Hurricane Harvey as a test case. Remote Sens. 11, 107, https://doi.org/10.3390/rs11020107.

Chini, M., Pulvirenti, L., Pierdicca, N., 2012. Analysis and interpretation of the COSMO-SkyMed Observations of the 2011 Japan Tsunami. IEEE Geosci. Remote Sens. Lett. 9, 467–471, https://doi.org/10.1109/LGRS.2011.2182495.

Cohen, S., Raney, A., Munasinghe, D., Derek Loftis, J., Molthan, A., Bell, J., Rogers, L., Galantowicz, J., Robert Brakenridge, G., Kettner, A., Huang, Y.F., Tsang, Y.P., 2019. The Floodwater Depth Estimation Tool (FwDET v2.0) for improved remote sensing analysis of coastal flooding. Nat. Hazards Earth Syst. Sci. 19, 2053–2065, https://doi.org/10.5194/nhess-19-2053-2019.

Currey, D.T., 1977. Identifying flood water movement. Remote Sens. Environ. 6, 51–61.

Dasgupta, A., Grimaldi, S., Ramsankaran, R.A.A.J., Pauwels, V.R.N., Walker, J.P., 2018. Towards operational SAR-based flood mapping using neuro-fuzzy texture-based approaches. Remote Sens. Environ. 215, 313–329, https://doi.org/10.1016/j.rse.2018.06.019.

Deutsch, M., Ruggles, F.H., 1978. Hydrological applications of Landsat imagery used in study of 1973 Indus river flood, Pakistan. Water Resour. Bull. 14, 261–274.

DeVries, B., Huang, C., Lang, M.W., Jones, J.W., Huang, W., Creed, I.F., Carroll, M.L., 2017. Automated quantification of surface water inundation in wetlands using optical satellite imagery. Remote Sens. 9, 807, https://doi.org/10.3390/rs9080807.

Durand, M., Gleason, C.J., Garambois, P.A., Bjerklie, D., Smith, L.C., Roux, H., Rodriguez, E., Bates, P.D., Pavelsky, T.M., Monnier, J., Chen, X., Di Baldassarre, G., Fiset, J.M., Flipo, N., Frasson, R.P.D.M., Fulton, J., Goutal, N., Hossain, F., Humphries, E., Minear, J.T., Mukolwe, M.M., Neal, J.C., Ricci, S., Sanders, B.F., Schumann, G., Schubert, J.E., Vilmin, L., 2016.

An intercomparison of remote sensing river discharge estimation algorithms from measurements of river height, width, and slope. Water Resour. Res. 52 (6), 4527–4549, https://doi.org/10.1002/2015WR018434.

El Hajj, M., Baghdadi, N., Bazzi, H., Zribi, M., 2019. Penetration analysis of SAR signals in the C and L bands for wheat, maize, and grasslands. Remote Sens. 11 (1), 31, https://doi.org/10.3390/rs11010031.

Faherty, D., Schumann, G.J.-P., Moller, D.K., 2020. Bare Earth DEM generation for large floodplains using image classification in high-resolution single-pass InSAR. Front. Earth Sci. 8.

Foga, S., Scaramuzza, P.L., Guo, S., Zhu, Z., Dilley, R.D., Beckmann, T., Schmidt, G.L., Dwyer, J.L., Joseph Hughes, M., Laue, B., 2017. Cloud detection algorithm comparison and validation for operational Landsat data products. Remote Sens. Environ. 194, 379–390, https://doi.org/10.1016/j.rse.2017.03.026.

Franceschetti, G., Iodice, A., Riccio, D., Ruello, G., 2003. SAR raw signal simulation for urban structures. IEEE Trans. Geosci. Remote Sens. 41, 1986–1995.

Giustarini, L., Matgen, R.H.P., Schumann, G.J.-P., Bates, P.D., Mason, D.C., 2013. A change detection approach to flood mapping in urban areas using TerraSAR-X. IEEE Trans. Geosci. Remote Sens. 51, 2417–2430.

Griffin, M., Burke, H.H., Mandl, D., Miller, J., 2003. Cloud cover detection algorithm for EO-1 Hyperion Imagery. In: 2003 IEEE International Geoscience and Remote Sensing Symposium (IGARSS), Toulouse, France. https://doi.org/10.1117/12.487297.

Grimaldi, S., Xu, J., Li, Y., Pauwels, V.R.N., Walker, J.P., 2020. Flood mapping under vegetation using single SAR acquisitions. Remote Sens. Environ. 237, 111582, https://doi.org/10.1016/j.rse.2019.111582.

Hess, L.L., Melack, J.M., Simonett, D.S., 1990. Radar detection of flooding beneath the forest canopy: a review. Int. J. Remote Sens. 11, 1313–1325.

Hirmas, D.R., Giménez, D., Nemes, A., Kerry, R., Brunsell, N.A., Wilson, C.J., 2018. Climate-induced changes in continental-scale soil macroporosity may intensify water cycle. Nature 561 (7721), 100–103, https://doi.org/10.1038/s41586-018-0463-x.

Hoefle, B., Vetter, M., Pfeifer, N., Mandlburger, G., Stoetter, J., 2009. Water surface mapping from airborne laser scanning using signal intensity and elevation data. Earth Surf. Process. Landforms 34, 1635–1649.

Hossain, F., Maswood, M., Siddique-E-Akbor, A.H., Yigzaw, W., Mazumdar, L.C., Ahmed, T., Hossain, M., Shah-Newaz, S.M., Limaye, A., Lee, H., Pradhan, S., Shrestha, B., Bajracahrya, B., Biancamaria, S., Shum, C.K., Turk, F.J., 2014. A promising radar altimetry satellite system for operational flood forecasting in flood-prone Bangladesh. IEEE Geosci. Remote Sens. Mag. 2, 27–36, https://doi.org/10.1109/MGRS.2014.2345414.

Hossain, F., Serrat-Capdevila, A., Granger, S., Thomas, A., Saah, D., Ganz, D., Mugo, R., Murthy, M.S.R., Ramos, V.H., Anderson, E., Schumann, G., Lewison, R., Kirschbaum, D., Escobar, V., Srinivasan, M., Lee, C., Iqbal, N., Levine, E., Searby, N., Friedl, L., Flores, A., Coulter, D., Irwin, D., Limaye, A., Stough, T., Skiles, J., Estes, S., Crosson, B., Akanda, A.S., 2016. A global capacity building vision for societal applications of earth observing systems and data: Key questions and recommendations. Bull. Am. Meteorol. Soc. 97 (7), 1295–1299, https://doi.org/10.1175/BAMS-D-15-00198.1.

Hostache, R., Matgen, P., Wagner, W., 2012. Change detection approaches for flood extent mapping: How to select the most adequate reference image from online archives? Int. J. Appl. Earth Obs. Geoinf. 19, 205–213, https://doi.org/10.1016/j.jag.2012.05.003.

Kinzel, P.J., Legleiter, C.J., Nelson, J.M., 2013. Mapping river bathymetry with a small footprint green LiDAR: Applications and challenges. J. Am. Water Resour. Assoc. 49, 183–204, https://doi.org/10.1111/jawr.12008.

Lane, S., 2009. Flood rich periods, flood poor periods and the need to look beyond instrumental records. In: EGU General Assembly 2009: Geophysical Research Abstracts, Vienna, Audtria.

Li, Y., Martinis, S., Wieland, M., 2019a. Urban flood mapping with an active self-learning convolutional neural network based on TerraSAR-X intensity and interferometric coherence. ISPRS J. Photogramm. Remote Sens. 152, 178–191, https://doi.org/10.1016/j.isprsjprs.2019.04.014.

Li, Y., Martinis, S., Wieland, M., Schlaffer, S., Natsuaki, R., 2019b. Urban flood mapping using SAR intensity and interferometric coherence via Bayesian network fusion. Remote Sens. 11 (19), 2231, https://doi.org/10.3390/rs11192231.

Markert, K.N., Chishtie, F., Anderson, E.R., Saah, D., Griffin, R.E., 2018. On the merging of optical and SAR satellite imagery for surface water mapping applications. Results Phys. 9, 275–277, https://doi.org/10.1016/j.rinp.2018.02.054.

Mason, D.C., Giustarini, L., Garcia-Pintado, J., Cloke, H.L., 2014. Detection of flooded urban areas in high resolution synthetic aperture radar images using double scattering. Int. J. Appl. Earth Obs. Geoinf. 28, 150–159.

Mason, D.C., Speck, R., Devereux, B., Schumann, G.J.-P., Neal, J.C., Bates, P.D., 2010. Flood detection in urban areas using TerraSAR-X. IEEE Trans. Geosci. Remote Sens. 48, 882–894.

Matgen, P., Hostache, R., Schumann, G., Pfister, L., Hoffmann, L., Savenije, H.H.G., 2011. Towards an automated SAR-based flood monitoring system: lessons learned from two case studies. Phys. Chem. Earth 36, 241–252.

McMillan, H.K., Brasington, J., 2007. Reduced complexity strategies for modelling urban floodplain inundation. Geomorphology 90, 226–243.

Muste, M., Hauet, A., Fujita, I., Legout, C., Ho, H.C., 2014. Capabilities of large-scale particle image velocimetry to characterize shallow free-surface flows. Adv. Water Resour. 70, 160–171, https://doi.org/10.1016/j.advwatres.2014.04.004.

Neal, J.C., Bates, P.D., Fewtrell, T.J., Hunter, N.M., Wilson, M.D., Horritt, M.S., 2009. Distributed whole city water level measurements from the Carlisle 2005 urban flood event and comparison with hydraulic model simulations. J. Hydrol. 368, 42–55.

Nevo, S., Anisimov, V., Elidan, G., El-Yaniv, R., Giencke, P., Gigi, Y., Hassidim, Avinatan Moshe, Z., Schlesinger, M., Shalev, G., Tirumali, A., Wiesel, A., Zlydenko, O., Matias, Y., 2019. ML for flood forecasting at scale. In: Thirty-second Conference on Neural Information Processing Systems (NIPS 2018), Montréal, Canada. NIPS 2018. https://doi.org/arXiv:1901.09583.

Pierdicca, N., Pulvirenti, L., Boni, G., Squicciarino, G., Chini, M., 2017. Mapping flooded vegetation using COSMO-SkyMed: Comparison with polarimetric and optical data over rice fields. IEEE J. Sel. Top. Appl. Earth Obs. Remote Sens. 10 (6), 2650–2662, https://doi.org/10.1109/JSTARS.2017.2711960.

Plank, S., Jüssi, M., Martinis, S., Twele, A., 2017. Mapping of flooded vegetation by means of polarimetric sentinel-1 and ALOS-2/PALSAR-2 imagery. Int. J. Remote Sens. 38 (17), 3831–3850, https://doi.org/10.1080/01431161.2017.1306143.

Prigent, C., Papa, F., Aires, F., Jimenez, C., Rossow, W.B., Matthews, E., 2012. Changes in land surface water dynamics since the 1990s and relation to population pressure. Geophys. Res. Lett. 39.

Robinove, C.J., 1978. Interpretation of a Landsat image of an unusual flood phenomenon in Australia. Remote Sens. Environ. 7, 219–225, https://doi.org/http://dx.doi.org/10.1016/0034-4257(78)90033-0.

Rodriguez-Alvarez, N., Podest, E., Jensen, K., McDonald, K.C., 2019. Classifying inundation in a tropical wetlands complex with GNSS-R. Remote Sens. 11, 1053, https://doi.org/10.3390/rs11091053.

Schumann, G., Matgen, P., Pappenberger, F., Hostache, R., Pfister, L., 2007a. Deriving distributed roughness values from satellite radar data for flood inundation modelling. J. Hydrol. 344, 96–111.

Schumann, G., Matgen, P., Pappenberger, F., Hostache, R., Puech, C., Hoffmann, L., Pfister, L., 2007b. High-resolution 3D flood information from radar for effective flood hazard management. IEEE Trans. Geosci. Remote Sens. 45, 1715–1725.

Schumann, G.J.-P., 2018. Satellite remote sensing of floods for disaster response assistance. In: Petropoulos, G.P., Islam, T. (Eds.), Remote Sensing of Hydrometeorological Hazards. CRC Press, Boca Raton, Florida, pp. 317–336.

Schumann, G.J.-P., 2017. Remote sensing of floods. In: Oxford Research Encyclopedia of Natural Hazard Science. Oxford University Press. https://doi.org/10.1093/acrefore/9780199389407.013.265.

Schumann, G.J.-P., 2015. Preface: Remote sensing in flood monitoring and management. Remote Sens. 7, 17013–17015.

Schumann, G.J.-P., Bates, P.D., 2018. The need for a high-accuracy, open-access global DEM. Front. Earth Sci. 6, 225, https://doi.org/10.3389/feart.2018.00225.

Schumann, G.J.-P., Bates, P.D., Neal, J.C., Andreadis, K.M., 2014. Technology: Fight floods on a global scale. Nature 507, 169.

Schumann, G.J.-P., Domeneghetti, A., 2016. Exploiting the proliferation of current and future satellite observations of rivers. Hydrol. Process. 30 (16), 2891–2896, https://doi.org/10.1002/hyp.10825.

Schumann, G.J.-P., Moller, D.K., 2015. Microwave remote sensing of flood inundation. Phys. Chem. Earth Parts A/B/C 83–84, 84–95, https://doi.org/http://dx.doi.org/10.1016/j.pce.2015.05.002.

Schumann, G.J.-P., Moller, D.K., Mentgen, F., 2016. High-accuracy elevation data at large scales from airborne single-pass SAR interferometry. Front. Earth Sci. 3, 88, https://doi.org/10.3389/feart.2015.00088.

Schumann, G.J.-P., Neal, J.C., Mason, D.C., Bates, P.D., 2011. The accuracy of sequential aerial photography and SAR data for observing urban flood dynamics, a case study of the UK summer 2007 floods. Remote Sens. Environ. 115, 2536–2546.

Schumann, G.J.P., 2019. The need for scientific rigour and accountability in flood mapping to better support disaster response. Hydrol. Process. 33 (24), 3138–3142, https://doi.org/10.1002/hyp.13547.

Schumann, G.J.P., Brakenridge, G.R., Kettner, A.J., Kashif, R., Niebuhr, E., 2018. Assisting flood disaster response with earth observation data and products: A critical assessment. Remote Sens. 10 (8), 1230, https://doi.org/10.3390/rs10081230.

Straatsma, M., 2009. 3D float tracking: In situ floodplain roughness estimation. Hydrol. Process. 23 (2), 201–212, https://doi.org/10.1002/hyp.7147.

Tarpanelli, A., Brocca, L., Barbetta, S., Faruolo, M., Lacava, T., Moramarco, T., 2015. Coupling MODIS and radar altimetry data for discharge estimation in poorly gauged river basins. IEEE J. Sel. Top. Appl. Earth Obs. Remote Sens. 8, 141–148, https://doi.org/10.1109/JSTARS.2014.2320582.

Ticehurst, C., Guerschman, J.P., Chen, Y., 2014. The strengths and limitations in using the daily MODIS open water likelihood algorithm for identifying flood events. Remote Sens. 6, 11791, https://doi.org/10.3390/rs61211791.

Yu, D., Lane, S.N., 2006. Urban fluvial flood modelling using a two-dimensional diffusion-wave treatment, part I: mesh resolution effects. Hydrol. Process. 20, 1541–1565.

Zhao, J., Zhao, X., Zhang, H., Zhou, F., 2017. Shallow water measurements using a single green laser corrected by building a near water surface penetration model. Remote Sens. 9 (5), 426, https://doi.org/10.3390/rs9050426.

Chapter 15

Emerging Techniques in Machine Learning for Processing Satellite Images of Floods

Mohammad Zare[a,b] **and Guy J-P. Schumann**[a,c,d,e]

[a]Research and Education Department, RSS-Hydro, Dudelange, Luxembourg; [b]University of Luxembourg, Faculty of Science, Technology and Communication (FSTC), Institute of Civil and Environmental Engineering (INCEEN), Luxembourg, Luxembourg; [c]School of Geographical Sciences, University of Bristol, Bristol, United Kingdom; [d]INSTAAR, University of Colorado, Boulder, CO, United States; [e]Remote Sensing Solutions, Barnstable, MA, United States

1 Introduction

Changing hydrological conditions are occurring all over the world, owing mostly to phenomena of climate change that affect atmospheric and earth surface processes. Temporal and spatial changes in rainfall have caused fundamental variation in surface water as well as flood events (IPCC, 2007). Losses due to all types of floods are not only economic (several billions of EUR every year at global level (Hirabayashi et al., 2013)) but also loss of lives. Responding appropriately to these threatening situations necessitates the use of innovative flood management techniques and technologies more than ever. The main priority of any flood management solution is to find suitable methods and models in order to manage floods better and to prepare facing this natural hazard and risk phenomenon and minimizing losses (Zare and Koch, 2014). Nowadays, scientific and technological advances, particularly in geospatial and remote sensing (RS) techniques have enabled the application of new tools for describing large areas affected by floods and also facilitating flood disaster management. The combination of these techniques and data-driven computing tools such as machine learning (ML) and artificial intelligence (AI) approaches have led to increased accuracy in satellite image processing, that is, practical information from satellite imagery during flood events can be extracted using ML and AI methods (Chen et al., 2018; Yang and Cervone, 2019). These methods are based on ideas how information is processed in biological systems. One of the advantages of such "soft" computing methods in system modeling is getting relatively accurate results without having well-defined nonlinear physical relations between variables (Nayak et al., 2013; Zare and Koch, 2018).

Earth Observation for Flood Applications. http://dx.doi.org/10.1016/B978-0-12-819412-6.00015-8

RS image processing using these data driven methods can be entwined with two main challenges. On one hand many parameters including different image provider, weather condition, spatial resolution, number of spectral bands, time interval between two overpasses and etc., should be considered for using images (Quinn et al., 2018). On the other hand, finding answer to a research questions of "which types of ML are suitable for processing satellite image of floods?" is difficult because of a multitude of methods. In this context, this chapter is focusing on these challenges and is organized as follows. Section 2 addresses the early history of applications of ML/AI methods in satellite image processing. Section 3 highlights the theory of recent ML methods for satellite image processing, more specifically the deep learning (DL) methods. Section 4 presents some illustrative case studies and the perspectives on the impacts of DL in satellite images processing during flood hazards studies are given in Section 5. Finally, the chapter concludes with Section 6.

2 Early history of methods

2.1 Application of machine learning in satellite image processing

ML is the ability of a machine to improve its performance by imitating human learning methods (repetition and experience) using artificial intelligence (AI) techniques (Mitchell, 1997; Witten and Frank, 2005). ML methods can enhance the computing infrastructure of data driven methods including statistics, AI, data mining, and pattern recognition. Therefore, it makes sense to apply it to solve a variety of data classification and process problems, including image segmentation. In this regard, many researchers have been using ML for RS image processing in flood studies, mainly because of the following reasons:

- A satellite image is a snapshot of a land surface (Liang et al., 2013), whereas, a flood event is taken place because of different time-dependent parameters (e.g., heavy rainfall). Moreover, some parameters cannot be seen in an image such as the effect of unsaturated zone on the generation of a flood event, ergo, a satellite images lacks knowledge about the whole process of flooding. In this situation ML uses its ability to learn by repetition.
- Flooding is a complex physical process (Mosavi et al., 2018), so ML can simplify the complexity by training a system using input/output data.

2.2 History of application in remote sensing (RS) satellite images for flood hazards

ML was applied for satellite image classification in flood studies. This has been of interest to Earth Observation (EO) researchers for a relatively long period of time. Typically, an ML method follows the workflow illustrated in Fig. 15.1.

Some notable ML approaches for efficient detection and classification of flooding in remote sensing imagery are k nearest neighbors (Thakur

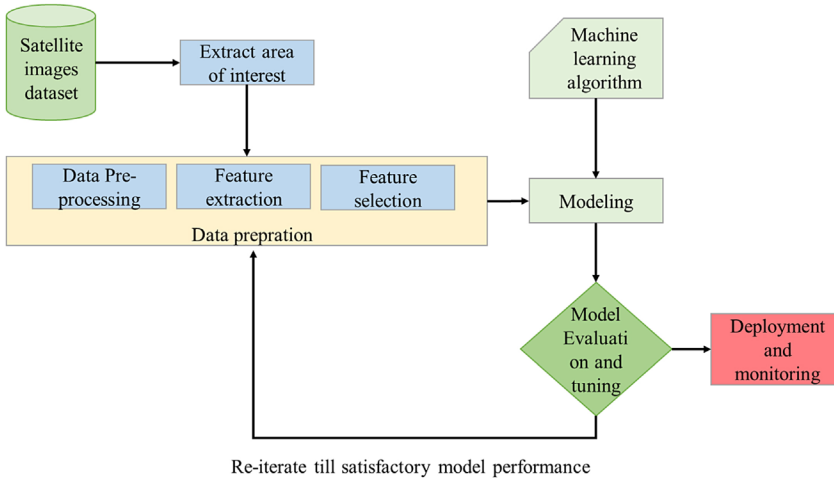

FIGURE 15.1 **Machine learning standard workflow.** *(From Sarkar et al. (2018).)*

et al., 2020), decision trees (Chapi et al., 2017; Janizadeh et al., 2019; Tehrany et al., 2013), random forests (Chaabani et al., 2018), support vector machine (Bui et al., 2019; Choubin et al., 2019; Dodangeh et al., 2020), and feed forward neural networks (FFNN) (Badrzadeh et al., 2015; Jensen, 2016; Skakun, 2010).

2.2.1 *k nearest neighbors (kNN)*

k nearest neighbors (kNN) is one of the simplest unsupervised ML algorithms in classification problems, it is also called the laziest learning method which was introduced by Fix and Hodges (1951) for the first time as a non-parametric method for pattern classification (Fig. 15.2).

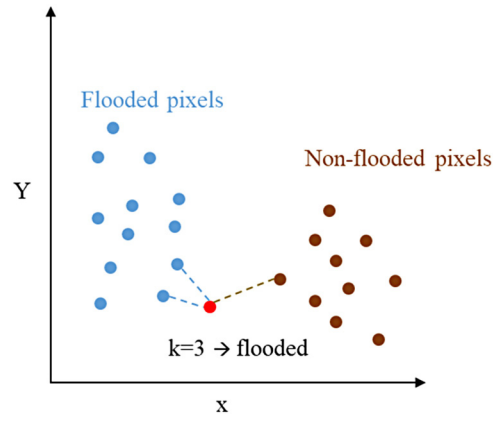

FIGURE 15.2 **Example of kNN classification.**

2.2.2 *Random forests (RF)*

Random forests (RF) is a classification ensemble learning algorithm that was introduced by Breiman (2001). It consists of multiple decision trees (DT); each tree has a single vote for a class (see Fig. 15.3). The most votes from all the trees in a forest will be selected as a final decision for assigning a class to unclassified data; such data could be a pixel in a satellite image for instance (Jensen, 2016; Rodriguez-Galiano et al., 2012).

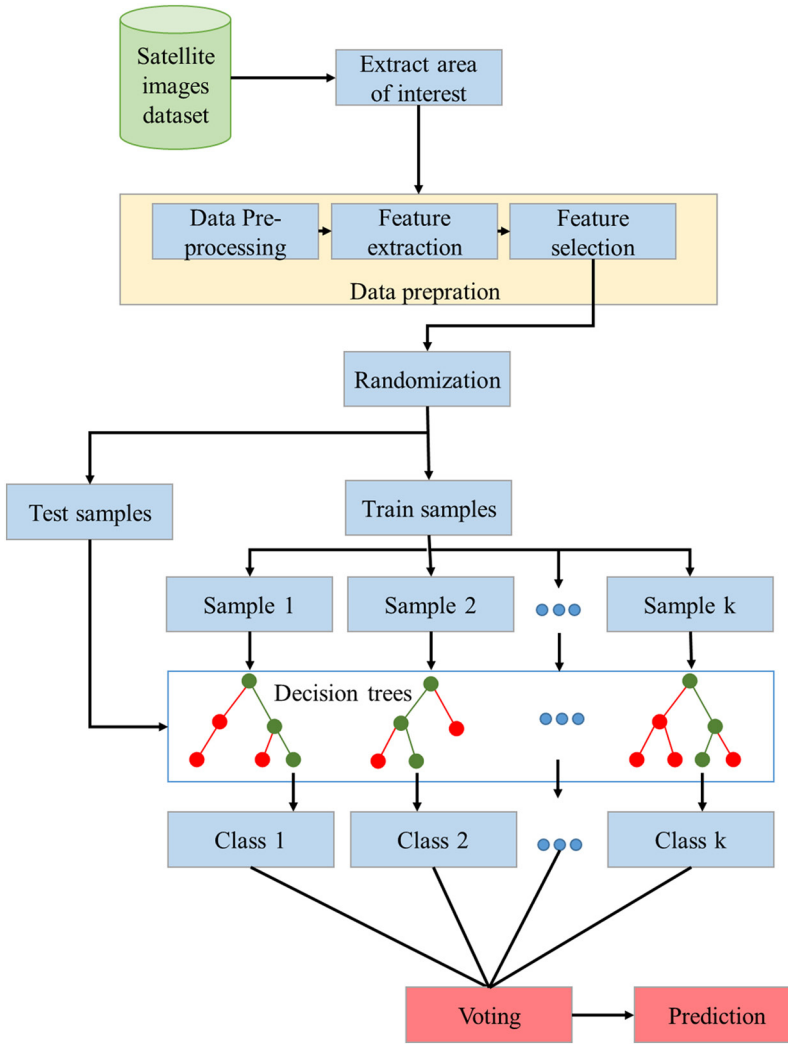

FIGURE 15.3 Random forest workflow. *(From Wang et al. (2015).)*

2.2.3 Support vector machine (SVM)

Support vector machine (SVM) might be the most popular classifier ML method that is used for processing remotely sensed data (Scheunders et al., 2018; Scholz, 2019). It was proposed by Boser et al. (1992). The main idea of SVM is to find the optimal separating hyperplane by maximizing the margin space which causes maximum separation between two classes (Fig. 15.4A). For this separation, the data on the boundaries of the margin—called support vectors (SV)—play an important role in the SVM classification problem because the middle of the margin is the optimal solution (Diop et al., 2018; Jensen, 2016; Scheunders et al., 2018). As Fig. 15.4 shows, in satellite image processing studies, the input space has a non-linear relation with output classes, ergo, kernel functions (e.g., sigmoid, polynomial, and spectral angle mapper kernels) are applied to project the spatial features into the higher dimensional space (Jensen, 2016).

2.2.4 Feed Forward Neural Network (FFNN)

The basic concept of an artificial neural network (ANN) is derived from an analogy with the biological nervous system of the human brain and how the latter processes information through its millions of neurons interconnected to each other by synapses. Borrowing this analogy, an ANN is a massively parallel system composed of many processing elements (neurons), where the synapses are actually variable weights, specifying the connections between individual neurons and which are adjusted, that is, may be switched on or off during the training- or learning- phase of the ANN, similar to what happens in the biological brain (Heaton, 2005; Zare and Koch, 2016). Multilayer FFNN is one of the

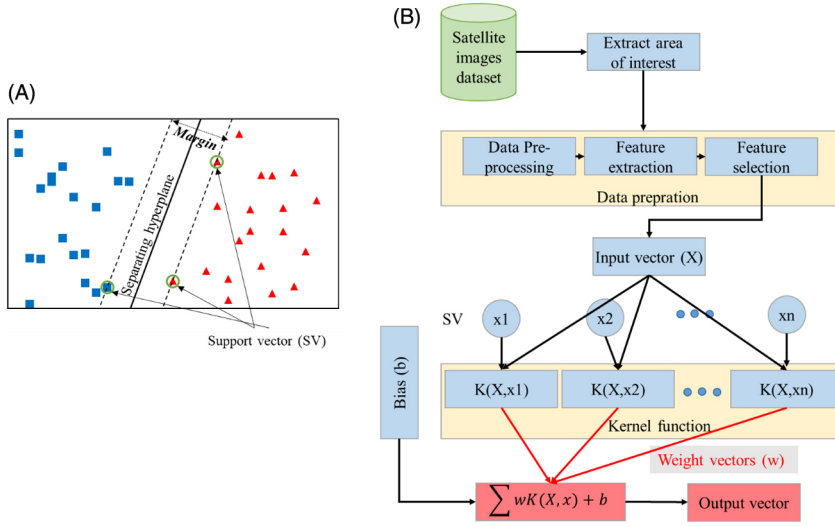

FIGURE 15.4 (A) Classifying objects with a SVM, (B) SVM workflow.

most popular and most widely used ANN-models. It is also a biologically inspired classification algorithm and consists of a number of simple neuron-like processing units, organized in layers. Every unit in a layer is connected with all the units in the previous layer (Fig. 15.5) by weights. The latter encode the knowledge about the network and are estimated during the training process, discussed later. Data enters at the inputs and passes through the network, layer by layer, until it arrive at the outputs. During normal operation, that is, when it acts as a classifier, there is no feedback between layers. This is why they are called FFNNs. When the network-weights and -biases are initialized, the network is ready for training. The multilayer FFNN can be trained for nonlinear and complex patterns. Essentially, the training consists mathematically of the adaptive computation (back-projection) of the weights between the various input- and output-units, by a local, or better, a global optimization method, such that some (squared) error- (objective) function

$$|E(w)|^2$$

between observed and ANN-predicted output is minimized (Daliakopoulos et al., 2005; Møller, 1993).

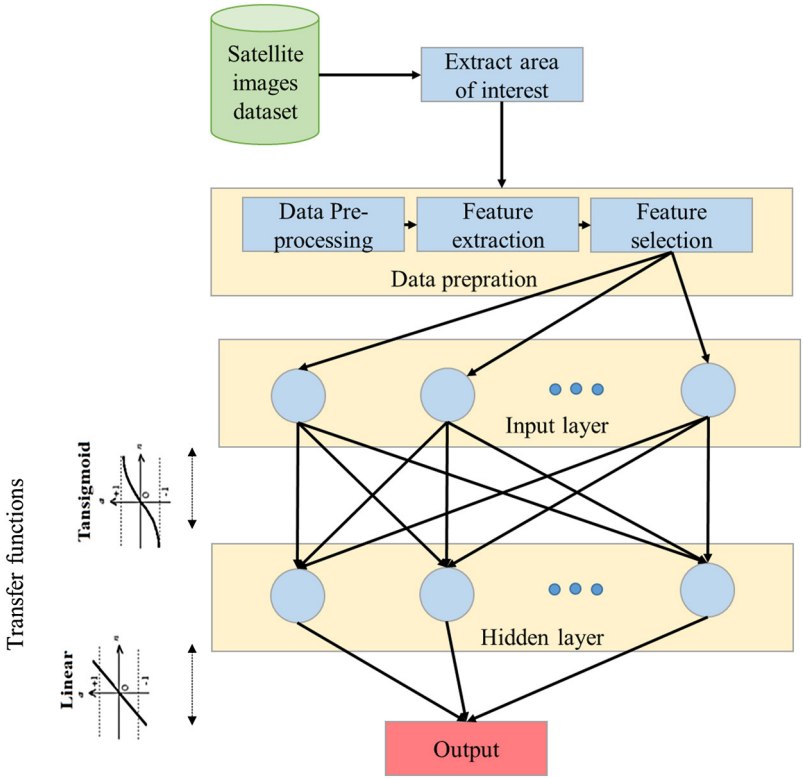

FIGURE 15.5 Architecture of FFNN with one hidden layer.

In recent years, there has been a significant improvement in satellite image processing using a cutting-edge implementation of FFNN called deep learning. This will be described and discussed in the next section.

3 Recent methods

3.1 Deep learning (DL)

DL is a subfield of AI and ML as shown in Fig. 15.6. The notion of "*deep*" in this approach comes from a multilayer structure in learning process, and therefore it is not necessarily related to the *deeper* understanding of this methodology for problem solving. Hence, it could be also called "*layered representations learning*" and "*hierarchical representations learning*" (Chollet, 2017).

Although the idea of DL was first introduced in 1993, it was not really applied for more than a decade because of the lack of data and high-performance computing hardware as well as popularity of other ML models at the time like support vector machine (SVM). However, a lot of labeled data have been collecting since 2006 and, moreover, significant progress in computers and data training methods have been made in recent years that removed obstacles to apply DL methods (Fig. 15.7). In fact, more recently it has become a rather hot topic in image processing, specifically the convolutional neural networks (CNN) DL model (Chollet, 2017; Hatt et al., 2019).

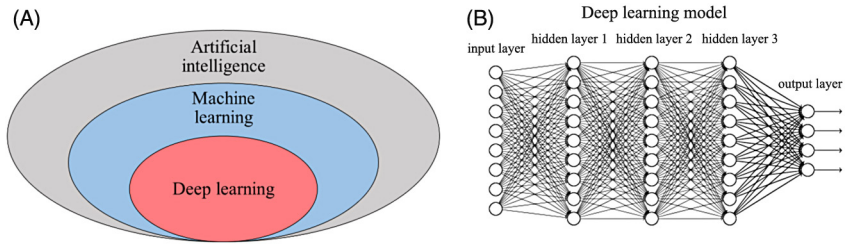

FIGURE 15.6 (A) artificial intelligence (AI), machine learning (ML), and deep learning (DL); (B) Architecture of a DL model (Chollet, 2017).

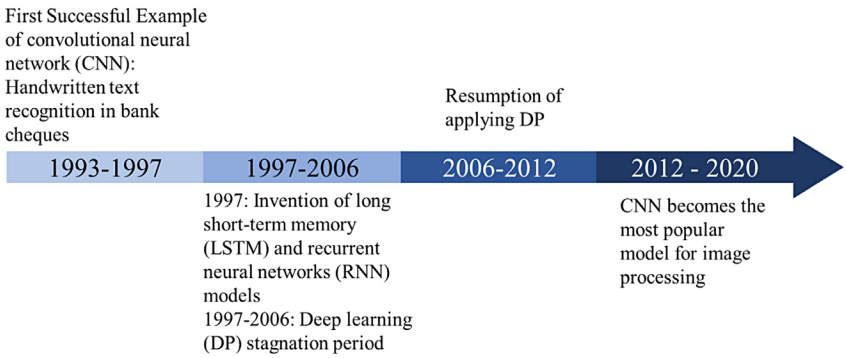

FIGURE 15.7 History of DL.

3.2 Application of deep learning to flood mapping

DL algorithms can classify the labeled data to make prediction for unlabeled ones (Bishop, 2006). For instance, when training and validating a DL algorithm like CNN for classifying satellite images as either flooded or non-flooded labeled pixels, it can be applied for classifying new unlabeled satellite images as either flooded or non-flooded areas (Fig. 15.8).

In flood studies, satellite imagery data are often used for identifying flood extent. Although optical satellite images are used for mapping of floods by many researchers, on numerous occasions optical satellite images are not really applicable for flood mapping because of frequent cloud cover during flood events as well as the problem of image acquisition during nighttime. In addition, flood events can occur outside satellite overpasses. Therefore, microwave wavelengths of the electro-magnetic spectrum, especially synthetic aperture radar (SAR) are mostly used to overcome these typical problems when using ML/DL algorithms in flood studies (Wagenaar et al., 2019). The most popular DL algorithm for satellite image classification is CNN, which is a multi-layer feed-forward artificial neural network comprising convolution, non-linearity, and pooling layers at each feature-extraction stage (Potnis et al., 2019). Flood mapping from SAR image processing using CNN generally consists of following steps (Chaabani et al., 2018; Hansen and Jorgensen, 2015; Li et al., 2019; Skakun, 2010):

- *SAR satellite imagery pre-processing*: (1) terrain distortion should be corrected using a digital elevation model (DEM) (2) exact geographic coordinates of pixels (geopositioning) should be determined

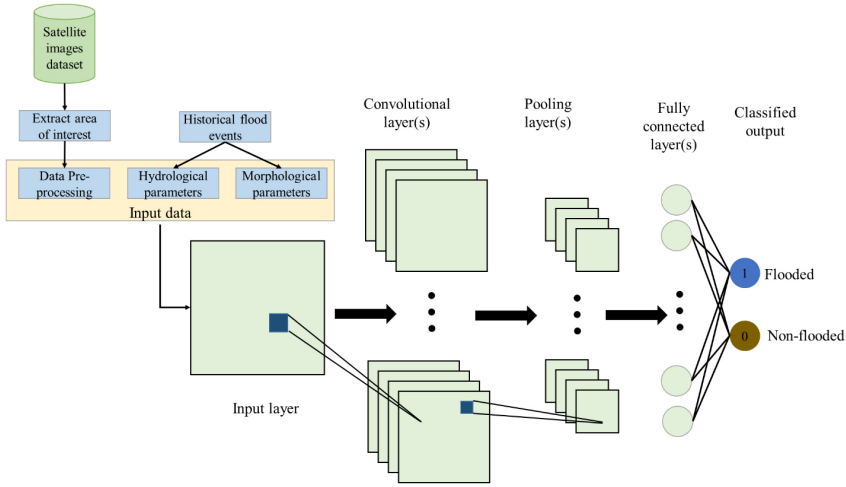

FIGURE 15.8 Architecture of convolutional neural network (CNN) classifier for flood susceptibility mapping (Wang et al., 2020).

- *Segmentation of image*: generating several feature maps are extracted by convolution, consequently the dimensions (Width × Height) will be reduced (downsampling) in pooling layer
- *Classification*: of final feature maps (learned representation), a conversion (e.g., linear classifier) is used to determine position/categories on the input map and apply it for prediction of new SAR images.

In the next section, classification of SAR satellite images of floods using ML methods will be described in detail using illustrative case studies.

4 Illustrative case studies

Illustrative examples/cases of techniques in ML for processing the satellite images of floods are based on outcomes of three notable research papers. It reflects the ability of three data driven models, namely, RF, SVM, and CNN for using remote sensed data to generate flood maps.

4.1 Flood mapping in Quebec, Canada

This research shows the results of assessing the flood mapping capabilities of SAR imagery acquired by the bistatic pair TanDEM-X/TerraSAR-X (TDX/TSX). Chaabani et al. (2018) provided a RF method to classify different land cover types of flooded areas based on multi-temporal input data of TDX/TSX SAR intensities and their bistatic InSAR coherence on the following acquisition dates:

- May 14, 2011, during a flood event
- July 14, 2011, after a flood event
- August 29, 2012, after a flood event

Due to the lack of flood extent ground measurements during SAR data acquisition, authors decided to utilize the LISFLOOD-FP hydraulic model (Neal et al., 2011) in order to cross evaluation the ML algorithm. For validating the LISFLOOD-FP model simulation, a flood map was extracted manually from a high-resolution GeoEye-1 optical image. The results showed very good agreement with an overall accuracy (OA) of 98% and a critical success index (CSI) of 94% between observed flood extent and model results for the May 14, 2011 flood event. As a next step, a RF classifier was employed to categorize all SAR image pixels into 10 different land cover classes during a flood event including flooded pixels (river, flooded agricultural zone, flooded forest zone, and flooded residential) and non-flooded pixels (dry agriculture, dry forest zone, dry urban zone, dry roads, dry grass, and buildings roofs). The most accurate RF model showed an OA of 79% when evaluated with the result of LISFLOOD-FP which was considered as a reference. As Fig. 15.9 shows, flood areas obtained with the RF model agree well with those simulated by the LISFLOOD-FP model. The authors finally concluded that the generated flood

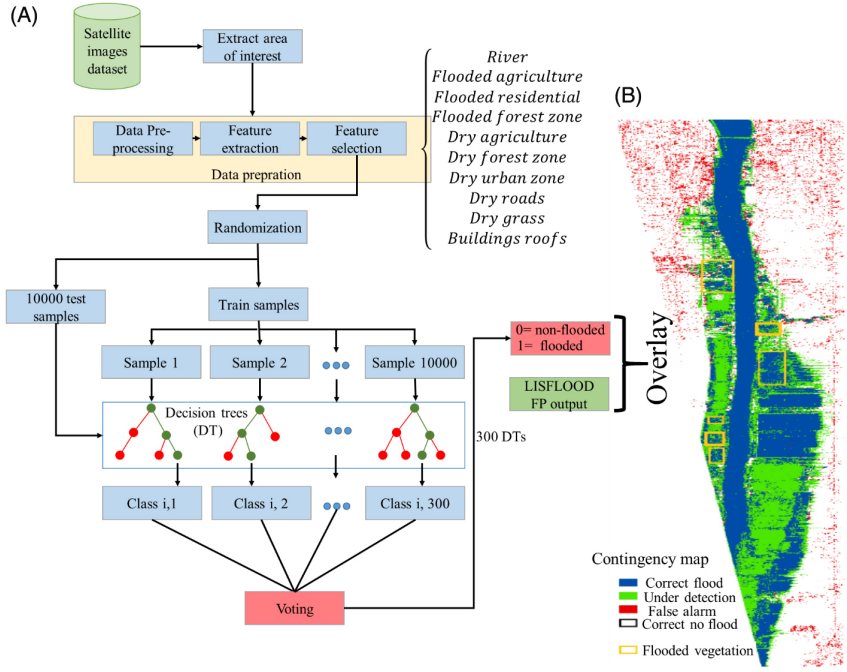

FIGURE 15.9 (A) Chaabani et al. (2018) research paper workflow and (B) contingency maps that show the agreement between hydraulic model-derived flood extent and RF classified maps.

extents map by remotely sensed satellite images can be applied for either ML data driven methods or physical models to improve their capability of flood simulations or predictions.

4.2 Flood susceptibility assessment in Kuala Terengganu, Malaysia

Tehrany et al. (2015) did some research on generating flood susceptibility maps with a SVM model. 181 flooded areas were determined by using TerraSAR-X imagery of the Nov 27, 2009 flood event, this was validated by several field surveys. The same numbers of flooded and non-flooded areas were chosen, that is, 362 locations consisting of flooded and non-flooded areas were introduced to the SVM model as input data. As expected, most of the flooded areas were located near rivers and flat floodplains. In order to develop a ML model, data were divided into two sets, wherefore the length of the training data set was 70% (127 flooded + 127 non-flooded cases) and test (prediction) data made up the remaining 30%. In the next step, the SVM model was then evaluated by using the spatial distribution of 10 flood condition factors including altitude, slope, curvature, stream power index (SPI), topographic wetness index (TWI), distance from the river, geology, land use/cover (LULC),

soil, and surface runoff. These factors were introduced to the SVM model as complementary GIS-maps. The results indicated that the auxiliary data (in this case the additional factors) can improve the precision of the ML model. As Fig. 15.4 shows, one of the crucial elements in the structure of SVM model are the kernel functions. Tehrany et al. (2015) used four kernel functions, namely, linear (LN), polynomial (PL), radial basis functions (RBF), and sigmoid (SIG) functions to study the impact of changing functions on final results. The authors also used the frequency ratio (FR) statistical method to show the proficiency of their SVM model. Both SVM and FR models were validated by the area under the curve (AUC) method where a value of AUC = 1 shows a prefect classification. The calculated success rate of AUC for all SVM models was between 0.82 and 0.89 for the training phase and 0.82 and 0.85 for the testing (prediction) phase, whereas the rate for the FR model was 0.72 and 0.61 in training and testing phases, respectively. Finally, they concluded that their SVM model can be used as an accurate and reliable ML model for producing flood susceptibility maps.

4.3 Urban flood mapping in Houston, United States

Li et al. (2019) research objectives were to first study the performance of different SAR information on flood mapping problems applying CNN. Second, develop an innovative semi-supervised deep neural network framework. The case study focused on floods during hurricane Harvey in August 2017. Authors showed that flooded pixels in SAR imagery have different appearances related to the backscattered energy between two classes (flooded and non-flooded). They used five different scenarios combining several SAR information and found the most important information from SAR data for urban flood mapping to be multi temporal intensity. Merging this information with SAR coherence information separate the flooded and non-flooded classes more effectively in ML algorithms. In a subsequent step, two parallel deep CNNs were used in the classification process. The input data were consisting of four TerraSAR-X HH-polarized Stripmap datasets: one pre-flood image (August 10, 2017), one co-flood image (September 01, 2017), and two post-flood images (October 26, November 17 and 28, 2017). The CNNs were connected to each other so that the weights of the second one (teacher model) would be updated by the first one (student model) in each iteration. The most innovative part of their research is using pseudo labeling of unlabeled sampling which updated the training data, hence the name of their model "active self-learning" CNN model or "A SL-CNN." The workflow of A SL-CNN is shown in Fig. 15.10. The advantage of this self-learning model is reducing the effect of limited training samples. Moreover, the A SL-CNN framework is applicable not only to TerraSAR-X data but also to the other SAR mission data like Sentinel-1 satellite images.

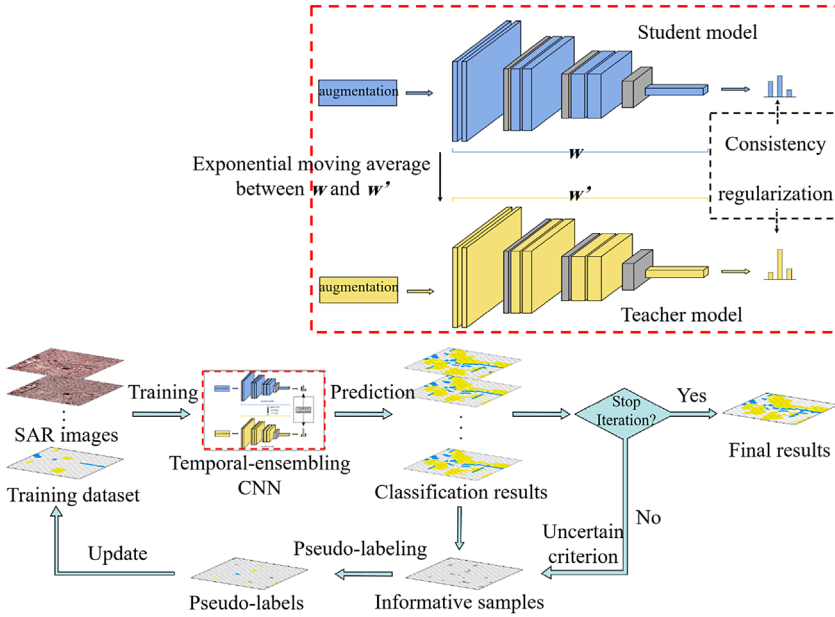

FIGURE 15.10 Active self-learning CNN (Li et al., 2019).

5 Perspectives

ML and AI are very popular topics in all basic and applied science and, more recently, also flood management. The most recent subfield of ML and AI is DL, which facilitates satellite image processing for flood studies. The biggest challenges of ML models in Earth observation and generating flood maps are recognizing that one is working with extreme value data, that is, flood extents of two similar rainfall storms are not the same, not even for the same location. Everything is highly stochastic, and the second challenge is that most (if not all) of existing ML models are "Data-In, Model-Out," this black box approach is not desirable for hydrologist because the physical relation between input and output are missed. To overcome the first problem, the combination of ML and cloud computing can be the solution. A cloud-based system can be easily used to manipulate a wide range of data aggregators (satellite images, digital elevation models, climate data, and infrastructure data). The collected data would be sent to a cloud platform instantly. In the backend, the real-time data stream and previous action experiences are sent to the designed DL model. In the case of a new flood event, which is not available in the historical dataset, the DL model immediately generates a new event and outputs will be updated by Internet of Things (IoT) event hub (Fig. 15.11). The problem of black box can be overcome by using parallel physical modeling. In other words, the ML data-driven

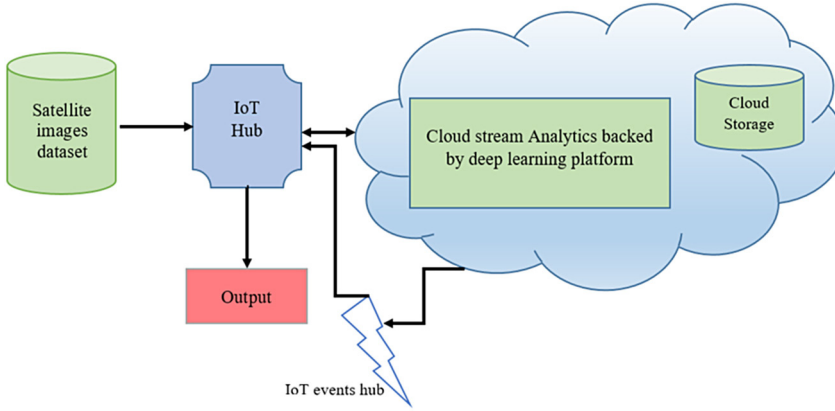

FIGURE 15.11 Cloud computing and deep learning.

methods run complementary to physical models and feed the physical model to calibrate involved parameters and vice versa. For example, a flood extent map simulated by ML uses as an input a 2D flood hazard model to calibrate a parameter like the SCS curve number (CN) or the runoff coefficient (C).

6 Conclusion

Currently, several ML methods are being applied to extract features from satellite images for flood mapping and consequently obtain spatial distribution of flood risks with acceptable levels of accuracy. This chapter introduced the basic concepts of ML algorithms and their application in flood studies. Through the illustration of different notable case studies, it is becoming clear that ML techniques for generating flood maps can be of great practical value for decision-making in water resource management and disaster response; however, important challenges remain. One of the bigger challenges is clearly that variables, which both scientists and practitioners involved with flood risk management, would like to measure or estimate during a flood event, and hopefully over different spatial and temporal scales, might include not only flooded area but also discharge, flow velocity and direction, water volume and level. Remote sensing can provide information about most of these with varying degrees of accuracy, however discharge and flow velocities can only be obtained indirectly through integration with a hydrodynamic model or gauging networks. Also, water volume and in some cases water level estimation requires the use of a topographic data set. So far, however, most studies using remote sensing data and ML approaches for floods are focusing on flooded area or extent. Future studies should be looking at the use of remote sensing and ML methods to estimate the many other flood parameters that remote sensing can inform about either directly or indirectly.

References

Badrzadeh, H., Sarukkalige, R., Jayawardena, A.W., 2015. Hourly runoff forecasting for flood risk management: Application of various computational intelligence models. J. Hydrol. 529, 1633–1643. doi: 10.1016/j.jhydrol.2015.07.057, Part 3.

Bishop, C.M., 2006. Pattern Recognition and Machine Learning (Information Science and Statistics). Springer-Verlag.

Boser, B.E., Guyon, I.M., Vapnik, V.N., 1992. A training algorithm for optimal margin classifiers. In: Proceedings of the Fifth Annual Workshop on Computational Learning Theory. Association for Computing Machinery, Pittsburgh, Pennsylvania, USA, pp. 144–152. DOI:10.1145/130385.130401.

Breiman, L., 2001. Random forests. Machine Learn. 45 (1), 5–32. DOI:10.1023/A: 1010933404324.

Bui, D.T., et al., 2019. A novel hybrid approach based on a swarm intelligence optimized extreme learning machine for flash flood susceptibility mapping. CATENA 179, 184–196. doi: 10.1016/j.catena.2019.04.009.

Chaabani, C., Chini, M., Abdelfattah, R., Hostache, R., Chokmani, K., 2018. Flood mapping in a complex environment using bistatic TanDEM-X/TerraSAR-X InSAR coherence. Remote Sens. 10 (12) doi: 10.3390/rs10121873.

Chapi, K., et al., 2017. A novel hybrid artificial intelligence approach for flood susceptibility assessment. Environ. Model. Softw. 95, 229–245. doi: 10.1016/j.envsoft.2017.06.012.

Chen, Y., et al., 2018. Multilevel cloud detection for high-resolution remote sensing imagery using multiple convolutional neural networks. ISPRS Int. J. GeoInform. 7 (5) doi: 10.3390/ijgi7050181.

Chollet, F., 2017. Deep Learning with Python. Manning Publications Co.

Choubin, B., et al., 2019. An ensemble prediction of flood susceptibility using multivariate discriminant analysis, classification and regression trees, and support vector machines. Sci. Total Environ. 651, 2087–2096. doi: 10.1016/j.scitotenv.2018.10.064.

Daliakopoulos, I.N., Coulibaly, P., Tsanis, I.K., 2005. Groundwater level forecasting using artificial neural networks. J. Hydrol. 309 (1–4), 229–240. doi: 10.1016/j.jhydrol.2004.12.001.

Diop, L., et al., 2018. The influence of climatic inputs on stream-flow pattern forecasting: case study of Upper Senegal River. Environ. Earth Sci. 77 (5), 182. doi: 10.1007/s12665-018-7376-8.

Dodangeh, E., et al., 2020. Integrated machine learning methods with resampling algorithms for flood susceptibility prediction. Sci. Total Environ. 705, 135983. doi: 10.1016/j.scitotenv.2019.135983.

Fix, E., Hodges, J.L., 1951. Discriminatory analysis, nonparametric discrimination: Consistency properties. Technical Report 4, USAF School of Aviation Medicine, Randolph Field, Texas.

Hansen, D.M., Jorgensen, M.N., 2015. Convolutional neural networks for SAR image segmentation. In: 2015 IEEE International Symposium on Signal Processing and Information Technology (ISSPIT). Abu Dhabi, United Arab Emirates, pp. 231–236. DOI:10.1109/ISSPIT.2015.7394333.

Hatt, M., Parmar, C., Qi, J., Naqa, I.E., 2019. Machine (deep) learning methods for image processing and radiomics. IEEE Trans. Rad. Plasma Med. Sci. 3 (2), 104–108. doi: 10.1109/TRPMS.2019.2899538.

Heaton, J., 2005. Introduction to Neural Networks with Java. Heaton Research Inc.

Hirabayashi, Y., et al., 2013. Global flood risk under climate change. Nat. Clim. Change 3, 816. doi: 10.1038/nclimate1911.

IPCC, 2007. Climate change 2007: The physical science basis. In: Solomon, S. et al. (Eds.), Contribution of Working Group I to the Fourth Assessment Report of the Intergovernmental Panel on Climate Change. Cambridge University Press, Cambridge, UK.

Janizadeh, S., et al., 2019. Prediction success of machine learning methods for flash flood susceptibility mapping in the Tafresh watershed, Iran. Sustainability 11 (19) doi: 10.3390/su11195426.

Jensen, J.R., 2016. Introductory Digital Image Processing : A Remote Sensing Perspective, fourth ed. Pearson.

Li, Y., Martinis, S., Wieland, M., 2019. Urban flood mapping with an active self-learning convolutional neural network based on TerraSAR-X intensity and interferometric coherence. ISPRS J. Photogramm. Remote Sens. 152, 178–191. doi: 10.1016/j.isprsjprs.2019.04.014.

Liang, S., et al., 2013. Global Land Surface Satellite (GLASS) Products: Algorithms, Validation and Analysis. Springer International Publishing.

Mitchell, T.M., 1997. Machine Learning. McGraw-Hill, p. 414.

Møller, M.F., 1993. A scaled conjugate gradient algorithm for fast supervised learning. Neural Networks 6 (4), 525–533, DOI:10.1016/S0893-6080(05)80056-5.

Mosavi, A., Ozturk, P., Chau, K.-w., 2018. Flood prediction using machine learning models: Literature review. Water 10 (11) doi: 10.3390/w10111536.

Nayak, P.C., Venkatesh, B., Krishna, B., Jain, S.K., 2013. Rainfall-runoff modeling using conceptual, data driven, and wavelet based computing approach. J. Hydrol. 493, 57–67. doi: 10.1016/j.jhydrol.2013.04.016.

Neal, J., et al., 2011. Evaluating a new LISFLOOD-FP formulation with data from the summer 2007 floods in Tewkesbury, UK. J. Flood Risk Manag. 4 (2), 88–95. doi: 10.1111/j.1753-318X.2011.01093.x.

Potnis, A.V., Shinde, R.C., Durbha, S.S., Kurte, K.R., 2019. Multi-class segmentation of urban floods from multispectral imagery using deep learning. In: IGARSS 2019-2019 IEEE International Geoscience and Remote Sensing Symposium, Yokohama, Japan, pp. 9741–9744. DOI:10.1109/IGARSS. 2019.8900250.

Quinn, J.A., et al., 2018. Humanitarian applications of machine learning with remote-sensing data: review and case study in refugee settlement mapping. Philos. Trans. Ser. A Math. Phys. Eng. Sci. 376 (2128) doi: 10.1098/rsta.2017.0363.

Rodriguez-Galiano, V.F., Chica-Olmo, M., Abarca-Hernandez, F., Atkinson, P.M., Jeganathan, C., 2012. Random Forest classification of Mediterranean land cover using multi-seasonal imagery and multi-seasonal texture. Remote Sens. Environ. 121, 93–107. doi: 10.1016/j.rse.2011.12.003.

Sarkar, D., Bali, R., Ghosh, T., 2018. Hands-On Transfer Learning With Python: Implement Advanced Deep Learning and Neural Network Models Using TensorFlow and Keras. Packt Publishing.

Scheunders, P., Tuia, D., Moser, G., 2018. Contributions of machine learning to remote sensing data analysis. In: Liang, S., (Ed.), Comprehensive Remote Sensing. Elsevier, Oxford, pp. 199–243. DOI: https://doi.org/10.1016/B978-0-12-409548-9.10343-4.

Scholz, M., 2019. Chapter 11—Classifying adaptive sustainable flood retention basins. In: Scholz, M. (Ed.), Sustainable Water Treatment. Elsevier, pp. 279–299. doi: 10.1016/B978-0-12-816246-0.00011-2.

Skakun, S., 2010. A neural network approach to flood mapping using satellite imagery. Comput. Inform. 29 (6), 1013–1024.

Tehrany, M.S., Pradhan, B., Jebur, M.N., 2013. Spatial prediction of flood susceptible areas using rule based decision tree (DT) and a novel ensemble bivariate and multivariate statistical models in GIS. J. Hydrol. 504, 69–79. doi: 10.1016/j.jhydrol.2013.09.034.

Tehrany, M.S., Pradhan, B., Mansor, S., Ahmad, N., 2015. Flood susceptibility assessment using GIS-based support vector machine model with different kernel types. CATENA 125, 91–101. doi: 10.1016/j.catena.2014.10.017.

Thakur, B., Kalra, A., Ahmad, S., Lamb, K.W., Lakshmi, V., 2020. Bringing statistical learning machines together for hydro-climatological predictions—Case study for Sacramento San joaquin River Basin, California. J. Hydrol. 27, 100651. doi: 10.1016/j.ejrh.2019.100651.

Wagenaar, D., et al., 2019. Invited perspectives: How machine learning will change flood risk and impact assessment. Nat. Hazards Earth Syst. Sci. Discuss. 2019, 1–23. doi: 10.5194/nhess-2019-341.

Wang, Y., Fang, Z., Hong, H., Peng, L., 2020. Flood susceptibility mapping using convolutional neural network frameworks. J. Hydrol. 582, 124482. doi: 10.1016/j.jhydrol.2019.124482.

Wang, Z., et al., 2015. Flood hazard risk assessment model based on random forest. J. Hydrol. 527, 1130–1141. doi: 10.1016/j.jhydrol.2015.06.008.

Witten, I.H., Frank, E., 2005. Data Mining: Practical Machine Learning Tools and Techniques, Second ed. Elsevier Science, p. 560.

Yang, L., Cervone, G., 2019. Analysis of remote sensing imagery for disaster assessment using deep learning: a case study of flooding event. Soft Comput. 23 (24), 13393–13408. doi: 10.1007/s00500-019-03878-8.

Zare, M., Koch, M., 2014. An analysis of MLR and NLP for use in river flood routing and comparison with the Muskingum Method. In: Eleventh International Conference on Hydroscience & Engineering (ICHE). Hamburg, Germany.

Zare, M., Koch, M., 2016. Using ANN and ANFIS models for simulating and predicting groundwater level fluctuations in the Miandarband Plain, Iran. In: Sustainable Hydraulics in the Era of Global Change, Proceedings of the fourth IAHR Europe Congress (Liege, Belgium, 27-29 July 2016). CRC Press, 2016, Taylor & Francis Group, London.

Zare, M., Koch, M., 2018. Groundwater level fluctuations simulation and prediction by ANFIS- and hybrid Wavelet-ANFIS/Fuzzy C-Means (FCM) clustering models: Application to the Miandarband plain. J. Hydro-environ. Res. 18 (Suppl. C), 63–76. doi: 10.1016/j.jher.2017.11.004.

Chapter 16

Merged AMSR-E/AMSR-2 and GPM Passive Microwave Radiometry for Measuring River Floods, Runoff, and Ice Cover

G. Robert Brakenridge[a], Son. V. Nghiem[b] and Zsofia Kugler[c]
[a]CSDMS, INSTAAR, University of Colorado, Boulder, CO, United States; [b]Jet Propulsion Laboratory, California Institute of Technology, Pasadena, CA, United States; [c]Budapest University of Technology and Economics, Budapest, Hungary

1 Introduction

Because of their importance to local economies, river flows have long been measured on the ground: at gauging stations (Fekete and Vorosmarty, 2007). However, the discharge data are not freely shared among all nations, and each station requires a sustained investment of personnel time, even after installation, in order to continually maintain and update the calibration to discharge. Also, and even though many river basins are transnational, efforts to compile data internationally must include data of varying quality and temporal and spatial coverage. This type of water data is regarded by some nations as state secrets; in other parts of the world, data collection is reduced due to funding issues (Shiklomanov et al., 2002). At some locations, flow observations have never been initiated (Fig. 16.1). As a result, the flow hydrology measurement needs and how they may be addressed are active topics of discussion in the hydrological community (Fekete et al., 2015; Famiglietti et al., 2015).

Accurate hydrological modeling also depends critically on improvements to the observational data: "processing more of the same poor quality data will only lead to poorer quality model results" (Fekete et al., 2016). Satellite-based measurements of the Earth's water cycle are therefore central to better understanding surface water fluxes and to modeling thereof (Pekel et al., 2016); as well as for understanding flood risk (Brakenridge, 2018). These observations are required for more efficient water resources management, and for better prediction of and responses to floods and droughts (Alsdorf et al., 2003,

Earth Observation for Flood Applications. http://dx.doi.org/10.1016/B978-0-12-819412-6.00016-X

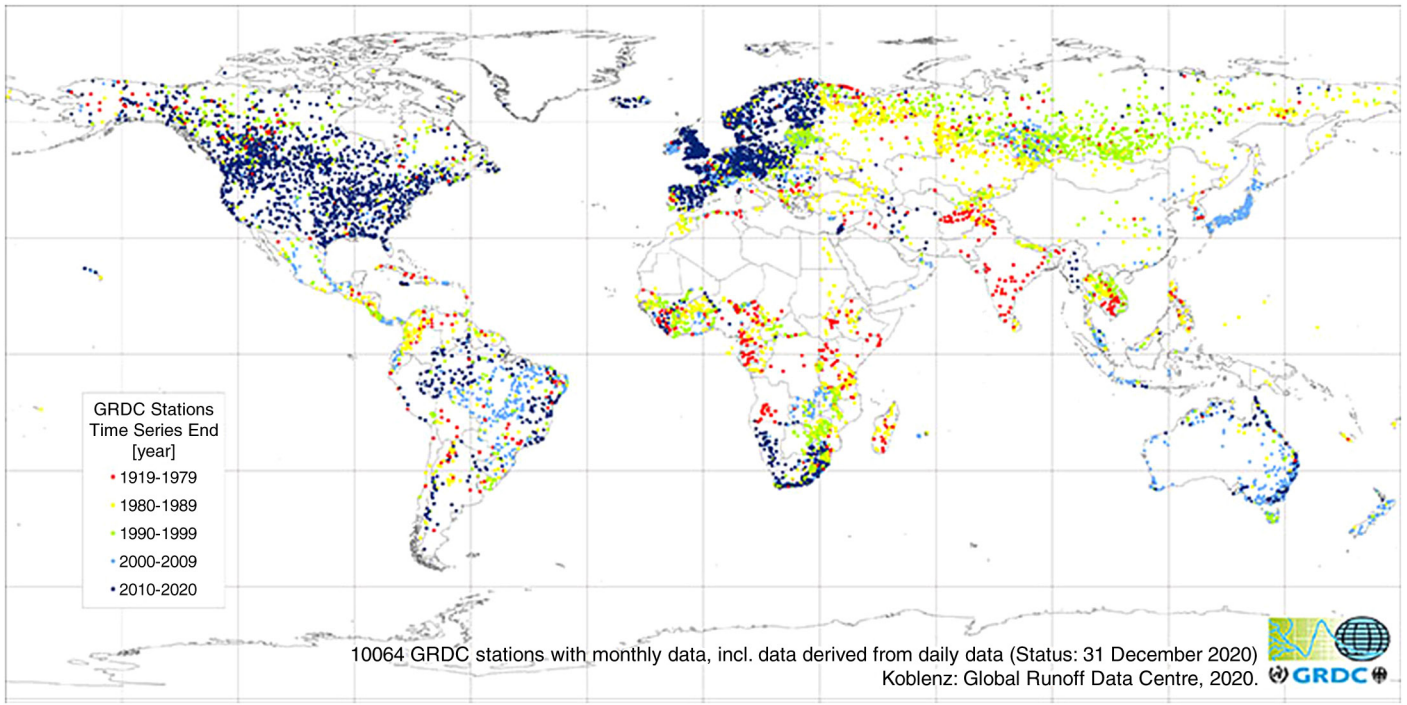

FIGURE 16.1 River discharge gauging stations with records collected at the Global Runoff Data Center (GRDC). Only *dark blue* stations are currently active; others are discontinued. Primarily monthly (only) data are available from GRDC; the shared archives of daily data are much more limited. Coverage by any data is sparse in portions of South America, some areas of Africa, and much of Asia (GRDC, 2010).

Brakenridge et al., 2016). Observational work using advanced technology on atmospheric components of the water cycle has made rapid progress: with the advent of satellite precipitation and also groundwater storage measurements at continental to global scales. Thus, the fluxes of water to and from the Earth's surface and its atmosphere are, increasingly, being directly measured. Now, another critical component of the cycle, *water surface runoff* (in mm) and *river discharge* (in m^3/s), is beginning to be measured via remote sensing. The two are similar measurements: discharge is converted to runoff by use of the contributing drainage area. We address here one method to accomplish direct measurements of river flow variation (discharge and runoff).

2 Definition of discharge and runoff

River and stream watersheds are defined in map view by the surface drainage network. During times of no precipitation or snowmelt, watersheds generate river base flow from groundwater discharge. The visible rivers, lakes, and wetlands in a watershed are the surface water expression of that ground water system. Also, during and after precipitation events or periods of snowmelt, higher runoff and discharge are achieved for various lengths of time (referred to as storm or flood hydrographs). *Discharge* (Eq. 16.1) is the volume of channeled water moving pass a measurement site along a river, and is expressed as

$$Q = wdv \tag{16.1}$$

where Q is discharge in m^3/s, w and d are flow width and depth, respectively, in m, and v is flow velocity in m/s. This simple flow continuity equation when applied to rivers includes abundant further complexity, because river channels are rarely rectangular, and each width increment across an actual flowing river includes a particular average depth and velocity.

Discharge is commonly measured on the ground via continuous river level (stage) recording, and then calibrated to discharge by intermittent sampling of the cross-sectional flow area and flow velocity. Current velocity meters are lowered into the river, and maximum depths and velocities (at different measurement depths in the flow column) are obtained in a series of measurements across the river. Intermittent measurements of Q by such field measurements of flow cross sectional area and velocity provide information about Q at different stage, as measured in the field at a permanent location. The relation between Q and stage is known as a rating curve, and it must be revised over time as channel dimensions, and thus the actual empirical relation, change. However, once the rating curves are established, instantaneous discharge is commonly measured (in many nations) to ±20% using only the stage value.

Runoff is essentially the same discharge information, but adjusted to watershed area and particular time intervals. Thus, an average discharge in m^3/s measured for the day, via stage, can be immediately transformed to total daily water volume/day using the total number of seconds in a day. This daily volume

is usefully recast to daily runoff by dividing volume by total upstream drainage area.

$$R = 86400 \times Q / A \tag{16.2}$$

where R is runoff in mm/day, Q is discharge converted to mm^3/s, and A is contributing watershed area, in mm^2.

Among the uses of this conversion from Q to R is that R is directly comparable to other relevant measurements or model results for watershed land surfaces, such as total millimeter of daily rainfall or evapotranspiration. Note that these units are conventionally used in hydrology, rather than the International System of Units.

3 Temporal sampling requirements

In the latter part of the 20th century, it was widely believed in the remote sensing/Earth Science community that discharge and runoff could not be directly measured from orbital platforms, but must instead be either modeled, or measured on the ground. There are two reasons for this:

1. Flow velocity is critical in any direct measurements of discharge (per equation 1), and, so far, there are only very experimental techniques of retrieving even surface flow velocities. Direct measurements of cross-sectional flow velocities from satellite remote sensing are not available at all.
2. Although, in principle, accurate river stages can be measured via satellite altimetry, discharge along many rivers can vary by an order of magnitude over time scales of only several days or even several hours (Fig. 16.2). An altimetric satellite system capable of retrieving stages on a global basis at this temporal resolution is difficult to accomplish. Like precipitation, runoff can be a very dynamic phenomenon, and difficult to adequately characterize unless revisits of at least daily can be attained. In addition, satellite altimetry is an along-track, nadir directional profiling tool that allows stage measurements only where the satellites ground track crosses the river channel: which imposes a significant spatially limitation to measurements.

In this regard, NASA's upcoming Surface Water and Ocean Topography Mission (SWOT) will offer, for the planned mission duration of ~3 years, river stage data at many locations across the world on a relatively coarse time step (weekly or twice-weekly, depending on latitude), but with a high precision of better than several centimeters. A major use of such data will be calibration of hydrological models which produce river stage and slope results along extensive drainage networks or even globally (Pavelsky et al., 2014). The calibrated models can then, in turn, be driven with daily climatology to predict river discharge and runoff at daily time steps. SWOT will be the first altimetry mission designed to monitor discharge and runoff changes, but its temporal sampling and limited mission duration constrain its utility for sustained observations.

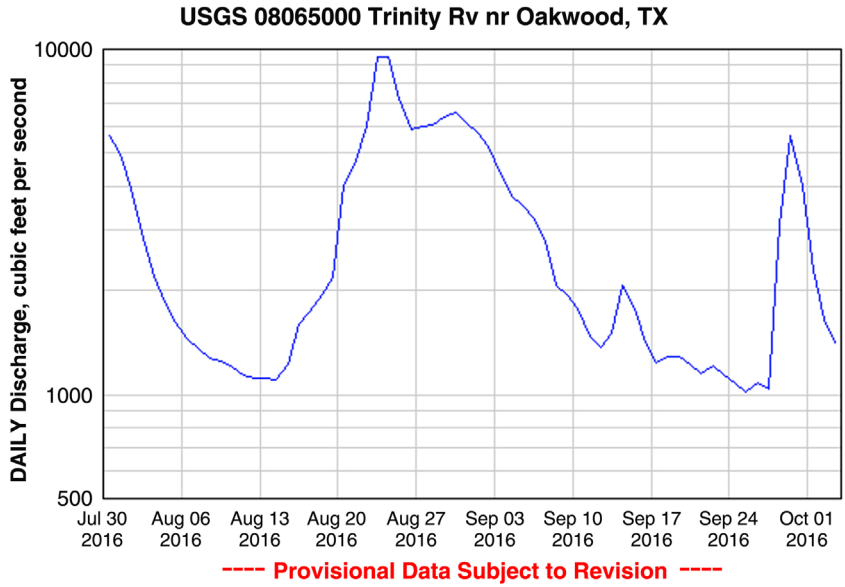

FIGURE 16.2 Portion of the gauging station discharge record for the Trinity River, Texas. In late September 2016, discharge rose from ~1000 ft^3/s to ~ 5000 ft^3/s in 3 days. In August of the same year, an order of magnitude increase occurred in 8 days.

Our work demonstrates that satellite microwave radiometry technology has the complementary ability to measure discharge and runoff with the advantage of a daily record extending back to at least 1998, and continuing indefinitely into the future, for as long as satellites such as GCOM-W, GPM, and follow-on's continue operating. The radiometry method does require accurate calibrations, which can be provided by river gauging, or in the future by SWOT measurements, thereby extending the value of SWOT backward in time before the SWOT launch and forward beyond the SWOT lifetime. Where there is no river gauge or SWOT coverage, the calibration can be accomplished by using a hydrology model such as the Water Balance Model (WBM) to estimate river discharge within the limit of model uncertainties (Brakenridge et al., 2012; Cohen et al., 2011). It should be noted that many of the world's *in situ* "gauging stations" monitor only stage and are also not calibrated to discharge: yet even such uncalibrated information provides useful monitoring, including relative flood magnitudes and durations, flow seasonality, and present flow status relative to a mean.

4 Potential of microwave radiometry

Satellite microwave satellites such as the Japanese Space Agency's GCOM-W and NASA's GPM provide global coverage of the radiation emitted from the Earth's land surface on a daily basis and, at certain wavelengths, without

major interference from cloud cover. Using a strategy first developed for wide-area optical sensors (Brakenridge et al., 2005), these sensors (e.g., AMSR-E, AMSR-2, TRMM/TMI, and GPM/GMI) can monitor river discharge changes via the accompanying changes in reach surface water extent. As rivers rise and discharge increases, water area within "satellite gauging sites" (selected parcels of floodplain land measuring approximately 10 km x 10 km; Figs. 16.3–16.5) also increases (Brakenridge et al., 2005, 2007, 2012; Van Dijk et al., 2016). Because at some frequencies the emission from water is much less than from land (even very wet land), the proportion of water and land within each pixel in a microwave image can be sensitively monitored by measuring the bulk or total emission.

The specific measurement parcels are selected from globally gridded microwave products whose pixels are at roughly 10 km spatial scale. A ~37-GHz

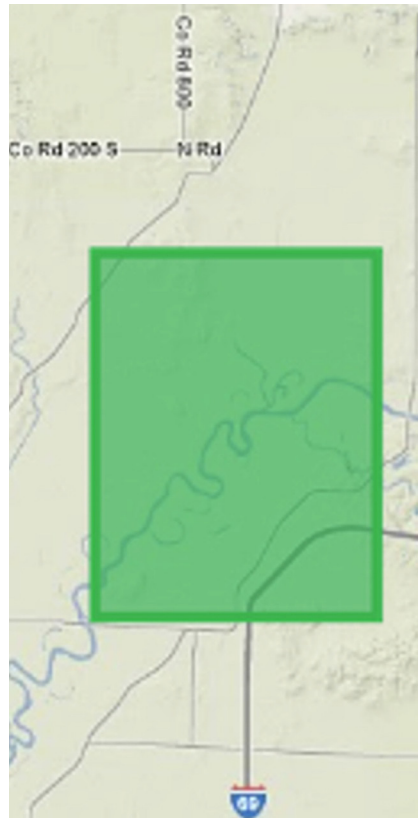

FIGURE 16.3 Footprint of a ~10 km measurement pixel from a daily global gridded microwave product produced at the JRC (Joint Research Centre, European Commission). This pixel is a measurement site for monitoring discharge changes along the Wabash River, southern Indiana, United States.

FIGURE 16.4 A meander bend covered by the measurement pixel showing the opportunity for flow area expansion onto the point bars and floodplain as stage and discharge increase.

FIGURE 16.5 View of a typical river meander, showing the point bar (inside of meander bend) and steeper cut bank (outside of bend). As flow increases, flow width and measurement site water area increase. This is the Brazos River below Possum Kingdom Lake, Texas. This image is courtesy of HuecoBear via Wikimedia Commons, https://commons.wikimedia.org.

image pixel of these dimensions centered over a river is commonly "mixed;" it includes both water (low emission), and land (much higher emission). As the proportion of water area rises, the bulk emitted radiation declines. The microwave signal is thereby sensitive to flow width changes (Fig. 16.6).

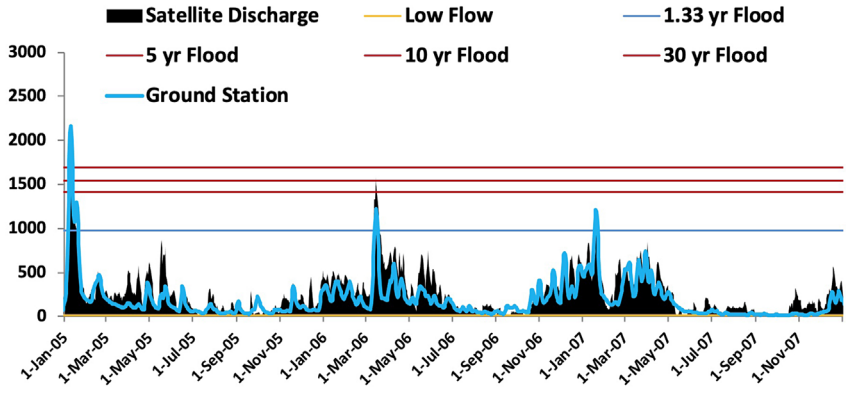

FIGURE 16.6 ***In situ*** **gauging station discharge (vertical axis is river discharge in m^3/s) can be compared with the satellite water flow area signal for co-located measurement sites/gauging stations in the United States.** In this example for River Watch site 446, Trinity River, Texas, the two independent time series of station data *(blue line)* and remote sensing *(black)* are shown for a portion of the 1998-present period of record. The satellite-based flow area measurements have been first transformed to discharge values using an empirical regression equation such as shown in Fig. 16.7.

For in-situ river gauging stations, transformation of the remote sensing signal to river discharge values must be accomplished using a rating equation. For an automated online satellite-based system (River Watch; http://floodobservatory.colorado.edu/Discharge Access.html), this is accomplished by runs of a global runoff model (Brakenridge et al., 2012; Cohen et al., 2011). Five years (2003–07) provide abundant model output for calibration.

The model produces daily discharge values for these years at each measurement site and daily maximum, mean and minimum values for each month of the 5-year period can be used (model global grid resolution is also 10 km). A rating curve equation then is constructed from the set of 180 daily discharge/remote sensing pairs (Fig. 16.7). Commonly, a linear or a second-order polynomial equation provides an acceptable fit. As is the case for *in situ* stage/discharge rating equations or curves, the relations are entirely empirical. The use of only 5 years of comparison of model to remote sensing is less than ideal (the rare very large flows may not be included); future work could compare longer time series.

The potential for remote sensing of streamflow is demonstrated in Figs. 16.6 and 16.7 (daily values) and 16.8 (monthly runoff). The use of *in situ* data provides the most accurate rating equation, but even the model-derived curve, though exhibiting a different slope, allows for useful results without the need for data from the ground. The model predictive strength is assessed by Nash-Sutcliffe (N-S) statistics (Nash and Sutcliffe, 1970), discussed in a section below.

Significant scatter is expected in the model and remote sensing plots of daily values, as both model and remote sensing errors are included. In this regard, global scale modeling may perform poorly at some sites in simulating daily

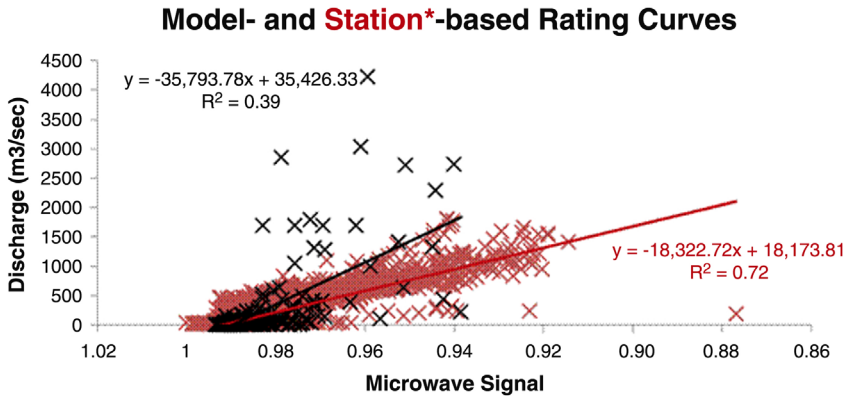

FIGURE 16.7 Two rating equations for site #460, Trinity River, Texas. The WBM model results are shown as *black crosses*, and, as expected, exhibit a large amount of scatter compared with the remote sensing. The scatter is expected in this case because the river includes control structures that are not part of the WBM model. The *in situ* gauging station discharges are more highly correlated to the remote sensing.

discharge changes, even while the remote sensing is tracking actual discharge and runoff changes very well (Fig. 16.8). Or the site may be poorly located and the remote sensing signal itself not be very sensitive to discharge changes (e.g., rivers within narrow mountain valleys). However, in many cases, at sites where discharge causes significant changes in surface water area, there is a strong correlation between modeled discharge and the remote sensing signal: both are independently tracking actual discharge changes (Figs. 16.9 and 16.10).

For most River Watch sites at present, there is no comparison to *in situ* data, and if the WBM model exhibits bias, this will be reflected in the rating curve and in the satellite-based daily discharge values. However, we stress that the observed model and remote sensing scatter in plots such as Fig. 16.9 does not

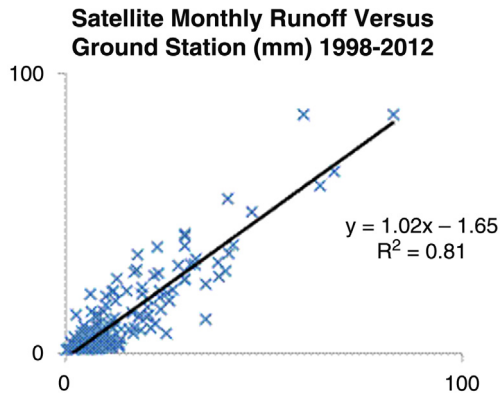

FIGURE 16.8 Satellite observation (*x*-axis) of Trinity River monthly runoff (mm) at River Watch site #460, compared to runoff (*y*-axis, mm) measured at the local gauging station.

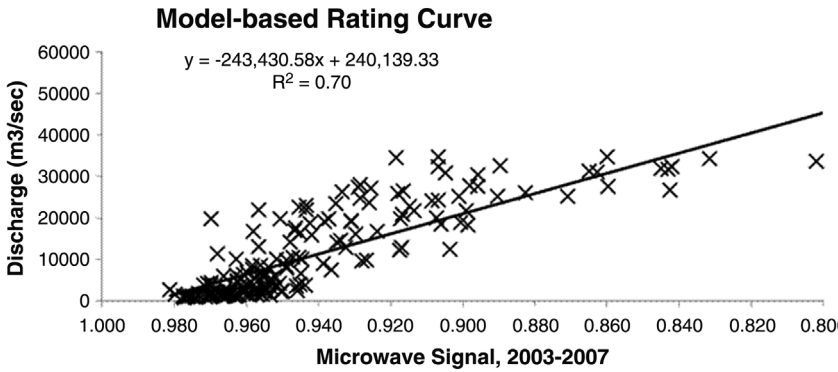

FIGURE 16.9 Scatter plot comparing WBM-modeled daily discharge over a 5-year period (January–December monthly daily maximum, minimum, and mean discharges) to the remote sensing for River Watch site #30 along the Ayeyarwady River, Myanmar. Although a better curve could be fit to these data, a straight line is a useful first-approximation rating equation. Some of the scatter is likely due to model errors.

necessarily represent errors in microwave signal or limits to the accuracy of the method, but instead is induced by model errors, including due to man-made structures (dams, levees, etc.) unaccounted in the model. This is the case for a number of rivers monitored by *in situ* gauging stations in the United States (Fig. 16.7).

We have obtained hundreds of rating curves, globally, similar to that in Fig. 16.9; but more work remains in order to improve the results: (1) the straight line rating illustrated in Fig. 16.9 is a simplistic fit to the data, (2) the amount of scatter appears to decrease with increasing discharge, and (3) attempts to calculate a daily confidence interval or error limits for daily values must thus consider that these will vary for low flow and high flow states (Figs. 16.8 and 16.9).

5 River Watch data processing

Data from River Watch version 3 and higher (Fig. 16.11) are available online, derived from the NASA/Japanese Space Agency Advanced Scanning Microwave Radiometer AMSR-E Ka-band at 36.5 GHz, the NASA/Japanese Space Agency TRMM Ka-band 37 GHz channel, and 37 GHz information from the AMSR-2 and GPM sensors. The discharge estimator (the remote sensing signal) is the ratio of the daily calibrating value ("C") that represent the 95th percentile of the day's driest (brightest) emissivity within a 9 pixel × 9 pixel array surrounding the site, and "M," the emissivity from a measurement pixel centered over the river and its floodplain. The 95th percentile is used instead of the hottest pixel to exclude outliers due to measurement noise. Explanation of why this ratio, instead of simply the M pixel radiance value, is used is below.

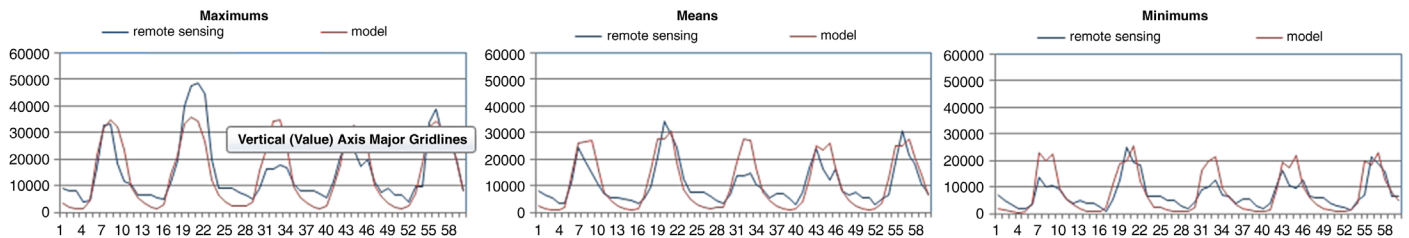

FIGURE 16.10 Same data as in Fig. 16.9 arranged as 5 year time series of maximum (left) mean (middle), and minimum (right) discharge values. The *red line* shows the model results and the *blue line* is the remote sensing transformed by the rating equation in Fig. 16.9.

Passive microwave signatures measured by a radiometer over a target area are related to the product ($T \times e_H$) of the physical temperature T and surface emissivity e_H for the horizontal polarization H (Brakenridge et al., 2012; Nghiem et al., 2012). Thus, the signatures at both the calibration target C and the measurement target M vary with the land surface temperature that drives the seasonal rhythm of the landscape. Unlike the polarization ratio or gradient ratio traditionally used in passive microwave remote sensing, the C/M ratio approximately cancels out the physical temperature while maintaining a high sensitivity to the surface water change conveyed in the measurement pixel emissivity (Brakenridge et al., 2007).

The sites within reach of TRMM (between 50° N and S) begin in January 1998; they add AMSR-E data when such became available in mid-2002 (the data are merged); continue using TRMM-only during the AMSR hiatus in 2012 and early 2013 (between AMSR-E and AMSR-2); and then extend to today using merged AMSR-2 and GPM. The record at higher latitude sites begins in mid-2002 (following launch of AMSR-E), and there is a gap in 2012–2013 between the termination of AMSR-E and initiation of AMSR-2 because no data was collected at these locations for this interval (Fig. 16.12). The gridding algorithm to produce the global daily images is accomplished at the JRC; the original data are near real time swath information from each sensor. A JRC Technical Report provides further information (De Groeve et al., 2015).

JRC produces a daily global grid at 10 km (near the equator) pixel resolution and provides daily ratio data for fixed pixels within that 4000 × 2000 pixel grid. Where data from more than one sensor are available, the merged gridded product uses all (De Groeve et al., 2015). At lower latitudes, the coverage is less than daily from AMSR-E and AMSR-2: River Watch Version 3.4 uses a forward moving 4-day running mean to avoid such data gaps and because river discharge exhibits strong temporal autocorrelation.

At the Flood Observatory (see link in Fig. 16.11), the ratio data from the JRC are ingested once each day, and the html displays for each site are updated and added to the Observatory web site at 14:30 local time in Denver, Colorado, United States. Each site outputs two html pages: one providing plots of the results but also some tabular data, the second, "data" html provides the rating curve and access to the complete record of satellite-measured discharge. For comparison purposes, a reference 20th percentile of the measured discharge for each day of the year, 2000–2010 is also calculated and provides a useful seasonally-adjusted low flow threshold. See individual site plots and data accessible from the (Fig. 16.11) online portal.

The River Watch approach to measuring river discharge is novel in that microwave sensors designed to monitor other aspects of the hydrologic cycle are here employed to measure river discharge changes and watershed runoff on the ground. Thus, in order to observe atmospheric conditions, such as precipitation, ground-sensing channels were included on AMSR, TRMM, and now GPM: these provide the background component of upwelling microwave radiation

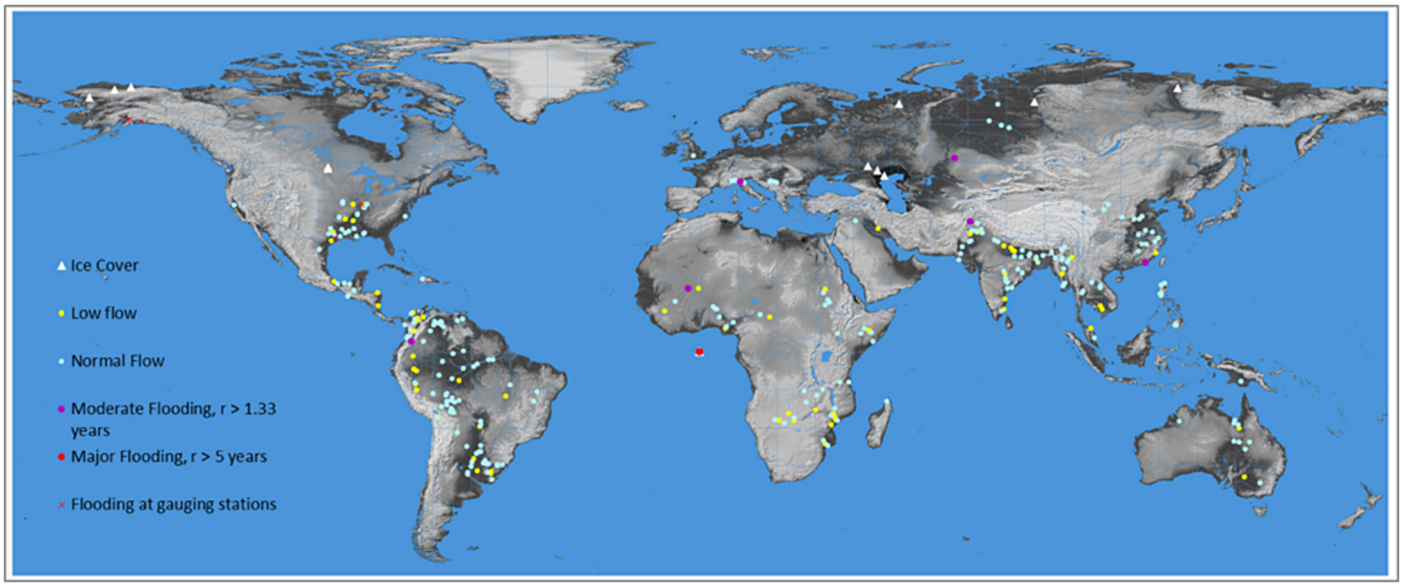

FIGURE 16.11 Status of River Watch version 3 online satellite gauging sites. *Yellow dots* for low flow, *blue dots* for normal flow, and *purple* (recurrence interval >1.5 y) and *red* (recurrence interval > 5 y) dots for moderate and severe flooding. Display is updated daily (Status: August 15, 2020). (https://floodobservatory.colorado.edu/DischargeAccess.html).

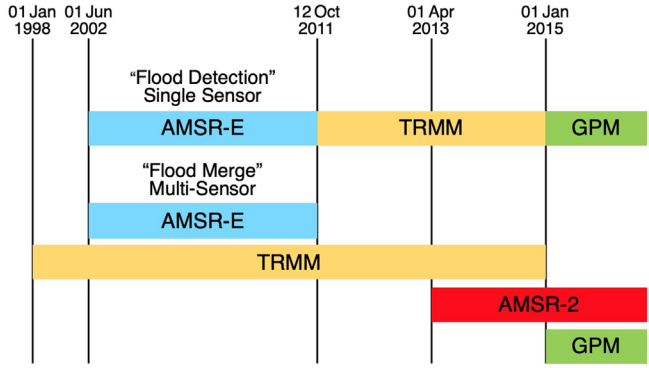

FIGURE 16.12 Temporal coverage, 1998 to present, of passive microwave sensors built and operated by NASA and by JAXA (Japanese Space Agency). Each satellite provides daily or near-daily imaging. *(From De Groeve et al., 2015.)*

against which precipitation can be observed via other microwave frequencies. River Watch uses the Ka-band channel to alleviate severe atmospheric effects compared to higher-frequency data while retaining a better spatial resolution compared to lower-frequency data.

6 Discharge measurement accuracy

Several studies examine the impact of various ground characteristics on the accuracy of this microwave radiometry approach (Revilla-Romero et al., 2014, 2015). As would be expected, there are locations where the method does not work well: (1) narrow straight, steep-gradient rivers where flow area expansion accommodates much less discharge variability than does velocity and depth, (2) channels with artificial levees that constrain all but rare floods from expanding onto the floodplain, (3) rivers with heavily vegetated floodplains where tree canopies obscure the signal variation as flow area expands, (4) ice-covered rivers, when ice cover is present (see next section), and (5) rivers in humid climate zones like tropical, subtropical, or monsoon climate where the potentially high atmospheric water vapor affects the flow observation quality. However, coupled with these constraints is the advantage that even small rivers (especially meandering rivers) can be reliably monitored, provided that the gauging site chosen allows for flow expansion into channel/lower floodplain features. These include in-channel and side-channel bars, point bars (Fig. 16.5), small tributary mouths, and negative floodplain relief (Lewin and Ashworth, 2014). Braided rivers can also be measured through this approach, as these rivers strongly respond to discharge changes though flow area expansions and contractions. Also, rivers with steep banks and large channels that contain sandbars and islands can be effectively monitored as flow rises and these features are submerged, even while *in situ* gauging methods may become inaccurate due to complex in-channel bathymetry and topography that changes. Channel cross-sectional area at a gauging

TABLE 16.1 Sample of microwave discharge (River Watch) measurement statistics at different sites along the Chindwin (108 and 23) and Ayeyarwady (26, 29, 30) rivers in Myanmar.

Site	S/M	Range[a]	Range[b]	S/N	r^2
108	VG	0.11	21	G	0.66
23	G	0.08	26	F	0.57
26	VG	0.09	17	F	0.67
29	G	0.12	36	F	0.57
30	VG	0.20	35	VG	0.70

Sites with high r^2 signal/model, "S/M" coefficient values suggest that both remote sensing and modeling are correlated and tracking actual discharge changes. Sites with larger signal range ([a]) and signal to noise (S/N) produce more stable daily values with smaller daily errors. Range[b] are discharge ranges between maximums and minimums observed in 10^3 m^3/s. F, G, VG, and E criteria are described in text.

station is subject to excavation and aggradation even within a flood event; these local changes are expected to have a less severe effect on rating curves when, instead, a 10-km long parcel of river and floodplain is used to monitor discharge passing through the reach.

The combined remote sensing and model output also allow assessments of the signal/noise characteristics and the model/remote sensing agreement exhibited by each gauging site (Table 16.1). As for *in situ* gauging stations, there is no expectation that each site records discharge changes with equal precision and accuracy. The *signal range* statistic records the total measured variability of the satellite discharge-estimator signal; larger values indicate that the remote sensing signal is more sensitive to discharge variation. The *noise* statistic refers to the average signal variability, day to day: larger values indicate more non-hydrologic noise as even small rivers commonly do not vary greatly, *on the average*, between sequential days. Also, comparison to the model results provides useful information aside from the rating curve: the r^2 values shown in Table 16.1 are the coefficient of determination of the remote sensing for the independent WBM modeling discharge results (over 5 years, 2003–07). If the remote sensing is first calibrated to discharge values by the rating equation, these values are identical to those calculated via the N-S equation (Nash and Sutcliffe, 1970).

The N-S statistic is often used to measure the predictive strength of hydrological models for actual measured discharge. In the present case, these values, for the global River Watch array, evaluate the predictive strength of the remote sensing as compared to the WBM global model results. This method commonly produces N-S values from 0.60 to 0.85. Also, as shown in Fig. 16.6, N-S and least squares coefficients of determination are sometimes much higher when the remote sensing is compared to *in situ* measured discharge rather than modeled discharge: the modeling is less accurate than the remote sensing.

These descriptive statistics allow useful summary assessments of relative measurement site utility. Thus, a somewhat arbitrary but still meaningful ranking of how the gauging sites perform as compared to the model runs is as follows: $r^2 > 0.8$, Excellent; >0.7, Very Good; >0.6, Good; >0.44, Fair; <0.44, Poor. Also, the S/N for all sites in the array can be assigned a ranking, as follows: >20, Excellent; >15, Very Good; >10, Good; >5, Fair; <5, Poor. Note that, in some cases, especially along large rivers, the n = 180 model output, such as illustrated in Fig. 16.10, when compared to the equivalent time series of remote sensing signal, is apparently offset by one unit forward or backward in time, suggesting that the model routes the flow too quickly or too slowly to the measurement site. In this case, because the purpose of the modeling is to develop a rating curve, shifting the model output to match the remote sensing is appropriate and greatly improves the N-S and coefficient of determination statistics (e.g., from initial values such as 0.3 to shifted values of 0.7). This situation demonstrates the potential usefulness of the remote sensing information in the calibration of hydrological model water routing formulae and coefficients.

7 Detection of river ice cover and spring flooding

The initiation and removal of river ice cover can also be detected via microwave C/M information and has clear relevance to flooding. Because the permittivity at microwave frequencies changes strongly between the liquid phase (water) and solid phase (ice) (Nghiem et al., 2012; Kong, 2008), the C/M ratio changes from >1 to <1 when a river changes from a liquid to solid remote sensing target, with the river permittivity magnitude switching from being larger to being smaller than that of soil as the river freezes up. This was demonstrated for the Lena and other rivers (Brakenridge et al., 2007; Kugler et al., 2010).

Fig. 16.13 shows, from an earlier version of River Watch, the independent microwave signals obtained from a measurement pixel centered over an Arctic river valley (River Watch site #100158, northern Pechora River, Russia) and from a pixel from adjacent land outside of the river valley. Fig. 16.14 illustrates only the ratio data from the same site, for years 2014 and 2015, as transformed via a WBM-based rating equation and a filter applied to screen the ice-covered intervals. The filter automatically detects the dates in the spring and fall when the C/M data show minimum values, prior to the sharp rise as ice cover dissipates, and also just prior to re-establishment of ice and matching C and M in the fall.

In temporal and spatial detail along river valleys, ice-break up and establishment can be complex. Ice jams may form and temporarily dam flow: producing backwater effects and disturbing the rating equation's validity (but the flooding is directly observed in any case). These processes can be examined in detail using optical sensors such as the NASA Moderate Resolution Imaging Spectroradiometer (MODIS) in clear-sky conditions, but we use such data here to pro-

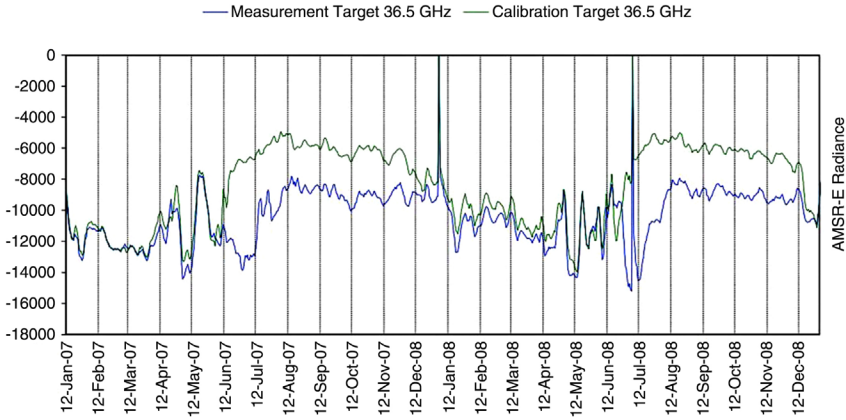

FIGURE 16.13 Brightness temperatures (digitized radiance values, vertical axis) measured by AMSR-2 for 2 years over River Watch site #100158 on the Pechora River, Arctic Russia. The (lower) *blue line*, M, shows data from the measurement pixel, over the river; the *green line*, C, is from a near-by comparison pixel outside of the river valley. Transition to ice-free conditions occurs in latest May/early June (sharp drop in *blue line*); full ice cover is established by late December (the lines diverge, then, as ice cover is established, merge). The C/M ratio provides the discharge signal during the period without ice cover. Early summer high discharge progressively decreases during the mainly dry high Arctic summer.

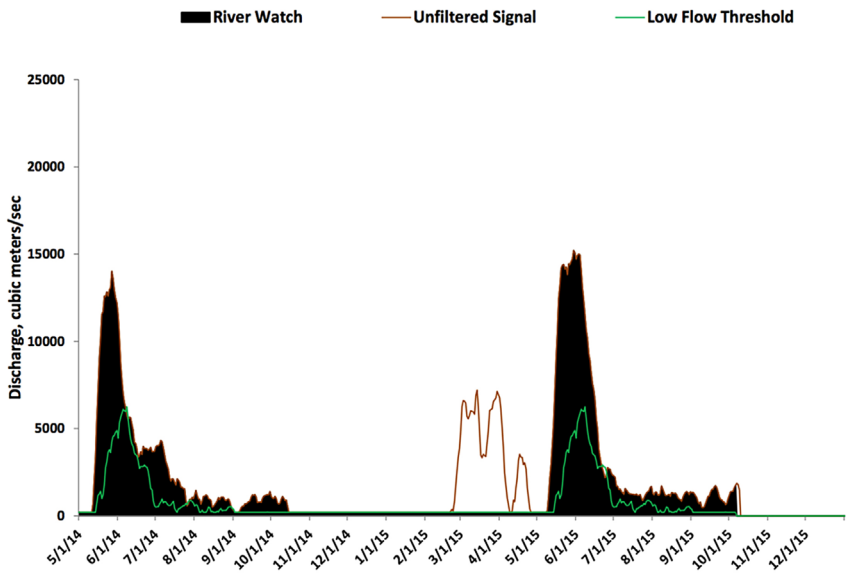

FIGURE 16.14 River Watch output for site #100158 showing two annual hydrographs, and the ratio signal prior to filtering *(brown line)* and after filtering (*brown line* underlain by black shading). Also shown is the 20th percentile discharge for each day used to identify unusually low flow or drought conditions *(green line)*.

vide a sample validation of the microwave results. Shown in Fig. 16.15 are four MODIS scenes over this river reach during the 2014 spring and summer. They can be compared to the microwave signal independently obtained (Fig. 16.14).

River Watch (versions 3.4 to the current 3.8) uses source data processed at the Joint Research Centre that is provided only as C/M ratio information. Thus,

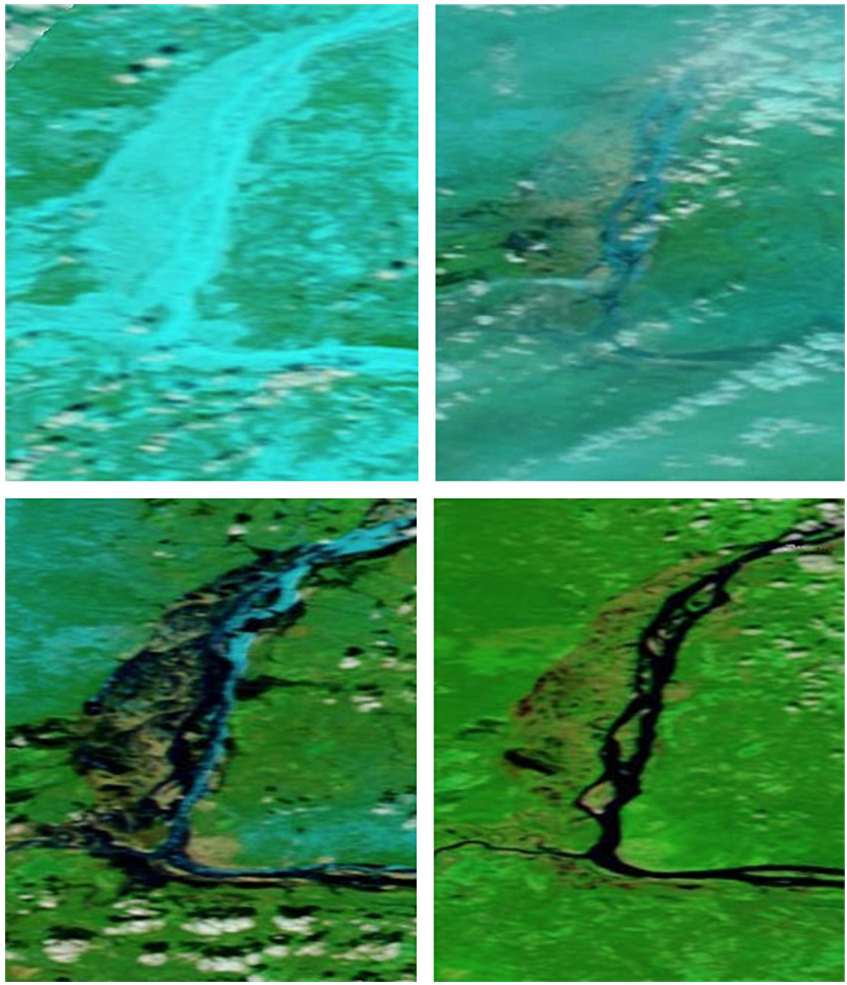

FIGURE 16.15 Four sample scenes from optical (MODIS bands 1,2,7) imaging of the Pechora River location used to provide confirmation of the timing of spring ice-out and the following discharge changes. Compare with Fig. 16.14. Top left: May 4, 2014. Top right: May 14. Bottom left: May 16. Bottom right: June 17. According to these images, ice cover was fully in place still on May 4, but break-up was underway by May 14 (there is significant haze and cloud obscuration in this scene). Already by May 16, the flow area and discharge had greatly expanded: the "spring freshet" was underway. By June 17, the spring flood was declining into the lower discharge values that would prevail for the rest of the summer.

the ice cover filter must detect ice-covered time periods using only the ratios. We locate the transition point in each season by determining the minimum ratio value within spring and autumn; the system then computes discharge values only between the times of these signal minimums. A constant sub-ice flow is estimated for the period of ice cover and from the modeling results. Fig. 16.16 provides the monthly runoff time series at the Pechora River site; Fig. 16.17 shows the annual runoff values and changes in the ice-free season for each year. There is utility in maintaining such observations into the future for attempts to understand and monitor climate change in the Arctic. In this regard, excessive terrestrial heat flux into the Arctic Ocean via river discharge can impact sea ice retreat processes (Yang et al., 2015; Nghiem et al., 2014). As well, the seasonal timing of ice break-up controls spring flooding, and is itself likely to be responsive to climate change.

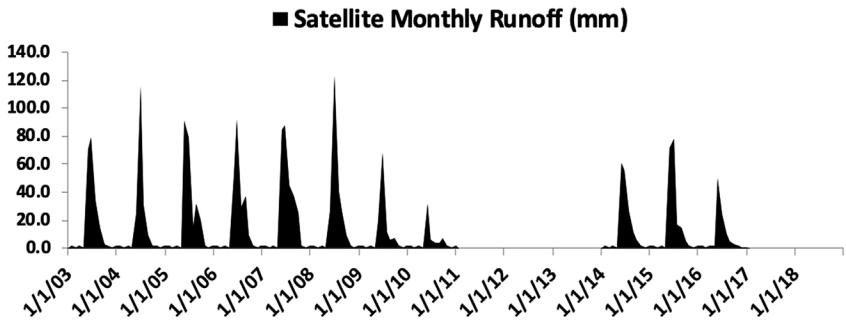

FIGURE 16.16 Monthly runoff for the Pechora River gauging site, showing low runoff amounts for 2010 but higher peak monthly runoff amounts for 2008 instead of 2007 (compare with Fig. 16.17). 2008 had a larger initial spring flood, but high discharge was sustained for a longer period through summer 2007. These data could also be used to determine if unusually long seasons were caused by early ice release, late establishment of ice cover, or both.

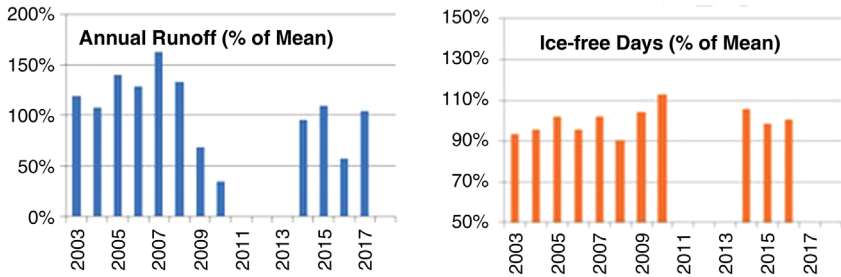

FIGURE 16.17 Total annual runoff at the Pechora River Watch site, upstream watershed area of 247,665 km^2 (left) and number of ice-free days (right), both expressed as percent of the mean. The year 2010 experienced an unusually long ice-free season, and also unusually low annual runoff. The year 2007 had unusually large total annual runoff during an ice-free season of normal length.

The spatial distribution of ice break-up events over Arctic rivers may help to characterize the effects of climate change on continental river ice cover and its duration; it also has implications for flood hazard in many high latitude communities situated along rivers. The lack of *in situ* hydrological measurements in these remote regions in harsh environments makes the use of satellite data a key technique to obtain basic information regarding river flow regime and flood history. Positioning microwave satellite measurement pixels every 50 km along Arctic rivers allows observations of river ice changes not only through time but also geospatially. From upstream to downstream, the melting in spring can thereby be monitored.

For example, and for the River Ob in western Siberia, Russia, Fig. 16.18 shows that the timing of the ice break up is not gradually changing from earlier dates at upstream (lower latitude) to later dates downstream (higher latitude). In 2004, regions on higher latitude were affected by above average temperatures in spring. For this reason, sites between 62° and 65° N were observed to have earlier ice melting during the spring. Thus, close monitoring of Arctic rivers enables an identification of locations where floating ice may accumulate and pose a threat of severe ice-jam flooding (e.g., on the River Tom, a tributary of the Ob River Zemtsov et al., 2014).

The location of river control structures can also change the timing of river ice melting in spring or freezing in late autumn or winter. This is the case above

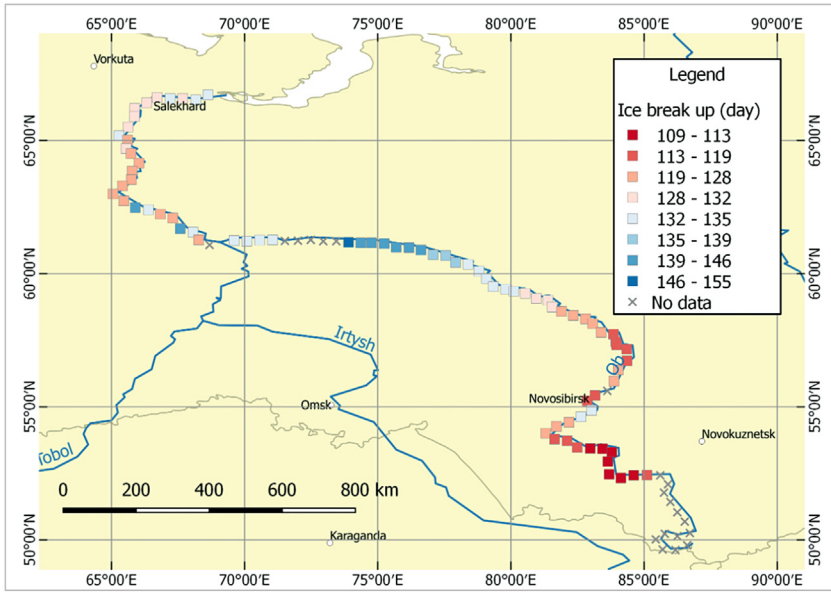

FIGURE 16.18 Ice break up times in 2004 derived from AMSR-E observations set every 50 km along the Ob River, Russia. Ice break-up times do not gradually vary from upstream to downstream.

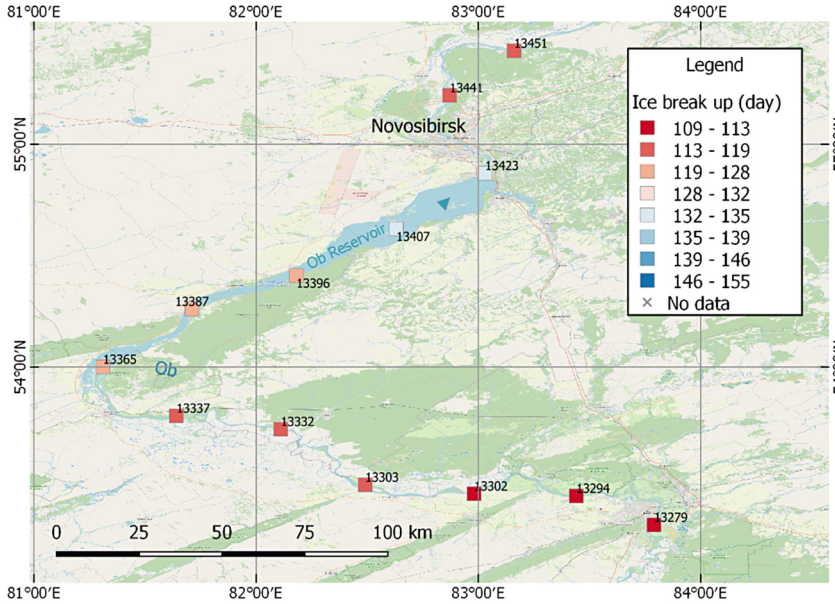

FIGURE 16.19 Ice break up times derived from AMSR-E observations over the Novosibirsk Reservoir (Ob River), Russia in 2004. Ice break up times shift to later dates near the dam (Sites 13423, 13407) in the wider and deeper waterbody of the Ob Reservoir compared to the narrower upstream parts (Sites 13396 to 13365).

Novosibirsk on the River Ob where the 200-km long, ~17-km wide Novosibirsk Reservoir (often called Ob Sea) alters the duration of ice-free periods. In the year 2004 and also in subsequent years, AMSR-E observed a delayed melting of the ice cover at the upstream end of the reservoir nearer to the dam (Fig. 16.19). This delay is due to wider and deeper bathymetry of the upstream part of the reservoir. AMSR-E observations confirm the results of hydrothermal simulation which outputs seasonal water temperature conditions in the reservoir (Kravtchenko et al., 2019). The temperature distribution in May shows a more intense melting of the ice in the shallower upstream part in the south and a later warming of the deeper part of the reservoir in the north.

8 Summary and conclusion

Passive microwave radiometry has a surprising power to monitor river discharge changes at an appropriate temporal sampling interval and with considerable accuracy over multiple decades and continuing into the future. This capability was unanticipated as the TMI, AMSR-E, AMSR-2, and GMI sensors aboard TRMM, AQUA, GCOM-W, and GPM satellites, respectively, were being designed. Yet such measurements are crucial to understanding the magnitudes of river floods, and to improving the estimation of future flood risk. Also, because

of the continued maintenance of the pre-1998 Ka-band microwave records in data archives, and new processing techniques, the way is open for extending consistent river discharge and watershed runoff observational records back in time by at least another decade (Paget et al., 2016). The demonstrated capability can be incorporated into future missions, such as the Copernicus Imaging Microwave Radiometer (CIMR) with radiometers from L to Ka bands providing observations out to 2040. As is the case also for precipitation observations, the identification of floods (anomalies) along rivers requires a long time series, so that unusual events can be distinguished from normal seasonal variability. The orbital microwave sensors are ideally configured to provide such, and also because high spatial resolution is not essential and cloud cover interference is relatively small.

This chapter notes several areas where current methodology is less than ideal, and more sophisticated methods of analysis could be employed. For example, signal to discharge rating curves are empirical in character, and could instead be created via adaptive regression methods that allow the derived curves and equations to fit as closely as possible to the constraining data. Also, the discharge values are derived from imperfect global runoff models. Although these have the advantage of being driven from observational precipitation amounts and land surface variables, it would be advantageous to develop a systematic method of comparing space-based to ground-based discharge measurements in order to detect model bias, and allow accurate extension of the ground-based data; even while accurate altimetry measurements from future satellites can be utilized as calibration data. In addition to Ka-band radiometers, satellite L-band radiometers, such as SMOS, SMAP, and the future CIRM, can improve river discharge measurements in the tropics (Nghiem et al., 2019; Kugler et al., 2019).

Finally, the microwave information also has the capability, in many cases, to automatically detect the timing and duration of ice cover over high latitude rivers. The removal of ice cover is an important environmental/ecological variable throughout northern North America and Asia and over the Arctic Ocean, and the existing microwave sensors are sensing this variable. The spring flood can be automatically detected, when and where it occurs. The challenge is to process such data from many more measurement sites, link such to available ground sensors and other orbital data, and thereby provide important new and trusted information regarding Arctic river flow changes. This area of work is ready for rapid progress providing new measurement and analysis capabilities.

Acknowledgments

River Watch is a cooperative project among scientists at the University of Colorado, Boulder, CO, United States; at GDACS-GFDS (Global Disaster Alert Coordination System, Global Flood Detection System), European Commission Joint Research Centre, Ispra, Italy; at the University of Alabama; and at the Jet Propulsion Laboratory. G. R. Brakenridge acknowledges grant support from NASA's Earth Sciences and Applied Sciences programs. The research carried out at the Jet Propulsion Laboratory (JPL), California Institute of Technology, by S.V.

Nghiem was supported under a contract with NASA; in particular the work related to Arctic discharge and ice cover was supported by the NASA Cryosphere Science Program and the work related to river stage and discharge was supported by the NASA Terrestrial Hydrology Program. The work carried out at the Budapest University of Technology and Economics in Hungary was supported by the "TKP2020, Institutional Excellence Program" of the National Research, Development and Innovation Office in the field of Water Sciences & Disaster Prevention (BME IE-VIZ TKP2020).

References

Alsdorf, D., Lettenmaier, D., Vorosmarty, C.J., 2003. The need for global, satellite-based observations of terrestrial surface waters. EOS, Trans. Am. Geophys. Union 84, 274–276.

Brakenridge, G.R., 2018. Flood risk mapping from orbital remote sensing. In: Schumann, G.J.-P. (Ed.), Global Flood Hazard: Applications in Modeling, Mapping and forecasting. AGU Monograph Series. John Wiley & Sons.

Brakenridge, G.R., Anderson, E., Nghiem, S.V., Chien, S., 2005. Space-based measurement of river runoff. EOS, Trans. Am. Geophys. Union, 86.

Brakenridge, G.R., Cohen, S., Kettner, A.J., De Groeve, T., Nghiem, S.V., Syvitski, J.P.M., Fekete, B.M., 2012. Calibration of orbital microwave measurements of river discharge using a global hydrology model. J. Hydrol. 475, 123–136, http://dx.doi.org/10.1016/j.jhydrol.2012.09.035.

Brakenridge, G.R., Nghiem, S.V., Anderson, E., Mic, R., 2007. Orbital microwave measurement of river discharge and ice status. Water Resour. Res. 43, 1–16.

Brakenridge, G.R., Syvitski, J.P.M., Niebuhr, E., Overeem, I., Higgins, S.A., Kettner, A.J., Prades, L., 2016. Design with nature: causation and avoidance of catastrophic floods in Myanmar. Earth Sci. Rev. 165, 81–109.

Cohen, S., Kettner, A.J., Syvitski, J.P.M., 2011. WBMsed: a distributed global-scale riverine sediment flux model - model description and validation. Comp. Geosci. 50, 80–93. doi: 10.1016/j.cageo.2011.08.011.

De Groeve, T., Brakenridge, G.R., Paris, S., 2015. Global Flood Detection System Data Product Specifications. Publications Office of the European Union.

Famiglietti, J.S., Cazenave, A., Eicker, A., Reager, J.T., Rodell, M., Velicogna, I., 2015. Satellites provide the big picture. Science 349, 684–685.

Fekete, B.M., Pisacane, G., Wisser, D., 2016. Crystal balls into the future: are global circulation and water balance models ready? Proc. IAHS 374, 41–51.

Fekete, B.M., Robarts, R.D., Kumagi, M., Nachtnebel, H.-P., Odada, E., Zhulidov, A.V., 2015. Time for in situ renaissance. Science 349, 685–686.

Fekete, B.M., Vorosmarty, C.J., 2007. The current status of global river discharge monitoring and potential new technologies complementing traditional discharge measurements. IAHS Publications, 309, Proceedings of the PUB Kick-off meeting held in Brasilia.

GRDC, 2010. https://www.bafg.de/GRDC/EN/Home/homepage_node.html.

KONG, J.A., 2008. Electromagnetic Wave Theory. EMW Publishing, Cambridge, Massachusetts.

Kugler, Z., Brakenridge, G.R., De Groeve, T. 2010. Microwave satellite data to quantify effects of global climate change on arctic rivers. SPIE Proceedings Volume 7825, Remote Sensing of the Ocean, Sea Ice, and Large Water Regions 2010, 782508(2010), https://doi.org/10.1117/12.866021.

Kravtchenko, V.V., Golubeva, E.N., Tskhai, A.A., Tarhanova, M.A., Kraineva, M.V., Platov, G.A., 2019. The Novosibirsk reservoir hydrothermalregime model. Bull. Nov. Comp. Center, Num. Model. Atmosph. 17, 31–49.

Kugler, Z., Nghiem, S.V., Brakenridge, G.R., 2019. L-Band passive microwave data from SMOS for river gauging observations. Remote Sens. 11, 835.

Lewin, J., Ashworth, P.J., 2014. The negative relief of large river floodplains. Earth Sci. Rev. 129, 1–23.

Nash, J.E., Sutcliffe, J.V., 1970. River flow forecasting through conceptual models part I—A discussion of principles. J. Hydrol. 10, 282–290.

Nghiem, S.V., Hall, D.K., Rigor, I.G., Li, P., Neumann, G., 2014. Effects of Mackenzie River discharge and bathymetry on sea ice in the Beaufort Sea *Geophys*. Res. Lett., 41. doi: 10.1002/2013GL058956.

Nghiem, S.V., Kugler, Z., Brakenridge, G.R., 2019. River Gauging with SMAP, SMOS, AMSR-2, and Jason-2 Satellite Data. Abstract for American Geophysical Union Fall Meeting.

Nghiem, S.V., Wardlow, D.B., Allured, D., Svoboda, M.D., Lecomte, D., Rosencrans, D., Chan, K.S., Neumann, G., 2012. Microwave remote sensing of soil moisture–Science and applications, Chapter 9, part III. Remote Sensing of Drought–Innovative Monitoring Approaches. Taylor and Francis.

Paget, A.C., Brodzik, M.J., Long, D.G., Hardman, M.A., 2016. Bringing Earth's microwave maps into sharper focus. EOS, 97.

Pavelsky, T., Durant, M.T., Andreadis, K.M., Beighley, R.E., Paiva, R.C.D., Allen, G.H., Miller, Z.F., 2014. Assessing the potential global extent of SWOT river discharge observations. J. Hydrol. 519, 1516–1525.

Pekel, J.-F., Cottam, A.N.G., Belward, A.S., 2016. High-resolution mapping of global surface water and its long-term changes. Nature, 20584.

Revilla-Romero, B., Feyera, A.H., Thielen-Del Pozo, J., Salamon, P., Brakenridge, G.R., Pappenberger, F., De Groeve, T., 2015. On the use of global flood forecasts and satellite-derived inundation maps for flood monitoring in data-sparse regions. Remote Sens. 7, 15702–15728.

Revilla-Romero, B., Thielen, J., Salamon, P., De Groeve, T., Brakenridge, G.R., 2014. Evaluation of the satellite-based Global Flood Detection System for measuring river discharge: influence of local factors. Hydrol. Earth Syst. Sci. 18, 4467–4484.

Shiklomanov, A.I., Lammers, R.B., Vorosmarty, C.J., 2002. Widespread decline in hydrological monitoring threatens pan-Arctic research. AGU Eos Trans. 83, 16–17.

Van Dijk, A.I.J.M., Brakenridge, G.R., Kettner, A.J., Beck, J.E., 2016. River gauging at global scale using optical and passive microwave remote sensing. Water Resour. Res., 52.

Yang, D., Shi, X., Marsh, P., 2015. Variability and extreme of Mackenzie River daily discharge during 1973-2011. Quat. Int. 380–381, 159–168.

Zemtsov, V.A., Vershinin, D.A., Inishev, N.G., 2014. Imitation modeling of ice dams (case study of Tom' River, Western Siberia). Ice and Snow 54 (3), 59–68, 10.15356/2076-6734-2014-3-59-68.

Index

Note: Page numbers followed by “f” indicate figures, “t” indicate tables.

D

E

F

G

H

I

N

O

P

Q

R

S

T

U

V

W

Z

EARTH OBSERVATION FOR FLOOD APPLICATIONS
PROGRESS AND PERSPECTIVES

A volume of the series Earth Observation, edited by George Petropoulos

Earth Observation for Flood Applications: Progress and Perspectives describes the latest scientific advances in Earth Observation. With recent floods around the world becoming ever more devastating, there is a need for better science enabling more effective solutions at a fast pace. This book aims at stretching from the current flood mapping to diverse real data so as to estimate the flood risk and damage. **Earth Observation for Flood Applications: Progress and Perspectives** includes three parts containing each a separate but complementary topic area under floods. Each chapter unfolds various applications, case studies, and illustrative graphics. In terms of flood mapping and monitoring, the usage of multi-sensor satellite data, web-services information, microwave remote sensing methods are discussed in depth. So, this book is a valuable resource for scientists, researchers, and students in the area of earth observation.

- Focuses in on one specific application field of Earth Observation
- Brings the latest scientific advances and perspectives from experts around the world
- Includes extensive figures, tables, and case studies to illustrate real-life applications

About the Editor

Guy J-P. Schumann

Dr. Guy Schumann is the founder and a principal scientist at RSS-Hydro. Dr. Schumann is also a Research Fellow at Geographical Sciences, University of Bristol and an affiliate at the Dartmouth Flood Observatory (DFO), INSTAAR at the University of Colorado Boulder, CO. He received both the MSc (Remote Sensing) and PhD (Geography) degrees from the University of Dundee (United Kingdom) in 2005 and 2008, respectively. Dr. Schumann has more than 15 years of experience in the field of remote sensing data integration with hydrodynamic modeling and particularly radar remote sensing and its use in flood models. Dr. Schumann has over 150 publications, including papers, book chapters, and edited books. Most of his current work and projects focusing on simulating river hydrodynamics and floodplain inundation and integration with remote sensing. Dr. Schumann is also involved in the Interoperability Program activities of the Open Geospatial Consortium (OGC).

COVER IMAGE: ©USGS / NASA EARTH OBSERVATORY

ELSEVIER elsevier.com/books-and-journals

ISBN 978-0-12-819412-6

9 780128 194126